DEVELOPMENT OF AN EXPANDED POLYSTYRENE GEOFOAM COVER SYSTEM FOR PIPELINES AT FAULT CROSSINGS

by

Bret Nils Lingwall

A dissertation submitted to the faculty of
The University of Utah
in partial fulfillment of the requirements for the degree of

Doctor of Philosophy

Department of Civil and Environmental Engineering

The University of Utah

May 2011

The University of Utah Graduate School

STATEMENT OF DISSERTATION APPROVAL

The dissertation of **Bret Nils Lingwall**

has been approved by the following supervisory committee members:

Steven F. Bartlett	, Chair	**12-20-2009** Date Approved
Aurelian Trandafir	, Member	**12-20-2009** Date Approved
Chris Pantelides	, Member	**12-20-2009** Date Approved
Evert Lawton	, Member	**12-20-2009** Date Approved
Pedro Romero	, Member	**12-20-2009** Date Approved

and by **Paul J. Tikalsky**, Chair of the Department of **Civil and Environmental Engineering**

and by Charles A. Wight, Dean of The Graduate School.

ABSTRACT

Questar Corporation commissioned and funded this research, in partnership with the University of Utah and Bechtel Corporation, to develop methods of protecting steel natural gas pipelines crossing zones of permanent ground deformation. The goal of this research was the development and testing of an Expanded Polystyrene (EPS) Geofoam cover system for such pipelines across active faults or areas of permanent ground deformation (e.g., landslides, permafrost thaw, liquefaction-induced lateral spread). The goal of an EPS Geofoam cover system atop a buried pipeline is to reduce the lateral, longitudinal and vertical forces induced on the pipe as the surrounding ground undergoes permanent deformation. The properties of EPS Geofoam have distinct advantages that lead to improved pipe performance during large ground deformation. The most important of these are its low unit weight and relatively high compressibility. These advantages are the primary focus of this research. Further, the interaction of a pipe and EPS Geofoam was explored and analyzed in a loading case where the pipe was pushed directly into the EPS. In addition to laboratory-scale tests, full-scale tests were conducted with vertical and horizontal plane strain movement of pipe interacting with EPS Geofoam cover systems. Subsequently, numerical modeling was done of the field tests to further evaluate the use of an EPS cover system for applications experiencing large, permanent deformation. The results of the research program have shown that EPS Geofoam can be used as a cover system for steel pipelines crossings at active normal faults, or for other

types of permanent ground deformation where the expected offset is predominately vertical.

TABLE OF CONTENTS

Appendices

LIST OF SYMBOLS

Symbol	Definition
a	Constant
a*	Constant Adjusted for Strain Rate
b	Constant
b*	Constant Adjusted for Strain Rate
c	Constant
c*	Constant Adjusted for Strain Rate
C	Apparent Cohesion of Soil or Geomaterial (F/L^2)
C'	Effective Cohesion of Soil or Geomaterial (F/L^2)
D	Diameter (L), Damping Ratio (dim)
D_{10}	Particle Size of 10% Passing (L)
D_{50}	Particle Size of 50% Passing (L)
D_{60}	Particle Size of 60% Passing (L)
d	Constant
d*	Constant Adjusted for Strain Rate
E	Young's Modulus (F/L^2)
E_{it}	Initial Tangent Young's Modulus (F/L^2)
E_r	Reloading Young's Modulus (F/L^2)
E_t	Tangent Young's Modulus (F/L^2)

E_u	Unloading Young's Modulus (F/L^2)
E_{ys}	Secant Young's Modulus at Yield Stress (F/L^2)
F	Force (F)
F_{max}	Maximum Force (F)
G	Shear Modulus (F/L^2)
G_o	Initial or Maximum Shear Modulus (F/L^2)
H	Height, Pipe Burial Depth (L)
I	Moment of Inertia (L^4)
K	Bulk Modulus (F/L^2)
K_i	Initial Bulk Modulus (F/L^2)
K_o	Coefficient of Lateral Earth Pressure (dim)
k_h	Horizontal Stiffness (F/L)
k_n	Normal Coupling Stiffness (F/L)
k_s	Shear Coupling Stiffness (F/L)
k_v	Vertical Uplift Stiffness (F/L)
L	Length (L)
M	Moment (FL)
M_{max}	Maximum Moment (FL)
m	Strain Rate Exponent (dim)
N	Number of Cycles
N_h	Horizontal Normalized Force (dim)
N_v	Vertical Normalized Force (dim)
P_N	Peak Number (dim)

Pu	Uplift Factor (dim)
R_c	Radius of Curvature (L)
R_o	Ratio of Tensile to Compressive Strengths (dim)
S_u	Undrained Shear Strength (F/L^2)
T	Temperature (deg), Tensile Strength (F/L^2)
t	Pipe Wall Thickness (L)
W	Weight (F)
z_u	Dimensionless Displacement (dim)
ε	Strain (dim)
ε_a	Axial Strain (dim)
ε_b	Bending Strain (dim)
ε_p	Plastic Strain (dim)
ε_v	Vertical Strain (dim)
ε_{ys}	Strain at the Yield Stress (dim)
f	Frequency (1/t)
δ	Displacement (L)
δ_h	Horizontal Displacement (L)
δ_{max}	Maximum Displacement (L)
δ_v	Vertical Displacement (L)
ϕ	Friction Angle of Soil or Geomaterial (deg)
ϕ'	Effective Friction Angle of Soil or Geomaterial (deg)
ϕ'_{cs}	Critical State Friction Angle of Soil or Geomaterial (deg)
ϕ'_{pk}	Peak Friction Angle of Soil or Geomaterial (deg)

γ	Unit Weight (F/L^3)
γ_c	Cyclic Shear Strain (dim)
γ_f	Final Soil Unit Weight after Shear (F/L^3)
γ_o	Initial Soil Unit Weight before Shear (F/L^3)
ν	Poisson's Ratio
π	PI
ρ	Density (M/L^3)
σ	Stress (F/L^2)
σ_a	Axial Stress (F/L^2)
σ_d	Deviator Stress (F/L^2)
σ_r	Radial Stress (F/L^2)
σ_t	Tensile Stress (F/L^2)
σ_y	Yield Stress (F/L^2)
σ_1	Major Principle Stress (F/L^2)
σ_{1f}	Major Principle Stress at Failure (F/L^2)
$\sigma_{1\%}$	Stress at 1% Strain (F/L^2)
$\sigma_{5\%}$	Stress at 5% Strain (F/L^2)
$\sigma_{10\%}$	Stress at 10% Strain (F/L^2)
$\sigma_{15\%}$	Stress at 15% Strain (F/L^2)
σ_3	Minor Principle Stress (F/L^2)
σ'_c	Effective Confining Stress (F/L^2)
σ'_{df}	Effective Deviator Stress at Failure (F/L^2)

σ'_h	Horizontal Effective Stress (F/L^2)
σ'_v	Vertical Effective Stress (F/L^2)
ψ	Dilation Angle (deg)

ACKNOWLEDGEMENTS

I wish to thank Questar Gas Company and Bechtel Corporation for funding this research and collaborating on some of the topics, especially the lateral loading tests. I wish to thank ACH Foam Products for their gracious donation of the EPS Geofoam used in my experiments. I thank my committee members for their guidance, review and suggestions for improvement of this document. Further, I note that Dr. Aurel Trandafir assisted greatly in testing of Geofoam cylinders and blocks and development of the large strain characteristics of EPS Geofoam, as well as conducting all the cyclic triaxial tests and reducing that data. Timothy Mitchell assisted in the pipe interaction experiments and modeling, and without the help of Byron Foster, the full-scale uplift and lateral load tests would not have been possible. Finally, I thank my wife Dureece who has been supportive throughout.

INTRODUCTION

This research was funded by a research contract with Questar Corporation of Salt Lake City, Utah and a Research Technical Grant from Bechtel Corporation of San Francisco, California. The impetus for this research originates from conversations between Mr. Peter McDonough of Questar Gas Company and Dr. Steven Bartlett of the University of Utah. The laboratory work to explore the concept of using a light-weight cover system was conducted at the University of Utah's Department of Civil and Environmental Engineering in Salt Lake City, Utah. Exploratory numerical modeling was conducted during the summer of 2007 using a grant provided by Questar Gas Company

Subsequently, a more comprehensive research plan was developed for Questar and Bechtel Corporations and a jointly funded project began in the spring of 2008 when laboratory testing commenced. The full-scale tests began in the summer of 2008 and the subsequent analyses and evaluation activities ended in May 31, 2009.

Bechtel Corporation also provided personnel services to model a case of a strike-slip fault using full-scale test results from a series of trench box experiments that were conducted at the University of Utah. The modeling evaluations performed by Bechtel Corporation are not included herein and the conclusions of this report are independent of the efforts of Bechtel Corporation.

All Expanded Polystyrene (EPS) Geofoam used in this research was donated to the University by ACH Foam of Murray, Utah.

This research project had six phases. The first phase was an evaluation of the material properties of Expanded Polystyrene (EPS) Geofoam. The strength, stiffness, large-strain and cyclic behaviors of various EPS Geofoam density were investigated. The second phase was a laboratory-scale experiment that explored the 2D and 3D interactions as a pipe was pushed downward into an EPS block in unconfined axial compression. The third phase consisted of a series of full-scale tests of a buried pipe being pushed laterally by a hydraulic actuator into various thicknesses of EPS Geofoam that had been placed and buried in a steel-walled trench box. This was done to replicate strike-slip faulting or other modes of horizontal ground displacement within the trench. The fourth phase was a series of full-scale field tests that compared the uplift performance of an EPS Geofoam cover system with a traditional backfilled trench. A 890-kN capacity crane was contracted to perform these uplift tests. The fifth phase of this research project was a numerical evaluation of the various laboratory and full-scale tests. The sixth and final stage of the research was an exploration of the effects of an asphalt pavement constructed atop the cover system.

CHAPTER 1

REVIEW OF LITERATURE

Manufacturing of EPS Geofoam

Expanded Polystyrene (EPS) is a manufactured plastic product made by expanding plastic beads in a block mold. In the manufacturing process, small, expandable polystyrene beads (diameters from 0.2 to 3.0 mm) are preheated, which causes expansion of the bead due to the pentane gas found at their core. These expanded spheres (called pre-puff) contain numerous closed cells that have an expanded diameter which is about three to four times greater than the initial bead size. In the second stage, the pre-puff beads are furthered expanded by steam heating in a fixed, steel-walled mold. During this latter heating, the beads are further expanded and coalesced to produce relatively rigid blocks of various sizes (Athanasopoulos, 1999). These blocks can be used as EPS Geofoam for construction applications, or they can be further cut and shaped for various packaging and insulation purposes.

Advantages of EPS

There are two primary advantages that EPS Geofoam has over traditional earthen materials when used for geotechnical applications. The first advantage is the relatively low mass density of EPS, which typically ranges from about 10 to 40 kg/m^3. This

advantage is useful in reducing the vertical and horizontal stresses on buried structures, utilities and compressible soils. The use of light-weight fill reduces the settlements caused by geotechnical construction and its potential damage to adjacent structures and facilities. The first documented use of EPS for light-weight roadway embankment was in Norway in 1975 (Negussey, 2006). Since then, numerous EPS Geofoam construction projects have been carried out, mainly in Japan, Scandinavia and North America. Of importance to the Salt Lake Valley was the light-weight application of EPS Geofoam used for embankment construction atop soft clays during the I-15 Reconstruction Project from 1998 to 2001. In this application, the EPS was used to reduce consolidation settlement in the foundation soils (Bartlett et al., 2000; Farnsworth and Bartlett 2008). The light-weight nature of Geofoam has also been used to reduce soil pressures on buried culverts (Kentucky DOT, 2004) and to decrease static lateral earth pressure against buried walls (Negussey and Sun, 1996). Lastly, EPS Geofoam has been used in the mitigation strategy for landslides and to improve slope stability of embankments (http://Geofoam.syr.edu/GRC_rt23a.asp).

The second advantage of EPS Geofoam is its use as a ‘compressible inclusion’ for systems undergoing static, monotonic and dynamic loadings (Horvath, 2005). Upon stress application, Geofoam is somewhat compressible and controlled compression can be used to reduce earth pressure against buried structures as well as deformation induced by structural loadings. The loadings that cause compression may include static and dynamic lateral earth pressures (Bathurst et al., 2007), swell and frost-heave pressures, settlements of support soils, faulting, liquefaction, landslides and traffic loads (Zou et al., 2000).

Typical Properties and Behavior of Geofoam

Extensive laboratory testing has been done to establish the properties of EPS Geofoam under static load conditions. Many researchers have presented elastic and volumetric material parameters for EPS. In short, typical densities of EPS block that are manufactured in the U.S. range from 10 to 40 kg/m^3. (The density of the manufactured EPS in kg/m^3 is used in naming Geofoam block. For example, EPS19 is the name given to EPS Geofoam that has a nominal density of 19 kg/m^3.) This weight is approximately one% of the density of soil. Because of its extremely light-weight nature and cellular structure, the void ratio of EPS varies from 40 to 100, compared to typical void ratios for soils of 0.5 to 1. However, despite its light-weight and extremely high void ratio, EPS is moderately stiff in the elastic range, and not significantly compressible under typical loads encountered in most field and embankment applications. The Young's modulus from full-block tests on EPS ranges from about 10 MPa for EPS19, and is greater for higher EPS densities (Negussey, 2006) For comparison, typical Young's moduli for saturated clayey soils range from about 5 MPa to 20 MPa (Negussey, 2006).

In addition, when used in roadway applications, EPS Geofoam is often, but not always, protected from overstressing by a capping load distribution slab. This typically consists of a 100 to 152-mm reinforced concrete slab that is poured directly atop the Geofoam. Its function is to distribute the tire loadings over a larger area; hence, overstressing of the Geofoam is avoided. Thus, in roadway applications, the EPS is maintained within the elastic range and no plastic deformation occurs. Also, if elastic behavior is maintained, long-term creep of the EPS is also minimized. For trenches that

cross or underlie roadways, the load distribution slab can either be poured in place, or constructed of prefabricated panels.

The elastic range of EPS is approximately between 0 to 2% compressive axial strain. Beyond this range, Geofoam yields and behaves plastically and the secant modulus remains relatively constant. However, with continued strain, strain hardening occurs. Hazarika (2006) and Horvath (1995) suggest that this occurs at about 60% axial strain in unconfined compression. However, no laboratory test results were published to quantify the EPS behavior at large strains for the applications invisioned by this research.

Many researchers have investigated the shear strength properties of EPS Geofoam since its initial use. The unconfined compressive strength of EPS has been investigated by numerous researchers, which is about 90 to 120 kPa for EPS19 at 10% axial strain. The internal angle of friction, shear strength and shear dilatancy behavior have been investigated by Hazarika (2006), Shelley and Negussey (2000), Negussey (2006), Xenaki and Athanasopoulos (2001) and Chun et al.. (2004). In addition, interface frictional properties for Geofoam-soil and Geofoam-structure interactions have been investigated by Xenaki and Athanasopoulos (2001), Shelley and Negussey (2001), and Negussey (2006). For cyclic loading, Athanasopoulos et al. (1999) have developed shear modulus degradation and damping curves for two commonly-used densities of Geofoam using resonant column testing and cyclic uniaxial compression tests.

Geofoam Use in Buried Applications

The concept of using Geofoam as a “compressible inclusion” between walls or foundation elements and a soil mass was conceptualized about 15 to 20 years ago

(Horvath, 1991, 1995, 1998, 2000, 2005). These publications explore this concept by simple numerical analyses and conceptual models for estimating the developed static earth pressures against buried structures using Geofoam inclusions. In addition, Reeves and Filz (2000) demonstrated that Geofoam-like products reduce compaction induced lateral earth pressures on retaining walls using full-scale tests. They also demonstrated that such products can reduce cyclic lateral pressures caused by thermal expansion and frost expansion on walls. For the dynamic loads, Bathurst and Zarnani (2006, 2007) have used shake table results and numerical modeling to evaluate the effectiveness of EPS in reducing lateral earth pressures behind rigid retaining walls. However, the developed numerical approach was relatively simple in that it treated the reinforced mass of the retaining wall as a rigid block that was allowed to displace horizontally under cyclic loading.

For pavement and subgrade applications, Zou et al. (2000) showed that lateral restraint on EPS Geofoam has little effect on its performance as a pavement sub-base. In fact, they showed that higher deformations were observed in laterally confined blocks than in unconfined blocks under repeated traffic type loading. They also demonstrated the need for a load distribution slab to protect the underlying Geofoam when constructed with an overlying flexible pavement system.

Yoshizaka and Sakanoue (2003) investigated EPS Geofoam as a method to reduce lateral force-displacement relationships for buried pipelines. They found a 33 to 60% reduction in the lateral soil-pipe forces when Geofoam was used as light-weight trench backfill for pipe undergoing horizontal displacement. However, Yoshizaka and Sakanoue (2003) did not place Geofoam in the sidewalls of the trench, but used it as a light-weight

cover to reduce vertical loads. More recently, Choo et al. (2007) explored the use of Geofoam as a cover system for buried steel pipelines subjected to vertical fault offset. They used centrifuge testing of scaled models to show the benefits of EPS as a light-weight material in reducing pipeline stresses undergoing vertical offset. Choo et al. (2007) demonstrated that the light-weight cover application of Geofoam can assist in reduction of pipeline damage, but they did not address the compressible inclusion effects of the Geofoam cover in reducing the stresses.

Summary of Current Design/Evaluation Methods

Except for the scaled-model evaluations of Choo et al., (2007), relatively little research has been done to investigate the effects of vertical offset caused by normal faulting on buried steel pipelines (MCEER, 1999).

However, considerable work has been done for the case of rigid steel pipelines undergoing horizontal offset from strike-slip faults, liquefaction-induced lateral spread and slope failure. Newmark and Hall (1975), Wang and Yeh (1985), and Kennedy et al. (1979) developed solutions for the stresses and strains imposed on a steel pipeline by permanent ground deformations. Their solutions were for horizontal or axial deformation.

For normal fault offset and its impact to pipelines, ASCE TCLLE (1985), MCEER (1999) and ASCE-ALA (2001-2005) recommend using the Newmark and Hall (1975), Kennedy et al. (1979) and Finite Element Method (FEM) approaches for evaluating vertical movements. (ASCE TCLLE, MCEER and ASCE-ALA recommend that finite element method (FEM) and elastic methods are best suited for horizontal movements and are applicable to cases where the pipeline is buried sufficiently deep so as not to reach

ground surface.) In addition, ASCE TCLLE (1984), MCEER (1999) and ASCE-ALA (2005) recommend using Trautmann and O'Rourke (1985) soil-pipe springs.

Despite these advances in evaluating pipelines undergoing horizontal displacement, ASCE TCLLE, MCEER and ASCE-ALA recommend that pipeline crossings of normal faults require further investigation. Essentially no published research has been performed on the evaluation and design of EPS Geofoam as a cover system for controlled (i.e., engineered) pipe uplift during vertical permanent ground deformations. It should be noted that Yoshizaka and Sakanoue (2003) used EPS block as a method of reducing vertical stress and therefore horizontal force-displacement reactions for horizontal PGD, but did not examine the controlled uplift case to mitigate potential pipeline damage.

Recent Advances in Numerical Modeling of Pipe Displacement

Perhaps numerical modeling offers the best method of evaluating complex Geofoam/soil/pipe interactions. The finite element method (FEM) has been used extensively to model horizontal permanent ground deformations and their effects on buried steel pipelines (Takada, 2001 and Desmond et al., 1995). Recently, Karamitros et al. (2007) used the FEM to develop a strike-slip model for pipelines crossing active faults based on the earlier work of Wang and Yeh (1985) and Kennedy (1979).

Trautmann and O'Rourke (1985) demonstrated that lateral and vertical movements of pipes through soil are essentially the same as for flat anchor plates undergoing lateral or vertical movements in soils. Their findings were confirmed by Cheuk et al. (2005). The objective of both Trautmann and O'Rourke and Cheuk et al. was to develop soil-pipe interaction Winkler springs for FEM modeling. The Winkler (1867) spring approach is

based on developing relations that assume the soil and structure will interact as a non-damped uncoupled spring. Soil spring constants are generally dependent upon the sectional configuration and the dimensions of an underground structure, rigidity of soil deposits, direction of loading and boundary conditions (Matsubara and Hoshiya, 2000).

There are several constitutive models that can be implemented in finite element methods (FEM) or finite difference methods (FDM) to simulate the stress-strain behavior of soils (e.g., hyperbolic, bilinear, double-yield, Mohr-Coulomb, etc.). Some of these may be applicable to modeling Geofoam behavior depending on the anticipated strain range of the soil-Geofoam system.

One of the most widely used constitutive models is the 'hyperbolic' model, in which the stress-strain relationship is elastic in the low strain range and nonlinear at higher strains that are less than 25%. Konder (1963) proposed the first hyperbolic model. Subsequently, the hyperbolic nonlinear elastic mathematical model for soil-soil interaction was fully developed by Duncan and Chang (1970) and Duncan et al. (1980). For soil-structure interaction problems, Clough and Duncan (1971) showed that a hyperbolic model could be used to simulate the soil-structure interaction for lateral earth pressures on retaining walls. Gomez et al. (2003) extended the soil-structure interface hyperbolic model past the Clough and Duncan version and demonstrated its reasonableness for soil-structure interaction problems. Duncan and Mokwa (2001) demonstrated that the hyperbolic model accurately predicts the passive earth pressures in numerical model/test comparisons.

For Geofoam applications, the most widely used model is a linear-elastic material, or a bilinear elastic material. For the latter, the initial loading (and unloading) modulus

reaches a yield point after some degree of elastic strain; following this, a secant modulus is used to describe the post-yield behavior, which is a line segment with very small positive slope that represents a slight strain-hardening.

Nonlinear models have been developed to describe the post-yield behavior of EPS by Chun et al. (2004) and Hazarika (2006). These researchers showed the stress-strain relationship is nonlinear elastic and hyperbolic in shape. However, neither of these models is applicable for cases where the axial strains are greater than about 20%. Thus, there are very few constitutive models for Geofoam at very large strain. The very large strain regime of EPC Geofoam behavior shows dramatic strain hardening which typical hyperbolic models cannot describe. The double yield model (Itasca, 2005) and similar compressible models which only roughly approximate the large strain behavior have been used to model Geofoam behavior at large strain (Hazarika, 2006), but this has not been fully validated.

CHAPTER 2

EXPLORATORY WORK

During the summer of 2007, Questar Gas Company requested that the University of Utah evaluate a conceptual EPS Geofoam cover system for a 610-mm steel, natural gas transmission pipeline crossing the Wasatch fault in Salt Lake City, Utah. The Wasatch fault is a normal fault, and the expected fault offset is about 2 m of dip slip (i.e., downward) displacement. The fault rupture is expected to produce a M7.0 to 7.5 earthquake in the Salt Lake Valley. For additional information beyond that presented in this report, see Lingwall and Bartlett (2007). This exploratory modeling was done as "proof-of-concept," and is refined in later chapters of this dissertation using the laboratory and field experimental data that are presented subsequently. This work had no verification to testing or case histories. The purpose of the dissertation was to provide the verification and validation to the numerical modeling concept.

Geofoam Properties Used in Numerical Modeling

A series of numerical simulations were performed using the general finite difference method (FDM) computer program named Fast Lagrangian Analysis of Continua 2D (FLAC 2D) (Itasca, 2005). Each material within FLAC was modeled as a Mohr-

Coulomb material, which treats the material as elastic for states of stress below the yield surface and as plastic for states of stress above the yield surface.

The EPS properties most important for the numerical modeling are the density, stiffness and compressive strength (Table 1). Typically, the density of EPS Geofoam ranges from about 10 to 40 kg/m^3; however, for roadway applications (i.e., where the trench crosses or is under a roadway) EPS19, or higher densities, is recommended based on the work performed on the I-15 Reconstruction Project (Bartlett et al. 2000). The minimum density specified by the Utah Department of Transportation standard drawings for EPS Geofoam placed under pavement systems is EPS19. Thus, EPS19 properties were used in the models developed in this section.

Table 1. Material properties used in exploratory modeling

Material	γ	E	ν	ϕ'	c'	ψ
----------	*kN/m3*	*MPa*	----------	*deg*	*kPa*	*deg*
Asphalt Pavement	145	3450	0.40	0	14500	0
UTBC	140	75	0.35	42	0	6
Load Distribution Slab	150	9570	0.20	0	29000	0
Bedding Sand	125	38	0.35	35	0	6
Native Sand	135	41	0.35	35	0	6
EPS Geofoam	1.3	12	0.10	0	250	0

Modeling Approach

There were two different numerical models developed in the preliminary evaluation approach: transverse and longitudinal. The transverse model consisted of a 2D transverse cross section of a hypothetical 0.6-m diameter pipeline and trench (Figure 1). The transverse model was used to determine force displacement functions (nonlinear springs) in the cover system during pipeline uplift using an approach similar to that of Trautmann and O'Rourke (1985). Results from the transverse model were then used in the longitudinal model to estimate the axial, shear and bending stresses, moments, and strains on the pipeline during and after vertical fault offset.

The transverse and longitudinal models were analyzed with two cases: (1) sand cover and bedding and (2) EPS Geofoam block cover and bedding. These will be referred to as the sand and Geofoam cover systems, respectively, for convenience. The sand cover system was model and then compared with the results from the Geofoam cover system to determine the reduction in stress obtained from the use of Geofoam in the system.

The sand cover system consists of (bottom to top): 0.7 m of bedding sand, 0.6-m diameter steel pipe, 1.4 m of sand cover, 0.3 m of untreated base course (UTBC) and 0.2 m of asphalt pavement. The Geofoam cover system consists of 0.7 m of bedding sand, 0.6-m diameter steel pipe, 0.1 m of sand cover, 1.2 m of Geofoam block, 0.1 m thick reinforced concrete load distribution slab (LDS), 0.3 m of UTBC and 0.2 m of asphalt pavement. For the latter system, the 0.1-m thick sand cover atop the pipe is required for the cathodic protection system of the pipeline.

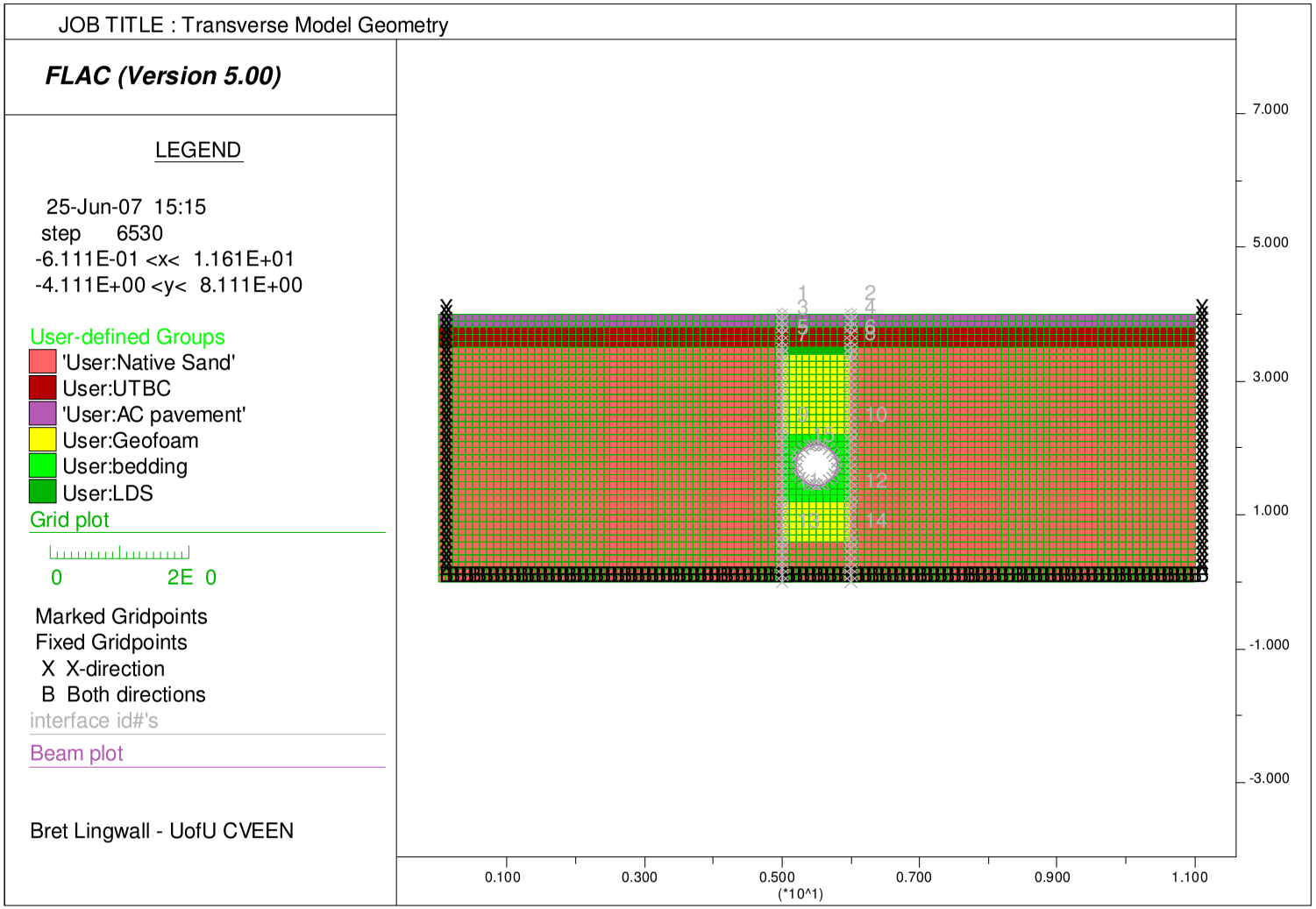

Figure 1. FLAC transverse model of Geofoam cover system with 0.6 m diameter pipe

Transverse Model

Trautmann and O'Rourke (1985) showed that for plane-strain conditions, the force-displacement behavior of a buried pipe in uplift is essentially the same as that of a plate in uplift. Thus, the pipe geometry shown in Figure 1 was simplified to a rectangular box (Figure 2) that was more computationally efficient.

A constant uplift velocity was applied in the numerical model to the box to represent the pipe and load distribution slab as they are forced upward into the cover system. The load distribution slab is approximately 1 m wide, thus the width of the rectangular matches this dimension.

The first step in exploratory FLAC modeling was to analyze a transverse cross-section model (i.e., plane-strain model) to capture the uplift behavior of the pipeline as it was forced upward through the cover system. The force-displacement relations were calculated at various points within the cover system to capture the nonuniform strains that developed at various points within the Geofoam cover system. The ultimate uplift capacity of the sand cover system from the FLAC transverse model is approximately 5.5 MPa (Figure 3). Similarly, the uplift capacity of 1.4 MPa for the Geofoam cover system is shown in Figure 4. Thus, the use of EPS block atop the pipe appears to have reduced the vertical stress in uplift by approximately a factor of 4, which in turn, is beneficial in reducing the shear and bending stresses that develop in the pipe during following normal faulting. The numerical model indicated that covering the sides of the Geofoam block with a geomembrane will further reduce the vertical uplift stress by reducing frictional forces between Geofoam and the trench sidewall. In addition, placing a geomembrane around the Geofoam block will provide added protection against petroleum spill. The

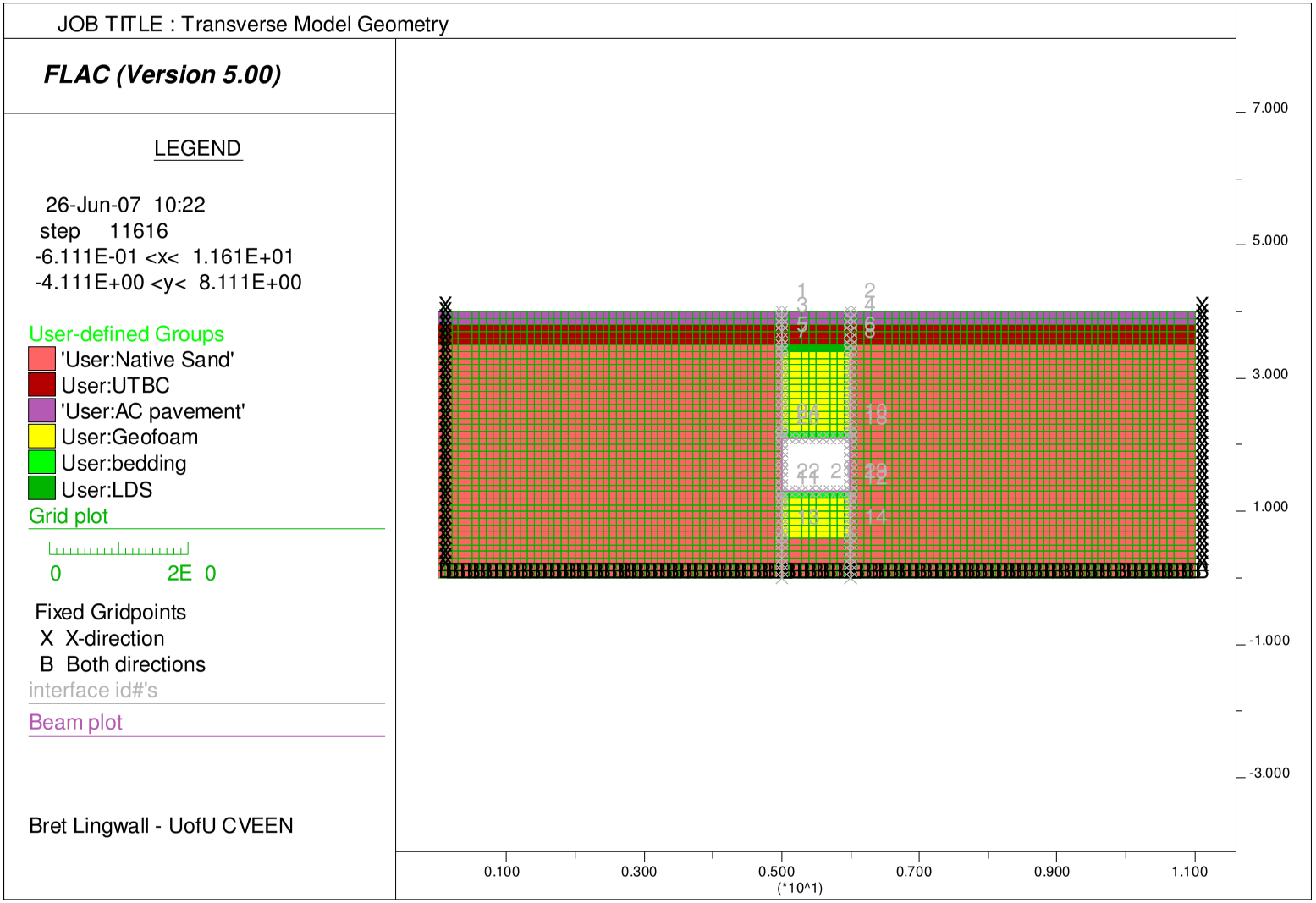

Figure 2. FLAC transverse model with rectangular box representing the pipe

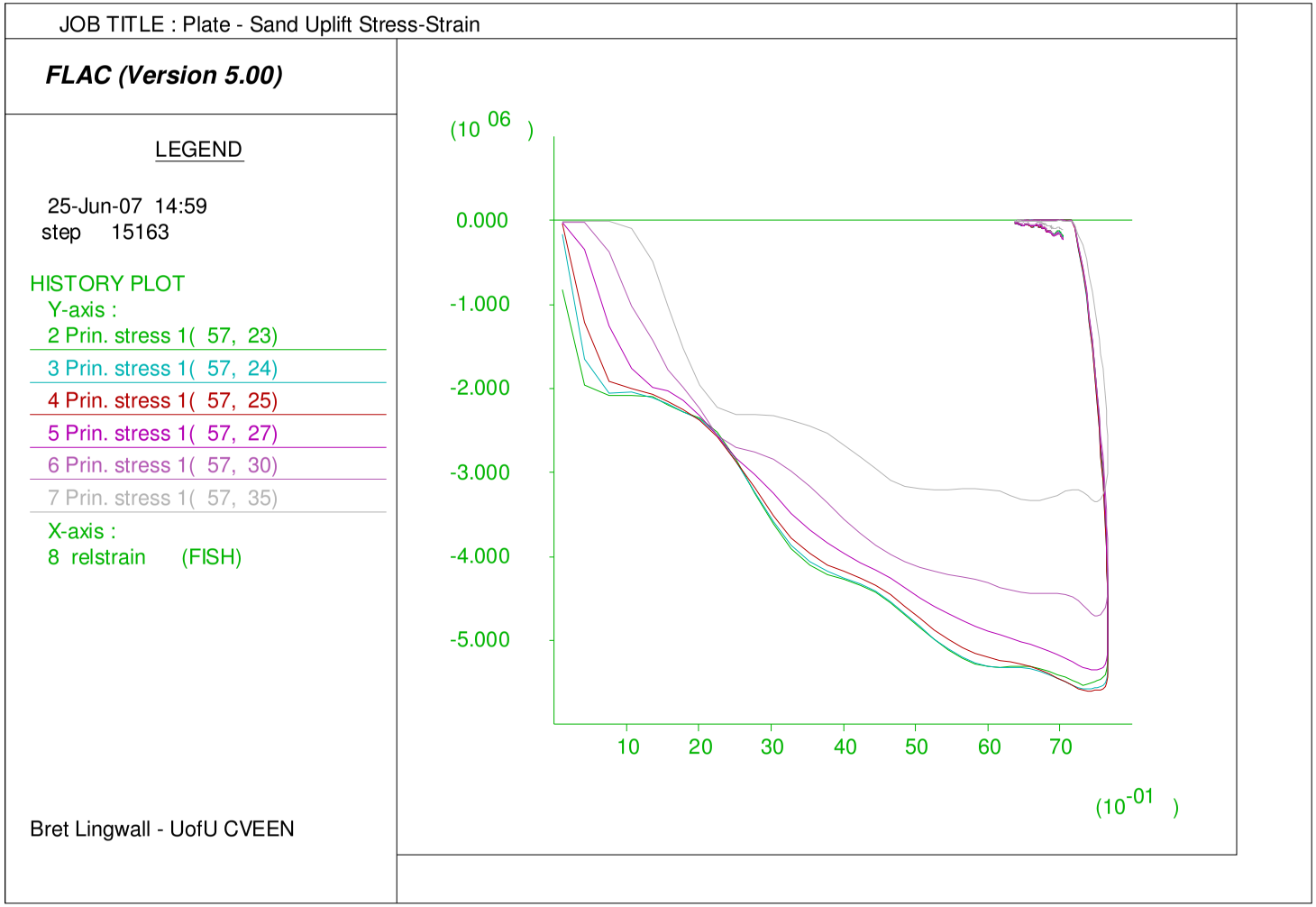

Figure 3. Plot of vertical stress (Pa) versus vertical strain for sand cover system

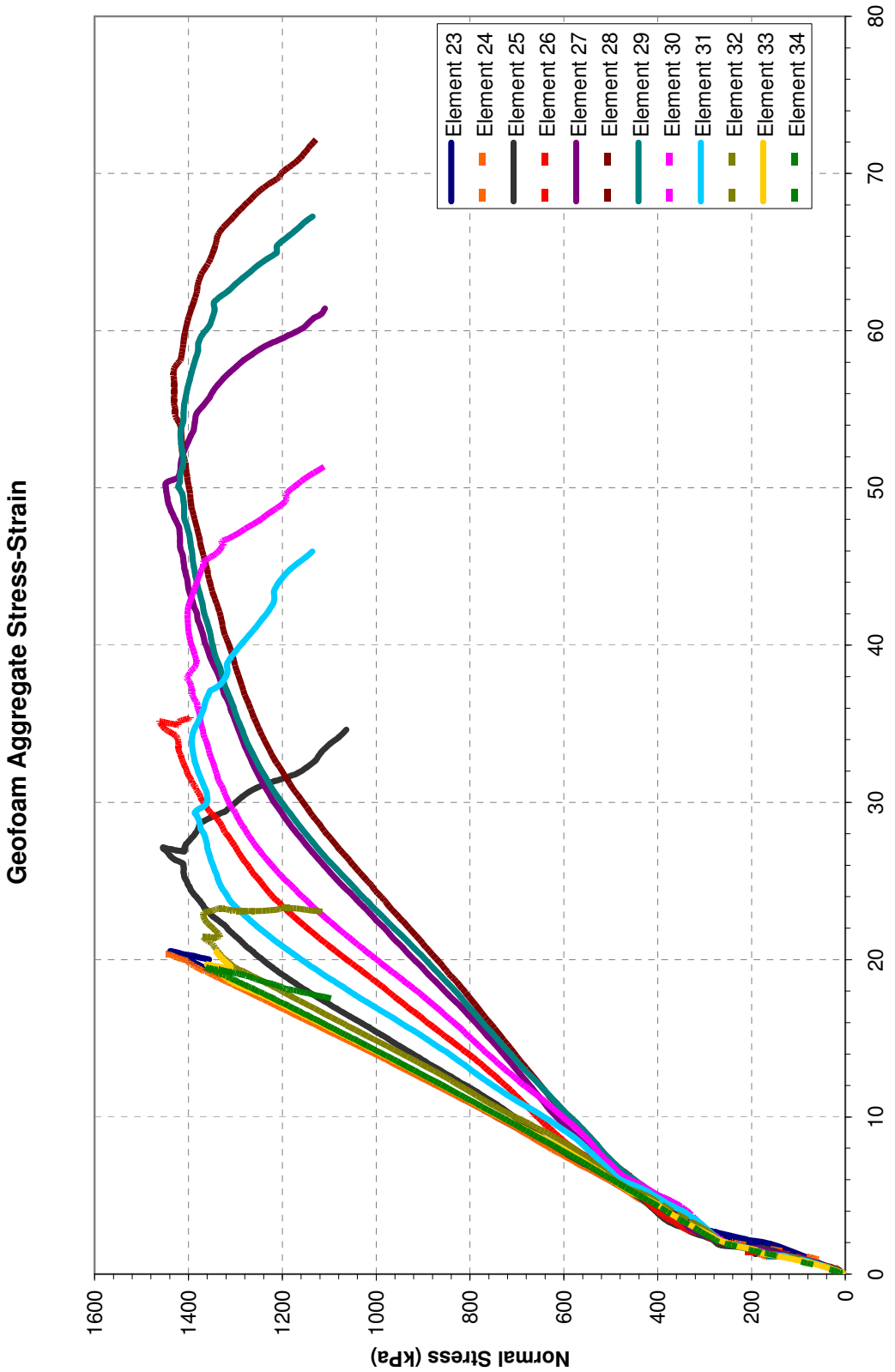

Figure 4. Plot of vertical stress versus strain at various points in the Geofoam cover system

light-weight Geofoam cover provides an additional benefit because it can accommodate more vertical movement before a failure state is reached. The compressive strain required to reach the ultimate stress is about 20 to 60% for the Geofoam cover system (Figure 4) and only about 7% for the sand cover system (Figure 3). The higher compressive strain allowed by the Geofoam system will also reduce the potential damage to the pipe. Figures 5 and 6 show the sand and Geofoam cover systems developed an ultimate uplift force of about 5 MN and 1.6 MN, respectively. Thus, in terms of total force per 1 m length of pipe, the Geofoam cover system reduces the maximum uplift force by a factor of about 3.

The deformation pattern of the Geofoam cover system during uplift is shown in Figure 7. This figure also shows the compressible inclusion concept where the Geofoam has been considerably compressed. Such action reduces the interaction stress between the pipe and cover system and reduces the deformation in the overlying layers. However, no strain hardening was used in this preliminary model, thus the plastic deformations increased at a constant rate after yield. (This modeling convenience will tend to overstate the efficiency of the compressible inclusion.) The compressible inclusion concept will be further evaluated using laboratory and field testing, as discussed later.

Longitudinal Model

The longitudinal FLAC model (Figure 8) requires the force-displacement relations in Figures 5 and 6 to define the vertical spring stiffness used in the longitudinal model. These results shown in these figures were coded into the FLAC program using FLAC's

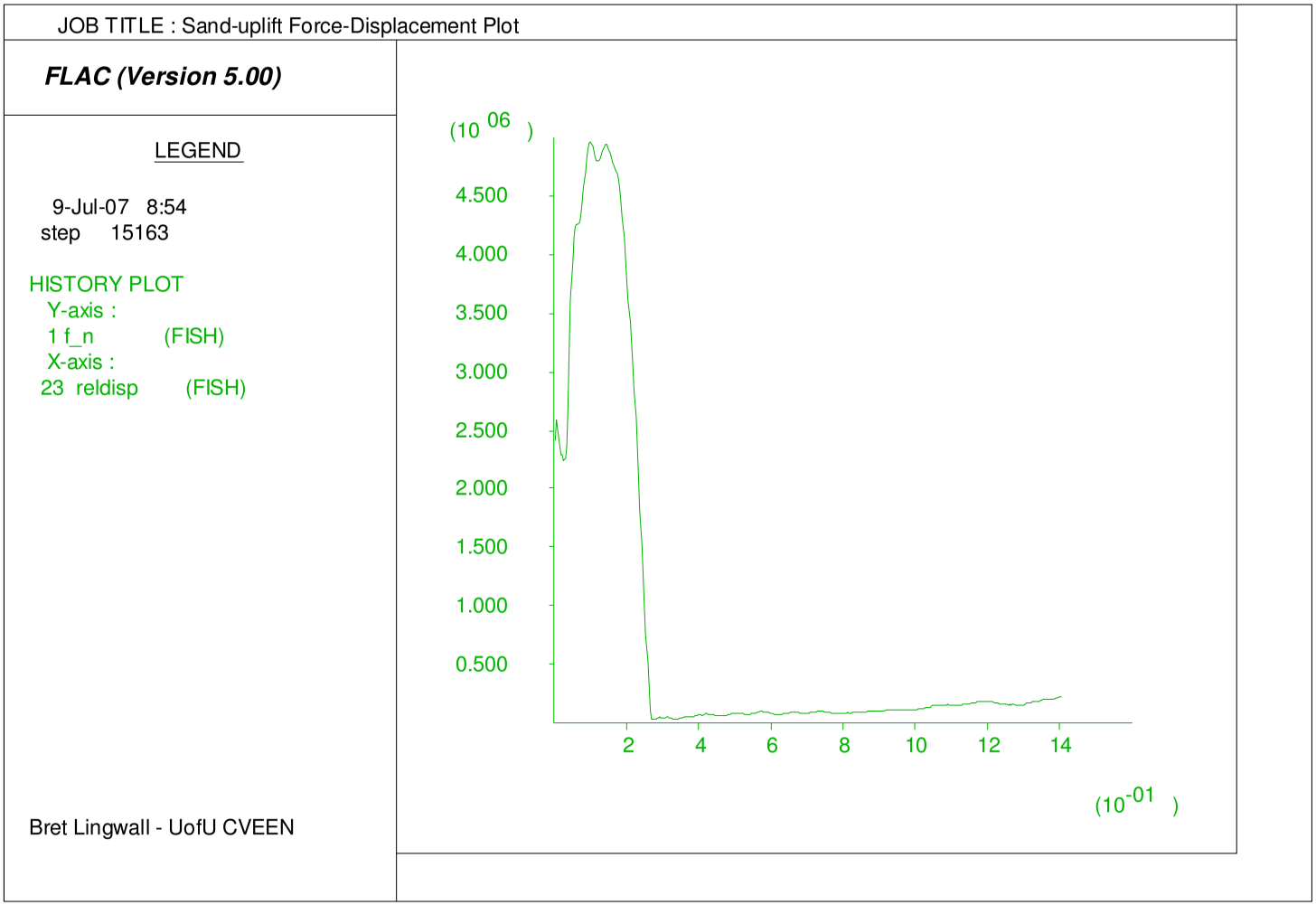

Figure 5. Total force (MN) versus displacement (m) for the sand cover system

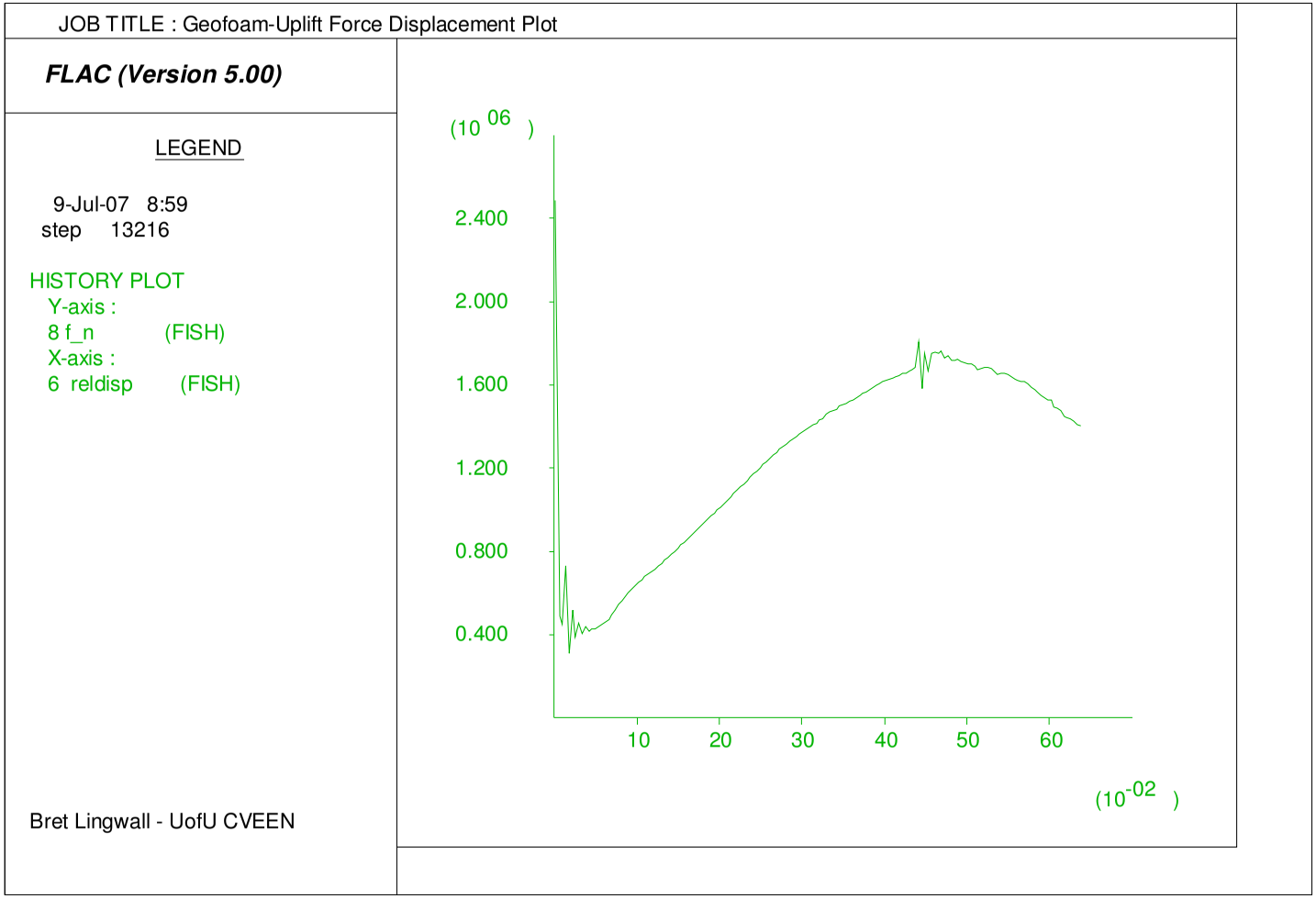

Figure 6. Total force (MN) versus displacement (m) for the Geofoam cover system

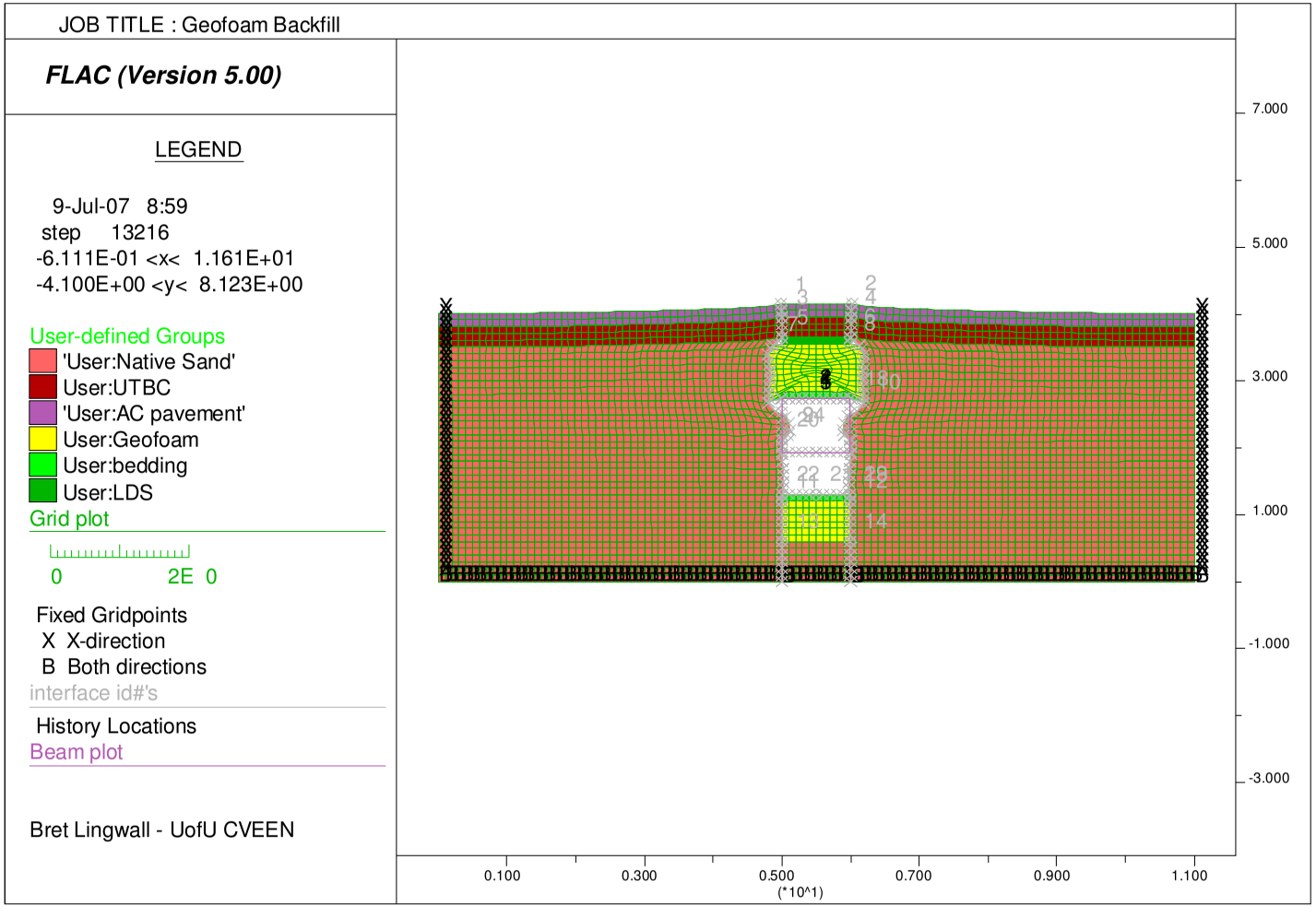

Figure 7. Deformed Geofoam cover system during uplift

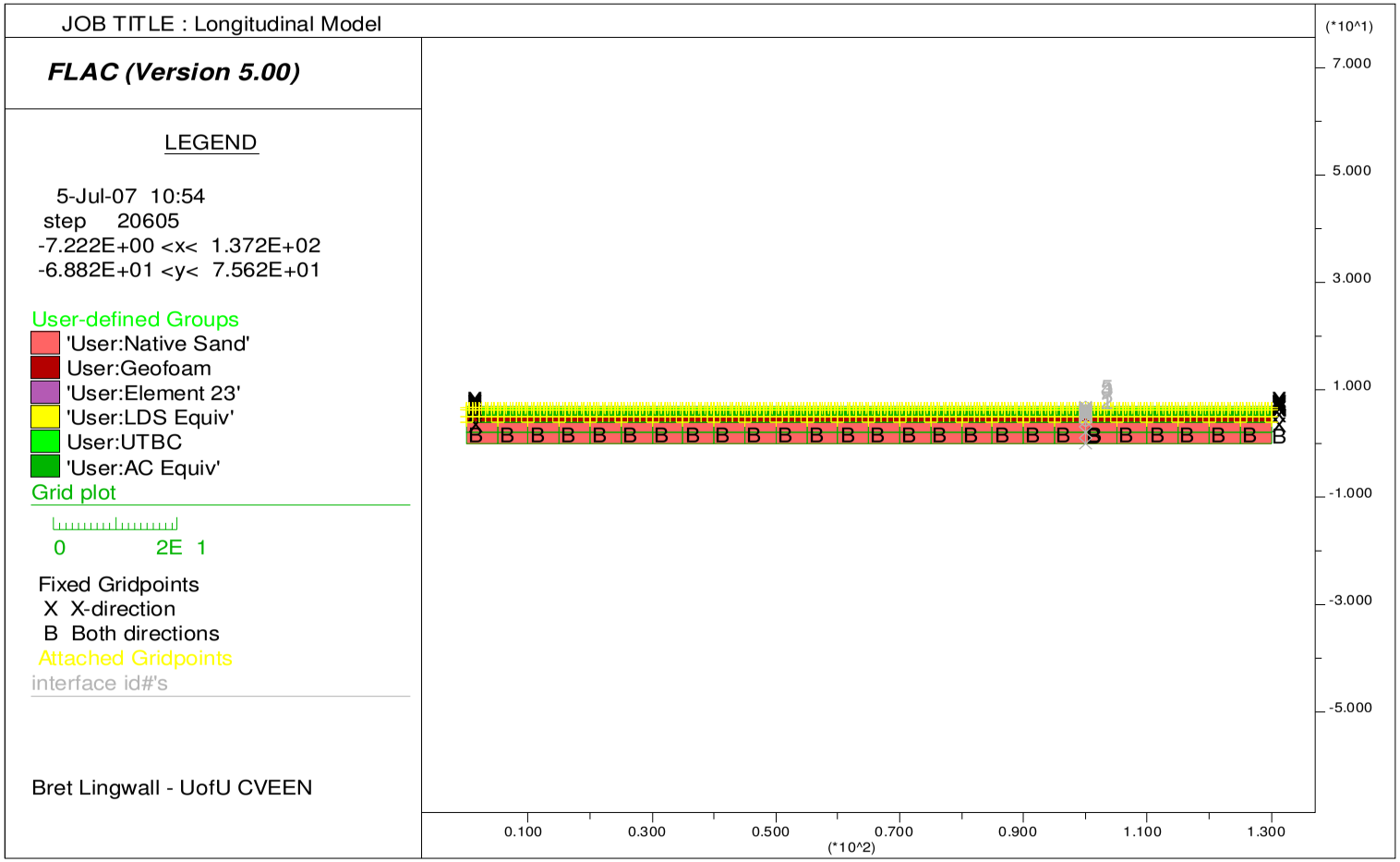

Figure 8. Longitudinal model geometry

programming language. The longitudinal model is 130 m long with 1030 beam elements. The normal fault was placed at the 100 m mark in the model and a vertical offset was forced on a vertical line at this mark. The right 30 m of the model was displaced 2 m upwards to create the fault offset. As was done for the transverse model, the longitudinal model had two cases: one model with the vertical spring constants applicable to a sand cover and another with vertical spring constants representing the Geofoam cover system.

Figure 9 shows the moments induced by fault offset on the pipeline with the sand cover system at failure of the pipeline. The maximum moment was 1.35×10^8 Nm. This model also shows that the maximum allowable offset was about 0.6 m, beyond which yielding of the pipeline occurs. Similarly, Figure 10 shows a moment of about 9.0×10^7 Nm after about 2 m of vertical offset, which is a typical offset expected on the Wasatch fault in Salt Lake Valley. This model indicates that the fault can displace about 2.5 m before the pipeline reaches its yield condition. This marked improvement realized in the displacement behavior of the Geofoam cover system was caused by the lower vertical stiffness and light-weight properties of this Geofoam cover system. In contrast, the vertical stiffness of the sand cover system is approximately an order of magnitude higher as shown by comparing the slopes of the force-displacement plots given in Figures 5 and 6. The vertical spring relation calculated from the FLAC results for the transverse model of the Geofoam cover system (Figure 6) plays a vital role in determining the stresses in the pipeline; thus, simplified methods were also used to estimate the value for this spring and compared with the FLAC results. Table 2 shows vertical spring constant values (K_v) from various methods with those predicted by the FLAC model. Vesic's method (MCEER, 1999) compared well with the FLAC results for the cases that were analyzed.

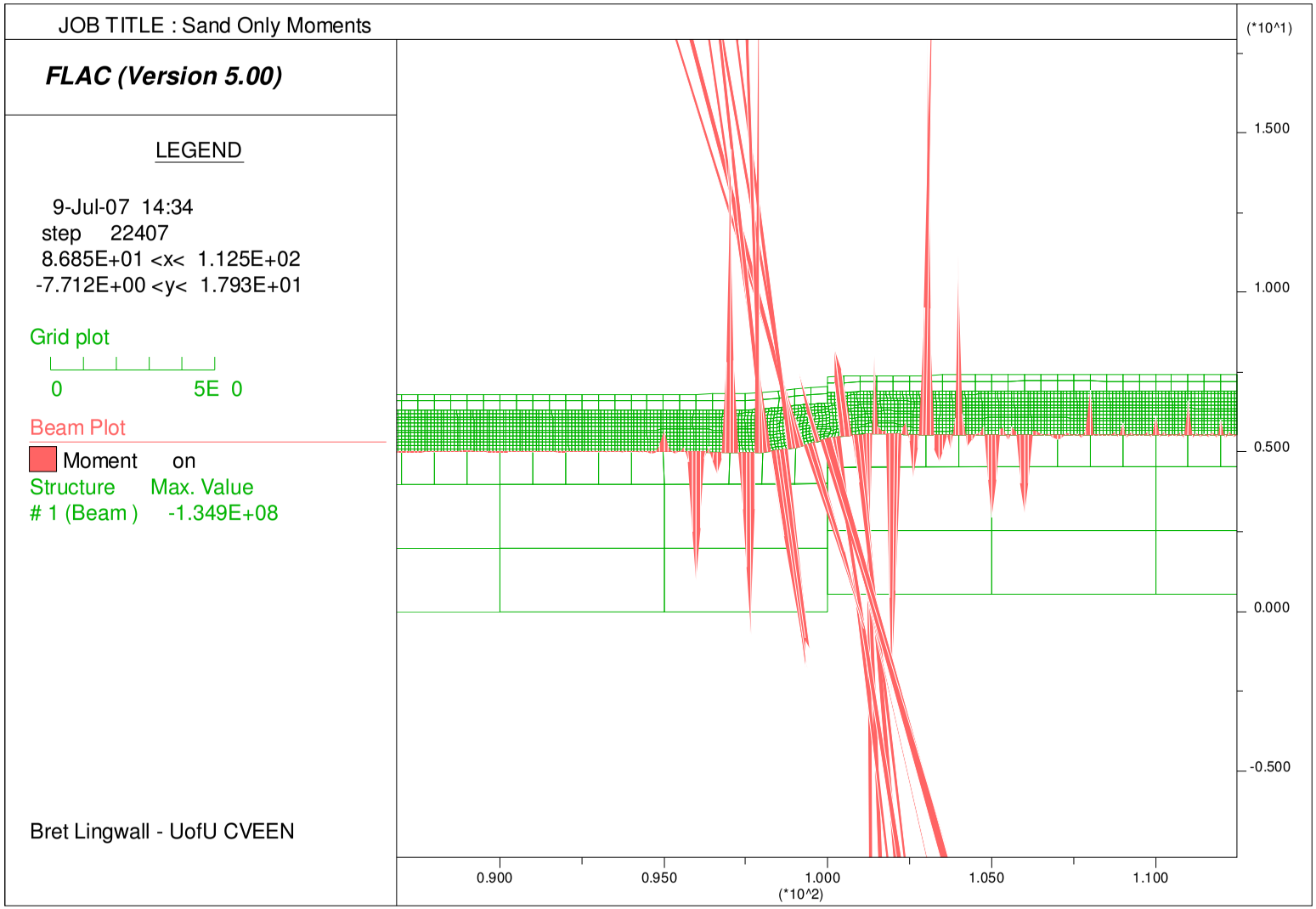

Figure 9. Pipeline moments (N-m) at pipe yielding for sand cover system

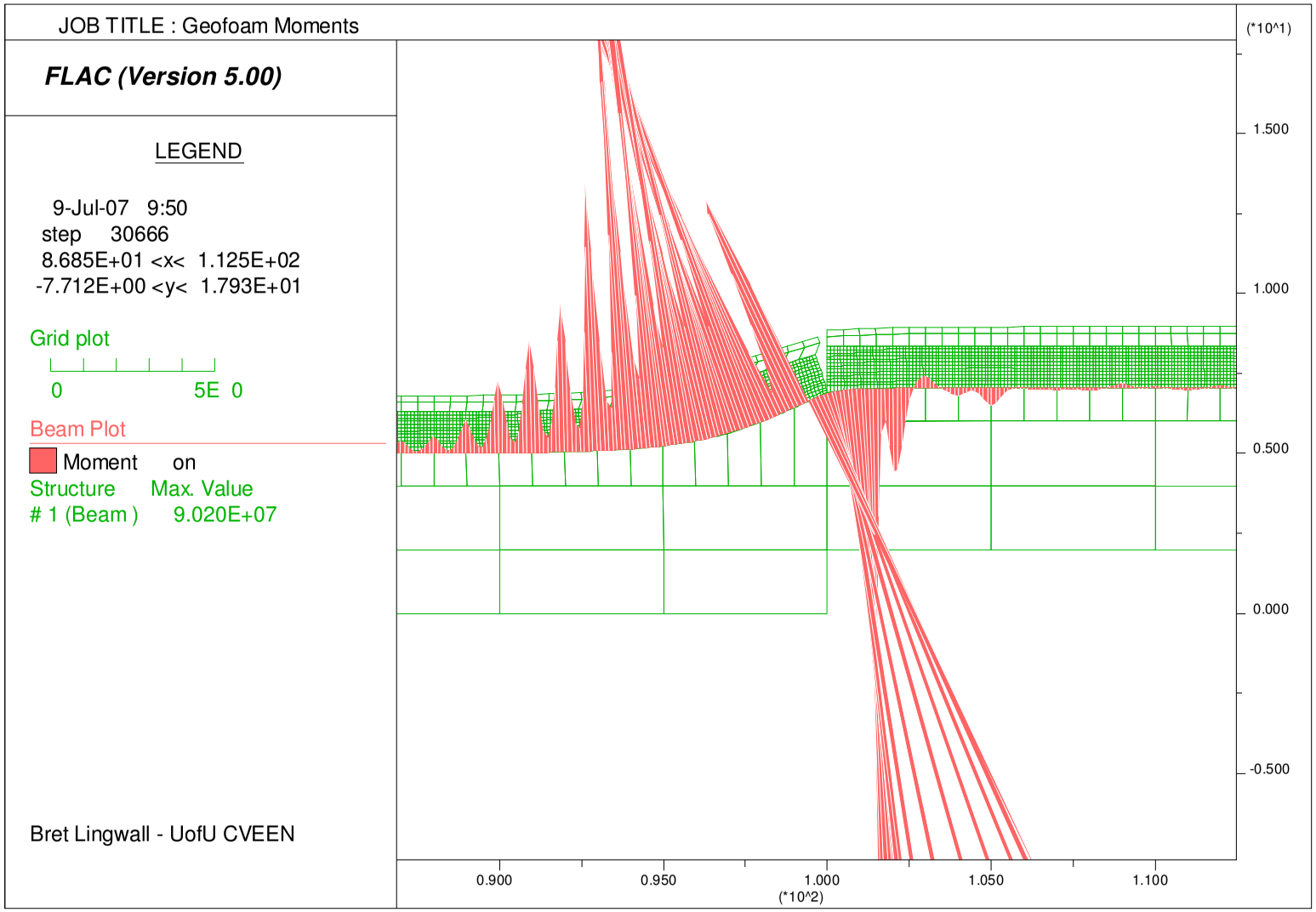

Figure 10. Pipeline moments (N-m) after 2 m offset with Geofoam cover system

Table 2. Vertical spring comparisons

Method	Pu	Zu	Constant	Kv
----------	*kN/m*	*M*	----------	*kN/m*
ASCE – Sand	114	0.025	2	9120
FLAC – Sand	NA	NA	NA	25000
Vesic - Sand	NA	NA	NA	28500
ASCE – Geofoam	504	0.061	2	16520
FLAC – Geofoam	NA	NA	NA	2890
Vesic - Geofoam	NA	NA	NA	3298

Recommendations from Preliminary Evaluations

The exploratory evaluations discussed in this section suggest that an EPS Geofoam cover system offers a substantial benefit in improving the expected uplift performance of steel pipelines that cross normal faults. When compared with a sand cover system, the pipeline covered by the Geofoam system can undergo approximately 4 times greater vertical displacement before pipe yielding is predicted.

The preliminary modeling suggests that placing a geomembrane in the sidewalls of the trench and in contact with the Geofoam can further reduce the uplift forces in the system and improve its efficiency. It was recommended that this be considered for future design and construction.

The findings of this section are based on numerical modeling of a conceptual design and appear to be reasonable when compared with simplified approaches. However, it

was recommended that additional laboratory and field testing be conducted to calibrate and verify the numerical results by constructing a test Geofoam cover system. This additional testing is described in the subsequent chapters of this dissertation. In these tests, a prototype Geofoam cover system was tested in uplift to the failure state. In addition, it was recommended that additional laboratory testing be performed on Geofoam and asphalt to support the evaluations. During a seismic event, the Geofoam is strained at a very rapid rate (in the order of milliseconds) as the fault is offset; no experimental data for Geofoam is available at such high strain rates. Because EPS Geofoam is stiffer when strained rapidly, further research is required to quantify this effect. For the purposes of this preliminary evaluation, a 30% increase in stiffness was assumed. In addition, the behavior of the asphalt pavement in a buckling uplift failure needs to be quantified.

It was also recommended that the cover system be further analyzed using 3D finite element or difference programs such as FLAC-3D. A 3D approach has several advantages over a 2D approach. A 3D model allows for application of internal pipeline pressure, exploration of effects of elbows and T-connections where needed, and allows for the use of more advanced structural elements such as shell elements. The more advanced structural elements that compose the pipeline allow for more precise predictions of pipeline curvature, shear, moments and axial strain.

It was also understood that Questar Gas Company had interest in the potential use of Geofoam to reduce pipe stress resulting from lateral (i.e., horizontal) permanent ground displacement. This type of ground displacement can be caused by land-sliding, liquefaction-induced lateral spread and horizontal (i.e., strike-slip) fault movement.

CHAPTER 3

EPS GEOFOAM TESTING

A series of laboratory unconfined compression tests were performed on EPS Geofoam of varying nominal densities. Two series of tests were performed. The first series consisted of uniaxial monotonic axial compression tests on 152-mm diameter cylinders. Samples of EPS15, EPS22 and EPS39 (i.e., 15, 22 and 39 kg/m^3, respectively) were used. The second series of tests consisted of uniaxial monotonic compression tests on 608 x 608 x 813-mm blocks. The second series of tests used the same densities as the first. All tests were performed using computer controlled load devices with electronic data acquisition of force and displacement.

A variety of strength and stiffness properties for EPS Geofoam were found from the two series of tests. These properties are summarized and recommendations are made regarding which properties are appropriate for different loading and design situations.

Test Equipment

The monotonic uniaxial compression tests on the 152-mm diameter EPS cylinders were conducted using a GeoComp test apparatus. The GeoComp system includes a load frame, LVDT, S-Type Load cell and computer control/data acquisition software. A load frame LOADTRACK II load device and data acquisition system are shown in Figure 11.

Figure 11. GeoComp test apparatus, courtesy of GeoComp Corporation

The 608 x 608 x 813-mm block tests were conducted using the University of Utah Civil and Environmental Engineering Department load frame, which was designed for testing full-sized structural beams and columns. The lower portion of this load frame is shown in Figure 12. The entire load frame is over 9 m high, and was not photographed.

This large load frame utilizes MTS electronic control and data acquisition. The actuator ram has a maximum capacity of 8900 kN with a stroke of 608 mm. The maximum displacement rate for the ram was 1.2 m/min. The ram is powered by a MTS pneumatic pump with computer controlled manifold and servo. Feedback for the system was through the displacement transducer, and the tests were displacement controlled. The load cell used was a 4450 kN Houston Scientific rod-end type load cell with an accuracy of +/-0.1%. The displacement transducer was a Temposonics brand magnetic slider displacement transducer. The MTS control equipment monitored the forces and displacements with a sampling interval of 0.5 sec. This load frame was chosen due to the large size of the load platform, large enough for the 608x813 mm base of the EPS blocks as well as sufficient stroke to take the EPS Geofoam to extremely high strains at a strain rate of 100%/min. The Geofoam specimens were compressed between two 13 mm steel plates mounted to the ram and load frame.

Test Procedures

Before any tests were performed, the specimens were measured and weighed to confirm that the specimens meet the minimum density specifications for their nominal EPS density according to ASTM D6817-02, Standard Specifications for Rigid Cellular Polystyrene Geofoam. Note that ASTM D6817-02 specifies that compression tests and

Figure 12. Large load frame for EPS block tests at full stroke

compression properties should be conducted on 50 mm cube specimens. These small samples were not used in this test program, because of their small size which may not represent the true stiffness and strength of full-sized EPS block in situ.

For a baseline comparison of the minimum compressive resistances of EPS Geofoam, see Table 1 of ASTM D6817-02, which is based on unconfined compression testing 50-mm EPS cube samples. It is important to note that the specifications in ASTM D6817-02 are only for minimum densities and compressive resistances for a specific EPS density. In reality, a given test specimen may have a higher density than the nominal density and often a higher compressive resistance than values given in ASTM D6817-02. Thus, the properties of EPS for a given application should be obtained and verified by laboratory testing that is appropriate for the loading conditions and scale of the application.

After specimens were measured and weighed, the cylinders for the uniaxial tests were trimmed on the ends in a miter-box with hot-wire cutter to assure that the ends were square before testing. The 608 x 608 x 813 mm blocks were factory trimmed. Each specimen was then placed on the bottom platen of the loading device.

For the monotonic uniaxial compression tests, the top platen was placed on the top of the specimen. The load platform was raised slowly into position until the specimen was loaded with a very small axial seating load (less than 2 N). The data acquisition was started and the specimens were compressed vertically in unconfined axial compression according to the loading rate programmed into the computer control module. At the end of the stroke of the actuator, the specimens were temporarily unloaded and a steel plate spacer was inserted below the specimens.

The compression of the specimen continued again to the end of the stroke. This process was repeated in some instances depending on the amount of compression of the specimen after the first reloading cycle.

For the 608 x 608 x 813 mm size block monotonic uniaxial compression tests, the large loading frame (8900 kN capacity) with its attached upper load platen (made from 13 mm steel plate) was lowered into place slowly until a small seating load (less than 40 N) was applied. The test was then started using the computer control system with a pre-specified vertical displacement rate. The specimen was compressed in vertical, confined compression without stopping until 90% axial strain, or greater, was achieved. Strains rates of 10 to 62.6% were performed to see if this had an effect on the material behavior. After loading was finished, the specimen was unloaded and removed from the large loading frame. Figure 13 is a photograph of a specimen in the large loading frame prior to compression of the specimen. Figure 14 shows the same specimen midway through compression testing at a strain of about 50%. Figure 15 shows the same specimen at the end of compression at about 90% vertical (i.e., axial) strain.

Monotonic Uniaxial Tests on Cylindrical Samples

Test Specimens

A total of 21 EPS cylindrical specimens were obtained from ACH Foam Products of Salt Lake City, Utah. These specimens were 152 mm in diameter and 152 mm in height. Three densities of Geofoam were obtained with 7 specimens obtained for each respective density. The nominal densities of EPS Geofoam used in these tests were EPS15, EPS22 and EPS39. Each specimen was measured and weighted to determine the actual density of the specimen.

Figure 13. EPS block positioned in large load frame prior to testing

Figure 14. EPS block during compression in the large load frame

Figure 15. EPS block at end of compression in the large load frame

All of the specimens were tested as part of the test program; however, some of the tests experienced problems and were not included in the test results. Some tests were rejected because the specimen did not deform uniformly in compression, causing the load platens to press at angles greater than 10° from horizontal. (If the load platen tilts excessively, the location and angle of the resultant force changes, leading to an increase of localized straining of the Geofoam cylinder.) Such tests were rejected due to the lack of reliability in the stress-strain data obtained from the angled loading condition.

The details for the acceptable tests are shown in Table 3. It can be seen from these results that for EPS39, the actual density was 57.2 kg/m^3, which was 47% denser than the nominal value. (This can be compared to the samples of EPS15 and EPS 22, which were 6% and 18% more dense, respectively, than the nominal density.) This density discrepancy between the actual and nominal values should be considered for design and installation of Geofoam block because EPS material properties are more closely correlated with the actual and not the nominal values.

The specimens shown in Table 3 were compressed at a variety of strain rates ranging from 3.3%/min to 26%/min to see if any strain rate effects could be observed. Note that the ASTM D6817-02 standard strain rate is 10%/min, which was performed as well for each Geofoam density.

Results

From the stress-strain plots of the test data, several material properties were calculated: initial tangent modulus, modulus to the yield stress, unloading and reloading moduli, yield stress, strain at yield and the stress level for a number of axial strains (1%,

Table 3. Monotonic uniaxial test specimen measurements and strain rates

Test	Nominal Density	Measured Density	Initial Diameter	Initial Height	Strain Rate
----------	*kg/m^3*	*kg/m^3*	*mm*	*mm*	*%/min*
3	15	15.9	150	150	10.0
5	15	15.9	150	152	12.5
6	15	15.9	150	1515	22.5
7	15	15.9	150	151	3.3
12	15	15.9	150	150	3.3
8	22	25.9	150	152	10.0
9	22	25.9	150	150	16.5
10	22	25.9	150	152	10.0
11	22	25.9	150	152	26.0
14	22	25.9	150	150	3.3
15	39	57.2	153	153	16.0
16	39	57.2	153	153	3.3
17	39	57.2	153	151	20.0
18	39	57.2	153	150	26.0
19	39	57.2	153	150	10.0

5%, 10%, 15% and 30%). The initial tangent modulus was determined by drawing a best-fit tangent line to the initial straight portion of the stress-strain curve. For several of the test results, the line was drawn after an initial upward curved portion of the stress-strain plot had become linear. This initial upward curved portion of the relationship is from seating effects of the Geofoam material. This was not observed in every test, but where it did occur, the results were adjusted to fit them with the elasto-plastic model used. See the results for cylinder test 15 in Figure 16 for a visual representation of this phenomenon.

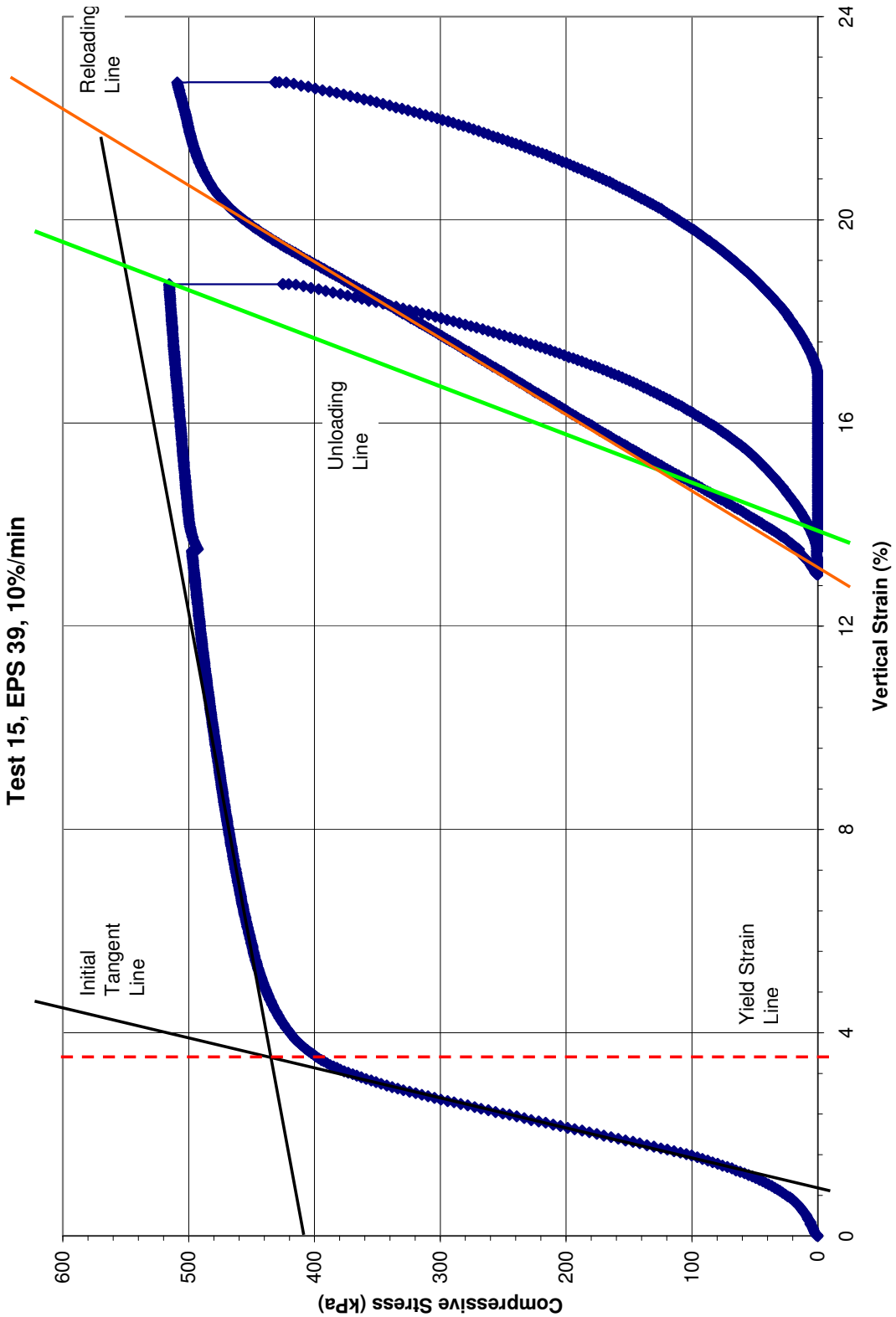

Figure 16. Definition of material properties obtained from the compression tests

The modulus to the yield stress is a secant modulus from the initial condition through the yield stress. This was found by dividing the yield stress by the yield strain.

For the purposes of this research, the unloading modulus was defined as the peak stress divided by the total remaining strain in the specimen just as the load on the specimen reaches zero. This is a secant modulus, and does not represent the actual unloading behavior, only a representation of the net unloading results. More details on the reasoning for this definition are presented in the discussion following these results. The reloading modulus was similar; it was taken as the best-fit tangent line between the beginning of the reloading path and the end of the straight line portion of the reloading curve.

The yield stress of EPS Geofoam is not clearly defined in the literature. It is occasionally defined as the stress at which the straight line initial portion of the stress-strain curve ends. Other researchers have stated that it is the stress found at the intersection of two tangent lines, one for the initial linear portion of the curve, and another for the straight line elasto-plastic portion of the curve above the yield stress.

NCHRP (2001) describes the yield stress as the stress on the stress-strain curve at the same strain as found by the intersection of the two best-fit tangent lines stated previously. In this report, the yield stress was defined in the same way as that of NCHRP (2001).

The results for the different monotonic load tests are summarized in Table 4. Note that not all the tests were reached 30% axial strain. Also, the unloading and reloading curves were not reported for all tests because of sample bending effects. Figure 16 shows a visual representation of the results of EPS Geofoam testing, the definitions of various engineering parameters are shown graphically.

Table 4. Six inch cylinder test results

Test	E_{it}	E_{ys}	E_u	E_r	σ_y	ε_y	$\sigma_{1\%}$	$\sigma_{5\%}$	$\sigma_{10\%}$	$\sigma_{15\%}$	$\sigma_{30\%}$
----------	*kPa*	*kPa*	*kPa*	*kPa*	*kPa*	*%*	*kPa*	*kPa*	*kPa*	*kPa*	*kPa*
3	2500	2091	NA	NA	46	2.2	24	60	70	78	100
5	4000	3333	1915	NA	50	1.5	38	70	83	89	NA
6	2310	2313	1620	NA	74	3.2	23	75	88	99	126
7	2105	2000	1667	1263	60	3.0	26	74	89	99	NA
12	2500	1600	2170	NA	48	3.0	24	62	72	80	NA
8	7500	4667	1920	1470	140	3.0	17	145	162	176	207
9	7500	4643	2045	1450	130	2.8	41	146	164	177	209
10	7778	6100	3000	NA	122	2.0	35	152	168	179	NA
11	8157	4083	1250	851	122	3.0	33	119	132	141	161
14	7500	3833	1471	930	115	3.0	32	127	141	151	173
15	18348	12222	10204	6667	440	3.6	69	341	481	503	NA
16	17241	13594	12750	10095	435	3.2	76	456	507	NA	NA
17	18811	11936	NA	NA	370	3.1	62	365	386	399	427
18	15873	12258	NA	NA	380	3.1	60	374	397	410	440
19	17094	13750	12683	8518	440	3.2	65	450	504	NA	NA

Monotonic Block Tests

Test Specimens

All block specimens were provided by ACH Foam Technologies of Salt Lake City, Utah. Three densities of foam were provided: EPS15, EPS22 and EPS39, which cover a wide range of EPS Geofoam densities. The specimen names, densities and strain rates are shown in Table 5 for the large blocks that were tested in compression up to the 90% strain range. The baseline strain rate of 10 %/min (See ASTM D6817-02) was used as the first set of tests. Subsequently, higher strain rates were used to observe if strain rate effects could be observed for more rapid strain rates.

Figure 17 shows an EPS Geofoam block prior to testing in the large load frame. Lines were drawn on the specimens to track the pattern of deformations during vertical compression as the test progressed. The internal strains could also be shown by these lines qualitatively throughout compression of the block.

Results

From the stress-strain plots, several material properties were calculated. These properties are the following: initial tangent modulus, modulus to the yield stress, unloading and reloading moduli, yield stress, strain at yield and the compressive resistance at various axial strain levels (1%, 5%, 10%, 15%, 30%, 50% and 90%). (The initial tangent moduli were determined by drawing a best-fit tangent line to the initial straight portion of the stress-strain curve.) For several of the test plots, the initial tangent modulus line was drawn after the seating of the sample was completed as was done for the 152 mm cylinder tests (Figure 16).

Table 5. Monotonic block test program

Test Name ----------	Measured Density *Kg/m3*	Deformation Rate *mm/min*	Strain Rate *% / min*
GF 1	39	61	10
GF 2	22	61	10
GF 3	15	61	10
GF 4	39	152	25
GF 5	22	152	25
GF 6	15	152	25
GF 7	39	381	62.5
GF 8	22	381	62.5
GF 9	15	381	62.5
GF 10	39	381	62.5
GF 11	22	381	62.5
GF 12	15	381	62.5

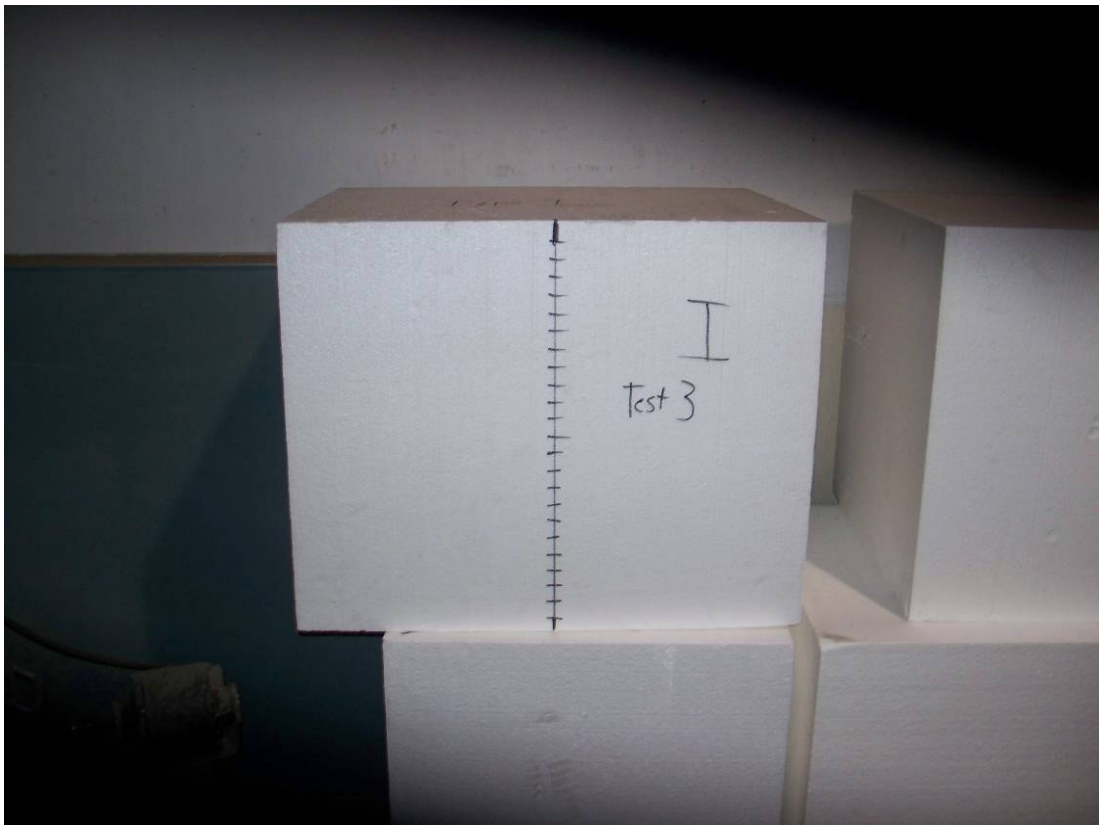

Figure 17. EPS block before testing in large load frame

The definition of all material properties calculated for the block tests were the same as those defined for the 152 mm cylinder tests. The results for the block tests are given in Table 6.

In Figure 18 it can be seen that the final thickness of a 608 mm block after compression was about 2.5 inches (63.6 mm), which corresponds to an axial strain of about 90%. It was also interesting to note that essentially no horizontal bulging of the Geofoam occurred during compression (Figure 15), suggesting that lateral deformation during axial loading was very small, especially in the plastic and strain hardening range

Table 6. 608-mm block test results

Test	E_{it}	E_{ys}	σ_y	ε_y	$\sigma_{1\%}$	$\sigma_{5\%}$	$\sigma_{10\%}$	$\sigma_{15\%}$	$\sigma_{30\%}$	$\sigma_{50\%}$	$\sigma_{90\%}$
----------	*kPa*	*kPa*	*kPa*	*%*	*kPa*	*kPa*	*kPa*	*kPa*	*kPa*	*kPa*	*kPa*
GF 1	15455	12692	330	2.3	129	378	406	423	473	609	3976
GF 2	7273	6190	130	2.1	75	156	168	178	206	244	1880
GF 3	3846	2889	52	1.8	37	71	77	81	82	123	1198
GF 4	13158	15000	360	2.4	159	415	444	465	528	645	4797
GF 5	7767	6250	150	2.4	71	177	190	199	225	285	2108
GF 6	1371	2927	60	2.0	35	76	83	86	87	138	1315
GF 7	14706	13571	380	2.8	120	432	470	494	570	675	4985
GF 8	15625	13333	400	3.0	128	448	484	506	574	700	5080
GF 9	7143	5600	168	3.0	45	180	196	205	233	297	2026
GF 10	6667	6120	153	2.5	66	178	193	200	222	284	2029
GF 11	3333	2393	67	2.8	25	81	88	91	95	152	1430
GF 12	2976	2333	70	3.0	25	82	88	91	95	155	1430

Figure 18. EPS block height at end of compression in the large load frame

of the EPS. Lateral bulging is an indication of Poisson's ratio in the elastic behavior of materials, and of dilation in the plastic behavior of materials. In EPS geofoam, with strain gradients, the block, in compression, experiences zones of both elastic compression behavior as well as zones of plastic compression behavior. It is likely that at very large strains that the entire block is in plastic compression. The presence of no lateral bulging, or even necking as was observed in the compression tests, indicates that the dilation of the material is possible negative. This warrants future research in geofoam behavior, to assess the volume change behavior at large strains, and the plastic volume behavior at very large strains.

Test Results

The results of both the cylinder and large block tests are compared in Table 7 for the EPS15 nominal specimens. Included are the average material properties for the tested specimens and a comparison with the ASTM D6817-02 standard minimum specifications for the corresponding property. (The ASTM information is presented only for comparison purposes because the ASTM standards are based on testing of 50 mm cube specimens.) From this table, it was concluded sample size effects in EPS Geofoam can be significant. Generally, larger specimens have greater compressive resistance and stiffness when compared with smaller specimens. (Sample size effects are best judged by using the average of all samples because there is reasonably variability when comparing individual test results.)

For all three of the Geofoam nominal densities tested, our test results exceeded ASTM minimum specifications with the exception of a few of the EPS15 cylinder

Table 7. EPS 15 test results

Test	Strain Rate	E_{it}	E_{ys}	σ_y	ε_y	$\sigma_{1\%}$	$\sigma_{5\%}$	$\sigma_{10\%}$	$\sigma_{15\%}$	$\sigma_{30\%}$
--------	*% / min*	*kPa*	*kPa*	*kPa*	*%*	*kPa*	*kPa*	*kPa*	*kPa*	*kPa*
GF 3	10	3846	2889	52	1.8	37	71	77	81	82
GF 6	25	3571	2927	60	2.1	35	76	83	86	87
GF 11	62.5	3333	2393	67	2.8	25	81	88	91	95
GF 12	62.5	2976	2333	70	3.0	25	85	88	91	95
3	10	2500	2091	46	2.2	24	60	70	78	100
5	12.5	4000	3333	50	1.5	38	70	83	89	NA
6	22.5	2310	2313	74	3.2	23	75	88	99	126
7	3.3	2105	2000	60	3.0	26	74	89	99	NA
12	3.3	2500	1600	48	3.0	24	62	72	80	NA
Average	----------	3016	2431	59	2.5	28	72	82	88	98
ASTM Standard	10	NA	2500	NA	NA	25	55	70	NA	NA

specimens. It is common that EPS Geofoam blocks are manufacturered to higher densities than the ASTM standard minimums. Batch quality control testing at manufacture plants typically only verify that the blocks meet the minimum standards for the nominal EPS density and verify that the properties do not exceed those of the next highest grade. Because of this, project-specific testing of Geofoam is recommended to confirm the properties of the Geofoam. The actual block may have properties between those of the nominal and the next highest grade of EPS. The project-specific test results should also be compared to the design values used in the engineering calculations. Tables 8 and 9 present the aggregated results for EPS 22 and EPS 39.

The yield strain, as calculated using the method proposed in this report, varies between 2.5 and 3% axial strain with the yield strain increasing with increasing EPS density (Tables 7 to 9). However, the linear portion of the stress-strain curve in the elastic range was generally found at strain levels below about 2% axial strain. This suggests that for most EPS specimens, the linear-elastic part of the stress-strain curve is below 2% axial strain and the yield strength occurs at about 2.5% strain. Between these values, the behavior is transitional between the elastic and plastic state (Figure 16).

The compressive resistance at 1% axial strain obtained for the 152 mm cylinder tests was consistently equal to or below the ASTM D6817-02 minimum standard for 1% compressive resistance. This effect may be due to the test apparatus and the applied seating load not being sufficient to eliminate the occasional curvature in the initial portion of the stress-strain relationship (Figure 16). Results for the 152 mm cylinders and 608 x 608 x 813 mm block tests showed that the initial tangent modulus is a function of

Table 8. EPS 22 test results

Test	Strain Rate	E_{it}	E_{ys}	σ_y	ε_y	$\sigma_{1\%}$	$\sigma_{5\%}$	$\sigma_{10\%}$	$\sigma_{15\%}$	$\sigma_{30\%}$
--------	*% / min*	*kPa*	*kPa*	*kPa*	*%*	*kPa*	*kPa*	*kPa*	*kPa*	*kPa*
GF 2	10	7273	6190	130	2.1	75	156	168	178	206
GF 5	25	7767	6250	150	2.4	71	177	190	199	225
GF 9	62.5	7143	5600	168	3.0	45	180	196	205	233
GF 10	62.5	6667	6120	153	2.5	66	178	193	200	222
8	10	7500	4667	140	3.0	17	145	162	176	207
9	16.5	7500	4623	130	2.8	41	146	164	177	209
10	10	7778	6100	122	2.0	85	152	168	179	NA
11	26	8157	4083	123	3.0	33	119	132	141	161
14	3.3	7500	3833	115	3.0	32	127	141	151	176
Average	----------	7476	5273	137	2.6	52	153	168	178	205
ASTM Standard	10	NA	5000	NA	NA	50	115	135	NA	NA

Table 9. EPS 39 test results

Test	Strain Rate	E_{it}	E_{ys}	σ_y	ε_y	$\sigma_{1\%}$	$\sigma_{5\%}$	$\sigma_{10\%}$	$\sigma_{15\%}$	$\sigma_{30\%}$
--------	*% / min*	*kPa*	*kPa*	*kPa*	*%*	*kPa*	*kPa*	*kPa*	*kPa*	*kPa*
GF 1	10	15455	12692	330	2.6	129	378	406	423	473
GF 4	25	13158	15000	360	2.4	159	415	444	465	528
GF 7	62.5	14706	13571	380	2.8	120	432	470	494	570
GF 18	62.5	15625	13333	400	3.0	128	448	484	506	574
15	16.5	18348	12222	440	3.6	39	441	481	503	NA
16	3.3	17241	13594	435	3.2	76	456	507	NA	NA
17	10	18811	11936	370	3.1	62	365	386	399	427
18	20	15873	12258	380	3.1	60	374	397	410	440
19	10	17091	13750	440	3.2	65	450	504	NA	NA
Average	----------	16257	13151	393	3.0	93	384	453	457	502
ASTM Standard	10	NA	10300	NA	NA	103	241	276	NA	NA

EPS density (Figure 19). The coefficient of correlation for the two different sample sizes is 0.98, or greater. We also noted that the 152 mm cylinder tests tend to produce slightly higher initial tangent moduli than the 24 608 mm block test, except for the EPS15 specimens. The results of this program tend to be somewhat higher than those recommended by NCHRP (2004), though not significantly higher.

The yield stress as a function of nominal EPS Geofoam density for both specimen sizes is shown in Figure 20. The 152 mm specimens show a higher yield stress for the EPS39 specimens and lower compressive resistance for the EPS15 specimens when compared with the 608 mm block specimens.

These trends were similar to the trends observed in the initial tangent modulus. However, there was more scatter for the 152 mm cylinder test result when compared with the block results for yield stress as a function of nominal EPS density. The results of this program tend to be higher than those recommended by NCHRP (2004), especially at higher nominal EPS densities. Figure 21 shows a similar trend for stress at 10% strain.

For more information on the effects of EPS Geofoam specimen size and compression test results, see Elragi et al. (2000). These authors found that 608 mm block EPS specimens had much higher modulus than 50 mm cube specimens. Figure 21 shows the results from this testing program on 608 mm block specimens. The results of the Elragi et al. (2000) test program show higher initial tangent modulus than those found by this test program (see Figure 22 with star symbols superimposed on this plot representing test results from this program).

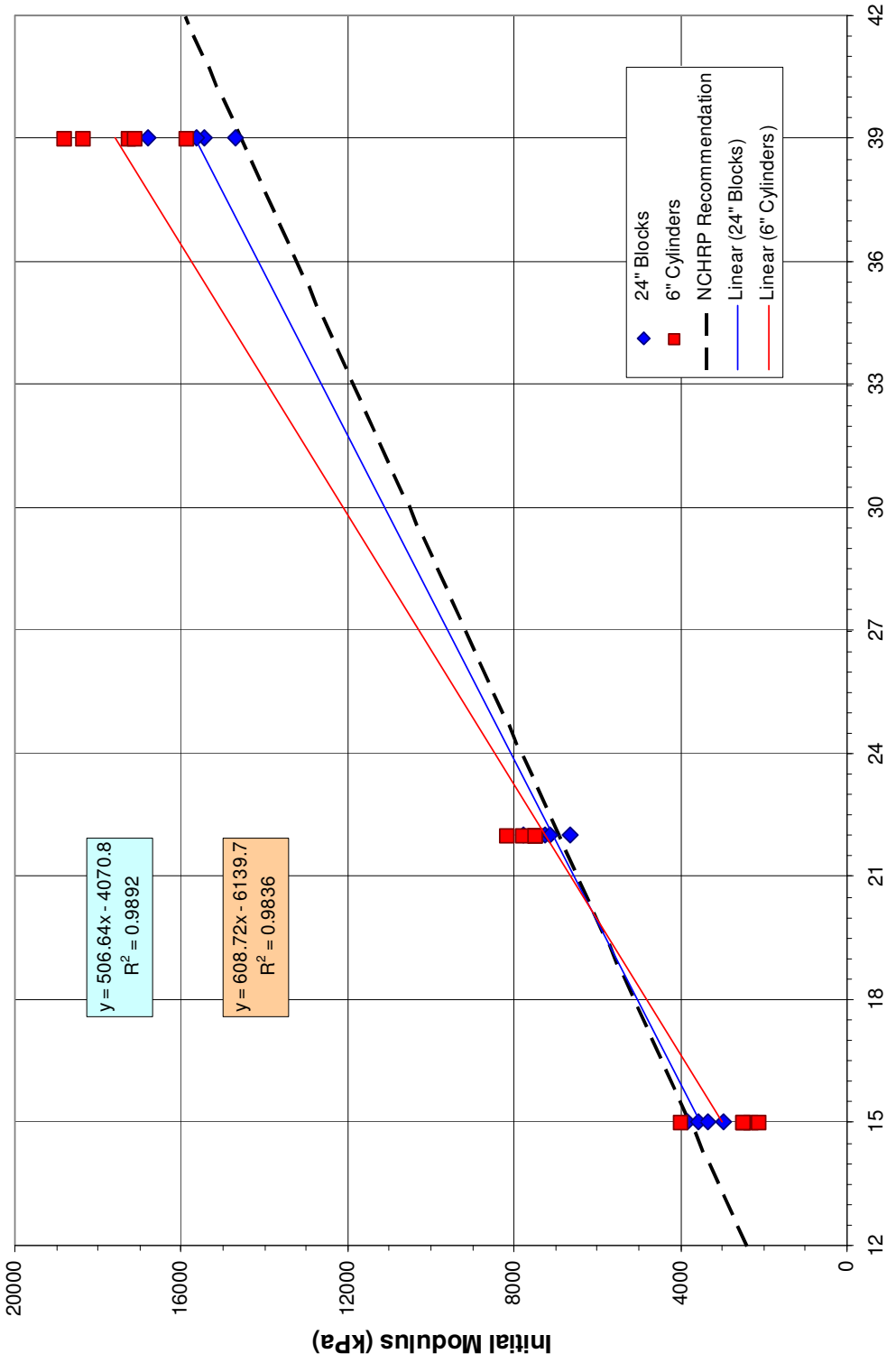

Figure 19. Comparison of initial tangent modulus for two specimen sizes

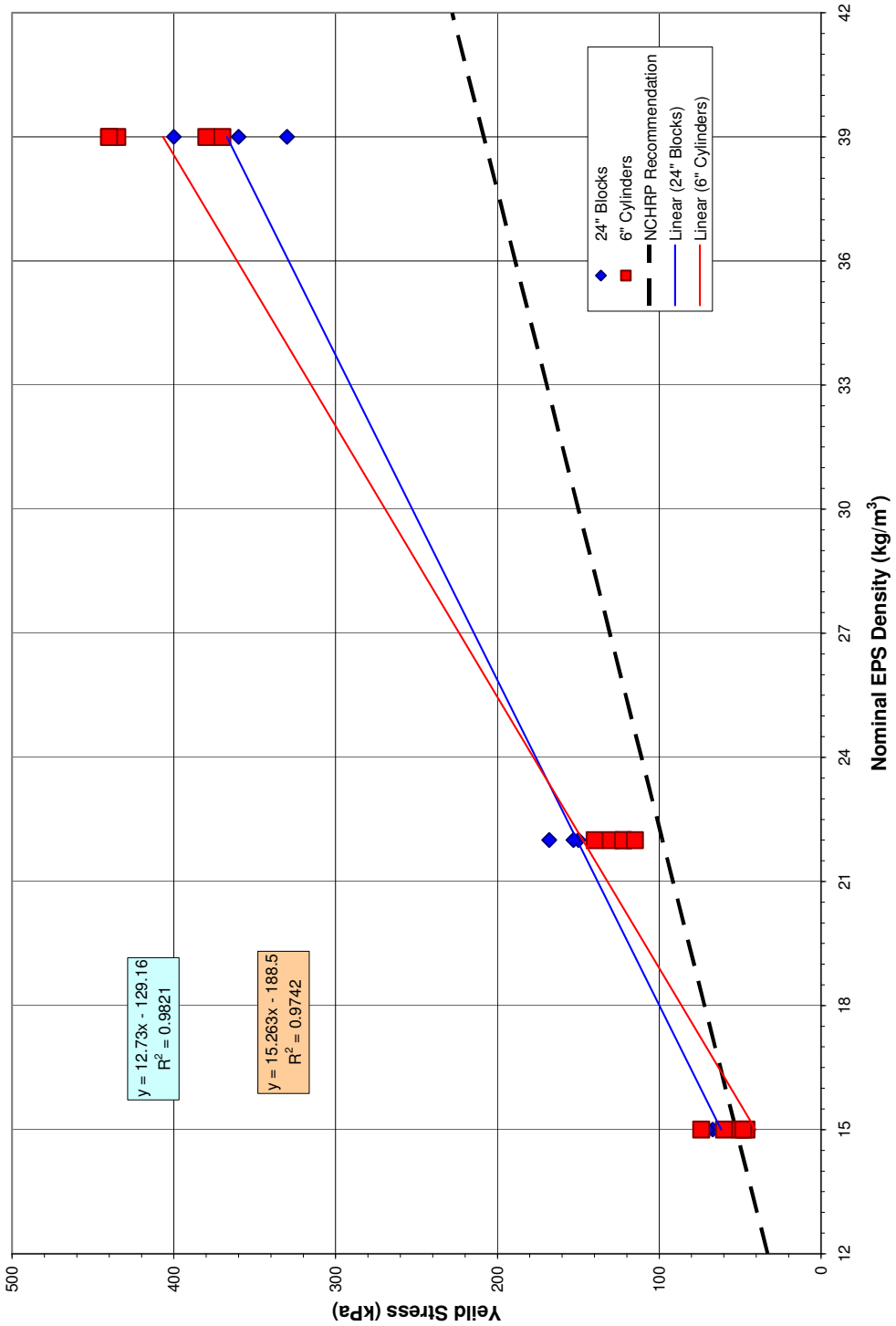

Figure 20. Yield stress for 608 mm block and 152 mm cylindrical sample sizes

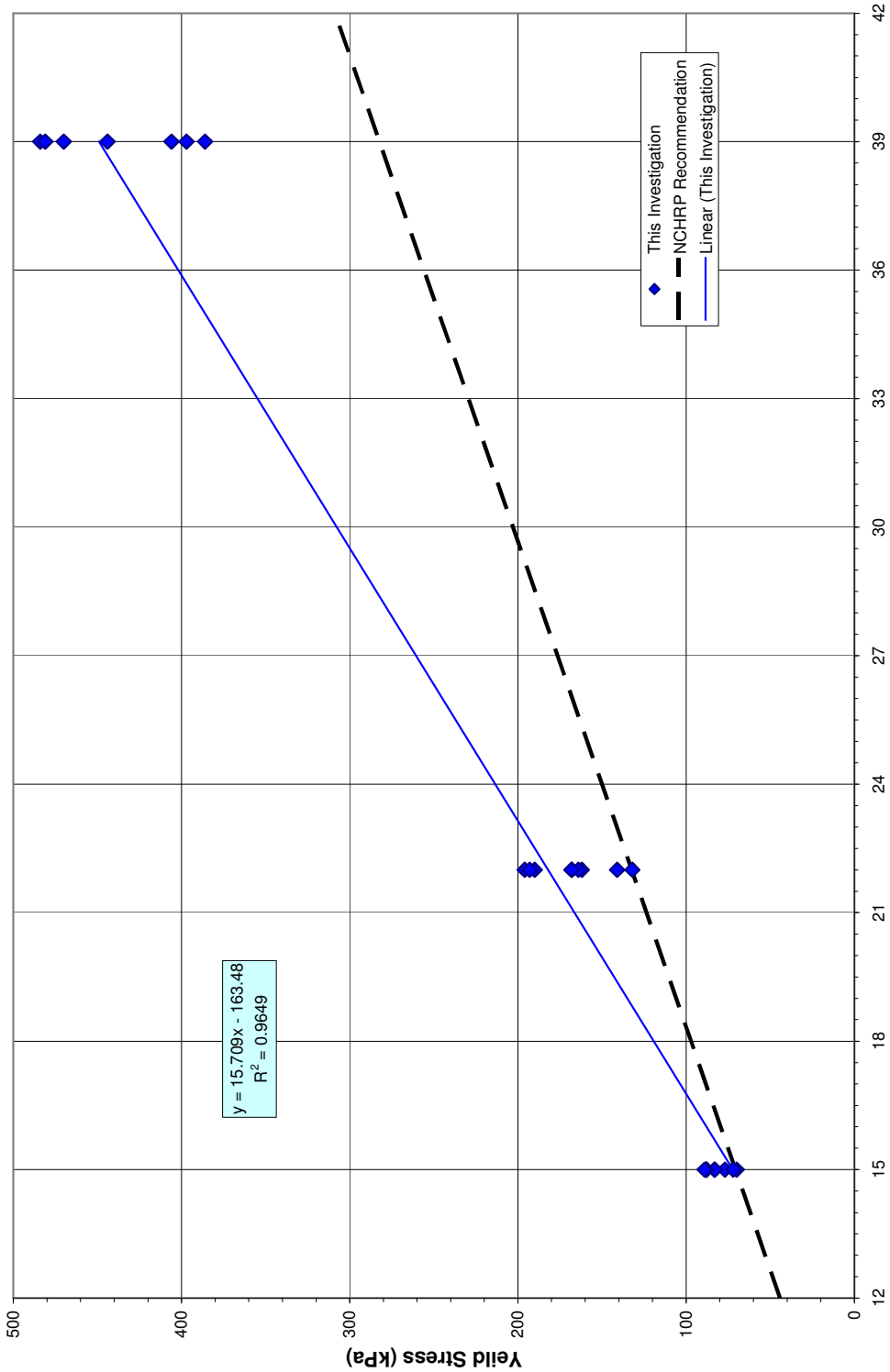

Figure 21. Compressive stress at 10% axial strain for 608 mm block specimens

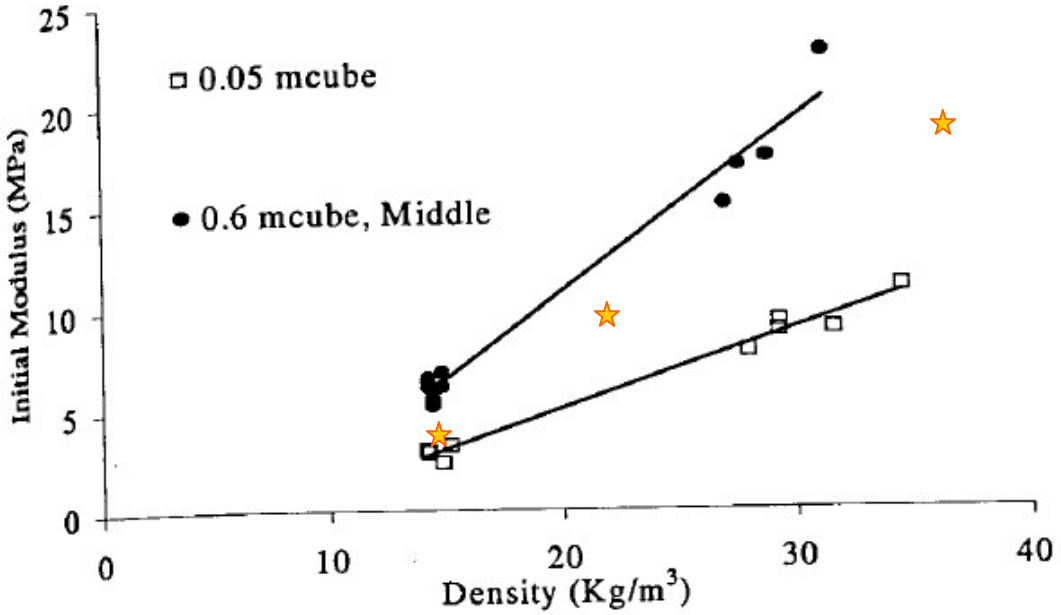

Figure 22. Specimen size effects on EPS modulus (after Elragi et al., 2000)

However, Elragi et al. (2000) used internal strain measurements to determine the axial strain. The moduli in this study were found by the global deformation of an entire EPS block or cylinder. The entire block was measured before, during and after compression to assess strain level. Despite the lower modulus measured by this test program, both these test data and those of Elargi et al. (2000) show that larger EPS test specimens have higher compressive strength and stiffness when compared with results obtained from smaller test specimens. This means that the typical compression of 50 mm specimens for quality control and property determination may under estimate actual properties. This leads to more conservative designs than planned and may lead to higher costs in constructed sections and fills.

Discussion of Test Results

The large block test specimens clearly show a sigmasoidal strain hardening behavior of EPS Geofoam. This behavior involves a significant strength gain of the material beyond about 30% axial strain. This finding has important implications regarding the efficiency of a compressible inclusion at higher strain levels. If the EPS block is strained to this amount, or greater, as expected for the case of fault offset, the compressible inclusion behavior may not be very efficient due to subsequent strain hardening of the EPS. Thus, it is recommended that the target strain level be considered in the Geofoam applications that involve postelastic straining and the associated compressive resistance developed at that level of strain.

As for the yield stress and stress at 10% strain being larger than those of NCHRP, it is unclear if the NCHRP results are a conservative recommendation, or the average of actual test data. It is also supposed that the NCHRP testing was done with small cube specimens rather than larger cylinders or blocks, which would cause significant differences.

Unloading Modulus

The unloading modulus is simply defined as the slope of the stress-strain curve for Geofoam from the end of loading to the end of unloading. The behavior of Geofoam in unloading is very nonlinear, so it is difficult to define the unloading modulus due to the shape. For the purposes of this research, the unloading modulus was defined as the peak compressive stress divided by the total remaining compressive strain in the specimen at the point where the load on the specimen reached zero (Figure 16). This is a secant

modulus and does not represent the actual nonlinear unloading behavior. It is only a representation of the net unloading results.

The behavior of Geofoam at peak load is time dependent (i.e., visco-elastic), meaning that the longer the specimen is held at the peak load there will be more plastic strain upon unloading. In addition, there tends to be a considerable amount of compressive strain rebound after the specimen was completely unloaded and the displacement imposed by the load frame was removed. This rebound occurs regardless of the length of time that the specimen was held at the peak stress.

Geofoam rebound behavior was difficult to describe mathematically, but was observed in every test specimen. In addition, the unloading curve behavior was difficult to describe because in the time between the end of loading and beginning of unloading, there was significant vertical stress relaxation in the EPS Geofoam as the peak compressive strain at the end of loading is maintained. This stress relaxation was measured on some occasions. It was observed that as much as 30% of the peak stress was lost in the specimen due to relaxation.

Reloading Modulus

The shape of the reloading part of the stress-strain curve is approximately linear for Geofoam, and so the reloading modulus is also linear (Figure 16). To calculate the reloading modulus, a best-fit line is drawn through the reloading data. This testing shows that at the same compressive stress level (i.e., after reloading is completed), the compressive strain at the end of the reloaded part of the curve was greater than the initial loading part of the curve, i.e., an accumulated plastic strain has occurred. The magnitude

of plastic strain varies with the elapsed time between reloading and unloading. It is also dependent upon the rate of loading. The visco-elastic behavior of EPS requires further research.

Another important observation is that the reloading modulus for EPS was significantly less than the initial loading modulus. In contrast, the reloading modulus for soils is usually similar to the initial loading modulus. The test data in Figure 16 show the reload modulus was about 50% less than the initial loading modulus. Similar values were measured for all EPS specimens tested in unloading and reloading. These unload-reload cycles were done at compressive strains greater than the elastic limit on the material; hence, the results are influenced by plastic behavior of the Geofoam. It is also noted that these unload and reload moduli should not be used for cyclic analyses (e.g., earthquakes or machine vibrations) because of the plastic behavior at large compressive strain. However, these moduli may be appropriate for smaller compressive strains, such as occurs during freeze-thaw and expensive soil loadings.

Strain Rate Effects

From the plots shown in Figure 22, it is concluded that compressive strain rate has only a minor effect on compressive resistance and modulus of EPS, at least for strain rates that range between 3% to 62.5%/minute. Figure 22 shows the initial tangent modulus as a function of nominal EPS Geofoam density for 4 different strain rates. The baseline strain rate of 10%/min, as prescribed in the ASTM D6817-02 standard, was included in the test program for comparison purposes. Similarly, Figure 23 shows the yield stress as a function of strain rate. Based on these figures, it was concluded that

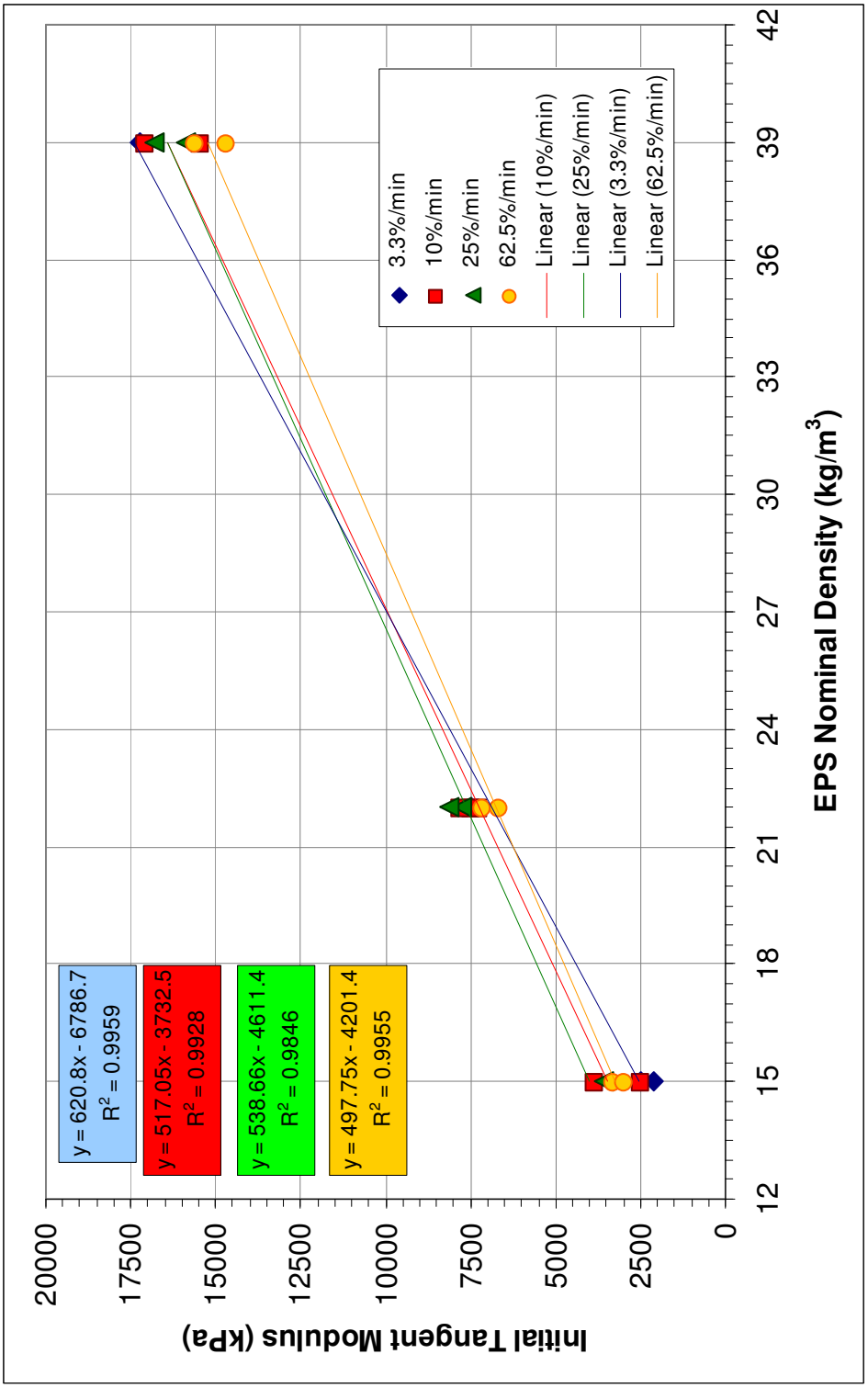

Figure 23. Initial tangent modulus for different strain rates

there is little difference in modulus and yield strength as a function of rate. However, loading from fault offset are essentially instantaneous (i.e., duration of a few to tens of milleseconds) and impact loading behavior of EPS needs to be further explored.

Figure 24 shows the yield stress at various strain rates for three nominal Geofoam densities. This figure shows that strain rate effects have little effect on the yield stress, though the fastest strain rate did show slightly higher resistance to compression than the other three strain rates used in the testing program. If a much higher strain rate was possible in the test equipment, the effects may have been more pronounced. This needs to be further explored if more rapidly loading test equipment becomes available.

Stiffening of EPS due to Creep Strain

EPS Geofoam installed in underground and embankments can undergo creep strains. This is long-term strain that occurs from the in situ state of stress. Such strain, with significant passage of time) will impact the compressive resistance and stiffness of the EPS. For example, test results on samples subject to very slow strain rates (i.e., 1%/year) show that the compressive strength of EPS increases to values higher than preloaded values (NCHRP, 2004). This creep behavior and its impact on the properties of EPS highlight the importance of the visco-elastic nature of Geofoam.

Poisson's Ratio

In the elastic range, Poisson's ratio for EPS is typically relatively low with values of about 0.1 for EPS19 (Negussey, 2006). However, in the plastic range, Poisson's ratio

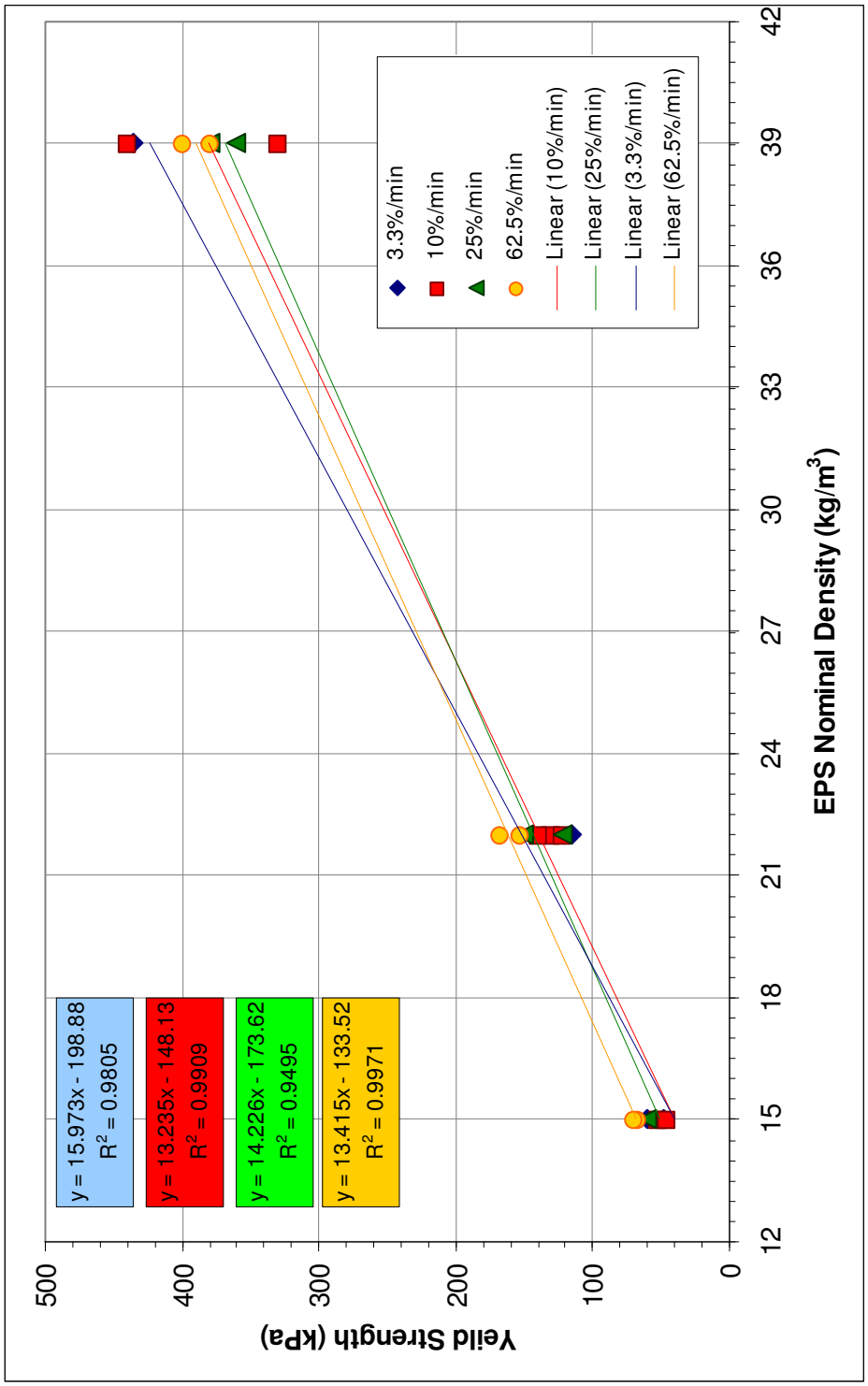

Figure 24. Yield stress at various strain rates

may actually be slightly negative. (Note that Poisson's ratio is an elastic property and is not strictly applicable to the plastic range.)In the plastic range, a negative dilation angle can produce similar behavior. The EPS behavior at large strain can be seen by examining Figure 25. This figure shows the shape of a 608 mm block specimen at the end of extreme compression.

Note that the sidewall of the sample has a concave shape rather than a typical convex (i.e., bulging) shape that is observed when soil is compressed. A concave shape seen in Figure 25 implies a negative Poisson's ratio and/or dilation angle, because the sample is slightly contracting laterally during axial loading. This slight concave shape at the edge was observed throughout the duration of the test.

Comparison to Published EPS Geofoam Testing

The test results discussed in the last section of this chapter can be compared with published data from other researchers. In particular, it is useful to compare them to the NCHRP (2004) report's findings. Figures 20 and 21 show the lab testing of this investigation compared to those recommended by NCHRP (2004). The trend between the testing done in this investigation and that found in the NCHRP recommendations is that the two have similar trends for low values of nominal EPS density. As the nominal EPS density increases, there is greater divergence between the two trend lines. This is mostly due to sample size effects. The NCHRP recommendations were developed largely with 50-mm cube specimens, while larger specimens were used in this research. This is the same trend as shown in Figure 22 when comparing sample sizes. In short, the finding

Figure 25. Shape of EPS block edge at end of compression in large loading frame

that increasing the EPS density and/or sample size will cause an increase in the measured strength and stiffness properties is still observable in these data and trends.

Mathematical Model of EPS Behavior at Large Strains

It is most important to evaluate the stiffness of EPS during its compression and uplift interaction with the pipe resulting from the displacement event. It is this stiffness and its change during compression that governs the forces that ultimately develop in the EPS when EPS blocks are used as a compressible inclusion in a buried interaction application.

For a standard hyperbolic model for 0 to 30% axial strain, Equation 1 is proposed:

$$\frac{\varepsilon}{\sigma} = a\varepsilon + b \Rightarrow \sigma = \frac{\varepsilon}{a\varepsilon + b} = \frac{\varepsilon}{\frac{\varepsilon}{(\sigma_1 - \sigma_3)_{ult}} + \frac{1}{E_{it}}} \tag{1}$$

where ε is axial strain, σ_1 and σ_3 are the major and minor principal stresses, respectively, E_{it} is the initial tangent modulus and a and b are hyperbolic model parameters that are determined using a best-fit method to experimental data.

For axial strains above 30% strain, another hyperbolic form is proposed, but with its beginning point matched with the end point of the first hyperbolic model (Figure 26). This will be refered to as a "matched double hyperbolic model." For axial strains above 30%, Equation 2 is proposed:

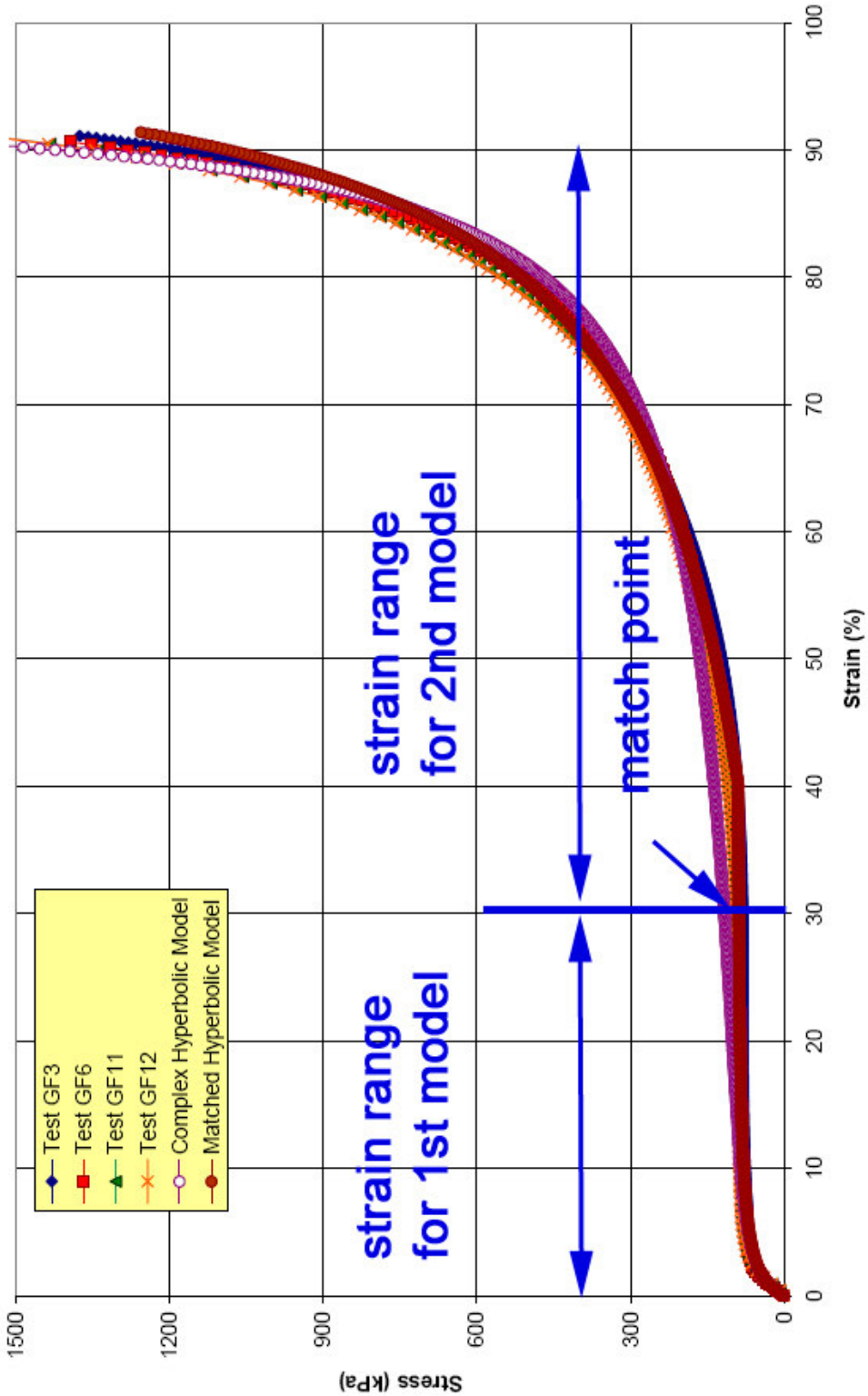

Figure 26. Matched double hyperbolic model

$$\frac{\varepsilon}{\sigma} = c\varepsilon^2 + d \Rightarrow \sigma = \frac{\varepsilon}{c\varepsilon + d} \tag{2}$$

where c and d are best-fit hyperbolic model parameters for the second part of the complex curve. Thus, for the matched double hyperbolic model, 5 fitted parameters are required (a, b, c, d) and a parameter for the match point where the curves connect. To adjust for strain rate effects, the test data can be normalized to the strain rate using Equation 3:

$$\sigma^* = \frac{\sigma}{\left(\dot{\varepsilon}\right)^m} = \frac{TestStress}{StrainRate^m} \tag{3}$$

where m = 0.05 is used for Geofoam. The stress-strain relationship becomes:

$$\frac{\varepsilon}{\sigma^*} = a^*\varepsilon^2 + b^* \Rightarrow \sigma = \frac{\varepsilon\left(\dot{\varepsilon}\right)^m}{a^*\varepsilon + b^*} \tag{4}$$

,

with opposite signs and parameters c and d used for the second part of the model. It was found that the above approach works well for EPS15; however it does not work as well for EPS of higher density. The matched parameters for the EPS15 model are shown in Table 10. In Table 10, the match point for the two curves is selected at 30% axial strain. This was an arbitrary match point that was chosen after inspection of Figure 26.

We also explored the application of a complex hyperbolic model, which is written as Equation 5.

Table 10. EPS 15 matched hyperbolic model parameters

Coefficient	Value
a*	0.0123
b*	0.0234
c*	-0.0084
d*	08548

$$\frac{\varepsilon}{\sigma} = a\varepsilon^3 + b\varepsilon^2 + c\varepsilon + d \Rightarrow \sigma = \frac{\varepsilon}{a\varepsilon^3 + b\varepsilon^2 + c\varepsilon + d} \tag{5}$$

In Equation 5, ε is the axial strain in%. This formulation has the advantage that the functional form covers the complete stress range; hence, only 4 parameters are required. It was found that the complex hyperbolic model performs well for EPS22 and EPS39. It did not provide as good of fit as the matched double hyperbolic model for EPS15, although Equation 5 reasonably approximates the EPS15 test data.

As before, the test data can be normalized for strain rate by, with exponent m, m = 0.05 for Geofoam as shown in Equation 6, with σ the compressive stress.

$$\sigma^* = \frac{\sigma}{\left(\dot{\varepsilon}\right)^m} = \frac{TestStress}{StrainRate^m} \tag{6}$$

.

and the stress equation becomes Equation 7.

$$\frac{\varepsilon}{\sigma^*} = a^*\varepsilon^3 + b^*\varepsilon^2 + c^*\varepsilon + d^* \Rightarrow \sigma = \frac{\varepsilon\left(\dot{\varepsilon}\right)^m}{a^*\varepsilon^3 + b^*\varepsilon^2 + c^*\varepsilon + d^*} \quad (7)$$

In Equation 7, a*, b*, c* and d* are fitted parameters for the complex hyperbolic model that has been normalized to strain rate. Values for the complex hyperbolic model parameters are shown in Figure 27. These plots show the parameters as a function of nominal EPS Geofoam density for both the regular and normalized data from the large block tests. Plots of the stress-strain data and the hyperbolic mathematical function can be seen in Appendix B. For reference, Type I Geofoam is EPS15, Type II Geofoam is EPS22 and Type III Geofoam is EPS39. Table 11 shows the complex hyperbolic model parameters for all three nominal Geofoam densities. Table 11 includes the normalized strain parameters. The parameters in Table 11 are all very small, even up to seven orders of magnitude less than 1. These values are to be used with equations 5 and 7 to find the stress at any imposed strain assuming constant compression and no relaxation in the specimen or Geofoam block.

The value of the d parameters was used to adjust the fit for the initial tangent modulus of the Geofoam. For example, increases in d causes a steepening of the initial portion of the curve. In addition, the value of the c influences the yield stress. Higher values of c increase the yield stress on the stress-strain curve. The inputted values for the a and b parameters affect the shape of the curve at strains higher than the match point.

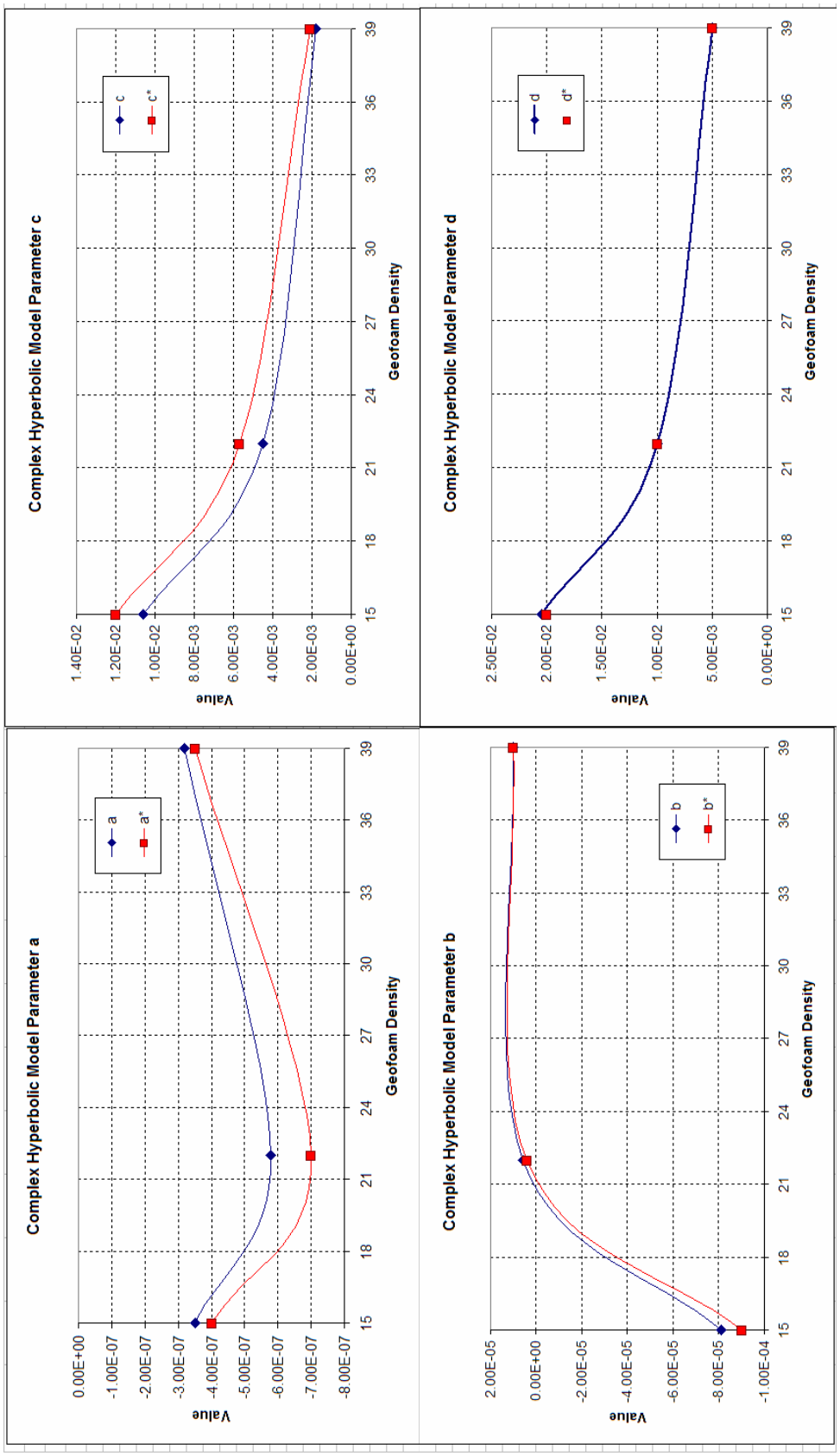

Figure 27. Complex hyperbolic model parameters as a function of EPS density

Table 11. Parameters for complex hyperbolic model

γ	a	b	c	d	a*	b*	c*	d*
15	-3.5E-07	-8.1E-05	1.06E-02	2.05E-02	-4.0E-07	-9.0E-05	1.20E-02	2.00E-02
22	-5.8E-07	6.00E-06	4.50E-03	1.00E-02	-7E-07	4.00E-06	5.70E-03	1.00E-02
39	-3.2E-07	1.00E-05	1.80E-03	5.00E-03	-3.5E-07	1.00E-05	2.10E-03	5.00E-03

The tangent modulus at any point along the stress-strain curve can be calculated for the various hyperbolic models. For the standard hyperbolic model, Equation 8 is the mathematical form. In Equation 8, E_{it} is the initial tangent modulus, E_t is the tangent modulus at any compressive stress level, σ_1 is the major principal, σ_3 is the minor principal stress.

$$E_t = \frac{b}{(a\varepsilon + b)^2} = \frac{\frac{1}{E_{it}}}{\left(\frac{\varepsilon}{(\sigma_1 - \sigma_3)_{ult}} + \frac{1}{E_{it}}\right)^2} = \left[1 - \frac{(\sigma_1 - \sigma_3)}{(\sigma_1 - \sigma_3)_{ult}}\right]^2 E_{it} \quad (8)$$

Equation 8 is the stress-strain equation differentiated. The squared term represents the amount that E_{it} is reduced at any point. At zero stress, $E = E_{it}$. At very large stress, E=0, which means that the stress-strain curve is horizontal and that there is continued strain with an increase in stress (i.e., perfect plastic behavior). Note that in the last part of Equation 8, the use of the stress ratio removes strain from the formulation. If strain is

desired in the formulation, an approximation can be made with curve-fitting techniques wherein Equation 9 should be used. In this equation, C is a constant found from curve fitting. For EPS15, C is equal to 1.75 for modulus in units of kPa.

$$E_t = E_{it} \frac{1}{1 + C\varepsilon} \tag{9}$$

For the matched double hyperbolic model, the tangent modulus is shown in Equation 10 using differentiation of Equation 2.

$$\frac{d\sigma}{d\varepsilon} = E_t = \frac{b}{(a\varepsilon + b)^2}, \frac{d}{(c\varepsilon + d)^2} \tag{10}$$

To determine the tangent modulus for the complex hyperbolic model, differentiate the stress-strain relationship for the complex hyperbolic model as in Equation 11.

$$\frac{d\sigma}{d\varepsilon} = E_t = -\frac{2a\varepsilon^3 + b\varepsilon^2 - d}{(a\varepsilon^3 + b\varepsilon^2 + c\varepsilon + d)^2} \tag{11}$$

Note that ε remains in both the complex and matched double hyperbolic formulations of the tangent modulus. In contrast, in the standard hyperbolic model, there is a failure stress which removes the need for strains in the formulation. In the complex hyperbolic

model, there is no failure stress, just stresses that lead to changes in the modulus. A comparison of Tangent Modulus between data and Equations 9 and 11 is presented in Figure 28. Figure 28 shows tangent modulus as a function of strain level. Note that the tangent modulus from the complex hyperbolic model and the data completely over-lap. The tangent modulus from Equation 9 has a slight difference from the data at strains from 1% to 2.5%.

Conclusions

EPS Geofoam specimens of two sizes and three nominal densities were tested vertically in monotonic and axial compression to large compressive strain. The test results showed that the compressive resistance of EPS is a function of its density. The test results also showed that the material undergoes significant strain hardening after yield, especially after about 30% axial strain. There are several data plots contained in Appendix B. These plots are applicable to the hyperbolic model developed and discussed in the previous section, as well as the Geofoam compression test data. In the plots, Type I refers to EPS15, Type II refers to EPS22 and Type III refers to EPS39.

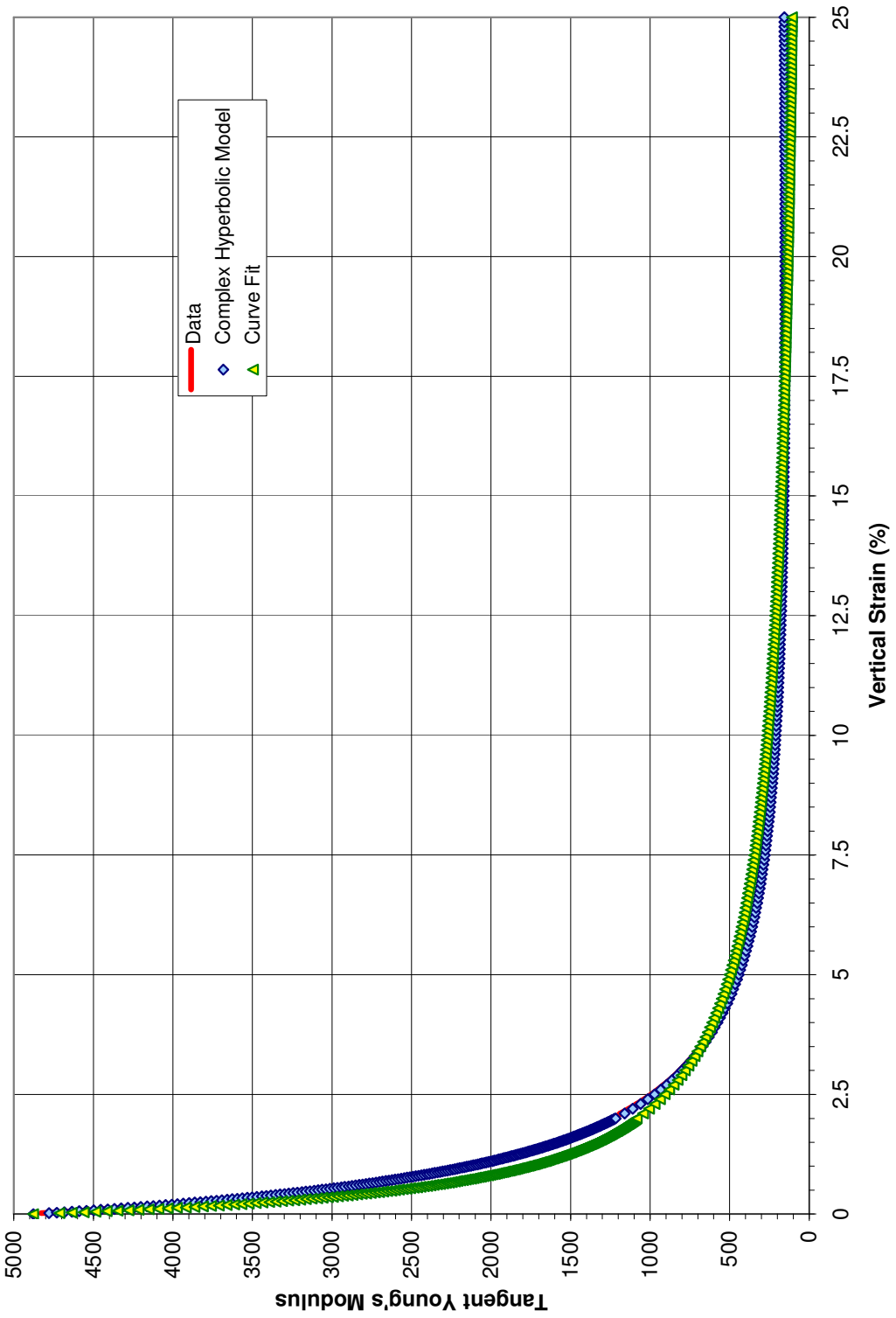

Figure 28. Comparison of Tangent Modulus for EPS15

CHAPTER 4

GEOFOAM – PIPE INTERACTION TEST

The laboratory tests thus far described have solely focused on EPS Geofoam behavior in axial compression. In this section, a bench-scale test involving the interaction between a block of EPS Geofoam and a steel pipe is described.

Objectives

The objectives of this Geofoam-pipe interaction test were: (1) to gain insight into the behavior of Geofoam in more complex loading conditions other than uniform axial compression, (2) to measure the Geofoam-pipe interaction in terms of total axial load, gross sample deformation and localized strain measurements as the test progressed and (3) to use these measurements to develop a realistic numerical model of the EPS Geofoam for this loading case. The test data obtained were used to develop a numerical model, or method, that reasonably reproduces the experimental behavior. Ultimately, these activities aided in developing an evaluation method for EPS Geofoam cover systems for buried pipelines that undergo permanent ground displacement.

Description of Test Setup

The pipe used for the test was a 101.6 mm OD steel pipe (6.4 mm wall thickness) and a 457 x 457 x 457 mm cube of EPS15 (measured density of 14.4 kg/m^3). The interaction of the pipe and the block was created by pushing the EPS block downward onto the top of the fixed pipe using a 457.2 mm square plate that was a 25 mm thick steel plate positioned atop the EPS block (Figure 29). The steel pipe was centered at the base of the block and held in position by the cross-brace of the hydraulic jack reaction frame. The Geofoam block was forced downward via a hydraulic jack while the steel plate atop the block distributed the axial load and produced a uniform, downward displacement of the top of the block. In essence, this test setup produces the same force reaction and block deformation as if the pipe was being displaced into the EPS block that is rigidly restrained on its opposing side.

Linear variable differential transformers (LVDTs) and an S-type load cell were used to measure the total vertical displacement and force developed in the system. The LVDTs and load cell were connected to a Campbell Scientific^{TM} CR 1000 data acquisition system, which was set at a sampling rate of 0.5 Hz. In addition, the LVDTs and load cell were calibrated prior to performing the test to ensure the acquisition of reliable data. In addition to the electronic sampling, a photographic technique was used to measure the localized vertical deformation pattern that developed as the test progressed. A 35 mm digital still camera and a digital video camera were positioned to record changes in the 25 mm square grid pattern that had been drawn on the face of the EPS block. These cameras were set up so that the center of their focal plane was positioned parallel with the center

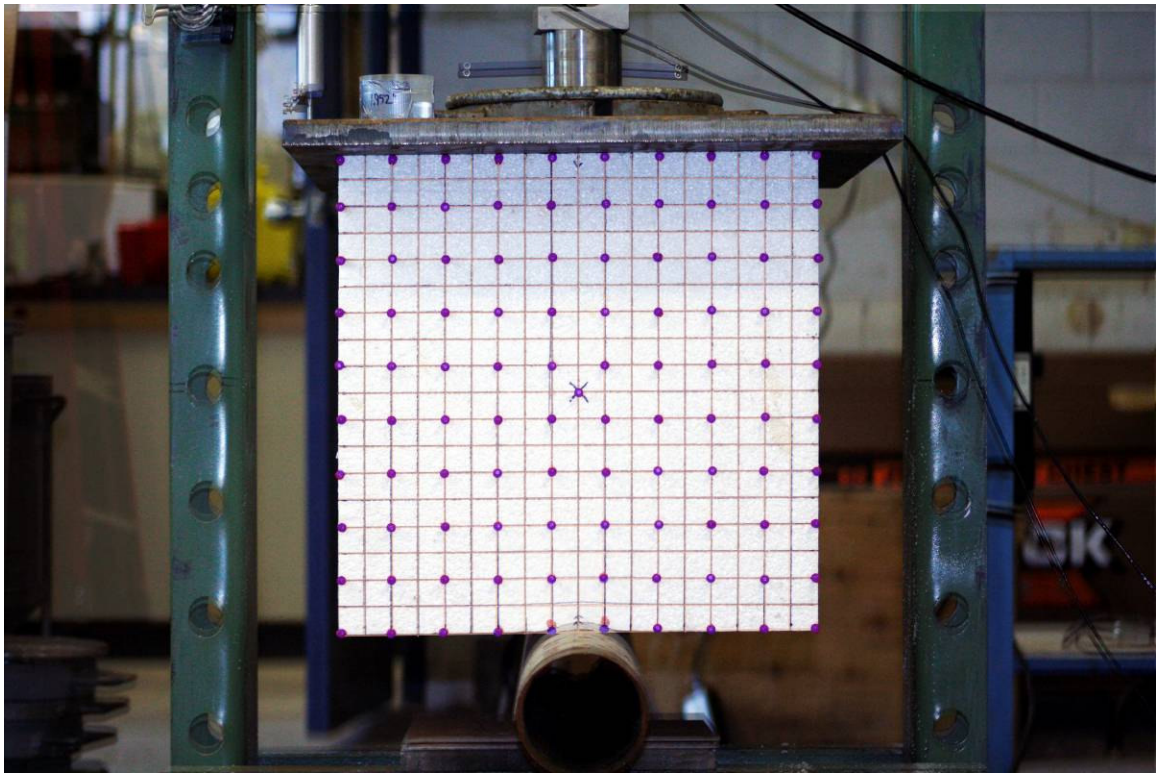

Figure 29. Beginning condition for EPS Geofoam pipe interaction test

elevation of the Geofoam block. This was done to minimize any photographic distortion of the photographed grid.

The test setup consisted of positioning a 1.2 m length of pipe in the reaction frame. The Geofoam block was then centered on the top of the pipe and was capped by the steel plate to distribute the vertical load imparted by the piston of the hydraulic jack. One LVDT was placed atop the plate near its center, and a second LVDT was placed near the edge of the plate to measure any differential displacement (i.e., rotation) of the plate as the test progressed. The load cell was positioned at center-top of the steel plate and steel cylinder spacers were used to fill the gap between the load cell and the steel plate (Figure 29).

In addition, the top of the load cell was connected to the hydraulic piston via a threaded steel rod coupler. Thus, the hydraulic jack could push downward on the load cell which in turn applied the vertical load to the steel plate placed atop the Geofoam block.

The hydraulic jack used was a pump-action that is manually operated with a lever. Prior to the test, it was affirmed that the jack could be manually advanced at an approximately constant displacement rate of about 6.4 mm per minute in a consistent manner, as measured by the LVDTs and the data acquisition system.

Pipe Load Test

A uniform square grid was marked on two faces of the Geofoam block to allow the cameras to photograph the deformation of the block as the test progressed. The grid was marked at 25 mm intervals in both the horizontal and vertical directions (Figure 29). Red push-pins were added at every other grid intersection (i.e., 50 mm spacing) to highlight the mesh on the face of the block for the photography.

The data acquisition system and video camera were started before testing began to establish baseline readings. The still camera was manually operated to record a frame every 10 seconds throughout the test. The hydraulic piston was advanced at a rate of approximately 6.6 mm per minute.

As the load was applied, the EPS block began to deform at the pipe-Geofoam contact point. In Figure 29 and subsequent photograph Figure 30, the undeformed grid pattern has been superimposed on the deformed grid pattern to give an idea of the relative movement of each grid point. The steel plate was advanced until approximately 118 mm of vertical displacement had occurred before the test was stopped. The Geofoam block

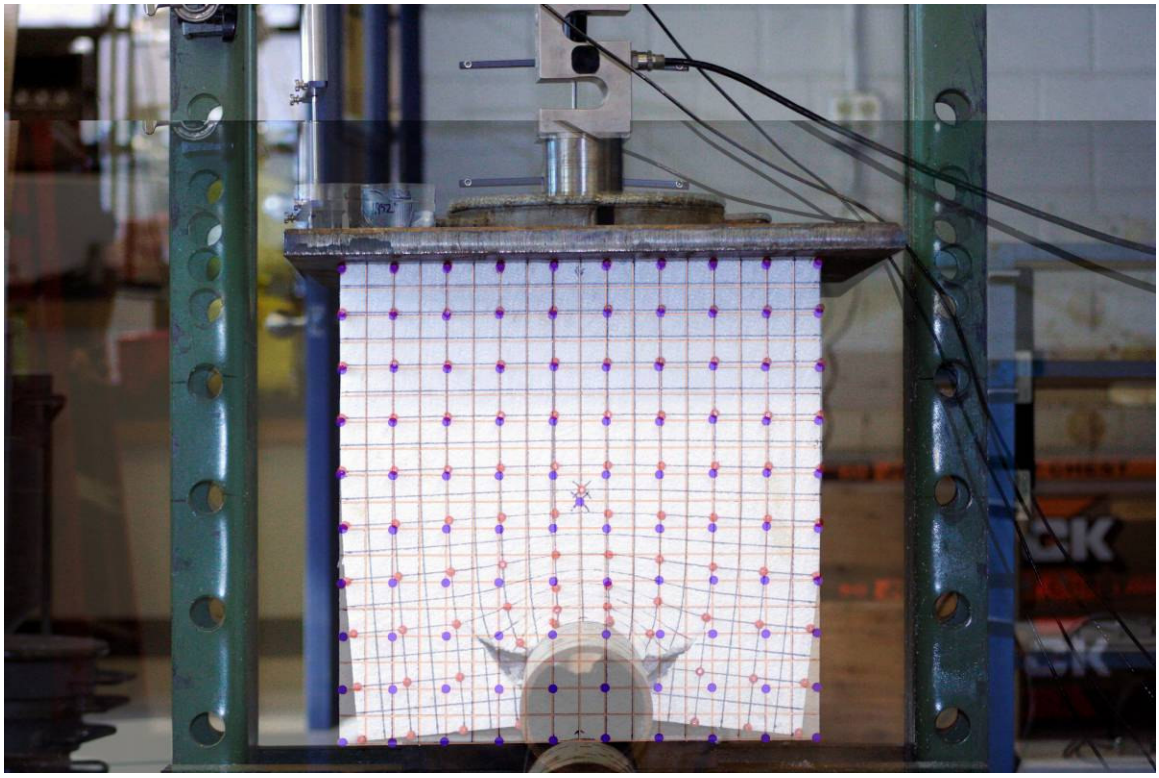

Figure 30. Deformation state of EPS15 Geofoam block after 89 mm of displacement

was not restrained on it sides, and the base of the block placed atop the pipe was free to rotate about the axis of the pipe during the test. After the test was completed, compliance testing of the load frame and load cell was done to correct the experimental data for compliance of the load frame, steel plate, loading apparatus and load cell. The corrections due to distortions of the load frame and load cell were minimal, but the displacement data were still corrected.

Test Results and Observations

As the test progressed, tensile cracks began to form after approximately 33.83 mm of advancement. The tensile cracks continued to develop throughout the test following their

initial formation (Figure 30). Note that this figure include an overlay of the original, undeformed shape of the Geofoam shown with blue dots and lines. The deformed state shows the same nodal points in red with black lines.) The cracks initiated at the interface of the pipe and Geofoam approximately 51 mm on either side of the center line of the Geofoam block. These cracks formed along the entire contact length of the Geofoam and pipe in the direction perpendicular to the photos. The test was terminated after about 118 mm of vertical displacement.

Figure 31 shows the force-displacement data collected during the pipe interaction test. The displacement at end of test, as shown in Figure 31, was 11.8 cm. The shape fo the curve is initially linear and begins to develop a hyperbolic shape with softening until a displacement of approximately 9.5 cm, when the test data experienced hardening.

Figure 32 shows that most of the compressional strain in the EPS occurred in a zone near the top and edges of the pipe. However, vertical strain can be detected throughout the block. In addition, very little lateral bulging of the block occurred along its sides; but as the test progressed, there was a slightly curling inward of the EPS block toward the pipe as seen in the lower right and left hand corners of the block (Figure 30b). Prominent tensile cracks also developed at a 45 degree angle from the horizontal where the EPS was in contact with the pipe (Figure 30b).

Vertical Load and Displacement

The data from this test were used to produce a load versus displacement plot (Figure 31). Figure 31 shows that the Geofoam compressed somewhat linearly to a vertical load of about 5.34 kN and displacement of about 23 mm (i.e., 5% axial strain).

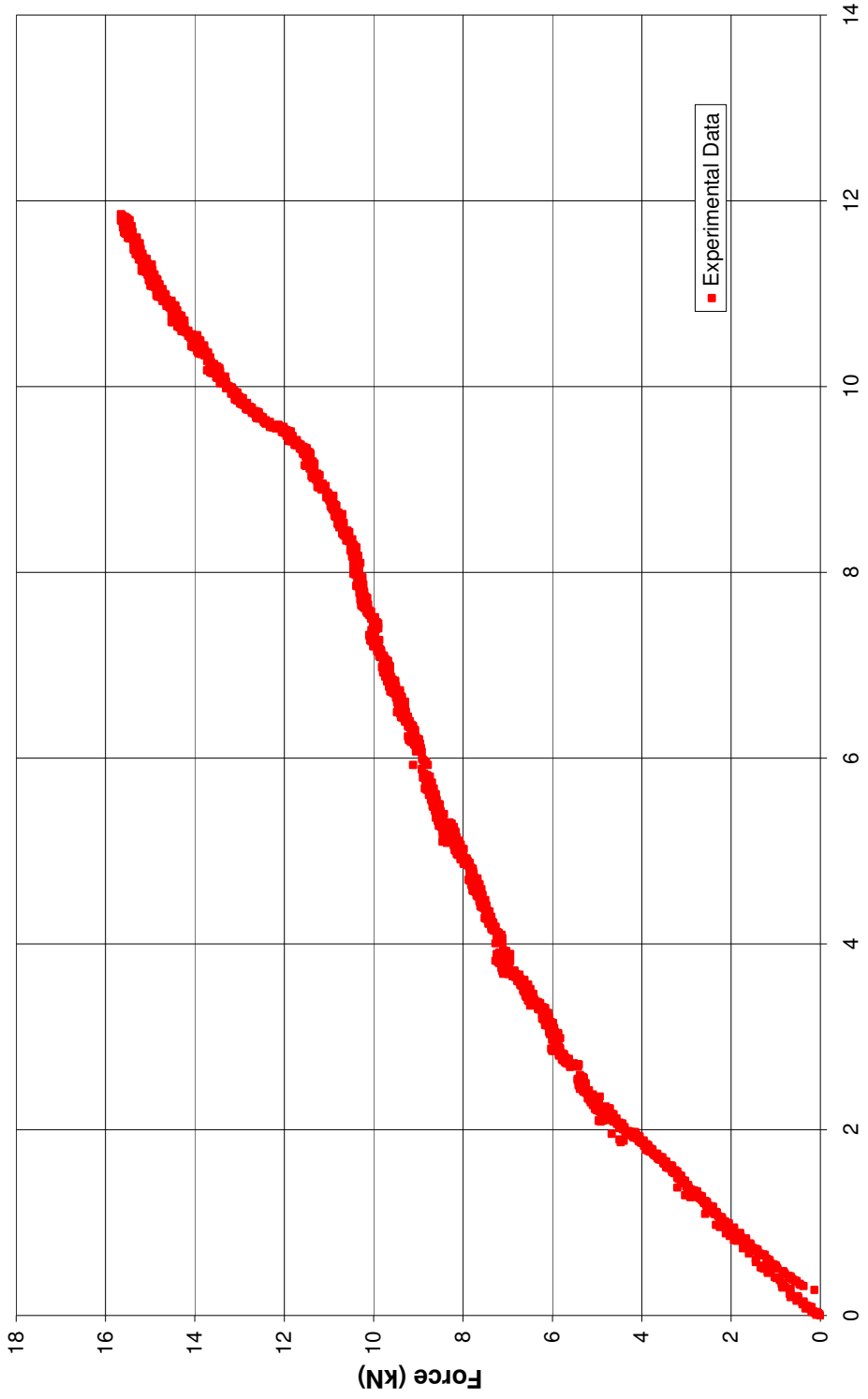

Figure 31. Force versus displacement plots of pipe interaction test results

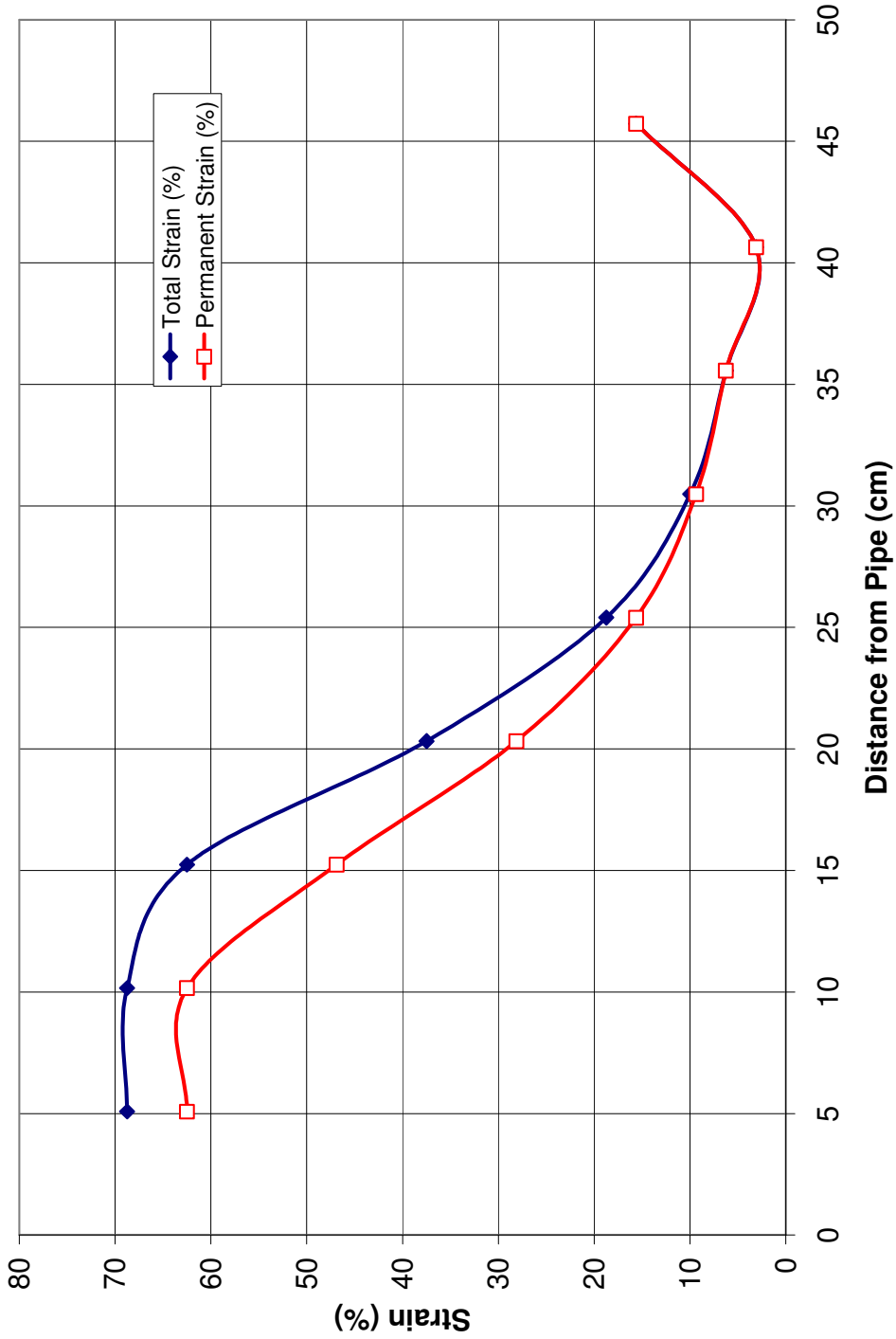

Figure 32. Localized vertical stain distribution along the vertical centerline of the Geofoam block

Following this, the behavior shows a slight strain softening. At about 92 mm of vertical displacement, the slope of the load-displacement increases, suggesting that strain hardening is occurring within the block. The test photos (Figures 30) show that high, localized strain develops in the zones near the pipe-Geofoam contact surface where the compression of the Geofoam is at its greatest. Severe damage of the EPS occurred in this zone which produces the changes in slope of the load-displacement curve, as seen in Figure 31. It appears that this zone initially softens, due to plastic behavior, and then later strain-hardens, producing the increase in load. In contrast, other regions of the block, which are further removed from the penetration zone, behaved more elastically. Thus, there are regions of the EPS that are behaving elastically, some are behaving plastically and some zones have strain hardened. This complex material behavior causes a very nonlinear behavior in the total force-displacement relation (Figure 31).

As the test progressed, tensile failure developed; hence, the localized, nonuniform strain and its influence on the overall load-displacement behavior is quite complex. Such behavior is not observed in simple uniaxial compression tests (Figures 16 and 25). A comparison of Figure 31 with these figures shows that uniaxial compression tests cannot be used to fully explain the complex deformation that results from a localized loading caused by a pipe penetration.

Final Vertical Strain Distribution

After the loading plate had finished, but prior to unloading, the vertical deformation and strain of the Geofoam block were measured. The amount of vertical displacement of the 50-mm grid was measured with a ruler and compared to photographs at a later time

(Figures 30). The vertical strain for each initial 50-mm grid on the centerline of the block was calculated as the distance at the end of loading divided by 50- mm. Figure 32 shows the localized vertical strains at 50-mm intervals along the vertical centerline of the Geofoam block. The total vertical strain for the entire block along the centerline axis was 33%. The highest strain, of about 70%, was measured near the pipe. Much of the vertical strain is concentrated in the lower 8 inches of the block. Near the top of the block, where the steel plate contacted the EPS, the vertical strains are about 5 to 15%. The block was then unloaded and the strains were recalculated at the end of unloading (Figure 32). The strains that remain represent the plastic strain of the block. The permanent vertical strain has a maximum value of about 62% near the pipe and diminishes to about 5 to 15% near the steel plate (Figure 32)

.

Numerical Modeling of Pipe Interaction Test

Understanding and predicting the force-displacement behavior of a pipe push against a Geofoam block is an important design consideration for applications where the Geofoam is placed against a pipe and is subsequently compressed by movement of the adjacent ground. Exploratory numerical modeling of the pipe penetration experimental data was done using the computer program FLAC. FLAC is an acronym for Fast Lagrangian Analysis of Continua and was developed by Itasca (2005) as a general finite-difference program used in geotechnical and mining engineering. Figure 33 shows the results of several modeling attempts as well as the experimental data.

The preliminary modeling was done using the Mohr-Coulomb constitutive model implemented in FLAC. The model properties used to obtain he FLAC results for the

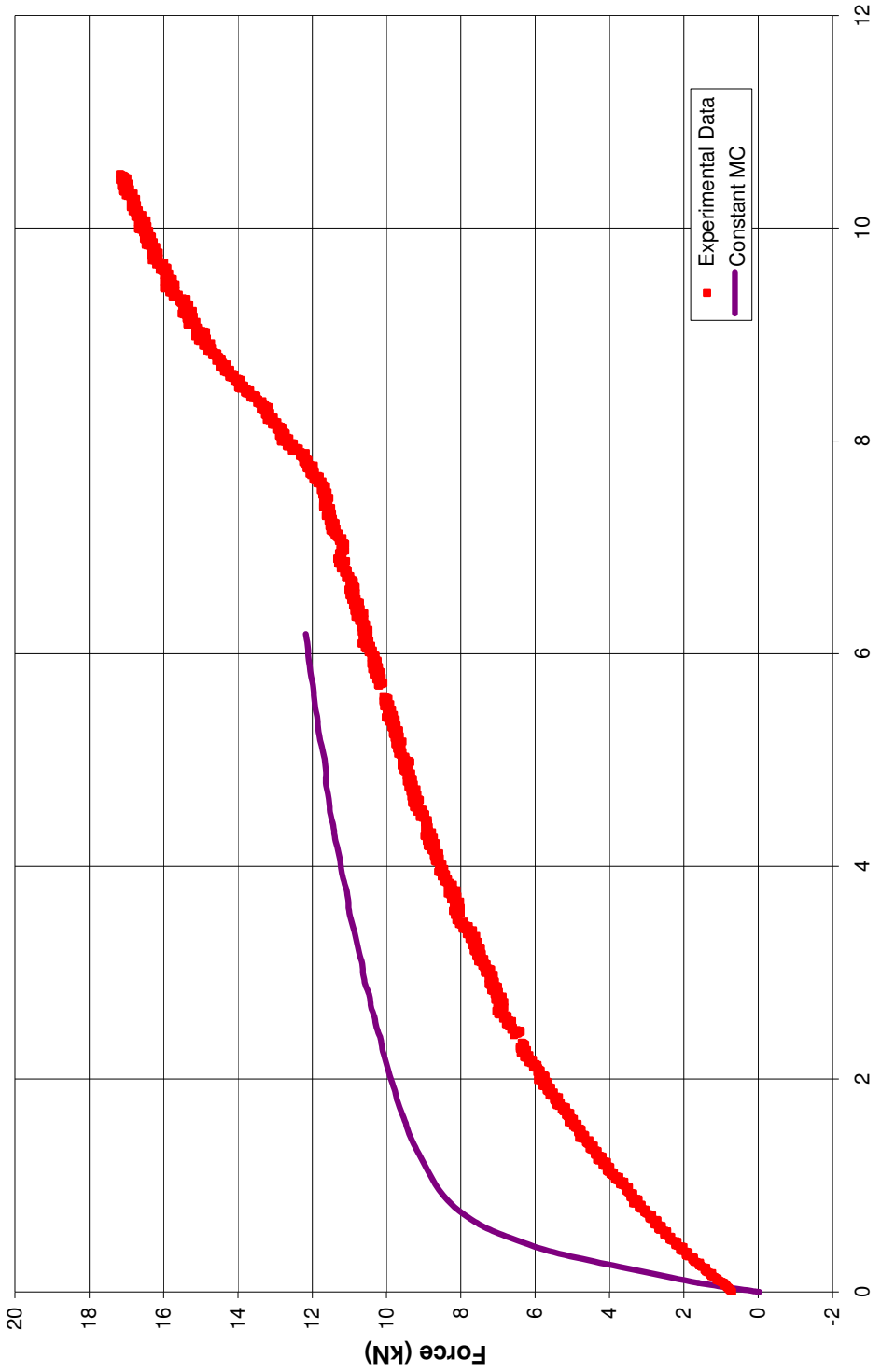

Figure 33. Force versus displacement plots of pipe interaction test and numerical modeling results

preliminary modeling are given in Table 12 and shown in Figure 33. The Mohr-Coulomb model, as implemented in FLAC, uses linear-elastic behavior for states of stress below the Mohr-Coulomb failure envelope. Upon reaching failure, a perfectly plastic material is approximated by the FLAC code for the elements that have exceeded their respective strength envelope. Figure 33 shows that the use of simple linear elasto-plastic Mohr-Coulomb material properties from EPS Geofoam testing did a relatively poor job of matching the test data. In response, several other elastic behavior implementation schemes with the Mohr-Coulomb material model were attempted.

Table 12. Mohr-Coulomb material properties for EPS Geofoam

	ρ kg/m^3	K MPa	G MPa	ϕ deg	c kPa	T kPa
FLAC model	15	1.00	1.50	0	50	200
Nominal EPS15	15	1.25	1.36	0	50	200
Softened Modulus	15	0.50	0.75	0	50	200

Because the Mohr-Coulomb material properties did not match the experimental results well, a parametric study was done to find better ways of modeling the pipe interaction problem in FLAC. A calibrated, "softened," FLAC model was completed first, where the elastic modulus in FLAC were parametrically adjusted, "softened," until a match to the experimental data was found. The elastic and Mohr-Coulomb properties for a typical EPS15 block are also shown below those used in the calibrated FLAC model in Table 12. A comparison of the various moduli shows that a reduction by about a factor of 2 was required for the FLAC model to match the experimental data. This severe of a reduction in the FLAC properties suggests that the block reached the plastic state rather quickly in the vicinity of the pipe. Thus, the FLAC softened model moduli are more representative of near-yield moduli.

In an effort to model the pipe interaction with data from compression testing, rather than using parametric curve matching, two methods of varying the elastic moduli of EPS Geofoam were attempted. The first method was to divide the stress-strain curve for EPS15 into three linear segments with constant elastic modulus (i.e., trilinear model). Figure 34 shows the three linear segments on an accompanying experimental plot. FLAC was programmed to keep the elastic moduli constant until a triggering stress was reached. After the triggering stress, the moduli were softened to the second linear segment. A second triggering stress was placed at the boundary between the second and third segments of the stress-strain curve. At the moment the stress in a FLAC zone reached the triggering stress, the moduli in that zone were then changed accordingly. Table 13 shows the moduli and triggering stresses.

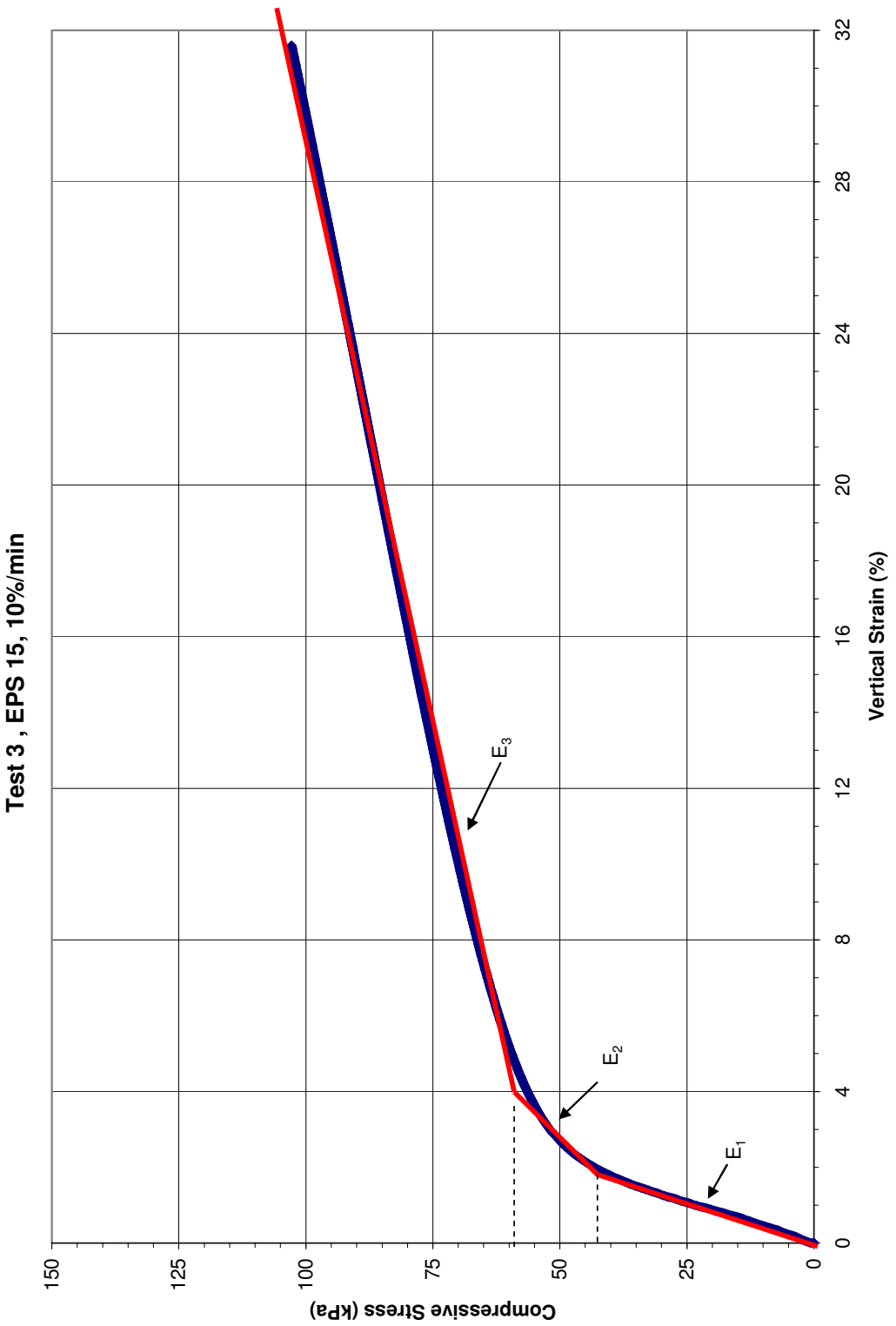

Figure 34. Trilinear modulus approach

Table 13. Trilinear modulus approach parameters

Zone ----------	Elastic Modulus *kPa*	Lower Stress *kPa*	Upper Stress *kPa*
1	3500	0	43
2	1000	43	59
3	250	59	150

Figure 35 shows the FLAC model mesh before compression. This can be compared to the photographs of the test shown previously. Figure 36 shows that the stress-based trilinear modulus did a much better job at predicting the force-displacement relationship of the pipe interaction problem than the constant elastic property model, but it did not match the shape of the curve as well as the constant elastic moduli model or the parametrically reduced modulus model.

A second attempt at modeling the curve was then attempted. This second attempt used a constantly softening nonlinear modulus based on strain in the EPS Geofoam block. The nonlinear modulus approach sets the elastic moduli initially elastic, and the same as for the constant Mohr-Coulomb model. The modulus was then made to change as a function of strain. The functional form of the reduction equation is shown in Equation 12, where K is the bulk modulus, 230 is a constant from curve-fitting, and ε is the vertical or axial strain. Note that Equation 12 is the same in form as Equation 9. The shear modulus was calculated using a constant Poisson's ratio of 0 from the results of Equation 12. Note that Equation 12 is based on Equations 6 through 11.

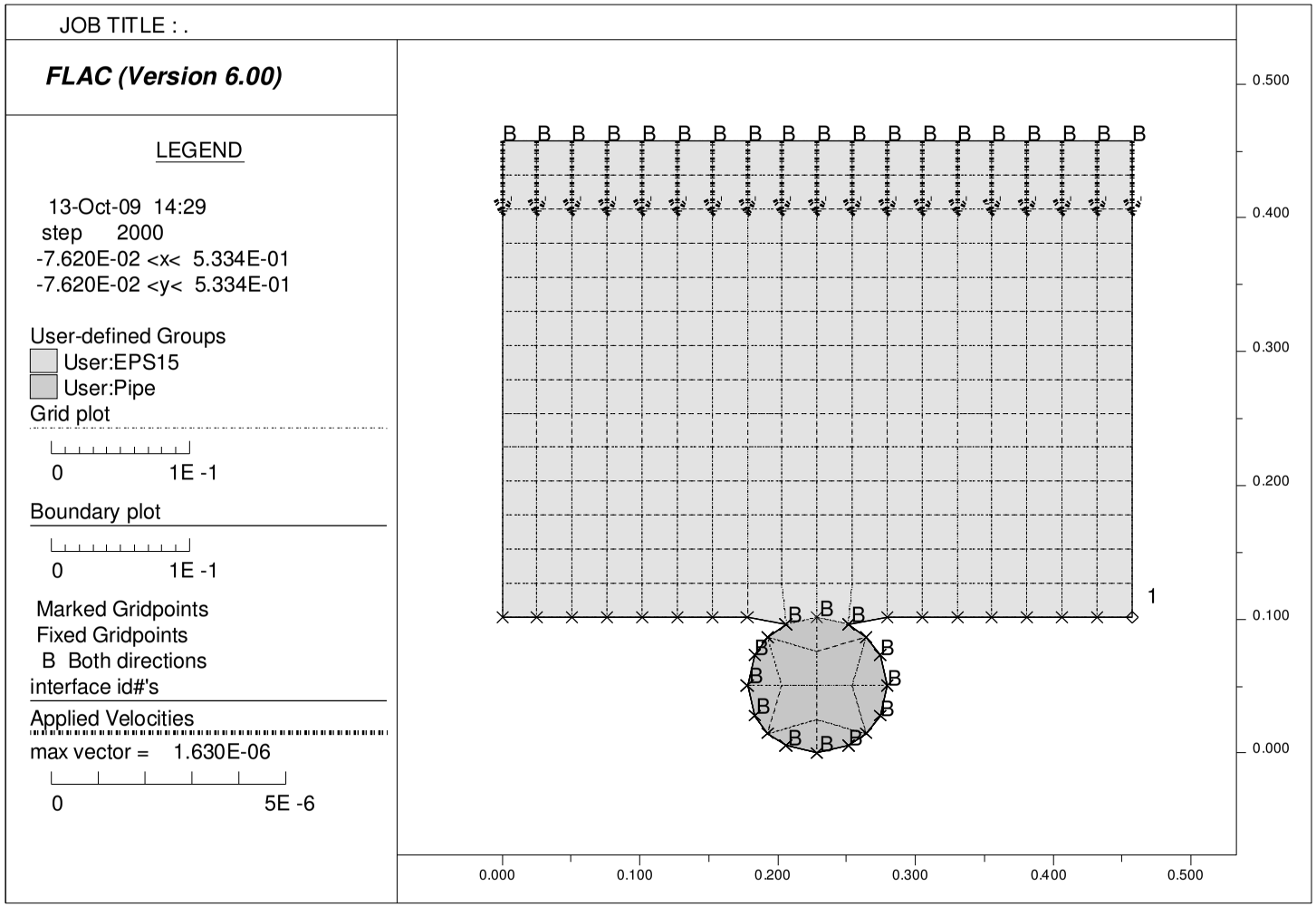

Figure 35. Initial FLAC model with 4-inch pipe fixed at the bottom

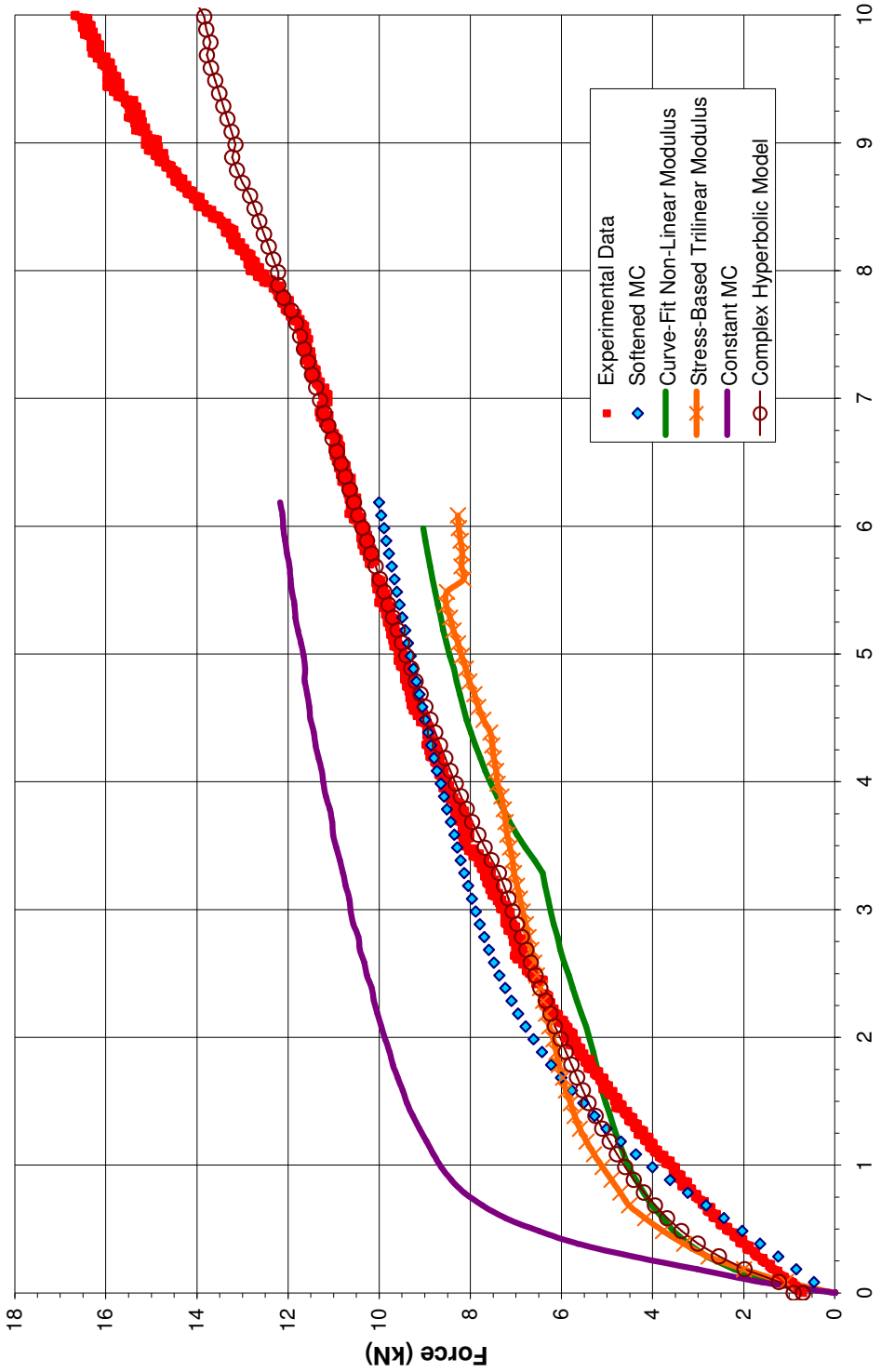

Figure 36. FLAC modeling results of pipe interaction test

$$K = K_i \frac{1}{1+(\varepsilon)*230} \tag{12}$$

The nonlinear modulus was implemented in the FLAC code as a Mohr-Coulomb material with the same failure criteria as the other models. Figure 36 shows that the nonlinear modulus did a better job than the trilinear softened modulus at matching the experimental data, although it did not perform as well as the parametrically reduced modulus.

Due to the amount of empirical fitting involved in the previous modeling attempts, a final model was attempted using the complex hyperbolic model for EPS 15 (see previous chapter for discussion of the development of this model). Figure 36 presents the modeling results for this attempt.

The FLAC model graphical output representing the pipe test is shown in Figure 37. This model has nodal points at 25 mm square spacing, which corresponded to the grid drawn on the EPS block (Figure 29). The upper boundary nodes of the model, representing the steel plate, were fixed together in both directions, so that this boundary would displace uniformly downward in the y-direction. The lower boundary of the model, where the circle is present to present the pipe, was fixed in both directions to represent a rigidly mounted pipe. The remaining nodes in the Geofoam zone of the model were free to move in both the x and y-directions.

The Geofoam to pipe contact surface was treated as a rigid-frictionless interface in the FLAC model. The properties of the pipe were set to be essentially rigid to prevent internal pipe deformation and the nodes of the pipe were fixed within the model to not allow internal movement.

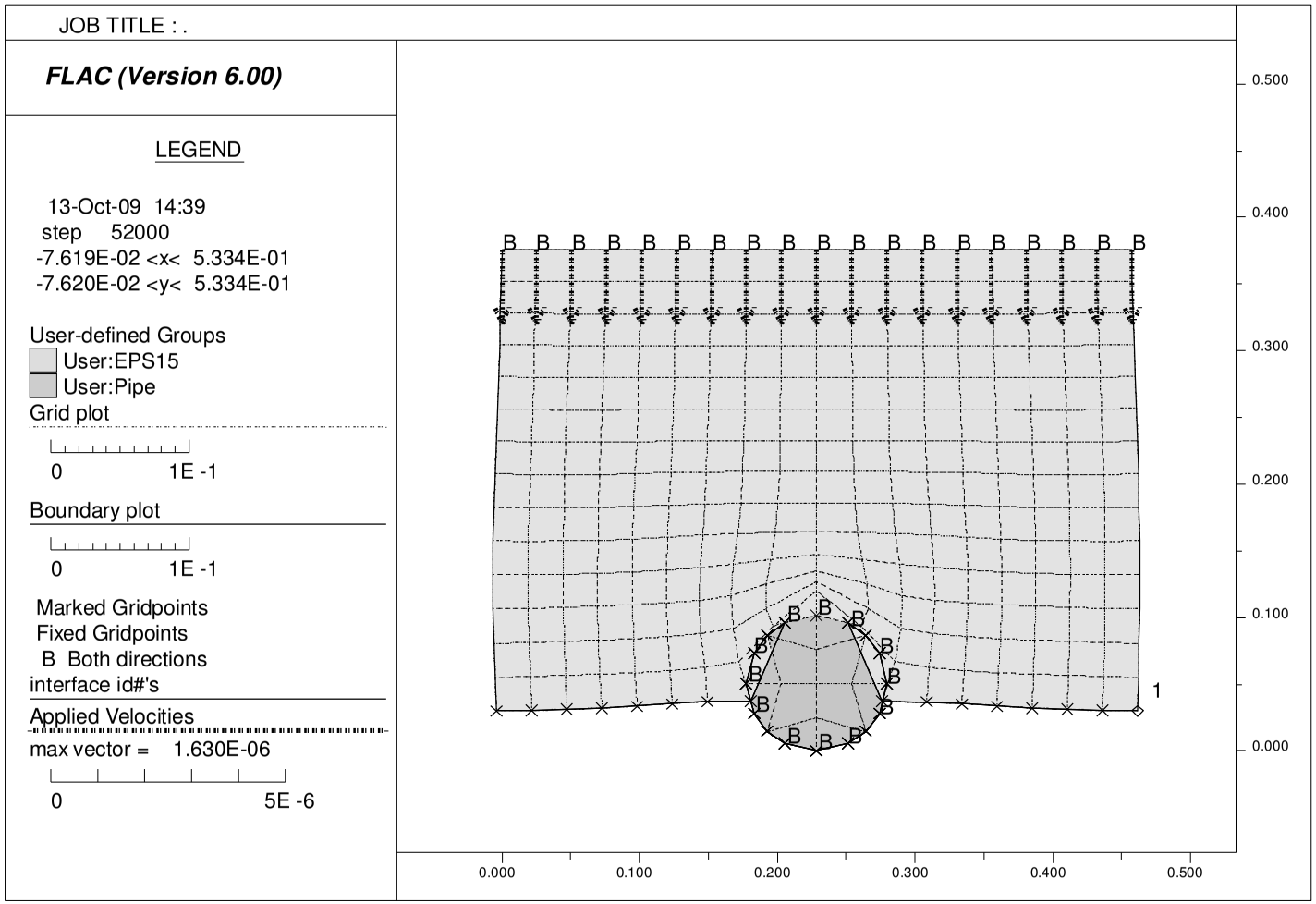

Figure 37. Deformed mesh after 81 mm of vertical displacement

The model was initiated by allowing equilibrium to be established under the self-weight of the system. Following this, displacement of the upper plate was initiated by moving the upper boundary, representing the plate, at a constant velocity. The model geometry became unstable at 81 mm of displacement; thus, a velocity of $1.00e^{-6}$ was applied to all the nodes that form the top boundary of the model in order to allow unbalanced forces to equalize in the model.

Modeling Results

The total vertical load carried by the EPS block was calculated by summing the vertical nodal forces for all nodes in the Geofoam block at each time step (Figure 35). The displacement for this figure is the displacement of the top center node of the mode, which represents the center of the downward moving plate. The FLAC model can reasonably replicate this behavior, until the model becomes unstable (i.e., tensile failure of the Geofoam near the pipe causes the nodal geometry to become too deformed to continue the calculation). Figure 36 shows all the modeling attempts using the various constitutive models.

From an examination of Figure 36, the relations producing the best fit to the experimental data were the complex hyperbolic model and the softened Mohr-Coloumb model. The curve-fit and trilinear modulus approaches worked better than the constant Mohr-Coloumb model, but had deficiencies at larger displacements. The comparison shows that the best method of modeling EPS Geofoam interacting with a pipe in direct compression is to use the complex hyperbolic model that incorporates the nonlinear elastic behavior of the Geofoam as well as its strain hardening behavior at larger strains.

Figure 37 shows the modeling results after 81 mm of vertical displacement. The deformed shape reasonably represents the experimental photo (Figures 30); however, near the end of the computer run, as the pipe was making full penetration into the Geofoam, the outer face of the block expanded slightly outward in the bottom one-half of the model. In contrast, the observed Geofoam behavior did not expand outward (Figure 30), suggesting that the bulk modulus model parameters and/or the constitutive relations are somewhat deficient. Nonetheless, the force-displacement and strain distribution obtained from this test are reasonably represented by the FLAC model using the complex hyperbolic constitutive relation.

Conclusions

The results of the Geofoam-pipe interaction test showed that the interaction of EPS with a penetrating steel pipe is a nonlinear problem that involves strain softening and ultimately strain hardening. The compressional strain in the Geofoam block concentrates near the Geofoam-pipe interface and spreads through the Geofoam mass in a complex, nonlinear manner. Ultimately, tensile failure occurred in a zone of highly localized compression that occurs near the top of the pipe. This type of behavior was not seen in simple axial compression tests of Geofoam, where high, nonuniform stress concentrations were not developed.

The Mohr-Coulomb material model, as implemented in FLAC, can be calibrated to match this behavior. However, the elastic material properties (i.e., bulk and shear moduli) must be significantly softened to approximately 50% of their initial values, or be softened with a continuous function based on stress or strain. Also, the Mohr-Coulomb

model cannot be used to represent strain-hardening at higher compressive strains. A model that includes an initial elastic range, a plastic range and a strain-hardening range is required, such as the complex hyperbolic model developed in Chapter 3.

CHAPTER 5

LATERAL SOIL-GEOFOAM-PIPE TESTS

A series of experiments using a 171.5 mm OD steel pipe were conducted to obtain the force-displacement behavior for pipe horizontal movement interacting with EPS block. For this series of tests, the steel pipe was pushed laterally in a box that included various backfill and cover configurations. These tests were done to explore the benefits of using EPS as a compressible inclusion against a pipe undergoing horizontal displacement. The primary goal of the research described in this chapter was to measure the reduction in stress on the pipe for the various cases and to later use this information for numerical modeling of the interaction. Four full-scale experiments were conducted at the University of Utah's Department of Civil and Environmental Engineering in the Summer and Fall of 2008.

Experimental Setup

A self-contained test system (i.e., trench box) was locally manufactured for the experimental program. This test system included a loading device, reaction system (i.e., reinforced external walls of the box), a load device (i.e., actuator), a test chamber for the soil-Geofoam interaction testing and the required instrumentation for measurements.

Test Box Setup

A steel box was constructed for the University of Utah by Knox fabrication of Salt Lake City, Utah. The box's overall dimensions were 5.34 m long, 1.83 m wide and 6 1.83 m high (Figure 38). The box was constructed of 6.35 mm thick steel plates. The horizontal load capacity of the box was approximately 111 kN. Both ends of the trench box were reinforced and braced with structural steel to withstand the forces involved in the experiments and to minimize the reaction deflections of the ram against the wall. A reinforced door was constructed on one end, which allowed side entry into the box. The top of the box was also left open; this allowed for sand to be placed in the box from above.

Internally, the trench box was divided into two chambers by a 10 mm thick steel partition wall (Figure 39). The smaller chamber houses the actuator and is 2.13 m long. In the smaller chamber, the actuator reacts internally against the end wall of the steel box. Three struts extended from the actuator, through the partition wall, into the second or test chamber. Thus, the actuator imposes the horizontal force on the pipe via these steel struts that extend into the second chamber. Both chambers were 1.83 m wide. The second chamber was 3.14 m long and houses the pipe, Geofoam and sand backfill used in the test program. In this chamber, a 171.5 mm O.D. steel pipe was welded onto the struts. This allowed sand and EPS Geofoam to be placed around the pipe, and the pipe to be pushed laterally into the backfill system. The center of the pipe rests 0.457 m above the bottom of the box, which produces a height to pipe diameter ratio (H/D) of 10.

Figure 38. Photo of steel trench box used for lateral tests

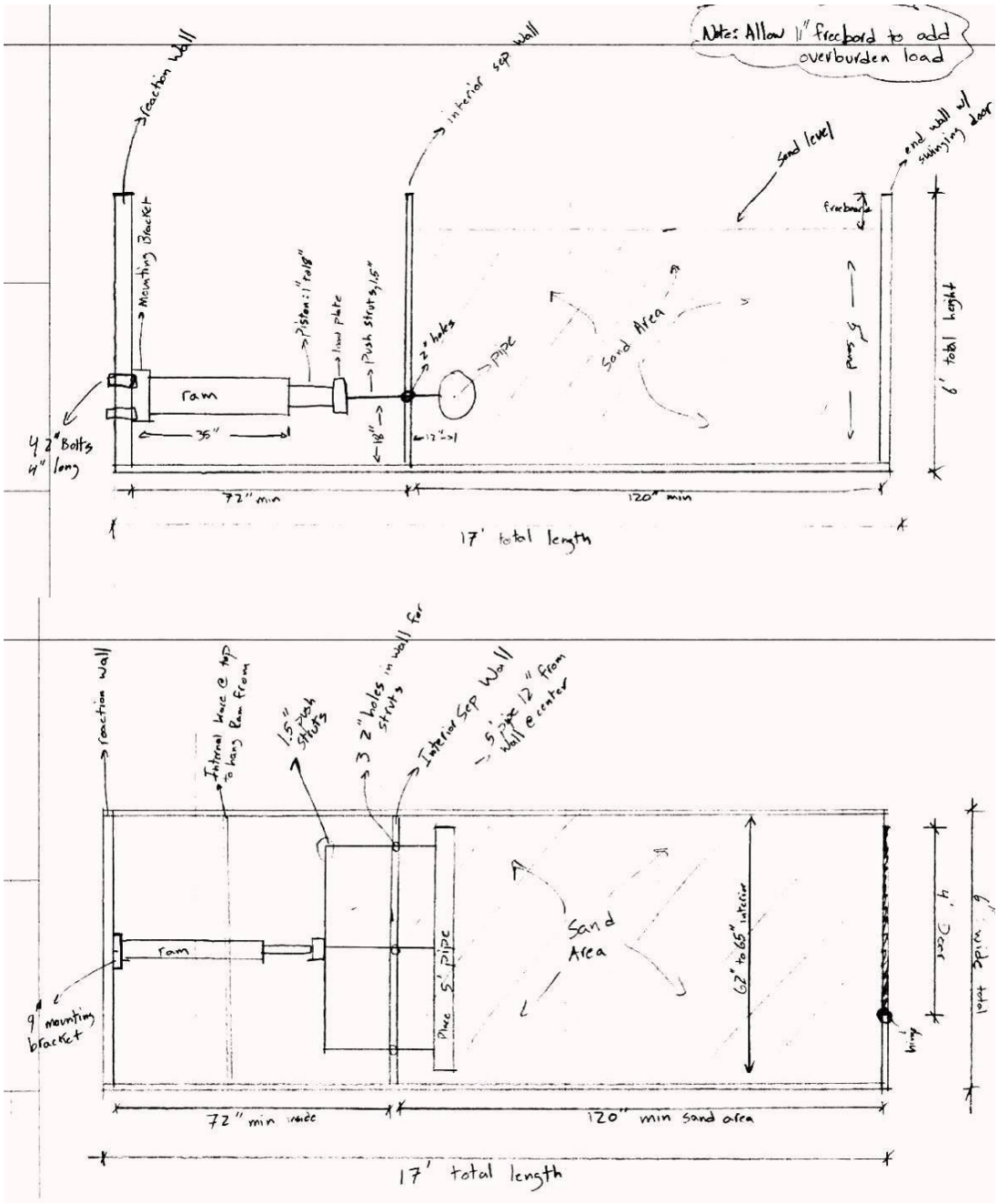

Figure 39. Sketch of steel trench box section and plan view

Materials

In the trench box test program, only two materials were used as backfill material: sand and EPS block. Both were chosen for their relatively uniform properties which aided repeatability between tests and in the numerical modeling of the test results. Also, sand is typically used as a backfill soil in pipeline trenches.

EPS Geofoam

EPS15 was used exclusively for these experiments as it is more compressible than higher density Geofoam. High compressibility is desired for compressible inclusion applications to reduce lateral forces on a pipe when it is pushed into a sidewall of the trench lined with EPS. The properties of EPS15 were obtained from the laboratory testing described previously, The EPS15 blocks were obtained from ACH Foam Technologies of Salt Lake City, Utah. The blocks used for tests 1 and 3 measured 608 x 608 x 1828 mm. The foam blocks used for test 4 were 608 x 914 x 1828 mm. The long dimension of the blocks was purposely slightly undersized to allow for sliding between the block ends and the side walls of the trench box. This produced a relatively low frictional boundary condition. Silicone lubricant was sprayed on the trench box side walls and floor, and two layers of plastic sheeting were placed against the side and end walls to reduce frictional effects. This is the method recommended by Tongon et al. (1999), who studied the best way to reduce boundary effects for chamber tests with pipes.

Sand Backfill

Loose, well-graded sand was used for the tests (Figure 40). The sand was a standard ASTM C33 fine aggregate. This sand was angular and rough. The gradation was defined by 100% passing the 3/8 inch sieve and 2.5% fines (i.e.,% passing the #200 sieve). Figure 40 also shows D_{10}, D_{50}, and D_{60} for the backfill sand. The fines were nonplastic. The sand was dumped through the top of the box by a skid steer, hand-placed and compacted with a vibrating plate compactor to an average dry density of 16 kN/m^3. The average in place moisture content was 2.5%. The average total unit weight of the sand was 16.42 kN/m^3.

Procedures

The experimental procedures for this testing program are as follows: (1) before any sand is placed in the sand chamber of the test box, the hydraulic ram was moved back to its initial position, (2) the sensors were recalibrated and (3) the pipe and push rods were all leveled and in-plane. The pretest position of the pipe in the trench box is shown in Figure 41.

The sand was placed in 150 to 200 mm lifts. Thus placed, the sand was in a loose condition. The lifts were made uniform by shovel spreading and subsequently compacted using a vibrating plate compactor. Following compaction, the in-place density of the sand was measured with a Troxler^{TM} nuclear density gauge. The water content of each lift was also checked with the density gauge. This particular gage provides estimates of the total unit weight, dry unit weight, and moisture content for each test. The rod was extended

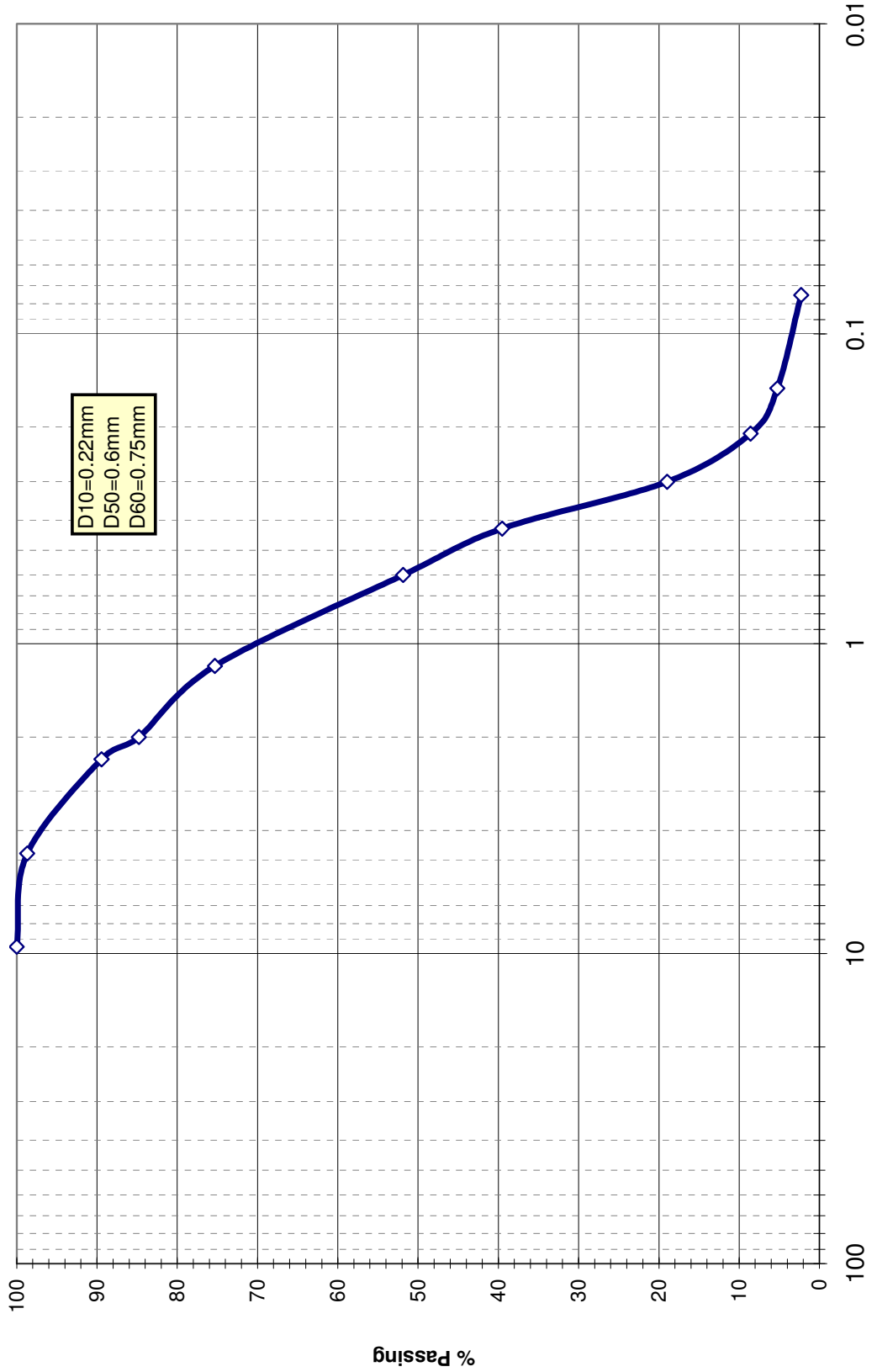

Figure 40. Gradation of C33 sand used in trench box

Figure 41. Initial position of pipe in trench box before sand placement

200 mm into the soil for each lift; except for the initial lift, where the rod was extended 100 mm. Each lift was checked with 5 tests at random locations. To avoid interference with the steel walls of the box, no tests were conducted within 150 mm of the walls. Figure 41 shows the test box sand chamber before any sand or Geofoam is placed. Note the pipe supported by three stiff rods coming through the partition wall.

When the sand had been brought up to the appropriate level, the sand was carefully leveled (raked) and the EPS bocks were placed in direct contact with the pipe. Placement

of sand and foam was done until sand was within 152 mm of the top of the box (Figure 42). The top sand surface was marked with paint in a uniform grid.

An elevation survey was done on these painted surface points so that they could be compared with the posttest elevations to determine the amount of heave and/or subsidence. The survey instrument was a Sokkia self-reading level that has an accuracy of ± 0.1 mm, with repeated measurements. The points were surveyed in a referenced pattern for comparison between pre and posttest. Survey was taken in reference to a benchmark.

Following box preparation, the equipment in Appendix E was readied. The equipment includes the hydraulic ramp and data acquisition. Appendix E details the attributes and specifications for all test equipment. The test data were constantly sampled by the data acquisition system using a laptop that was running on an noninterruptible power supply. After the test was completed, the grid points atop the sand were resurveyed. Figure 43 shows top surface and grid points after completion of a test, as well as the developed cracking pattern.

Following the survey, the ram was retracted to its pretest position. The sand was excavated out of the box and the Geofoam blocks were removed for examination. The data from the various instruments were then imported into MS Excel™ for data processing. The VW pressure cell data were also imported into Excel™ and included with the automatically retrieved data.

Figure 42. Completely filled trench box with survey grid ready for testing

Figure 43. Posttest photograph of top of box and developed cracking pattern fissured sand after testing

Testing Program

The testing program consisted of 4 tests with differing configurations. The objective of the program was finding the most efficient system for a soil-Geofoam backfill system. The first test was configured with a single 610 x 610 x 1828 mm EPS15 block placed along the side of the pipe. The block was positioned so that the center elevation of the 171.5 mm OD steel pipe was at the center elevation of the EPS block. This first test investigated the efficiency of a conceptual system that had been modeled previously in FLAC3D^{TM} by Bechtel Corporation. The second test was the baseline experiment for the testing program. Because it consisted solely of sand backfill, the effectiveness of other configurations could be compared with the base case. Also, the results from the second test were compared with the results obtained by Trautmann and O'Rourke (1984) for pipes pushed laterally into sand. The third test was a double Geofoam block configuration. For this test, two 610 x 610 x 1828 mm EPS15 blocks were placed side-by-side adjacent to the pipe; thus, the pipe was pushed laterally into 1.22 m of EPS15. The rationale for this configuration was to see if the thickness of the compressible inclusion had a significant impact on the load-displacement behavior. (It was thought that a thicker compressible inclusion would allow for a softer loading behavior and delay the strain hardening behavior that was seen and described in the test program conducted in the previous chapter.) The fourth test was based on a different concept for reducing the pipe stresses. Instead of using a compressible inclusion in the side wall of the trench; this test sought to achieve lower horizontal soil resistance by minimizing the weight of the cover system (Figure 44). Thus, it was devised to test a light-weight cover system instead of a compressible inclusion. The goal of this configuration was to use EPS as a

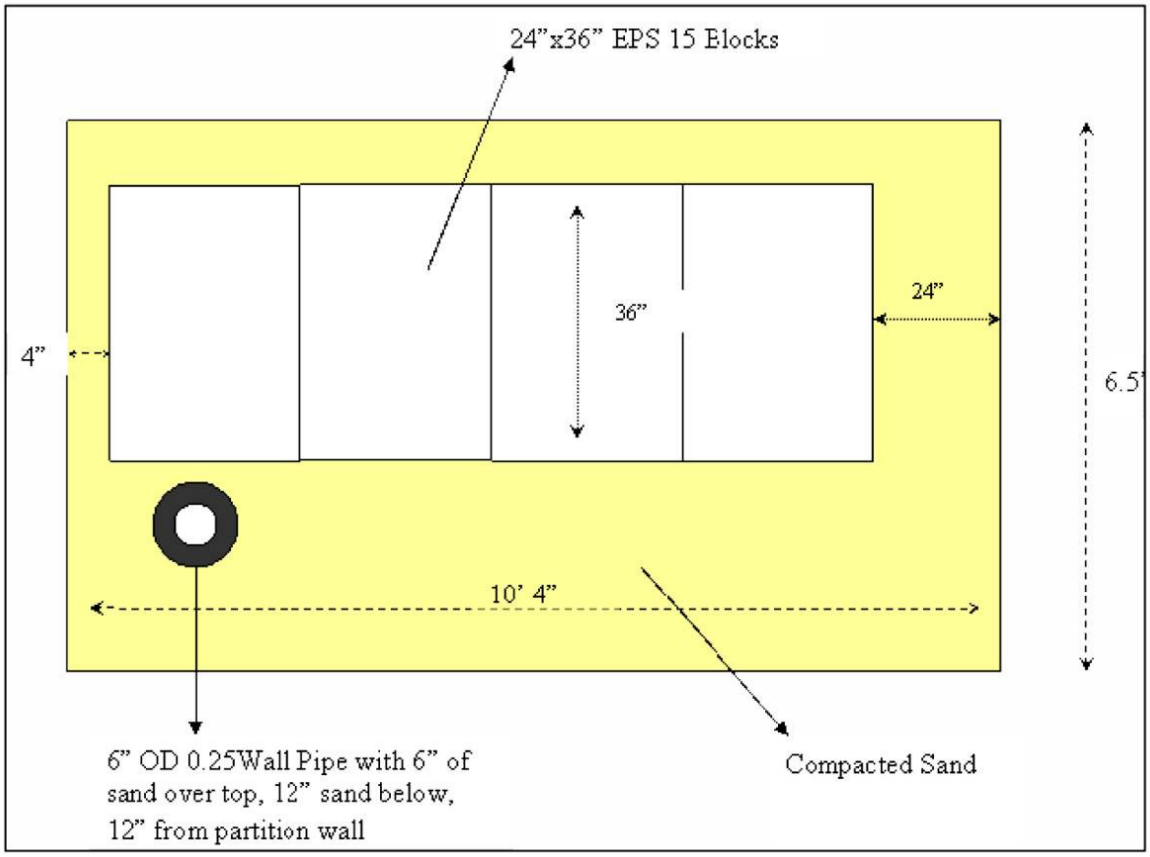

Figure 44. EPS block layout for test 4

super light-weight cover system and effectively reduce both the vertical and horizontal earth pressures that act on the pipe as it is pushed horizontally. Because of this, the stiffness and shear strength of the back sand placed adjacent to the pipe would be reduced significantly, thus allowing the pipe to displace more easily through the backfill and reduce the total load transferred to the pipe. The idea being to simulate very shallow embedment for a geometry that has a deep embedment. Shallow embedment has long been known to be an effective mitigation technique for fault crossings.

Lateral Movement Experimental Results

The data from all four tests have been normalized for comparison purposes. The total force measured by the load cell attached to the actuator was normalized and made dimensionless by dividing the total load by the product of the pipe's length, diameter, depth of embedment and the total unit weight of the sand backfill. The total displacement of the pipe can be made dimensionless by dividing this displacement by the diameter of the pipe. These normalizations were introduced by Trautmann and O'Rourke (1984) and are done in this report. Other load displacement plots presented in this chapter have not been normalized.

Test 1 – Single 610 mm Block Placed Adjacent to Pipe

Figure 45 shows the force-displacement curve for test 1. In addition, this figure shows the earth pressures that developed in the soil mass at 4 locations at the same total displacement of the pipe. The earth pressure cells were arranged so that the horizontal pressure that developed immediately behind the Geofoam was measured. Two cells were positioned 1 foot behind the block at two locations. In addition, the horizontal pressure that developed at a distance halfway between the EPS15 block and the box back wall was measured, and the horizontal pressure near the back wall was also measured. However, unfortunately, a short occurred in the cable for the sensor placed near the back wall which produced erroneous readings and these data were rejected.

The peak horizontal load from test 1 was 123.7 kN and occurred at a displacement of 280 mm. (This peak load and its displacement convert to a normalized force of 16, and a dimensionless displacement of 1.65.) The peak stress between the EPS15 block and the

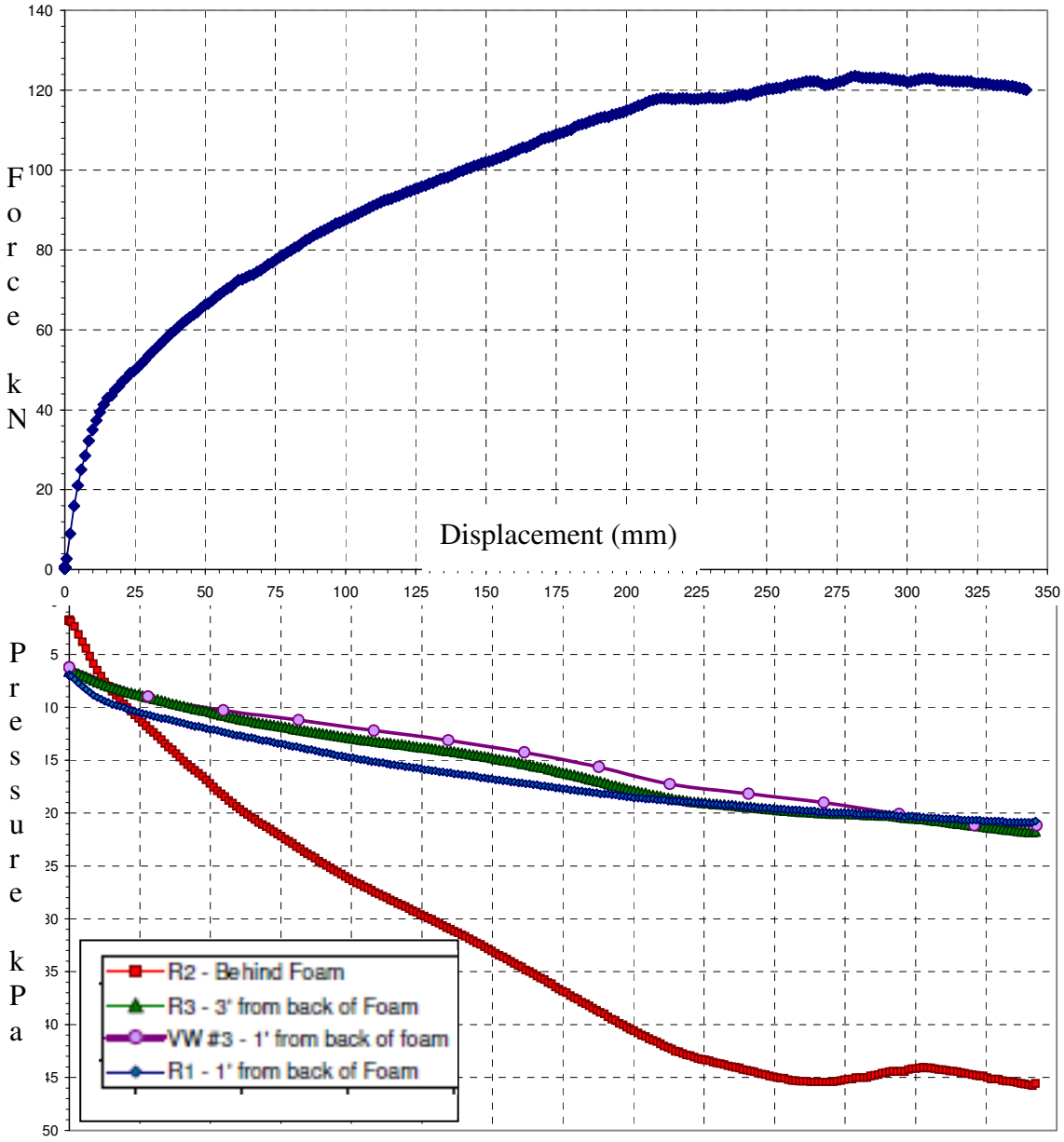

Figure 45. Force versus displacement (mm) and horizontal pressure (stress) plots results for test 1 – single EPS block against pipe with sand backfill

sand was 45.5 kPa at a pipe displacement of 266.7 mm. The peak stress 305 mm behind the block decreased to 20.6 kPa at a pipe displacement of 330 mm, and the peak stress midway between the block and the back of the test box was 21.8 kPa at 343 mm of pipe displacement.

The shape of the force-displacement curve for test 1 has a typical hyperbolic shape similar to the shape of the force-displacement curves for loose sands and/or normally consolidated clays.

The shape of the curve does not, however, resemble those published by Trautmann and O'Rourke (1984). The peak normalized force and dimensionless displacements also do not compare favorably to those developed by Trautmann and O'Rourke (1984). The curve presented here is higher than the loose sand curves developed by these researchers. In the first test, the total pipe force reached a higher peak than was expected. The peak force was much larger than Trautmann and O'Rourke (1984) curves for loose to medium dense sand. This lead to the need for a baseline test with only sand for comparison.

Test 2 – Sand Backfill Only

Test 2 was performed with sand backfill and bedding. This was the baseline case for comparison with literature and the other tests in the program. Figure 46 shows the data and results for this configuration including lateral pressures that developed within the sand backfill. The earth pressure cells were arranged in test 2 such that the pressure was measured at 305 mm, 610 mm, and halfway to the backwall behind the pipe. The pressure on the chamber backwall was also measured.

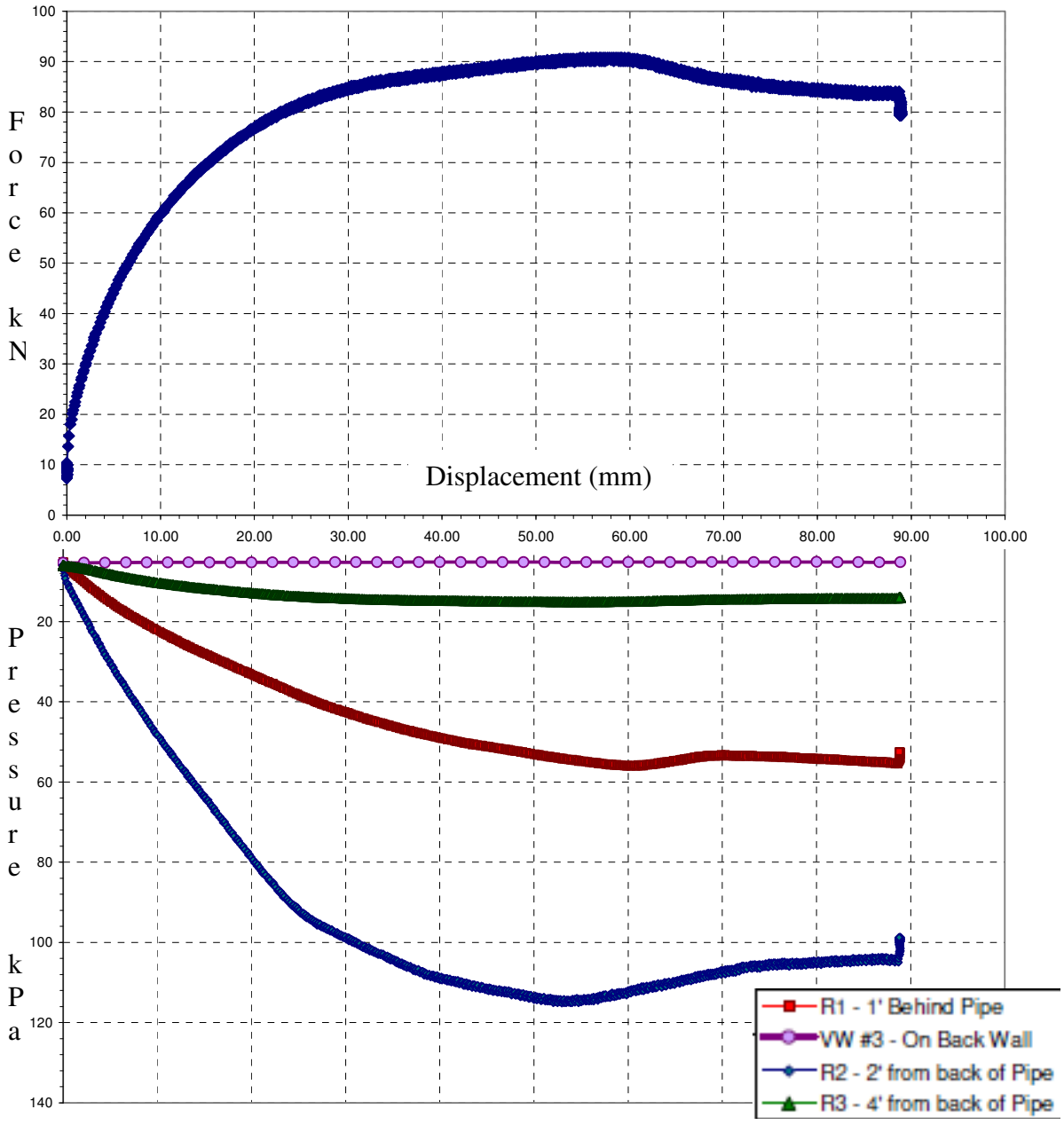

Figure 46. Force versus displacement (mm) and horizontal pressure plots for test 2 - pipe with sand backfill

The shapes of the force displacement and pressure displacement curves are similar to those seen for medium dense sands and heavily over-consolidated clay having a decrease in force or stress after a peak that occurs at a relatively small displacement. In test 2, the peak load measured by the force load cell for the pipe was 90.7 kN at a horizontal pipe displacement of 57.2 mm. The peak earth pressure, measured 305 mm behind the pipe, was 115 kPa at 54 mm of horizontal displacement. The highest horizontal earth pressure measured 610 mm behind the pipe was 56 kPa at a pipe displacement of 63.5 mm.

Halfway between the pipe and the back wall, the peak horizontal pressure was 15.1 kPa at a horizontal pipe displacement of 56 mm. There was essentially no change in horizontal pressure measured along the back wall compared to the start of the test, indicating that the failure plane for the sand came upward well before encountering the trench box back wall.

The peak results for test 2 produced a normalized force of 11.8 at a dimensionless displacement of 0.33. The results compared fall somewhere between the Trautmann and O'Rourke (1984) results for medium dense sand with a cover ratio of 5.5 and loose sand with a depth of cover ratio of 11. Note that the 1984 research used a smaller pipe and test chamber, which may contribute to difference between the experimental results.

Test 3 – Two 610 mm Blocks Placed Adjacent to Pipe

In test 3, two 610 x 610 mm EPS15 blocks were placed adjacent to the pipe which provided a 1.22 m EPS15 compressible inclusion for the pipe. It was thought that this larger compressible inclusion would allow for more horizontal displacement before reaching the peak force. Figure 47 shows the force-displacement and pressure-

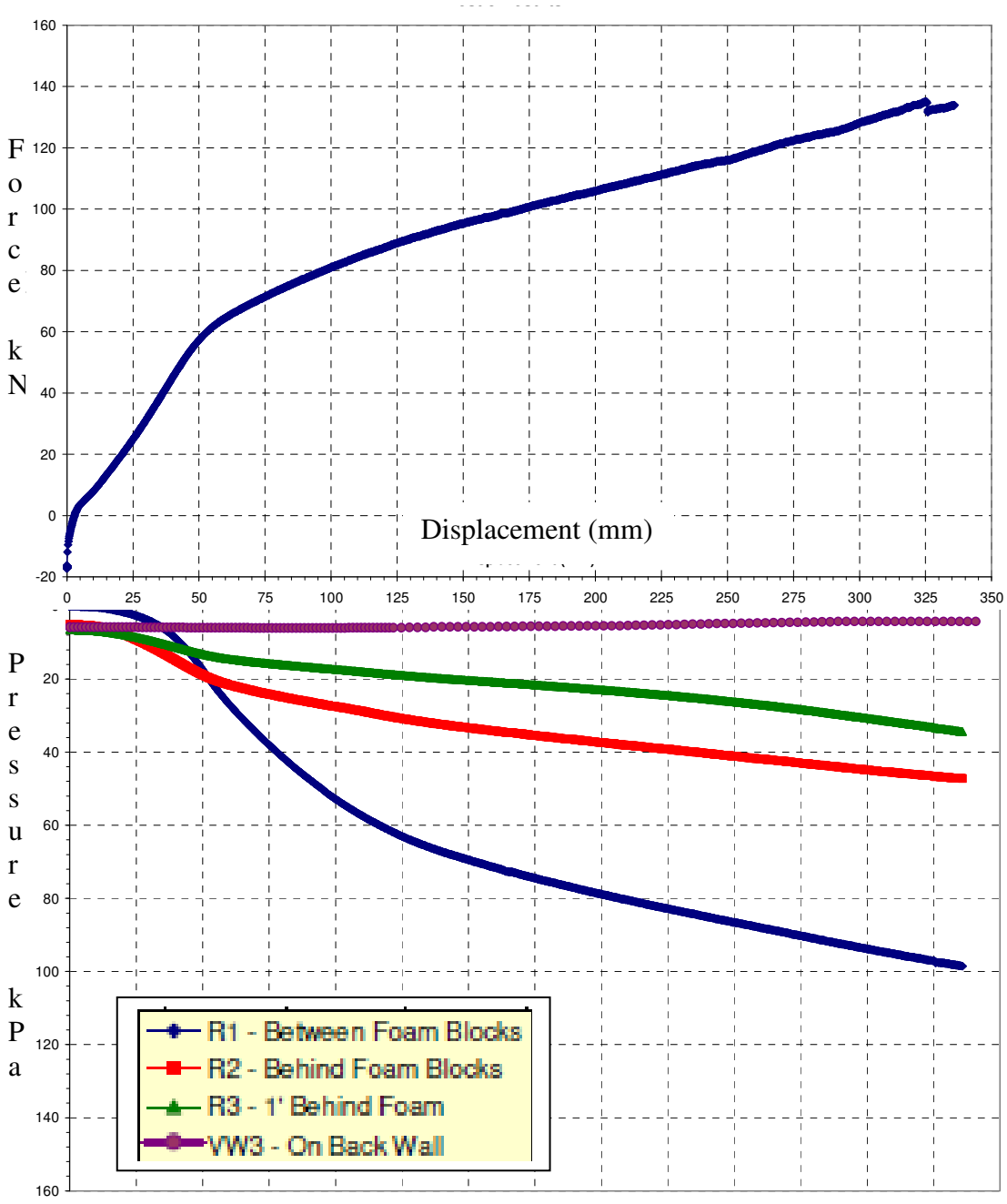

Figure 47. Force versus displacement and horizontal pressure plots for test 3 – two EPS block against pipe with sand backfill

displacement curves for this configuration. The earth pressure cells were arranged in test 3 so that the horizontal pressure between the Geofoam blocks was measured. This was done to see if this configuration effectively decreased the horizontal stresses produced by the pipe at the same location measured by test 1.

The horizontal pressure just behind the second block was measured at a distance which was halfway between the back of the second block and the trench box back wall. The horizontal pressure along the back wall of the box was also measured.

The shape of the force-displacement and the pressure-displacement curves in Figure 47 are dissimilar to those published for sands or clays by Trautmann and O'Rourke (1984). The shape in Figure 47 shows an initial stiffer linear behavior followed by a less stiff, but continually increasing load that forms a bilinear strain hardening curve. Note the horizontal earth pressure versus displacement curves have an initial relatively flat behavior and that the load cell shows an initial negative value. This behavior resulted from the hydraulic ram, which for some unknown reason, retracted slightly from its initial position when pressurized. The actuator pulled back from the starting position, placing the force load cell in tension and leading to this anomaly at the beginning of the earth pressure curves. Note also the pressure cell placed between the Geofoam blocks initially recorded a pressure of nearly zero before initiating the test and the retraction of the actuator.

In test 3, the peak force measured by the load cell was 134.8 kN at a total pipe displacement of 325 mm. (This test was terminated at this horizontal force due to concerns about damaging the end walls of the trench box.) The highest horizontal earth pressure measured between the Geofoam blocks was 98.6 kPa at a displacement of 335.3

mm. The highest horizontal earth pressure measured 305 mm behind the blocks in the sand backfill was 47.4 kPa at a displacement of 335.3 mm. Midway between the back of the blocks and the back wall, the highest horizontal pressure was 34.5 kPa at a pipe displacement of 335.3 mm. There was virtually no change in horizontal pressure measured along the back wall compared with the start of the test, indicating that the displaced soil from the test did not engage the soil near the back wall.

The highest force for test 3 was normalized to 17.5 at a dimensionless displacement of 1.9. The total horizontal force in this test is much higher than that of loose and medium dense sands (Trautmann and O'Rourke, 1984) and the dimensionless displacement as a function of normalized load is much greater. This finding will be discussed in greater detail later in a subsequent section of this chapter.

Test 4 – Light-weight Cover with No Compressible Inclusion

In test 4, a thin lift of sand back was placed over and around the pipe (Figure 41). The top of this lift of sand was 152 mm above the top of the pipe. The cover above this lift consisted of EPS block which was configured with four 610 x 914 x 1828 mm EPS15 blocks placed adjacent to each other to form a 914 mm thick light-weight cover. EPS blocks were subsequently covered with 305 mm of compacted sand. Thus, the total amount of sand in the cover system was approximately 457 mm, as measured from the top of the pipe.

Figure 48 shows the force-displacement and pressure-displacement curves for this configuration. The earth pressure cells were arranged in test 4 so that the horizontal pressure 610 mm behind the pipe was measured. This pressure cell was placed in this

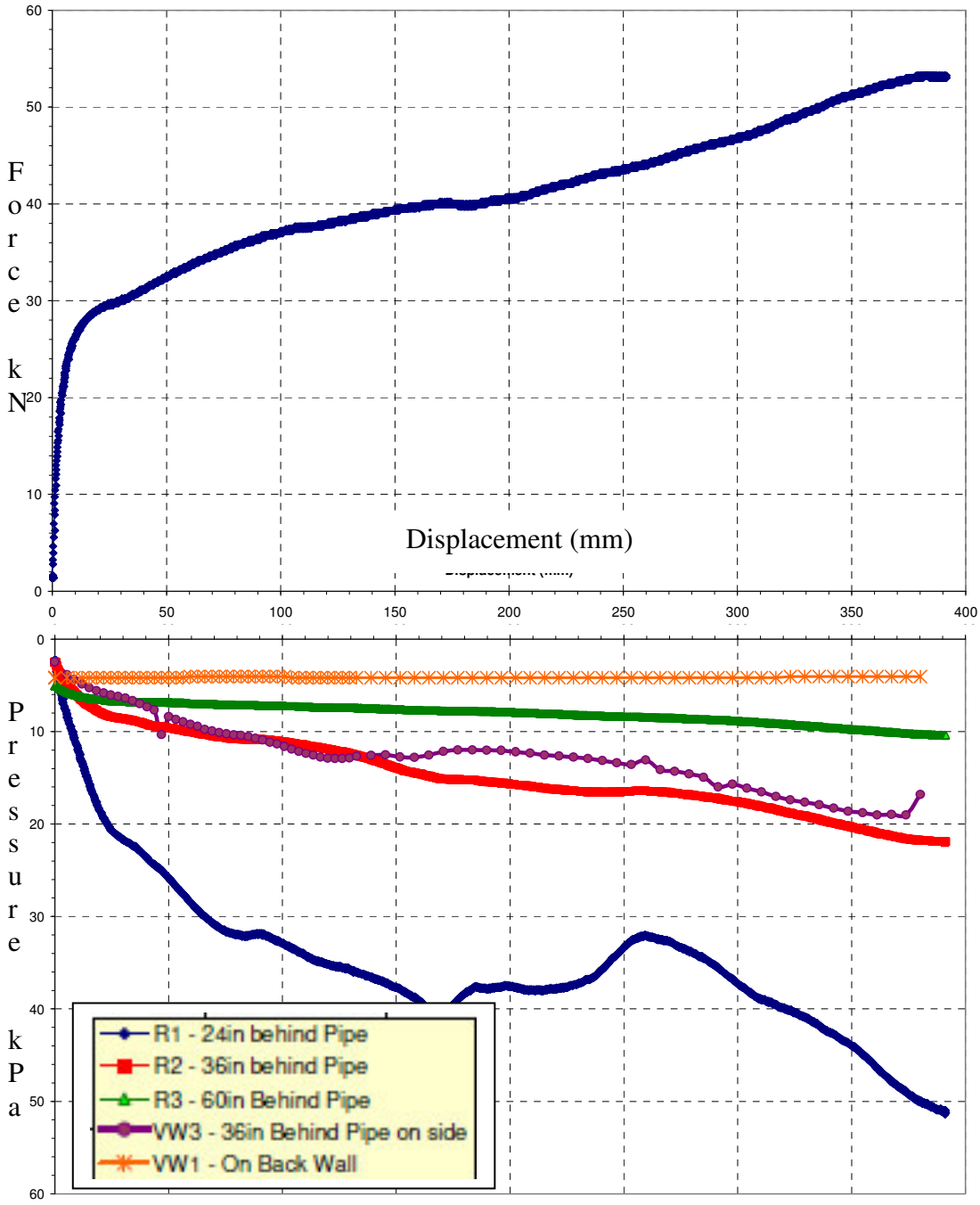

Figure 48. Force versus displacement and horizontal pressure plots for test 4

location to avoid damage by the large, expected movement of the pipe. The horizontal pressure at a distance of 914 mm behind the pipe was measured at two locations. Lastly, the horizontal pressure halfway between the pipe and the trench box back wall was measured, as was the horizontal pressure at the back wall of the box. The shapes of the force-displacement and pressure-displacement curves are similar to those of loose sand at low confining stress from Trautmann and O'Rourke (1984). They show a continually increasing load that follows an initial linear part of the curve (i.e., bi-linear strain hardening curve.) Note that the horizontal earth pressure curves have an initial peak, followed by a small drop in pressure and then show a rapid increase in pressure to the true peak at the end of the test. This test was terminated at the maximum stroke of the actuator, which is about 381 mm.

In test 4, the peak force measured 53.4 kN at a pipe displacement of 381 mm. The peak horizontal earth pressure, measured 610 mm behind the pipe, in the soil underneath the Geofoam was 51.2 kPa at 394 mm of displacement. A false peak of 40.7 kPa at 170 mm was also seen. The highest horizontal earth pressure measured 914 mm behind the pipe was 22 kPa at a displacement of 388.6 mm. Midway between the pipe and the back wall, the peak horizontal pressure was 10.5 kPa at a pipe movement of 391.2 mm. There was essentially no change in horizontal pressure along the back wall compared with the start of the test, indicating that the sand backfill was not mobilized in this area.

The peak force results for test 4 were normalized to 6.6 at a dimensionless displacement of 2.0. The total load from this test is lower than that of loose and medium dense sand from these researchers. In addition, the dimensionless displacement for any given normalized load is much greater in test 4. This behavior will be discussed later in

the next section of the dissertation. Test 4 is the most efficient system of the 4 tests as will be discussed in the subsequent section.

Comparison of Test Results

The total force data for all four tests completed during this test program are against horizontal pipe displacement for comparison purposes (Figure 49). As expected, test 2 (sand only) had the stiffest initial response to pipe movement, due to the higher stiffness of compacted sand, when compared with EPS. In addition, test 2 had a lower peak force when compared with tests 1 and 3 (i.e., EPS compressible inclusion tests). Unfortunately, tests 1 and 3 had higher peaks than test 2, which occurred at a displacement that is approximately 2 to 3 times larger. For application purposes, this means that these systems mobilize more force, albeit at larger displacement, than the sand backfill case, which is not a favorable result for pipes that undergo large horizontal displacement (e.g., strike-slip displacement). This conclusion is true for loosely compacted sands, but may not be generalized to pipe/EPS systems that engage dense sands or cohesive soils.

The test results for test 4 are much more favorable from an application standpoint. This behavior shows an initially stiff behavior followed by a relatively flat force-displacement response. Thus, such a system produces the lowest peak force and maintains the relatively low force for considerable displacement. The data shown in Figure 49 can also be plotted in their dimensionless and normalized form (Figure 50). Normalized data are important to eliminate scale effects for direct comparison with

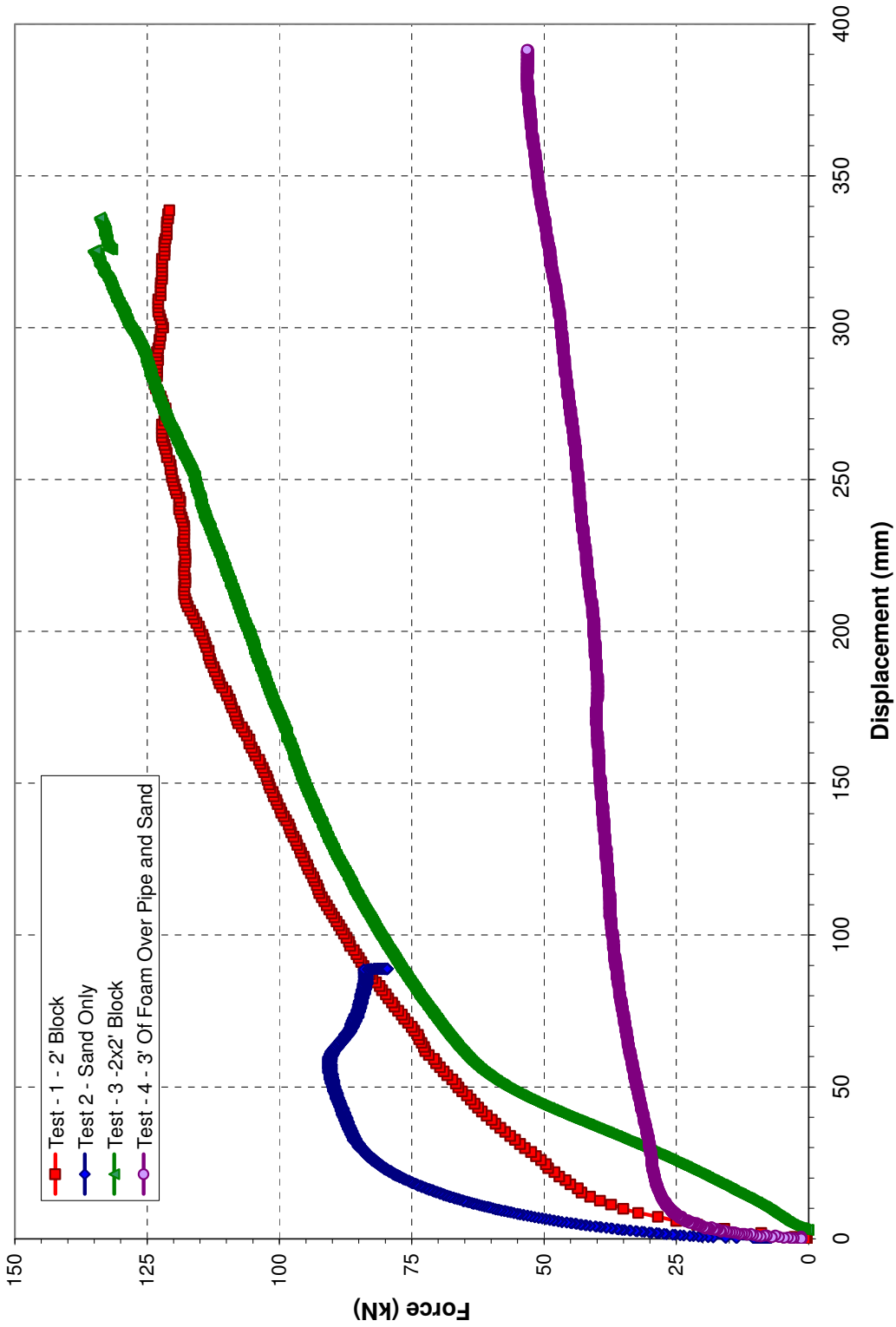

Figure 49. Comparison of force-displacement curves for all trench box tests

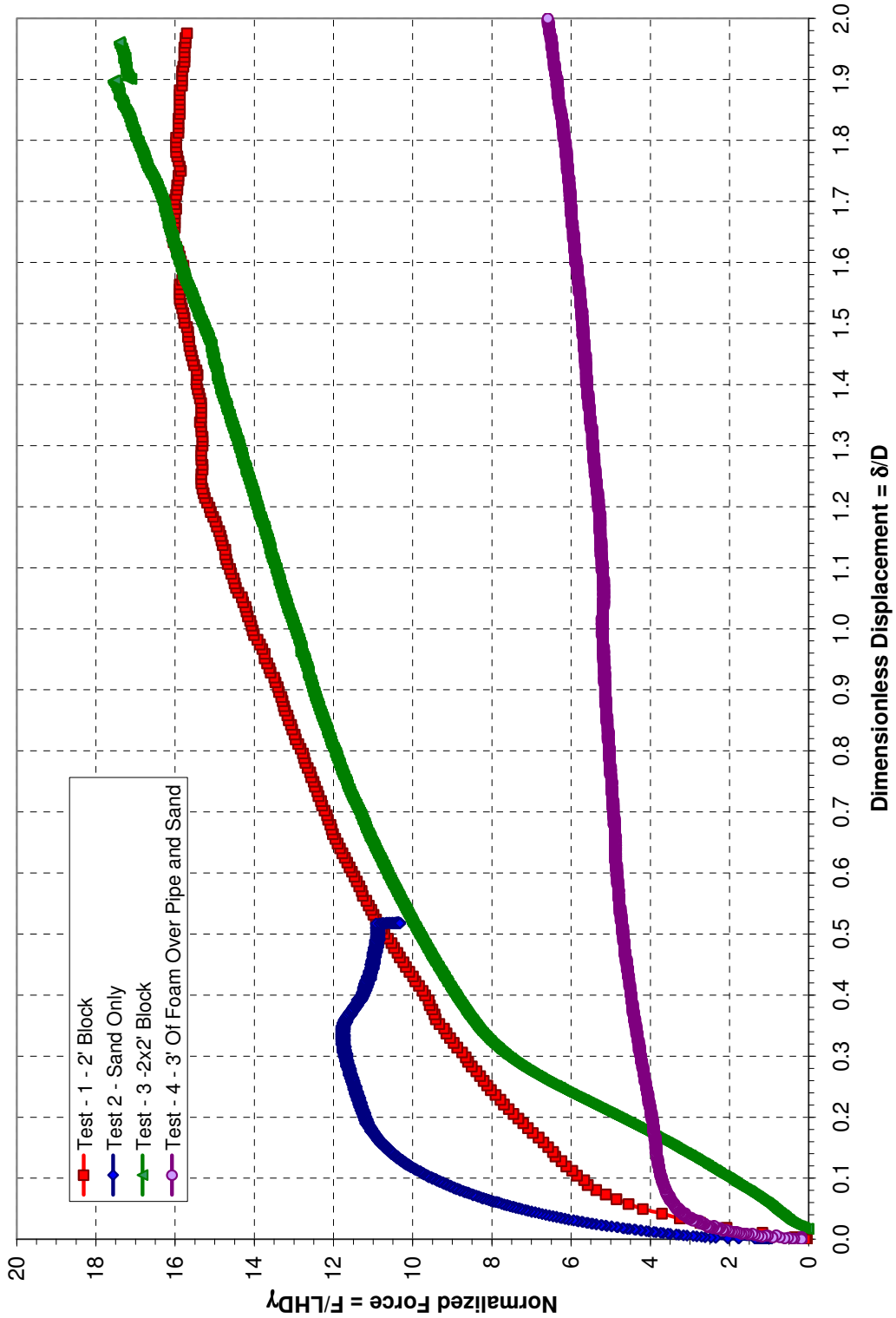

Figure 50. Dimensionless force and displacement curves for all trench box tests

literature compression data. Normalized data are the typical presentation in the geotechnical literature.

The normalized force is equivalent to the limit-equilibrium horizontal bearing capacity factor (Trautmann and O'Rourke, 1984) for that specific configuration of pipe, EPS Geofoam and soil. However, the bearing factor, N_h, does not represent the displacement needed to reach that peak normalized force. This research proposed a new term, called the peak number (P_N), which is the normalized force divided by the dimensionless displacement. Values of P_N are unit-less and represent the relative efficiency of a horizontally loaded pipe system. Higher P_N values represent systems with higher initial stiffness. In contrast, lower values represent systems that are more efficient in accommodating horizontal displacement. Values of P_N are intended to provide an indication of how much displacement is required for the bearing factor N_h to reach full mobilization of backfill soil's shear strength. Table 14 shows a summary of the peak forces and their corresponding displacements and P_N values for the four trench box tests.

Based on the P_N values shown in this table, the configuration corresponding to test 4 was the most efficient at accommodating horizontal pipe movement. (A relatively low total load and high accompanying displacement were achieved and the peak number represents this as a value of 3.3.) The two experiments with EPS Geofoam as a compressible inclusion (tests 1 and 3) showed higher peak numbers, which represents less efficiency; however, they still were more efficient than test 2. The P_N value for test 2 (soil only) was 35.8, which indicates that the system was relatively stiff and inefficient. However, this system did not continue to gain load at large displacements and a residual

Table 14. Normalized lateral test results

Test	F_{max}	δ_{max}	N_h	δ_{max}/D	P_N
----------	*lb/in*	*mm*	----------	----------	----------
1	386	279.4	16.0	1.65	9.7
2	283	58.4	11.8	0.33	35.8
2 residual	260	381.0	10.7	2.00	5.4
3	421	325.1	17.5	1.90	9.2
4	167	381.0	6.6	2.00	3.3

P_N value of 5.35 was defined for test 2 at large displacements to show that loose to medium dense sands have more efficiency in a residual state compared to tests 1 and 3.

The maximum force per unit length and accompanying displacement for that load can be found from Figure 51. This figure shows the force divided by displacement values of the 4 tests in the small displacement range of the curves. The slope of these curves at any displacement is the force/unit length/length or subgrade modulus of the system in pounds per square per unit length. Thus, a bilinear or multilinear representation of the subgrade modulus can be constructed by a designer to represent the force-displacement relationship per unit width of the system for numerical modeling of the system.

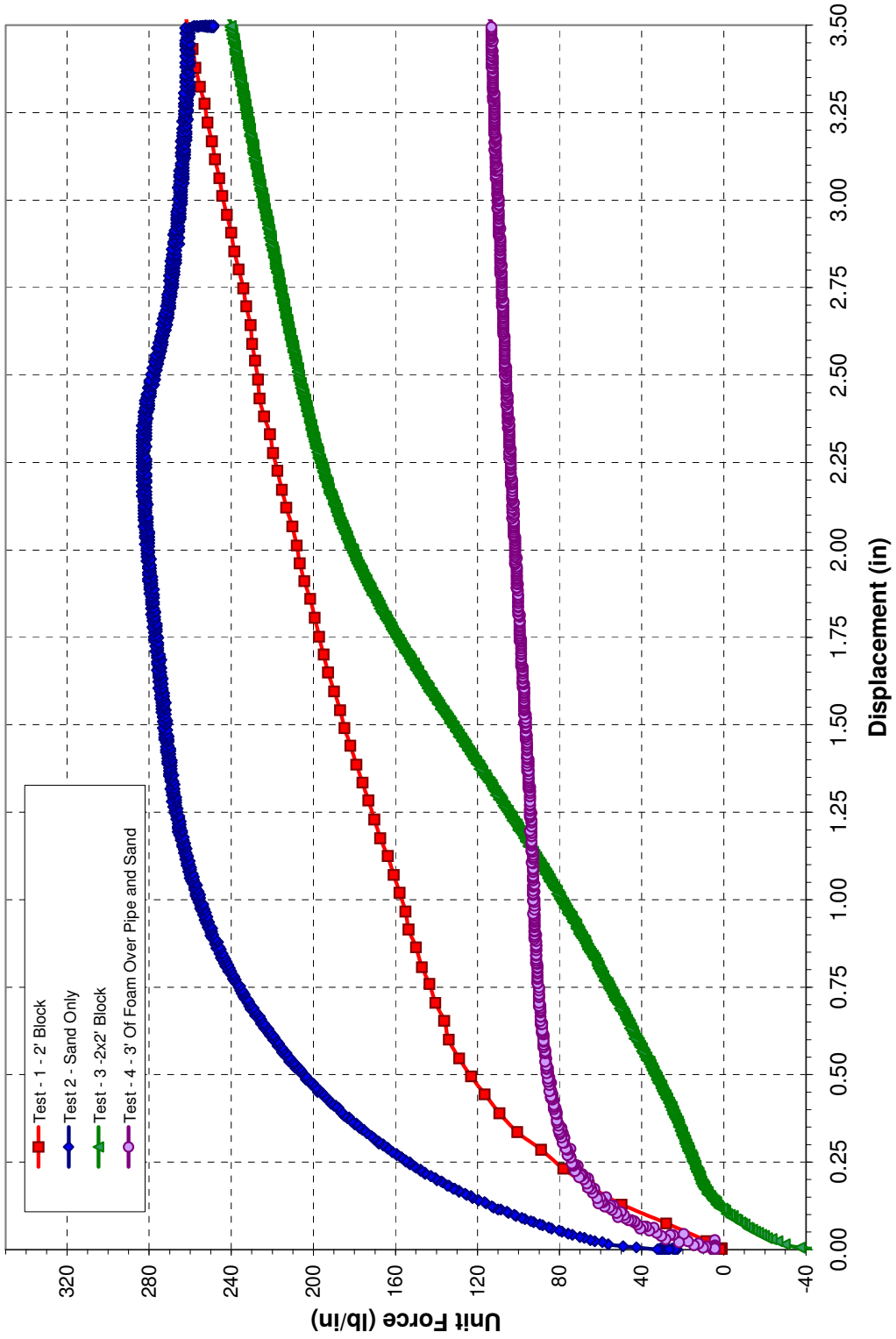

Figure 51. Force per unit width plots of trench box tests

Discussion of Experimental Results

It is apparent from the test program that EPS Geofoam did not perform significantly better than loose sand backfill when used as a compressible inclusion to reduce horizontal stresses imposed on the pipe system undergoing large displacement.

The EPS Geofoam trench sidewall system gave a less stiff response at low displacement compared to the loose sand; but at larger displacement, it developed higher loads. It is important to note that these experiments were conducted only with loose sand. Dense sands, well graded engineered fill or clays in undrained or unsaturated loading may give a stiffer and stronger response to the movement than loose sand.

It is recommended that numerical models be used to explore the effects of differing soil types when used in junction with EPS Geofoam in the sidewalls of the trench. EPS Geofoam may still provide a better system for allowing horizontal pipeline movements as a compressible inclusion when compared to other soil types. In addition, the system showed more complex behavior than initially conceived, and dismissing the idea of the compressible inclusion application of EPS Geofoam for laterally moving pipelines based solely on these results is premature.

Increasing the thickness of the compressible inclusion produced only marginally better response in loose sand. When considering the two compressible inclusion Geofoam tests (test 1 and 3), there were only minor differences in the force-displacement curves. Initially, it was hypothesized that by doubling the thickness of the Geofoam, this would produce a more desirable displacement behavior. Based on test 3 results, this is true only for pipes undergoing relatively small displacements.

Localized, nonuniform strain greatly influenced the behavior of the compressible inclusion. As the Geofoam block was loaded by the pipe, the zone immediately around the pipe compressed first in a nonuniform manner (Figure 52). From this figure, the location of the pipe against the Geofoam block is shown. In addition, there are matching failures zones on each side of the pipe's compression zone. These failures are likely a combination of tension and shear failure. More difficult to observe was how the Geofoam was compressed differentially by the pipe. The compressed material around the pipe seat exhibits rings of compressed Geofoam beads which gradually increase in size away from the pipe contact area until they finally disappear completely (Figure 52). These observations show that the EPS has developed nonuniform localized strain, especially around the pipe penetration. This localized strain and subsequent strain hardening of the EPS at large pipe displacement allowed for the block itself to be push laterally into the sand mass placed adjacent to the block. Thus, the block tended to act as a large plate moving through the soil mass, producing higher lateral resistance as the pipe displacements became larger.

The light-weight cover system of test 4 had superior performance to the other three tests. The concept of decreasing the lateral earth forces by reducing the weight of the cover material appears to be more efficient that using a compressible inclusion for loose sand backfill. This concept can be applied to the general construction of pipe-trench systems regardless of the backfill media placed around the pipe. In concept, a wide trench can be constructed and the pipe covered with a veneer of sand. The remaining backfill cover can be constructed with EPS block to the required elevation, which produces low vertical stress on the pipe.

Figure 52. Localized deformation of an EPS block loaded by pipe in the trench box

Thus, constructed in this manner, the pipe will act as if it is shallowly buried and move relatively freely through the thin sand bedding and cover. This light-weight cover behavior was explored by Yoshikaze and Sakanoue (2003). They used a similar configuration to test 4, and their results for normalized force are shown in Figure 53, with the EPS cover system reducing the normalized force by as much as 60%. The results for test 4 from this program show a 62% reduction. Thus, based on the results from this program, it appears that the light-weight application of EPS is more efficient than a compressible inclusion for reducing stresses on a pipe undergoing horizontal displacement in a trench, as long as the trench can be excavated sufficiently wide to accommodate the magnitude of the horizontal displacement.

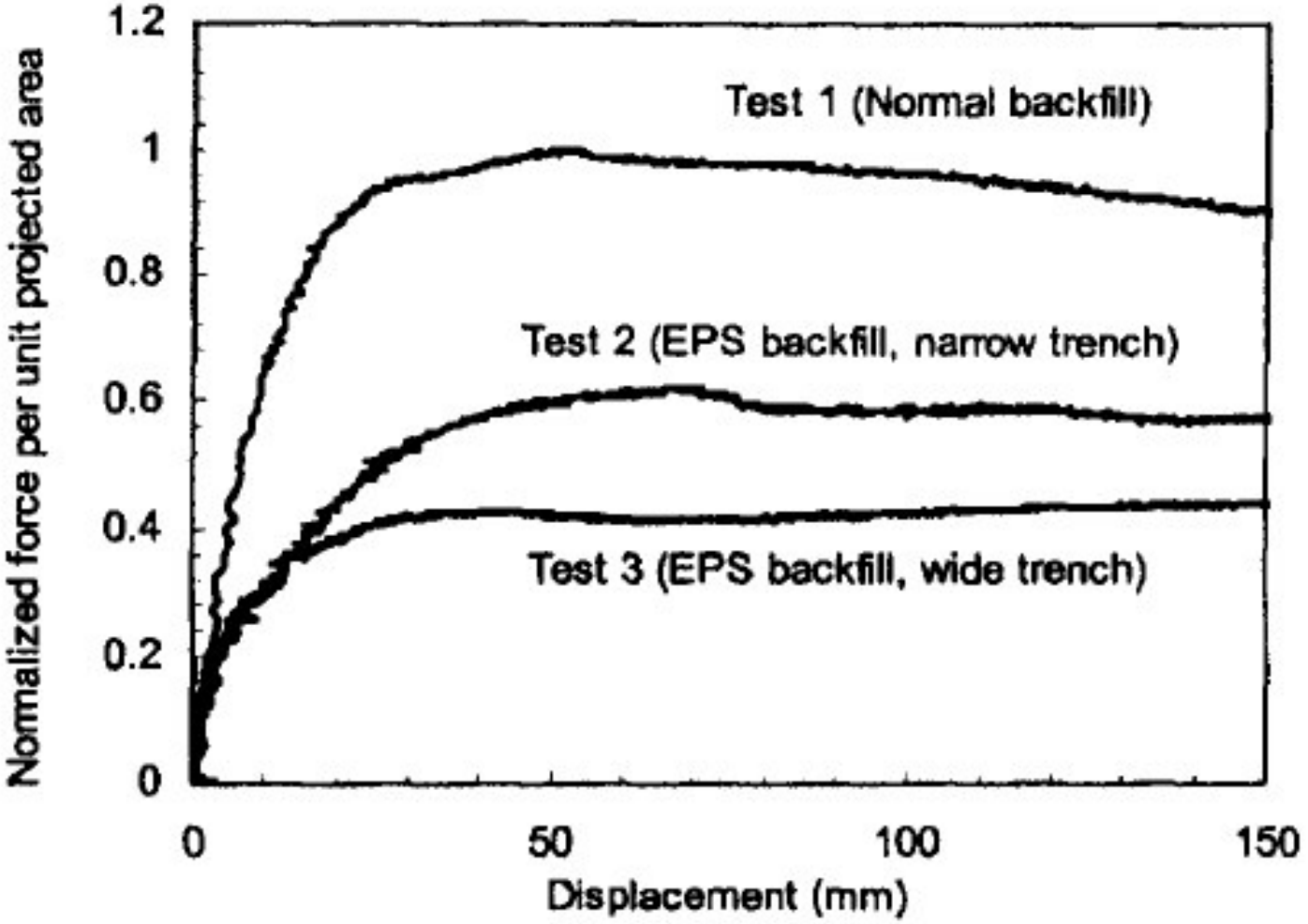

Figure 53. Test results from Yoshikaze and Sakanoue, 2003

CHAPTER 6

NUMERICAL MODELING OF LATERAL TESTS

Many different soil types, geometries and fault crossing scenarios are possible involving the future application of EPS Geofoam cover systems for steel pipelines crossing active strike-slip faults. Because it is cost prohibitive to conduct full-scale or even reduced-scale tests to evaluate the force-displacement characteristics for all cases, numerical modeling can play an important role in the development and assessment of these systems. Numerical modeling of various fault crossings is less expensive and allows the designer to parametrically examine ways of mitigating the potential damage to the pipeline by evaluating various Geofoam geometries and configurations. As part of this research program, a series of numerical models were developed to evaluate the experimental results of the uplift tests and see if such modeling could be used as an evaluation tool. In addition, the force-displacement relationships obtained from the experiments previously discussed provide the basis for development of other techniques that may not entirely rely on numerical modeling. Thus, the force-displacement relationships, or nonlinear springs, developed herein are important to the evaluation and design of pipeline crossings undergoing vertical offset, regardless of the numerical scheme developed to perform the evaluation.

Numerical Modeling Program

The numerical model chosen for this research is the finite difference analysis program FLAC version 5.01.432 (Fast Lagrangian Analysis of Continua) from Itasca software of Minneapolis Minnesota. FLAC uses the explicit finite difference method for its analysis. FLAC2D simulates the deformations and system response of continuous systems built of soil, rock or other materials that undergo plastic flow when their yield limits are reached. It also has the capability of modeling structural elements placed in and atop geomaterials. Geomaterials are represented in a manner similar to a finite element formulation by elements (i.e., zones) that form a grid which is adjusted by the user to fit the shape of the modeled object. However, unlike the finite element method, which does the calculations at the element level, the finite difference technique does the calculations at the nodes and the area properties as assigned to the nodes. Each element (i.e., zone) in the finite difference mesh behaves according to a prescribed linear or nonlinear stress-strain law in response to the applied forces or displacements. The material in the model can yield and flow in response to loads and the grid can deform (in large-strain mode) and move with the material that is represented. The explicit, Lagrangian calculation scheme used in FLAC ensures that plastic yield and flow of geomaterials are modeled accurately. Because no matrices are formed, large two-dimensional calculations can be made without excessive memory requirements. The finite element method, in contrast, does all the calculations in a series of local and global stiffness matrices.

The drawbacks of the explicit finite difference formulation are longer computer run time and a significant number of iterations required to find a convergent solution. In comparison, finite element programs generally obtain a solution more quickly, but

require much more memory. In addition, finite element programs also become unstable when large strain and/or grid separation develops in the model; both of these situations were encountered while modeling the Geofoam full-scale tests. In contrast, the explicit finite difference method is much more robust in dealing with large strain and grid separation and was successful in modeling these cases.

One additional feature that gives FLAC a distinct modeling advantage is the interfaces used between different geomaterials. Many numerical analysis programs contain interface elements between structural elements and geomaterial elements; nonetheless, FLAC is especially suited for placing interfaces between geomaterials elements themselves. These interfaces were required when dealing with EPS Geofoam and its interaction with the surrounding soil. EPS Geofoam has internal strength properties of cohesion and friction, but interacts with surrounding soil masses with distinctly different stiffness, cohesive, adhesive and frictional interface properties than defined by internal strength and stiffness properties.

The main advantage in using FLAC for the analysis of Geofoam systems is its powerful built-in programming language, FISH (short for FLACish). With this feature, the user can write FISH code that implements functions that give more control to the modeling process. In addition, FISH code can be used to define alternative constitutive soil models, if so desired. This is a unique capability to FLAC users who wish to tailor their analyses to suit specific needs that arise which are unique to specific geo-engineering problems.

Once the force-displacement behavior of the uplifting system is found from the FLAC modeling, the designer may choose to use a finite element program (e.g., ANSYS or

PIPLIN) to complete the analysis of the pipeline; or the designer may use FLAC and/or FLAC3D to do the same analysis and couple the pipe analysis with the soil/Geofoam modeling.

Benchmark Lateral Pipe Movement Modeling

The first step in the numerical modeling process is to begin with simple systems before progressing to more complex ones like those presented in the box testing discussed in Chapter 5. The process of building up the model begins with benchmarking, or comparing the simple model with results from the geotechnical literature. In this case, the benchmarking was done by comparing the modeling results with those from Trautmann and O'Rourke (1984). Their tests consisted of simple geometries and uniform sand placed carefully into a homogenous mass; afterwards, a small pipe was pushed laterally into the sand. This system is simple, and therefore more repeatable than the full-scale box tests with EPS Geofoam analyzed in this dissertation.

The FLAC model was initiated to the same dimensions as the Trautmann and O'Rourke (1984) tests. Although many tests were conducted by these authors, only a few were chosen for the benchmarking process. They used three different densities of sands in their testing, with a large number of burial depths.

In this benchmarking study, six of their tests were modeled herein. At least one model for each of the three relative densities of sand was analyzed and models were developed for three burial depths. The tests modeled are summarized in Table 15.

Table 15. FLAC bencharking models

Model	Burial Depth / Pipe Diameter	Relative Density of Sand Fill	Sand Density (kN/m3)	Friction Angle (deg)	Dilation (deg)
1	2	Loose	15.6	30	0
2	6	Loose	15.6	30	0
3	2	Medium Dense	17.0	34	0
4	6	Medium Dense	17.0	36	2
5	11	Medium Dense	17.0	36	2
6	6	Dense	18.4	42	10
7	11	Dense	18.4	48	16

A sample of the FLAC geometry for the models is shown in Figure 54. The dimensions of the sand volume and the pipe are the same as those in Trautmann and O'Rourke (1984). In the modeled geometry, the pipe was placed nearer to one side and pushed away from that side into the soil mass. The pipe was pushed at a constant rate in FLAC until numerical instability occurred, which was usually less movement than the end of the test data record. The sand was treated as a Mohr-Coulomb material with constant modulus, dilation and friction angle. No cohesive strength or tensile strength was assumed. The soil density, friction angle and dilation were provided by Trautmann and O'Rourke in their test background information. Bulk and shear moduli were assumed for each model from the relative density of the soil using similar materials found in the Duncan et al. (1980) soil library. The numerical code is presented in Appendix A.

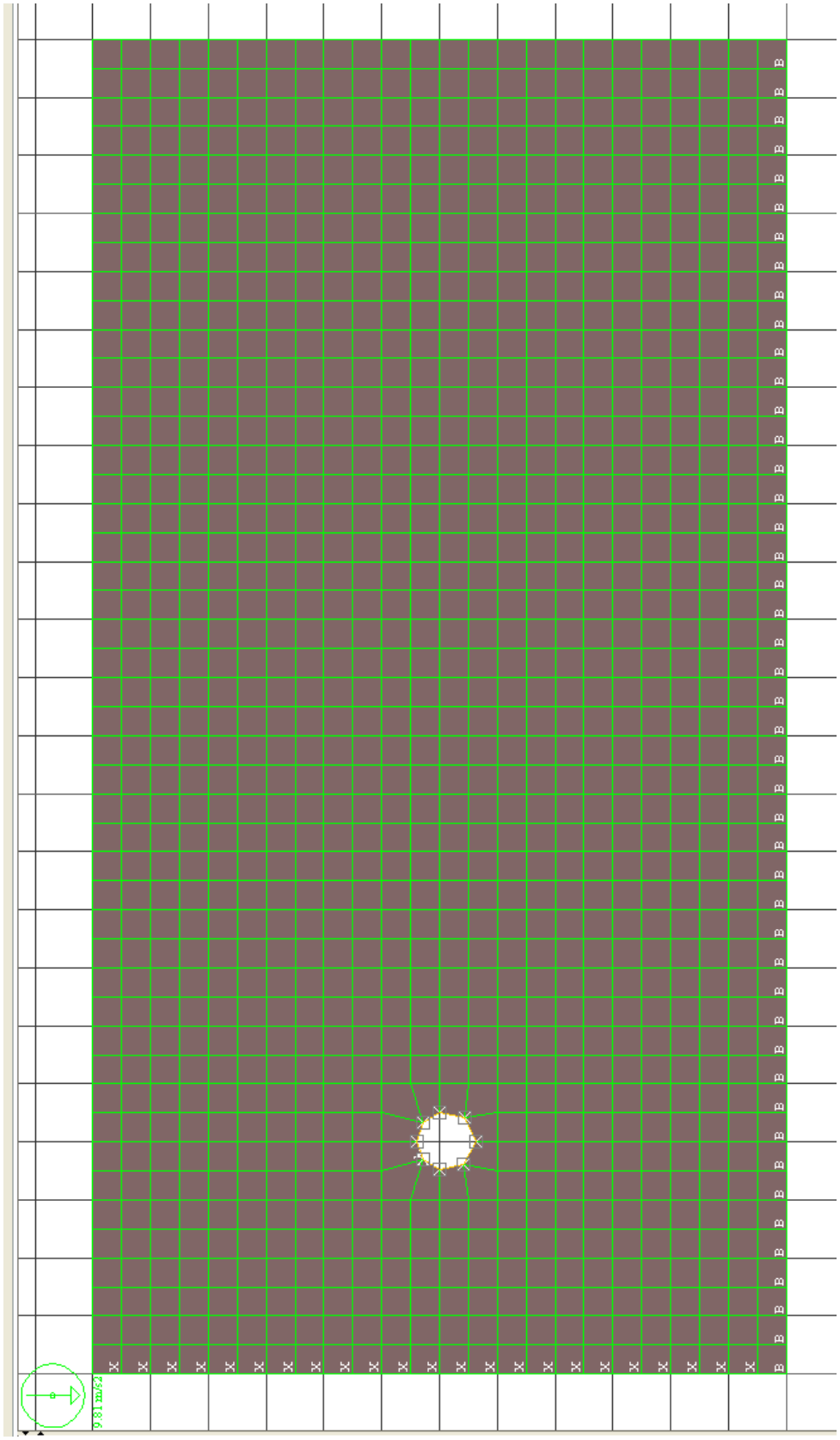

Figure 54. Lateral pipe movement FLAC model basic geometry

The model was initiated by adding the sand in lifts with the pipe added at the correct lift. The model was run to static equilibrium under gravity loading. The FLAC code was then switched to large strain mode, and the pipe is pushed at a constant rate into the soil mass (see left side in Figure 54). The normal forces on the pipe were tracked by FISH code and summed to produce the total soil resisting force at incremental displacements. The resulting force-displacement curves for all 7 tests modeled are plotted in Figure 55. In Figure 55, the force-displacement relationships are shown for comparison. Based on these results and common intuition, it is clear that modeling results for deeper pipe burial depths produce greater resisting forces for all soil densities modeled.

The individual test curves are plotted along with the original Trautmann and O'Rourke (1984) test data in Appendix I. The FLAC models for the loose sand tests tend to overpredict forces by 9%, especially for shallow embedment. For the medium dense sand tests, the FLAC model tends to match the test curves well, except for the case of shallow embedment. When the FLAC results are compared to the dense sand test data, the FLAC models tend to underpredict the postpeak behavior by 13%. The FLAC model performs better for deeper embedment depths and for medium dense sands; however, the model is less accurate for shallow embedment and for sands with large postpeak softening. In summary, it was concluded that the FLAC modeling approach was able to predict reasonably the force-displacement behavior of the benchmark test data done by Trautmann and O'Rourke (1984) with only a simple understanding of the sand's constitutive properties from basic testing provided by Trautmann and O'Rourke.

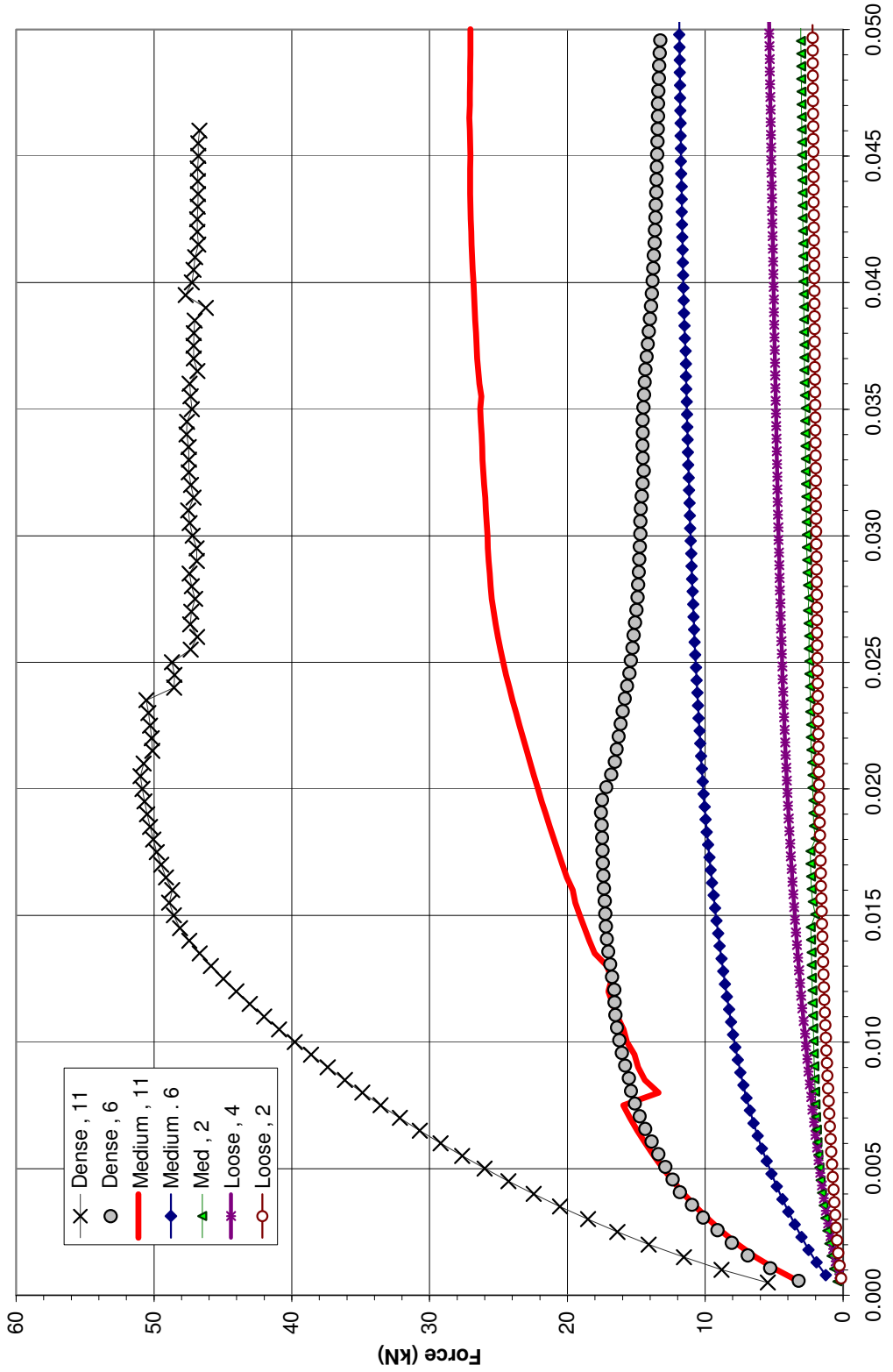

Figure 55. Lateral pipe movement benchmark FLAC modeling results

Lateral Pipe Test FLAC Modeling

The lateral pipe movement tests discussed in Chapter 5 were modeled in FLAC to see if the actual force-displacement relationships could be simulated by FLAC for the 4 tests conducted. The same numerical procedure used in the benchmark modeling was used. The model was first built up to an initial static solution under gravity forces, followed by the initiation of lateral pipe movement at a constant rate. The model geometry was developed for the same scale as the trench box tests. The sand was modeled as a Mohr-Coulomb material, while the Geofoam was modeled as a nonlinear elastic material defined by the complex hyperbolic model developed for EPS15 from Chapter 3. Properties of the sand material used in the FLAC models are shown in Table 16.

The modeling progression began with the sand only test (test 2), followed by the Geofoam cover test (test 4). These were evaluated before tests 1 and 3, which represent the test where the pipe pushed horizontally into Geofoam. This progression was chosen because it progressed from the simplest to most complex case.

Table 16. Sand material properties for lateral FLAC modeling

Density	K	G	ϕ	c	T	ψ
Kg/m3	kPa	kPa	deg	kPa	kPa	deg
1602	9300	5600	32	0	0	0

The FLAC model results for the sand only box test are shown in Figure 56. The FLAC output matches the experimental results well until a displacement of about 60mm. After this, the experimental results showed a slight decrease in the resistance of the sand to pipe penetration. The FLAC model continues with a slight increase. It is unclear what caused the divergence at this point, but it was concluded that the FLAC model had successfully predicted the force-displacement curve for this case.

Next, the case of the Geofoam cover overlaying the sand surrounding the pipe was modeled (test 4). The FLAC modeling results are shown along with the test data in Figure 57. This comparison demonstrates that the FLAC model matches the test data well until a displacement of about 12 mm. After this, the FLAC model tends to slightly overpredict the force-displacement behavior by about 11% which is considered to be a reasonable difference between numerical prediction and experimental data. At the end of the FLAC modeling results, this difference had decreased to about 4%.

The more complex models, including EPS15 placed in compression by the pipe, are presented as follows. The first test conducted was modeled (i.e., a single Geofoam block adjacent to the pipe) so that the pipe was horizontally into the EPS block backed by the surrounding sand backfill. The Geofoam was modeled using the complex hyperbolic model for EPS 15 (Chapter 4). Figure 58 shows the calculated force-displacement relationship versus the experimental data. The FLAC modeling (Figure 58) provides a reasonable estimate of the experimental data up to a displacement of about 140 mm; after this, numerical instability occurred in the FLAC model.

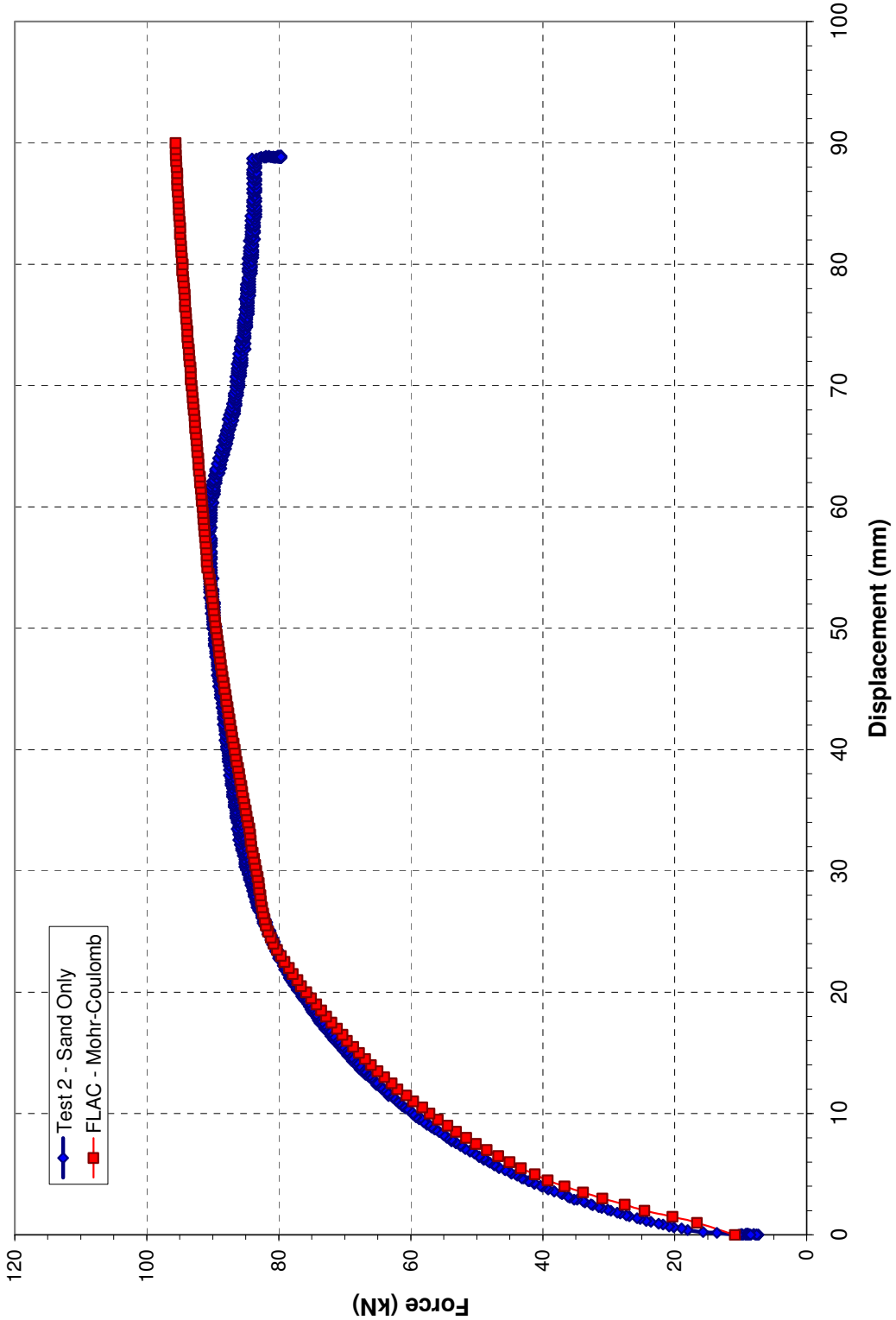

Figure 56. Comparison of sand only box test and FLAC

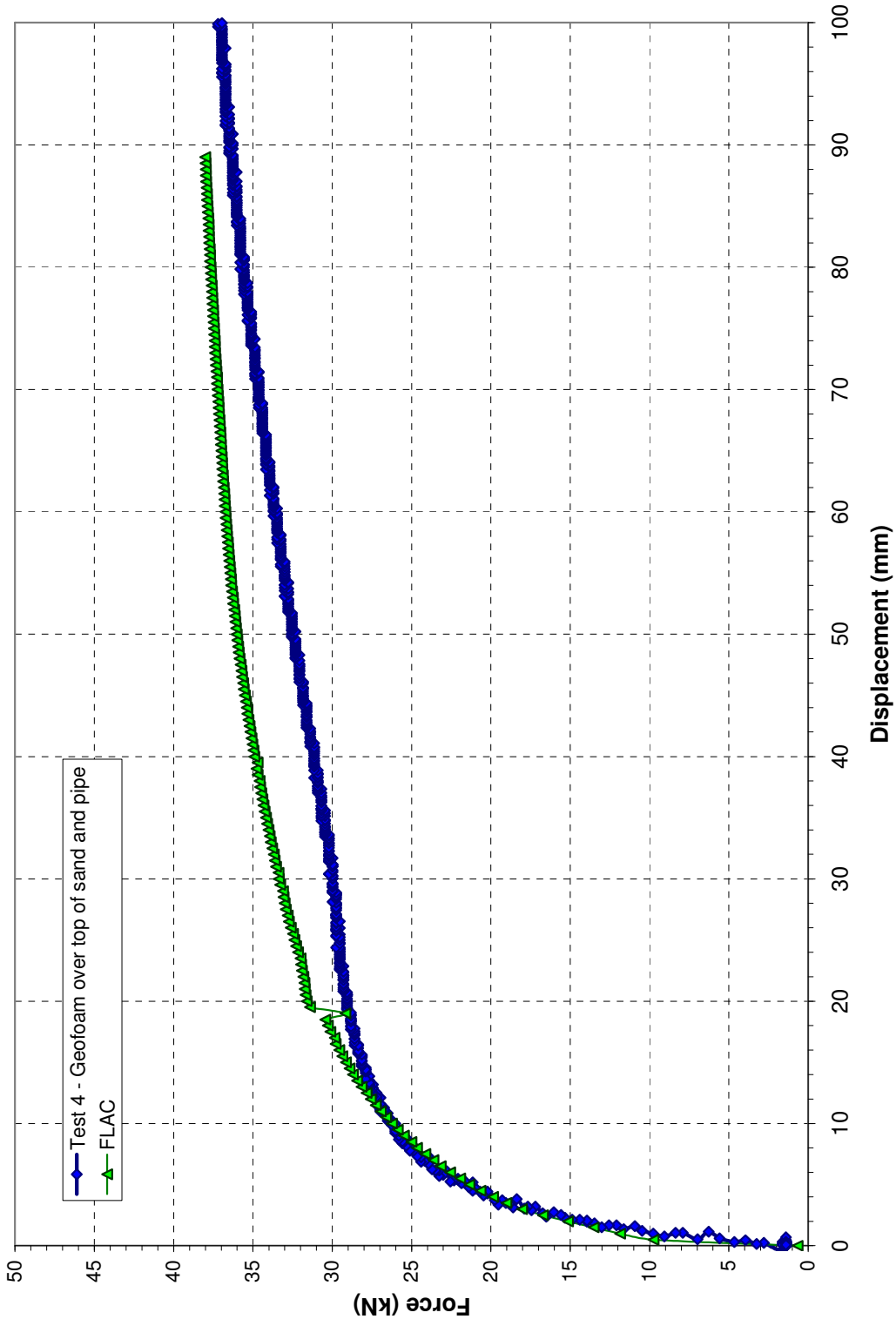

Figure 57. Comparison between foam-over-pipe box test and FLAC

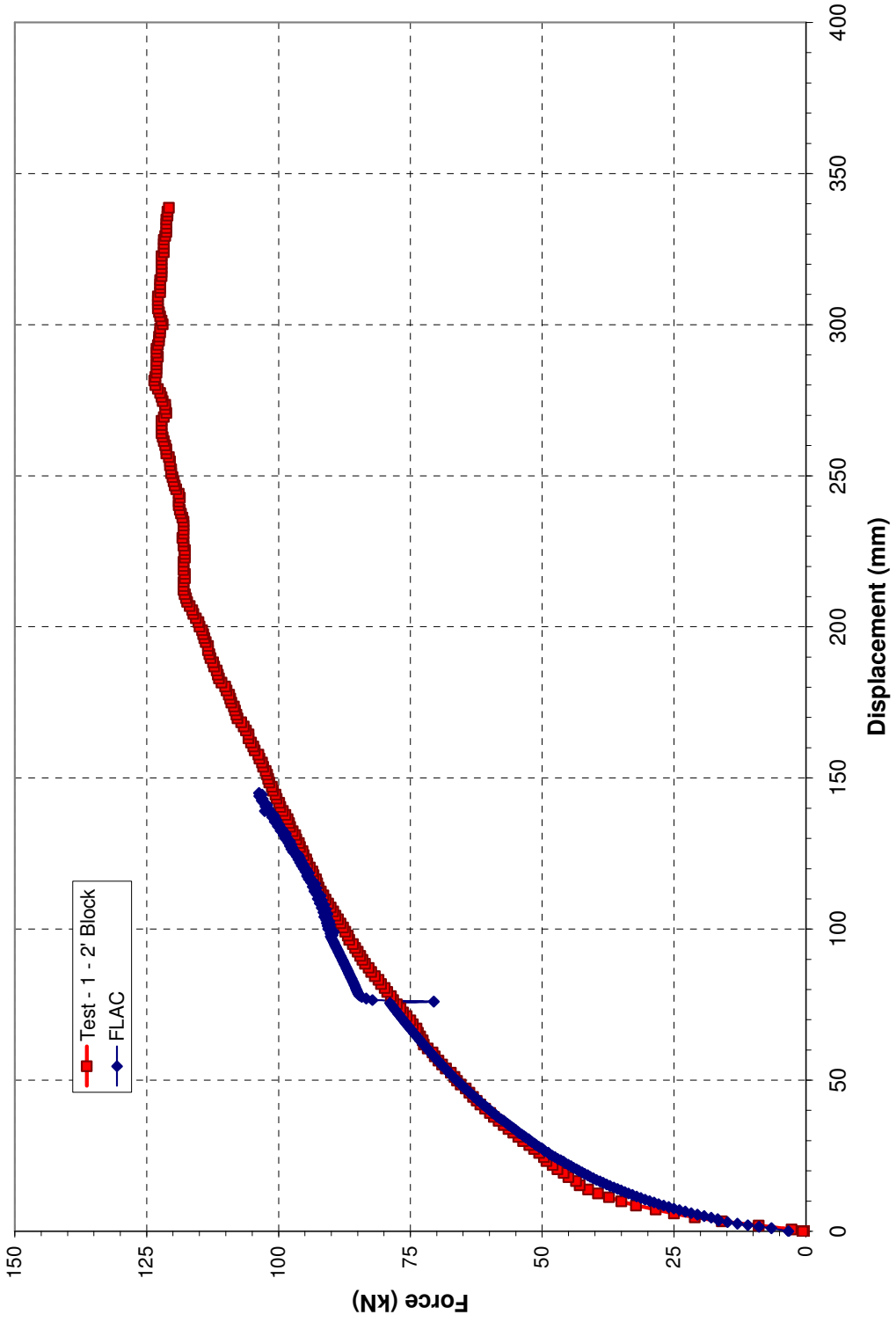

Figure 58. Comparison between single foam block against pipe test and FLAC

The final test modeled in FLAC (i.e., test 3) was that of two Geofoam blocks placed side-by-side abutting against the pipe with the remaining part of the trench box filled with sand. The FLAC modeling was conducted in the same manner as previous models with the additional width of Geofoam added (i.e., total of 2 blocks wide). The results of the FLAC model are compared with the experimental data in Figure 59. These results indicate that the FLAC modeling is reasonable for predicting the force-displacement relationship up to about 140 mm of displacement, after which numerical instability in the FLAC model occurred. The initial match of the curve is not perfect (i.e., displacement below 50 mm), but the FLAC modeling results matches the experimental data once again at 50 mm of displacement.

Conclusions

In all, the relatively simple FLAC models of horizontal pipe movement in backfill (with and without EPS) reasonably explain the experimental data. When this is considered with the benchmarking of the FLAC modeling using the Trautmann and O'Rourke (1984) results, as discussed in Chapter 5, it is concluded that FLAC can reasonably estimate the nonlinear force-displacement relationship for cases with or without Geofoam. In addition, it is also apparent that the Complex Hyperbolic Model (Chapter 3) can be used to model the Geofoam-pipe interaction of a pipe moving into the EPS block. The modeling exercises and comparisons of the FLAC modeling approach can be applied to more complex geometries and soil conditions, as subsequently discussed in Chapters 8 and 9.

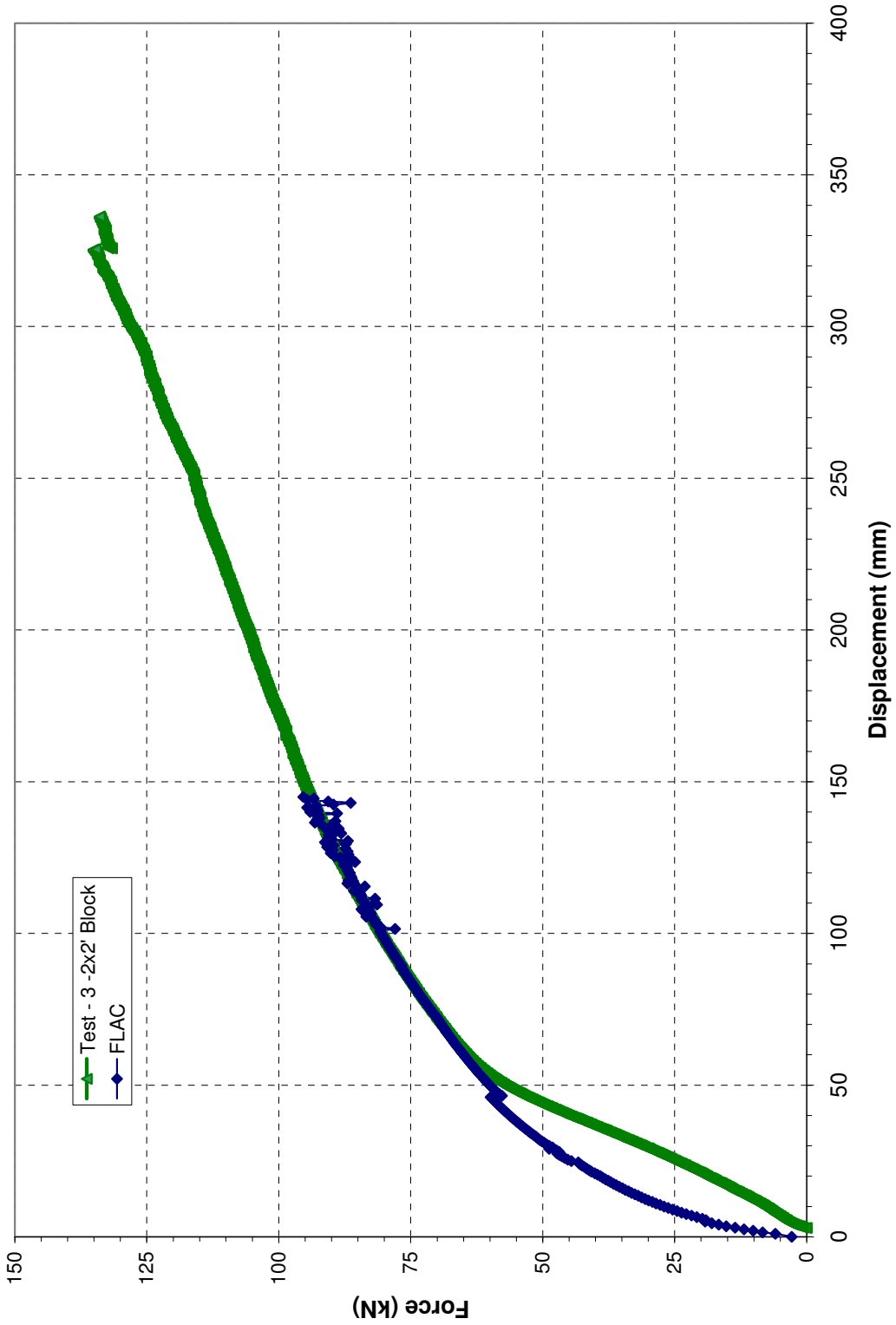

Figure 59. Comparison of two Geofoam block test to FLAC

CHAPTER 7

UPLIFT SOIL-GEOFOAM-PIPELINE TESTING

Background

Two full-scale uplift tests were performed on pipes with soil and Geofoam covers, respectively. The uplift tests were designed and constructed to obtain, as reasonably as possible, 2D plane strain conditions. The pipe was installed in trenches with uniform cross-sectional areas and end effects were minimized. The uplift imposed on the buried pipe was similar to that encountered by a steel pipeline during normal faulting on the downthrown side of the fault.

Two tests were performed at a location provided by Questar Corporation. The first test was a baseline test of a pipeline uplifting through a native soil backfill trench. The second was a pipeline test uplifting through an EPS Geofoam cover. The pipes were buried to the same depth below the surface and both included the same thickness of granular backfill that was compacted at the surface. The pipes used in the two tests were grade X42 with an outer diameter of 324 mm, and wall thickness of 6.5 mm. During each test, the uplift force, displacement of the pipe and the stresses within the backfill mass were monitored continuously. Photographs and video were taken of the experiments for additional analysis and modeling. A pressure film was also used to measure the contact stress on the Geofoam that developed at the pipe/Geofoam contact point.

The results of the tests showed that the EPS Geofoam cover system significantly reduced the uplift force when compared with the native backfill case. In addition, the vertical displacement required to reach the peak uplift force was increased over that of the native backfill case. From these data, the soil-structure interaction relation (i.e., nonlinear spring relation) of a pipeline undergoing normal faulting was developed. It was concluded that the reduction in forces from the soil-structure interaction with the Geofoam cover case can significant reduced steel pipeline distress for cases where the pipe is subjected to normal (i.e., vertical) faulting.

Purpose of Testing

When large, steel pipelines cross active faults, protection of the pipeline to potentially damaging permanent ground deformations must be considered. As the normal fault ruptures, the pipeline on the downthrown side of the fault attempts to lift upwards, relatively, through the trench backfill. This uplift places significant loads on the pipeline that could lead to excessive bending and/or rupture of the pipe.

This chapter investigates the placement of an EPS Geofoam backfill cover system over the pipeline to protect it from such damage. In order to design an EPS cover protection system, the uplift force-displacement relationship (i.e., nonlinear Winkler spring) must be evaluated. This can be done through a combination of laboratory and full-scale testing and numerical modeling of these test data. This chapter details the full-scale testing done to measure the force-displacement relationship of an EPS Geofoam cover system and a conventional backfill cover subjected to pipe uplift.

An initial modeling report for Questar Corporation was completed in August of 2007 that used numerical modeling of a prototype EPS cover system (Chapter 2). This evaluation suggested that a light-weight EPS cover can significantly reduce the stresses, strains and moments on a pipeline undergoing vertical faulting and/or other types of vertical permanent ground deformation. This chapter is a continuance of this work and presents the experimental data that were obtained to support additional numerical modeling described in Chapter 10.

Experimental Setup

Site Conditions

The pipe uplift tests were conducted at the Fugal and Sons Company equipment yard on 700 North Street in Lindon, Utah. The approximate latitude and longitude for the site are 40.3512°N and 111.7359°W. This location was a level, open site in Utah County in the State of Utah that currently is used as Fugal's construction yard. The upper 0.914 m of the existing soil profile was a sandy, random fill from previous site grading. This material included some cobbles and a significant amount of clay. Underneath the fill was a thick layer of medium stiff brown silty clay down to the bottom of the trench excavations. This layer also had some fine-grained sands and was plastic. The moisture content of the upper fill layer varied with depth. The water content at the bottom of this layer was 13.4%. The water content of the native, brown, silty clay ranged from 13.4 to 18%. Groundwater was not encountered in the construction of the two trenches, nor was it found in the samples obtained from the push-in hand sampler. Bulk samples were taken

of the soils from each of the two surficial layers. Details of the laboratory test program, including triaxial testing on the soil samples from the site, are presented in this report.

Backfill for the first test was a mix of surficial sandy fill and native silty clays excavated from the trenches which consisted of a clayey soil with sand and cobbles. The top 457 mm of the trench sections was a granular fill with 100% passing the 25 mm sieve. This fill was angular, well graded, with nonplastic fines.

Soils Characterization at Uplift Test

At the time of excavation and backfilling of the two trenches for the uplift tests, a number of soil samples were taken for evaluation. Samples were taken from each layer or soil type present and geotechnical tests were performed on the samples. These tests included grain-size analyses, Atterberg Limits and strength tests, including unsaturated triaxial tests. The results from these tests were used to characterize the soil's strength and deformation properties and relevant inputs for numerical modeling of the uplift tests.

The soil that was visually classified as the upper native sand layer shows a well-graded particle size distribution with 20% fines (Figure 60). In addition, the grain-size distribution for the various soils is shown in Figure 60. These curves are typical but may not represent the entirety of the site. The grain size distribution curves for the road base used for the two tests had similar grain size distributions, indicating that the samples were from the same stockpile. The native lower clay layer was poorly graded with 72% fines (less than 0.075 mm in diameter).

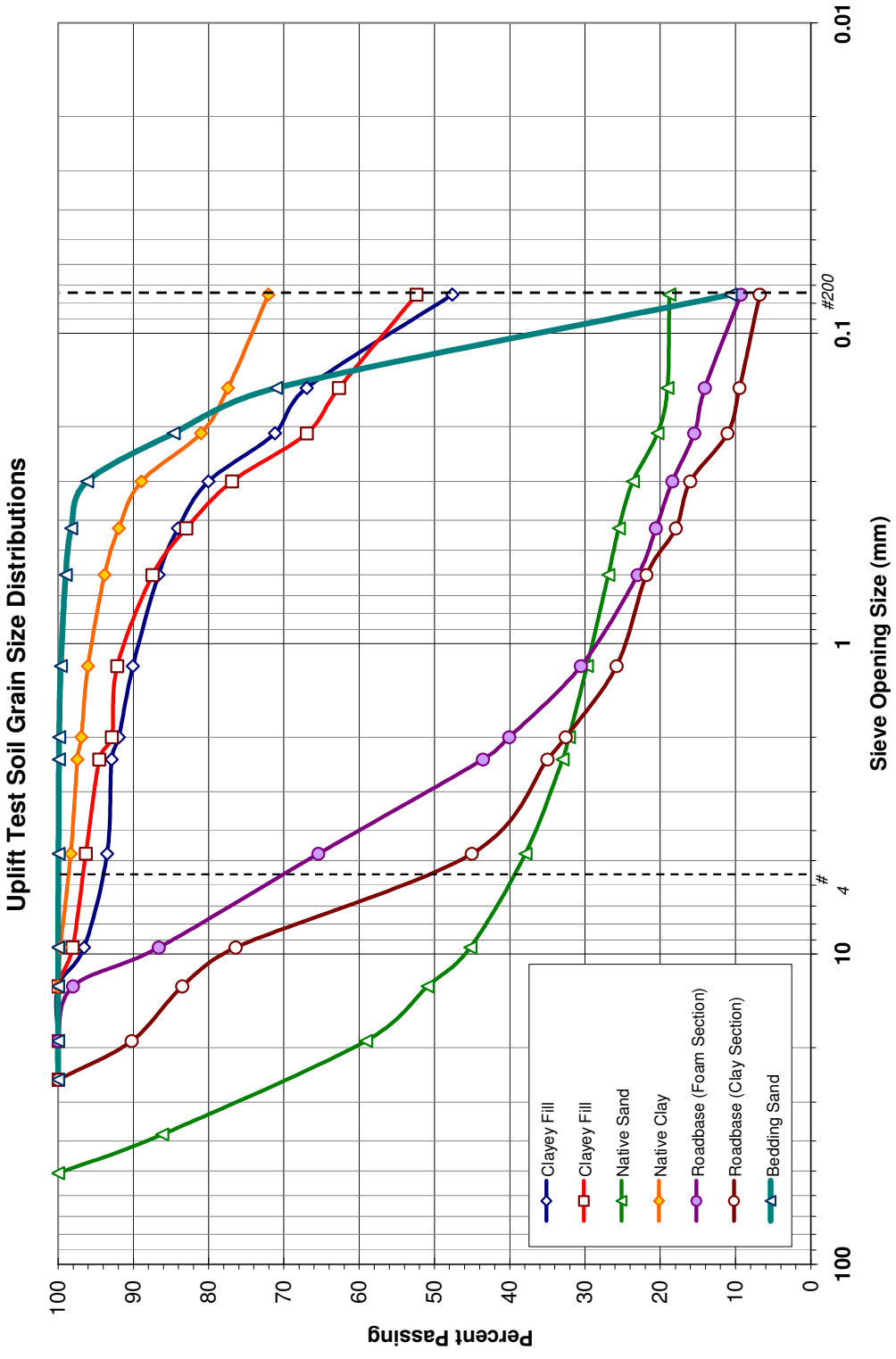

Figure 60. Grain size distributions

The strength and deformation characteristics of a given soil are highly influenced by the amount of fines present in the soil. Generally, soils with high fines content are softer, more susceptible to changes in moisture content and are more sensitive to the compaction method used.

Sand cone tests were also performed to measure the in-situ density of the soils. Four sand cone tests were completed: two on the compacted clayey fill used for the soil backfill test and two on the UTBC. The results of the sand cone tests are given in Table 17.

The water content of a soil and its plasticity index are important geotechnical properties, especially for soils with significant fines content. Table 18 shows the results of the water content tests performed on the various samples. Only the native clay layer and the clayey fill had any significant plasticity.

Table 17. Sand cone test results

Sample	Wet Soil	Dry Soil	Volume	Moist Density	Dry Density	Moist Unit Weight	Dry Unit Weight	Water Content
----------	*grams*	*grams*	*cm^3*	*g/cm^3*	*g/cm^3*	*kN/m^3*	*kN/m^3*	*%*
Clayey Fill	1957.8	1593.91	1081.35	1.81	1.47	18.12	15.64	15.92
Clayey Fill	1024.11	882.98	571.1	1.79	1.55	17.94	15.48	15.98
Road base (Clay Section)	1811.31	1727.02	923.8	1.96	1.87	19.61	18.70	4.88
Road base (Foam Section)	2102.94	2018.74	108.35	1.94	1.87	19.45	18.68	4.17

Table 18. Moisture content test results

Sample	Mass Wet Soil	Mass Dry Soil	Mass Soil	Water Content
---	*grams*	*grams*	*grams*	*%*
Bedding	844.28	742.59	101.69	13.69
Road base (EPS Section)	2102.91	2018.74	84.20	4.17
Road base (Clay Section)	1811.31	1727.02	84.29	22.83
Native Clay	1957.81	1593.91	363.90	13.44
Native Sand	785.44	692.38	93.09	15.92
Clayey Fill	725.98	626.25	99.73	4.88
Clayey Fill	1024.11	882.98	141.13	15.98

Several tests were performed to characterize the shear strength of the soils, including direct shear and triaxial shear tests. The direct shear test was chosen for the road base samples because of the angularity of the particles and the sharpness of the gravels. For these tests, the soil sample recompacted to the appropriate in situ, compacted density. The sample was then sheared to determine its strength along the shearing plane located at midheight of the 50.8 mm sample. A series of tests at increasing confining pressures were performed to estimate the Mohr-Coulomb envelope for the soil. The direct shear force-displacement curves for the UTBC are presented in Figure 61, and the failure envelope is shown in Figure 62. The results in Figure 62 indicate that the failure envelope for the road base was slightly curved. A straight line fit through the data at low stresses suggests that the drained friction angle of the UTBC was about 43°.

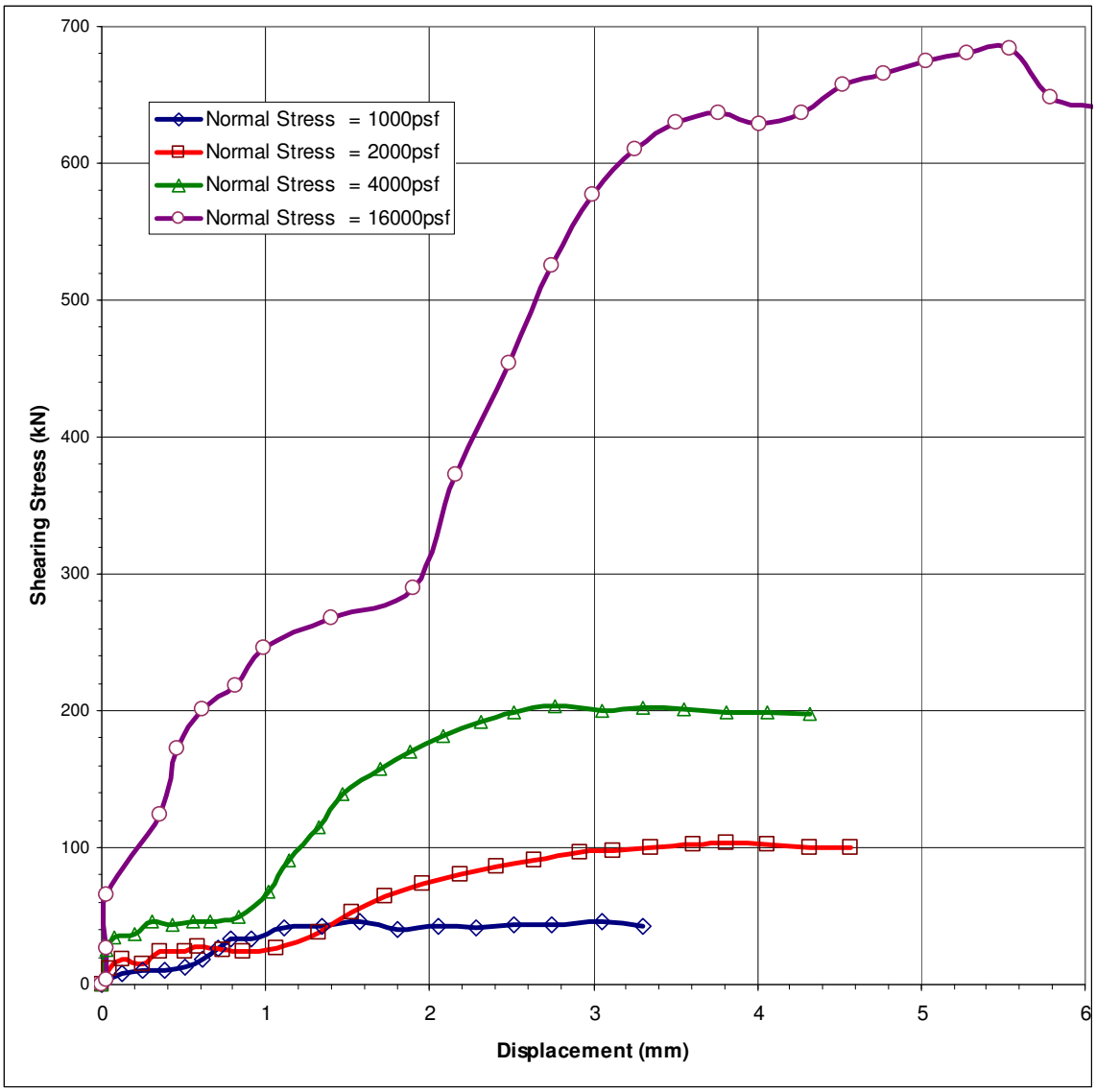

Figure 61. UTBC direct shear test curves

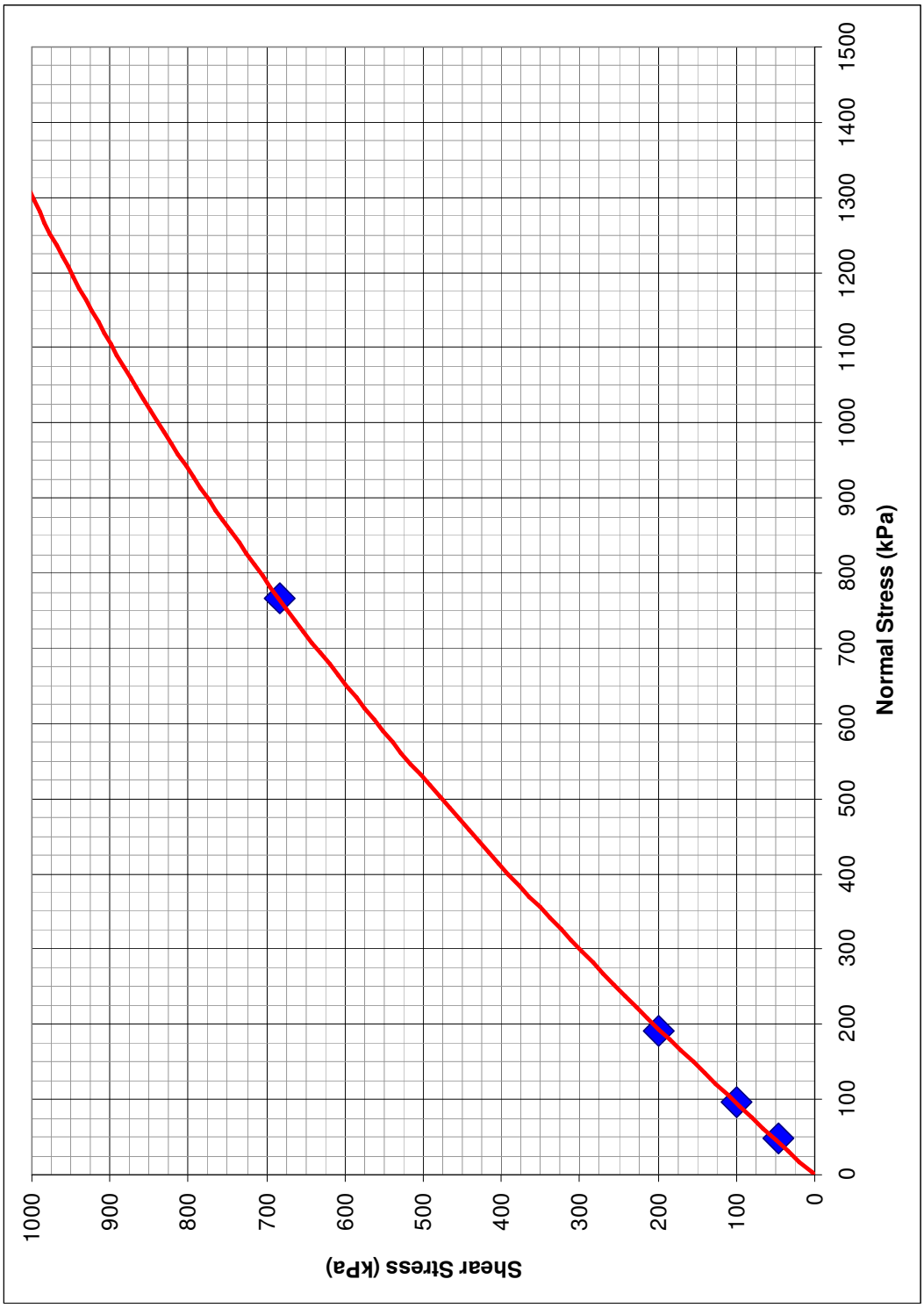

Figure 62. UTBC failure envelope

In addition to the direct shear tests, triaxial testing was performed that consisted of 12 tests: 4 tests on each of the clayey fill, native clay and native sand, respectively. The samples for these tests were consolidated and sheared in a manner to better represent their actual failure behavior. Both consolidated undrained (CU) and consolidated drained (CD) triaxial tests were performed. The CU tests were performed on backpressure saturated specimens. Pore pressure measurements were made in CU testing to determine the drained strength properties of the soils in addition to their undrained strength properties.

Table 19 shows the results for the 4 CU tests performed in the triaxial test series. Among the output results of the CU test are the total and effective cohesion intercept and the total and effective friction angle. The CD tests were performed on unsaturated samples, save for one exception: one CD test was run on a backpressure saturated sample to assess the effects of saturation on the strength of the soils at the site.

Table 19. CU test results

Layer	γ_o	ω_o	σ'_c	σ_{3f}	σ'_{3f}	σ'_{df}	Su	c	ϕ	c’	ϕ'
--------	*kN/m^3*	*%*	*kPa*	*kPa*	*kPa*	*kPa*	*kPa*	*kPa*	*deg*	*kPa*	*deg*
Native Clay	17.56	17.7	77.8	390.4	39.4	112.1	56.1	60	0	14.4	26.8
Native Clay	17.64	17.8	143.6	442.9	61.1	131.3	65.6	60	0	14.4	26.8
Native Sand	18.34	13.3	191.5	504.1	102.9	209.9	104.9	60	6	0	30.3
Clayey Fill	18.33	16.5	239.4	203.4	122.2	304.9	152.5	60	15.3	0	33.7

A typical stress-strain curve for two of the triaxial tests is shown in Figure 63. This figure shows the curves for two unsaturated consolidated drained (CD) triaxial tests on the lower native clay layer. (The CD test is performed on the consolidated sample; but sheared at a sufficiently slow rate so water can escape the sample; hence, no excess pore water pressure is generated during the shear phase.) In a CD test for an unsaturated soil, the sample is consolidated and tested at its in situ or compacted water content. Drainage is allowed and the test is run sufficiently slowly so shear-induced pore water pressures are not generated. Volume change in the sample for an unsaturated CD triaxial test is calculated by measuring changes in water volume in the outer cell. In contrast, for a saturated CD test, the sample volume change is calculated for the amount of water flowing in or out of the sample from the inner cell. Table 20 shows the consolidated drained (CD) triaxial compression test results, Figure 63 shows typical triaxial data and Table 21 shows the unsaturated CD triaxial test results. The triaxial results for the entire series are given in Table 22, which includes the water content, Atterberg Limits and unit weight for the various soils at the uplift test site.

Table 20. CD triaxial test results

Soil Layer	γ_f	γ_o	ω_o	σ'_c	σ'_{3f}	σ'_{1f}	σ'_{df}	Stress Ratio	c’	ϕ'	ϕ'_{cs-pk}
--------	*kN/m^3*	*kN/m^3*	*%*	*kPa*	*kPa*	*kPa*	*kPa*	--------	*kPa*	*deg*	*deg*
Native Sand	19.75	17.40	13.49	77.8	77.8	273.2	195.4	3.51	0	34.6	33.8

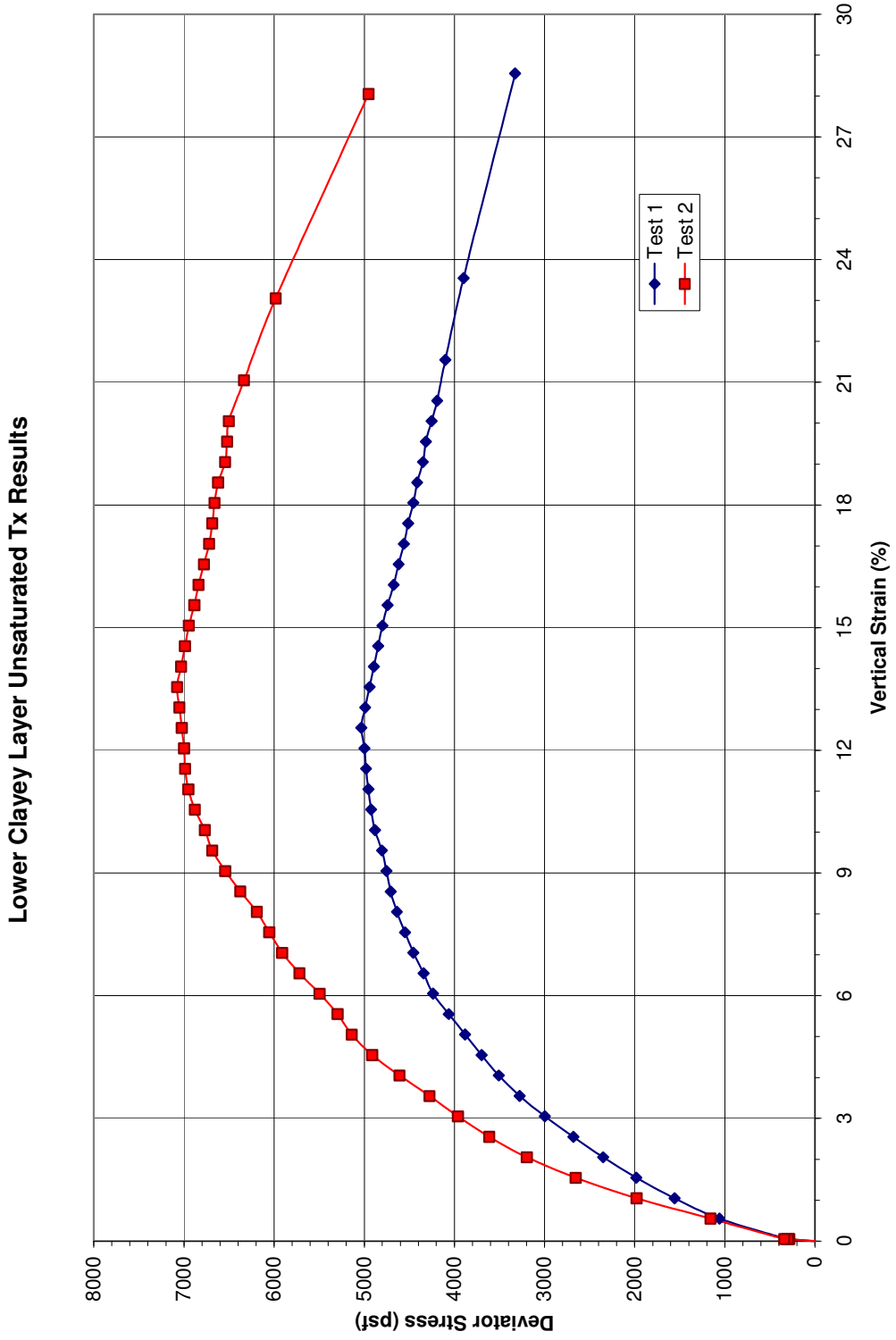

Figure 63. Typical CD triaxial test data

Table 21. CD unsaturated triaxial test results

Soil Layer	γ_f	γ_o	ω_o	σ'_c	σ'_{3f}	σ'_{1f}	σ'_{df}	Stress Ratio	c'	ϕ'
--------	*kN/m³*	*kN/m³*	*%*	*kPa*	*kPa*	*kPa*	*kPa*	--------	*kPa*	*deg*
Native Clay	20.90	18.32	14.07	77.8	77.8	346.6	268.8	4.45	1250	23.2
Native Clay	16.69	17.30	13.84	143.6	143.6	479.9	336.2	3.34	1250	23.2
Native Sand	20.62	17.46	18.01	77.8	77.8	318.8	241.0	4.10	750	27.2
Native Sand	20.93	17.96	16.58	143.6	143.6	482.4	338.8	3.36	750	27.2
Clayey Fill	20.93	18.09	15.67	240	240	771.9	532.5	3.22	750	28.0
Clayey Fill	20.95	18.07	15.98	95.8	95.5	359.7	263.9	3.76	750	28.0

Table 22. Final geotechnical test results

Material	Moist Unit Weight	Water Content	Liquid Limit	Plastic Limit	Plasticity Index	Cohesion	Friction	Dilation
--------	*kN/m^3*	*%*	*%*	*%*	*%*	*kPa*	*deg*	*deg*
Bedding	15.48	13.7	0	0	0	0	32	2
Road base	19.54	4.5	0	0	0	0	43	7
Native Clay	17.62	22.8	37.4	21.4	16	60	23	0
Native Sand	18.34	13.4	0	0	0	35.9	27	0
Clayey Fill	18.02	15.9	24.4	20.4	4	35.9	28	0

Pipe and Geofoam

The pipes that were used in the uplift tests were grade X42 with an outer diameter of 323.9 mm and a wall thickness of approximately 6.5 mm. The pipe was cut into two 4.57 m lengths. Both sections of pipe were visually inspected for defects, and none were observed prior to placement in the trenches. On each end, a 3 m #4 reinforcing bar tell-tale was welded in a vertical position to assist in measuring the displacement uplift. The reinforcing bar was observed to be in good condition.

The Geofoam blocks that were used in the Geofoam cover trench were EPS 29 (i.e., density of 29 kg/m^3), which is a relatively dense and stiff EPS Geofoam block manufactured by ACH Foam in Murray, Utah. The blocks were molded and cut in the factory prior to delivery. (EPS 29 is in the mid to upper range of Geofoam products in terms of its strength and stiffness. This density was chosen by Questar Corporation because EPS 29 was used along existing pipeline alignments, such as the reconstruction done along 3300 South Street in Salt Lake City.) There were four blocks used in the experiment; each was visually inspected and observed to be in good condition with only a few surface markings from shipping and handling. No tool marks from onsite installation were observed on the blocks prior to placement. The blocks came in two pairs with approximately the same dimensions. Two of the blocks were 1219 x 914 x 914 mm and the other two blocks were 1067 x 914 x 914 mm. Slots were cut in the block on site during installation to allow the crane rigging to pass between blocks. These slots were cut using a chain-saw and were no larger than 127 mm wide and 50 mm deep on the side of the block.

Experimental Design

The trench and cover cross-sections were predetermined by Questar gas Company and the University of Utah for the tests prior to construction. The first test cross-section was that of the native soil backfill. This served as a baseline test to compare with the results from the EPS Geofoam cover system. A schematic drawing of the native soil backfill test cross-section is shown in Figure 64. In constructing this test, the trench was over-excavated 150 mm and bedding sand was placed beneath the pipe. The pipe was fitted with crane rigging and placed atop the bedding sand. Subsequently, other lifts of sand were placed along the sides of the pipe until the pipe was covered with 150 mm of sand. This bedding and sand was placed loosely and was not compacted.

Above the 150 mm of bedding sand, the excavation spoil was placed and compacted in the trench up to 457 mm below the ground surface. This material was compacted with an impact-type compactor (i.e., "jumping jack"). The backfill was tested with a sand cone test to measure its density. Two total earth pressure cells were horizontally embedded in the backfill at 304 mm and 610 mm above the top of the pipe. Above the random clayey backfill from the site, and beneath the 457mm of UTBC, another earth pressure cell was placed, and the 457 mm of granular material (UTBC) was placed and compacted with a self-propelled tamping foot compactor with vibrating drums.

The crane rigging that was attached to the pipe was kept as vertical as possible throughout backfill and compaction. String pod potentiometers were attached to the rebar tell-tale. The string pods were suspended by lumber reference frames that were founded outside the zone of uplift so that absolute uplift measurements could be made.

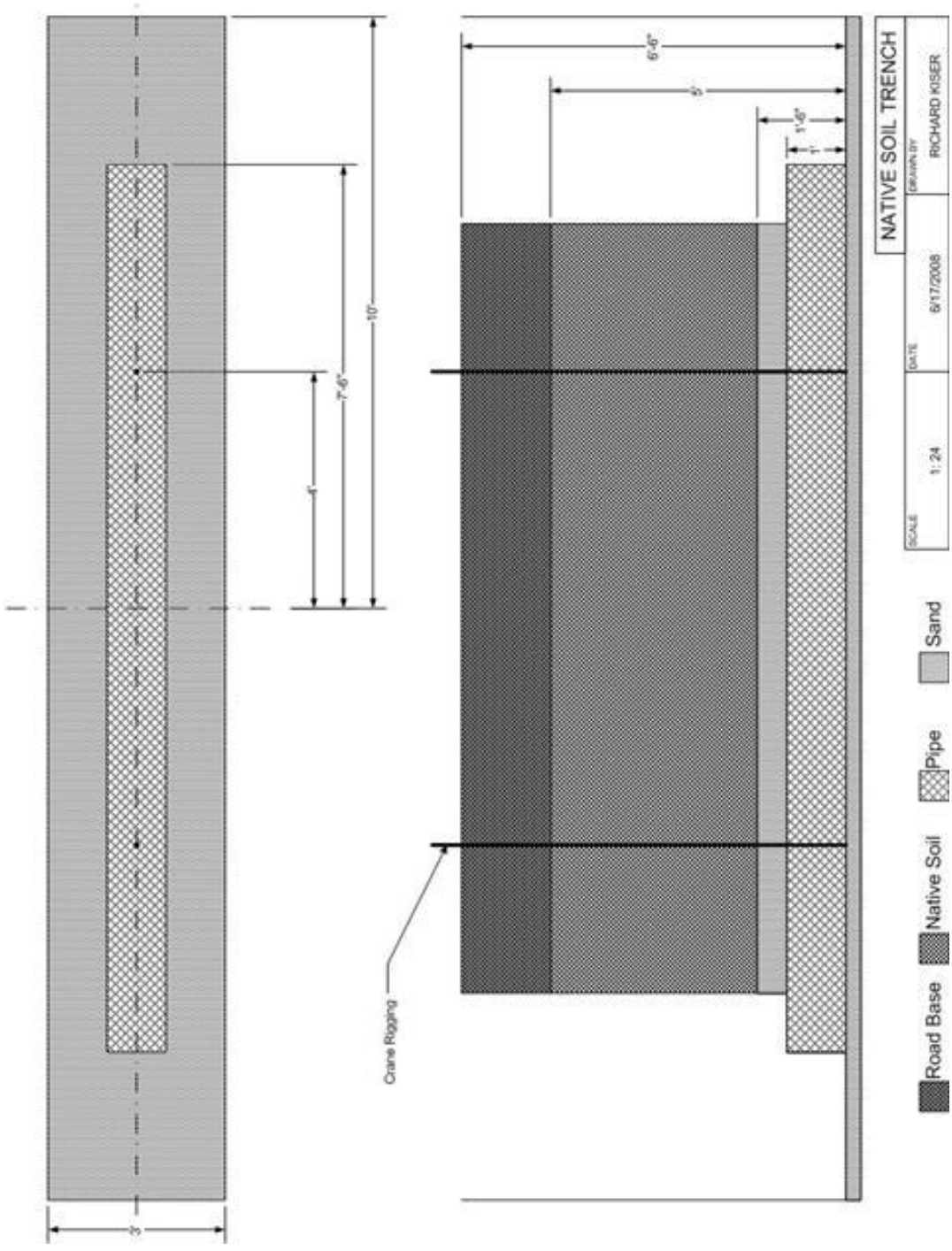

Figure 64. Soil backfill trench schematic

The second trench was the EPS Geofoam cover system cross-section. For this test, the trench was excavated and the pipe was placed in bedding sand similar to the first trench. The crane rigging was again placed at 1.143 m from each end of the pipe and kept vertical throughout backfill and compaction. An earth pressure cell was placed on the top of the bedding sand. The EPS Geofoam blocks were then placed on the bedding sand, which were overlain by the reinforced concrete load distribution slab. A 457 mm layer road base was placed over the load distribution slab and compacted.

During the construction of this trench, it must be noted that the clayey soils on the sides of the trench remained vertical during Geofoam block placement. In some places, the trench walls did not fit tightly against the Geofoam blocks. In these locations, small gaps remained throughout the test.

An earth pressure cell was placed on top of the Geofoam blocks at the center of the trench to measure vertical total earth pressure during testing. A thin layer (< 150 mm) of bedding sand was then placed on the blocks to level the next course. The next layer in the system was a 152-mm reinforced concrete load distribution slab. The slab was not continuous, but consisted of panels that were 1067 mm wide, so that the panels slightly overhung the outer edge of the Geofoam blocks. These slabs ran the length of the pipe with 152 mm spaces to allow crane rigging to pass through at 1.143 m from each end. Above the reinforced concrete slabs, 417 mm of granular material was placed and compacted. Figure 65 shows the schematic for this trench and cover system.

Figures 66 and 67 show the two completed trench cross sections after construction. These figures show the crane rigging which comes to the surface of the soil at the outer quarter points of the pipe and trench.

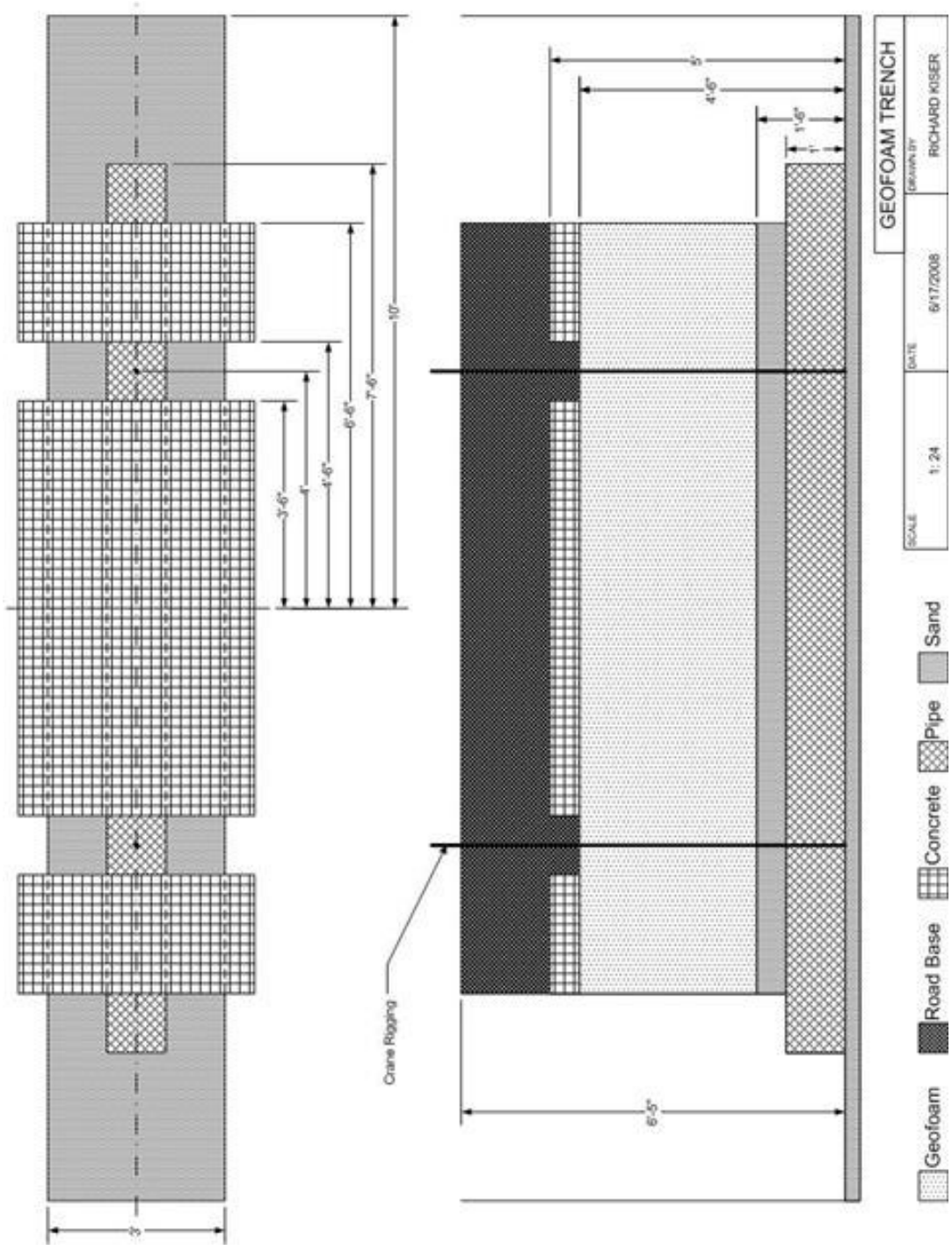

Figure 65. EPS Geofoam cover trench schematic

Figure 66. Soil backfill trench, with compacted fill

Figure 67. EPS Geofoam backfill trench

Procedures

After construction of the two trenches and cover systems, the site was inactive for two days because of scheduling of equipment and personnel. This waiting period allowed the soils and Geofoam to come to self-weight equilibrium under their respective vertical and horizontal stress states. Appropriate caution signs, fall protection and warnings were placed around the site during the delay. No tampering with the equipment and test site was observed prior to testing.

For the uplift tests, an 890 kN truck mounted crane was mobilized to the site (Figure 68). A large capacity crane was need for two reasons: (1) the long boom and reach allowed the rigging to be pulled up vertically, to limit horizontal forces to a minimum and (2) the high capacity of the crane allowed the uplift to be done in a controlled and slow manner in order to avoid any jerking or sudden movement.

Figure 68. Tire mounted crane used for uplift tests

After the crane arrived on the site, the boom was raised and the rigging connected to the inline tension load cell. The instrumentation cables were connected to the datalogger (for resistance-based instruments) and to the readout box (for the two vibrating wire earth pressure cells). The data acquisition system was initiated and began to gather data to establish the zero-uplift readings. The crane raised the rigging until all slack was taken out of the cables and a small amount of tension was placed on the lines. At this time, the test was paused as a verification of test setup and instrumentation was performed.

When all parties were ready, including video and photography, the crane operator was given the signal to begin uplift, as slow as possible (152 mm per minute). At two times in each test, uplift was paused for a few seconds to allow the crane operator to inspect the rigging to ensure its condition and safety. Data was monitored continuously through these pauses and continued until the pipe had completely ruptured the cover system or the pipe/cable system had reached a predetermined criterion. The test stopping criterion for the soil backfill test was a displacement of 417 mm, or a tensile force in the cables of 712 kN, or a sudden dramatic failure of the soils in uplift that rendered the displacement data useless. For this case, the third criterion was first met. For the EPS Geofoam cover system, the stopping criterion was 762 mm of uplift, or tensile force of 356 kN, or a sudden dramatic failure of the soils in uplift. The displacement criterion was first met for this test.

After the uplift was stopped, additional video and photography of the posttest conditions were done to document the failure state of each experiment. The pipe was then lowered slowly by the crane operator until slack was observed in the lines. Data acquisition was stopped at this point. After both tests were completed, each trench was

excavated carefully to retrieve instruments and ascertain the conditions of both pipes and the EPS Geofoam blocks.

Observations

Soil Backfill Test

The uplift of the soil backfilled trench test was actually performed second. This test proceeded much slower than the EPS Geofoam cover testing due to the larger force required to uplift the backfill-soil system. Because of this, the crane was able to lift this system at a much slower rate, allowing for more time series data to be acquired. The uplift of this section was unremarkable, until the peak uplift force was reached. After this, the west end of the pipe began to uplift much faster than the east end. A few seconds after the creation of this imbalance, the west end of the pipe rapidly uplifted through the backfill while the east end continued to uplift slowly. This eccentric uplift placed the pipe severely out of level and the sudden uplift of the west end destroyed the string pot potentiometer on that end of the pipe, rendering further displacement data useless. Fortunately all this occurred after the peak force of uplift had been recorded, so this behavior only affected the latter part of the postpeak displacement. In addition, no detectable bending in the pipe was observed before or after the catastrophic failure on the west end of the trench system. Figure 69 shows the differences in uplift displacements between the pipe ends for the soil backfill trench section.

Figure 69. Uplifted soil backfill system

EPS Geofoam Test

Figure 70 shows the uplifted EPS Geofoam section. During uplift of the EPS Geofoam section, very little compression of the Geofoam was observed during testing. The ends did not appear to be compressed to any observable degree even after the peak force was reached. (A grid had been drawn on the Geofoam block face to track the deformations of the foam block.) However, after excavation of the Geofoam blocks, it was seen that along the length of the pipe, the Geofoam compressed about 50 to 75 mm. Figure 71 shows the deformations along the bottom of one of the EPS Geofoam blocks.

Figure 70. Uplifted EPS Geofoam system

Figure 71. Deformations along bottom of Geofoam block

In contrast to the soil backfill test, the uplift of the EPS Geofoam system was very uniform with little rotation of the pipe occurring during uplift. The string pods attached to the east and west sides of the pipe showed approximately 30.5 mm of maximum differential displacement during the test. Because the uplift resistance was so low for the EPS cover, this offered little resistance to the crane during uplift; maintaining a slow uplift rate was difficult. As before, no pipe bending was observed at any time.

Figure 71 shows that there was no significant internal deformation of the Geofoam block as seen by the uniform grid that had been marked on the block prior to testing. Figure 70 also shows the amount of final displacement achieved during this test. It was

noted that the load distribution slab had protected the Geofoam from damage during uplift and the failure was a sliding failure along the block-trench wall interface.

Vertical Pipe Movement Results

The force-displacement and stress data gathered during the tests were imported into Excel for analysis. The results of the force and displacement data for the soil backfill test are shown in Figure 72. Both the raw data gathered by the instruments and the net results are presented. (The slopes of the curve are the nonlinear spring relations needed for pipeline evaluations for this case). Note that the soil backfill system had a peak force of 520 kN at a displacement of 70 mm. The soil backfill system also had an initial force of about 100 kN at very small displacement (Figure 72). This approximately corresponds to the weight of the system and represents the vertical uplift force prior to any significant mobilization of the soil strength in the cover. SP18 and SP20 are the two vertical displacement transducers from the soil backfill test.

There is a large amount of scatter in the displacement data gathered in the testing. However, the force data had very little scatter. The source of the scatter in the displacement data is unknown, but there is a possibility that the string-pot displacement transducers are affected by changes in displacement rate that occurred at the beginning of the soil uplift test, as well as during a pause for safety check during test uplift. The soil backfill section showed a large decrease in force after the peak until an approximately 300 kN residual force was achieved through the end of the test.

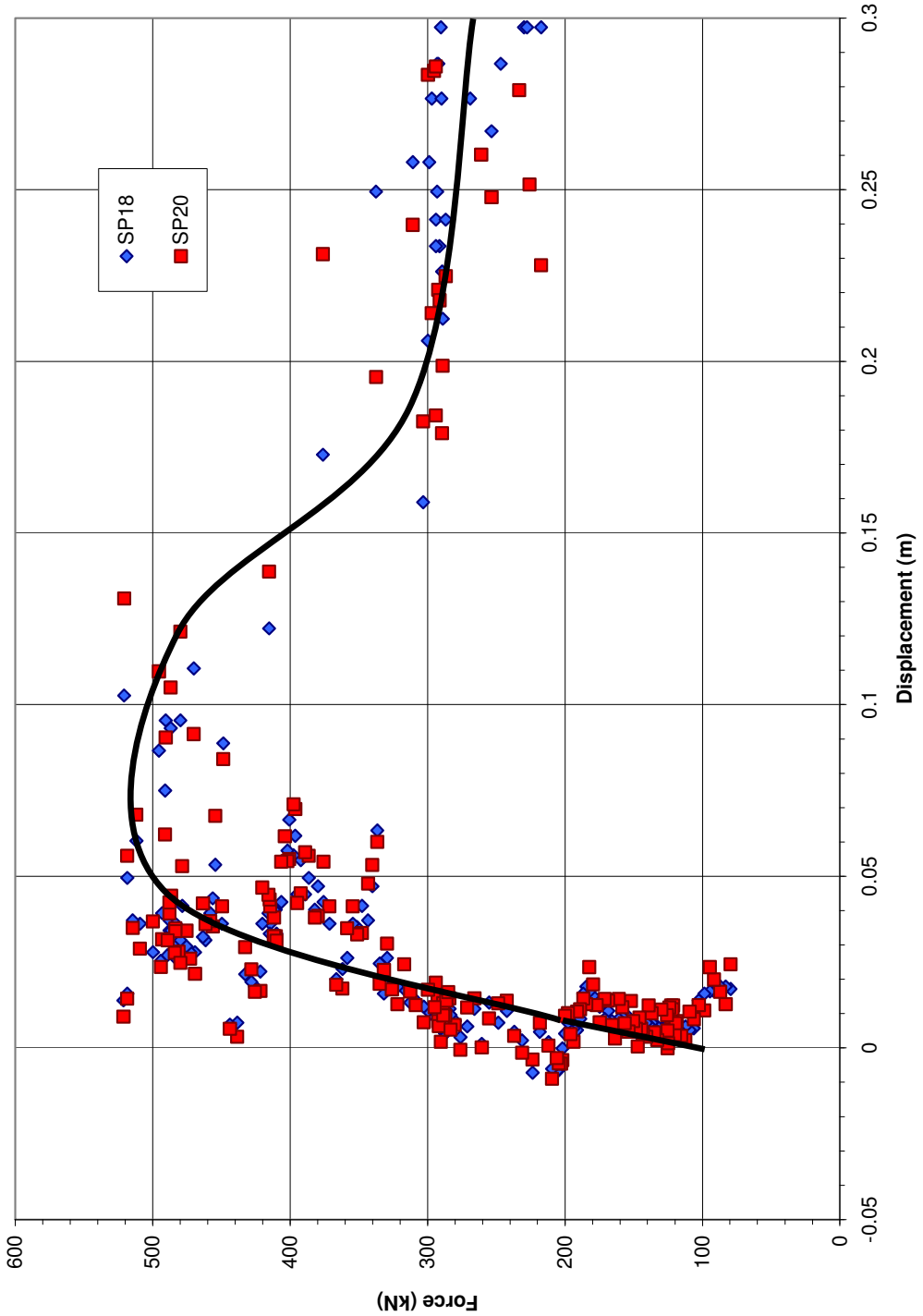

Figure 72. Raw data from native soil test with average curve

The Geofoam section test displacement data are shown in Figure 73 as raw instrument readings as a function of time. These instrument readings are in mV/V excitation, with two different symbols for the two different displacement transducers used. The scatter in the displacement data is more pronounced in one of the transducers, so the net results were developed largely from the data set that is more consistent. The relationship between readings and displacements is highly nonlinear, and the initial jump in readings corresponds to a small actual displacement.

The force and displacement data are plotted in Figure 74. The two displacement data sets are paired with the force data to show individual data points for the Geofoam section. The net force-displacement relationship is overlain in Figure 74 by the individual data points. The EPS Geofoam section had an uplift resistance force of 35 kN before any displacement was detected in the system, approximately the weight of the system. The weight of the system for both sections was mobilized before any displacement was recorded by the transducers. This occurred as friction was mobilized along the slip planes of the system. The peak force for the EPS Geofoam section was 136 kN at a displacement of 188 mm. It is seen in Figure 74 that the slope of the uplift curve was relatively linear until approximately 188 mm of displacement where the peak of 136 kN was encountered.

Figure 74 shows that the shape of the uplift curve was reasonably linear until the peak is reached. Postpeak behavior is manifest by a rapid decrease in force until a vertical pipe displacement of about 400 mm. A constant load of 88 kN was attained after a displacement of 400 mm. This constant force was measured until the end of the test. This force is largely the resistance of the sliding Geofoam block against the trench side walls, since at that range of displacements, the UTBC atop the section had completely sheared.

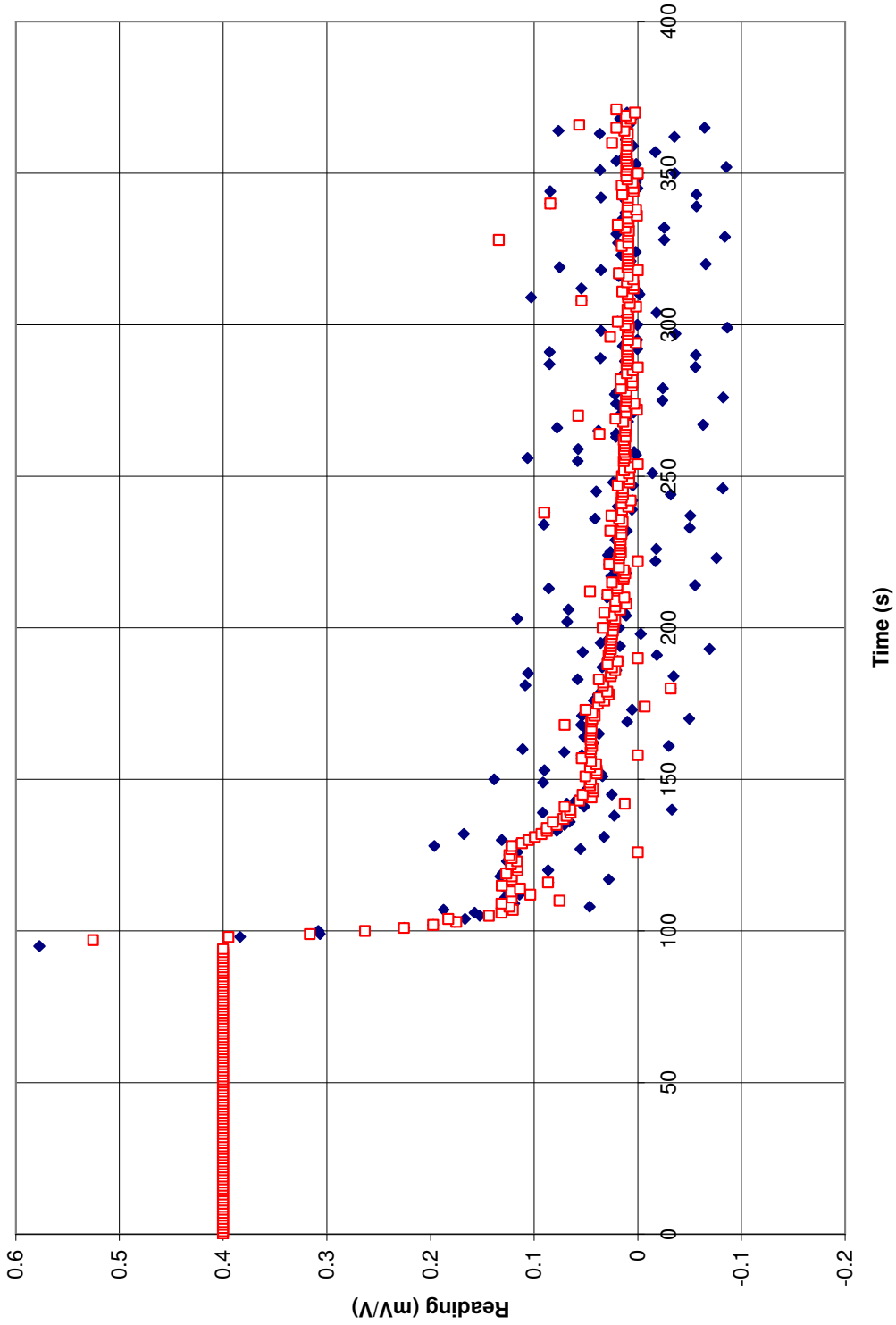

Figure 73. Geofoam test displacement data at time

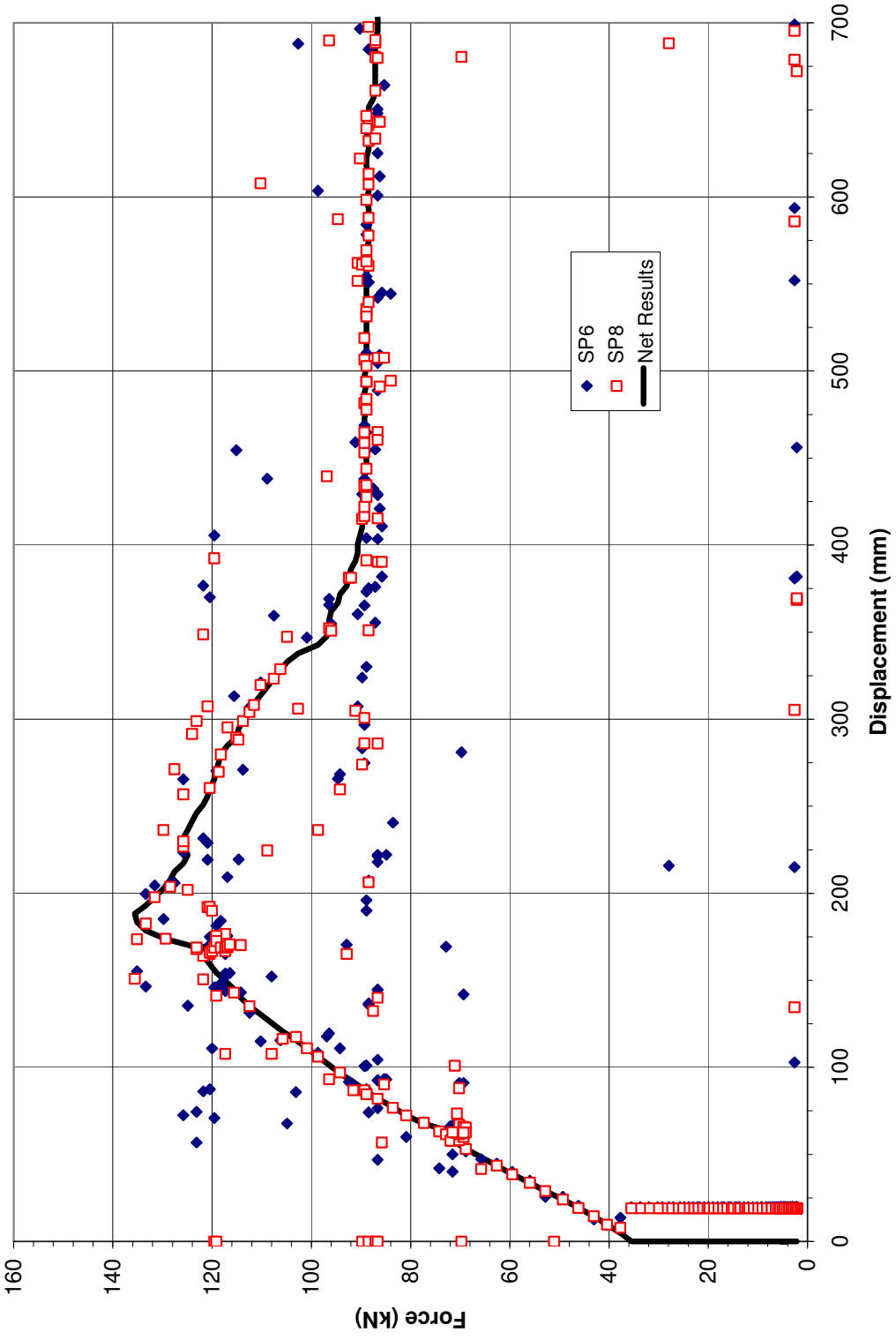

Figure 74. Raw Geofoam test data overlain by net curve

The net results of both the soil and Geofoam sections are shown together in Figure 75 without data points.

Figure 75 is for comparison of the two tests. The slope of a force-displacement curve is the stiffness of the system and in linear systems represents the spring constant. However, this slope may change depending on the nonlinearity of the uplift behavior. Both sections show initial linear behavior. The soil backfill section becomes less linear as the peak force is approached than the Geofoam section. The Geofoam section retains a much more linear shape through the entire test. Both sections show a decrease in force after the peak, though the soil backfill section had a much large decrease both as a total force and a percentge of the peak force.

The data in Figure 75 show that the stiffness of the EPS Geofoam system was approximately an order of magnitude less than that of the soil backfill system. The uplift force at peak is divided by the length of the pipe (4.572 m) to find the force/unit length of the system. For the soil backfill system, the force/length was 113.7 kN/m. For the EPS Geofoam section, the force/length was 29.7 kN/m. Thus, the uplift resistance of the EPS Geofoam system was approximately less than that of the soil backfill system by a factor of 3.8.

A useful way to present the results is to normalize the force displacement data (Trautman and O'Rourke, 1985). The normalization accounts for length of pipe, burial depth, and pipe diameter and removes these effects from the results so that the tests can be compared more directly. This technique is very common in determination of parameters for pipeline design crossing faulting (ALA, 2001, ASCE, 1984, and Trautmann and O'Rourke, 1984).

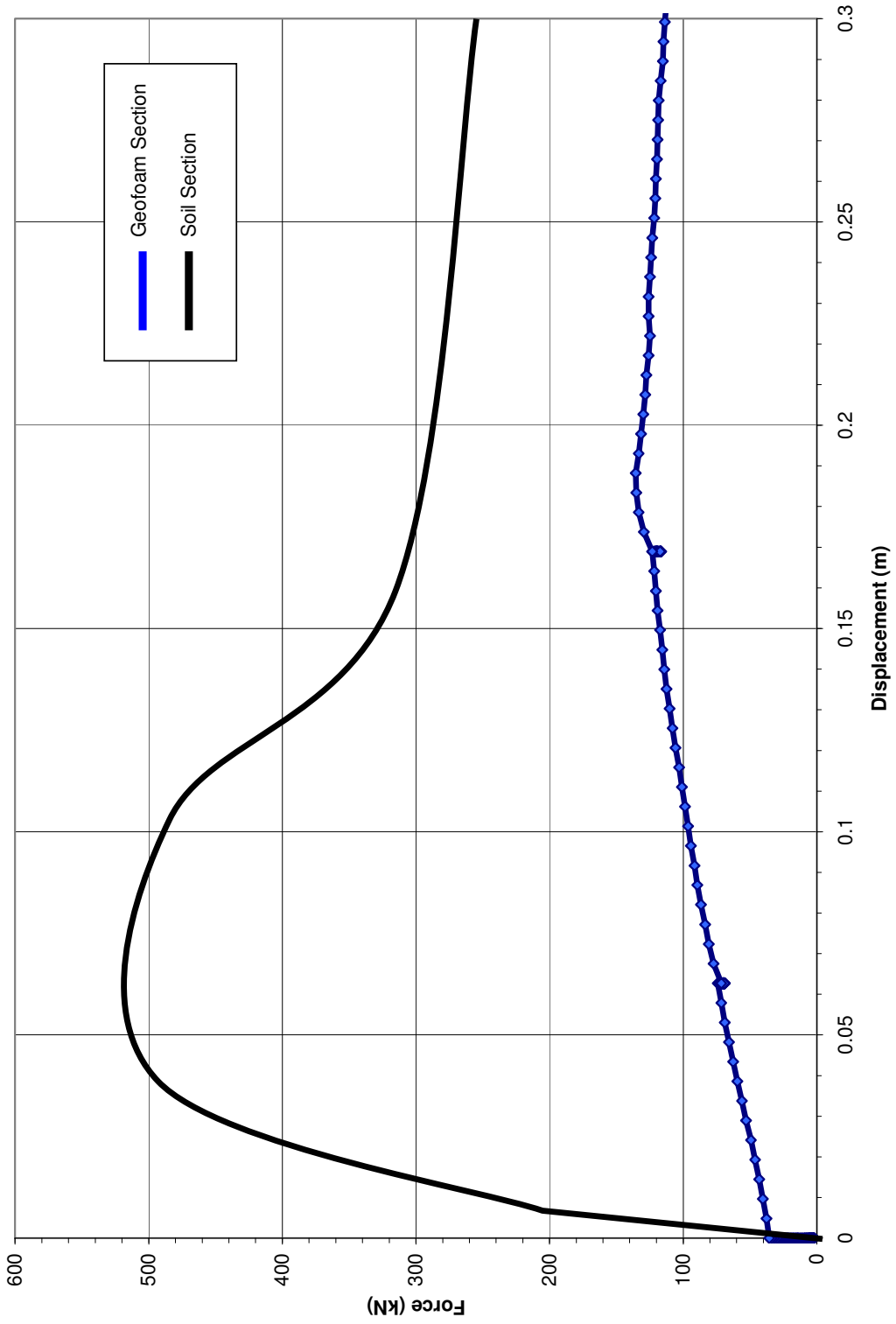

Figure 75. Force data for the two tests

Figure 76 shows the normalized uplift curves for the two systems. The displacement of a pipe in uplift was made dimensionless by dividing the displacement by the pipe diameter. The force was normalized for a homogenous trench system by dividing the uplift force by the length of the pipe, the pipe diameter, the burial depth and the unit weight of the backfill. For a system with several layers, such as these tests, the total uplift force was normalized by dividing the total force by the pipe length, the pipe diameter and the vertical stress on the pipe. Figure 76 has both test curves normalized to the vertical stress of a homogeneous soil cover system. Figure 77 shows the normalized data, when each curve was normalized by the stress on the pipe from the actual vertical load on the pipe in the respective test.

From Figure 76, the normalized curves still showed a significant advantage of EPS Geofoam in reducing uplift stiffness on the pipe when normalized by a soil unit weight as is traditionally done. Note that the relative shapes of the curves did not change between Figures 75 and 76. The peak of the normalized force curve is called the uplift factor and corresponds to a traditional bearing capacity factor used for downward loading in foundation design. The normalized curves recommend for future design are shown in Figure 77. This figure shows less of a normalized difference as the masses of the system are much different and affect the scale when normalized. Figure 76 is more dramatic a presentation, but Figure 77 should be used for design purposes.

Figure 77 shows that when normalized to the low vertical stress of an EPS cover system, the uplift factors only differ by 38% despite the large difference in total uplift force and peak uplift force shown in Figure 75.

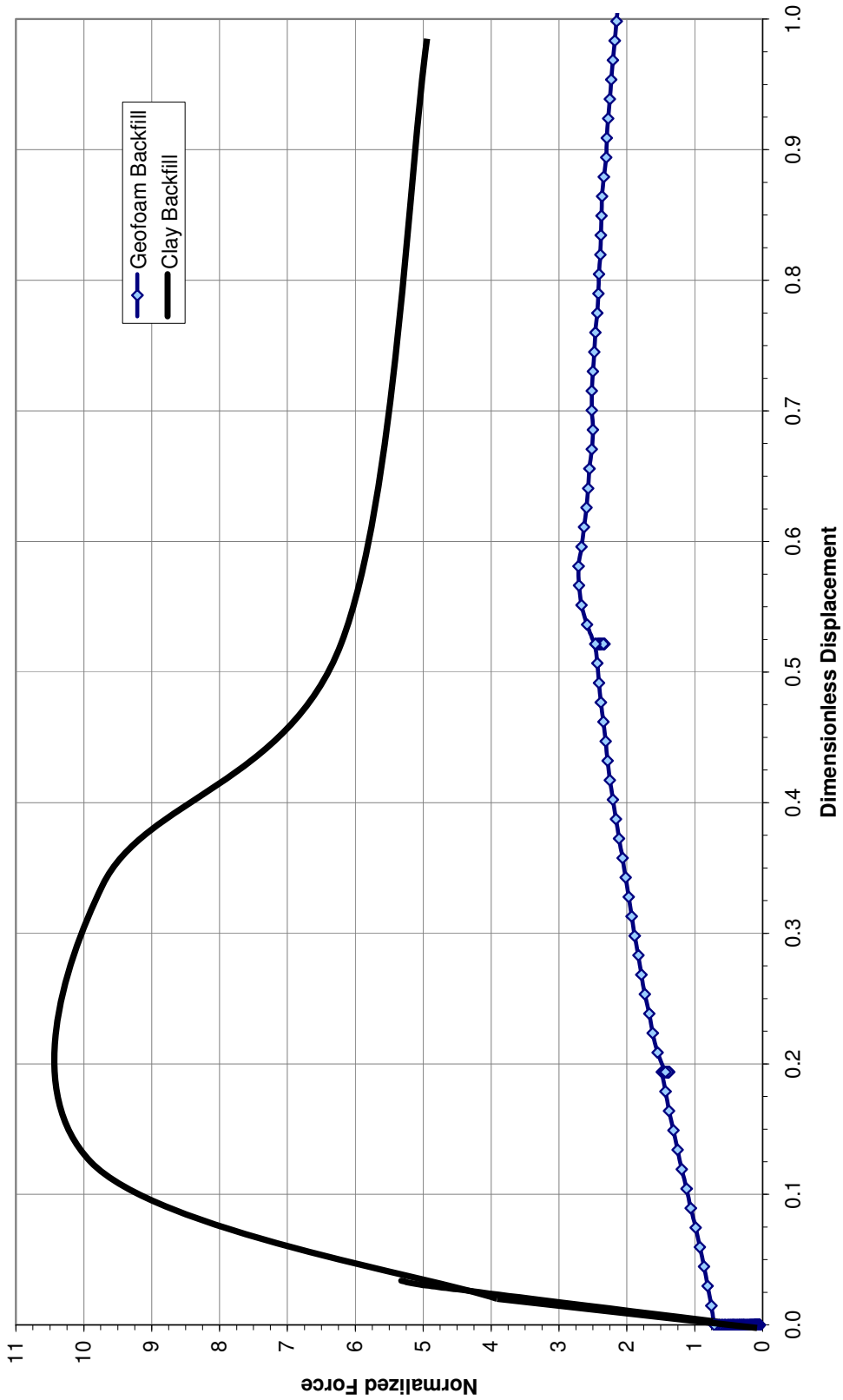

Figure 76. Force normalized to the mass of the soil system

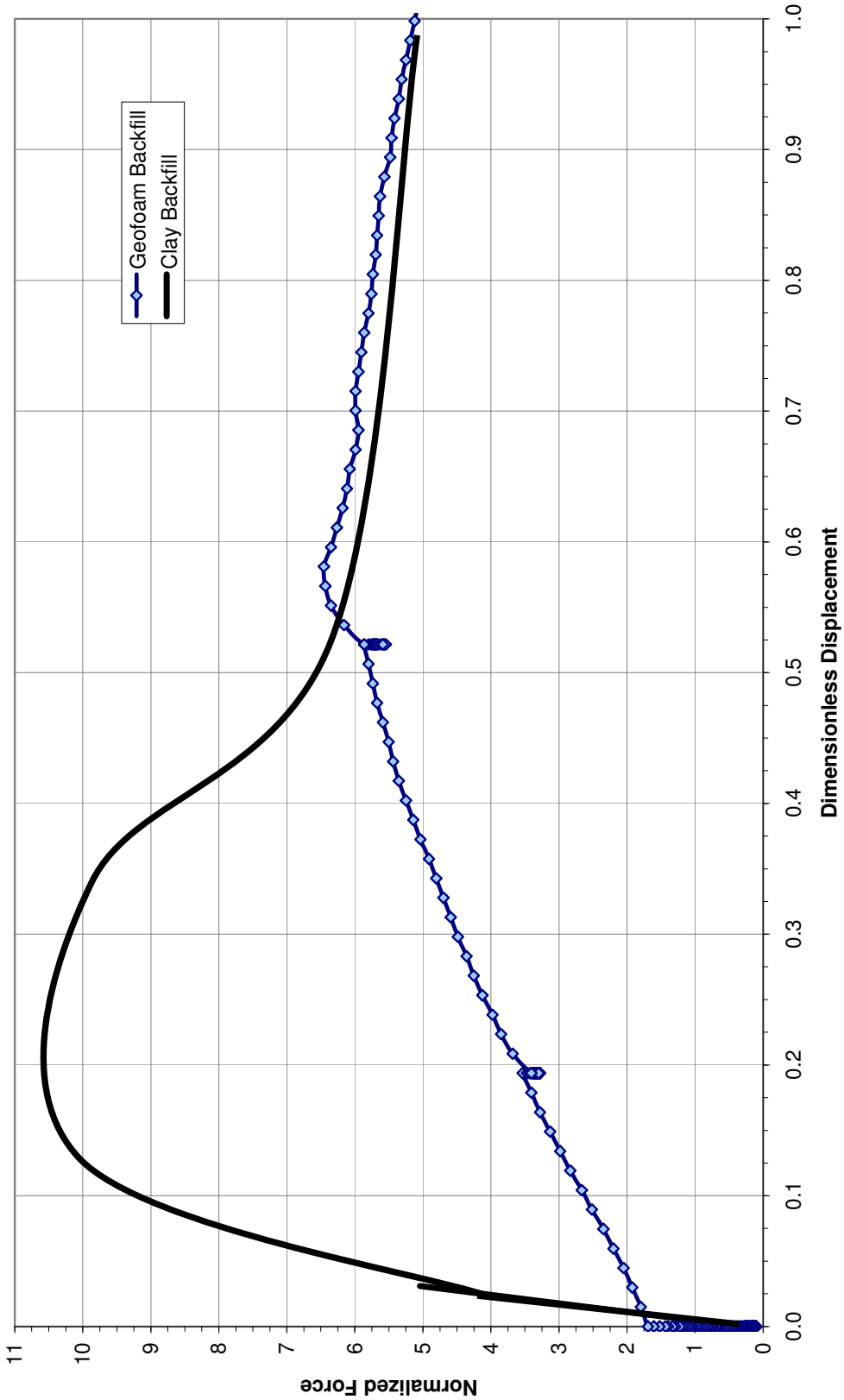

Figure 77. Force normalized to the mass of each system

The uplift factor for the soil backfill system from this experiment was 10.5. The uplift factor for the EPS Geofoam cover system from this experiment was 6.5. A summary of the parameters found in these tests for pipeline design crossing normal faults is presented in Table 23. Figures 75 through 77 show that the dimensionless displacement of the EPS Geofoam section was 2.75 times larger than that of the soil backfill system.

Figure 78 shows the earth pressures from the EPS Geofoam test, while Figure 79 shows the earth pressures measured in the soil backfill test. These results give insight into the behavior of the trench system. There are three earth pressure cell stress curves shown in Figure 78. The pressure cell placed between the pipe and the Geofoam blocks had the

Table 23. Experimental pipe uplift results

	Stiffness *kN /m/m*	Uplift Factor ----------
Soil Backfill System	1625	10.5
EPS Geofoam System	158	6.5

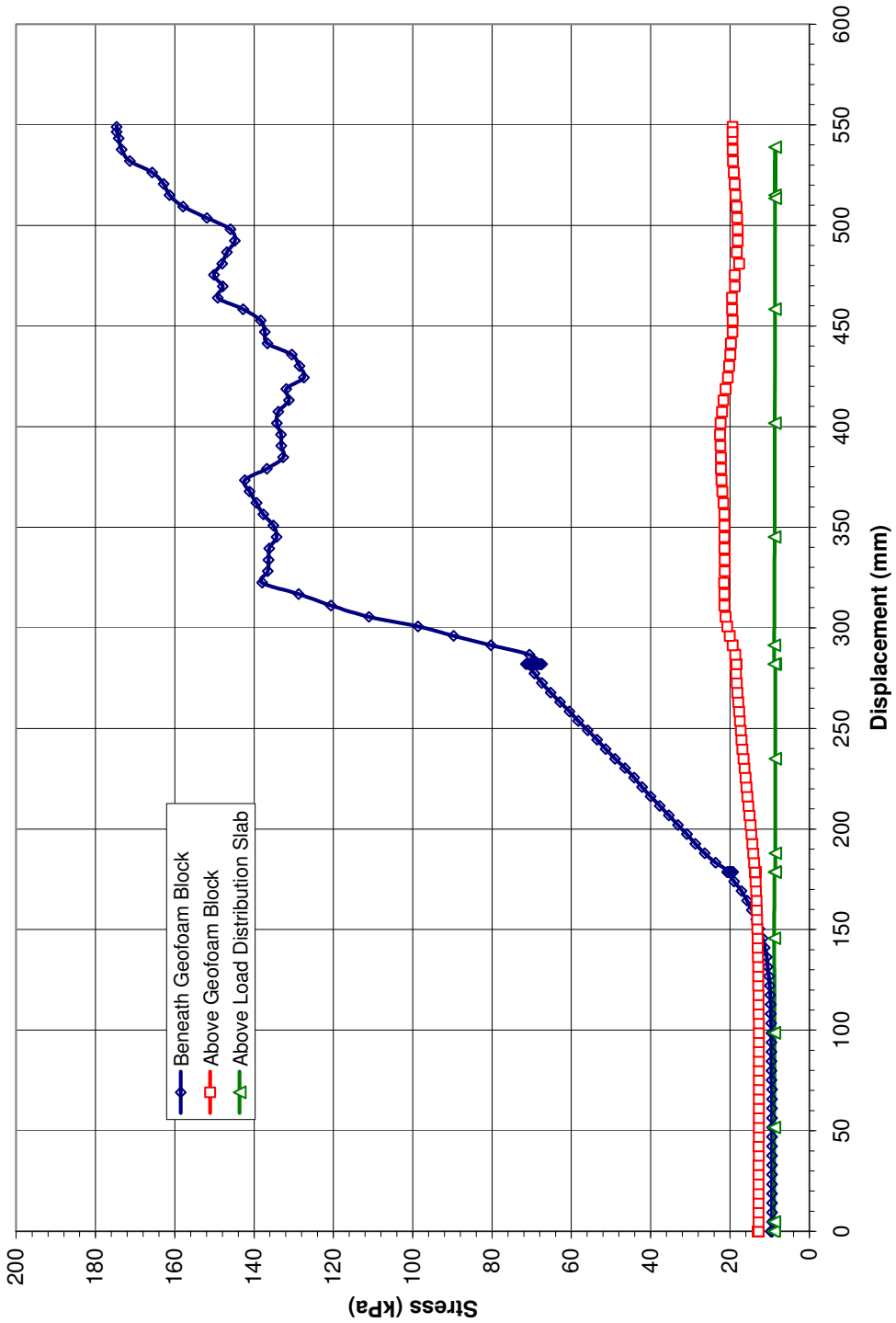

Figure 78. Stresses in the EPS Geofoam trench system

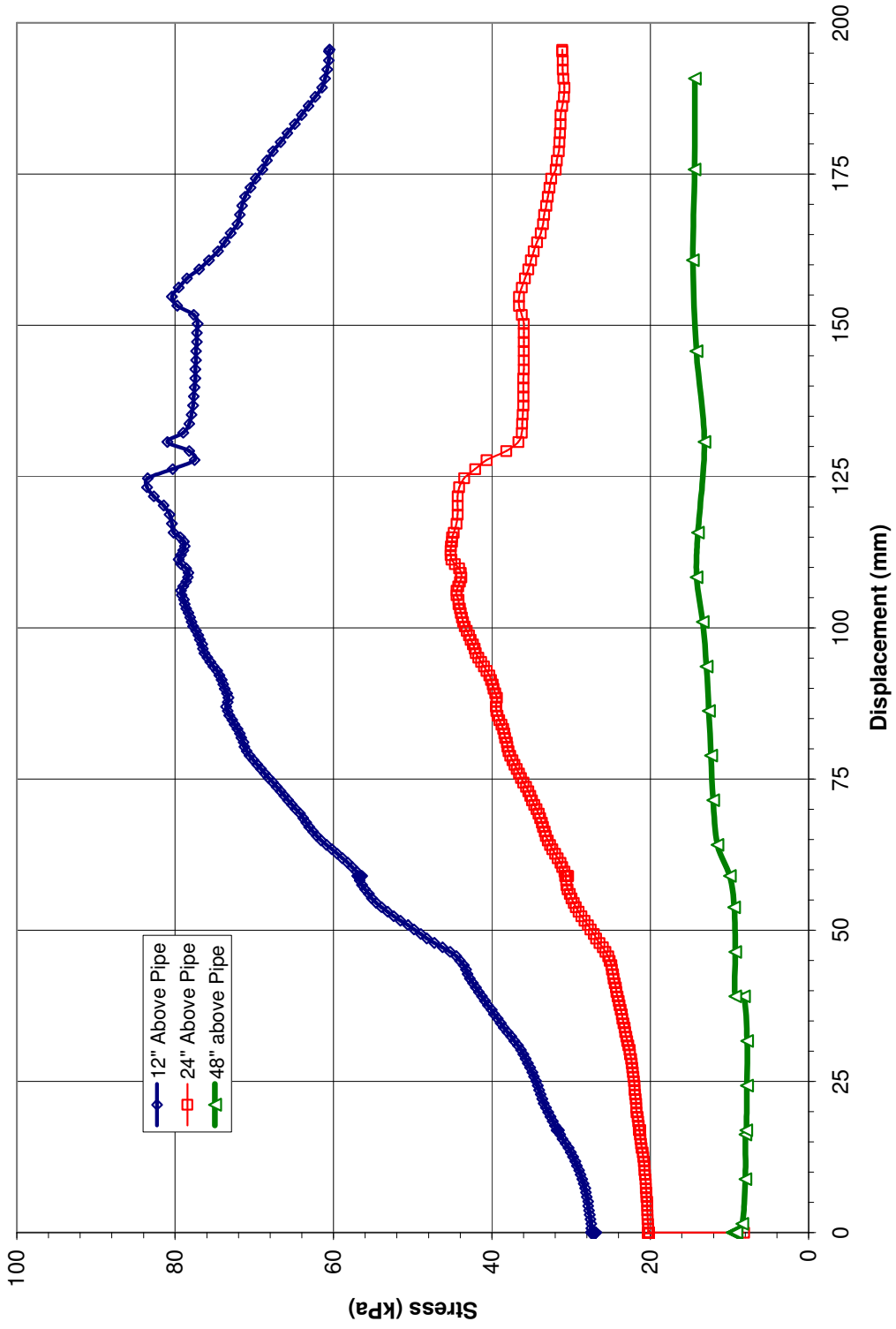

Figure 79. Stresses in the soil backfill section

largest recorded force; however, its peculiar shape may be a result of the bedding sand flowing downward during uplift between the pipe and blocks in the area of the cell producing pressure readings as the stresses concentrated on the cell in a local area. This was likely the reason why the EPS Geofoam stress is higher than any of the soil backfill stresses that were measured.

An important observation from the EPS system was that no significant loads were recorded by any of the three pressure cells until 114 mm; this corresponds to about the same displacement where there was a change in the slope of the force-displacement curve (Figure 75).

The pressure cell that was atop the concrete load distribution slab experienced essentially no significant increase in vertical stress, suggesting that this part of the system moved as a unit, and that the reinforced concrete isolating the stresses. The cell positioned underneath the slab, but above the Geofoam block, saw an approximate doubling of the vertical stress at that location, and notwithstanding, had a relatively minor vertical stress increase when compared to the cell placed beneath the EPS block (Figure 78).

Unfortunately, the pressure cell placed between the pipe and the EPS Geofoam blocks had erroneous vertical earth pressure readings, probably due to excessive stress concentration. This prevented the modulus of uplift reaction from being calculated from this particular test.

Figure 79 shows the vertical earth pressure stress results for the soil backfill system. The intercept of the curve for the pressure cell placed closest to the pipe shows that vertical resistance immediately developed and rapidly increased when compared with the

Geofoam system. The pressure cell located farther from the pipe (i.e., pressure cell located 1219 mm above the pipe) experienced an initial slight decrease in vertical stress and the magnitude of the initial stress increase at this location was about 4.8 kPa. This suggests that the zone of significant stress increase and the development of the potential failure surface were reasonably removed from the centerline of the trench.

The cell positioned 610 mm above the pipe showed a significant decrease in load at a displacement of 119 mm, which approximately corresponds to the marked drop off in total uplift force seen in Figure 75. It is interesting to note that the cell located 304 mm above the pipe did not experience any decrease in load until about 57 mm of additional displacement.

The final observation obtained from the review of the earth pressure cell data was that none of the pressure cells recorded initial vertical stress conditions corresponding to those predicted by a simple vertical stress calculation. All the recorded initial vertical stresses were lower than expected, except the cell atop the load distribution cell (which was nearly that of predicted). For the pressure cells placed in the EPS Geofoam system, this is easily explained. The blocks were placed tightly into the trench, with the side walls of the trench gripping the blocks in areas at some locations, preventing a complete seating of the blocks on the underlying bedding sand. Also, the load distribution slab overhung the EPS blocks and rested on native material along its edges. These two facts likely contribute to the behavior seen in the pressure cells for the EPS cover system. For the soil backfill system, the lower vertical stresses may be due to the development of arching.

Conclusions

Two full-scale uplift tests were performed for steel pipes in plane strain uplift to determine design parameters for steel pipelines crossing active, normal faults. One of the tests used EPS Geofoam backfill cover as a potential mitigation strategy. The other test used soil backfill for a comparison case. The EPS Geofoam section had four times less uplift resistance than the soil backfill section. The EPS Geofoam section also had 2.75 times more displacement at the peak resistance. The stiffness of the EPS Geofoam system was an order of magnitude less than the stiffness of the soil backfill system. The results showed that EPS Geofoam gives a less stiff and more manageable uplift condition on a steel pipeline than native backfill soil.

CHAPTER 8

HAND CALCULATION OF UPLIFT RESISTANCE

Though not capable of estimating the displacements at which uplift resistance occurs, simple calculations can be used to estimate the uplift of a pipe with or without an EPS Geofoam cover system. These simple hand calculations are limit equilibrium solutions, and are similar in their construction and derivation to bearing capacity problems. The most basic hand calculations for uplift resistance are based on the uplift of plate anchors (Trauntman et al., 1984). More complex hand calculations include dilation (Cheuk et al., 2005). Previously published equations for the uplift of pipes assume a homogenous media through which the pipe is uplifting. Those equations assume one of three failure modes, as illustrated in Figure 80. The first failure mode is the simple sliding block with vertical slip surfaces (e.g., trench side walls). The second failure mode is a sliding block with inclined slip surfaces (e.g., sand), while the third is soil flow around the pipe (e.g., liquefied soils and very loose sands). For uplift in sands, Cheuk et al. (2005) recommend their equation because it incorporates both the stress state at the beginning of uplift and dilation. For the uplift in clays, Trautmann et al. (1984) recommend Vesic's equation of uplift from cavity expansion theory. The effects of pipelines in uplift have also been grossly accounted for in the simplified test results for homogeneous sand systems by Trautmann and O'Rourke (1984) and other authors from the results of small-scale laboratory tests and extrapolations of cavity expansion theories.

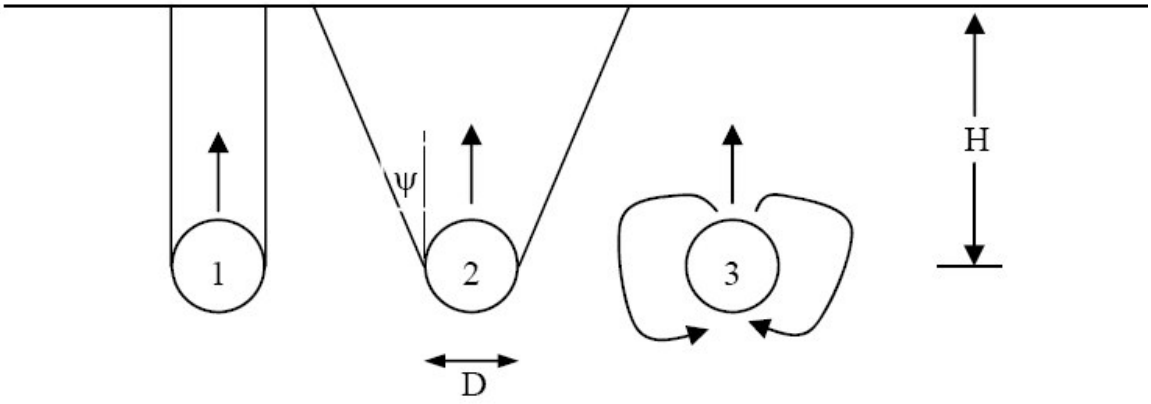

Figure 80. Possible uplift scenarios

The field uplift tests performed in this research had complicated geometry and were heterogeneous, so a calculation assuming a simple vertical sliding block in a multi-layered system is preferable.

The simple sliding vertical sliding block is a limit-equilibrium solution that assumes that the resistance to uplift is formed from two components, the weight of the uplifting block and the shear resistance along the sides of the uplifting block. The general equation for a simple sliding block is shown in Equation 13, or alternatively in Equation 14.

$$F = \sum_{1}^{n} \tau_i A_i + LD\sigma_{pipe} \tag{13}$$

$$F = 2 * L\sum_{1}^{n} \tau_i t_i + LD\sum_{1}^{n} \gamma_i t_i \tag{14}$$

where F is equal to the uplift force, τ is the shear stress induced by uplift on the trench side wall, or portion thereof, and A is the area of the side walls on which the stress is acting. The first term in the equation is the sliding block and the second term is the mass of the uplifted block. The term L is the length of the pipe, D is the width of the uplift block, while γ is the unit weight of the layer, and t is the thickness of a particular layer. The shear stress τ is a function of the normal stress (σ_N), friction (ϕ) and adhesion (a) between uplifting mass and the trench walls. The normal stress for a vertically uplifting mass of soil between the mass and trench walls is the horizontal stress (σ_H). The equation for the maximum shear stress τ between two moving bodies (assuming no dilation to the soil) is calculated with Equation 15.

$$\tau_i = \sigma_h \tan \phi_i + a_i \tag{15}$$

The friction angle can be replaced in this equation by an interface friction angle (δ). The friction and adhesion between two bodies can be determined through laboratory direct shear tests. The horizontal stress σ_H is calculated by multiplying the vertical stress σ_V by a constant K_o.

$$\sigma_h = \sigma_v K_o \tag{16}$$

The vertical stress is found by summing the unit weight times the thickness of all layers above the point of interest. For calculation simplicity, it is common to use the vertical (and horizontal) stress at the midpoint of the area on which the shear stress is

being calculated, i.e., the midpoint of a layer. The coefficient of lateral earth pressure, K_o, is estimated by one of three ways in the absence of direct testing of the lateral earth pressure. The first way is common to geotechnical engineering, the Jaky Equation, (Jaky 1944) and is Equations 17 and 18. Equations 17 and 18 differ in that Equation 17 is for normally consolidated soils, and/or sands, while Equation 18 is for overconsolidated soils and/or clays.

$$K_{o-sand} = (1 - \sin\phi) \tag{17}$$

$$K_{o-clay} = (1 - \sin\phi)OCR^{0.8} \tag{18}$$

The term OCR is the over-consolidation ratio of the soil and is defined as the ratio between the maximum past pressure of the soil (or its yield stress) divided by the current stress state. The OCR of a soil is the most difficult parameter in the above equation to estimate. It can be found from direct testing, indirect in-situ test result correlations or by empirical correlations from the geotechnical literature. The second way to estimate K_o is from empirical correlations to soil index properties from the geotechnical literature. The Massarsch equation (Holtz and Kovacs, 1981), Equation 19, is preferable for this instance because the soils are unsaturated and other correlations require the soil to be saturated and knowledge of OCR. For the cohesive soils at this site, we have no direct knowledge of OCR. This empirical correlation relies heavily on the Jaky Equation and OCR in its development. The third method of estimating K_o is to relate it to Poisson's ratio through elastic theory, Equation 20 (Itasca, 2005).

$$K_o = 0.44 + 0.42 * \left(\frac{PI}{100} \right) \tag{19}$$

$$K_o = \frac{\upsilon}{1 - \upsilon} \tag{20}$$

For the existing (native) soils present at the full scale uplift tests, there are estimates of the water content, liquidity index, friction angle, adhesion and Poisson's ratio. There is also a known geometry of the problem, including layer thickness, and the unit weights of the materials involved. The largest unknown is which is the appropriate vertical stress and K_o value to use in the estimate of uplift force for the EPS Geofoam section. In the soil backfill section, the properties of the trench walls and trench backfill were very similar, so it can be assumed that the horizontal stress between uplifting mass and the trench walls at the time of uplift are similar. However, the compaction of the backfill has altered the horizontal stress state between trench wall and backfill to some unknown value. For a simple calculation, it was assumed that the natural (i.e., Ko) horizontal stress state exists. In the EPS Geofoam section, the trench walls and the EPS Geofoam did not have full contact during the uplift test, nor did the EPS Geofoam section have the same stress state as the surrounding media naturally does.

Equation 14 can be extended for the soil backfill section into Equation 21. In Equation 21, the adhesion between clayey fill and native clay will be taken as the lower of the cohesions of the two materials. The frictional interaction between the clayey fill and native clay can be treated likewise. The full internal friction angle of the road base was

used. All vertical stresses were calculated at the midpoint of each layer. The loose bedding sand was ignored, as it flowed around the pipe very quickly in the field tests. The sand provided little uplift resistance in the field, and the flow around the pipe is very complex and difficult to predict. No predictive equations for loose flowing sands providing uplift resistance are available for pipes.

$$F_{soil} = 2L\left[t_{UTBC}(\sigma_{UTBC}K_{UTBC}\tan(\phi)) + t_{fill}(\sigma_{fill}K_{fill}\tan(\phi) + (c_{fill})/2)\right] + DL\left[t_{UTBC}(\gamma_{UTBC}) + t_{fill}(\gamma_{fill})\right] \quad (21)$$

Equation 14 can also be extended for the Geofoam section into Equation 22. In Equation 22, the adhesion between EPS and frictional interaction between the clayey fill and native clay is taken from direct shear testing shown in Appendix D. The full internal friction angle of the road base (UTBC) will be used. The adhesion and friction between native sand and the reinforced load distribution slab were estimates at 50% of those of the native sand.

$$F_{EPS} = 2L\begin{bmatrix} t_{UTBC}(\sigma_{UTBC}K_{UTBC}\tan(\phi)) + \\ t_{LDS}(\sigma_{LDS}K_{LDS}\tan(\delta) + a) + t_{EPS}(\sigma_{EPS}K_{EPS}\tan(\delta) + a) \end{bmatrix} + LD\left[t_{UTBC}(\gamma_{UTBC}) + t_{LDS}(\gamma_{LDS}) + t_{EPS}(\gamma_{EPS})\right] \quad (22)$$

The properties to use in the calculation are derived in Chapter 7 and found on Table 20. (These properties can be varied to show the sensitivity of the analysis in a qualitative manner. The properties are here varied by 16% to show a best estimate of the uplift resistance by simple sliding block, along with an upper and lower bounds.) Though arbitrary, a 16% variation in properties is sufficient to show the sensitivity in the analysis.

Table 24 shows a selection of the inputs of simple hand calculations using Equations 21 and 22 with the material properties shown in Table 20 along with the geometries shown in Figures 62 and 63. Interface properties for EPS 39 and native clay are presented in Appendix D. Table 25 presents the results of the simple sliding block uplift calculations.

The results of the simple sliding block, as shown in Table 25, are that the soil backfill section test was estimated within 6% for the best estimate case and 10 and 24%, respectively, for the upper and lower bounds. The EPS Geofoam section was estimated within 4% for the best estimate case and 21 and 13%, respectively, for the upper and lower bounds.

These results show that a simple sliding block is an adequate method for prediction of the peak uplift resistance for a multilayered system for an uplifting pipe at a normal or reverse fault crossing. It does not, however, estimate the stiffness of a system, nor the displacement at which the peak resistance is mobilized. The postpeak behavior cannot be estimated with limit-equilibrium methods; numerical modeling is one option to evaluate both the peak uplift resistance and the associated displacement for complex and/or multilayered cover systems.

Table 24. Select simple sliding block uplift inputs

Parameter	Soil Backfill Section			EPS Geofoam Section		
	Lower Bound	Best Estimate	Upper Bound	Lower Bound	Best Estimate	Upper Bound
Fill Ko	0.416	0.482	0.559	0.096	0.111	0.129
UTBC Ko	0.274	0.318	0.369	0.274	0.318	0.369
LDS Ko	NA	NA	NA	0.431	0.500	0.580
Fill Unit Weight *(kN/m3)*	15.53	18.02	20.90	0.284	0.33	0.383
UTBC Unit Weight *(kN/m3)*	16.84	19.54	22.67	16.84	19.54	22.67
LDS Unit Weight *(kN/m3)*	NA	NA	NA	20.30	23.55	27.32
Fill:Native Adhesion *(kPa)*	40	46	53	10	12	14
Fill:Native Friction (°)	23	27	31	17	20	23
UTBC Friction (°)	39	43	47	39	43	47

Table 25. Simple sliding block uplift calculation results

Results	Soil Backfill Section				EPS Geofoam Section			
	Lower Bound	Best Estimate	Upper Bound	Test Result	Lower Bound	Best Estimate	Upper Bound	Test Result
F (kN)	472	551	646	520	108	130	154	136

CHAPTER 9

NUMERICAL MODELING OF SIMPLE PIPELINE UPLIFT

Many different soil types, geometries and fault crossing scenarios are possible involving the future design of EPS Geofoam cover systems for steel pipelines crossing active normal faults. In order to develop a modeling procedure of pipelines in uplift that predicts both uplift resistance and displacements, it is necessary to begin the numerical analyses with simple geometries and case histories from the geotechnical literature. Numerical modeling is best done when a rational procedure is followed in which simple hand calculations and limit equilibrium techniques are first explored. Then, simple numerical models that match case histories and benchmark tests (Validation and Verification) are developed. Once the modeling procedure is developed and benchmarked against simple geometries, it can be extended to more complicated systems.

In geotechnical modeling, the simplest conditions are those that have sand as the geo-material. For this reason, case histories from the literature using sand as the bedding material for pipes in uplift were chosen. Cheuk et al. (2008) conducted uplift testing of small pipes in sand. Their research included detailed characterization of the sand backfill used in their testing. Two different sands were used by Cheuk et al. (2008), a fine grained clean sand and a coarse grained clean sand. Tests were conducted using each sand in two

cases, dense compaction and loose compaction. This provided 4 case-histories with appropriate background information to conduct FLAC benchmarking for pipes in uplift.

Four FLAC models were developed using the geometry and soil conditions from Cheuk et al. 2008. Symmetry was assumed at the center line of the pipe in the FLAC model geometry. The soil properties appear in Table 26. Included in the sand characterization by Cheuk et al. (2008) was critical state friction angle and dilation. The only properties in Table 26 not provided by Cheuk et al. (2008) were Bulk and Shear Modulus. These properties were obtained from the soil property library in Duncan et al. (1980) from similar sands at similar relative density. The geometry for the FLAC models is shown in Figure 81. The pipe was modeled as 100 mm rigid pipe. Interface elements were placed between structural elements and the surrounding sand media as required by Itasca (2005) with interface properties developed using the procedure required for interface elements. The FLAC model was run to an initial static equilibrium before pipe uplift was initiated with the base of the model fixed in both directions, while the edges are fixed horizontally. The pipe was uplifted at constant rate in the FLAC model until numerical stability occurred. Figure 82 shows the deformed mesh at the end of uplift for one of the FLAC models. Normal nodal forces on the pipe were monitored continuously during pipe uplift using FISH code in FLAC. The sum of the uplift resisting forces was multiplied by two and plotted against pipe displacement for comparison to the results from Cheuk et al. (2008). Figure 83 shows the results of the FLAC modeling, while Figure 84 shows a comparison of the FLAC results and the test results from Cheuk et al. (2008). Figure 85 is after Cheuk et al. (2008).

Table 26. FLAC model properties for simple pipe uplift

Sand	I_D	γ	ϕ'_{cs}	ϕ'_{pk}	ψ'_{pk}	K	G
----------	*%*	*kN/m3*	*deg*	*deg*	*deg*	*kPa*	*kPa*
Coarse/Dense	92	17.2	32	52	25	458	211
Coarse/Loose	36	15.6	32	42.5	13.1	375	173
Fine/Dense	92	15.8	32	52	25	458	211
Fine/Loose	30	14.1	32	39.9	9.9	375	173

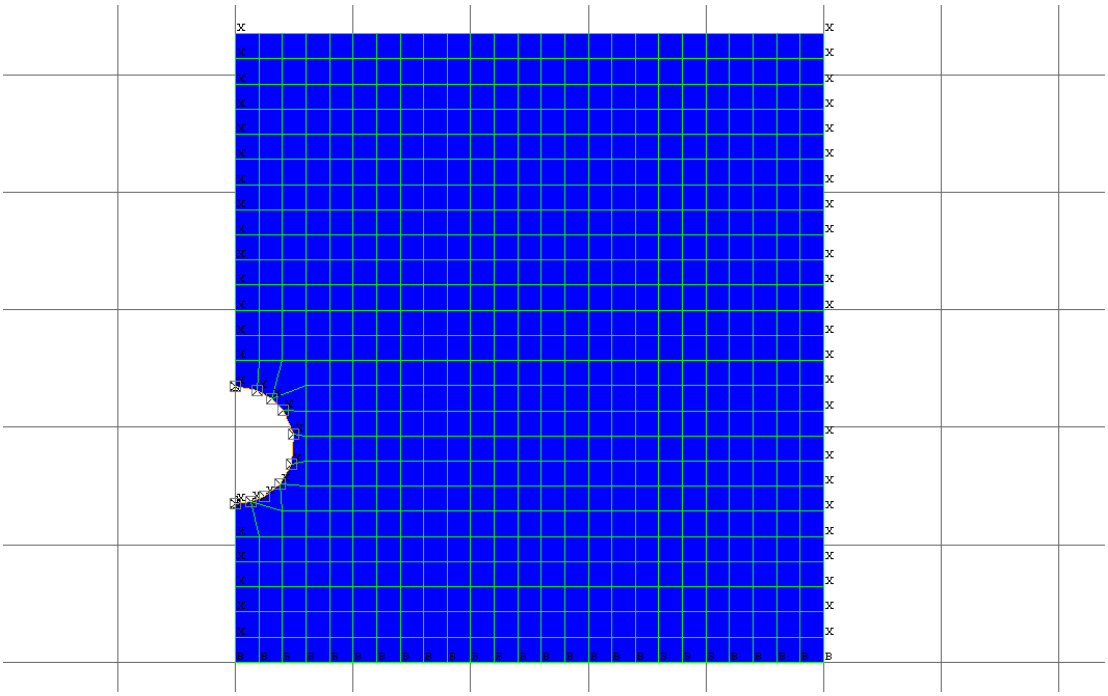

Figure 81. FLAC simple pipe uplift model geometry

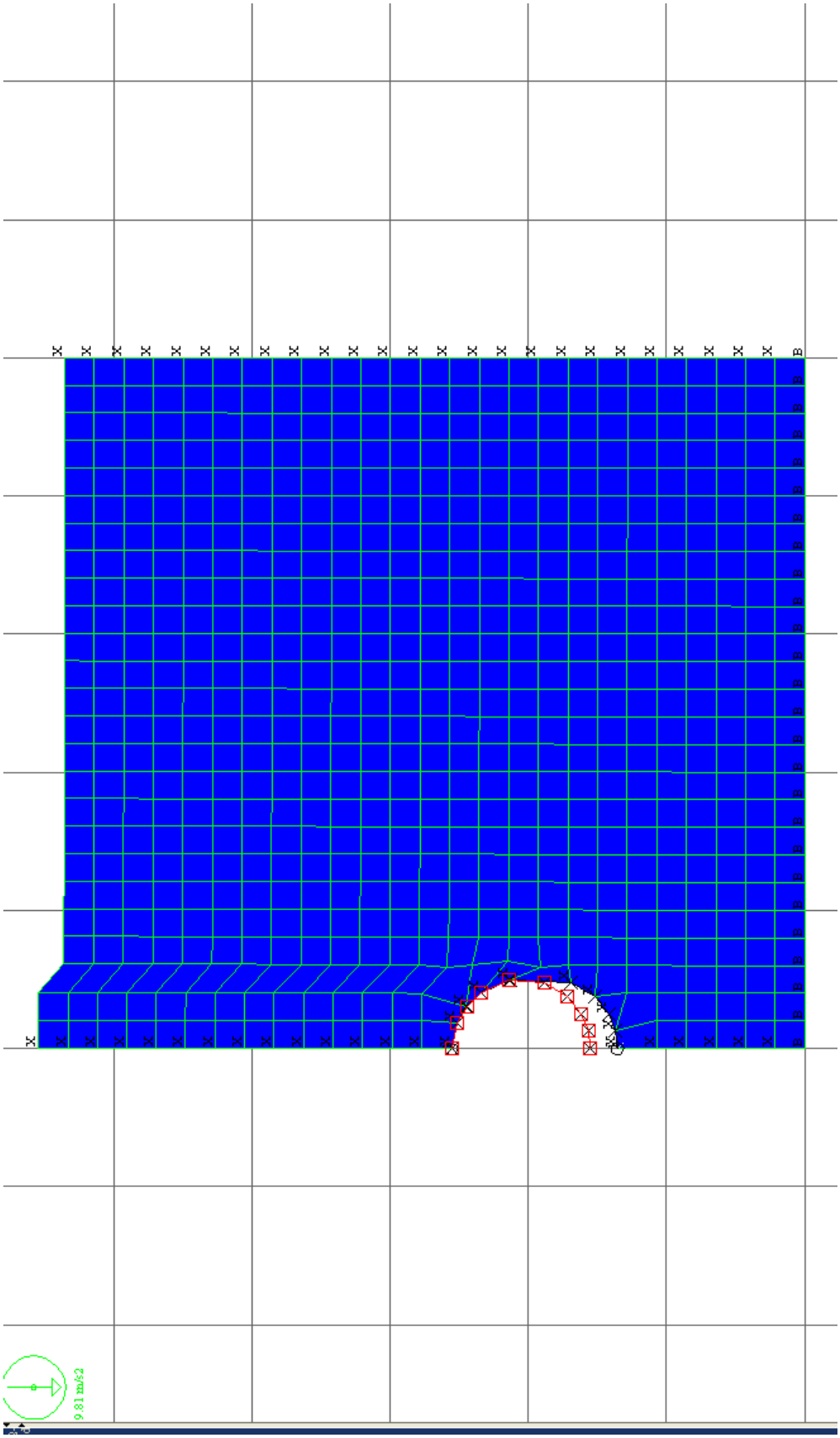

Figure 82. Deformed FLAC model geometry

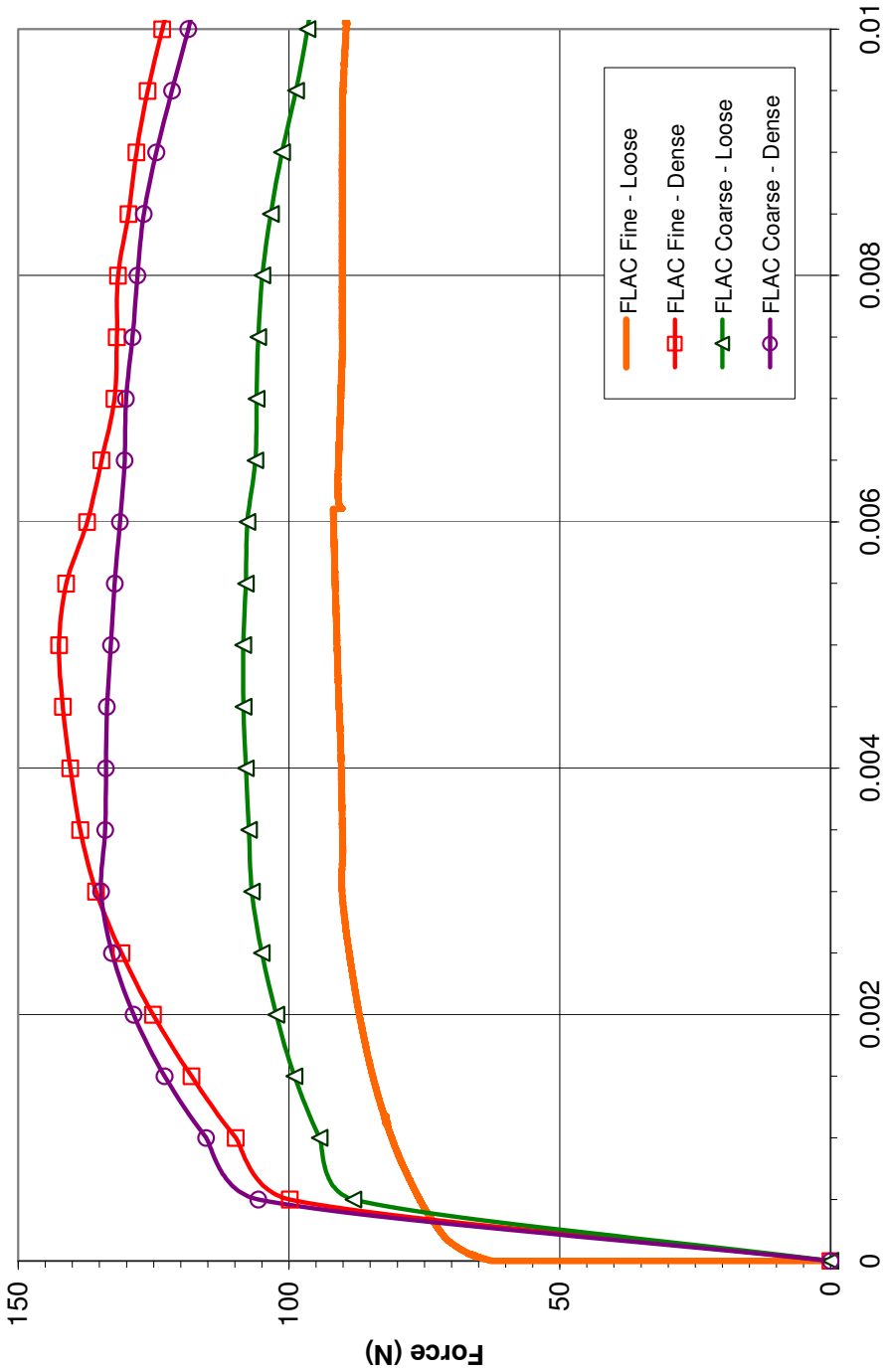

Figure 83. FLAC simple pipe uplift modeling results

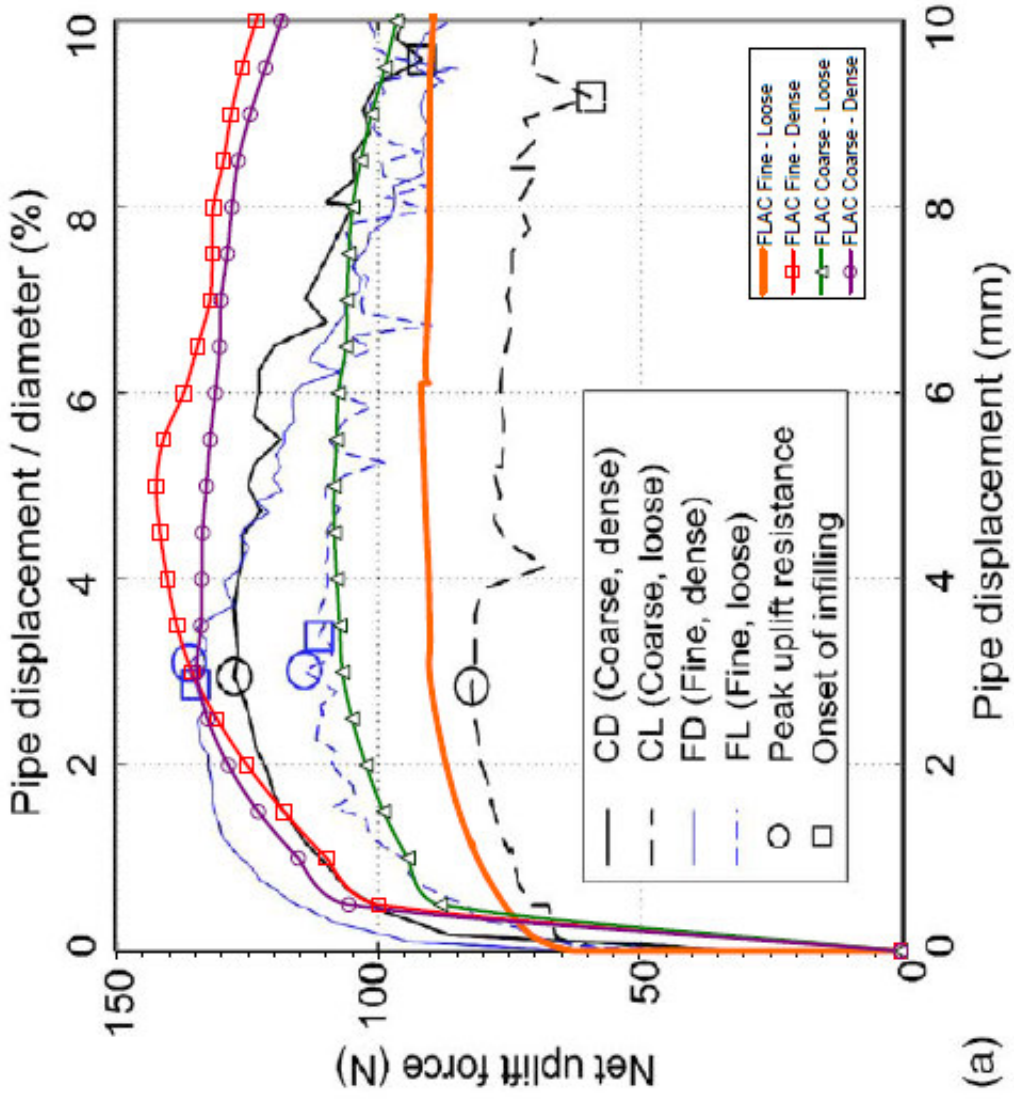

Figure 84. Comparison of Cheuk et al. (2008) test data and FLAC modeling (After Cheuk et al. (2008))

Figure 84 shows that the FLAC results compare well to the Cheuk et al. (2008) test results. The best fit between FLAC and test was the Course-Loose sand, while the Fine-Dense sand had the worst fit. In general, the FLAC models overpredict the peak uplift force up to 13%. The shape of the force-displacement curve is generally consistent between FLAC and test data. A better postpeak shape could have been achieved in the FLAC modeling by use of a strain softening model.

It is concluded from the simple FLAC pipe uplift modeling that FLAC can predict both peak forces and the shape of the force-displacement curve found from simple pipe uplift tests. This benchmarking exercise gives confidence that more complex pipe uplift systems can be modeled by FLAC.

CHAPTER 10

NUMERICAL MODELING OF UPLIFT TESTS

Many different soil types, geometries and fault crossing scenarios are possible that involve the future installation of EPS Geofoam cover systems for steel pipelines crossing faults or other types of permanent ground displacement (PGD) zones. Because it is cost prohibitive to conduct full-scale, or even reduced-scale, tests to evaluate the force-displacement characteristics for all cases, numerical modeling can play an important role in the evaluation and design of these systems. Numerical modeling of various fault/PGD crossings is less expensive and allows the designer to parametrically examine ways of mitigating the potential damage to the pipeline by evaluating various Geofoam geometries and configurations. As part of this research program, a series of numerical models were developed to evaluate the experimental results of the uplift tests to see if such models could be used as an evaluation tool.

In addition, the force-displacement relationships obtained from the experiments previously discussed provide the basis for development of other techniques that may not entirely rely on numerical modeling. Thus, the force-displacement relationships, or nonlinear springs, developed herein are important to the evaluation and design of pipeline crossings undergoing vertical offset, regardless of the numerical scheme developed to perform the evaluation.

Numerical Modeling Program

The numerical model chosen for this part of the research was FLAC version 5.01.432 (Fast Lagrangian Analysis of Continua) from Itasca software of Minneapolis Minnesota. FLAC3D version 3.01 was also used. FLAC2D is a two-dimensional explicit finite difference program and FLAC3D is the three-dimensional formulation of FLAC. (See Chapter 6 for additional discussion about the advantages and disadvantages of the selected numerical technique.) FLAC3D contains most of the advantages of FLAC2D, while extending the structural element models to PLATE and SHELL type elements (FLAC2D is restricted to BEAM and CABLE type elements). FLAC3D has disadvantages in its grid generation complexity and longer run time required to model 3D features.

Once the force-displacement of the uplifting system is found from the FLAC modeling, further evaluation of the pipe may be done in a finite-element program (e.g., ANSYS or PIPLIN); or FLAC2D and/or FLAC3D can perform similar analysis using structural elements.

FLAC Modeling

Two FLAC models were developed for the full scale tests in this research. The experimental results were used to develop and calibrate the numerical models. The first FLAC model was developed for the case of the native soil backfill trench; the second FLAC model was developed for the case of the EPS Geofoam cover system. The models were developed in plane-strain mode using FLAC2D.

The FLAC2D models were developed by uplifting the pipe at a constant rate (i.e., velocity) through the cover system and calculating the resultant stress. This was similar to the manner in which the field experiments were conducted. The mechanical properties of the soils and materials used in the field test were input into the FLAC models with only minor adjustments. The triaxial testing of the soils at the site made it possible to determine the requisite Mohr-Coulomb properties of the various materials. (The Mohr-Coulomb model is a basic model for geomaterials and was easy to implement.) Some behaviors were analyzed with more complex constitutive relations, such as the post-peak softening observed in the triaxial tests for the site soils and the tensile strength and large strain behavior of EPS Geofoam.

Modeling Approach

The first step was to develop the modeling layout and geometry of the two field tests into the input file as closely as possible to the actual test conditions. For the Geofoam section, the mesh was created in two ways. The mesh was created once nearly identical to that of the soil backfill section with no internal interfaces. It was created once with internal interfaces between the Geofoam and soil. Modeling results from the first case showed that interfaces were needed to accurately model the Geofoam cover system uplift.

In the second case, after the mesh was created and interfaces added, as appropriate, the mesh was divided up into "groups." The "groups" are the elements (zones) in the mesh that will be assigned to a common material type. As such, there was a "group" for the road base (UTBC) that was placed above the trench in the field experiments. The mesh and grouping of materials are shown in Figure 85 for the EPS Geofoam section.

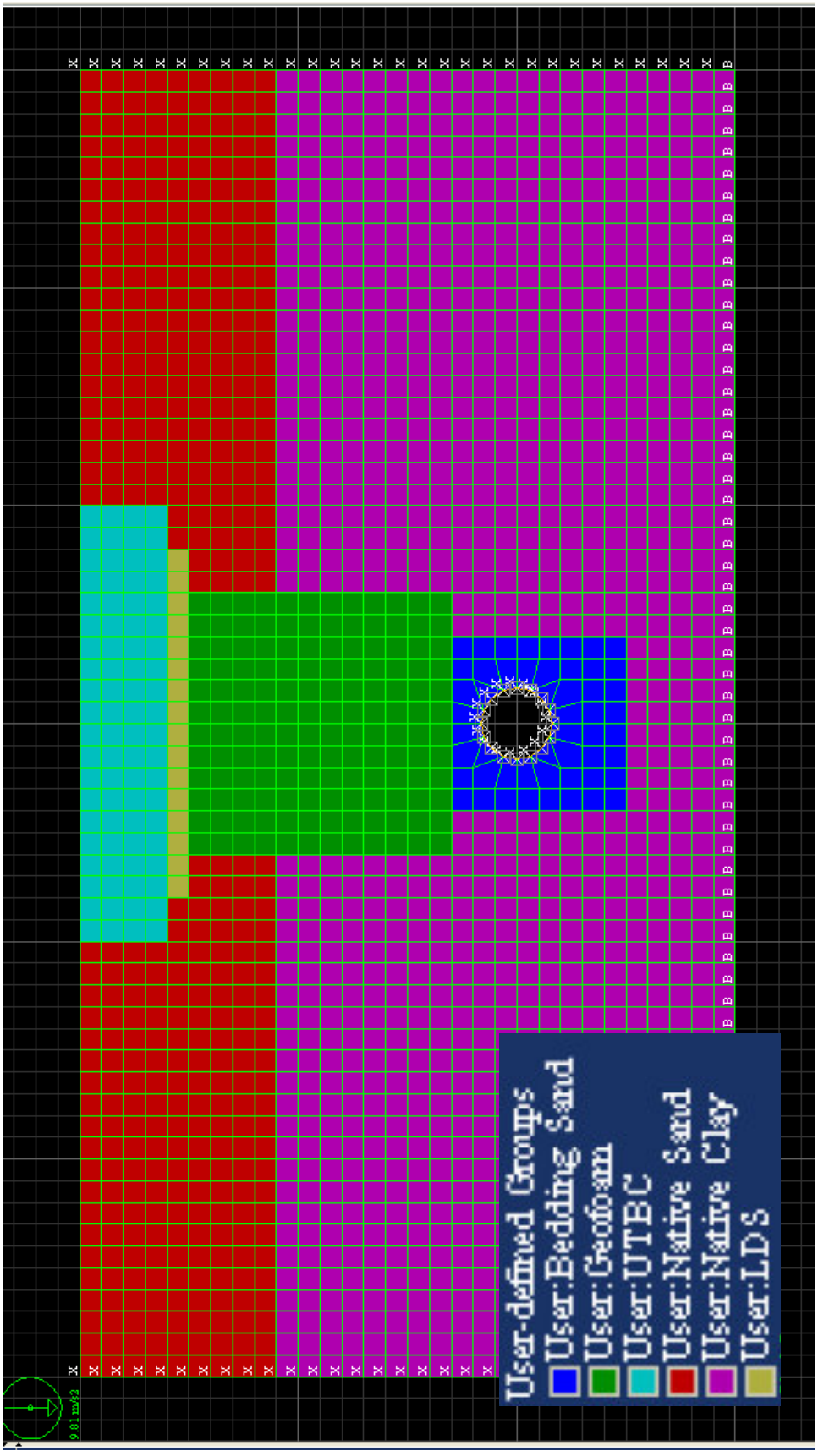

Figure 85. Geofoam section geometry without interfaces

Once the zones in the finite element mesh were assigned to a "group," the materials' properties added to the model. The materials are identified by a name, mass density, bulk and shear modulus. FLAC does not use Young's Modulus or Poisson's ratio in its formulation, but these properties can be calculated from elastic theory from the bulk and shear modulus. If the Mohr-Coulomb model is invoked, then additional properties are required (i.e., cohesion, tension and the friction and dilation angles).

After the material properties were entered into FLAC, and the materials assigned to their "group" the boundary conditions were established for the model. The base of the model is fixed in both the X (horizontal) and Y (vertical) directions, respectively. The sides of the model were fixed in the X direction, so that the materials at the model's edge may compress (i.e., move vertically) under applied loads, but no horizontal movement was allowed. This required that the model finite difference zone mesh be sufficiently large in the horizontal direction so that the deformations near the pipe were not influenced by the side boundaries.

Interface elements were required to properly model the interface conditions that develop between two dissimilar materials (Figure 86). The interfaces' nodes placed between the materials are shown by the white lines with crosses. The interfaces run along the edge of the geofoam block, the whole of the reinforced concrete load distribution slab, the contact between Road base and the native soils and the potential slip lines through the Road base. These potential slip lines were determined from inspection of the field test, where the Road base sheared along the line of the load distribution slab that sits atop the EPS Geofoam block.

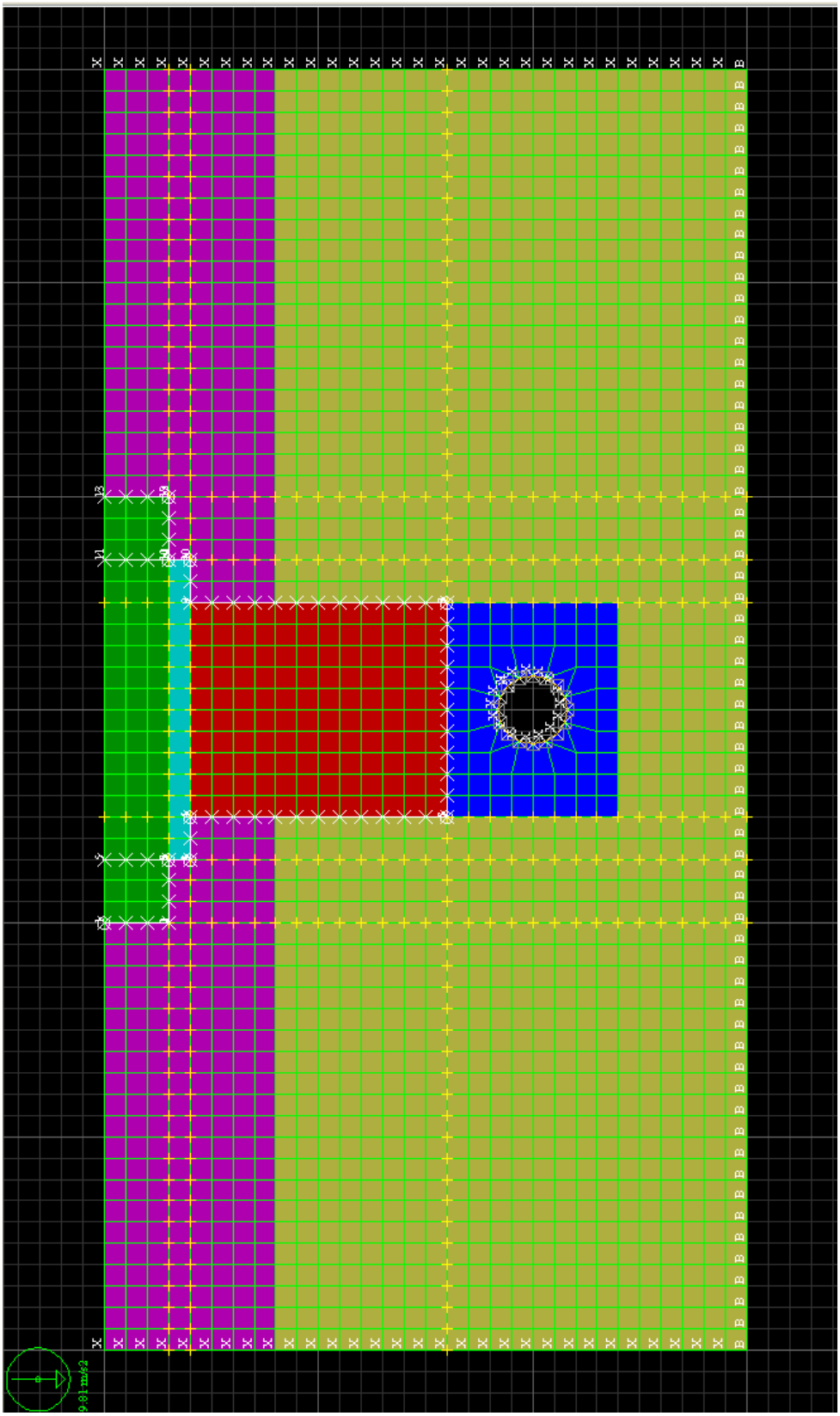

Figure 86. Geofoam section model with interfaces

Before the model can be used to evaluate the uplift tests, the initial stress conditions must be calculated under gravity loads. The model was built up one material layer at a time and the model was stepped through time to static equilibrium. This allowed the material to settle under its own weight and establish stress equilibrium before another overlying layer was added. Once equilibrium has been reached, the displacements in the grid were initialized to zero, because these displacements were not important to modeling the uplift tests. Once the in-situ soil stresses were established, the trench was excavated in the FLAC model, and the system was again solved to static equilibrium and the resulting displacements from the excavation event were zeroed in the model.

Lastly, the pipe and the backfill soil were added to the model. The model was then stepped again with gravity load present to find the stress state in the system prior to uplift. Any displacements calculated during this step were also reset to zero. The pipe was added as a series of plane strain beam elements that lined a cavity created in the mesh by using a "null" material. (A null material removes nodal points and mesh in the "null" zone.) The beams representing the pipe were attached to the grid mesh using interface elements. The interface elements used here were given the stiffness of the bedding sand and the adhesive and frictional strength properties assumed for steel-sand interface were assigned about 50 to 67% of the values for the adjacent soil. The beam elements were assigned the thickness of the pipe used in the uplift tests and given the modulus and yield stress of X42 steel pipe.

As an alternative, the pipe could also be modeled in a plane strain situation as a very rigid and unyielding material, so as not to introduce additional internal deformations during uplift. This approach was also deemed acceptable, because the model was being

used to estimate the nonlinear uplift characteristics of the cover system and the internal pipe deformation was deemed insignificant due to its stiffness and the shortness of the strand of pipe. In this approach, any possible pipe deformation for a longer strand of pipe could be evaluated during the subsequent structural assessment of the pipe using the force-displacement spring found from the FLAC modeling. Figure 87 shows the soil backfill section with the pipe embedded in the model. The pipe is the circular opening in the mesh at the center of the model. Once the pipe and backfill have been added to the model, initial stress conditions calculated and the displacements re-zeroed, the uplift protocol was coded into the FLAC model using FISH code. The FISH code was written such that every node of the pipe will uplift at the same rate. The FISH code was also programmed to track the nodal forces on the pipe so that the total force required to uplift the pipe could be calculated. In doing so, it was important to include only those forces that participate in resisting uplift to correctly calculate the force-displacement relation. In addition, FISH code was written to obtain the stresses at various locations in the mesh at every time step in the model, or at prescribed intervals.

Damping must be used in the numerical model to improve numerical stability. Because FLAC uses the equation of motion to solve both static and dynamic problems, damping is required for numerical stability even for “static” problems. There are several types of damping available; combined mechanical and material damping is recommended. The amount of damping used depends on the run time the user desires, but the maximum recommended mechanical damping is 5%. Additional damping may introduce inaccuracies in the solution.

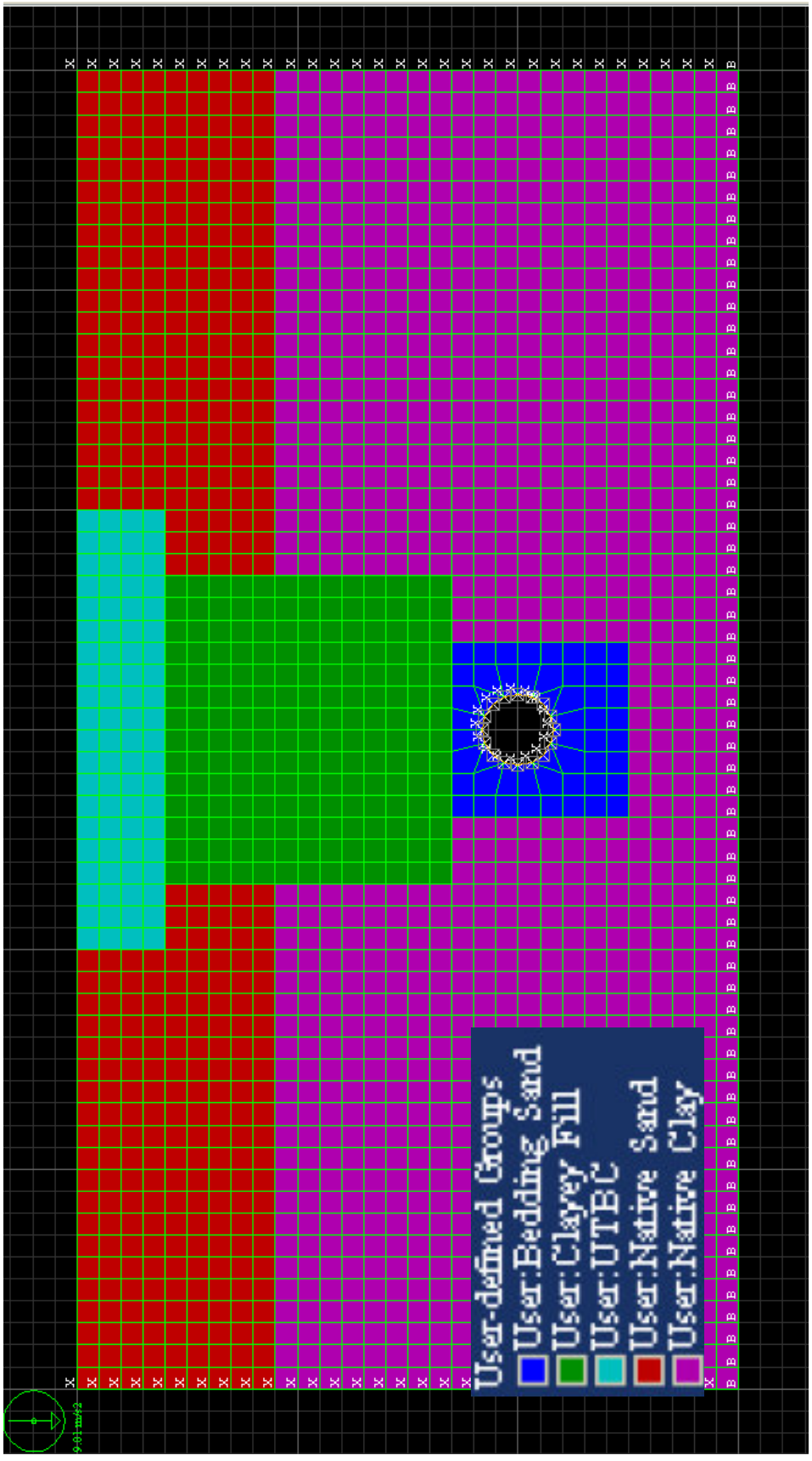

Figure 87. FLAC geometry for soil backfill section

The velocity chosen for uplift of the pipe requires special consideration in FLAC. FLAC is primarily a numerical model for static and dynamic loading of geomaterials and structures. It can be run using the actual test uplift velocity if and only if the correct visco-elastic material constitutive model and properties have been assigned. However, obtaining these properties for geomaterials is a very expensive and time consuming process. Instead, the visco-elastic model was not used; thus, the actual uplift velocity was not modeled. Instead, the Mohr-Coulomb model was used with a "virtual" velocity. This "virtual" velocity is not related to the actual velocity, but is a numerical velocity that is sufficiently slow to allow the model to properly track the model state. The virtual velocity used FLAC for non-visco-elastic modeling is quite small (i.e., ranges from 1e-5 to 1e-9 m/s). This rate allowed the numerical code to solve in a stable manner the stresses, stains, forces and displacements occurring in the geomaterials and the structural elements. The user can force the model to run the appropriate number of timesteps, at the specified velocity, in order to reach the desired pipe displacement. The optimal virtual velocity can be selected by monitoring the changes in the solution until a sufficiently slow rate has been found that no longer significantly affects the solution. This can be monitored by observing the deformations and system response by plots and histories at specified locations in the model as uplift is proceeding. Once the model has finished running, the user can examine the output graphically or export the history plots to a text file (to be imported into EXCEL or other data analysis program) for inspection.

Soil Backfill Section Modeling Results

The soil backfill model (Figure 87) was analyzed with no sliding interfaces except along the edge of the pipe. This figure shows the model geometry prior to beginning uplift. Figure 88 shows the FLAC deformed mesh at its final state. Note that the backfill (green material) and the road base (light blue material) have remained attached to the native clay and sandy layers. If an interface had been placed along the edge of the backfill, the fill material could have moved relatively along the sides of the trench.

The soil backfill section used the Mohr-Coulomb material model for the road base at the top of the model, but used the FLAC's strain softening model for the native soils and the clayey fill. The strain softening model is the same as the Mohr-Coulomb model in the elastic range, but differs in how it treats postyield plastic flow. The associated flow rule for the strain softening model uses strain softening or hardening friction, dilation, tension and cohesion as a function of plastic strain. For its implementation, the triaxial test results were used to find the strain softened postpeak properties (Appendix G). These are summarized in Tables 28 through 31.

Table 27 shows the inputs for the material properties in the FLAC model. In Tables 27 through 31, the bulk modulus of the material is shown by K, the shear modulus by G, the internal friction angle of the material is shown by the Greek letter phi, while the dilation angle of the material is shown by the Greek letter psi. The apparent cohesion of a material is designated by c, and the tensile strength is given the symbol T. Appendix G contains a demonstration of the use of the strain softening model and its implementation in FLAC.

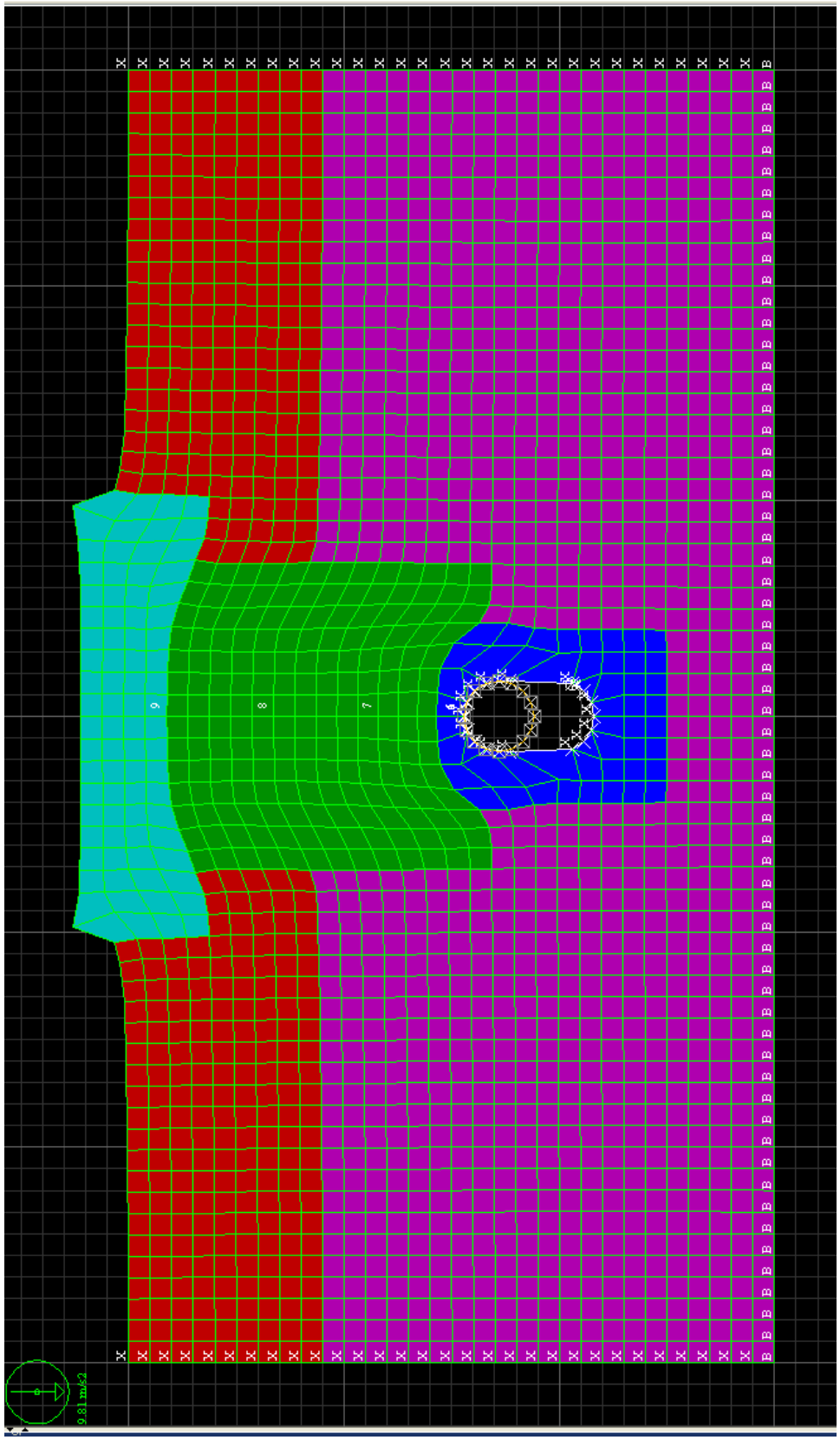

Figure 88. Soil backfill section deformed mesh

Table 27. Material properties for soil backfill section model

Material ---	Density *Kg/m3*	K *kPa*	G *kPa*	ϕ *deg*	ψ *deg*	c *kPa*	T *kPa*
UTBC	1990	53333	32000	43	3	2.5	0
Bedding	1700	8333	3846	32	0	0.0	0.0
Native Clay	1765	6666	2222	24	0	59.9	0.599
Native Sand	1842	7083	3269	27	0	35.9	0.359
Clayey Fill	1810	8333	1758	28	0	35.9	0.359

Table 28. Strain softening model friction angle

Material ---	0% Plastic Strain *deg*	9% Plastic Strain *deg*	15% Plastic Strain *deg*	30% Plastic Strain *deg*
Clayey Fill	28	26	21	18
Native Sand	28	26	21	18
Native Clay	24	23	20	18

Table 29. Strain softening model dilation angle

Material ---	0% Plastic Strain *deg*	9% Plastic Strain *deg*	15% Plastic Strain *deg*	30% Plastic Strain *deg*
Clayey Fill	0	0	0	0
Native Sand	0	0	0	0
Native Clay	0	0	0	0

Table 30. Strain softening model cohesion

Material ----------	0% Plastic Strain *kPa*	9% Plastic Strain *kPa*	15% Plastic Strain *kPa*	30% Plastic Strain *kPa*
Clayey Fill	35.9	23.9	12.0	10
Native Sand	35.9	35.9	15.9	10
Native Clay	59.9	59.9	15.9	10

Table 31. Strain softening model tension

Material ----------	0% Plastic Strain *kPa*	9% Plastic Strain *kPa*	15% Plastic Strain *kPa*	30% Plastic Strain *kPa*
Clayey Fill	0.36	0.36	0.12	0.10
Native Sand	0.36	0.36	0.16	0.10
Native Clay	0.60	0.60	0.16	0.10

Figure 89 shows the displacement vector pattern from the FLAC model at the end of uplift. In this figure, the majority of the vectors are vertical except along the failure plane, where they are approximately 60° from the horizontal. This failure angle was approximately predicted by Rankine passive earth pressure theory. The theoretical angle of failure in soils is 45° plus the friction angle divided by two. For the native soils and compacted clayey fill in this scenario, the friction angle was nearly 28°; thus, the failure angle is 59° from Rankine theory. When the failure plane encounters the compacted

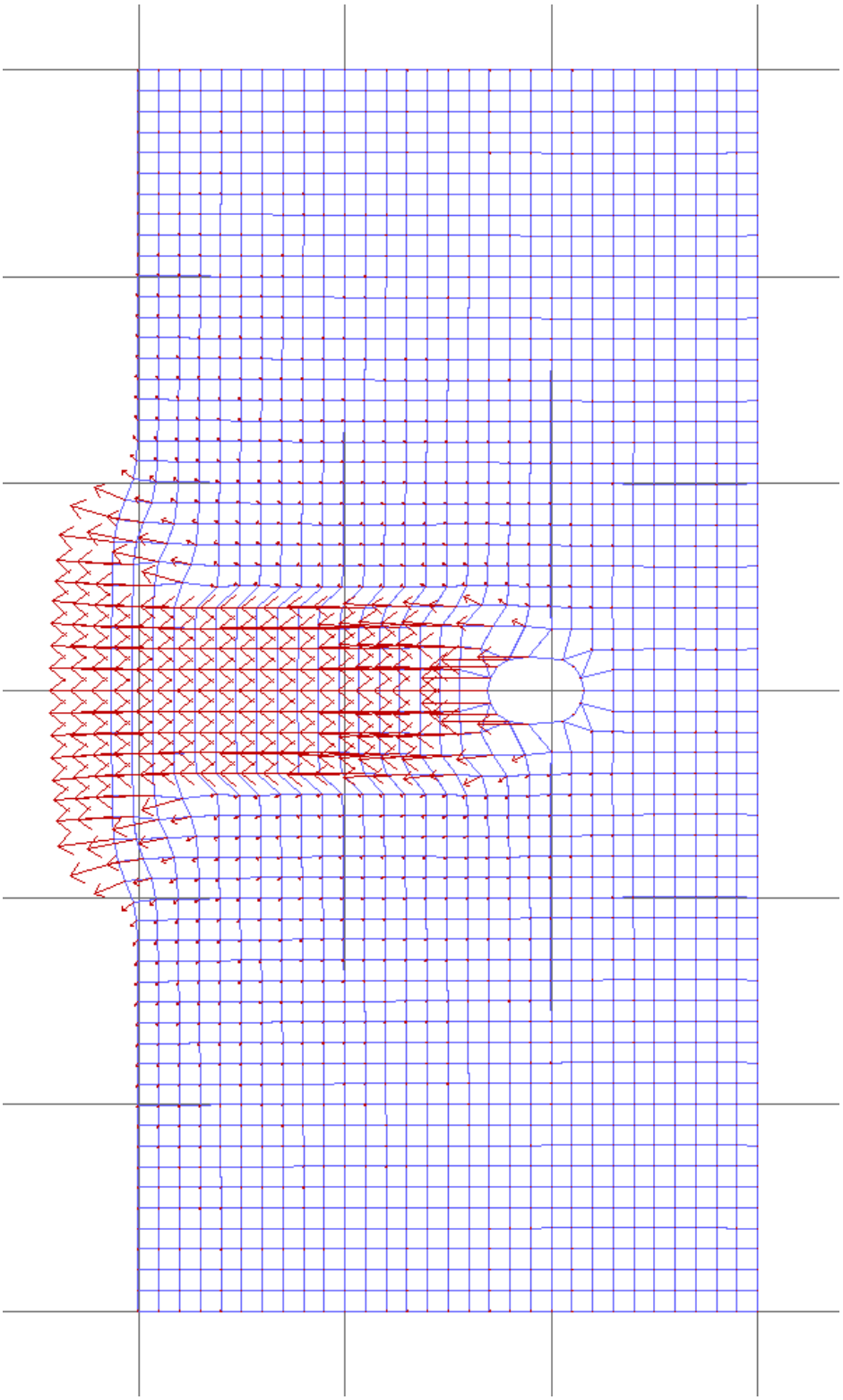

Figure 89. Soil backfill section vectors

road base at the top of the model, the angle became nearly 70° because the friction angle of the road base is about 45°.

Figure 90 shows the vertical stress distribution in the soil backfill system at the end of uplift. The green zones in this figure are zones of vertical stress less than 100 kPa. The light blue shows areas where vertical stress became negative (i.e., the soil is slightly in tension). In addition, the red shading along the top of the pipe and in the zones immediately around the pipe indicated that the vertical stress in the bedding sand at the end of uplift is between 400 and 500 kPa.

It should be noted that the peak pressure found in the actual field uplift test was around 100 kPa located approximately 305 mm above the top of the pipe. The FLAC model predicted 240 kPa at the same location, or about 140% more vertical stress than was measured in the experiment of the soil backfill section. However, at the pressure cell placed 1220 mm above the top of the pipe, the field measurement was 10 kPa and the FLAC model predicted 10 kPa of vertical stress.

Lastly, the total force-displacement curve from the soil backfill uplift test is plotted in Figure 91 with the FLAC results.

It can be seen from Figure 91 that the FLAC modeling results overpredicted the peak uplift force of 563 kN compared to the test result of 520 kN. The FLAC modeling results also overpredicted the displacement associated with the peak force by about 30% (100 mm of displacement predicted by FLAC compared to 70 mm displacement from the field experimental data).

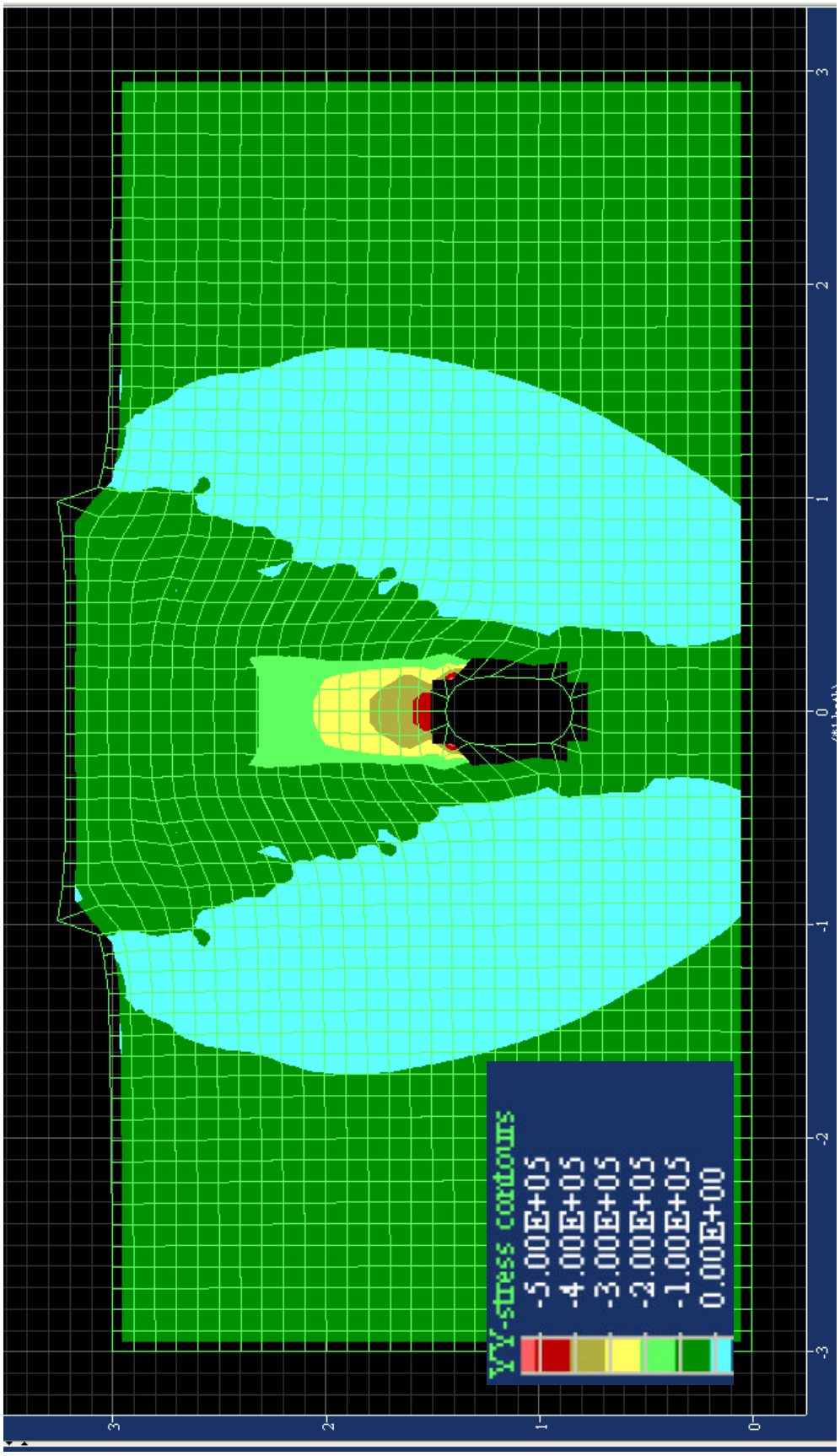

Figure 90. Soil backfill Section Vertical Stress Contours

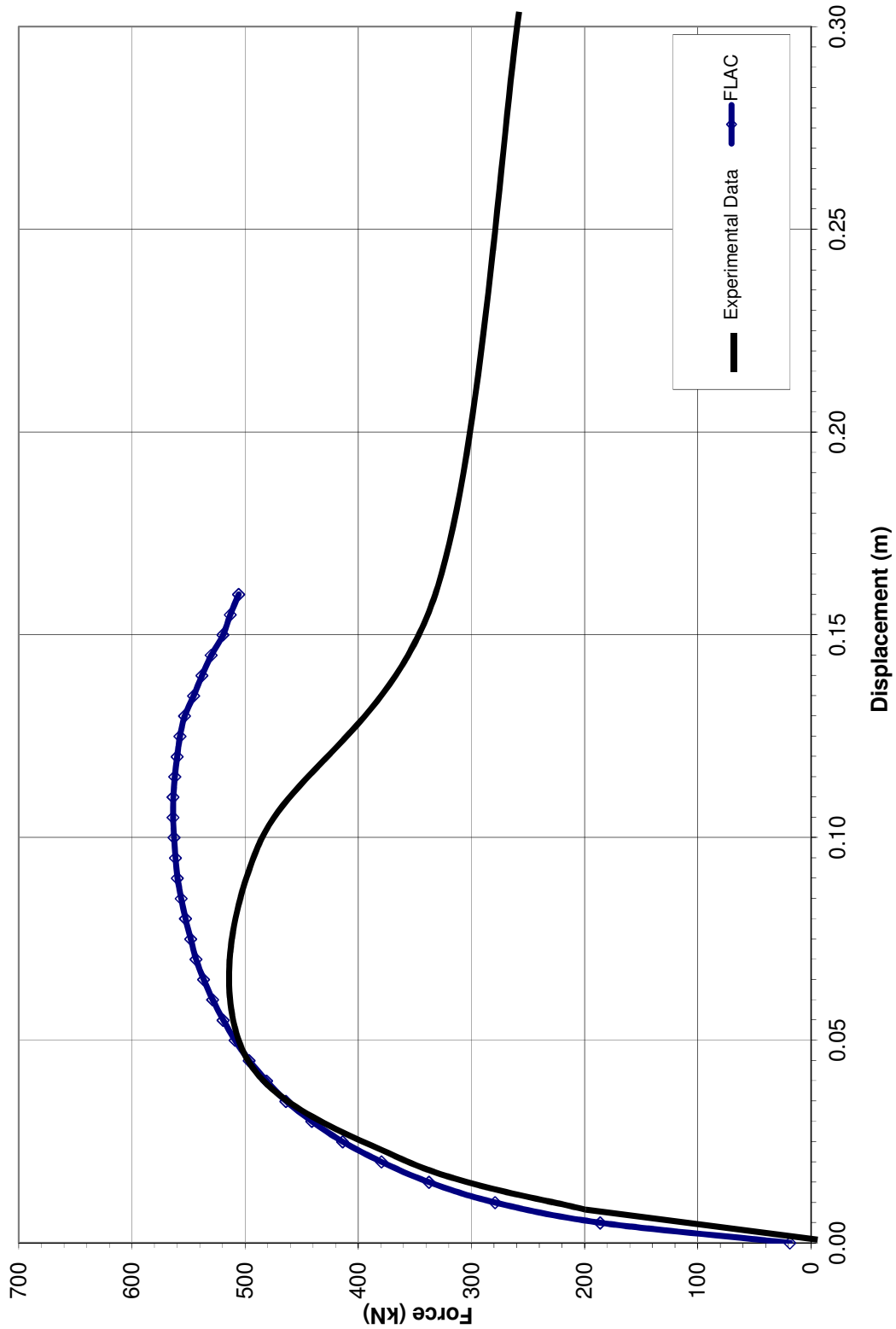

Figure 91. Soil backfill section force-displacement results

The peak secant stiffness of the soil backfill system from the FLAC was 1230 kN/m/m compared to 1625 kN/m/m obtained from the experimental data, a difference of 24%. Thus, the FLAC modeling appeared to reasonably predict the force displacement relationship for a pipe uplifting through a soil backfill system in regards to overall stiffness of the system.

The postpeak behavior in the FLAC model suggests a significant decrease in uplift resisting forces after the peak resistance and this was observed in the experimental data, although the decrease was even more significant in the experimental data. The postpeak softening of the curve was accomplished by using the strain softening soil model in FLAC. The use of the strain softening model appears to be appropriate for modeling the postpeak behavior of the system in uplift, but it may need more calibration.

EPS Geofoam Section Modeling Results

Figures 85 and 86 show the mesh and model setup for the Geofoam cross-sectional models developed without and with interface elements, respectively. The Geofoam model differs from the soil backfill model by the addition of the Geofoam block within the backfill and the reinforced concrete load distribution slab atop the Geofoam block. In the FLAC analysis, the reinforced concrete slab was treated as a linear-elastic material because the loads expected from pipeline uplift do not approach the yield strength of a 152 -mm thick reinforced concrete slab. The material properties for the model are shown in Table 32, while the interface properties are shown in Table 33. In Table 33, the interface properties were determined by guidance from the FLAC manual (Itasca, 2005). The values Ks and Kn are the shear and normal stiffness for the interface, respectively.

Table 32. Material properties for Geofoam section model

Material	Density	K	G	ϕ	ψ	c	T
---------	*Kg/m3*	*kPa*	*kPa*	*deg*	*deg*	*kPa*	*kPa*
UTBC	1990	53333	32000	43	0	2.5	0.25
Bedding	1800	8333	3846	32	0	0.0	0.0
Native Clay	1765	6666	2222	24	0	59.9	0.60
Native Sand	1842	7083	3269	27	0	35.9	0.36
LDS	2000	436667	325700	NA	NA	NA	NA
EPS Geofoam	29	3401	3269	0	0	50	100

Table 33. Interface properties for Geofoam section model

Material 1	Material 2	Ks	Kn	ϕ	ψ	c	T
---------	---------	*kN/m*	*kN/m*	*deg*	*deg*	*kPa*	*kPa*
EPS Geofoam	Native Clay	1000	11420	24	0	9	0
EPS Geofoam	Native Sand	1000	11420	24	0	9	0
EPS Geofoam	LDS	87333	87333	6	0	0	0
LDS	Native Sand	87333	87333	13	0	1	0
Bedding	EPS Geofoam	1000	11420	30	0	0	0
Bedding	Pipe	1350	13500	24	0	0	0

The stiffness of an interface between two materials is calculated from a combination of bulk and shear modulus divided by the zone widths along the interface. The shear and bulk modulus of the softer material along the interface is suggested, but not required (Itasca, 2005).

The elastic moduli for the EPS Geofoam were set to degrade as a function of strain in the complex hyperbolic model (Chapters 3 and 4). The EPS moduli used were therefore nonlinear and constantly softening as a function of compressional strain. Also, it was noted that these nonlinear moduli had little effect on the results because the failure was dominated by shearing at the Geofoam soil interface and the assigned interface properties controlled the uplift behavior in the FLAC model.

EPS Geofoam Section Modeling without Interfaces

The EPS Geofoam section was modeled twice: with and without interface elements. The result for the model without interfaces is presented first (Figure 92). The reason for not including interfaces in the first case was to evaluate their importance in the subsequent FLAC models. It can be seen in Figure 92 that this no-interface model predicts significant deformation of the EPS Geofoam block. Because this phenomenon was not observed in the full-scale field uplift test of the Geofoam cover system, this model does not produced reasonable results. Approximately 0.28 m of uplift occurred before the modeling was terminated.

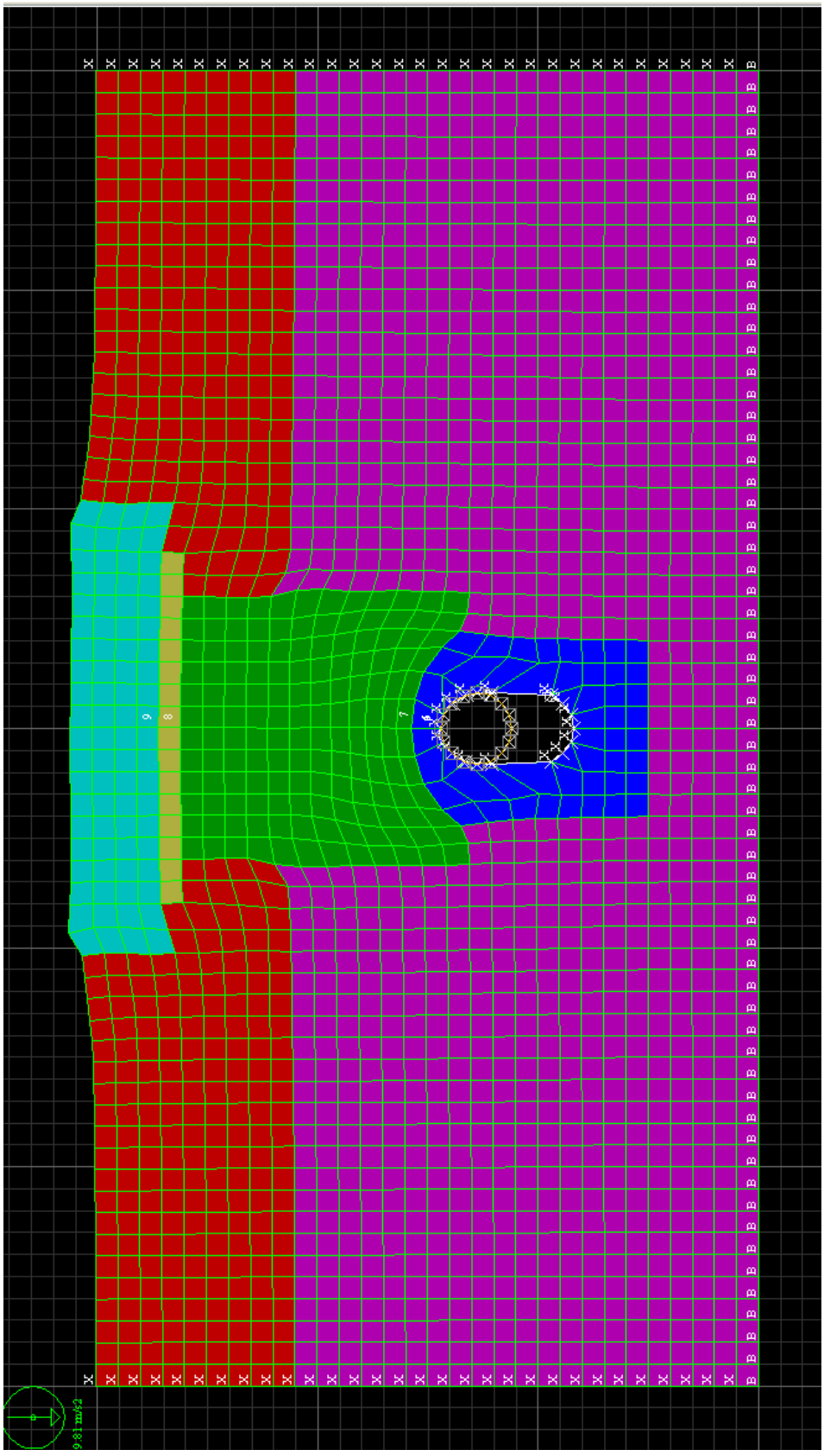

Figure 92. EPS section deformed mesh, no interfaces

Figure 93 presents the vertical displacement contours for the Geofoam model with no interfaces. This figure suggests that the angle of the displacement contours prorogated at roughly 60° from the horizontal in the zone outside of the Geofoam block.

It is important to note that most of the vectors in this model were concentrated in the bottom half of the EPS Geofoam block. This is similar to the observations of the Geofoam behavior in the Geofoam-pipe interaction and lateral Geofoam pipeline experiments. This behavior, however, was not observed in the uplift test of the Geofoam system. The compression in the Geofoam block suggested from the FLAC modeling was a result of the relatively large shear resistance that developed on the sides of the Geofoam block because no interface was present. This resistance restrained the block from uplift, hence producing compression in the block as the pipe attempts to uplift.

It is possible that if the full-scale uplift test been conducted by vigorously compacting soil around the EPS Geofoam block rather than digging a trench and placing the block in the open trench, this type of behavior may have resulted. However, because the trench was excavated in a somewhat cohesive soil, a stable trench wall was achieved and less side shear resistance developed.

The above observation is important for future applications. A system that allows the block to move upward rather freely will produce a less stiff system, giving the pipeline freer movement towards the surface as it uplifts. The reduction in frictional force between the Geofoam block and the trench walls can be achieved in several ways (e.g., geomembrane placed between the trench wall and the EPS). Consideration of this should be given during construction because of its highly beneficial effects.

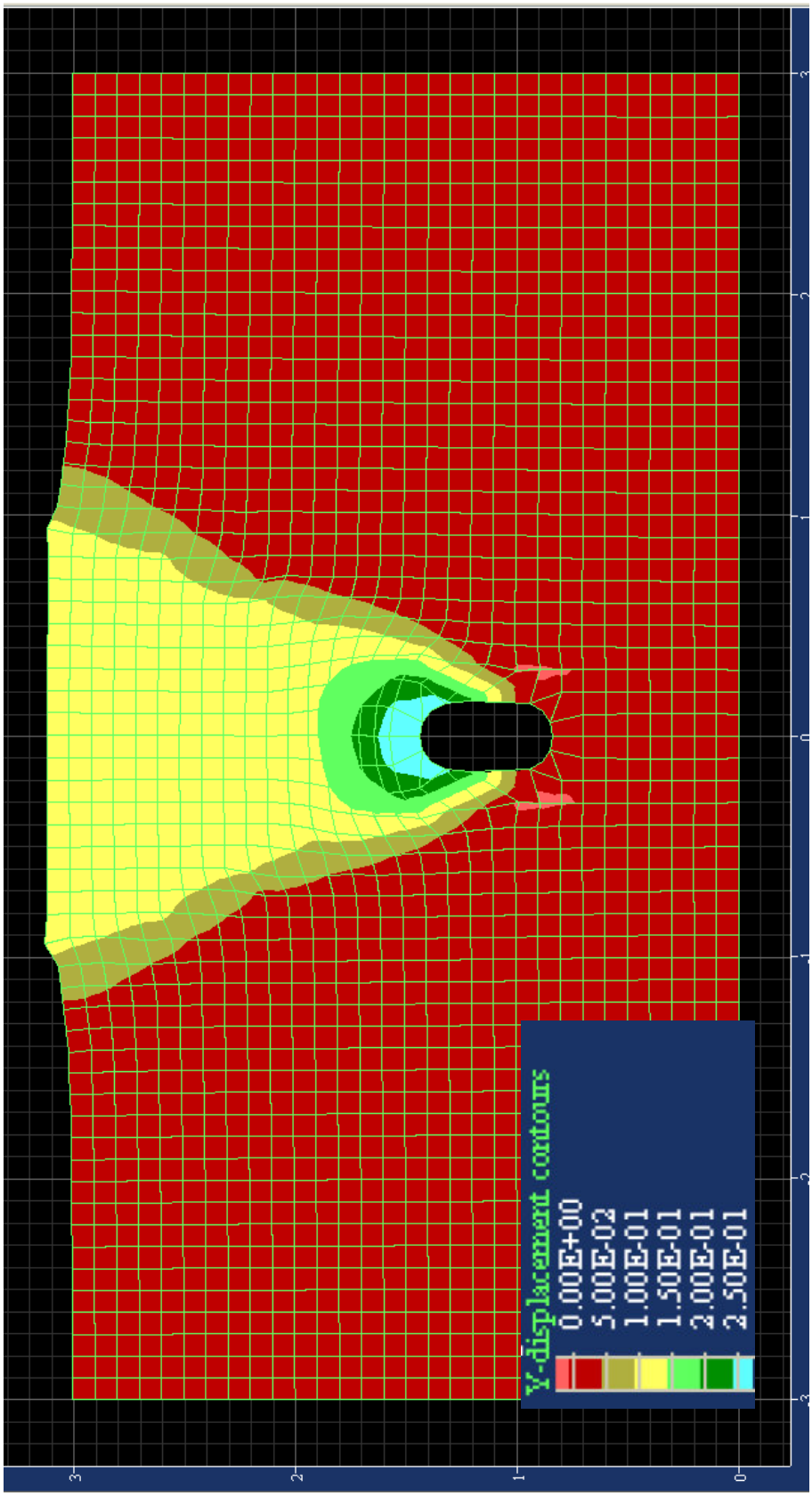

Figure 93. Displacement contours for Geofoam section with no interfaces

Figure 94 shows the vertical stresses in the model at the end of uplift for the case where no interfaces have been added to the model. The peak stress observed in the uplift of the EPS model with no interfaces is 600 kPa. The highest stress observed in the actual uplift test was 168 kPa. This again shows that the FLAC model predicted significant higher local stresses around the pipe than were observed from the test results. However, the stresses in the top part of the model were about 25 kPa, the same as was observed in the actual uplift test.

The force-displacement results for the Geofoam model without interfaces are shown in Figure 95 in combination with the actual test data for the Geofoam cover system. This figure shows that the FLAC model without interfaces exceeded the experimental data by about 100 kN. In summary, these modeling results indicate that interfaces should be used when modeling Geofoam block in a soil mass that is responding to an uplifting pipeline.

EPS Geofoam Model

Figure 96 shows the deformed mesh at the end of uplift for the Geofoam section model that utilized interfaces. The peak uplift for this model was 318 mm before a bad geometry error was encountered in the FLAC model.

The deformation pattern in Figure 96 at the end of uplift matched the observed deformation pattern from the full-scale uplift tests in the field. This model suggested that the Geofoam slightly compresses at the base, when uplifted out of the trench as an elastic unit while the load distribution slab supported the overlying compacted road base. In this model, the interface properties between the Geofoam and the surrounding soil are given

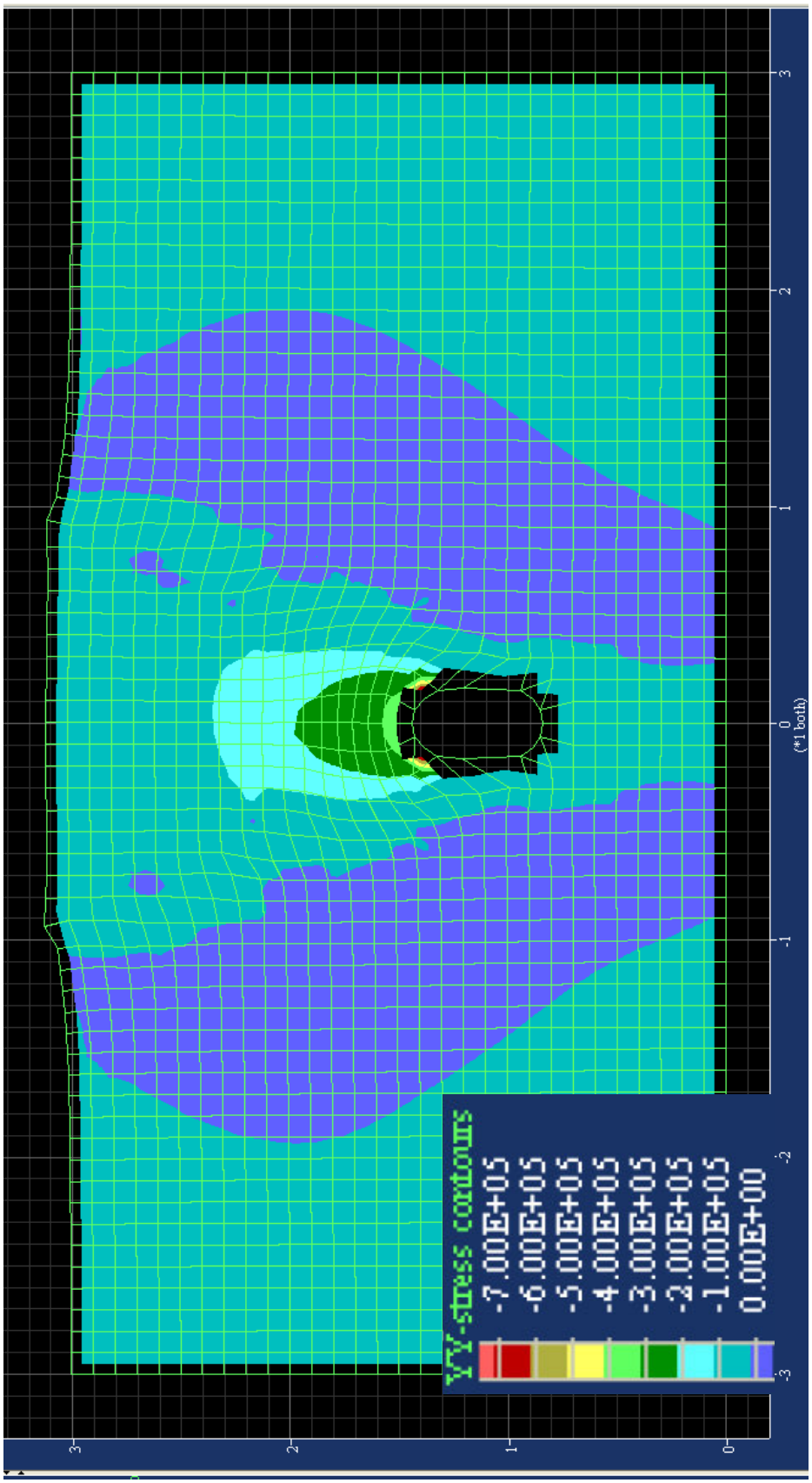

Figure 94. Vertical Stresses for EPS Geofoam section with no interfaces

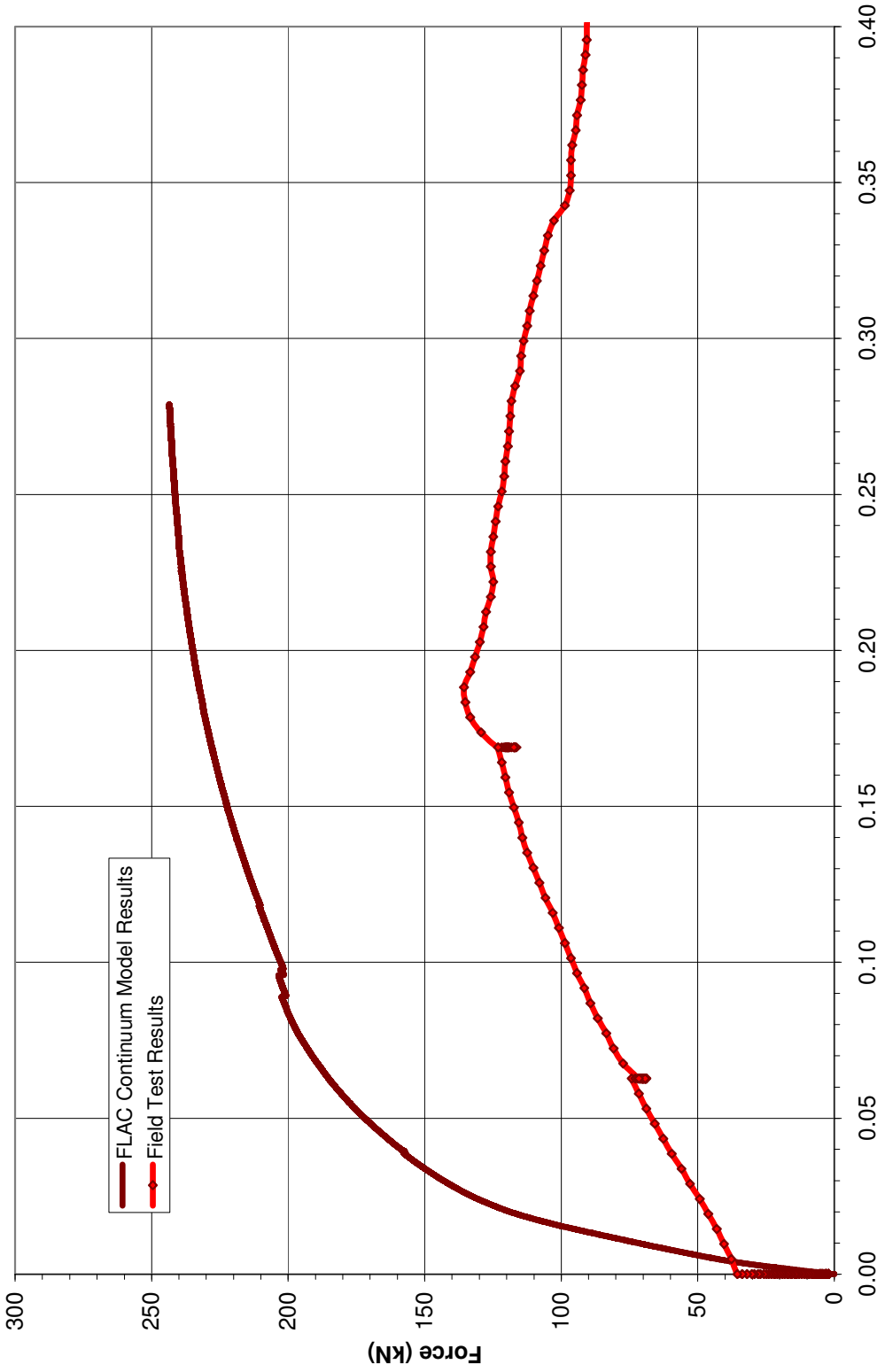

Figure 95. FLAC results for the Geofoam section with no interfaces

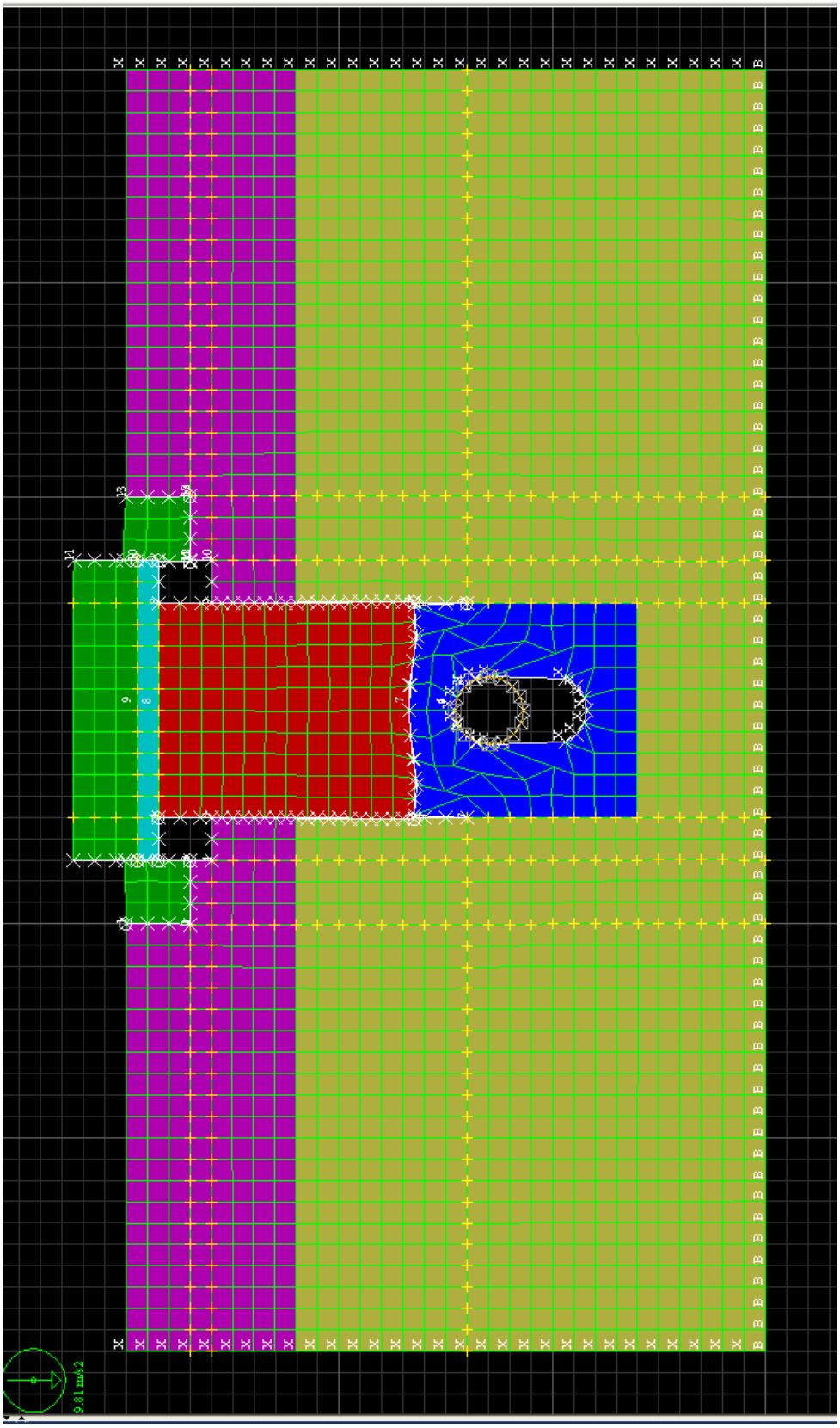

Figure 96. EPS Geofoam model with interfaces deformed mesh

in Table 33. The values in Table 33 were obtained from interface testing in a direct shear device using the EPS Geofoam and the native soils obtained from the site. Figure 97 shows the state of the Geofoam model at the end of uplift. This plot shows that the Geofoam had reached the yield point in compression and that the compacted road base above the load distribution slab had failed in tension. The load distribution slab protected the Geofoam to a certain degree in uplift and forced the failure plane vertically through the compacted road base.

Figure 98 shows the displacement vectors for the Geofoam model with interfaces. Figure 98 and Figure 99 show the Geofoam block uplifting as a single unit with some minor compression of the Geofoam immediately near the pipe and the bedding sand. The compression, however, is limited to the first 150 mm of the Geofoam block. This shows the strain gradient of Geofoam in compression that was observed in both the pipe-interaction test and the full-scale lateral pipe movement tests done as part of this research.

Figure 99 shows the vertical stress contours at the end of uplift for the Geofoam system with interface elements added. The peak vertical stress was found near the top of the pipe in this model and is about 300 kPa. This was approximately 40% larger than the field measured value. The vertical pressure at 152 mm above the pipe (i.e., the location of the lowest pressure sensor in the uplift experiment) was 200 kPa, which is only 16% higher than the measured value.

The final force-displacement results for the Geofoam section are shown in Figures 100 and 101. Figure 100 shows the results of the EPS Geofoam model with interfaces included. The match of the peak force and the shape of the curve is considered to be very

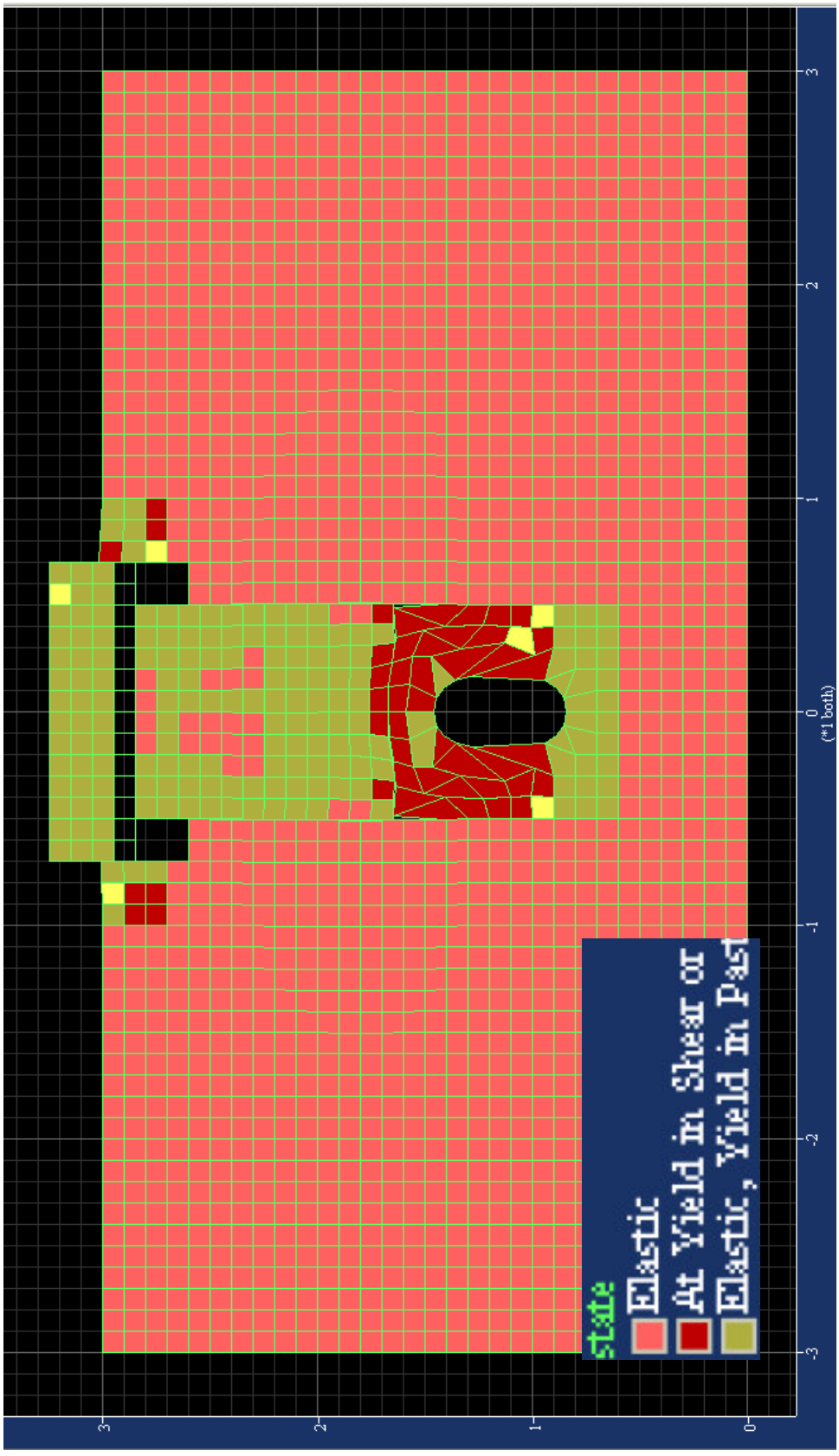

Figure 97. State of the Geofoam model with interfaces

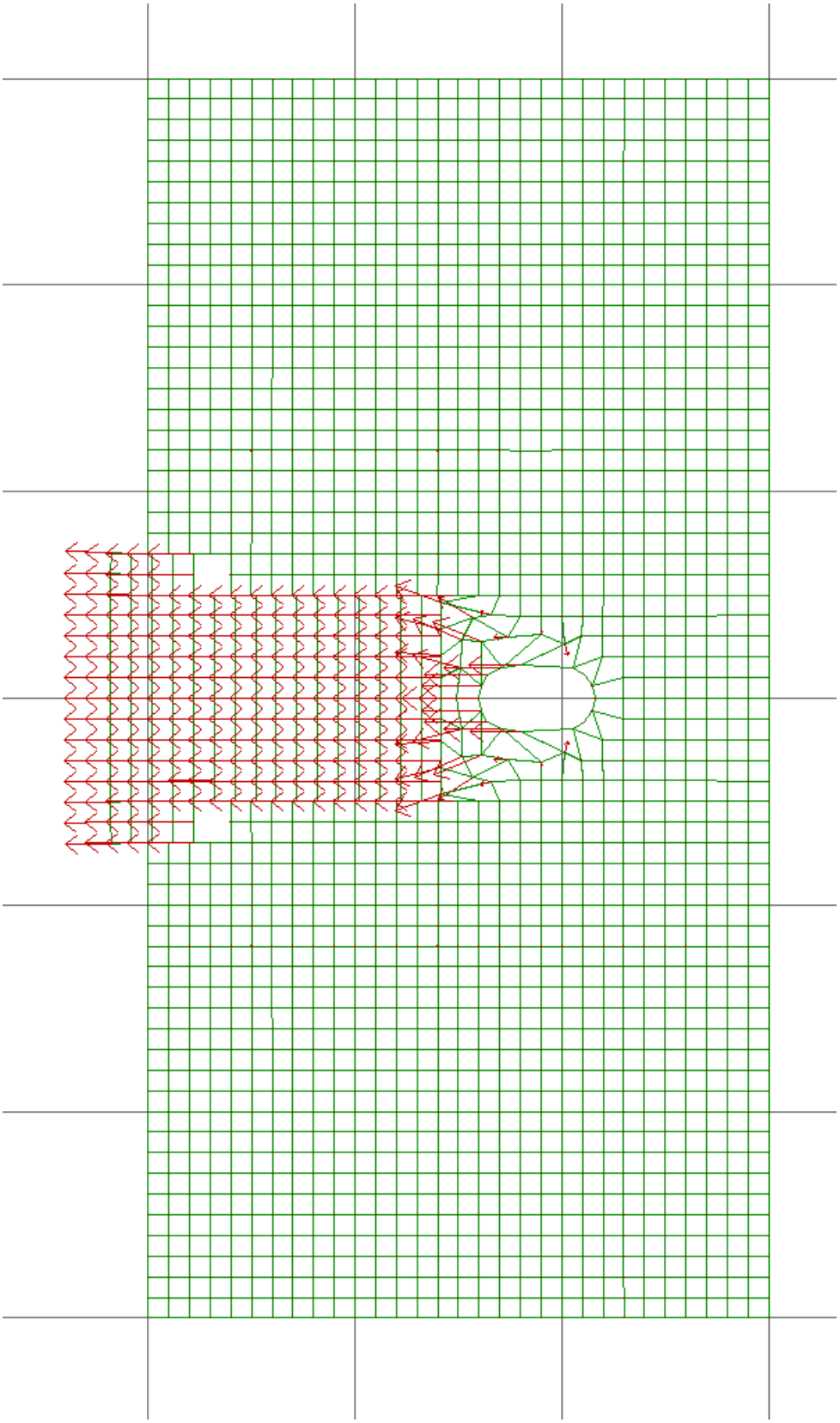

Figure 98. Vectors for the Geofoam model with interfaces

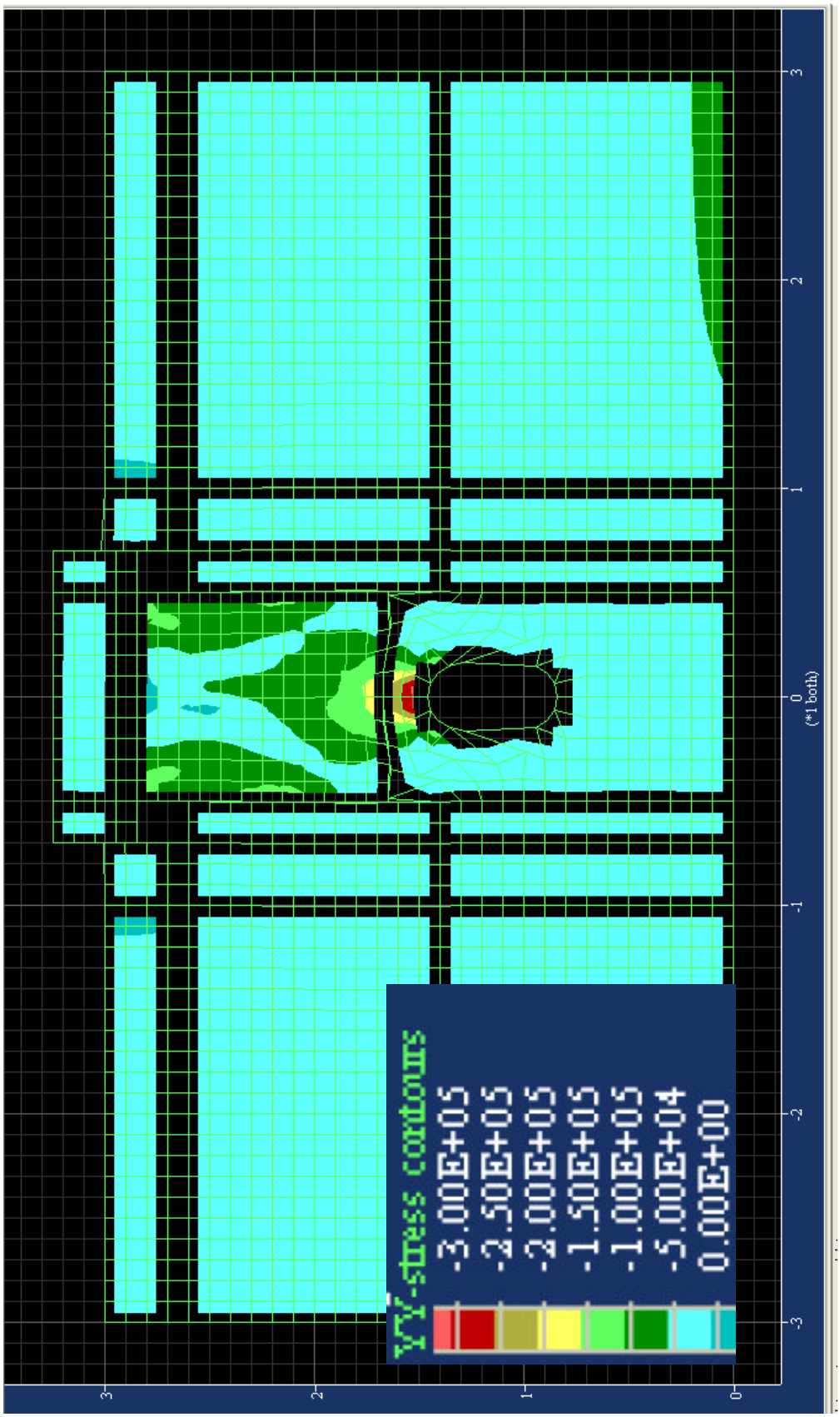

Figure 99. Vertical stresses of the Geofoam model with interfaces

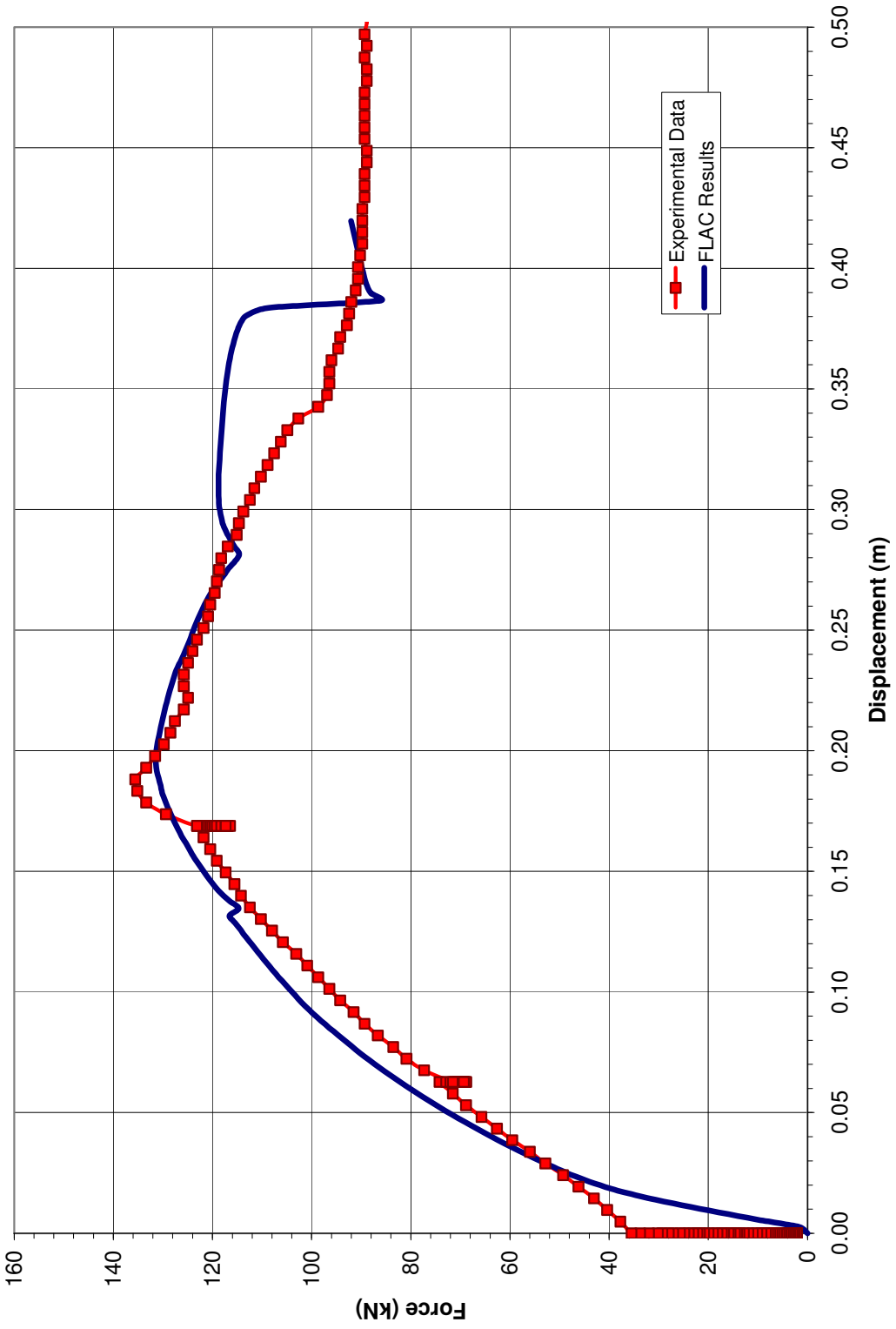

Figure 100. FLAC results for EPS Geofoam section with interfaces

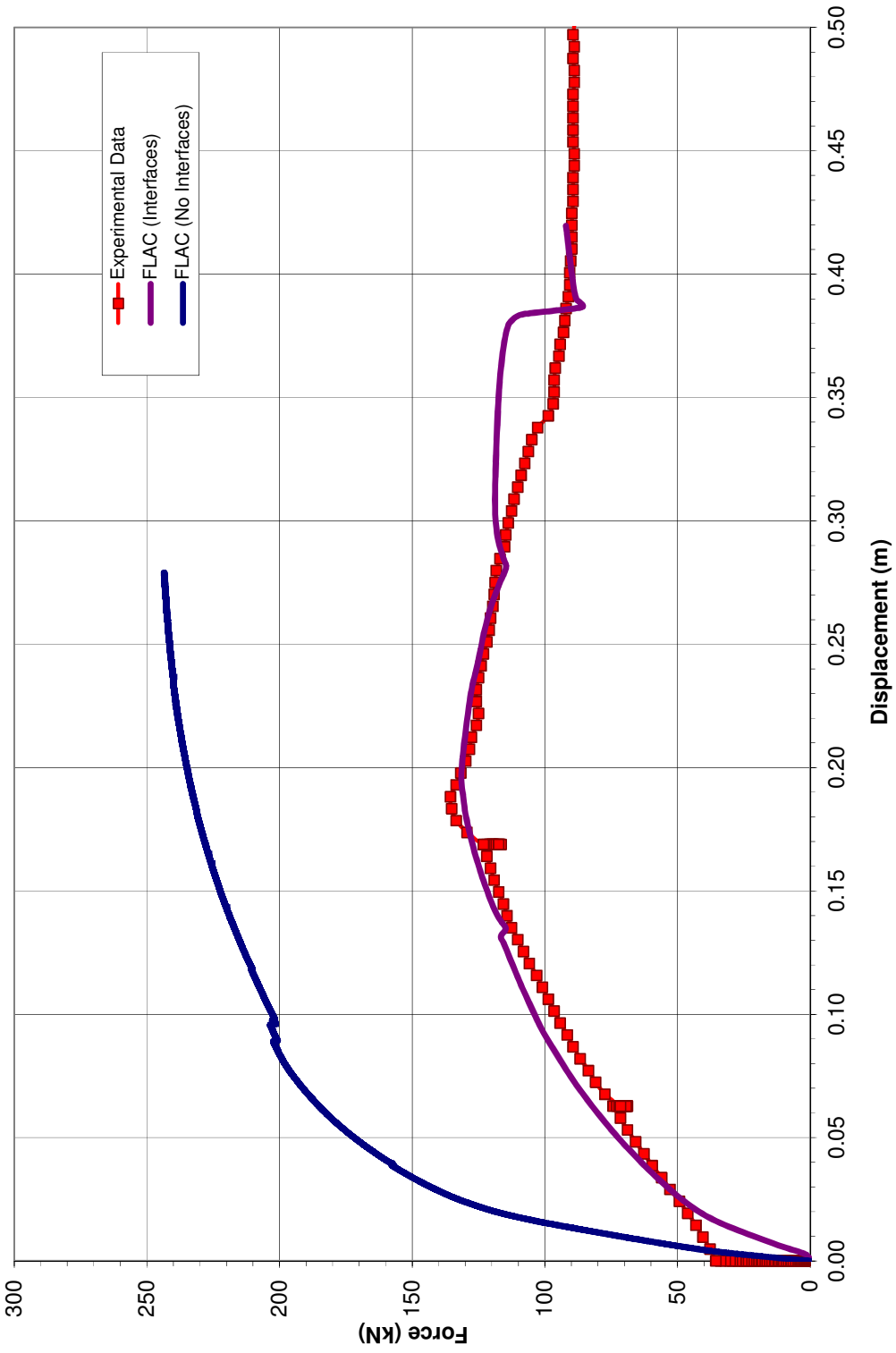

Figure 101. Force-displacement results for the Geofoam models

good throughout most of the displacement range. The initial displacement range did not match well, as the field test data showed no displacement until the mass of the system above the pipe was mobilized as well as some of the frictional resistance. The FLAC model shows more immediate displacement. This initial behavior is governed by the bedding sand around the pipe. In the field tests, the sand was observed to flow freely around the pipe before much uplift had occurred. In FLAC, the sand did not flow around the pipe. At a displacement of 270 to 370 mm, the FLAC model had some numerical instability that produced the "bump" in the FLAC curve compared to the field test data.

Figure 101 shows the field test data and the results of both the EPS FLAC models with and without interfaces. The FLAC model with interfaces predicted the peak force within 5% of the field results. The experimental peak occurred at nearly 180 mm of pipe uplift, while the FLAC model with interfaces showed the peak was achieved at 200 mm of vertical displacement.

Thus, it is concluded that the FLAC model with interfaces reasonably estimates the peak uplift resistance and the corresponding displacement required to reach that peak. It is also concluded that if proper interface properties are determined via laboratory testing, FLAC can reasonably model the uplift force-displacement behavior of a pipe in uplift for plane-strain conditions.

Figure 101 presents the recommended curves for evaluating the force-displacement relationship of an EPS Geofoam cover system for site, soil and construction details similar to those used in the field experiments. In application of Figure 101, it is important to remember these FLAC modeling results represent two distinct cases, one where the block is allowed to slide along trench side walls, and one where the block is fully coupled

with the trench side walls. In reality, the EPS block cannot be fully coupled with the trench sidewall, so that case represents the upper bound of behavior. The actual sliding resistance that develops at this interface is a function of the interface friction angle and the normal stress that develops between the EPS and the adjacent backfill. The latter is strongly influenced by the construction and degree of compaction used as the soil placed around the EPS block.

FLAC3D Modeling

A series of FLAC3D models were developed in conjunction with the FLAC2D models for the two field test sections (i.e., soil backfill and EPS Geofoam cover system). The purpose of these modeling exercises was to explore more closely the soil-structure and soil-Geofoam structure interactions in uplift. The FLAC2D models previously discussed used simple beam elements for the pipe. The FLAC3D analysis incorporated more complex plate and shell type elements to model the beam. The plate and shell elements have more degrees of freedom than simple beam elements. Additionally, the FLAC3D models allow the pipe to be "picked up" at two locations as occurred in the field tests. Rather than assuming a plane-strain condition, the actual uplift conditions can be more faithfully modeled, including end conditions, in FLAC3D.

In most respects, FLAC3D's formulation is similar to that of FLAC2D except that in the model setup, the user defines the geometry, structural elements, material properties, boundary conditions, etc., in terms of their location in real coordinate space rather than in nodal space as is done in FLAC2D analysis. The same constitutive material models are available in FLAC3D. In addition, the same computational procedure is implemented in

both codes and large strain mode calculations are handled in both models. FISH code was once again used in FLAC3D to control the model and request detailed outputs from the analyses during and after computation.

Modeling Approach

The same modeling approach used in FLAC2D was used as in FLAC3D. The model geometry was created as closely as possible to the actual field test conditions. The materials were added to the model and assigned to "groups" that divided up the mesh into regions. The boundary conditions were established with the additional restraint that displacement was restricted in the longitudinal direction along the base, sides and ends of the model. The soil in the area of the pipe was assigned as a "null" material and the pipe geometry was added as a series of SHELL elements with the same material properties as the actual pipe. The SHELL elements were not attached to the mesh with interface elements similar to the FLAC2D analysis, because the structural model in FLAC3D already contains such interfaces. These interfaces allow slippage and separation of the zones at the interface. They also allow for frictional interaction as specified by the friction angle at the contact point.

A series of runs were conducted to initialize the model to the in-situ and initial stress conditions. After the initialization of the model, the pipe was uplifted, at the locations in used the field test, at constant velocity until a numerically unstable state was reached (i.e., bad geometry error was encountered). Uplift was then halted and the results were extracted from the model.

FLAC3D Modeling Geometry

Figure 102 shows the three-dimensional finite-difference grid with the pipe positioned within. (This perspective was chosen for most of the subsequent plots because it shows the 3-dimensional shape of the grid as well as the results in a simple manner.) Note that the axes shown in Figure 102 show that the X-direction was transverse, the Y-direction was longitudinal and the Z-direction was vertical. The grid was centered in the X and Y directions, and the base of the model was set to zero in vertical (i.e., Z-direction). The base of the grid is the same length as the length of the pipe used in the field uplift tests. The end of the pipe was flush with both ends of the model. This was done because in the field tests, the ends of the pipe were not covered in the trench by the soil backfill or EPS cover system.

Figure 103 is similar to Figure 102 with the addition of the shading representing the different materials used in the soil backfill model. The structural elements for the pipe are not shown in Figure 103, but the pipe has been placed in the slot in the bedding sand.

FLAC3D Modeling of Soil Backfill Section

The various materials in the soil backfill model are also shown in a different manner on the mesh in Figure 104. This figure also shows shading representing the cohesive strength of the different materials. (The sidebar in Figure 104 indicates the range in cohesive strengths for a given color.) The blue shading represents zero cohesion which is sand. The native sand was been given some cohesive strength despite being an overall nonplastic soil. The amount of cohesion assigned was based on the results of the unsaturated triaxial tests performed (Tables 24 through 28).

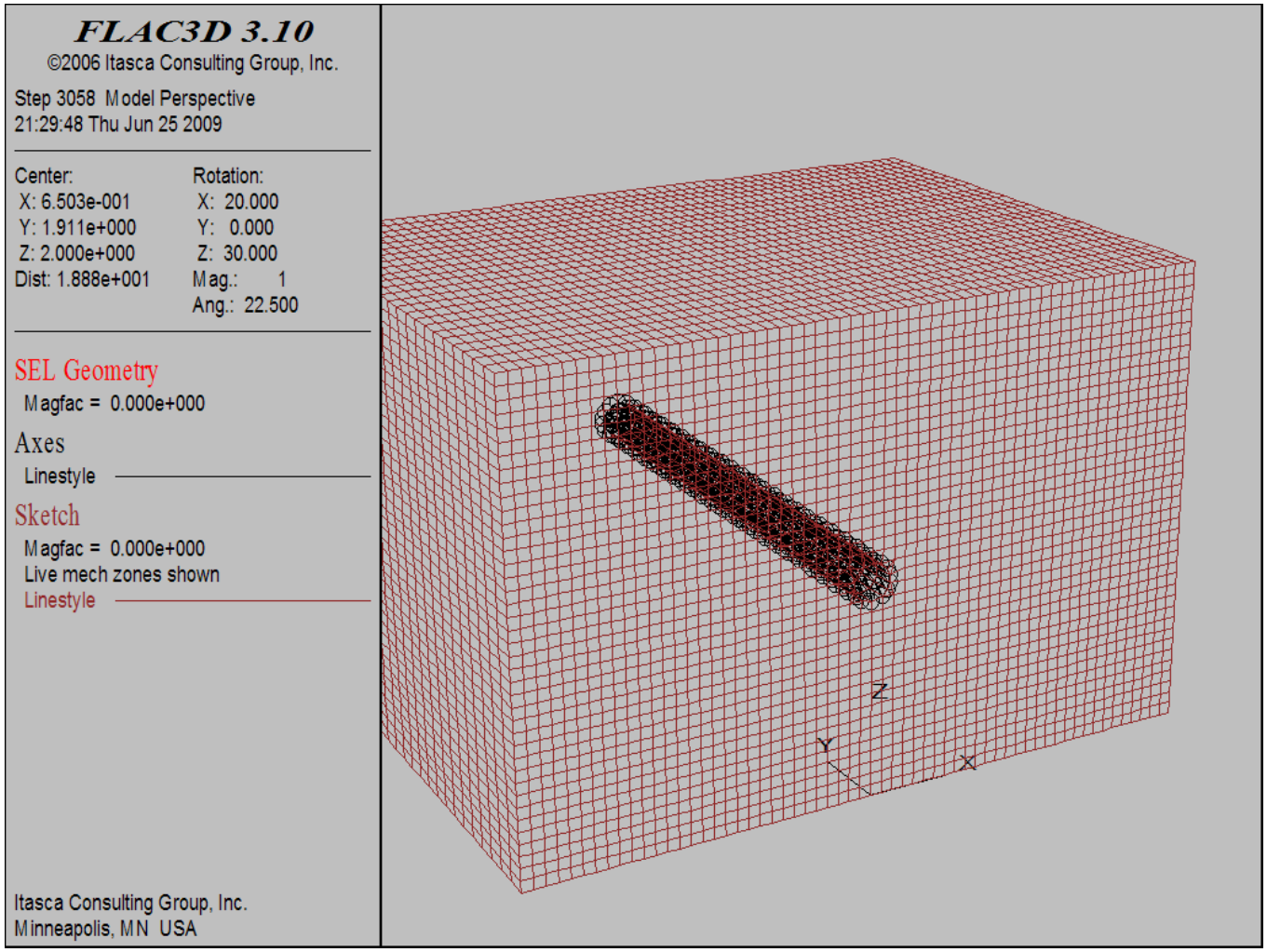

Figure 102. FLAC3D mesh

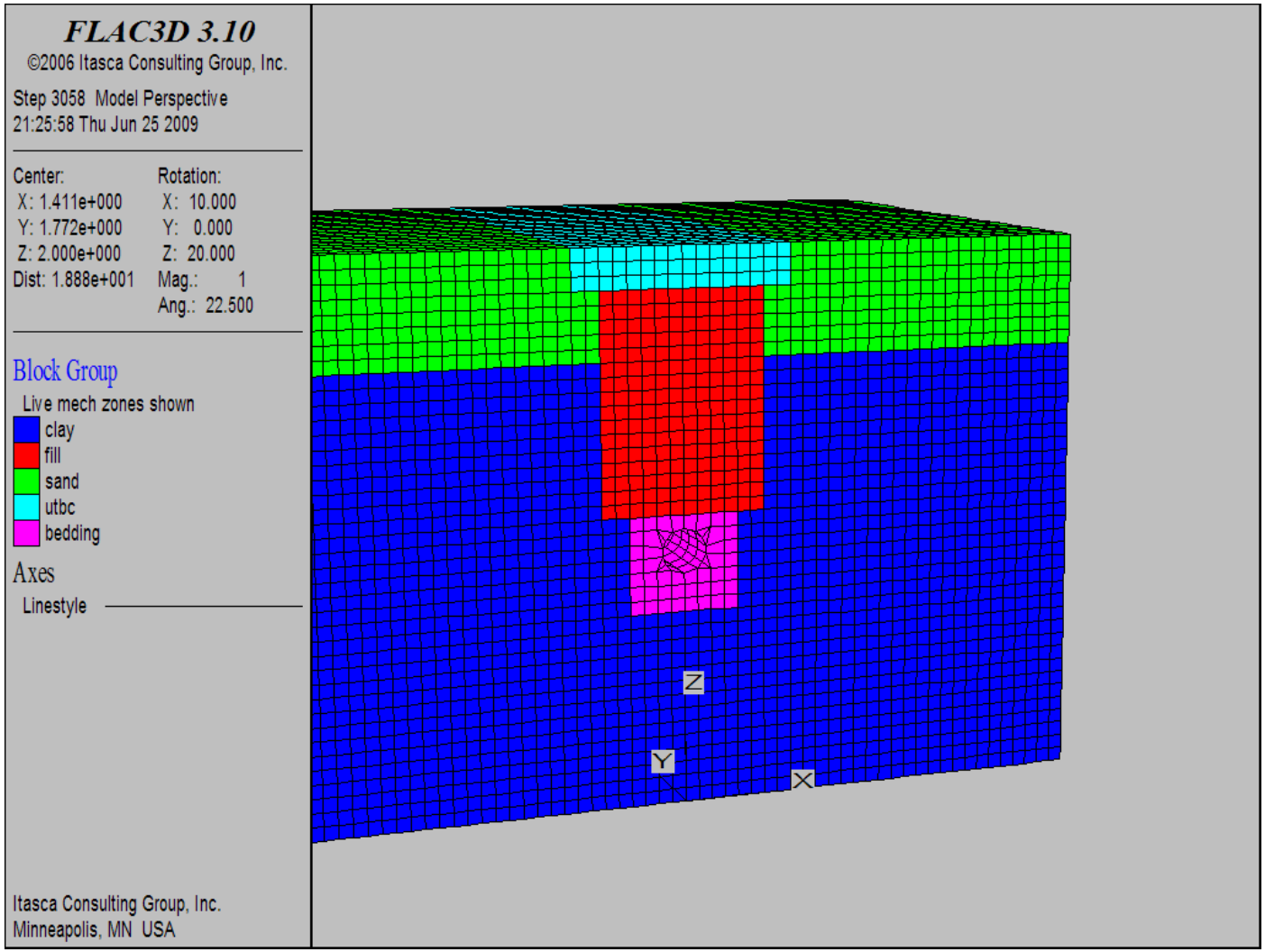

Figure 103. FLAC3D soil backfill model geometry

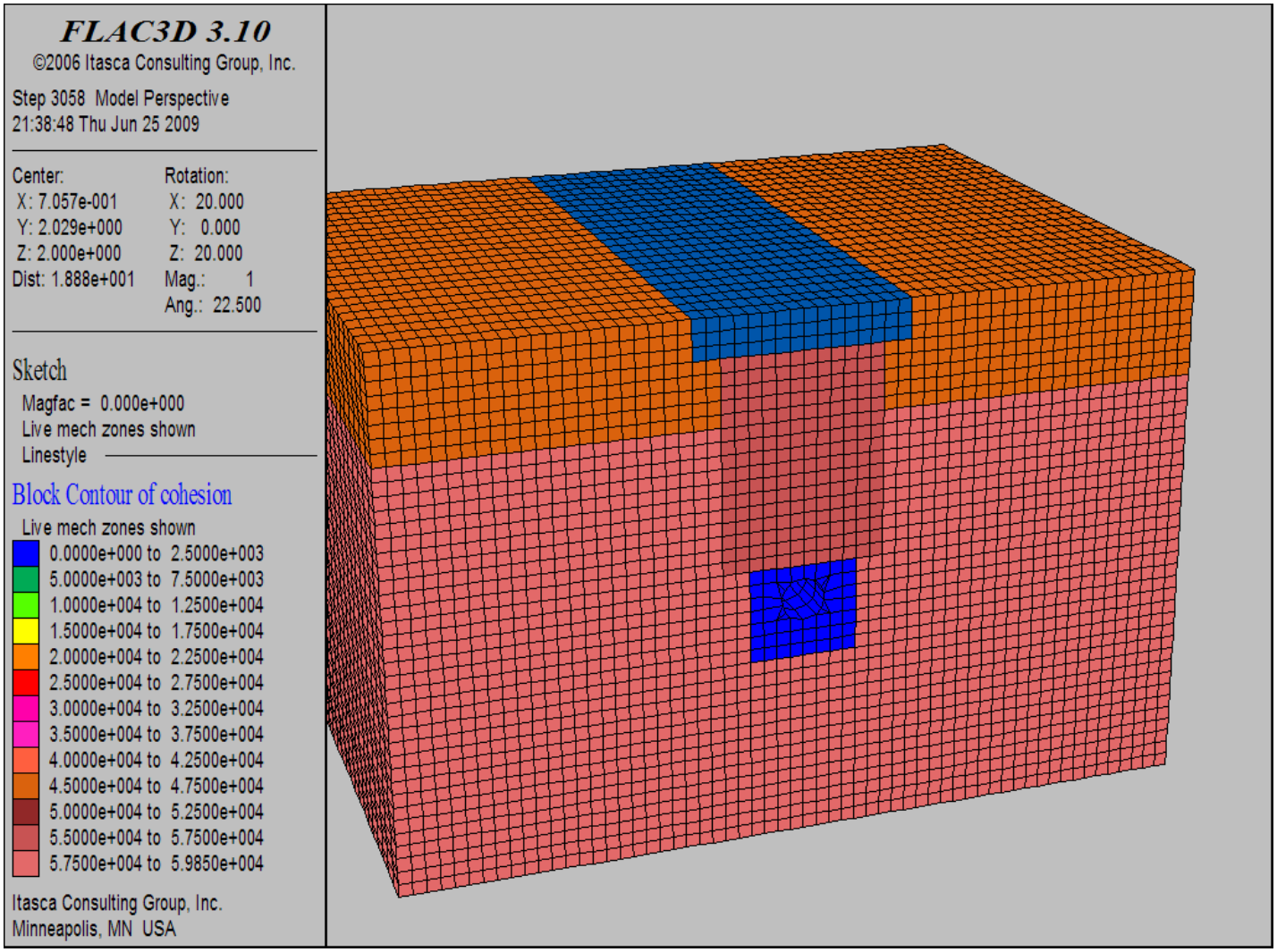

Figure 104. Soil backfill model cohesive strengths

Figure 105 shows the deformed mesh and pipe location at the end of uplift for the soil backfill section. Figure 106 shows the displacement contours on the deformed mesh. The pipe location at the end of uplift is shown in reds. Figures 105 and 106 show slightly more compression and distortion of the clay backfill than was obtained in the FLAC2D model (Figure 92). In addition, a less pronounced surface expression of the uplift failure planes was obtained in the FLAC3D results. Instead, the FLAC3D modeling showed that the uplift is more concentrated along the trench.

Figure 107 shows the vertical stress distribution in the soil backfill from the FLAC3D model at the end of uplift. The red shading in this figure shows the zones of the grid that were in tension. The blue shading indicates that the highest vertical stresses were concentrated within 150 mm of the pipe. The green shading indicates that most of the higher vertical stresses were concentrated within about 457 mm of the pipe during this stage of uplift. The FLAC3D modeling results overpredicted the vertical stresses in the zone located 915 mm above the pipe by about an order of magnitude compared to the FLAC2D model. This may be a 3D stress concentration effect not calculated by the plane strain formulation in FLAC.

It should be noted that the displacement of the pipe at the end of uplift, as shown in Figure 106, was nearly 250 mm. Uplift of the pipe during the modeling was halted by FLAC3D after 190 mm of uplift. Figure 108 shows the horizontal stress distribution of the soil backfill model at the end of uplift. The highest horizontal stress was concentrated around the top of the pipe and was in compression. The red shading in this figure indicates that the soil located directly beneath the compacted road base was in tension at the end of uplift.

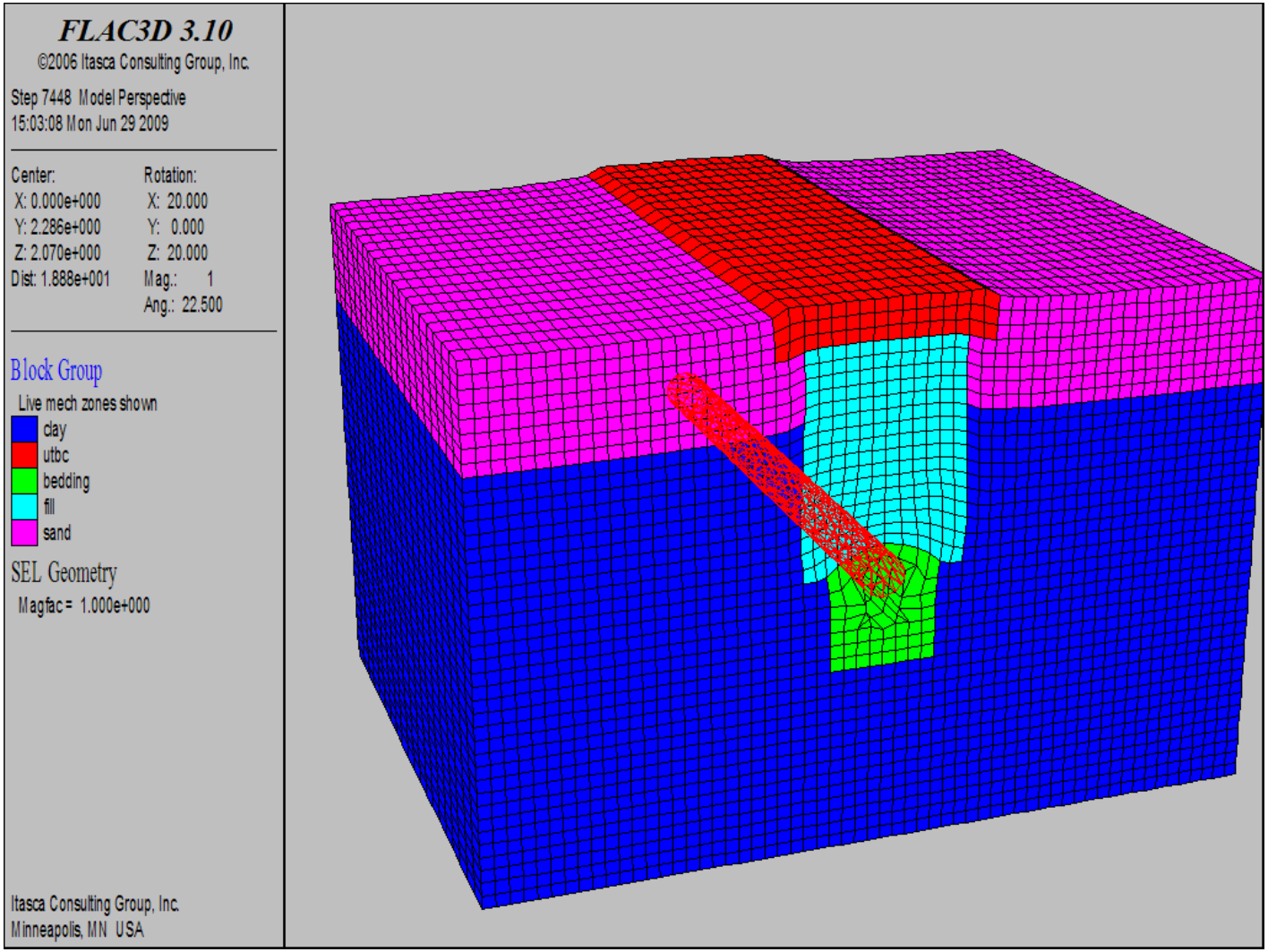

Figure 105. Deformed geometry for soil backfill model

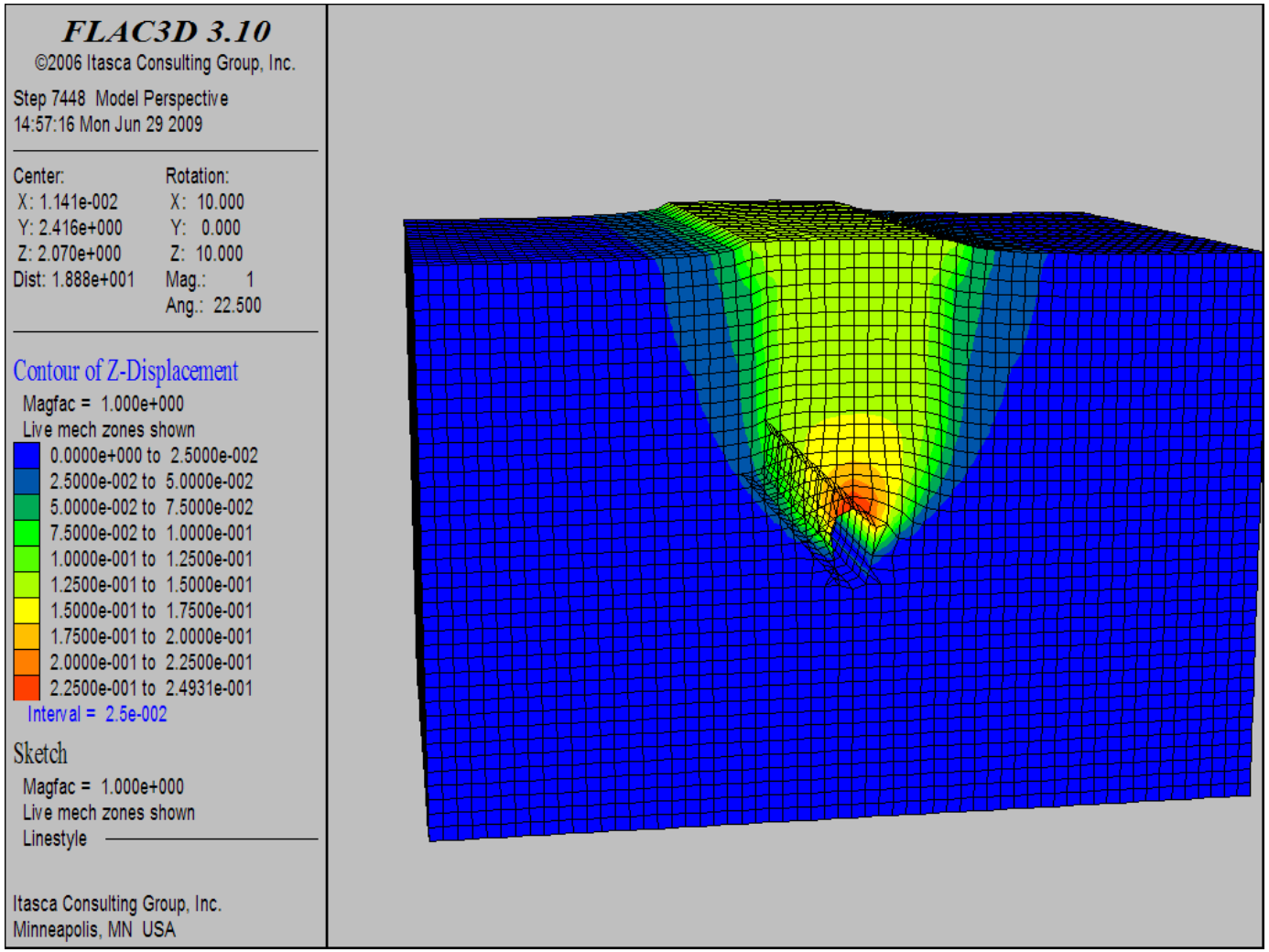

Figure 106. Vertical displacements for soil backfill model

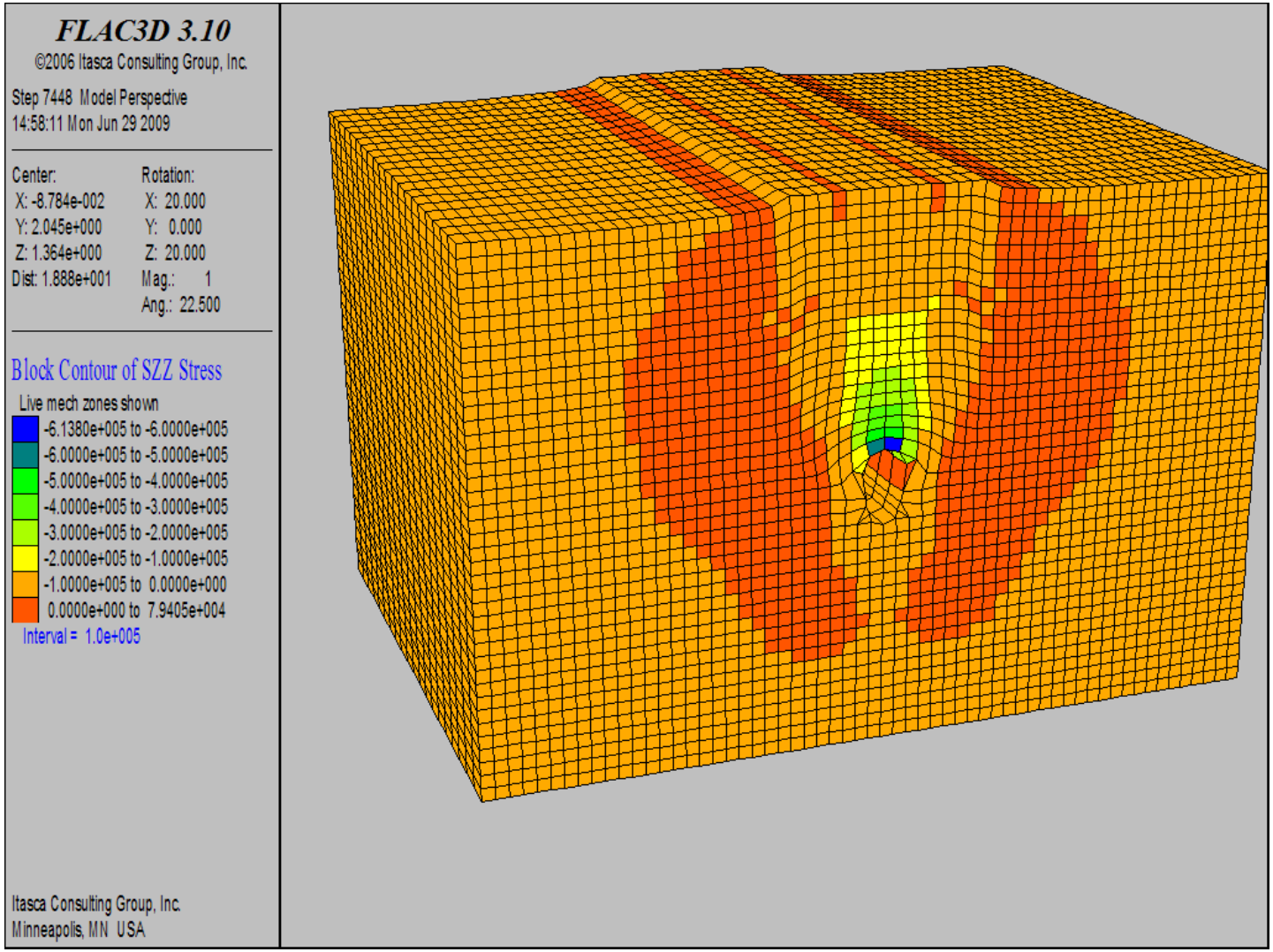

Figure 107. Vertical stresses in soil backfill model

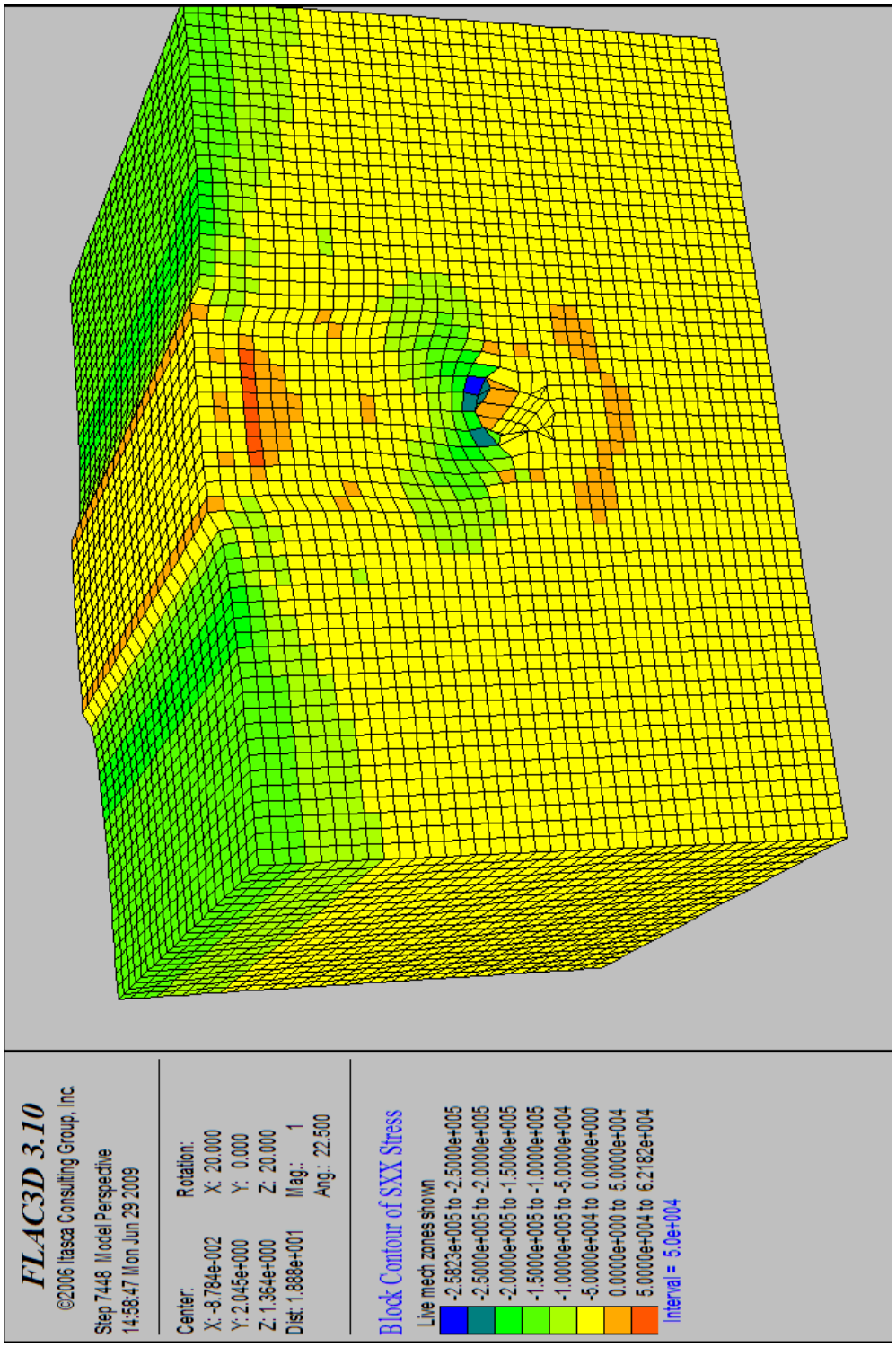

Figure 108. Horizontal stresses in soil backfill model

In addition, the model predicts a horizontal stress increase in the surficial soil near the ground surface starting from the edge of the trench and extending to the edge of the model. This increase in horizontal stress appears reasonable and was a result of the bulging of the clayey fill in the trench as it is pushed upward and outward by the uplifting pipe.

The normal stresses developed in the SHELL elements that compose the pipe are also shown in Figure 109 at the end of uplift. The shading of the pipe's SHELL elements indicates the magnitude of the normal stress at this time. The highest normal stress calculated was approximately 1 MPa and occurred along a thin strip that runs along both sides of the pipe near the crown. This zone of highest stress was located roughly 1/8 of a pipe radius from the crown of the pipe (45 degrees from vertical). The normal stress found directly above the crown of the pipe was significantly lower (about 600 MPa) which represents a 40% reduction from the maximum normal stress.

Figure 110 illustrates the vertical stress on the pipe at the end of uplift. This plot confirms the conclusions from Figure 109 in that the stresses on the pipe were concentrated at 45 degrees from vertical on the pipe, but not at its top. This vertical stress distribution on the pipe (Figure 110) shows that very high, localized vertical stresses occurred along the lines of highest normal stress. Figure 111 also shows that the bottom of the pipe had zero to slightly negative vertical stress acting on it in the zone where there was no contact with the underlying soil.

The shear coupling stress in the pipe at the end of uplift for the soil backfill model is shown in Figure 111. The highest shear coupling stress was also found where the normal and vertical stress were at their maxima. Figure 111 indicates the local shear stresses

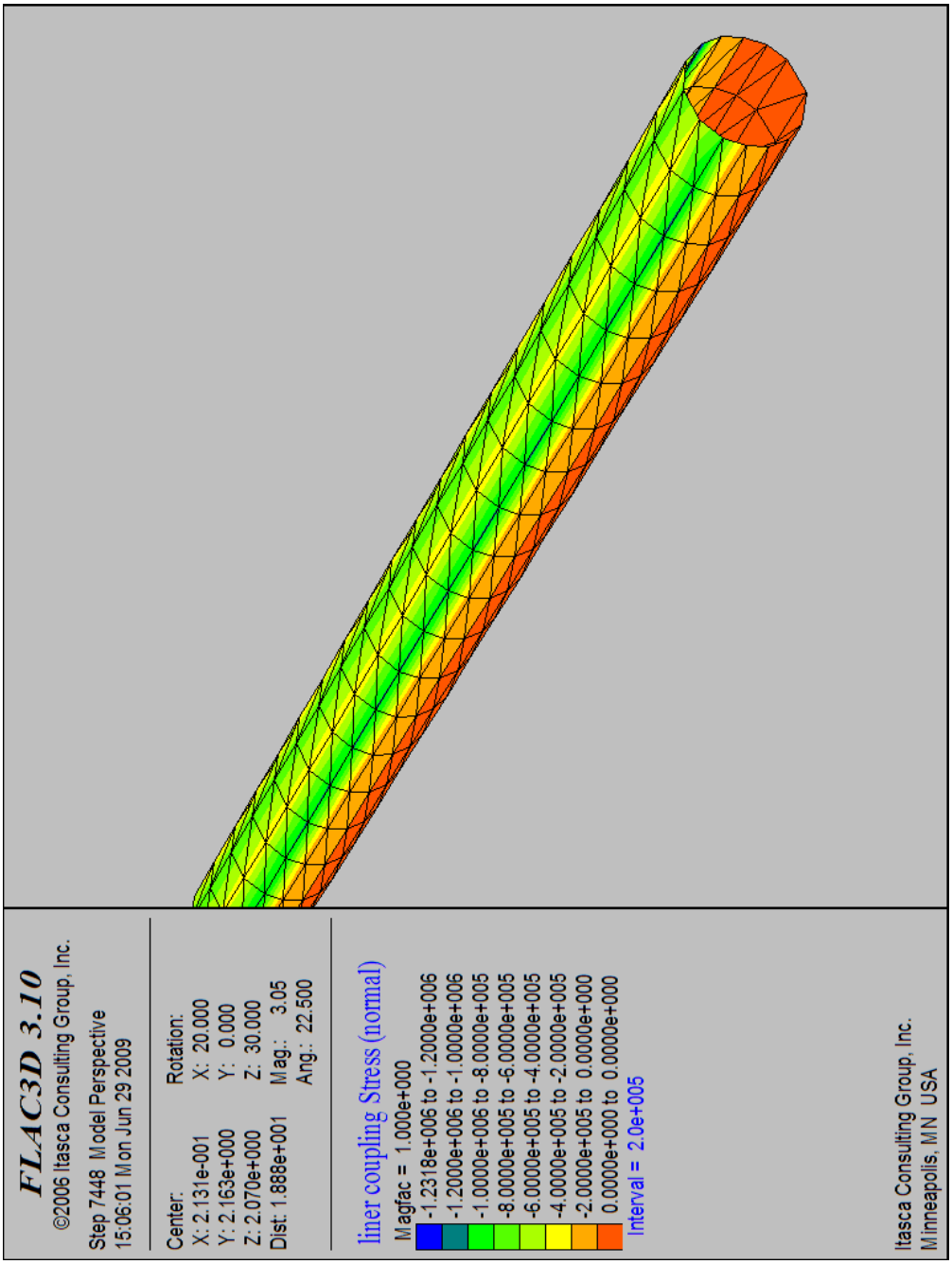

Figure 109. Pipe normal coupling stress from soil backfill model

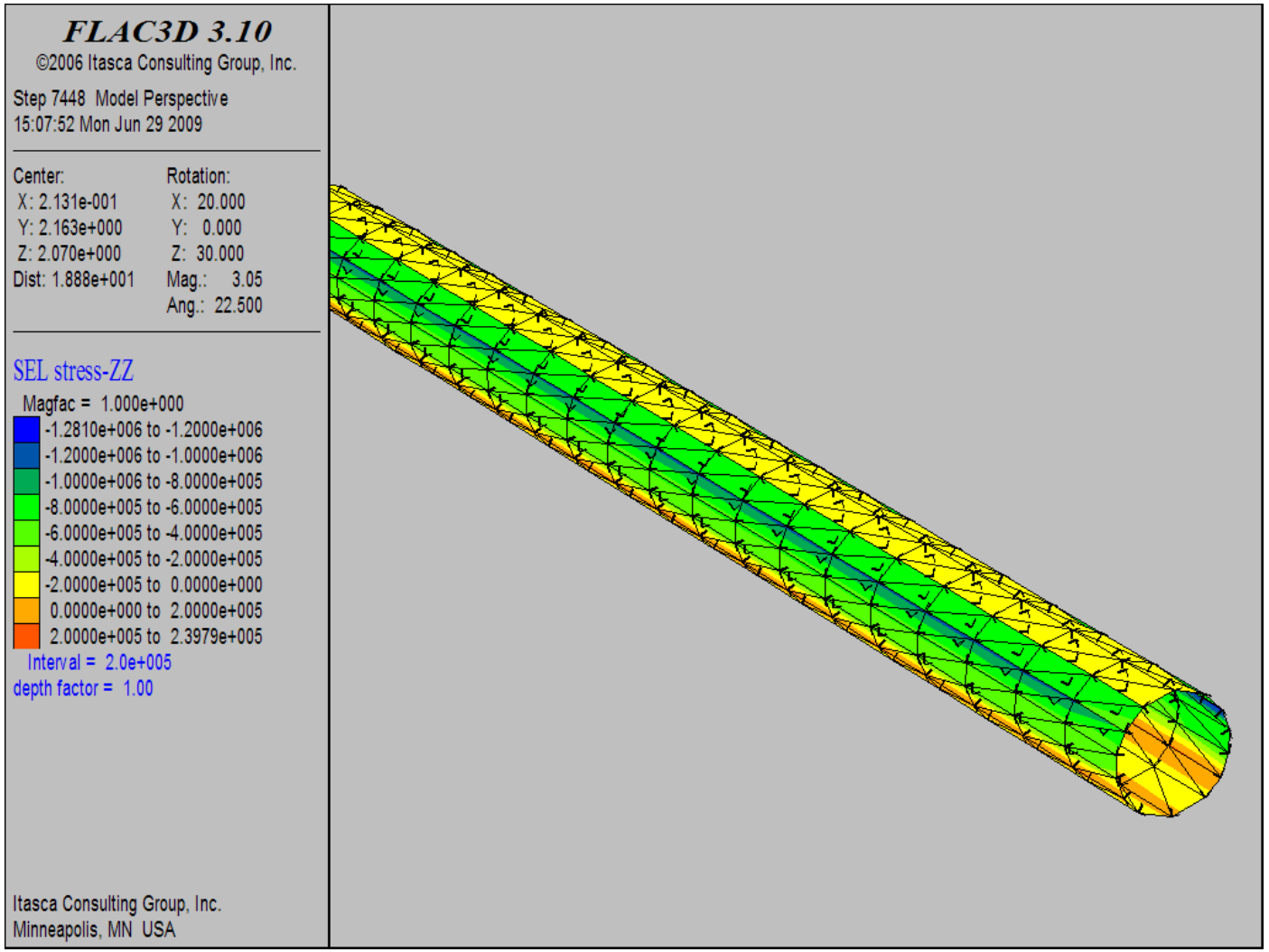

Figure 110. Pipe vertical stress from soil backfill model

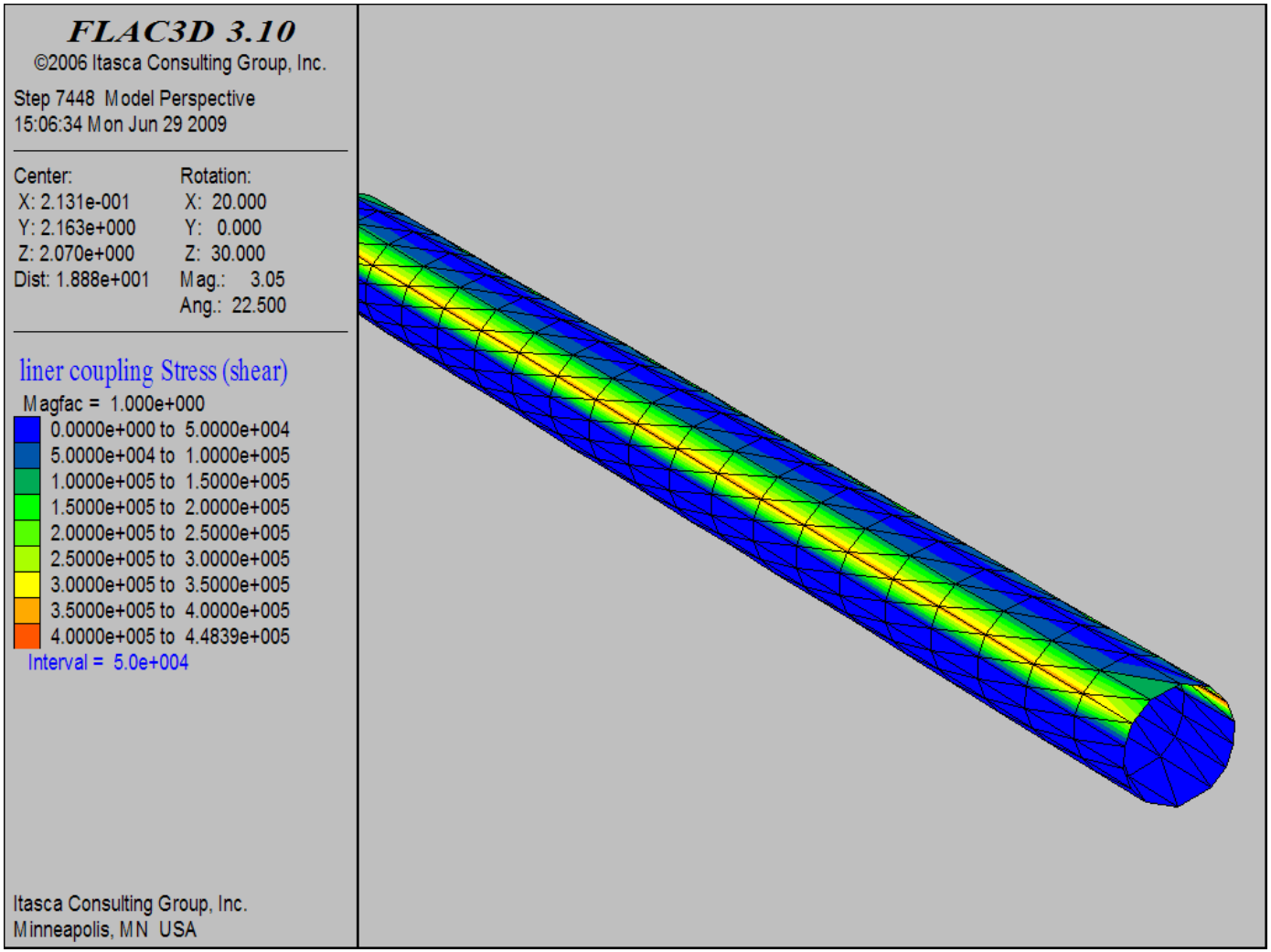

Figure 111. Pipe shear coupling stresses from soil backfill model

were quite high at this location and were nearly zero at other locations in the pipe. This suggests that the shearing of the soil was also occurring at this location (i.e., an angle of 45° from the center of the pipe).

In short, the modeling of the pipe showed that the highest vertical, normal and shear stresses were found in the same longitudinal zones. The highest horizontal stress on the pipe (not shown in this report), however, acted at the sides of the pipe at 90° from vertical. Figure 112 shows the moments induced on the pipe at the end of uplift. The magnitude of the induced moments are so small it is concluded that the uplift of the pipe at two locations had little influence on the pipe (i.e., the pipe behaved rigidly). This confirms the plane-strain assumptions used in the FLAC2D modeling.

FLAC3D EPS Geofoam Model

The EPS Geofoam section was modeled in FLAC3D. The FLAC3D Geofoam section model geometry with interfaces is shown in Figure 113. The interface locations in the EPS Geofoam section with interfaces are shown in Figure 114. Interfaces were placed in the same locations in the 3D model as the 2D model. Interfaces properties were the same in the 3D model as the 2D model (Table 30). The FLAC3D Geofoam model with interfaces was initialized in the same manner as was the FLAC3D soil backfill model. The same uplift code was used in the model with interfaces as the soil backfill section. The only difference in the two models was that the materials for which interfaces are to be added were “separated” from each other in the code, and an interface “wrapped” around them. The interfaces, as shown in Figure 114, were “wrapped” around the bedding sand, the EPS Geofoam block, the load distribution slab and the UTBC at the top

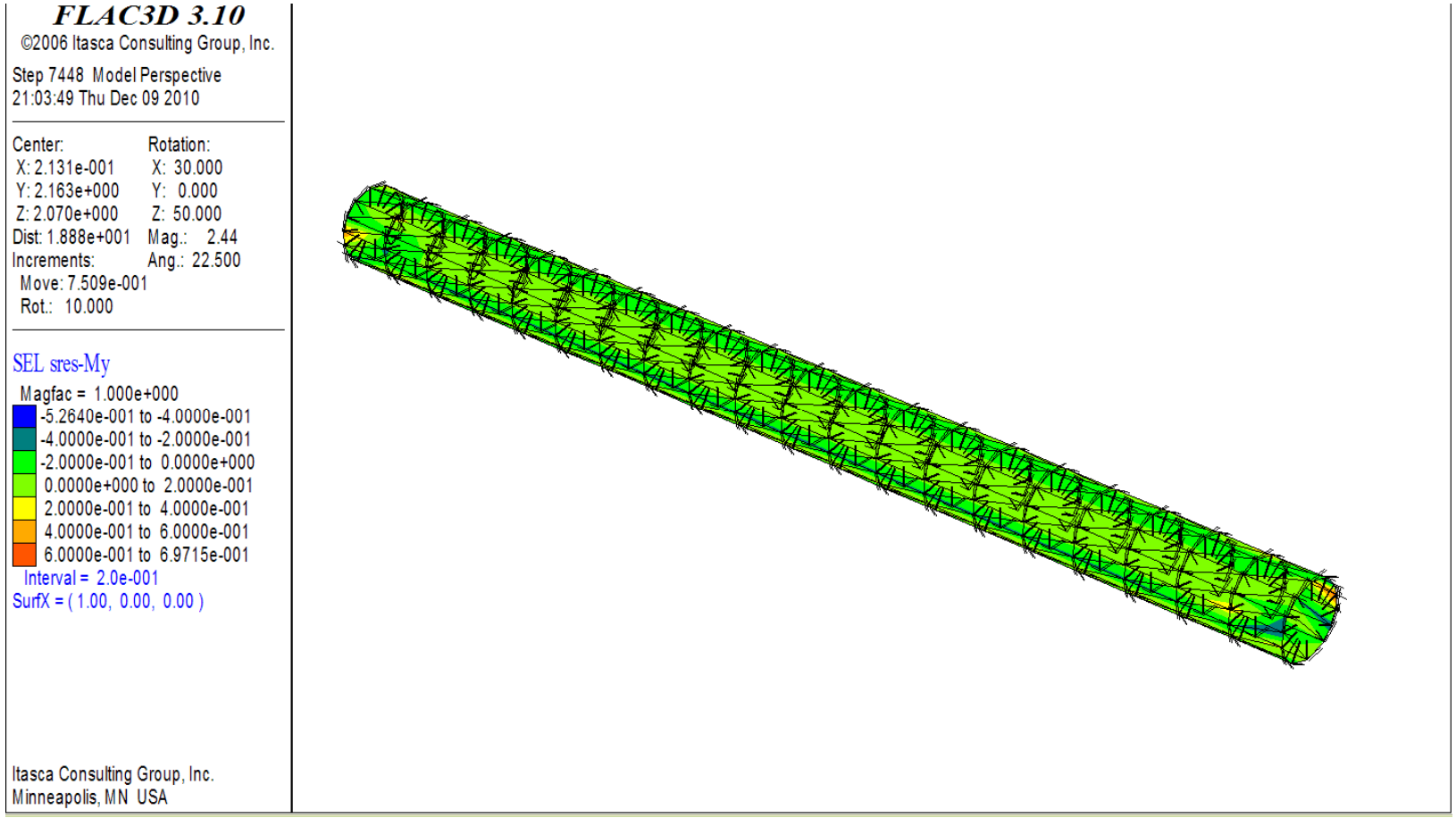

Figure 112. Resultant moments in pipe at end of pick-up

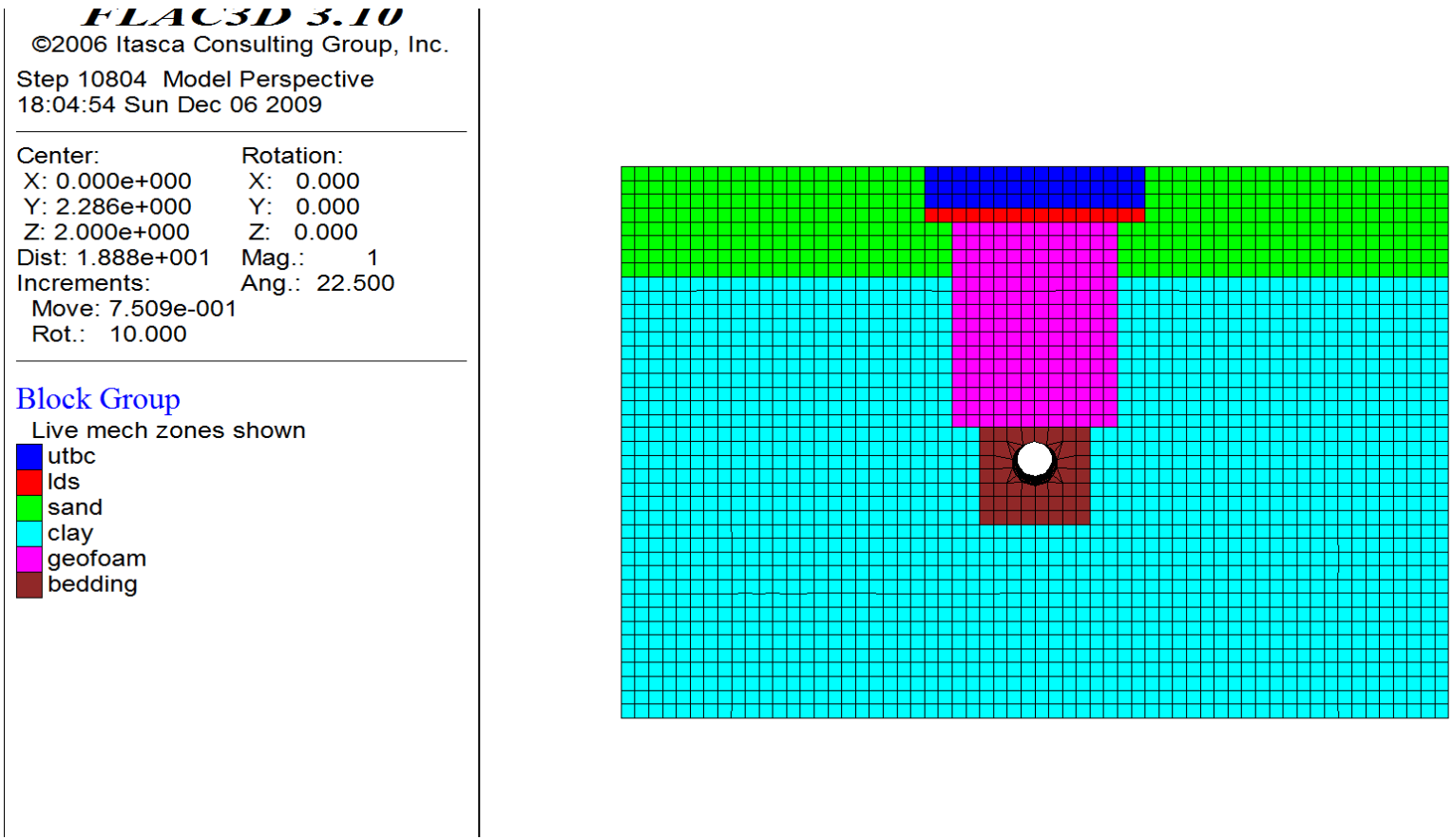

Figure 113. FLAC3D Geofoam model geometry with interfaces

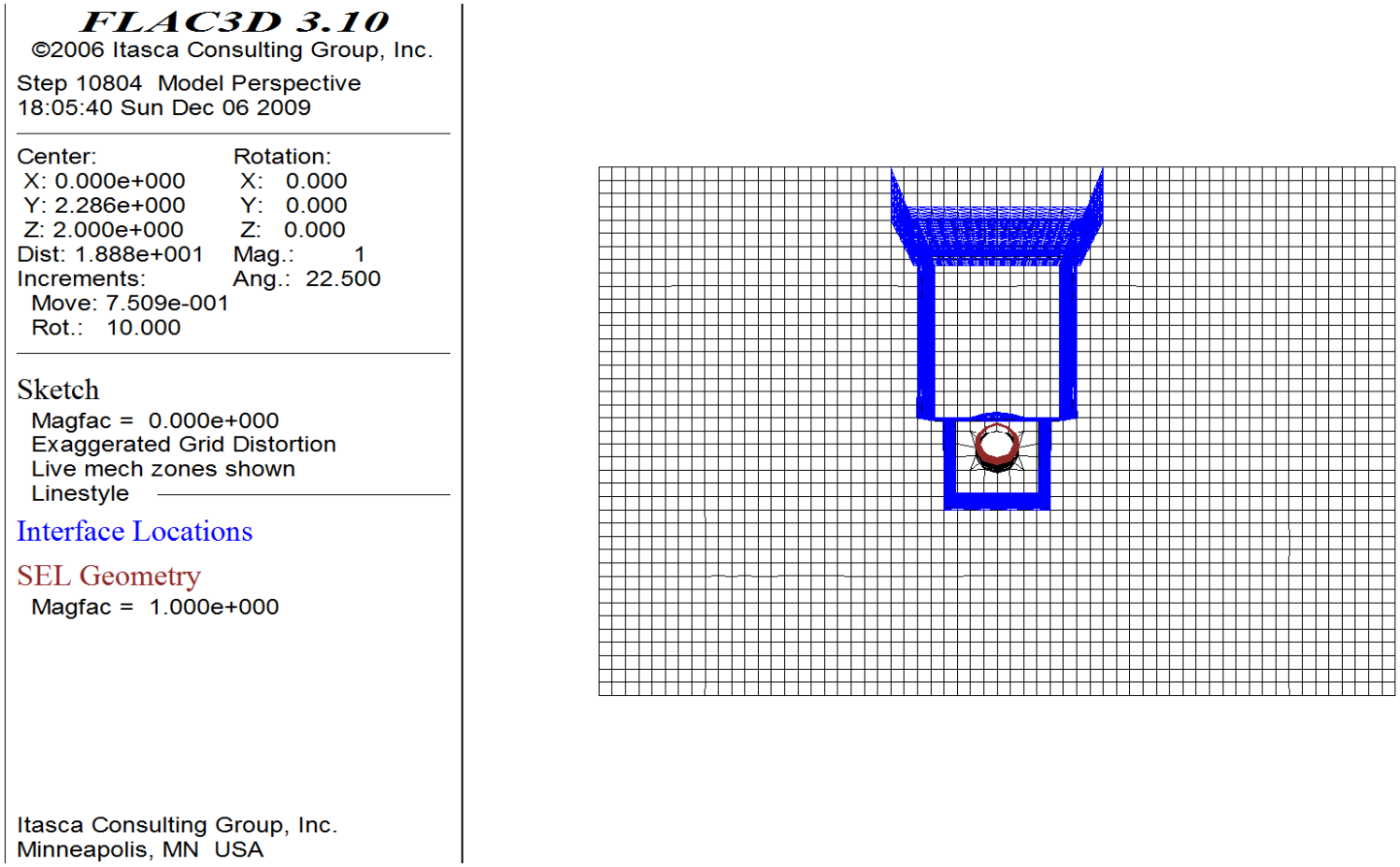

Figure 114. FLAC3D Geofoam model interface locations

of the trench backfill. The pipe was uplifted into the cover system with interface elements until numerical instability was reached at 152 mm.

In order to see the performance of the EPS Geofoam FLAC3D model with interfaces, the interfaces themselves were checked first. The normal stresses on the interfaces should reflect a reasonable stress condition. The contact between materials sliding past one another should also match the deformed geometry. The normal stresses on the interfaces at the end of uplift are plotted in Figure 115, while the contact between materials at the end of uplift is plotted in Figure 116.

The normal stresses on the interfaces in Figure 115 reflect a bulging of the Geofoam block. The shading in Figure 116 shows areas of normal stress between 40 and 140 kPa. The areas of higher normal stress were at the bottom sides of the Geofoam block, where the block was attempting to bulge (as a negative Poisson's ratio has not been applied for numerical stability). The bulging of the Geofoam block had increased the normal stress on the interface, and also increased the resisting shear force in uplift along that interface.

The shear resistance of the interfaces was fully mobilized by the end of uplift. At an uplift of 152 mm, the interfaces should be mobilized, and the contact should be lost between some elements near the top of the model. Figure 116 shows red and brown symbols for interface elements that had, or were in the process of, slipping past the material opposite them. Every interface element had been mobilized in the model at the end of uplift, and many elements towards the top of the model (road base and load distribution slab interfaces) had even lost complete contact with the adjacent materials. The final deformed geometry is shown in Figure 117. This deformed geometry closely matches the field uplift test geometry at the end of uplift.

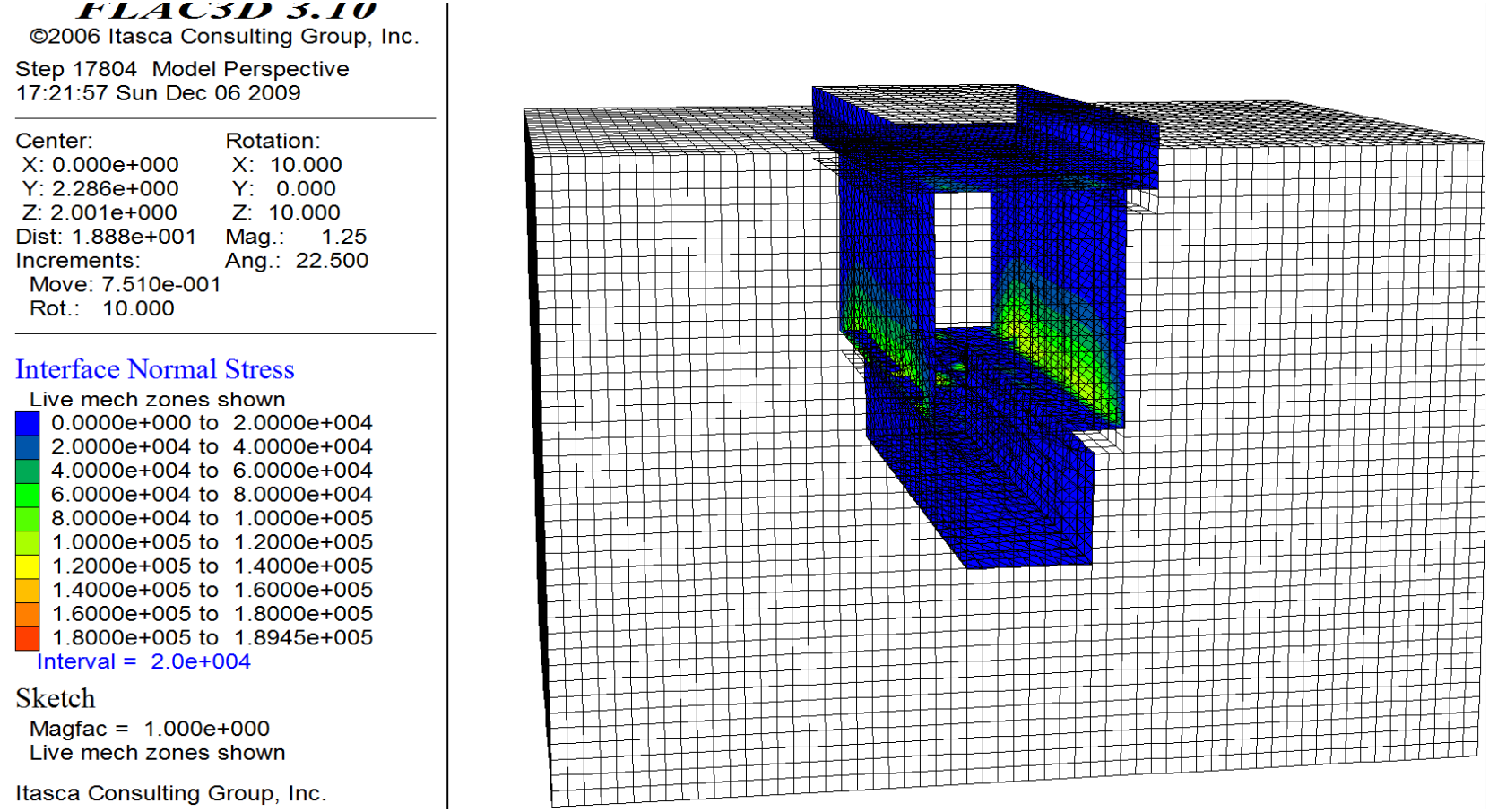

Figure 115. FLAC3D Geofoam model with interfaces, interface normal stress

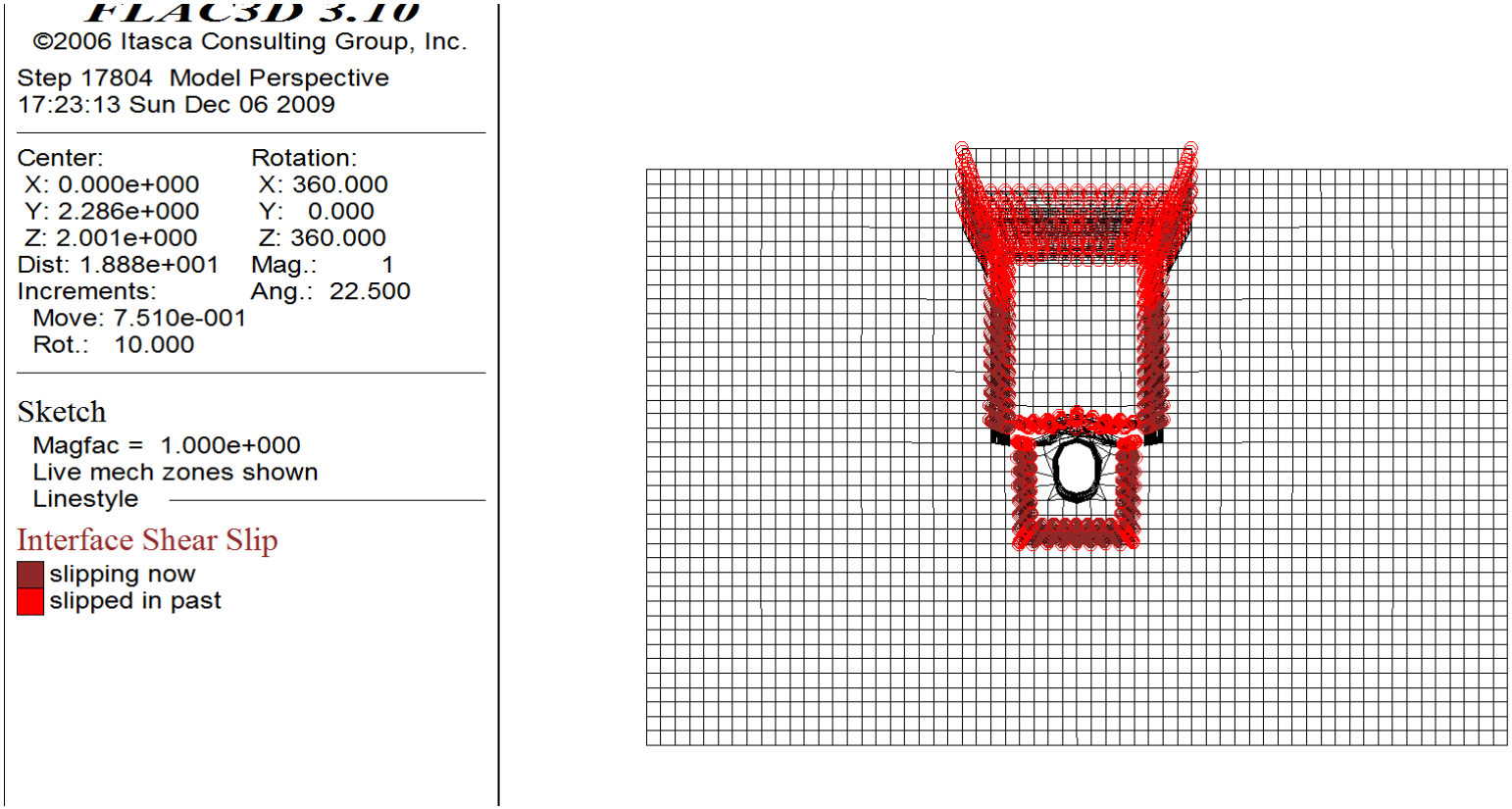

Figure 116. Interface contact at end of uplift for EPS Geofoam model with interfaces

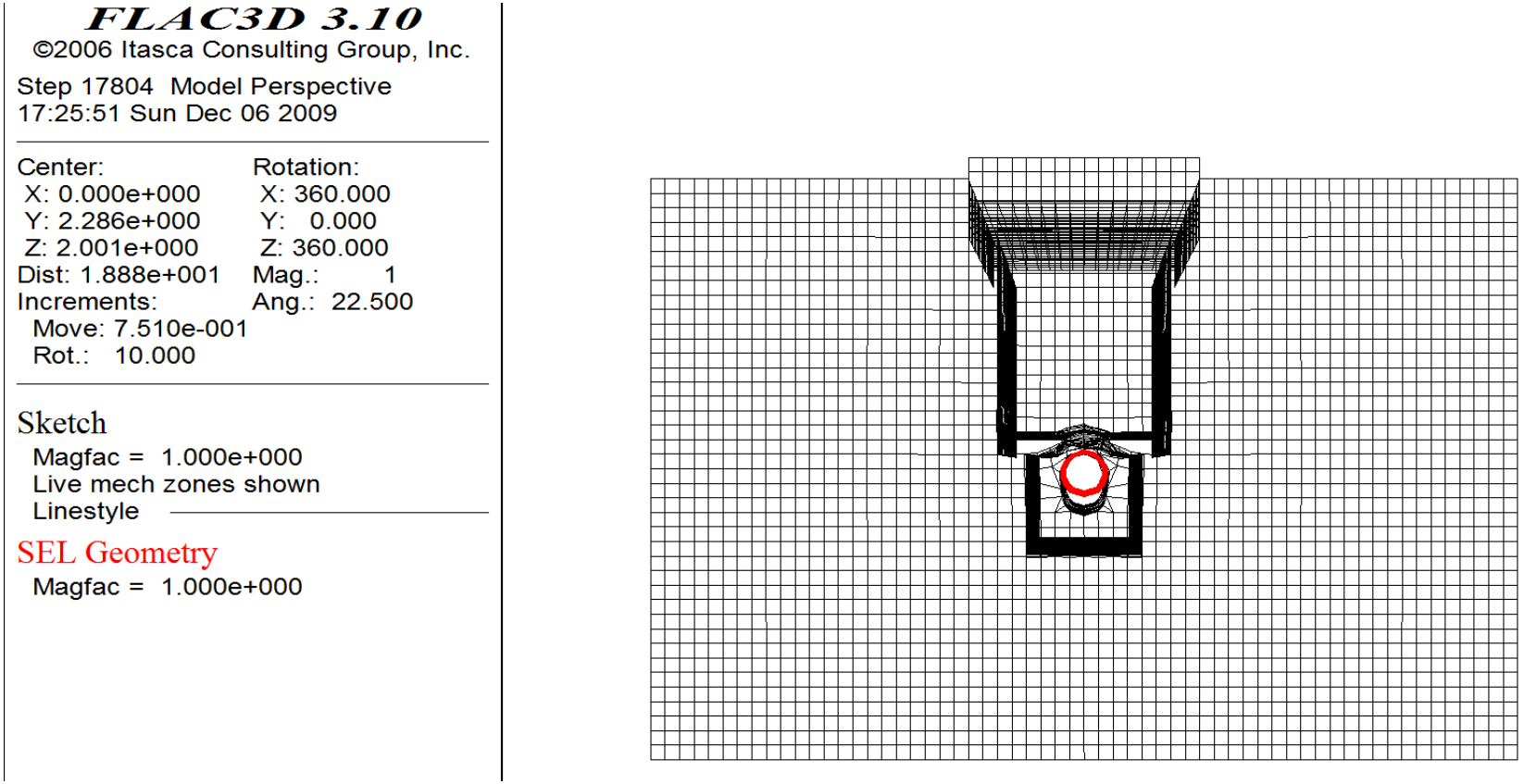

Figure 117. Final uplifted grid for Geofoam model with interface

Vertical stress contours at the end of uplift for the model and the vertical stresses on the pipe itself for the FLAC3D Geofoam model without interfaces are in Figures 118 and 119, respectively. The vertical stress contours in the grid (Figure 118) at the end of uplift show that the highest vertical stresses were in the Geofoam block. The vertical stresses on the pipe (Figure 119) show that the highest stresses on the pipe were at 45 degrees from vertical on the pipe.

The highest vertical stress in Figure 119 on the pipe was 485 kPa, while the highest vertical stress in Figure 118 for the grid was 113 kPa. The vertical stress at 300 mm above the pipe in the FLAC3D Geofoam model was 80 kPa. The field uplift test of the Geofoam section had a peak vertical stress of 80 kPa located 300 mm above the pipe.

The total resistance on the pipe during uplift is a function of normal and shear resistance. The shear resistance is plotted in Figures 120. The uniform distribution along the pipe, even at the two locations of the pick-up points, supports the assumption that the pipe remained rigid during the field test.

Conclusions

Numerical models using FLAC2D and FLAC3D were conducted to show that the uplift tests results can be reasonably modeled and estimated. The primary advantage of FLAC for modeling the uplift tests is its large-strain capabilities. The FLAC models were able to estimate reasonably the field test results for the EPS Geofoam section. The FLAC models were also able to estimate the field test results for the soil backfill section, though with less accuracy than the EPS Geofoam section. The modeling procedure of this chapter, together with the modeling and analyses of previous chapters shows that FLAC

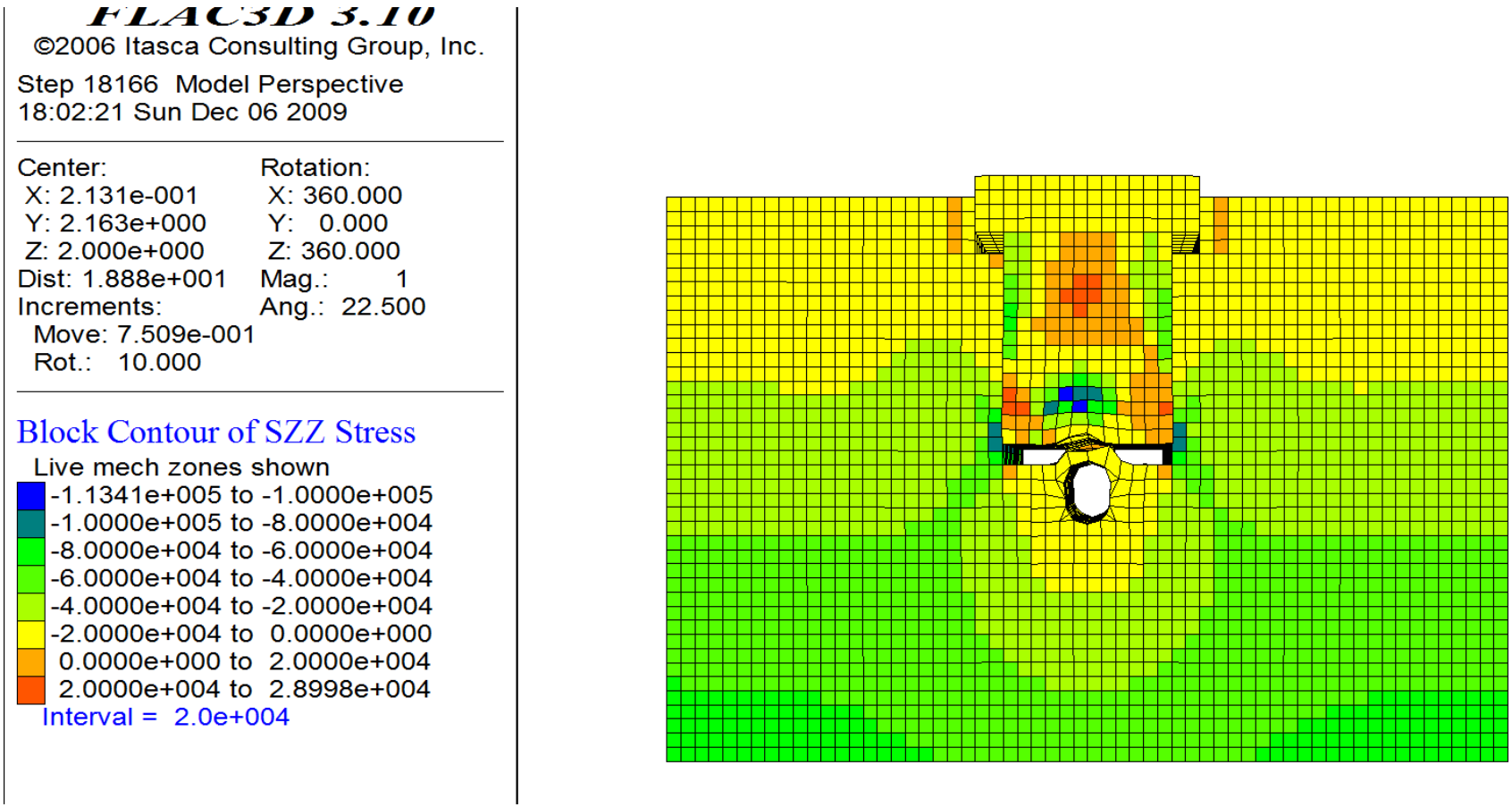

Figure 118. Vertical stress contours for Geofoam model with interfaces

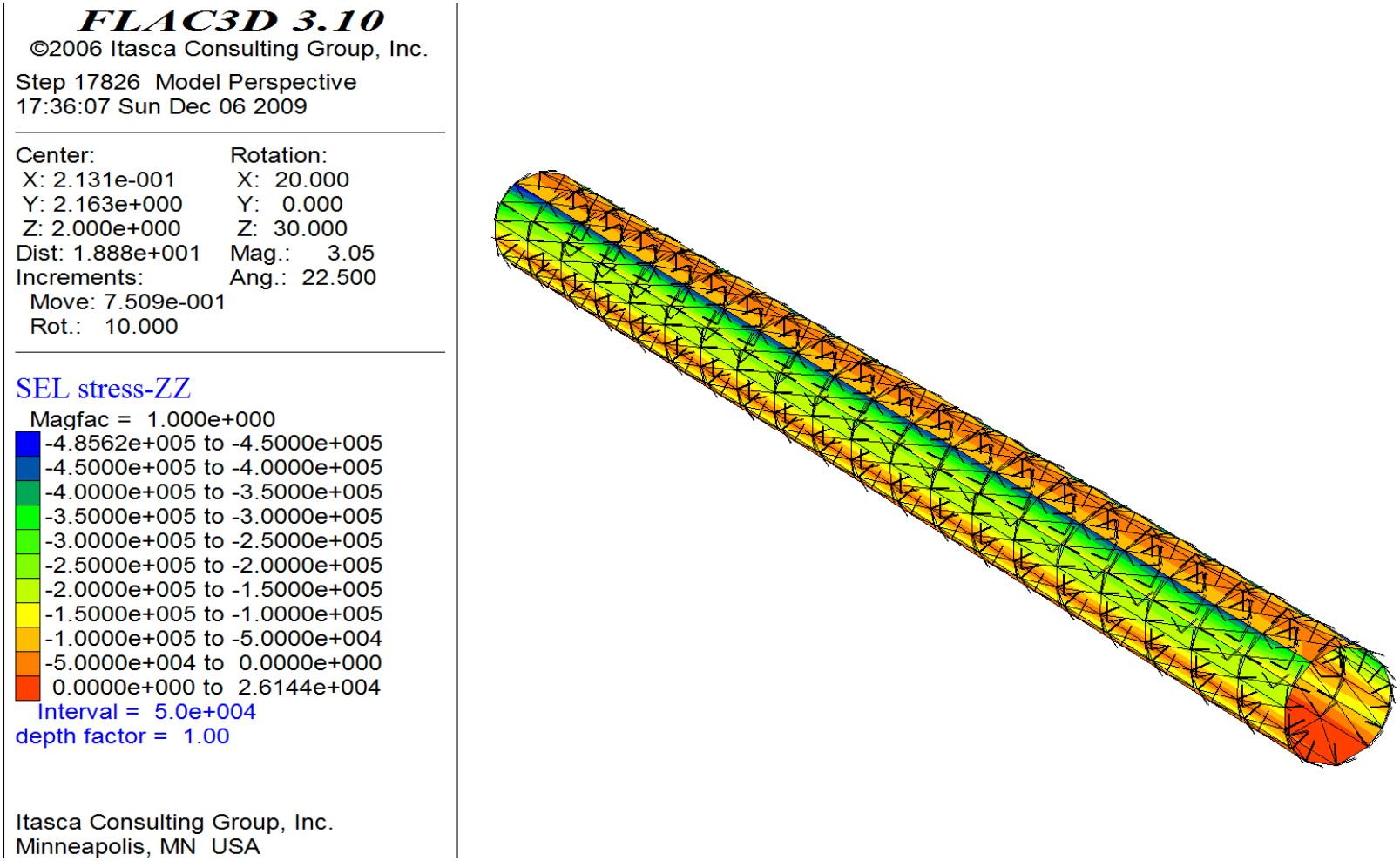

Figure 119. Vertical stress on pipe at end of uplift for Geofoam model with interfaces

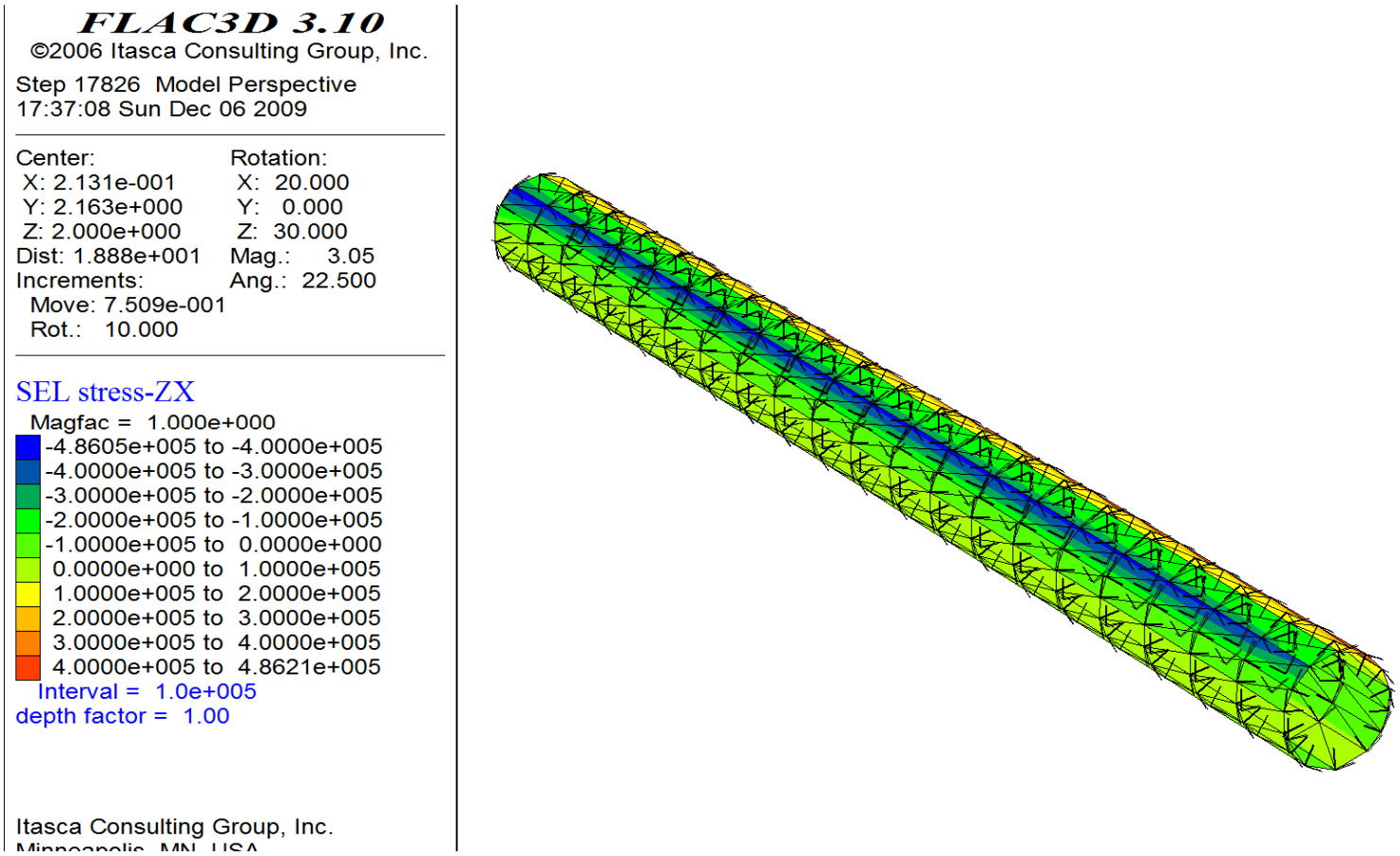

Figure 120. Shear stress on pipe in Geofoam model with interfaces

can be used to develop uplift force-displacement relationships for pipeline design at fault or permanent ground offsets. This means that engineers have a tool that can be used to develop springs constants for sand and clay using the modeling techniques presented herein. The FLAC modeling in conjunction with the experimental data show that EPS Geofoam cover systems can be used to reduce significantly the soil-pipe interaction forces for large vertical displacements of the pipe system.

CHAPTER 11

ASPHALT PAVEMENT EFFECTS ON UPLIFT

For the uplift of steel gas transmission pipelines due to fault offset, one important consideration is the behavior and rupture strength of the overlying asphalt pavement that commonly cover buried pipelines in urban settings. Asphalt Concrete (AC) pavements are commonly used for roadways in the western United States. During uplift, when an AC pavement is present, the pipeline must lift up against the relatively stiff and strong pavement layer at the ground surface. The strength and high stiffness of the pavement layer potentially provides significant resistance to uplift, so its behavior and material properties are important to the design of EPS Geofoam cover systems in urban settings.

Unfortunately, the shear strength and stiffness of an in-place asphalt pavement are difficult to define. The properties of the asphalt pavement material are dependent on a number of things (e.g., aggregate type, aggregate gradation, binder grade, binder content, temperature, age, rate of rupture, pavement thickness, pre-existing cracks in the pavement, etc.). Aged asphalt pavements with a great deal of cracking generally have less strength against uplift than newly placed pavements.

Most of the research done on the strength and deformation properties of asphalt concrete pavements has been directed at traffic loading, which is in the small strain regime. Traffic loads produce much smaller stresses and deformations than a large diameter pipeline undergoing uplift from fault offset through a pavement section.

Pavement engineers typically investigate asphalt and asphalt pavements for the range of stresses and deformations from a standard 80 kN truck load. These engineers have little interest in the extreme limit strength of asphalt.

For this report, a two-stage investigation was done to try to quantify the expected strength and stiffness of asphalt pavements undergoing uplift to a failure state. The first stage of the investigation was a survey of available information from the pavement engineering literature. The second state of the investigation was a set of beam tests on typical hot-mix asphalt as used in Utah. No discussion is given herein regarding the properties of cracked pavements or highly aged pavements. Instead, the study focuses on the properties of a new pavement, where environmental factors have not deteriorated the pavement. Such an approach is conservative in the engineering sense, because the evaluation of material properties appropriate for a new pavement will lead to the most extreme loading condition. However, for design, it is recommend that further site-specific and pavement specific studies/test be conducted if the pavement properties vary significantly from those used herein. A series of FLAC analyses were conducted from the baseline case in the previous chapter with the addition of a HMA pavement section at the ground surface. The results of these FLAC analyses demonstrate the effects of a pavement section on pipeline uplift.

Applicable Asphalt Strength and Rupture Studies

Goetz and Chen (1950) were perhaps the first to publish experimental data on the strength of hot mix asphalt (HMA). They conducted a series of triaxial compression tests on a range of mixes and binders, but did so with more bitumen and voids than commonly

are used today. Goetz and Chen reported friction angles between 21° and 57° and a ratio of tensile strength to compressive strength (R_o) ranging from 0.1 to 0.5, with a mean of 0.25. Thus, this study suggests that the tensile strength of HMA is roughly one quarter that of its compressive strength.

Hills and Heukelom (1969) continued the early work by Goetz and Chen. They conducted additional triaxial compression tests and found that for less rich mixes, R_o ranges from 0.15 to 0.30, with a mean of about 0.225. This additional study supports the generalization that the tensile strength of HMA is roughly 25% of its compressive strength. Hills and Heukelom (1969) further found that the ratio of the modulus in tension to that in compression for HMA ranges from 0.2 to 0.9, suggesting that the modulus of HMA in tension can be as little as 20% of the compressional value. They also found that for a given HMA mix, the ratio of modulus decreases with increasing temperature. They also found that the stiffness of the binder has a great effect on the strength and stiffness of the HMA. In addition, R_o increases with increasing binder stiffness and that the ratio of tensile to compressive stiffness dramatically increases with increasing binder stiffness. This indicates that as the stiffness of the binder increases, correspondingly, the tensile stiffness increases. Lastly, Hills and Heukelom (1969) relate the friction angle of HMA to compressive strength with Equation 24. In Equation 24, ϕ is the friction angle of the HMA.

$$\sin\phi = \frac{1 - R_0}{1 + R_0} \tag{24}$$

Li et al. (2008) found that the temperature history affects the tensile strength of HMA. They made two sets of HMA samples, identical in every way. The first set was aged for several days at room temperature (25 °C). The second set was conditioned in a 60 °C water bath for 24 hours after having spent two days in a -18° chamber. Li et al. (2008) found that the tensile strength of the HMA averaged 115kPa for the normal samples and 97kPa for the conditioned samples. This was a decrease in strength of 15%. This research indicates that thermal cycles affect the strength of HMA, though not significantly over a short period of time. The authors suggest that the affect of thermal cycling and aging would become more pronounced with more elapsed time.

El-Aziz Zahw (1999) conducted a study on the tensile strength of HMA and the influence of test temperature. He found that, depending on mix and binder, the strength of HMA at room temperature ranged from 1.6 to 3 MPa. These strength results were higher at room temperature than other researchers had reported by approximately an order of magnitude. El-Aziz Zahw (1999) found that the strength of the different mixes of HMA decreased to a range of 1 to 2 MPa at 45°C. This indicates that the strength of HMA can decreases from 230 psi to 145 psi on a hot day, a reduction of 37%. The strengths of the different mixes further decreased to a range of 0.6 to 0.9 MPa at 60°C. This is a decrease of 62% to 70% from the room temperature strength. El-Aziz Zahw (1999) also found that increasing the asphaltene content of the binder and decreasing the resin content of the binder increased the strength of HMA.

El-Naby et al. (2002) investigated the affects of different aggregate type and binder content on the strength of HMA. A series of compression and indirect tensile tests were done on 4 different mixes with three binder contents and three aggregate types. Tests

were done at standard temperature and pressure and at an unknown rate (not specified by authors). El-Naby et al. (2002) concluded that the denser the HMA, the higher the compressive and tensile strength of the HMA. (This is a logical conclusion since fewer voids in the compacted material means more aggregate and binder interacting.) The interaction of binder and aggregate, along with binder strength, leads to the strength of the mix. Figure 121 shows the results of El-Naby et al. (2002) research on the effects of compacted specimen unit weight and strength of HMA. This figure shows that the compressive and tensile strengths of HMA increase slightly with increasing compaction. El-Naby et al. (2002) also found that by increasing the asphalt binder content of the mix from 3% to 7%, the strength increased by 20% to 30% depending on aggregate type and gradation. Figure 122 shows the results of their research into binder content and strength of HMA at room temperature. Figure 122 also shows the trend in the data towards increasing strength with increasing binder content. These authors also found that aggregate type made a profound effect on the strength of HMA. El-Naby et al. (2002) concluded that aggregates with rougher surfaces make stronger HMA, which was also an obvious conclusion because of the higher friction angle and interface friction associated with rougher aggregate surfaces.

Wang et al. (2008) investigated the effects of gradation on HMA strength. They conducted a series of direct shear tests and indirect tensile tests to discover the effects of 4 different gradations on HMA strength. This evaluation used 5 gradations, including a Superpave gradation from the United States. The major differences in the gradations were their maximum particle size and fines content. In addition, one series of tests wasalso done on a single gradation but varying the binder content from 3.5% to 5.5%.

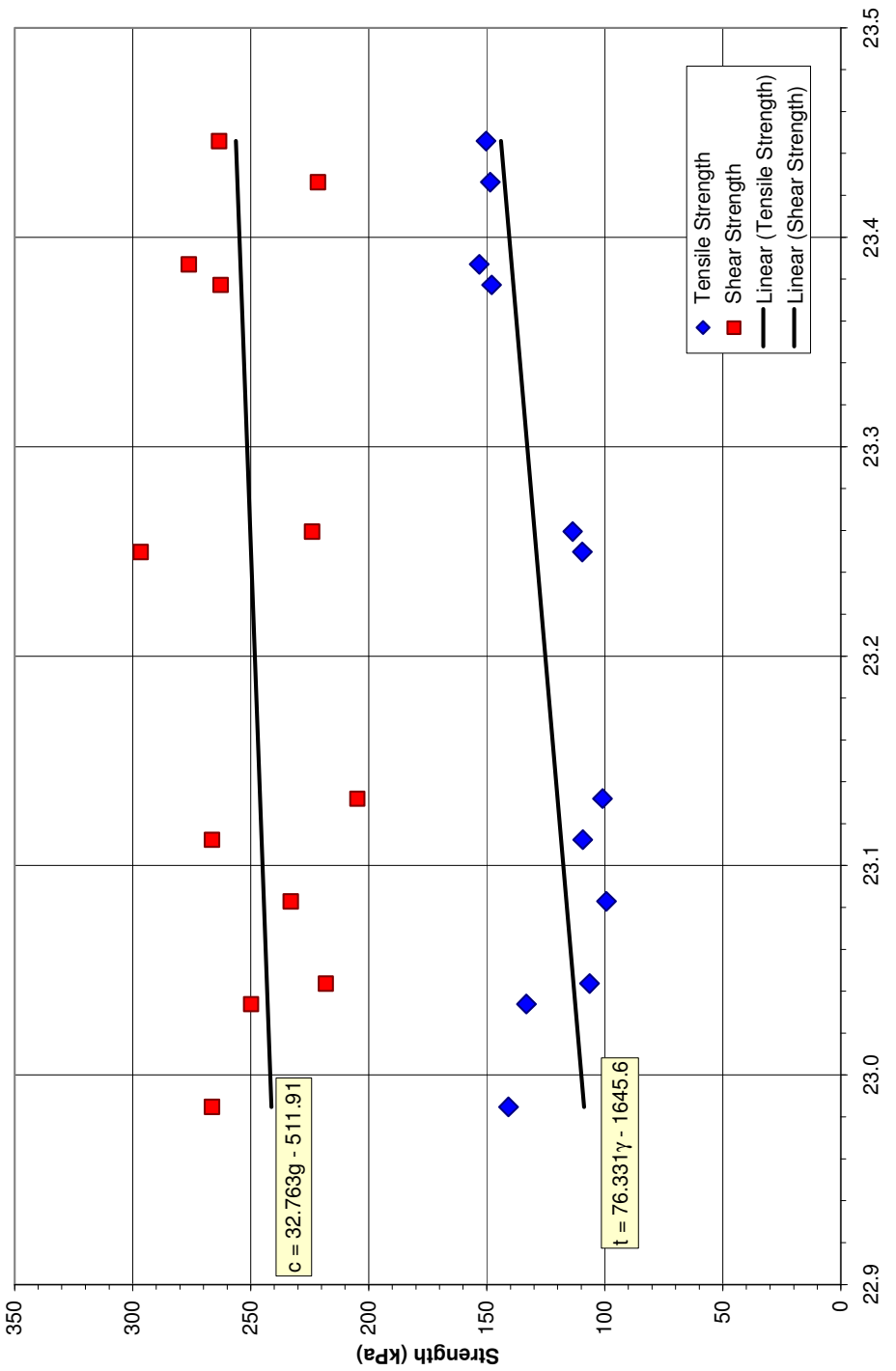

Figure 121. Compressive strength as a function of compacted unit weight (after El-Naby, 2002)

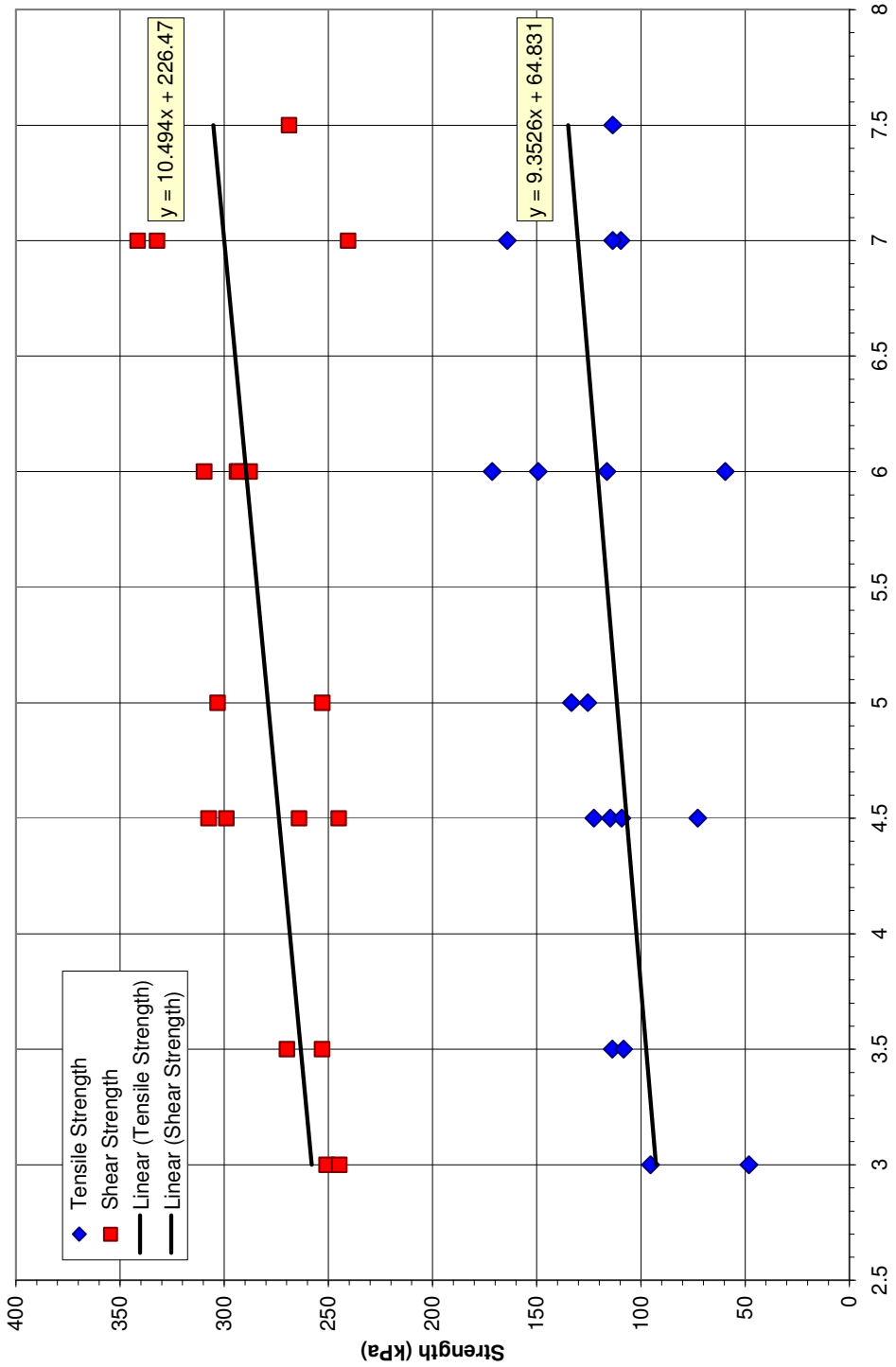

Figure 122. Compressive strength as a function of asphalt content (after El-Naby, 2002)

The series of tests where Wang et al. (2008) varied the asphalt binder content showed that the friction angle of the material decreased with increasing binder content. This stands in contrast to the findings of El-Naby (2002), who found increasing strength with increasing binder content. The results of the Wang et al. (2008) study indicate that although the tensile strength and unconfined compressive strengths of HMA may increase with increasing binder content, the friction angle and cohesive strength in simple shear decrease with increasing binder content. This finding suggests that aggregate roughness is a large portion of the shearing resistance of HMA rather than asphalt binder in direct shear.

Regarding the effects of gradation, Wang et al. (2008) found that gradations with a larger amount of larger aggregate had higher compressive strength. Likewise, they found that decreasing the fines content of HMA increased the friction angle. Wang et al. (2008) found that the average shear strength of HMA regardless of gradation at 60°C (150°F) is 393 kPa, the average compressive strength is 381 kPa, the average tensile strength of HMA is 67 kPa and the average friction angle is 46.6°. These values are applicable to a hot summer's day. For lower temperatures (i.e., 12°C) Wang et al. (2008) determined that the average shear strength of HMA regardless of gradation is 5 MPa, the average compressive strength is 780 kPa, the average tensile strength of HMA is 96.5 kPa and the average friction angle is 48°. These values are applicable to a cool day.

More recently, Pellinen and Xiao (2005) developed a set of Mohr-Coloumb failure criteria for HMA based on several factors including loading rate. They used 4 different mixes and 3 different binders in their investigation. They used indirect tensile tests and triaxial compression tests to determine tensile strength, cohesion and friction angle at

temperatures around 45 °C. They found that loading rate was the most critical variable in their testing when keeping temperature constant. This was confirmed by several sources that remind engineers that for asphalt and HMA, time and temperature can be superimposed. This means that for HMA, loading rate and temperature give analogous results. Slower rates correspond to warmer temperatures and visa versa. A fast rate on a cold sample will give the highest strength and stiffness, while a slow rate on a hot specimen yields the smallest strength and stiffness. For a loading rate of 50 mm/min, Pellinen and Xiao (2005) found that the average tensile strength for the 12 mixes and binders was 81 kPa (12 psi), the cohesion intercept for failure 200 kPa and a friction angle of 40.4°. At slower rate of 7.5mm/min, Pellinen and Xiao (2005) found that the average cohesion intercept for failure 126 kPa, and a friction angle of 43.3°. This means that at a slower rate, the cohesion intercept decreases and the friction angle of HMA increases.

In summary, the literature survey found that the tensile strength of HMA at room temperature ranges from 62 to 96 kPa, increases at low temperatures and decreases at high temperatures. The cohesion intercept of HMA at room temperature ranges from 124 to 207 kPa, increases at low temperatures and decreases at high temperatures. Finally, the friction angle of HMA at room temperature ranges between 42° and 48° and the friction angle decreases at low temperatures and increases at higher temperatures. The literature also indicates that the modulus of HMA increases dramatically for colder temperatures and more rapid loading. Denser HMA, larger aggregate, rough aggregate and less resin content in the asphalt binder increase the strength and friction angle of HMA. Increasing

amounts of asphalt binder increase the compressive and tensile strengths of HMA and decrease the shear strength.

Asphalt Rupture Tests

A series of small 3-point load beam tests were conducted on HMA to determine the tensile strength and stiffness of a typical HMA local to the Salt Lake City, Utah area. The HMA was taken from an asphalt placement in Salt Lake City out of the hopper of the asphalt spreader on a project site. The sampling temperature of the asphalt was 130 °C. The material was transported to the lab, reheated and a series of index tests on the sample were performed. The HMA sample was then reheated and compacted into three slabs. The slabs were compacted as slabs by a SLAB-TRAK kneading compactor at the University of Utah. The three slabs were cut with a diamond saw into nine small beams for three-point load testing after cooling for 48 hours.

The asphalt binder content of the sample was 6.7%. The Marshall value was 2.355, theoretical specific gravity was 2.433 and the Marshal unit weight of the HMA was 146.5pcf. The stability of the Marshall pucks was 17 kN. There were 3.2% voids in the compacted sample of which 82.1% were filled, with a VMA of 13.8%. Figure 123 shows the gradation of the aggregate in the sample. The aggregate was angular crushed rock. Compaction Temperature of the slabs was 130°C. The actual compacted unit weight of the slabs was 22.26 kN/m^3. Each beam was 320 mm long, 41.4 mm deep and 88.7 mm wide.

After cutting, the slabs were aged for three days at room temperature. Three of the beams were then aged for four days at room temperature. Three were aged for four days

in a 125 °F oven. The last three beams were aged for four days at -10 °F. The individual beams were left in their temperature environment until a few seconds before testing. Great care was used to test within one minute of removing a beam from the oven or freezer to ensure that the temperature of the beam would change as little as possible before testing.

The three-point beam load test is based on simple static principles. The beam is supported at each end by a roller which allows rotation of the ends, but no vertical movement. At the center point of the beam, the load is applied with another roller. The beam is thus loaded at the center with reaction on the ends. The loading device is applied rapidly (635 mm/min) so as to simulate the rate at which fault-induced pipeline uplift occurs. The force and displacement of the loading device is monitored and recorded continuously by the loading device. The loading device used was a GEOCOMP brand LOADTRACK load frame. The data acquisition of force and displacement are contained in the LOADTRACK. The support rollers sit on a small frame that sits on the load platen of the LOADTRACK. Figures 124 and 125 show the load frame and support rollers, along with the specimen.

The test is started as the loading roller is positioned on top of the beam with minimal contact force. The platen then lifts up, pushing the beam against the load roller. The force is recorded by the load cell attached to the load roller. The platen lifts until the beam has completely cracked. The platen is lowered, data removed retrieved and the specimen is removed. Figure 126 shows the asphalt beam after testing is complete.

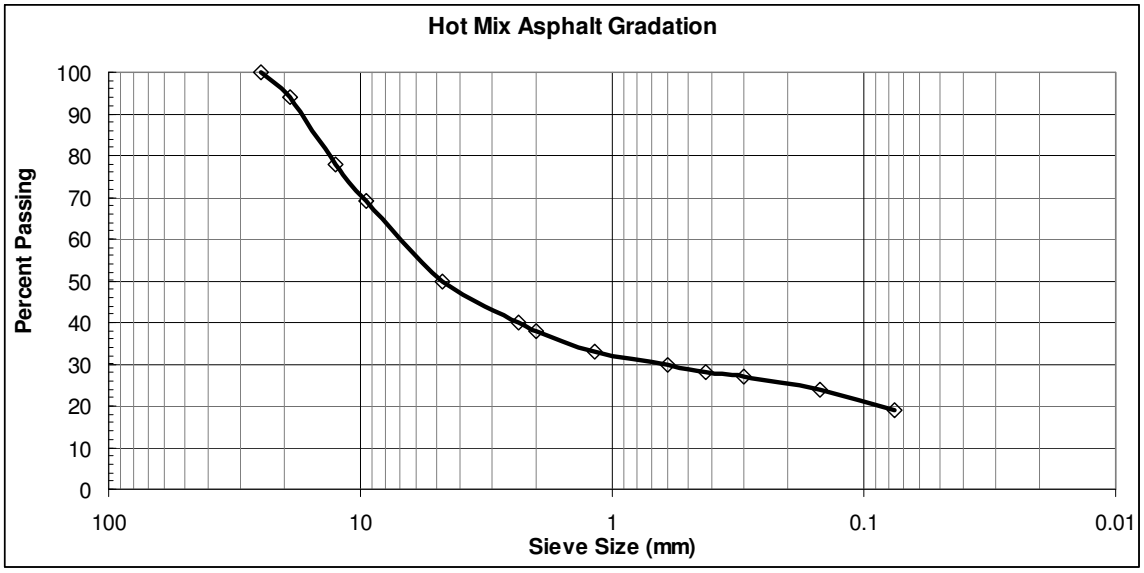

Figure 123. Gradation of HMA used in beam tests

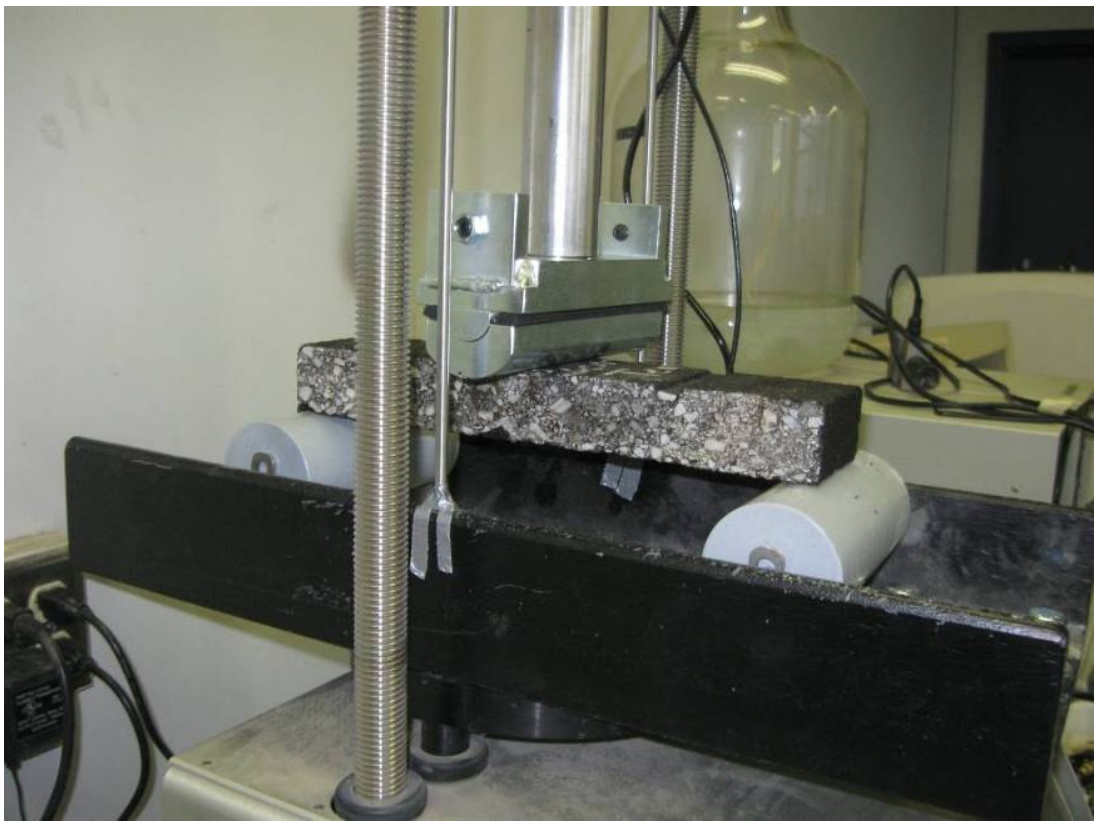

Figure 124. Asphalt beam on rollers

Figure 125. LOADTRACK and asphalt beam

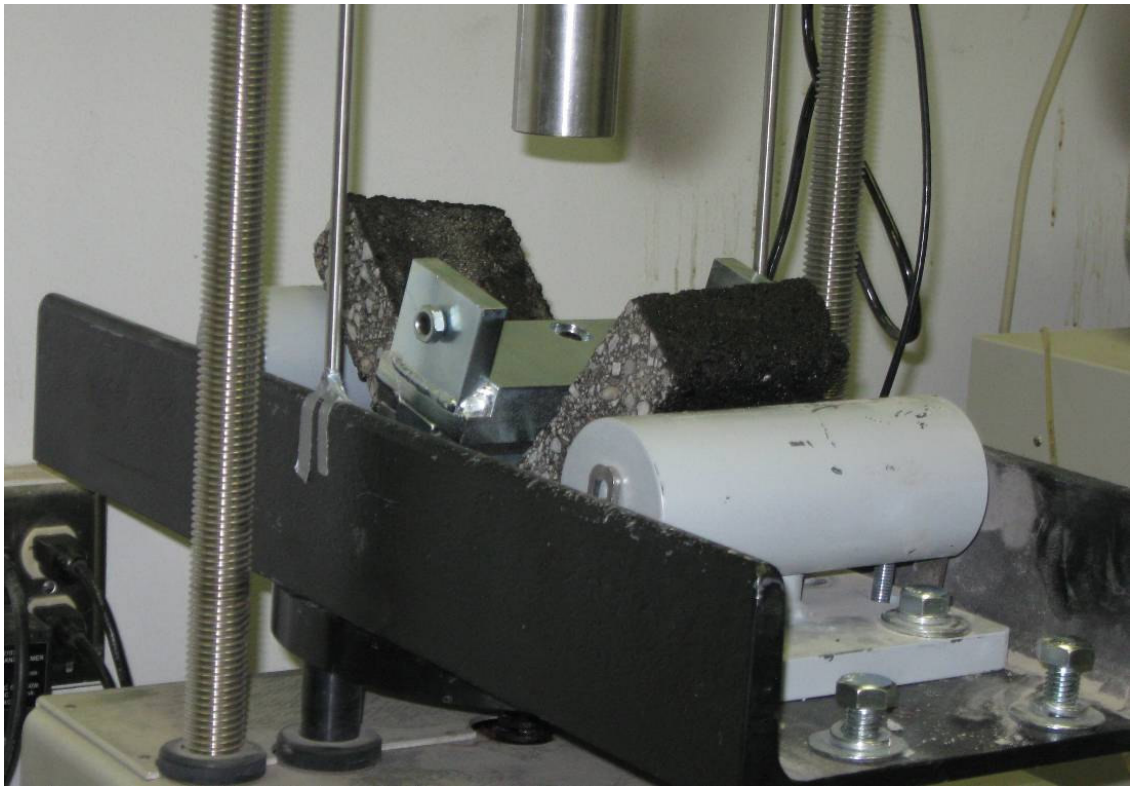

Figure 126. Cracked asphalt beam after 3-Point beam test

The tensile strength of the beam is calculated using statics principles. The calculation begins with the maximum moment. The maximum moment for a beam is calculated by Equation 25.

$$M_{\max} = \frac{F_{\max} L}{4} + \frac{WL}{8} \tag{25}$$

In Equation 25, L is the length of the beam and W is the weight of the beam. The maximum moment is assumed to be at the center of the beam. The tensile strength of the beam is calculated as the maximum tensile stress in the beam. This is also calculated using statics in Equation 26.

$$\sigma_t = \frac{M_{\max} c}{I} \tag{26}$$

In Equation 26, c is the depth to the neutral axis of the beam and I is the moment of inertia of the beam. From the above equations, the results of the 9 beam tests are summarized in Table 34. Table 34 shows that the tensile strength of the coldest specimens was about 35 kPa greater than that for room temperature specimens. The tensile strength of the room temperature specimens tended to be about 28 kPa higher than the warmest specimens. Table 34 also shows that the coldest specimens were up to 2 orders of magnitude stiffer than the warmest specimens. Table 35 shows the average results among all the beam tests. In addition to Table 35, the average results were plotted in Figure 127 which shows tensile strength as a function of temperature. Note that the polynomial fit had an excellent correlation in Figure 127. Table 34, 35, and Figure 127 are all based on the singular variable that the rate is fixed at 635 mm/min displacement. If the rate changes from this, the values shown in these figures and tables became less accurate since temperature and time are interrelated for visco-elastic materials such as hot mix asphalt.

For numerical modeling of a pavement overlaying a pipeline, the temperature will be the largest variable for the asphalt properties. The temperature at the time of fault offset is impossible to predict. An average temperature (and therefore strength) will be used for numerical modeling. The temperature chosen was 72°F. In the state of Utah, 72°F is a reasonable summertime temperature at night and in the spring/fall, an afternoon temperature in the sun.

Table 34. Asphalt beam test results

Test	Temp	Displacement Rate	Peak Force	Displacement at Peak	Max Moment	Tensile Strength	Stiffness
------	*°F*	*mm/min*	*kN*	*mm*	*N-m*	*kPa*	*kN/mm*
1A	72	635	0.525	1.54	14.01	77.22	0.341
1B	72	635	0.508	1.50	12.66	69.64	0.339
1C	72	635	0.542	1.08	13.33	73.09	0.502
2A	122	635	0.328	2.00	8.48	46.20	0.164
2B	122	635	0.246	1.79	7.46	41.37	0.137
2C	122	635	0.258	1.56	6.67	36.54	0.165
3A	-10	635	0.829	0.18	19.89	109.63	4.600
3B	-10	635	0.672	0.04	16.27	88.95	16.80
3C	-10	635	0.676	0.03	18.19	199	22.53

Table 35. Beam test tensile strengths

Temperature	Peak Force	Displacement at Peak	Maximum Moment	Tensile Strength	Stiffness
°C (°F)	*kN*	*mm*	*N-m*	*kPa*	*kN/mm*
22 (72)	0.525	1.37	13.33	146	0.383
50 (122)	0.278	1.78	7.54	83	0.156
-12 (-10)	0.731	0.08	18.11	198	9.138

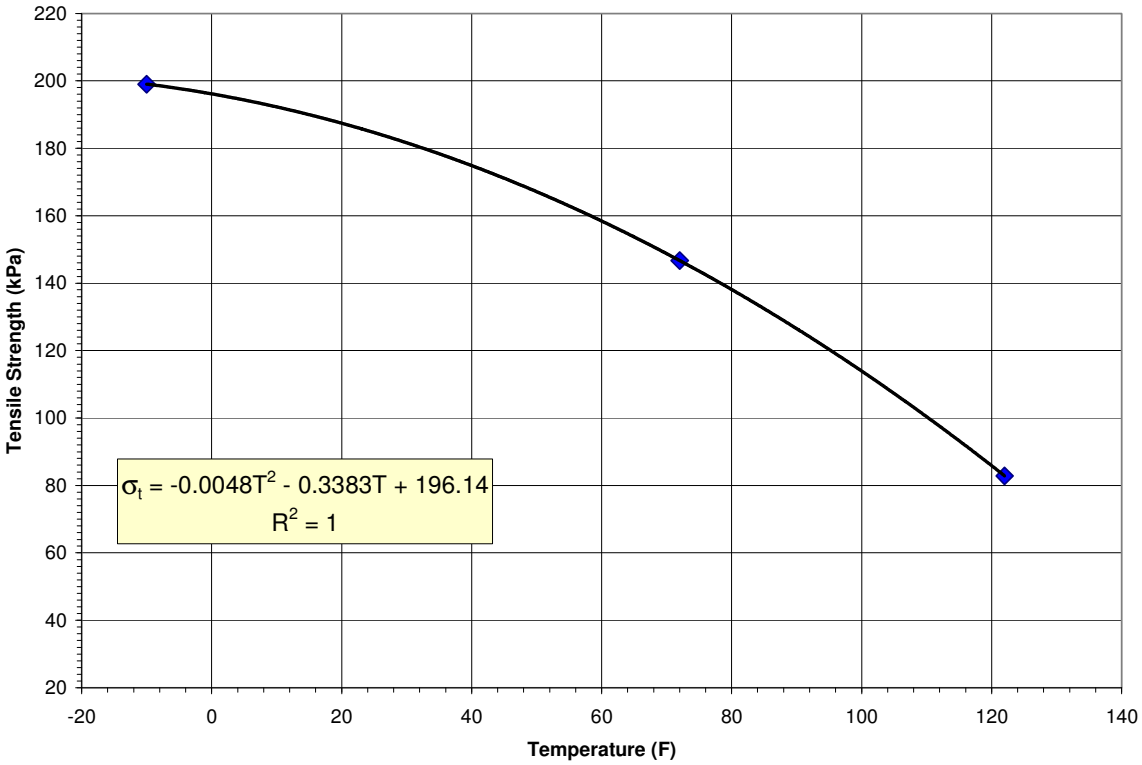

Figure 127. Relationship of tensile strength and temperature

FLAC Analysis with AC Pavement

A series of FLAC models were conducted identical to those in Chapter 10, with the exception that an asphalt concrete pavement was placed across the top of the model. The pavement properties were the same as those found in this chapter. The asphalt concrete in the models was 152 mm thick. The asphalt concrete pavement rested on 300 mm of road base. The intent of these models was to compare the uplift of a pipe (i.e., force displacement relationship) compared to those found in field experimentation and FLAC modeling done in comparison to the field uplift tests. The tensile strength came from the testing in this chapter. The cohesive strength was set to 1 times the tensile strength (as

shown earlier in this chapter). The modulus and friction angle were typical as shown earlier in this chapter for 72°F. Properties are summarized in Table 36.

The model geometry for the soil only FLAC section and EPS Geofoam section were shown previously. They are modified by the addition of the asphalt concrete pavement and are shown in Figures 128 and 129. Figure 128 shows the soil backfill section geometry modified with pavement section and Figure 129 shows the EPS Geofoam section modified with pavement section.

The asphalt concrete pavement was an order of magnitude stiffer than the UTBC in the soil model, and as a stiffer element, resisted more load. The asphalt pavement also had a much higher tensile strength than the soils and was able to stretch much more than the soil elements. The deformed shape behaved as a beam bending and bulging above the uplifting soil or EPS Geofoam mass. Figure 130 shows that for the soil backfill system, this was true, while Figure 131 shows the same for the EPS Geofoam sections. Figures 130 and 131 are the deformed FLAC mesh after the end of uplift.

Table 36. Properties of asphalt concrete for FLAC modeling

Density	Elastic Modulus	Poisson's Ratio	Friction Angle	Cohesive Strength	Tensile Strength
Kg/m3	*kPa*	----------	*deg*	*kPa*	*kPa*
2346.93	940000	0.25	45	146	146

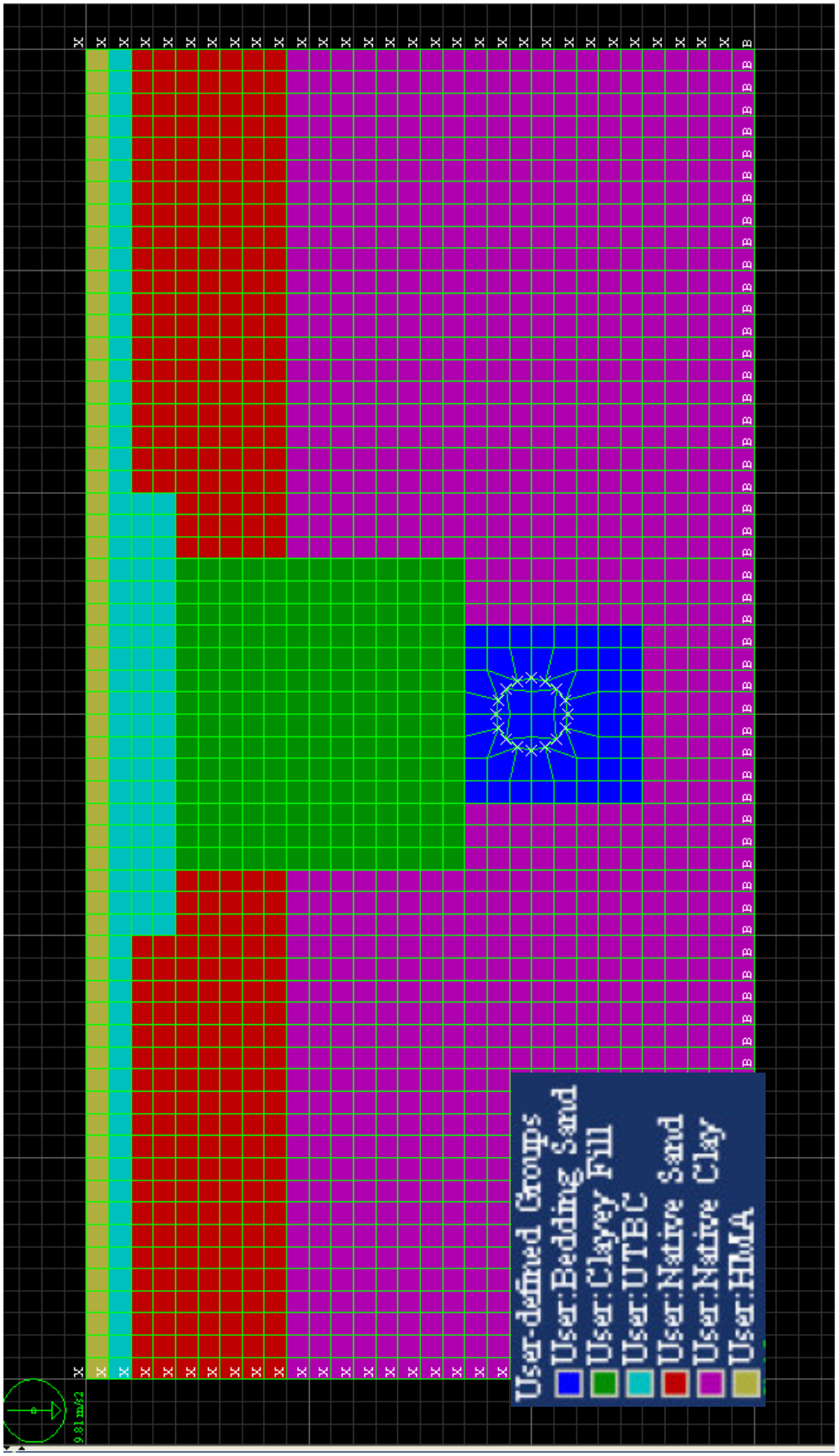

Figure 128. Soil backfill section FLAC model with AC pavement

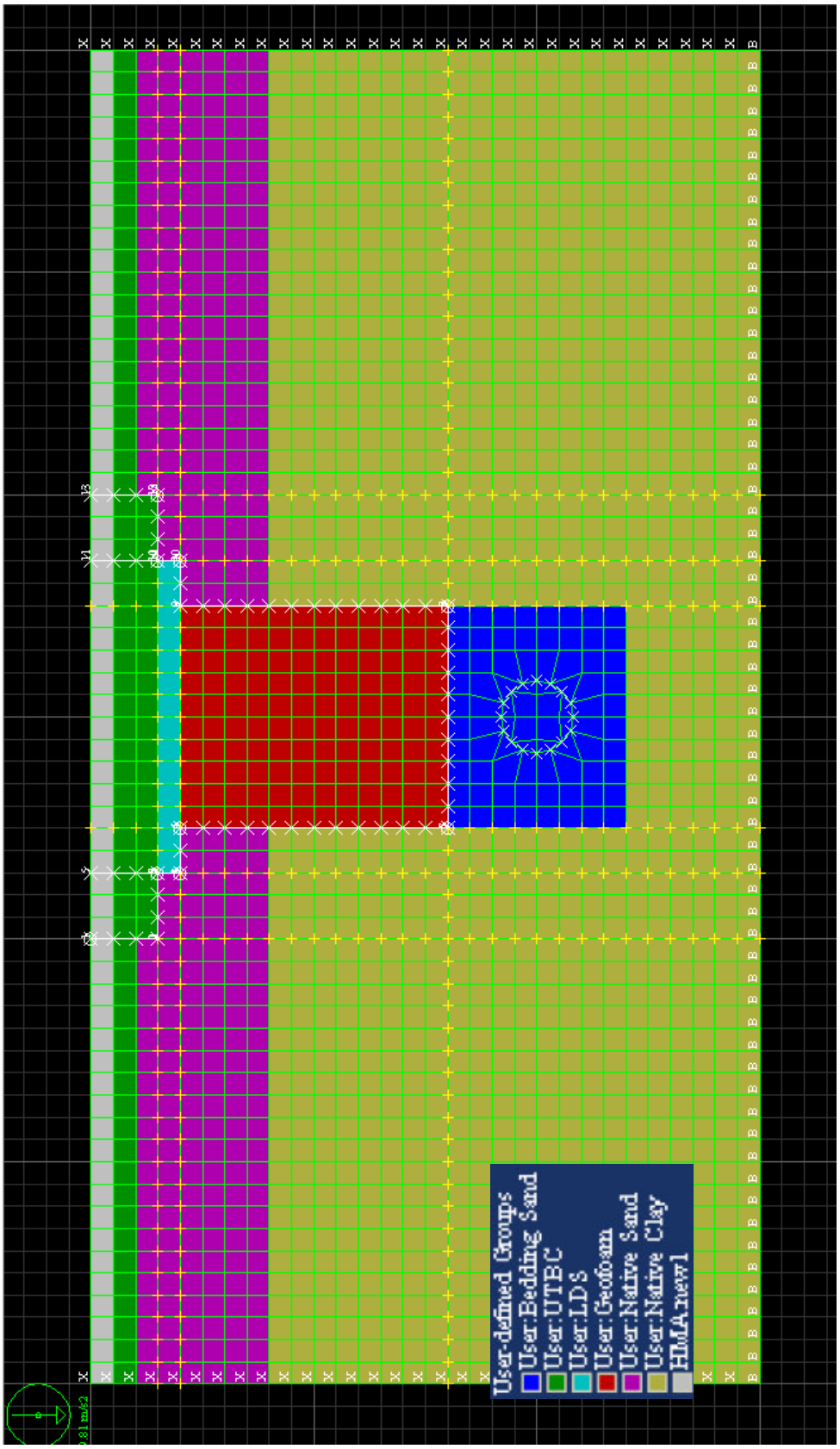

Figure 129. EPS Geofoam section FLAC model with AC pavement

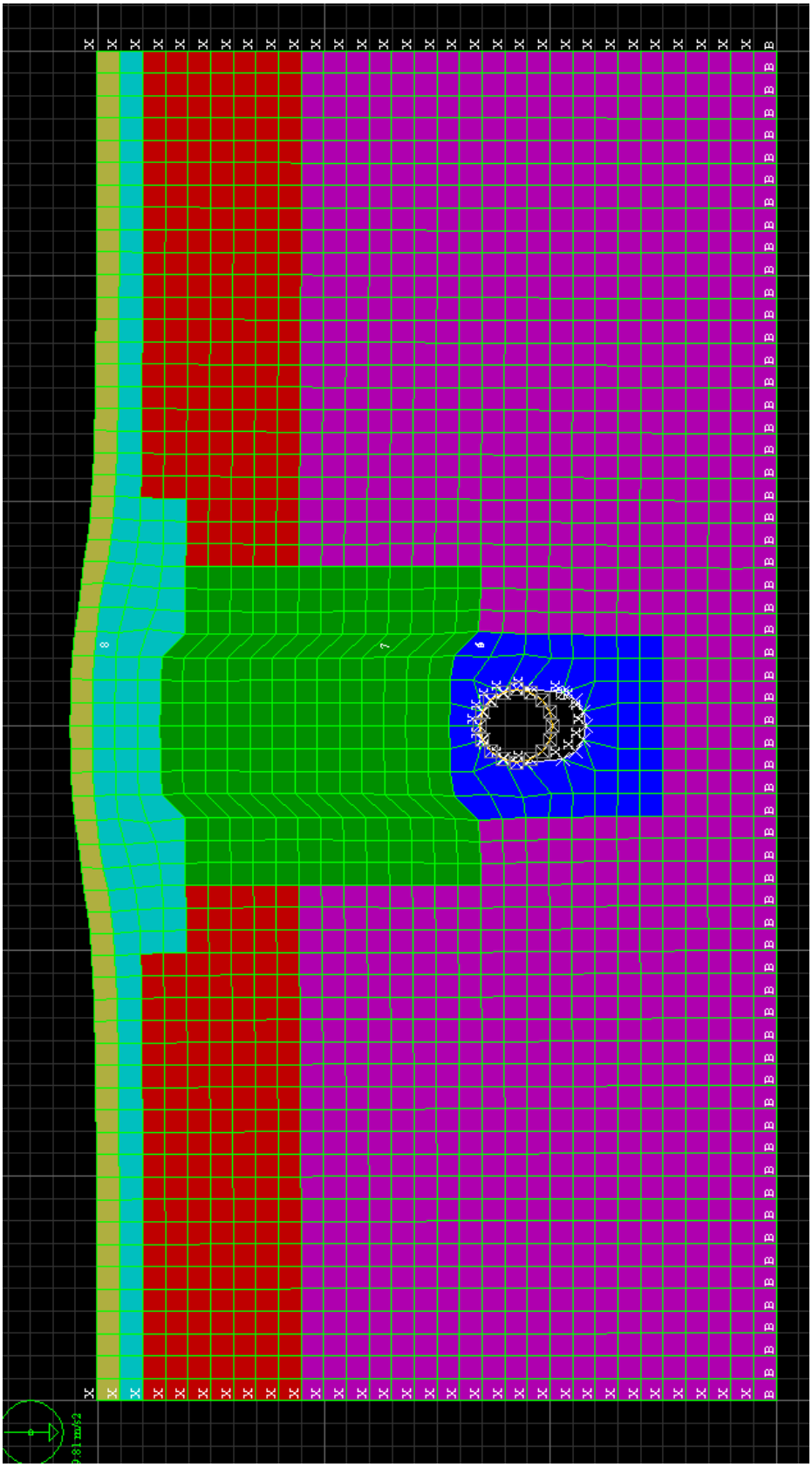

Figure 130. Deformed FLAC mesh with soil backfill and AC pavement

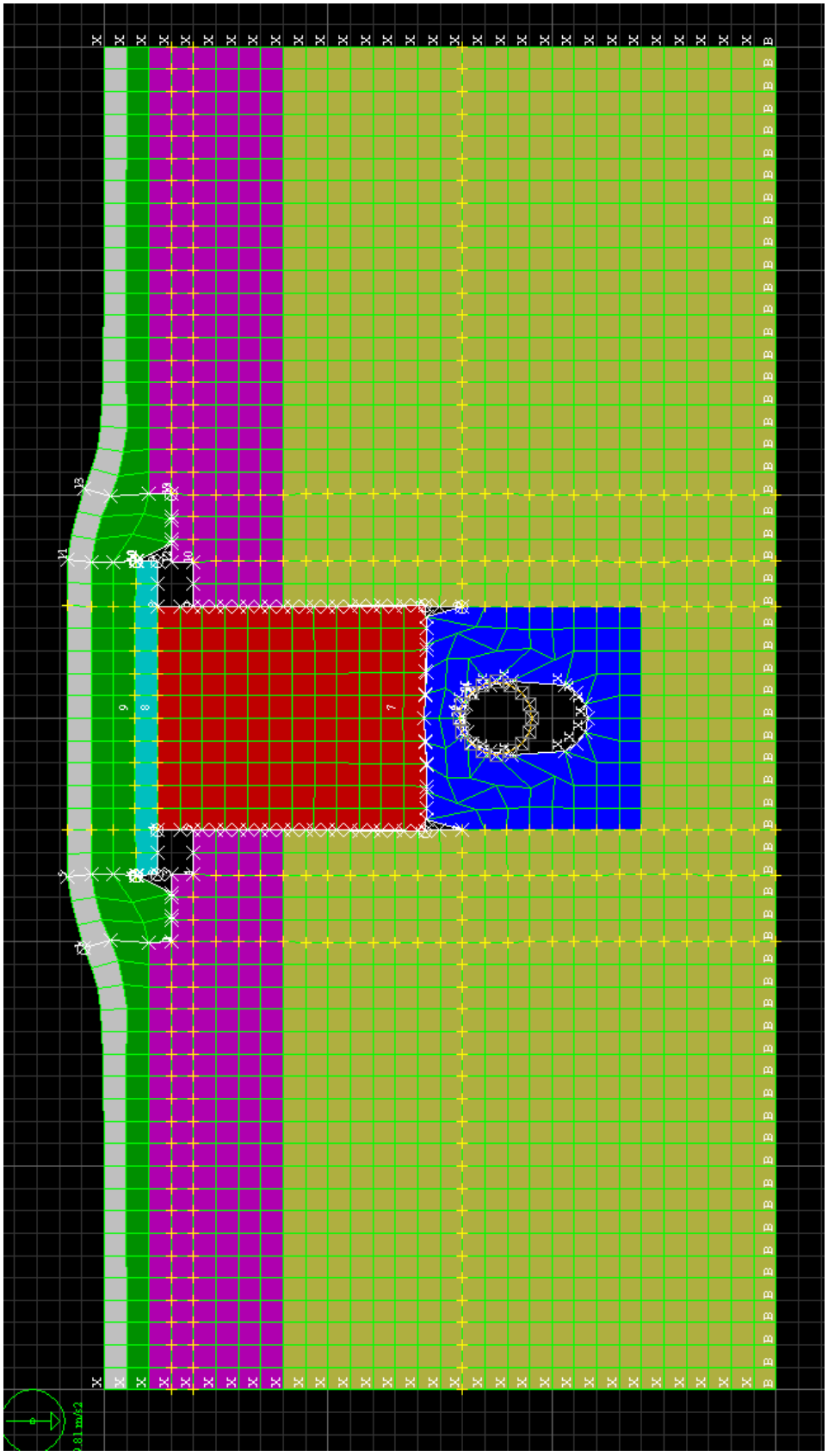

Figure 131. Deformed FLAC model with EPS Geofoam and AC pavement

The pavement section in Figures 130 and 131 appears to be intact, though deformed. In the soil backfill section, there had not been separation of elements because of the tensile strength, but the material had failed completely in shear. In the EPS Geofoam backfill section, conversely, the pavement section had failed in tension and was being held together by its shear strength. This was likely an effect of the stiff and rigid reinforced concrete load distribution slab that sits atop the EPS Geofoam block.

The force-displacement data from the FLAC models with an asphalt concrete pavement section were exported from FLAC and imported into EXCEL to plot with the field test data and the FLAC modeling without a pavement section. The curves from the asphalt concrete analyses are shown plotted together in Figure 132. Figure 132 shows, like the FLAC models without a pavement section, that the soil backfill section had more resistance to uplift than the EPS Geofoam section. Figure 133 shows the soil backfill section FLAC analysis for cases with and without a pavement section as well as the field data. Figure 134 shows the EPS Geofoam section FLAC analysis for cases with and without a pavement section as well as the field data.

The asphalt pavement system in the FLAC models increased both the peak resisting force to uplift and the stiffness of the system response when compared to the uplift behavior of the two systems in the actual field test. The force displacement curves in Figures 133 and 134 show that the asphalt pavement had two effects on the FLAC models in uplift. They first show that the peak uplift force increased when a HMA is added to the model. The peak force in the soil backfill section increased by 51 kN, a 9% increase. The peak force in the EPS Geofoam backfill section increased by 135 kN, a 100% increase.

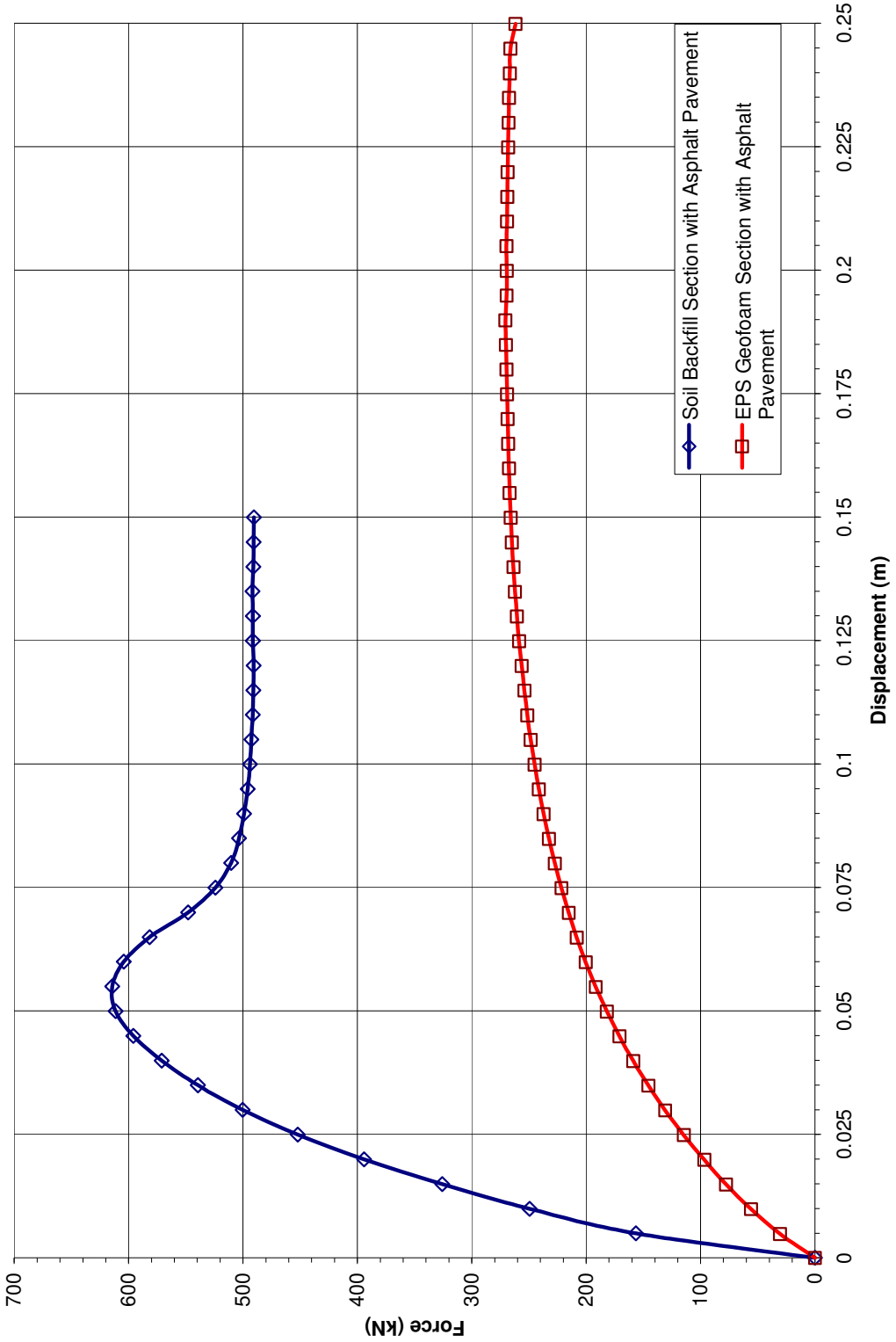

Figure 132. FLAC modeling results with an asphalt pavement added to model

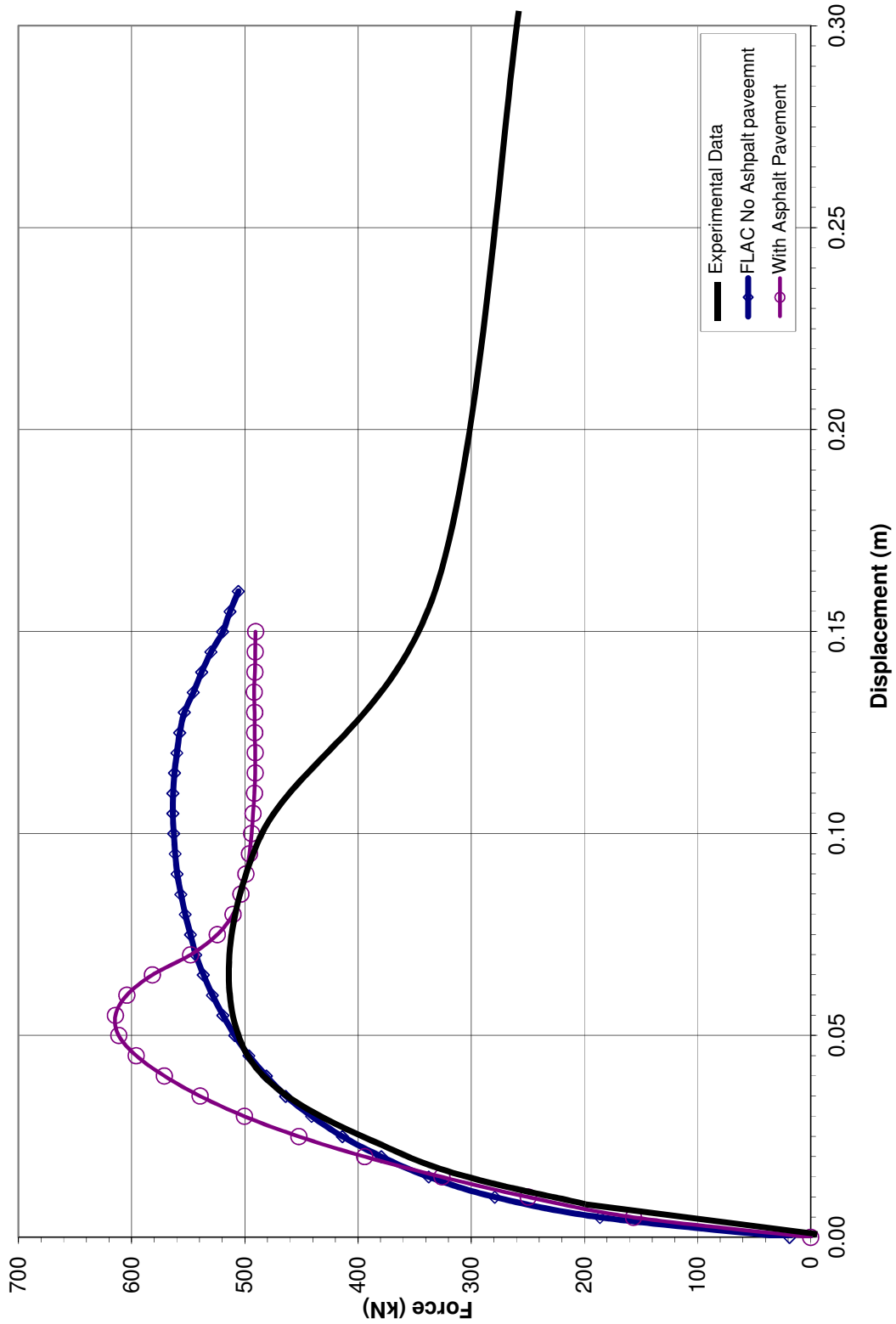

Figure 133. Comparison of soil backfill section with and without asphalt pavement added to model

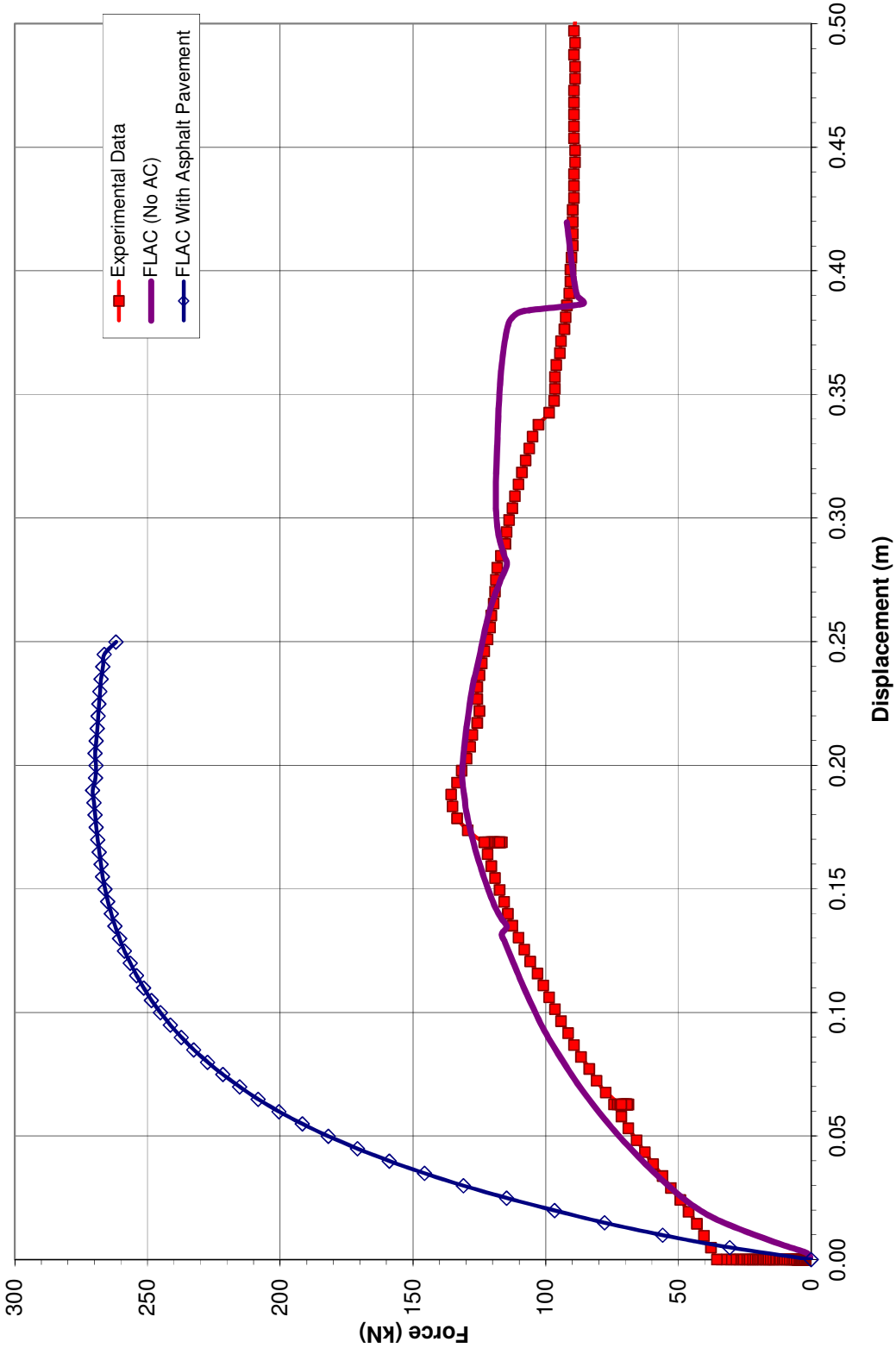

Figure 134. Comparison of EPS Geofoam section with asphalt pavement added to model

The second effect of the asphalt pavement above the uplifting pipe was the increased stiffness of the systems. The soil backfill section stiffness with the asphalt pavement system was 12220 kN/m/m, a 17% increase over the stiffness of the soil backfill section without an asphalt pavement system. The EPS Geofoam section stiffness from the FLAC models with asphalt pavement was 322 kN/m/m, a 95% increase over the EPS Geofoam section without an asphalt pavement section.

With this asphalt pavement investigation, it is important to note that some simplifying assumptions were made. It was assumed for the FLAC analysis that the pavement section was 152 mm thick. Actual pavement thicknesses can vary after years of maintenance. Temperature that lies in the median of the seasonal temperature spectrum was assumed. Had a colder temperature been assumed, the asphalt pavement in the FLAC models would have been much stronger and stiffer, and conversely had a warmer temperature been assumed, the asphalt modeled would have been softer. The condition of the pavement was assumed to be in good condition. No pre-existing cracking of the asphalt concrete was assumed. Cracking of asphalt concrete pavements reduces the strength and stiffness of the pavement system. The assumption of no traffic loads at the time of uplift was also assumed. The effects of pavement system thickness, temperature, pavement condition, traffic loading and other variables can be studied parametrically by changing the FLAC analysis as appropriate. This asphalt property investigation and FLAC modeling show that the presence of an asphalt pavement in good condition, at an average daytime temperature, has the effect of increasing both the stiffness and peak resisting force of a pipe in uplift with or without EPS Geofoam. The EPS Geofoam system, however, still provides less uplift resistance to the pipe.

CHAPTER 12

SUMMARY OF PIPE UPLIFT WITH EPS GEOFOAM COVERS

For pipeline design of an active fault crossing, or other location of permanent ground deformation, the normalized uplift resistance (N_v) and the system stiffness (K_v) are required. The design of pipelines in uplift using N_v and K_v was established by ASCE (1984) based on the work of Newmark and Hall (1975) and Kennedy et al. (1979). The uplift resistance and system stiffness results from field experimentation and numerical simulations for a pipe in uplift were normalized by Equations 27 and 28 to make them dimensionless (Trautmann and O'Rourke, 1984) for future design work of pipelines crossing active normal faults. The term N_v is the vertical uplift factor for a system, similar to a bearing capacity factor from foundation design. The term N_v was calculated by dividing the total uplift resistance on a pipe by the unit weight of the overburden material (γ), the diameter of the pipe (D), the vertical height of cover over the pipe (H) and the length of the pipe uplifting (L).

The parameter z_u is the dimensionless displacement at the peak. The dimensionless displacement in Equation 28 was calculated by dividing the displacement of the uplifting pipe by the diameter of the pipe. The stiffness of the system is denoted by the symbol K_v. The stiffness of the system can be taken as the tangent or secant slopes to the force displacement curve.

$$N_v = \frac{F_v}{\gamma HDL} \tag{27}$$

$$z_u = \frac{\delta_v}{D} \tag{28}$$

The ASCE (1984) and ALA (2005) guidelines for pipe design give three different ways to define the stiffness of the system (K_v) and the dimensionless displacement (z_u), similar to the uplift factor. The three ways to define system stiffness in uplift are denoted as K_{v1}, K_{v2} and K_{v3}, where K_{v1} is the initial tangent stiffness, K_{v2} is the secant stiffness at 50% peak stress and K_{v3} is the secant stiffness at the peak. The three ways to define normalized system resistance to uplift are denoted as N_{v1}, N_{v2} and N_{v3}, where N_{v1} is the uplift resistance at the end of the initial linear portion of the curve, N_{v2} is the 50% peak resistance and N_{v3} is the peak resistance. The three ways to define the dimensionless displacement are denoted as z_{u1}, z_{u2} and z_{u3}, where z_{u1} is the dimensionless displacement at the end of the initial tangent portion of the curve, z_{u2} is the dimensionless displacement at the 50% peak force and z_{u3} is the dimensionless displacement at the peak resisting force. The units for K_v are kN/m/m or kN/m^2.

For the soil backfill section, Table 37 summarizes the field test and FLAC analysis results including the effects of the addition of an asphalt pavement section. Table 37 includes the ASCE (1984) and ALA (2005) recommended values for clayey backfill. For the EPS Geofoam section, Table 38 summarizes the field test and FLAC analysis results including the effects of the addition of interface elements to the model and the addition of an asphalt pavement system to the section.

Table 37. Soil backfill section research program results

	ASCE - ALA Recommended	Field Test	FLAC	FLAC with Asphalt Pavement
N_{v1}	NA	4.0	3.8	3.8
N_{v2}	NA	5.3	5.7	6.2
N_{v3}	10	10.5	11.4	12.4
z_{u1}	NA	0.03	0.015	0.015
z_{u2}	NA	0.04	0.03	0.04
z_{u3}	0.32	0.20	0.31	0.17
K_{v1}	NA	5460	8135	6870
K_{v2}	NA	4375	6124	5470
K_{v3}	1260	1625	1230	2440

In the EPS Geofoam section results presented in Table 38, it is important to note that the FLAC analysis with no interfaces represented cases where there is complete, uniform contact between trench side walls and EPS Geofoam block such that the Geofoam is "gripped" by the trench side walls, with full frictional interaction. The FLAC analyses with interfaces had reduced friction, indicating cases where a geomembrane is placed between EPS Geofoam block and trench side walls or other cases where simple sliding is not impeded as occurred in the field test. To calculate the factors in Tables 37 and 38, the length of pipe was 4.572 m, the depth of cover was 2 m and the pipe diameter was 0.324 m. The unit weight of the clayey fill was 17.76 kN/m^3 and the unit weight of the EPS Geofoam was 0.3 kN/m^3.

Table 38. EPS Geofoam section research program results

	Field Test	FLAC No Interface	FLAC With Interface	FLAC with Asphalt Pavement
N_{v1}	1.7	4.9	1.8	2.7
N_{v2}	3.3	4.9	3.2	6.4
N_{v3}	6.5	9.7	6.3	12.7
z_{u1}	0.003	0.05	.05	0.03
z_{u2}	0.17	0.05	0.15	0.09
z_{u3}	0.58	0.28	0.62	0.46
K_{v1}	7775	1403	475	1230
K_{v2}	286	1403	300	970
K_{v3}	158	490	144	388

The field test with clay backfill, as shown in Table 34, was predicted very well by the ASCE (1984) and ALA (2000) recommendations and by the FLAC analysis. The effects of the asphalt concrete pavement on the uplift resistance of the system was that that dimensionless displacements were reduced by a factor of 2 from the section with no pavement section, and the stiffness of the system with asphalt pavement increased by a factor of 2 over the soils backfill system with no pavement section. The EPS Geofoam test had the peak force and uplift factors predicted well by the FLAC analysis with interfaces representing a decrease in block to soil friction (as could be achieved by placement of a geo-membrane between the EPS block and the adjacent soil). The addition

of the asphalt pavement system in FLAC had the effect of increasing the uplift factor by a factor of 2, and increasing the stiffness of the EPS Geofoam system 100%.

The terms N_{v1}, N_{v2}, N_{v3}, z_{u1}, z_{u2}, z_{u3}, K_{v1}, K_{v2} and K_{v3} are used in finite-element pipeline modeling. The finite element of the pipeline is done by first placing vertical uplift, bearing, longitudinal and transverse nonlinear springs at each pipe structural element (MCEER, 1999). The nonlinear springs are defined by N_{v1}, N_{v2}, N_{v3}, z_{u1}, z_{u2}, z_{u3}, K_{v1}, K_{v2} and K_{v3}. The pipeline distress to fault offset is modeled by displacing one half of the model vertically, while holding the far end of the pipe fixed in space (ASCE, 1984). This approach is well documented, and good agreement with observed case histories has been achieved (Arimin and Lee, 1991, and Meyersohn, 1991).

If the Kennedy et al. (1979) approach is used for pipeline design, the term N_{v3} and z_{u3} are used with Equations 29 and 30 (MCEER, 1999). Equations 29 and 30 use pipe diameter (D), pipe stress due to elongation (σ), pipe burial depth (H), pipe wall thickness (t) and bending strain (ε_b). The pipe bending strain (ε_b) is then checked against the steel structural failure model chosen by the designer. If the pipe bending strain is below the failure threshold, the design is finalized; if not, the design is iterated until the bending strains are tolerable.

$$\varepsilon_b = \frac{D}{2R_c} \tag{29}$$

$$R_c = \frac{\sigma \pi t}{\gamma H N_{v3}} \tag{30}$$

In summary, Tables 37 and 38 provide the designer directly the parameters required for pipeline fault-offset in uplift when using the EPS Geofoam cover system developed herein. The ASCE-ALA recommendations for a pipe uplifting through a clayey soil were matched by both the FLAC modeling and the field uplift test. The EPS Geofoam system input parameters are consistent between field test and FLAC model with interfaces.

CHAPTER 12

CONCLUSIONS

The use of an EPS Geofoam cover system for pipelines undergoing permanent ground displacement (PGD) from faulting and other geological mechanisms has been investigated using laboratory testing, full-scale testing and numerical modeling. The overall conclusion is that when used as a light-weight cover, EPS Geofoam cover systems offer significant reductions in resistance to buried pipelines displacing from fault offset or other forms of permanent ground deformation.

It was concluded that when EPS Geofoam is used as a compressible inclusion in the sidewalls or bottom of a trench, this application has limited value in reducing the forces that develop on the pipe for systems undergoing a significant amount of PGD. As the pipe is pushed into the EPS, a localized strain hardening zone develops within the EPS near the contact zone and such behavior significantly reduces the effectiveness of the compressible inclusion. It was found that EPS Geofoam behavior in compressive loading against the trench sidewalls or bottom is highly nonlinear and experiences significant strain hardening at higher compressive strains. In addition, localized shearing of the EPS block occurs near the corners of the block where shear stresses are maximized. Thus, it is recommended that significant strain-hardening behavior be avoided when using EPS as a compressible inclusion in the sidewalls or bottom of a trench. The recommendations for a compressible

inclusion concept were confirmed using a set of full-scale horizontal load tests conducted on a buried steel pipe pushed horizontally against a Geofoam compressible inclusion. These tests showed that at a relatively large horizontal displacement (greater than about 150 mm), the Geofoam strained hardened as it was compressed and the total force to the pipe increased to values greater than those measured using a sand backfill. However, a Geofoam compressible inclusion has some beneficial effect since these tests also showed that at smaller horizontal displacements (less than 150 mm), the compression of Geofoam from the pipe loading produced a smaller resisting force when compared with a sand backfill.

It is concluded that the application of EPS as a light-weight cover system should be considered for pipes that may undergo both vertical and horizontal PGD. Because of its extremely low mass density, a Geofoam cover system significantly reduces the vertical and/or uplift forces on a pipe system undergoing vertical PGD (e.g., normal faulting). In the case of vertical uplift of the pipe system, full-scale testing and numerical modeling demonstrated that the total force on the pipe is reduced by a factor of about 3 to 4 when compared with a trench backfilled only with soil. In addition, this research shows that if an EPS cover system is constructed atop a pipe that undergoes horizontal PGD (e.g., strike-slip faulting), the full-scale testing and numerical modeling suggests that the total force on the pipe can be reduced by a factor of about 2, even if the pipe is pushed horizontally into a sand backfill. This latter benefit occurs because the EPS light-weight cover system significantly reduces the in situ vertical stresses, which in turn reduces the resistance of the soil to horizontal displacement.

It was concluded that the presence of an asphalt pavement atop and uplifting EPS cover system significantly decreases the efficiency of the system in uplift. The strength

and stiffness of asphalt concrete in uplift rupture were investigated by literature survey and experimentation. The effects of an asphalt concrete pavement system atop a pipe uplifting were explored. It was found that the presence of an asphalt pavement system overlying a pipe uplifting from vertical PGD increases the peak resisting force and the stiffness of the system significantly and the modeling suggests the increase may be a 100%, or greater.

Finally, it was concluded that numerical modeling is an adequate tool for development of soil-Geofoam-pipe interaction. A series of numerical models were developed to demonstrate that such modeling can be used to evaluate a light-weight cover system for design of pipelines crossings of faults. The numerical models demonstrate that different configurations and materials can be incorporated into the investigation of system resistance to uplift of a pipe for future design work. The force displacement relationships obtained in such analyses of complicated EPS Geofoam configurations can be used to model pipeline distress from fault rupture according to methods developed by Newmark and Hall (1975), Kennedy et al. (1979) and the finite-element method.

APPENDIX A

FLAC SOIL BACKFILL SECTION CODE

```
config ats extra 1
grid 60,30
gen (-3.0,0.0) (-3.0,3.0) (3.0,3.0) (3.0,0.0) ratio 1.0,1.0 i=1,61 j=1,31
set gravity=9.81
fix  x y j 1
fix  x i 61
fix  x i 1
model elastic
gen circle 0.0,1.0 0.161925
group 'User:Bedding Sand' i 27 34 j 6 13
model mohr group 'User:Bedding Sand'
prop density=1800.0 bulk=8.33333E6 shear=3.84615E6 cohesion=0.0 friction=32.0
dilation=32.0 tension=0.0 group 'User:Bedding Sand'
group 'User:Clayey Fill' i 24 37 j 14 26
model ss group 'User:Clayey Fill'
prop density=1810.0 bulk=6.66667E6 shear=2.22222E6 ftab=1 ctab=2 dtab=3 ttab=4
group 'User:Clayey Fill'
group 'User:UTBC' i 21 40 j 27 30
model mohr group 'User:UTBC'
prop density=1990.0 bulk=5.33333E7 shear=3.2E7 cohesion=2500.0 friction=43.0
dilation=43.0 tension=2500.0 group 'User:UTBC'
group 'User:Native Sand' i 1 20 j 22 30
model ss group 'User:Native Sand'
prop density=1842.0 bulk=7.0833E6 shear=3.26923E6 ftab=5 ctab=6 dtab=7 ttab=8
group 'User:Native Sand'
group 'User:Native Sand' i 21 23 j 22 26
model ss group 'User:Native Sand'
prop density=1842.0 bulk=7.0833E6 shear=3.26923E6 ftab=5 ctab=6 dtab=7 ttab=80
group 'User:Native Sand'
group 'User:Native Sand' i 38 40 j 22 26
model ss group 'User:Native Sand'
prop density=1842.0 bulk=7.0833E6 shear=3.26923E6 ftab=5 ctab=6 dtab=7 ttab=8
group 'User:Native Sand'
group 'User:Native Sand' i 41 60 j 22 30
```

```
model ss group 'User:Native Sand'
prop density=1842.0 bulk=7.0833E6 shear=3.26923E6 ftab=5 ctab=6 dtab=7 ttab=8
group 'User:Native Sand'
group 'User:Native Clay' i 1 23 j 1 21
model ss group 'User:Native Clay'
prop density=1765.0 bulk=8.33333E6 shear=1.75871E6 ftab=9 ctab=10 dtab=11 ttab=12
group 'User:Native Clay'
group 'User:Native Clay' i 38 60 j 1 21
model ss group 'User:Native Clay'
prop density=1765.0 bulk=8.33333E6 shear=1.75871E6 ftab=9 ctab=10 dtab=11 ttab=12
group 'User:Native Clay'
group 'User:Native Clay' i 24 37 j 1 5
model ss group 'User:Native Clay'
prop density=1765.0 bulk=8.33333E6 shear=1.75871E6 ftab=9 ctab=10 dtab=11 ttab=12
group 'User:Native Clay'
group 'User:Native Clay' i 24 26 j 6 13
model ss group 'User:Native Clay'
prop density=1765.0 bulk=8.33333E6 shear=1.75871E6 ftab=9 ctab=10 dtab=11 ttab=12
group 'User:Native Clay'
group 'User:Native Clay' i 35 37 j 6 13
model ss group 'User:Native Clay'
prop density=1765.0 bulk=8.33333E6 shear=1.75871E6 ftab=9 ctab=10 dtab=11 ttab=12
group 'User:Native Clay'
table 1 0,28 .09,27 0.15,26
table 2 0,35910 .05,23940 .15,11970
table 3 0,14 .09,7 .15,0
table 4 0,35910 .09,23940  0.15,11970
table 5 0,27.2 .09,23.2 0.15,24.8
table 6 0,35910 .09,35910 .215,15940
table 7 0,14 .09,7 .15,0
table 8 0,35910 .09,35910 .15,15940
table 9 0,23.8 .09,23.0 0.15,20
table 10 0,59850 .90,35910 .15,20000
table 11 0,14 .09,7 .15,0
table 12 0,59850 .09,35910 .15,20000
hist 999 unbalanced
solve
ini ydisp=0
ini xdisp=0
fix  x mark
solve
model null region 30 11
group 'null' region 30 11
group delete 'null'
struct node 1 0.1495992,0.938034
struct node 2 0.161925,1.0
```

```
struct node 3 0.1495992,1.0619661
struct node 4 0.114498265,1.1144983
struct node 5 0.061966013,1.1495992
struct node 6 1.2359384E-15,1.161925
struct node 7 -0.061966013,1.1495992
struct node 8 -0.114498265,1.1144983
struct node 9 -0.1495992,1.0619661
struct node 10 -0.161925,1.0
struct node 11 -0.1495992,0.938034
struct node 12 -0.114498265,0.88550174
struct node 13 -0.061966013,0.8504008
struct node 14 1.2359384E-15,0.838075
struct node 15 0.061966013,0.8504008
struct node 16 0.114498265,0.88550174
struct beam begin node 1 end node 2 seg 1 prop 1001
struct beam begin node 2 end node 3 seg 1 prop 1001
struct beam begin node 3 end node 4 seg 1 prop 1001
struct beam begin node 4 end node 5 seg 1 prop 1001
struct beam begin node 5 end node 6 seg 1 prop 1001
struct beam begin node 6 end node 7 seg 1 prop 1001
struct beam begin node 7 end node 8 seg 1 prop 1001
struct beam begin node 8 end node 9 seg 1 prop 1001
struct beam begin node 9 end node 10 seg 1 prop 1001
struct beam begin node 10 end node 11 seg 1 prop 1001
struct beam begin node 11 end node 12 seg 1 prop 1001
struct beam begin node 12 end node 13 seg 1 prop 1001
struct beam begin node 13 end node 14 seg 1 prop 1001
struct beam begin node 14 end node 15 seg 1 prop 1001
struct beam begin node 15 end node 16 seg 1 prop 1001
struct beam begin node 16 end node 1 seg 1 prop 1001
interface 1 aside long from 33,10 to 33,10 bside from node 1,16 to node 1
interface 1 unglued kn=1.35e8 ks=1.35E8 cohesion=0.0 dilation=12 friction=24
tbond=0.0 bslip=On
struct prop 1001 e 2E11 area 0.048 I 2.3E-4
struct node range 15 16 fix x fix y
solve

ini ydisp = 0
ini xdisp = 0
step 2000
set large
set st_damping=combined 0.8
set st_damping struct=combined 0.8
structure node 1 ini yvel 1e-5
structure node 2 ini yvel 1e-5
structure node 3 ini yvel 1e-5
```

```
structure node 4 ini yvel 1e-5
structure node 5 ini yvel 1e-5
structure node 6 ini yvel 1e-5
structure node 7 ini yvel 1e-5
structure node 8 ini yvel 1e-5
structure node 9 ini yvel 1e-5
structure node 10 ini yvel 1e-5
structure node 11 ini yvel 1e-5
structure node 12 ini yvel 1e-5
structure node 13 ini yvel 1e-5
structure node 14 ini yvel 1e-5
structure node 15 ini yvel 1e-5
structure node 16 ini yvel 1e-5
set geometry=0.06
hist 1 node 1 ydisp
call str.fin
; F_n is the sum of the normal forces along the outside of the pipe
def F_n
        sum = 0.0
        pnt = imem(str_pnt+$ksnode)
        loop while pnt # 0
                sum = sum + fmem(pnt+$kndf2c)
                pnt = imem(pnt)
        endLoop
        F_n = ABS(sum)
end
step 28000
```

FLAC EPS Geofoam Cover System Code

```
config ats
grid 66,33
gen (-3.0,0.0) (-3.0,3.3) (3.6,3.3) (3.6,0.0) ratio 1.0,1.0 i=1,67 j=1,34
model elastic
;
;cut grid into chunks
model null i 21
model null i 25
model null i 28
model null i 46
model null i 42
model null i 39
model null j 30
model null j 28
```

```
model null j 15
;
;Move and attach the bottom chunks into correct geometry
gen -1.0,0 -1.0,1.4 -0.7,1.4 -0.7,0 ratio 1.0,1.0 i=22,25 j=1,15
attach aside from 21,15 to 21,1 bside from 22,15 to 22,1
gen -0.7,0 -0.7,1.4 -0.5,1.4 -0.5,0 ratio 1.0,1.0 i=26,28 j=1,15
attach aside from 26,15 to 26,1 bside from 25,15 to 25,1
gen -0.5,0 -0.5,1.4 0.5,1.4 0.5,0 ratio 1.0,1.0 i=29,39 j=1,15
attach aside from 29,15 to 29,1 bside from 28,15 to 28,1
gen 0.5,0 0.5,1.4 0.7,1.4 0.7,0 ratio 1.0,1.0 i=40,42 j=1,15
attach aside from 40,15 to 40,1 bside from 39,15 to 39,1
gen 0.7,0 0.7,1.4 1.0,1.4 1.0,0 ratio 1.0,1.0 i=43,46 j=1,15
attach aside from 42,15 to 42,1 bside from 43,15 to 43,1
gen 1.0,0 1.0,1.4 3.0,1.4 3.0,0 ratio 1.0,1.0 i=47,67 j=1,15
attach aside from 47,15 to 47,1 bside from 46,15 to 46,1
;
;Move and Attach the left chunks into correct geometry
gen -3,1.4 -3,2.6 -1,2.6 -1,1.4 ratio 1.0,1.0 i=1,21 j=16,28
attach aside from 1,15 to 21,15 bside from 1,16 to 21,16
gen -3,2.6 -3,2.7 -1,2.7 -1,2.6 ratio 1.0,1.0 i=1,21 j=29,30
attach aside from 1,29 to 21,29 bside from 1,28 to 21,28
gen -3,2.7 -3,3 -1,3 -1,2.7 ratio 1.0,1.0 i=1,21 j=31,34
attach aside from 1,30 to 21,30 bside from 1,31 to 21,31
;
;move and attach the chunks to the left of LDS incl UTBC
attach aside from 21,28 to 21,16 bside from 22,28 to 22,16
attach aside from 25,15 to 22,15 bside from 25,16 to 22,16
gen -1,1.4 -1,2.6 -0.7,2.6 -0.7,1.4 ratio 1.0,1.0 i=22,25 j=16,28
attach aside from 22,30 to 22,29 bside from 21,30 to 21,29
attach aside from 25,29 to 22,29 bside from 25,28 to 22,28
gen -1,2.6 -1,2.7 -0.7,2.7 -0.7,2.6 ratio 1.0,1.0 i=22,25 j=29,30
gen -1,2.7 -1,3 -0.7,3 -0.7,2.7 ratio 1.0,1.0 i=22,25 j=31,34
interface 1 aside from 21,34 to 21,31 bside from 22,34 to 22,31
interface 1 unglued kn=9.6E8 ks=9.6E8 cohesion=11250.0 dilation=0.0 friction=21.5.0
tbond=11250.0 bslip=On
interface 2 aside from 25,31 to 22,31 bside from 25,30 to 22,30
interface 2 unglued kn=9.6E8 ks=9.6E8 cohesion=11250.0 dilation=0.0 friction=21.5
tbond=0.0 bslip=On
;
;move and attach the chunks on the left and below of the LDS
attach aside from 26,28 to 26,16 bside from 25,28 to 25,16
attach aside from 28,16 to 26,16 bside from 28,15 to 26,15
gen -0.7,1.4 -0.7,2.6 -0.5,2.6 -0.5,1.4 ratio 1.0,1.0 i=26,28 j=16,28
interface 3 aside from 26,30 to 26,29 bside from 25,30 to 25,29
interface 3 unglued kn=8.7329997E9 ks=8.7329997E9 cohesion=1000.0 dilation=0.0
friction=13.5 tbond=0.0 bslip=On
```

```
interface 4 aside from 28,29 to 26,29 bside from 28,28 to 26,28
interface 4 unglued kn=8.7329997E9 ks=8.7329997E9 cohesion=1000.0 dilation=0.0
friction=13.5 tbond=0.0 bslip=On
gen -0.7,2.6 -0.7,2.7 -0.5,2.7 -0.5,2.6 ratio 1.0,1.0 i=26,28 j=29,30
interface 5 aside from 26,34 to 26,31 bside from 25,34 to 25,31
interface 5 unglued kn=9.6E8 ks=9.6E8 cohesion=0.0 dilation=0.0 friction=21.5
tbond=0.0 bslip=On
attach aside from 28,31 to 26,31 bside from 28,30 to 26,30
gen -0.7,2.7 -0.7,3 -0.5,3 -0.5,2.7 ratio 1.0,1.0 i=26,28 j=31,34
;
;move and attach the chunks of the model that are the foam and above the foam
interface 6 aside from 29,28 to 29,16 bside from 28,28 to 28,16
interface 6 unglued kn=1.14422736E8 ks=1.14422736E7 cohesion=0.0 dilation=0.0
friction=6.0 tbond=0.0 bslip=On
interface 7 aside from 39,16 to 29,16 bside from 39,15 to 29,15
interface 7 unglued kn=1.1442273E8 ks=1.1442273E8 cohesion=0.0 dilation=0.0
friction=32.0 tbond=0.0 bslip=On
gen -0.5,1.4 -0.5,2.6 0.5,2.6 0.5,1.4 ratio 1.0,1.0 i=29,39 j=16,28
attach aside from 29,30 to 29,29 bside from 28,30 to 28,29
attach aside from 39,29 to 29,29 bside from 39,28 to 29,28
gen -0.5,2.6 -0.5,2.7 0.5,2.7 0.5,2.6 ratio 1.0,1.0 i=29,39 j=29,30
attach aside from 28,34 to 28,31 bside from 29,34 to 29,31
attach aside from 39,31 to 29,31 bside from 39,30 to 29,30
gen -0.5,2.7 -0.5,3 0.5,3 0.5,2.7 ratio 1.0,1.0 i=29,39 j=31,34
;
; Move and attach the chuncks on the right of the goeofoam block zone
attach aside from 42,16 to 40,16 bside from 42,15 to 40,15
interface 8 aside from 40,28 to 40,16 bside from 39,28 to 39,16
interface 8 unglued kn=1.14422736E8 ks=1.14422736E7 cohesion=0.0 dilation=0.0
friction=6.0 tbond=0.0 bslip=On
gen 0.5,1.4 0.5,2.6 0.7,2.6 0.7,1.4 ratio 1.0,1.0 i=40,42 j=16,28
attach aside from 40,30 to 40,29 bside from 39,30 to 39,29
interface 9 aside from 42,29 to 40,29 bside from 42,28 to 40,28
interface 9 unglued kn=8.7329997E9 ks=8.7329997E9 cohesion=1000.0 dilation=0.0
friction=13.5 tbond=0.0 bslip=On
gen 0.5,2.6 0.5,2.7 0.7,2.7 0.7,2.6 ratio 1.0,1.0 i=40,42 j=29,30
attach aside from 40,34 to 40,31 bside from 39,34 to 39,31
attach aside from 42,31 to 40,31 bside from 42,30 to 40,30
gen 0.5,2.7 0.5,3 0.7,3 0.7,2.7 ratio 1.0,1.0 i=40,42 j=31,34
;
;Move and attach the chunks to the right of the LDS
attach aside from 43,28 to 43,16 bside from 42,28 to 42,16
attach aside from 46,16 to 43,16 bside from 46,15 to 43,15
gen 0.7,1.4 0.7,2.6 1.0,2.6 1.0,1.4 ratio 1.0,1.0 i=43,46 j=16,28
attach aside from 46,29 to 43,29 bside from 46,28 to 43,28
interface 10 aside from 42,30 to 42,29 bside from 43,30 to 43,29
```

```
interface 10 unglued kn=8.7329997E9 ks=8.7329997E9 cohesion=1000.0 dilation=0.0
friction=13.5 tbond=0.0 bslip=On
gen 0.7,2.6 0.7,2.7 1.0,2.7 1,2.6 ratio 1.0,1.0 i=43,46 j=29,30
interface 11 aside from 43,34 to 43,31 bside from 42,34 to 42,31
interface 11 unglued kn=9.6E8 ks=9.6E8 cohesion=0.0 dilation=0.0 friction=21.5
tbond=0.0 bslip=On
interface 12 aside from 46,31 to 43,31 bside from 46,30 to 43,30
interface 12 unglued kn=9.6E8 ks=9.6E8 cohesion=11250.0 dilation=0.0 friction=21.5
tbond=0.0 bslip=On
gen 0.7,2.7 0.7,3 1,3 1,2.7 ratio 1.0,1.0 i=43,46 j=31,34
;
; Move and attach the chunks of the grid on the far right side of the model
attach aside from 47,28 to 47,16 bside from 46,28 to 46,16
attach aside from 67,16 to 47,16 bside from 67,15 to 47,15
gen 1,1.4 1,2.6 3,2.6 3,1.4 ratio 1.0,1.0 i=47,67 j=16,28
attach aside from 67,29 to 47,29 bside from 67,28 to 47,28
attach aside from 47,30 to 47,29 bside from 46,30 to 46,29
gen 1,2.6 1,2.7 3,2.7 3,2.6 ratio 1.0,1.0 i=47,67 j=29,30
attach aside from 67,31 to 47,31 bside from 67,30 to 47,30
interface 13 aside from 47,34 to 47,31 bside from 46,34 to 46,31
interface 13 unglued kn=9.6E8 ks=9.6E8 cohesion=11250.0 dilation=0.0 friction=21.5
tbond=11250.0 bslip=On
gen 1,2.7 1,3 3,3 3,2.7 ratio 1.0,1.0 i=47,67 j=31,34
fix x i=1
fix x i=67
fix x,y j=1


set gravity=9.81
gen circle 0.0,1.0 0.161925
group 'User:Bedding Sand' i 29 38 j 7 14
model mohr group 'User:Bedding Sand'
prop density=1800.0 bulk=8.33333E6 shear=3.84615E6 cohesion=0.0 friction=32.0
dilation=21.333 tension=0.0 group 'User:Bedding Sand'
group 'User:UTBC' notnull i 22 45 j 31 33
model mohr notnull group 'User:UTBC'
prop density=1990.0 bulk=5.33333E7 shear=3.2E7 cohesion=1500.0 friction=43.0
dilation=43.0 tension=500.0 group 'User:UTBC'
group 'User:LDS' notnull i 26 41 j 29
model elastic notnull group 'User:LDS'
prop density=2000.0 bulk=4.36668E8 shear=3.27501E8 group 'User:LDS'
group 'User:Geofoam' i 29 38 j 16 27
model mohr group 'User:Geofoam'
prop density=22.0 bulk=3.401e7 shear=4.9505e7 cohesion=50000.0 friction=0.0
dilation=0.0 tension=50000.0 group 'User:Geofoam'
group 'User:Native Sand' notnull i 1 20 j 24 33
```

```
model mohr notnull group 'User:Native Sand'
prop density=1842.0 bulk=7.0833E6 shear=3.26923E6 cohesion=45000.0 friction=28.0
dilation=13.5 tension=45000.0 group 'User:Native Sand'
group 'User:Native Sand' notnull i 22 24 j 24 29
model mohr notnull group 'User:Native Sand'
prop density=1842.0 bulk=7.0833E6 shear=3.26923E6 cohesion=45000.0 friction=28.0
dilation=13.5 tension=45000.0 group 'User:Native Sand'
group 'User:Native Sand' i 26 27 j 24 27
model mohr group 'User:Native Sand'
prop density=1842.0 bulk=7.0833E6 shear=3.26923E6 cohesion=45000.0 friction=28.0
dilation=13.5 tension=45000.0 group 'User:Native Sand'
group 'User:Native Sand' i 40 41 j 24 27
model mohr group 'User:Native Sand'
prop density=1842.0 bulk=7.0833E6 shear=3.26923E6 cohesion=45000.0 friction=28.0
dilation=13.5 tension=45000.0 group 'User:Native Sand'
group 'User:Native Sand' notnull i 43 45 j 24 29
model mohr notnull group 'User:Native Sand'
prop density=1842.0 bulk=7.0833E6 shear=3.26923E6 cohesion=45000.0 friction=28.0
dilation=13.5 tension=45000.0 group 'User:Native Sand'
group 'User:Native Sand' notnull i 47 66 j 24 33
model mohr notnull group 'User:Native Sand'
prop density=1842.0 bulk=7.0833E6 shear=3.26923E6 cohesion=45000.0 friction=28.0
dilation=13.5 tension=45000.0 group 'User:Native Sand'
group 'User:Native Clay' notnull i 1 27 j 1 23
model mohr notnull group 'User:Native Clay'
prop density=1765.0 bulk=8.33333E6 shear=1.75871E6 cohesion=59850.0 friction=23.0
dilation=0.0 tension=89775.0 group 'User:Native Clay'
group 'User:Native Clay' notnull i 40 66 j 1 23
model mohr notnull group 'User:Native Clay'
prop density=1765.0 bulk=8.33333E6 shear=1.75871E6 cohesion=59850.0 friction=23.0
dilation=0.0 tension=89775.0 group 'User:Native Clay'
group 'User:Native Clay' i 29 38 j 1 6
model mohr group 'User:Native Clay'
prop density=1765.0 bulk=8.33333E6 shear=1.75871E6 cohesion=59850.0 friction=23.0
dilation=0.0 tension=89775.0 group 'User:Native Clay'
hist 999 unbalanced
solve


ini ydisp=0
ini xdisp=0
fix  x mark
solve
model null region 34 10
group 'null' region 34 10
group delete 'null'
```

```
struct node 1 0.114498265,1.1144983
struct node 2 0.061966013,1.1495992
struct node 3 -2.2471609E-17,1.161925
struct node 4 -0.061966013,1.1495992
struct node 5 -0.114498265,1.1144983
struct node 6 -0.1495992,1.0619661
struct node 7 -0.161925,1.0
struct node 8 -0.1495992,0.938034
struct node 9 -0.114498265,0.88550174
struct node 10 -0.061966013,0.8504008
struct node 11 -2.2471609E-17,0.838075
struct node 12 0.061966013,0.8504008
struct node 13 0.114498265,0.88550174
struct node 14 0.1495992,0.938034
struct node 15 0.161925,1.0
struct node 16 0.1495992,1.0619661
struct beam begin node 1 end node 2 seg 1 prop 1001
struct beam begin node 2 end node 3 seg 1 prop 1001
struct beam begin node 3 end node 4 seg 1 prop 1001
struct beam begin node 4 end node 5 seg 1 prop 1001
struct beam begin node 5 end node 6 seg 1 prop 1001
struct beam begin node 6 end node 7 seg 1 prop 1001
struct beam begin node 7 end node 8 seg 1 prop 1001
struct beam begin node 8 end node 9 seg 1 prop 1001
struct beam begin node 9 end node 10 seg 1 prop 1001
struct beam begin node 10 end node 11 seg 1 prop 1001
struct beam begin node 11 end node 12 seg 1 prop 1001
struct beam begin node 12 end node 13 seg 1 prop 1001
struct beam begin node 13 end node 14 seg 1 prop 1001
struct beam begin node 14 end node 15 seg 1 prop 1001
struct beam begin node 15 end node 16 seg 1 prop 1001
struct beam begin node 16 end node 1 seg 1 prop 1001
interface 14 aside long from 35,12 to 35,12 bside from node 1,16 to node 1
interface 14 unglued kn=1.35e8 ks=1.35E8 cohesion=0.0 dilation=12 friction=24
tbond=0.0 bslip=On
struct prop 1001 e 2E11 area 0.048 I 2.3E-4
struct node range 15 16 fix x fix y
solve

ini ydisp = 0
ini xdisp = 0
step 2000
set large
set st_damping=combined 5.0
set st_damping struct=combined 5.0
structure node 1 ini yvel 1e-5
```

```
structure node 2 ini yvel 1e-5
structure node 3 ini yvel 1e-5
structure node 4 ini yvel 1e-5
structure node 5 ini yvel 1e-5
structure node 6 ini yvel 1e-5
structure node 7 ini yvel 1e-5
structure node 8 ini yvel 1e-5
structure node 9 ini yvel 1e-5
structure node 10 ini yvel 1e-5
structure node 11 ini yvel 1e-5
structure node 12 ini yvel 1e-5
structure node 13 ini yvel 1e-5
structure node 14 ini yvel 1e-5
structure node 15 ini yvel 1e-5
structure node 16 ini yvel 1e-5
set geometry=0.06
hist 1 node 1 ydisp
call str.fin
; F_n is the sum of the normal forces along the outside of the pipe
def F_n
        sum = 0.0
        pnt = imem(str_pnt+$ksnode)
        loop while pnt # 0
                sum = sum + fmem(pnt+$kndf2c)
                pnt = imem(pnt)
        endLoop
        F_n = ABS(sum)
end
step 40000
```

FLAC3D Soil Backfill Section Code

```
;The clay section model with no interfaces 6-16-09
;Slightly larger than the 2D model
;
;GP Fixity for the model
fix z range z -.05 .05
fix x range z -.05 .05
fix y range z -.05 .05
fix y range y -0.05 0.05
fix y range y 4.5 4.6
fix x range x -3.05 -2.95
fix x range x 2.95 3.05
fix y range x -3.05 -2.95
fix y range x 2.95 3.05
```

```
;
;Add gravity
set grav 0 0 -9.81
;
;Add the SEL
sel liner range cyl end1=(0.0,0.0,1.838075)  end2=(0.0,4.572,1.838075) radius=0.161925
sel liner prop iso=(2.068423e10, 0.0) thick=0.0127 dens=3500
sel liner PROP cs_nk=8e8 cs_sk=8e8 &
            cs_ncut=0 cs_scoh=0 cs_scohres=0 cs_sfric=20.0
;
;fix the pipe against movement in x and y
sel node fix x y
;add material models
model mohr range group bedding
model ss range group fill
model mohr range group Clay
model mohr range group Sand
model mohr range group UTBC
;
;add material densities
prop den=1800 range group bedding
prop den=1810 range group fill
prop den=1765 range group clay
prop den=1842 range group sand
prop den=1990 range group UTBC
;
;add material stiffness
prop bulk=8.33333E6  shear=3.84615E6  range group bedding
prop bulk=6.66667E6  shear=2.22222E6  range group fill
prop bulk=8.33333E6  shear=1.75871E6  range group clay
prop bulk=7.0833E6  shear=3.26923E6  range group sand
prop bulk=5.33333E7  shear=3.2E7  range group UTBC
;
;add strength properties
prop coh=0.0  ten=0.0  fric=32  dil=32  range group bedding
prop coh=tab1  ten=tab2  fric=tab3  dil=tab4  range group fill
prop coh=59850  ten=89775  fric=23  dil=0 range group clay
prop coh=45000  ten=45000  fric=28  dil=13.5  range group sand
prop coh=2500  ten=500  fric=43  dil=43  range group UTBC
;
;solve the analysis for the in-situ conditions
solve
;
;reset the displacements to zero
ini ydisp = 0.0
ini xdisp = 0.0
```

```
ini zdisp = 0.0
solve
;
;Fix the pipe in the Z direction prior to uplift
sel node fix z
solve
;
;begin uplift of pipe
sel liner prop slide=on
sel node init xvel=0.0 yvel=0.0
sel node INIT zVel=5e-5
set large
set geometry 0.05
sel set damp combined
history id=1 unbal
history id=10 sel node zdisp id=1
step 5000
```

FLAC3D EPS Geofoam Cover System Code

```
;The EPS Geofoam section model with no interfaces 6-16-09
;Slightly larger than the 2D model
;
;GP Fixity for the model
fix z range z -.05 .05
fix x range z -.05 .05
fix y range z -.05 .05
fix y range y -0.05 0.05
fix y range y 4.5 4.6
fix x range x -3.05 -2.95
fix x range x 2.95 3.05
fix y range x -3.05 -2.95
fix y range x 2.95 3.05
;
;Add gravity
set grav 0 0 -9.81
;
;Add the SEL
sel liner range cyl end1=(0.0,0.0,1.838075)  end2=(0.0,4.572,1.838075) radius=0.161925
sel liner prop iso=(2.068423e10, 0.0) thick=0.0127 dens=3500
sel liner PROP cs_nk=8e8 cs_sk=8e8 &
            cs_ncut=0 cs_scoh=0 cs_scohres=0 cs_sfric=20.0
;
```

```
;fix the pipe against movement in x and y
sel node fix x y
;add material models
model mohr range group bedding
model elast range group LDS
model mohr range group Geofoam
model mohr range group Clay
model mohr range group Sand
model mohr range group UTBC
;
;add material densities
prop den=1800 range group bedding
prop den=2280 range group LDS
prop den=29   range group Geofoam
prop den=1765 range group clay
prop den=1842 range group sand
prop den=1990 range group UTBC
;
;add material stiffness
prop bulk=8.33333E6  shear=3.84615E6  range group bedding
prop bulk=6.66667E9  shear=2.22222E9  range group LDS
prop bulk= 3.4010e7  shear=4.95050e7  range group Geofoam
prop bulk=8.33333E6  shear=1.75871E6  range group clay
prop bulk=7.0833E6  shear=3.26923E6  range group sand
prop bulk=5.33333E7  shear=3.2E7  range group UTBC
;
;add strength properties
prop coh=0.0  ten=0.0  fric=32  dil=32  range group bedding
prop coh=50000  ten=75000 fric=0  dil=0  range group Geofoam
prop coh=59850  ten=89775  fric=23  dil=0 range group clay
prop coh=45000  ten=45000  fric=28  dil=13.5  range group sand
prop coh=2500  ten=500  fric=43  dil=43  range group UTBC
;
;solve the analysis for the in-situ conditions
solve
;
;reset the displacements to zero
ini ydisp = 0.0
ini xdisp = 0.0
ini zdisp = 0.0
solve
;
;Fix the pipe in the Z direction prior to uplift
sel node fix z
solve
;
```

```
;begin uplift of pipe
sel liner prop slide=on
sel node init xvel=0.0 yvel=0.0
sel node INIT zVel=5e-5
set large
set geometry 0.05
sel set damp combined
history id=1 unbal
history id=10 sel node zdisp id=1
step 4000
```

FLAC EPS Geofoam Pipe Interaction Code

```
config dynamic extra 5
grid 18,18
set dynamic off
set=large
set geometry=0.05
set st_damping=combined 10.0
set st_damping struct=combined 10.0
model elastic
gen circle 9.0,2.0 2.0
ini x mul 0.0254
ini y mul 0.0254
fix  x y j 19
fix  x y i 9 11 j 5
fix  x y i 12 j 2 4
fix  x y i 9 11 j 1
fix  x y i 8 j 2 4
model null i 1 7 j 1 4
group 'null' i 1 7 j 1 4
group delete 'null'
model null i 12 18 j 1 4
group 'null' i 12 18 j 1 4
group delete 'null'
model null i 11 j 1
group 'null' i 11 j 1
group delete 'null'
model null i 11 j 4
group 'null' i 11 j 4
group delete 'null'
model null i 8 j 4
group 'null' i 8 j 4
group delete 'null'
```

```
model null i 8 j 1
group 'null' i 8 j 1
group delete 'null'
interface 1 aside from 1,5 to 19,5 bside from 9,5 to 11,5
interface 1 unglued kn=4032e6 ks=4032e6 cohesion=0.0 dilation=0.0 friction=0
tbond=0.0 bslip=Off
group 'User:EPS15' j 5 18
model mohr notnull group 'User:EPS15'
prop density=15.0 bulk=0.12E6 shear=0.18E6 cohesion=37e3 friction=0.0 dilation=0.0
tension=74e3 notnull group 'User:EPS15'
group 'User:Pipe' i 9 10 j 1 4
model elastic group 'User:Pipe'
prop density=500.0 bulk=3.3e9 shear=3.6e9 group 'User:Pipe'
group 'User:Pipe' i 11 j 2 3
model elastic group 'User:Pipe'
prop density=500.0 bulk=3.3e9 shear=3.6e9 group 'User:Pipe'
group 'User:Pipe' i 8 j 2 3
model elastic group 'User:Pipe'
prop density=500.0 bulk=3.3e9 shear=3.6e9 group 'User:Pipe'
set gravity 9.81
his unbal 999
his syy 10 i 10 j 18
his ydisp 998 i 10 j 19
his ydisp 101 i 10 j 5
his ydisp 102 i 10 j 6
his ydisp 103 i 10 j 7
his ydisp 104 i 10 j 8
his ydisp 105 i 10 j 9
def sumforce
  totforce = 0
  vertdisp = 0
   loop i (1,izones)
   loop  j (1,jzones)
   totforce = totforce + yforce (i,j)
   sumforce = totforce*(-0.225)
   vertdisp = ydisp(10,19)*100/2.54*(-1)
   end_loop
   end_loop
end
his vertdisp 106
his sumforce 107
step 2000
apply yvelocity -1.1E-6 from 1,19 to 19,19
apply xvelocity = 0 from 1,19 to 19,19
step 75000
hist write 10 vs 9 begin 1 skip 20
```

```
set = large
set geometry=0.05
set st_damping=combined 10.0
set st_damping struct=local 10.0
set update=5
config
grid 18,18
model elastic
;
; Geofoam properties
prop density = 20 bulk = 1.77e6 shear = 2.65e6;
ini x mul 0.0254
ini y mul 0.0254
fix  x y j 1
his unbal 999
set gravity 9.81
step 2000
ini ydisp = 0
apply yvelocity -1.235E-6 from 1,19 to 19,19
apply xvelocity 0 from 1,19 to 19,19
def install
  avgstress = 0
  avgstrain = 0
  totalxforce = 0
  whilestepping
  loop i (1,izones)
    loop j (1,jzones)
      vstrain = ((0- ydisp(i,j+1) - (0 - ydisp(i,j)))/0.0254)
      vstress = syy(i,j)*(-1)
      avgstrain = avgstrain + vstrain/18/18
      avgstress = avgstress + vstress/18/18
      totalxforce = totalxforce + xforce(i,j)
      if vstrain > 0.01
           bulk_mod(i,j)= 1.77e6/(1+(vstrain-0.01)*230)
           shear_mod(i,j) = 1.5*bulk_mod(i,j)
           if vstrain > 0.10
             bulk_mod(i,j)= 78e3
             shear_mod(i,j) = 117.5e3
          endif
      endif
    end_loop
  end_loop
end
his avgstrain 998
his avgstress 997
his bulk_mod 996
```

```
his shear_mod 995
his totalxforce 994
history 999 unbalanced
cycle 10000
cycle 5000
cycle 5000
cycle 5000
cycle 5000
cycle 5000
cycle 5000
cycle 5000
set st_damping=combined 10.0
set st_damping struct=combined 10.0
def EQ_Modulus
  Whilestepping
   loop i (1,izones)
     loop j (5,18)
       vstrain = ((0- ydisp(i,j+1) - (0 - ydisp(i,j)))/0.0254)
      vstress = syy(i,j)*(-1)
      avgstrain = avgstrain + vstrain/18/18
      avgstress = avgstress + vstress/18/18
      totalxforce = totalxforce + xforce(i,j)
      if vstrain > 0.01
           bulk_mod(i,j)= 1.77e6/(1+(vstrain-0.01)*230)
           shear_mod(i,j) = 1.5*bulk_mod(i,j)
           if vstrain > 0.10
             bulk_mod(i,j)= 78e3
             shear_mod(i,j) = 117.5e3
          endif
      endif
     end_loop
   end_loop
end
EQ_Modulus
solve
apply yvelocity -1.000E-6 from 1,19 to 19,19
step 45000
his write 3 vs 4
```

APPENDIX B

GEOFOAM EXPERIMENTAL DATA

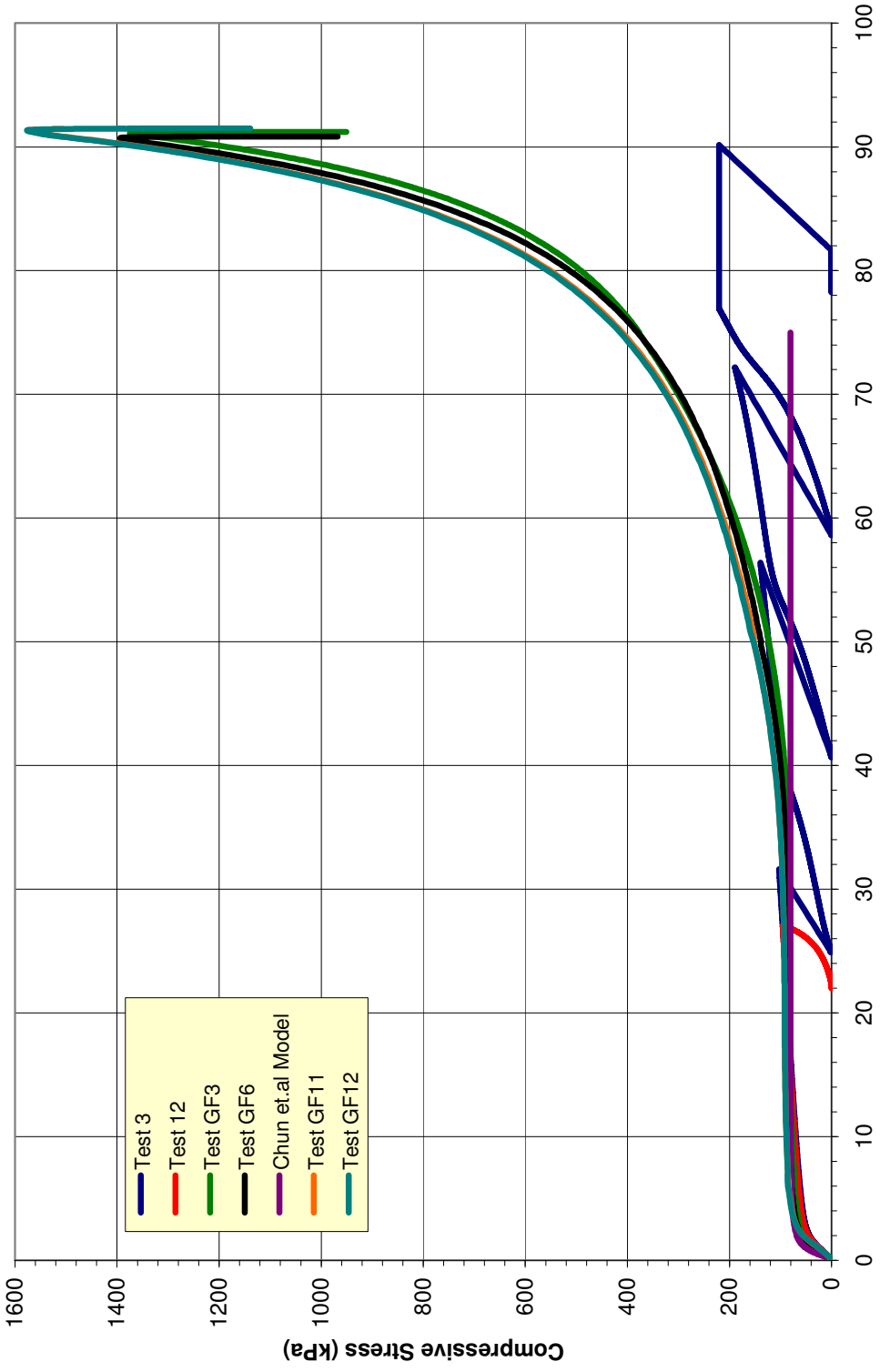

Figure 135. EPS 15 experimental stress:strain curves

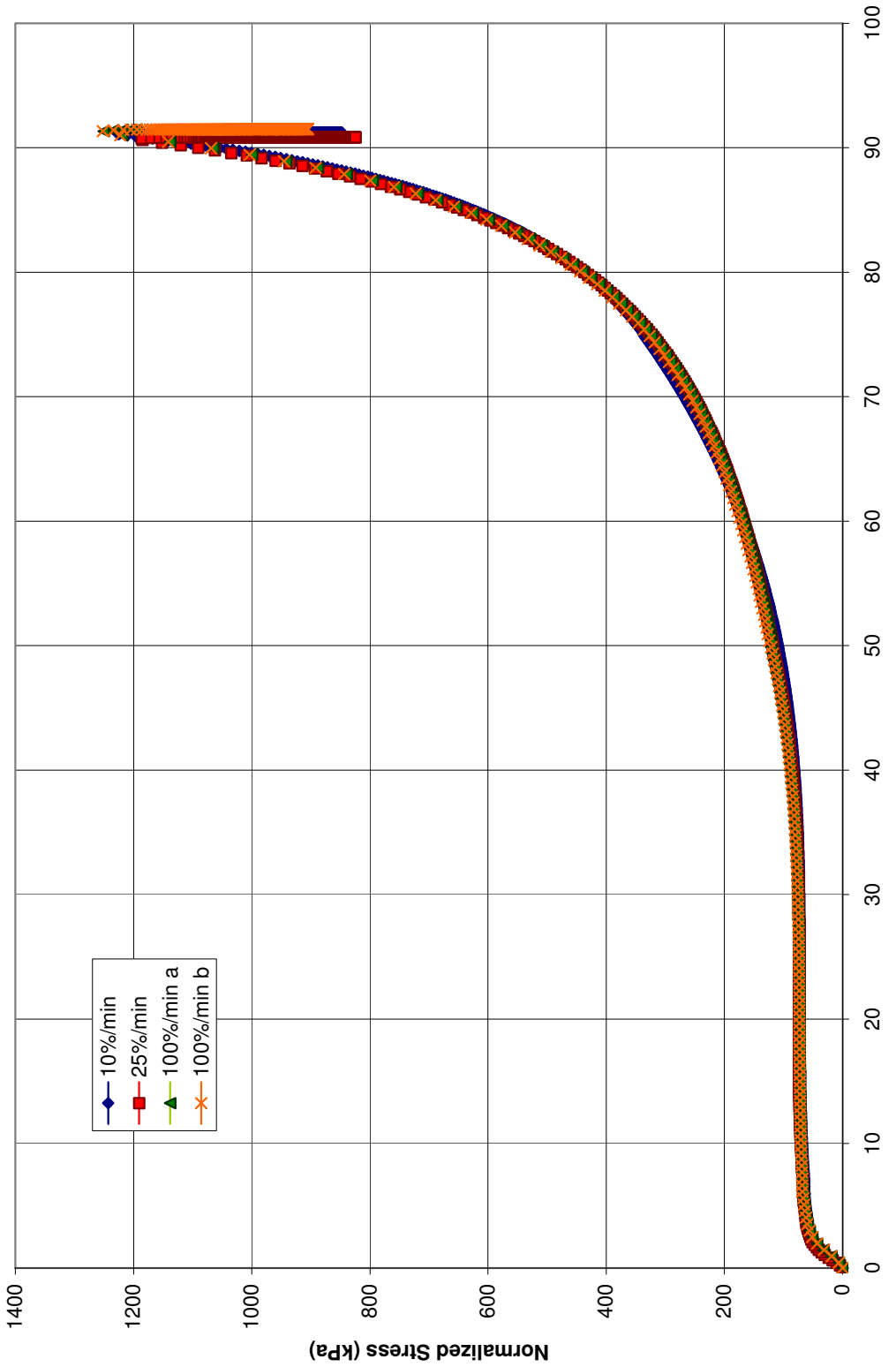

Figure 136. EPS 15 normalized experimental data

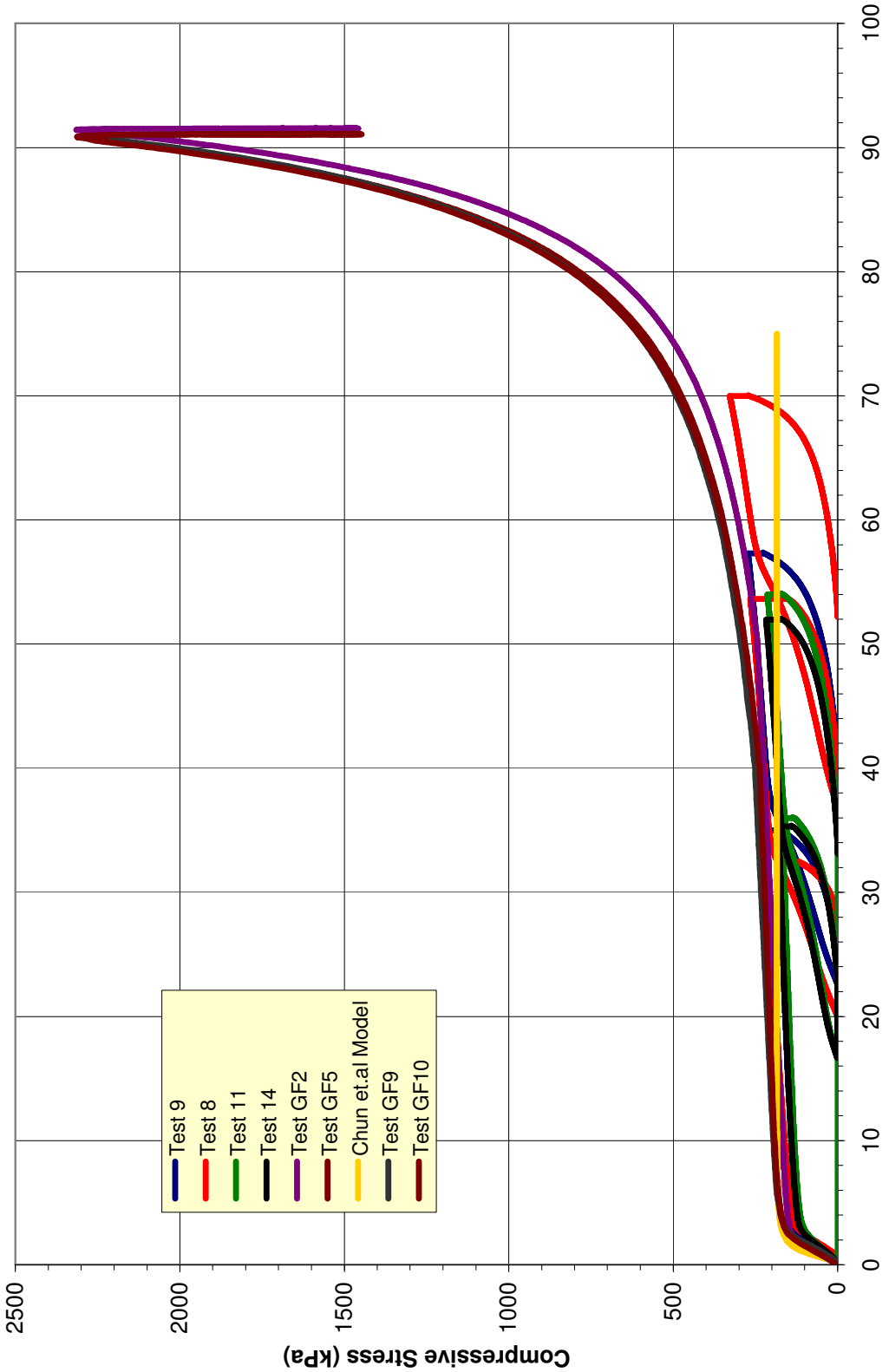

Figure 137. EPS 22 experimental stress:strain curves

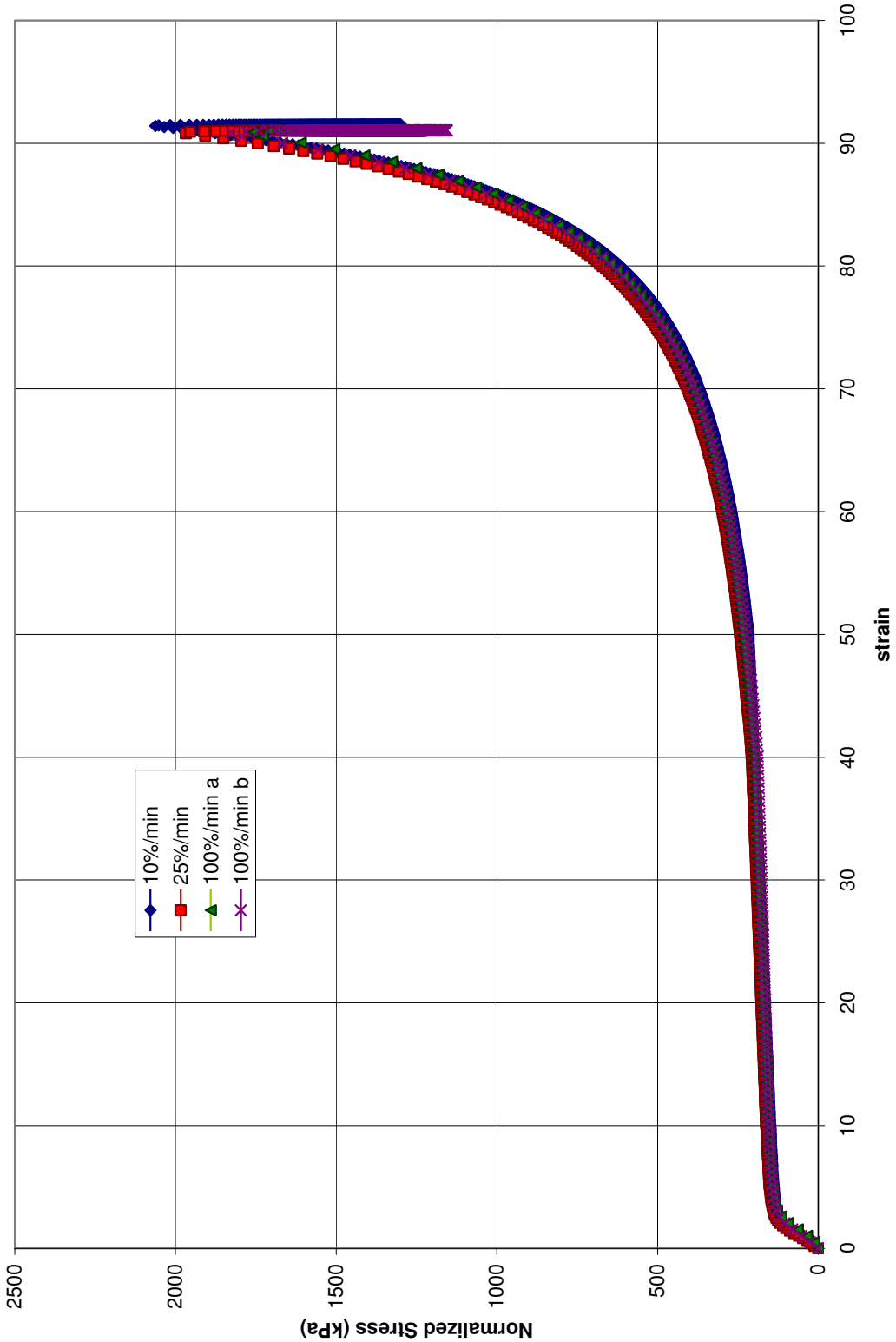

Figure 138. EPS 22 normalized experimental stress:strain curves

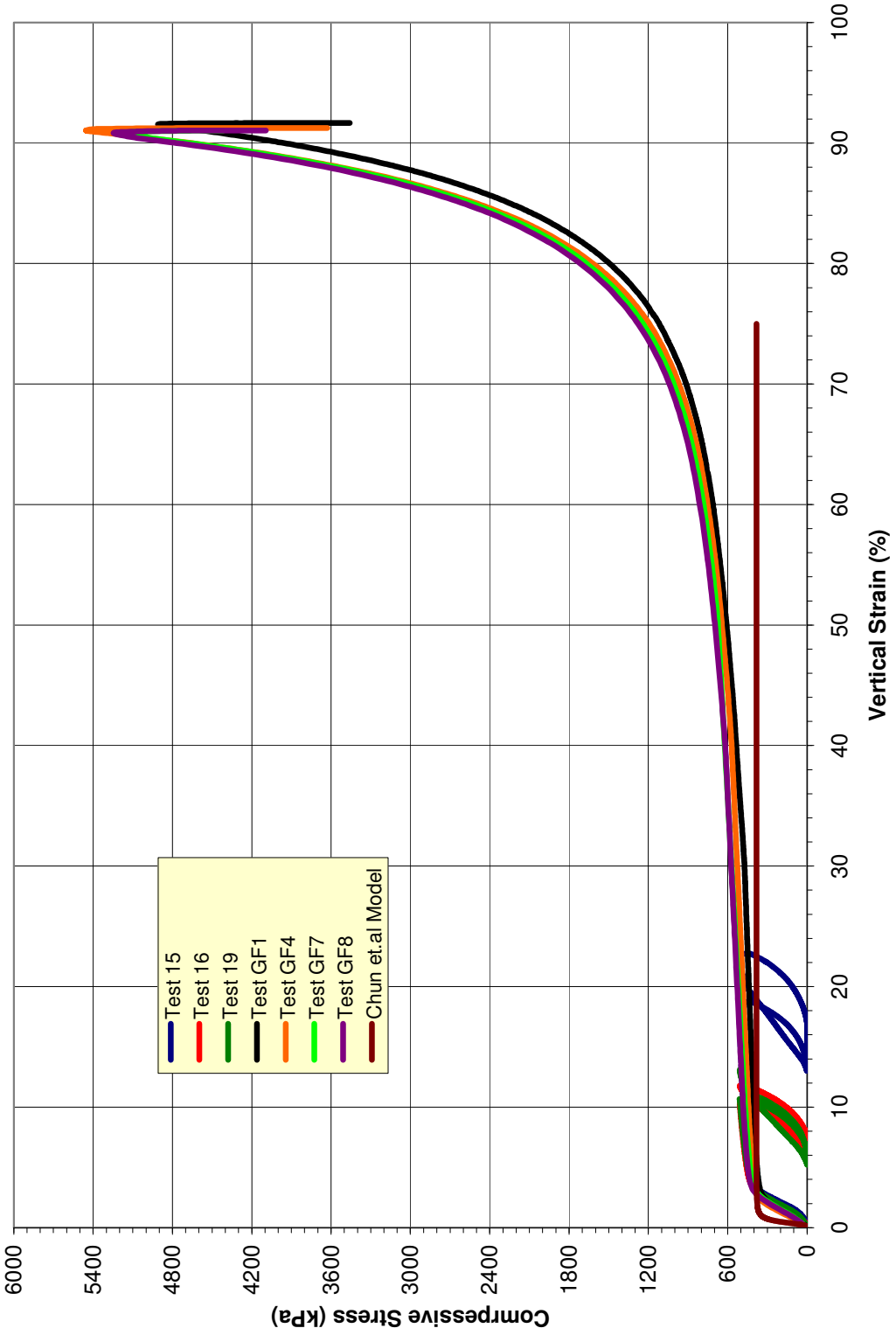

Figure 139. EPS 39 experimental stress:stain curves

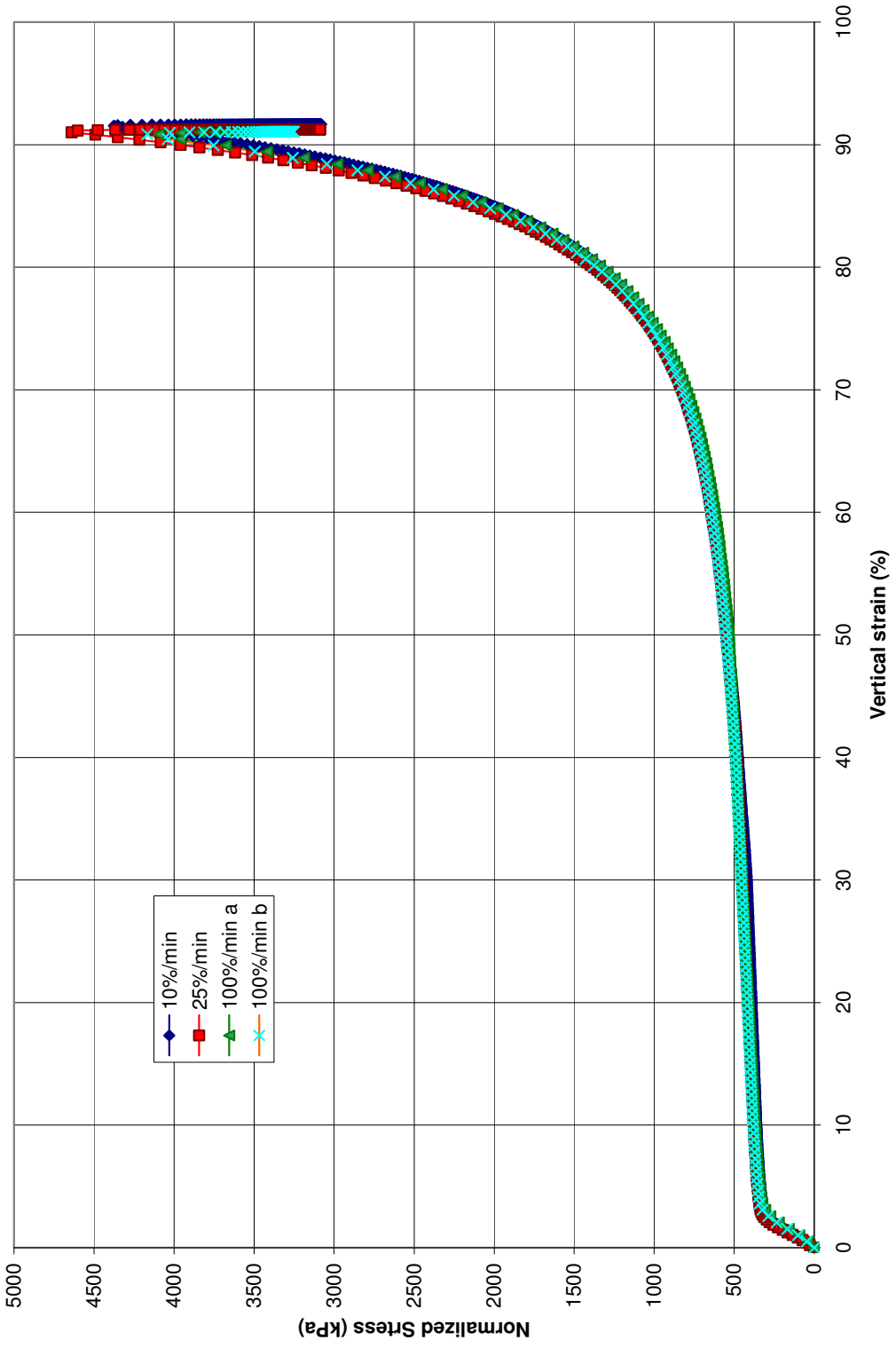

Figure 140. EPS 39 normalized experimental curves

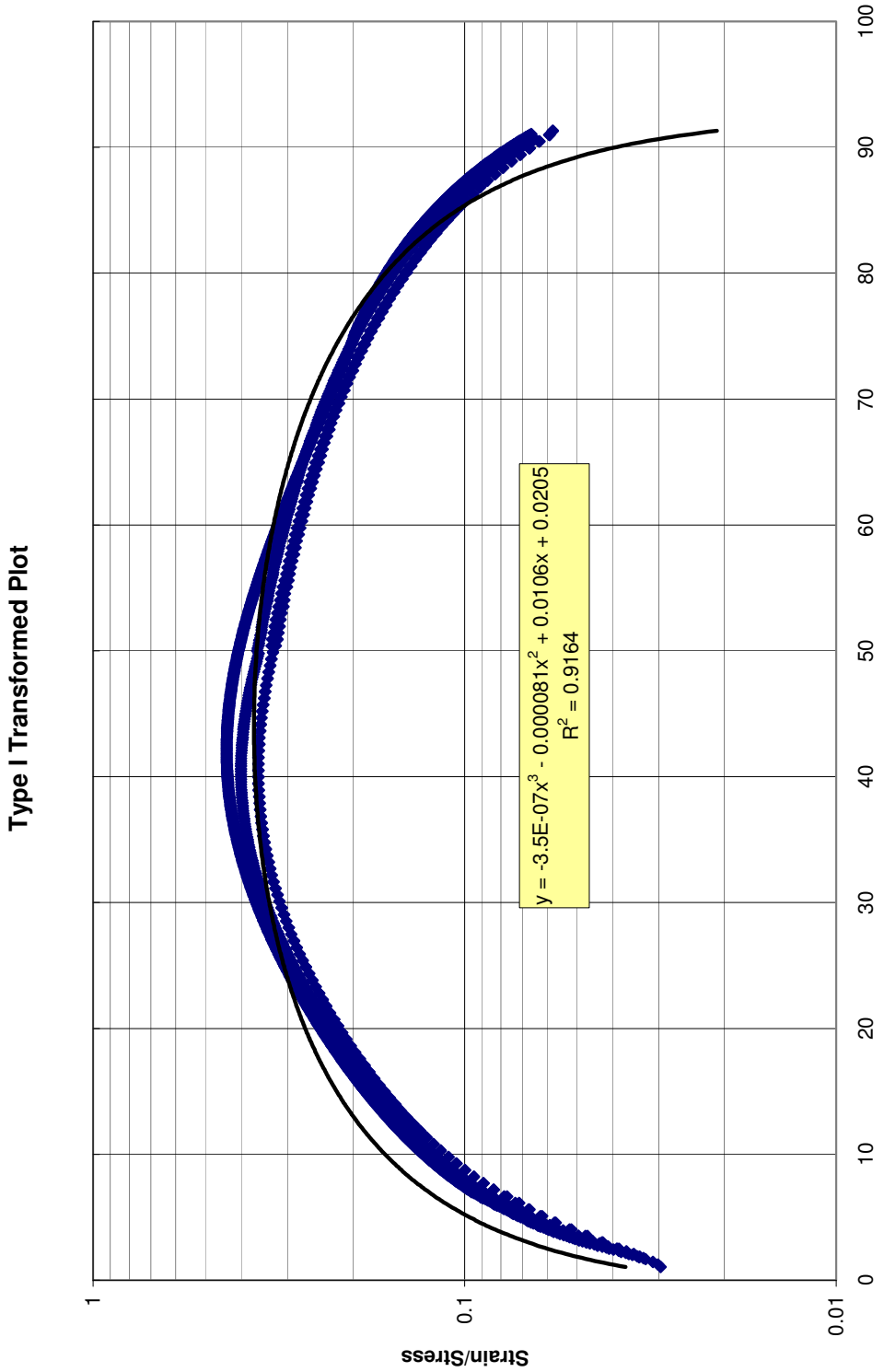

Figure 141. EPS 15 Transformed Hyperbolic Plot

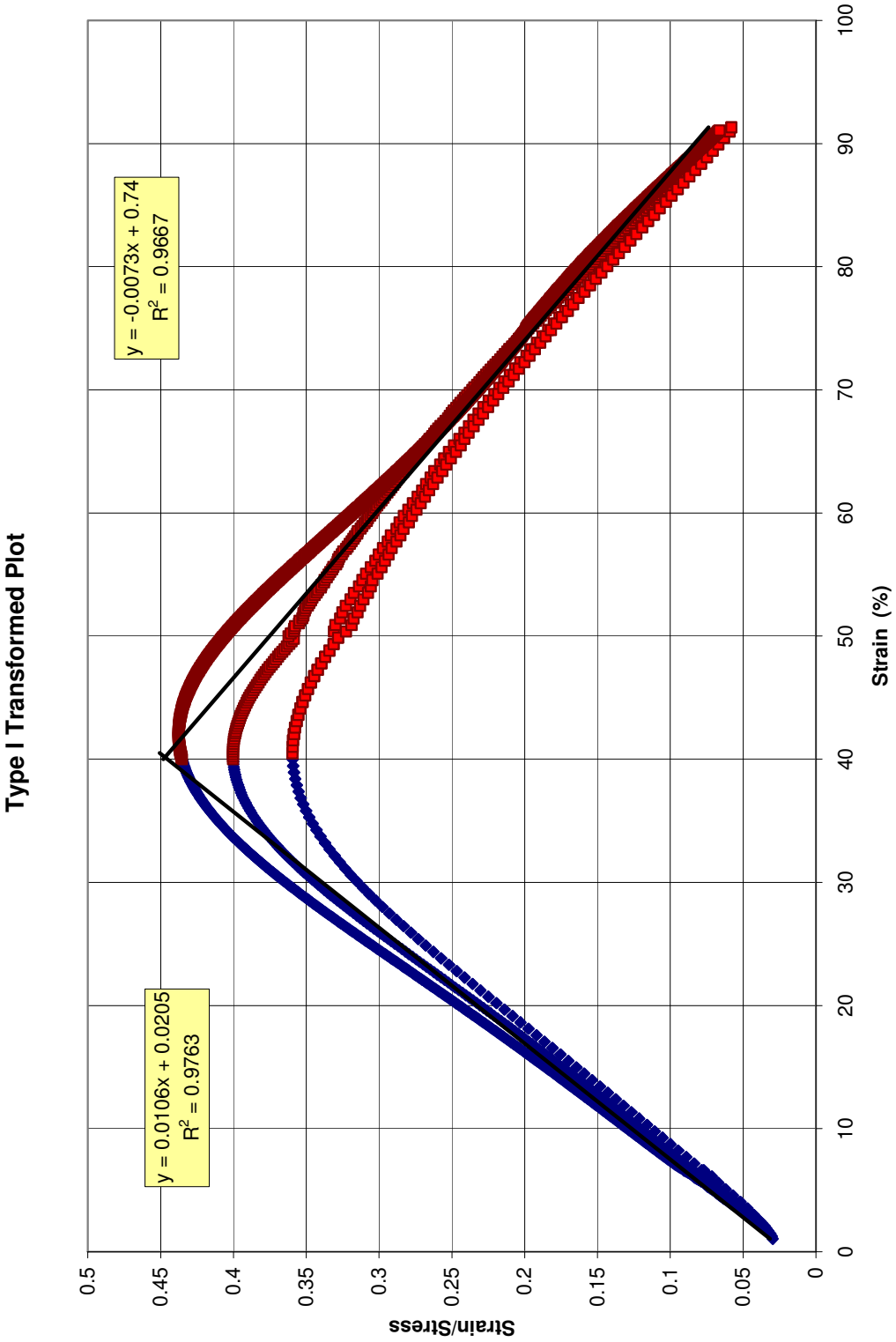

Figure 142. EPS 15 Matched Transformed Plot

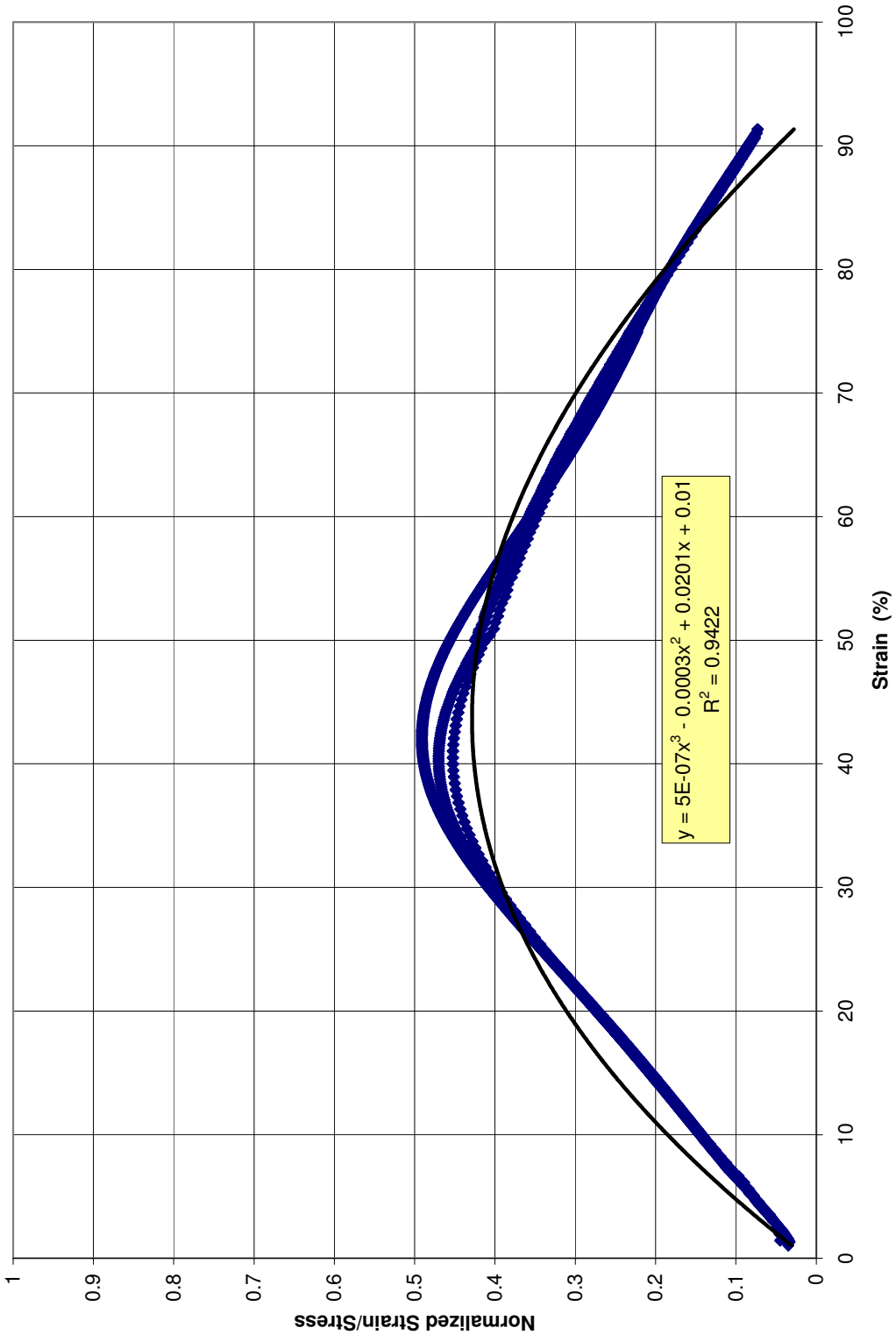

Figure 143. EPS 15 normalized transformed hyperbolic plot

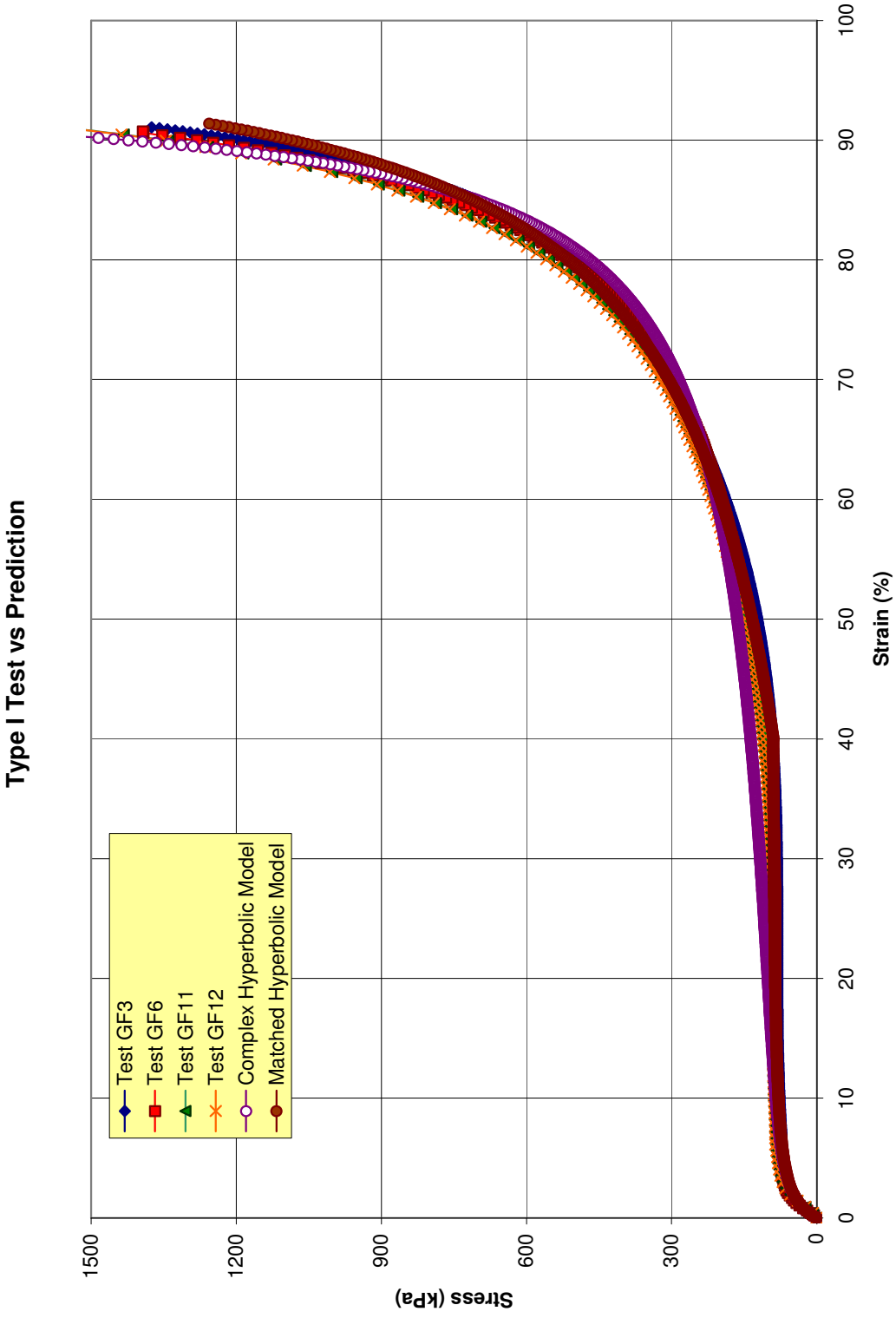

Figure 144. EPS 15 compression comparison plot

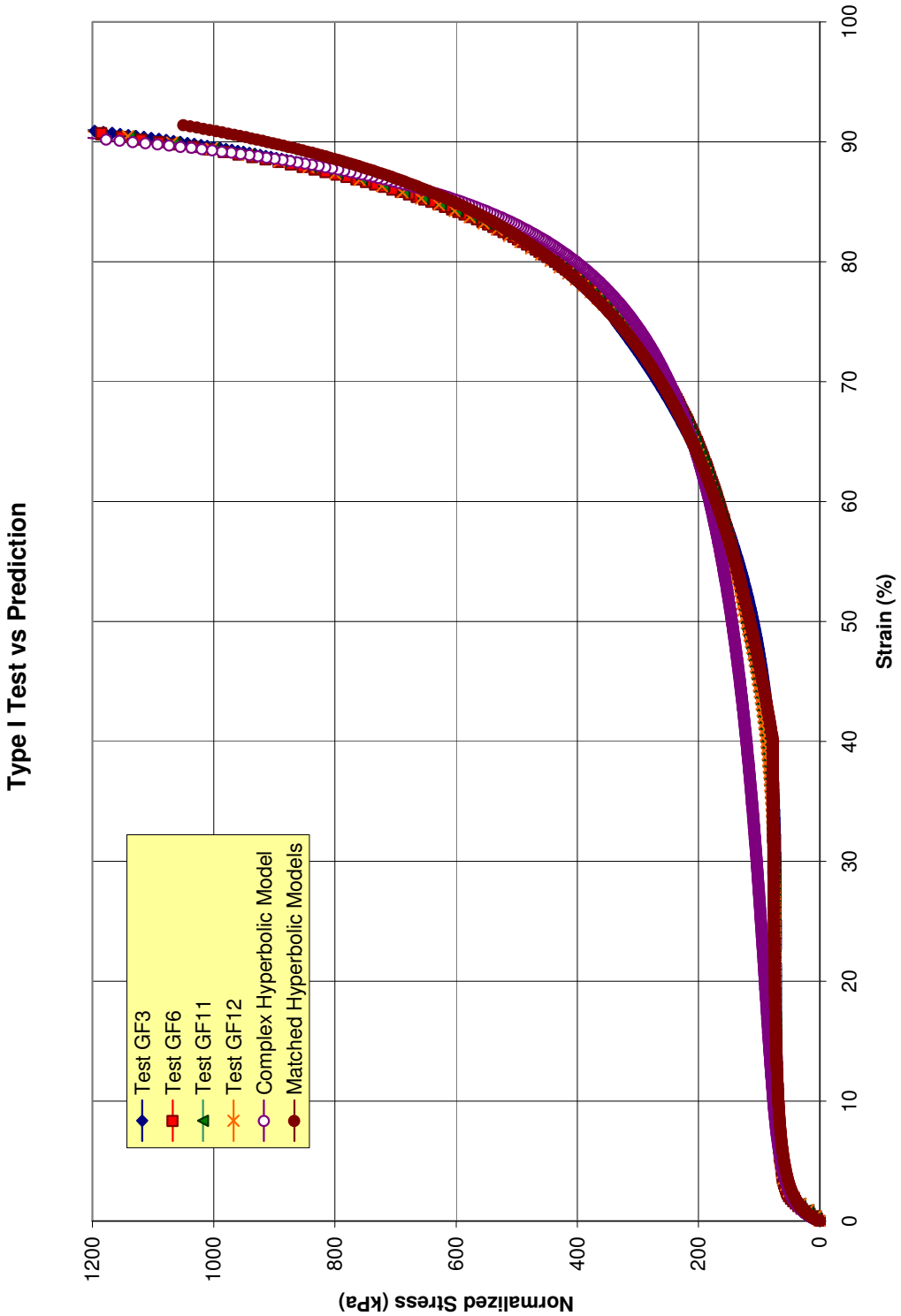

Figure 145. EPS 15 normalized compression comparison plot

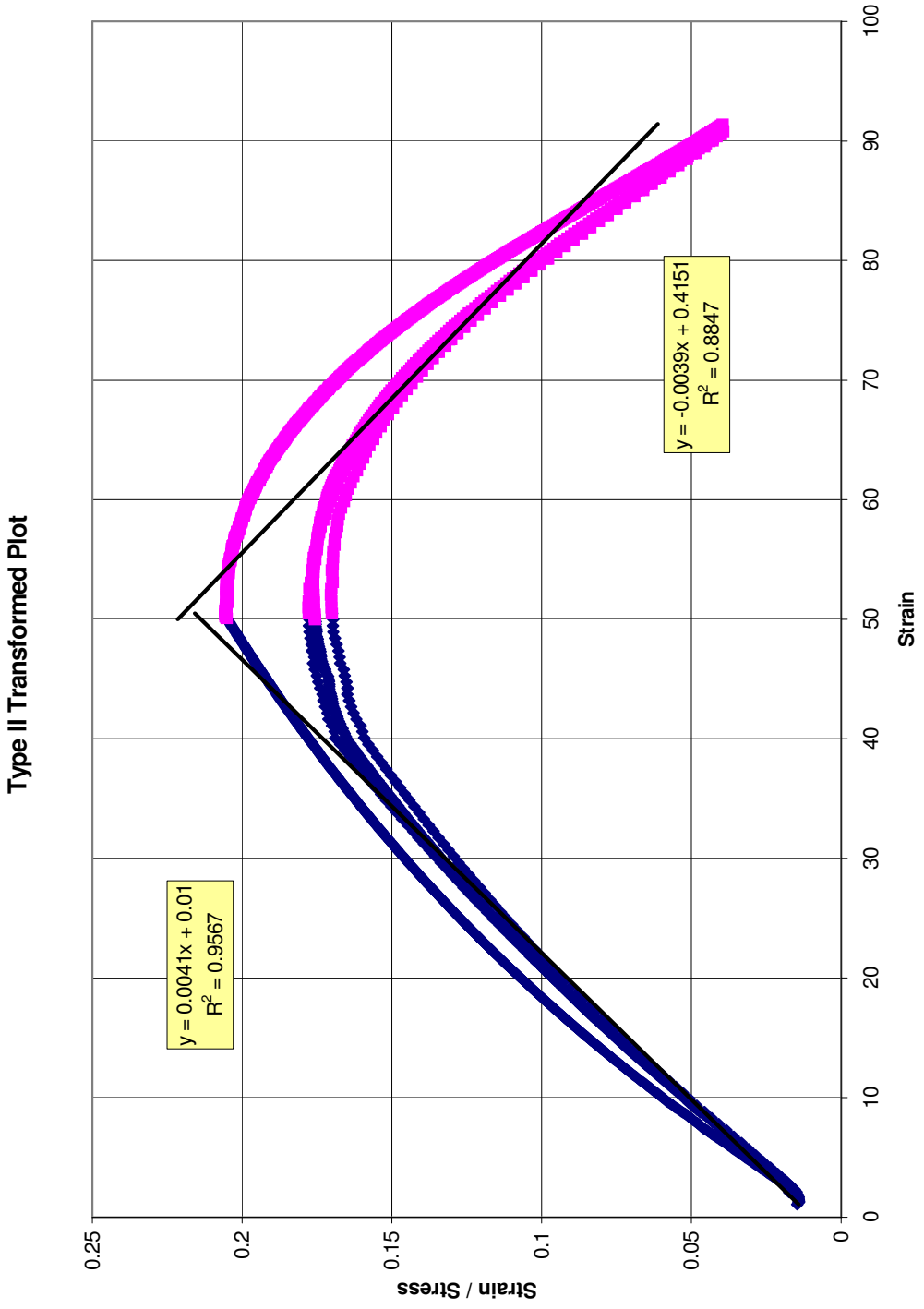

Figure 146. EPS 22 transformed hyperbolic plot

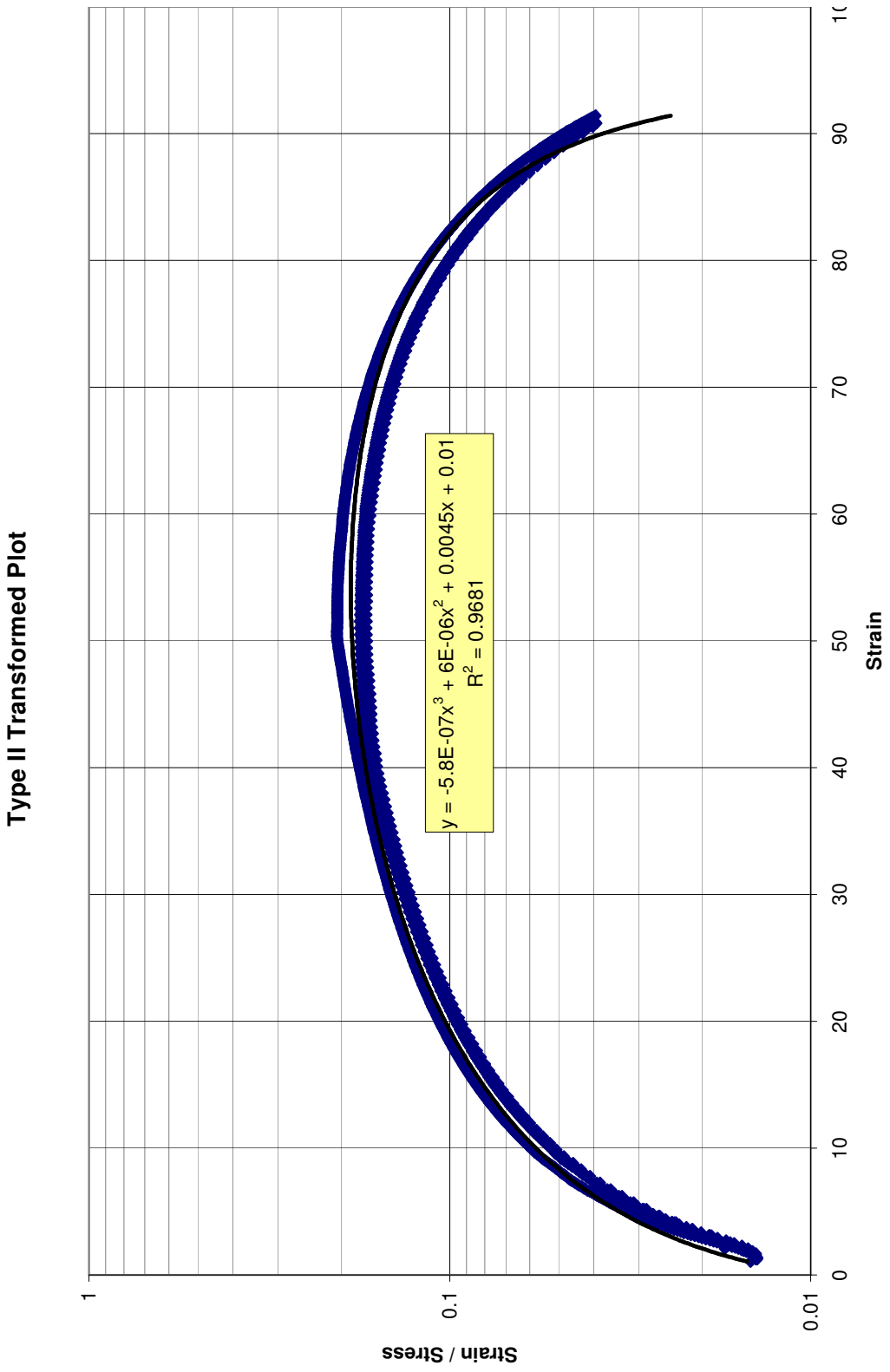

Figure 147. EPS 22 transformed hyperbolic plot (2)

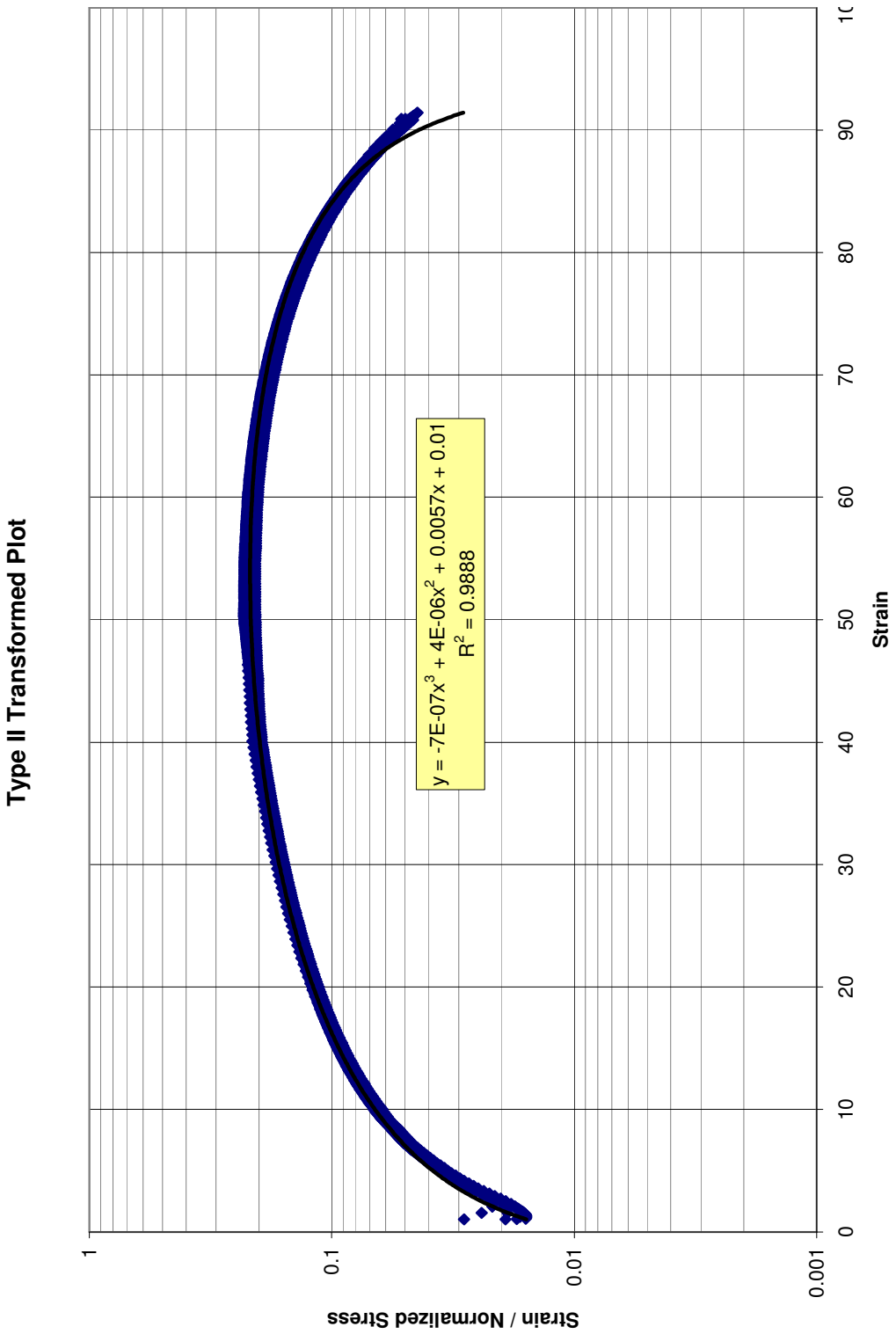

Figure 148. EPS 22 Transformed and normalized hyperbolic plot

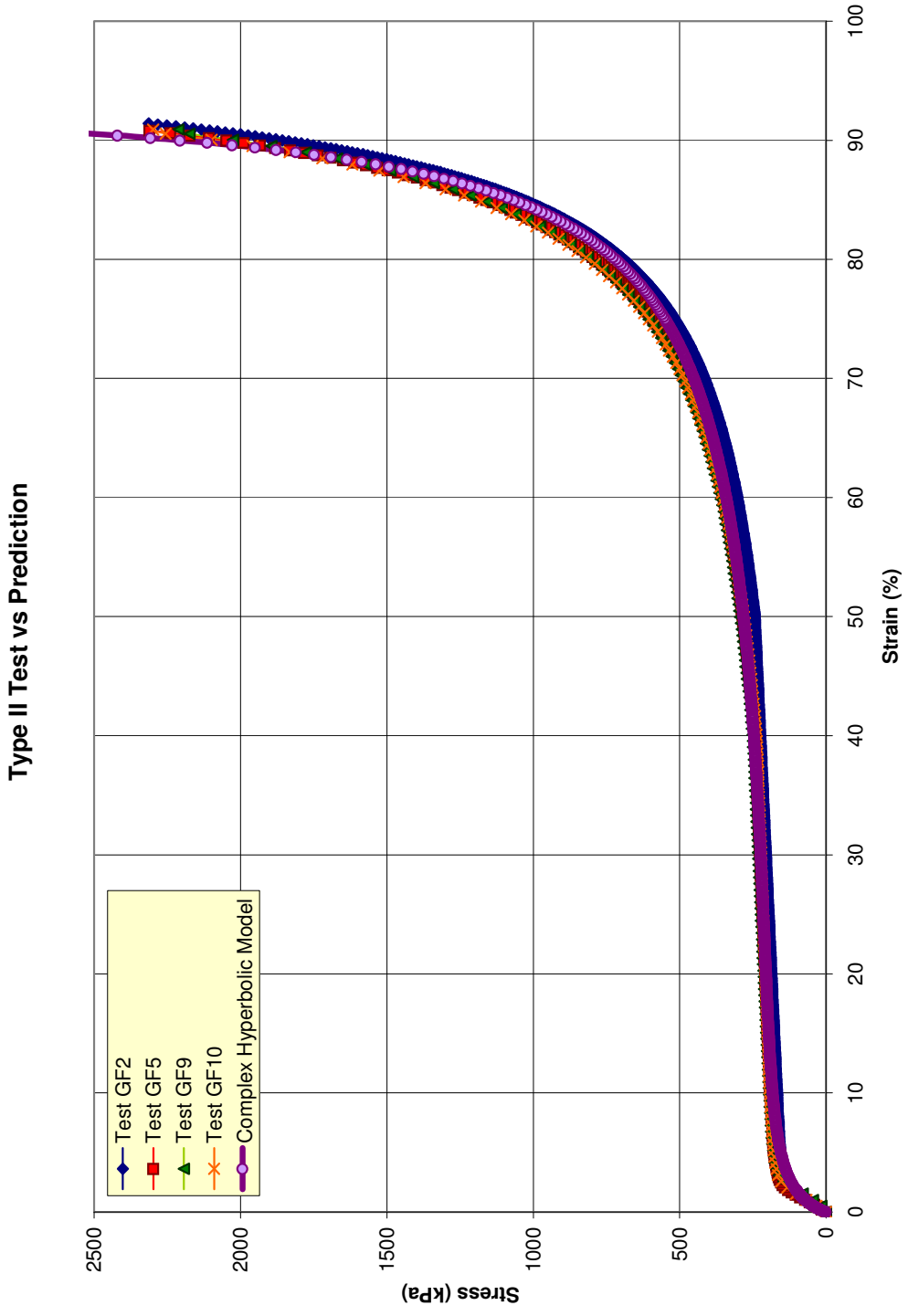

Figure 149. EPS 22 comparison stress:strain curves

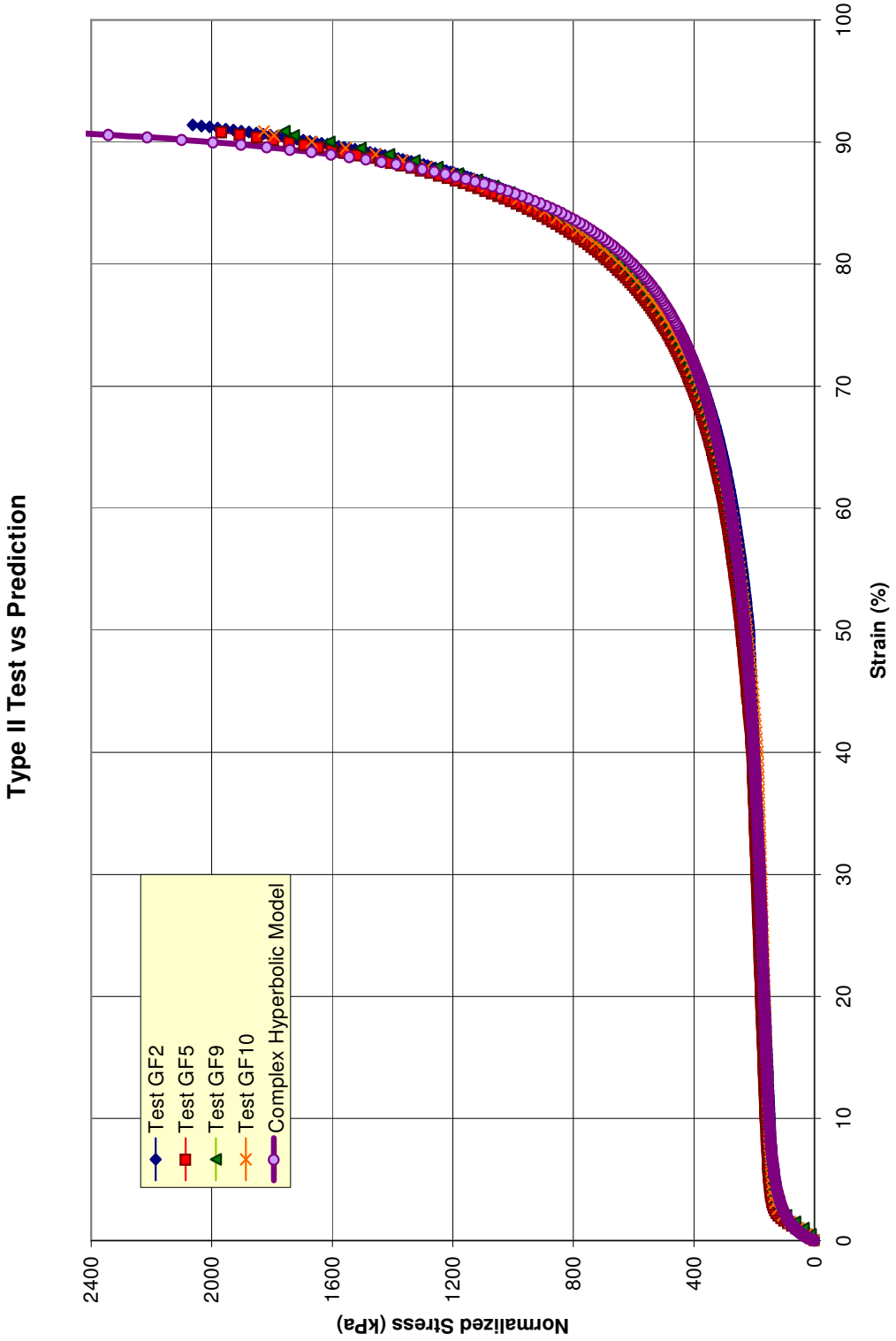

Figure 150. EPS 22 comparison normalized stress:strain curves

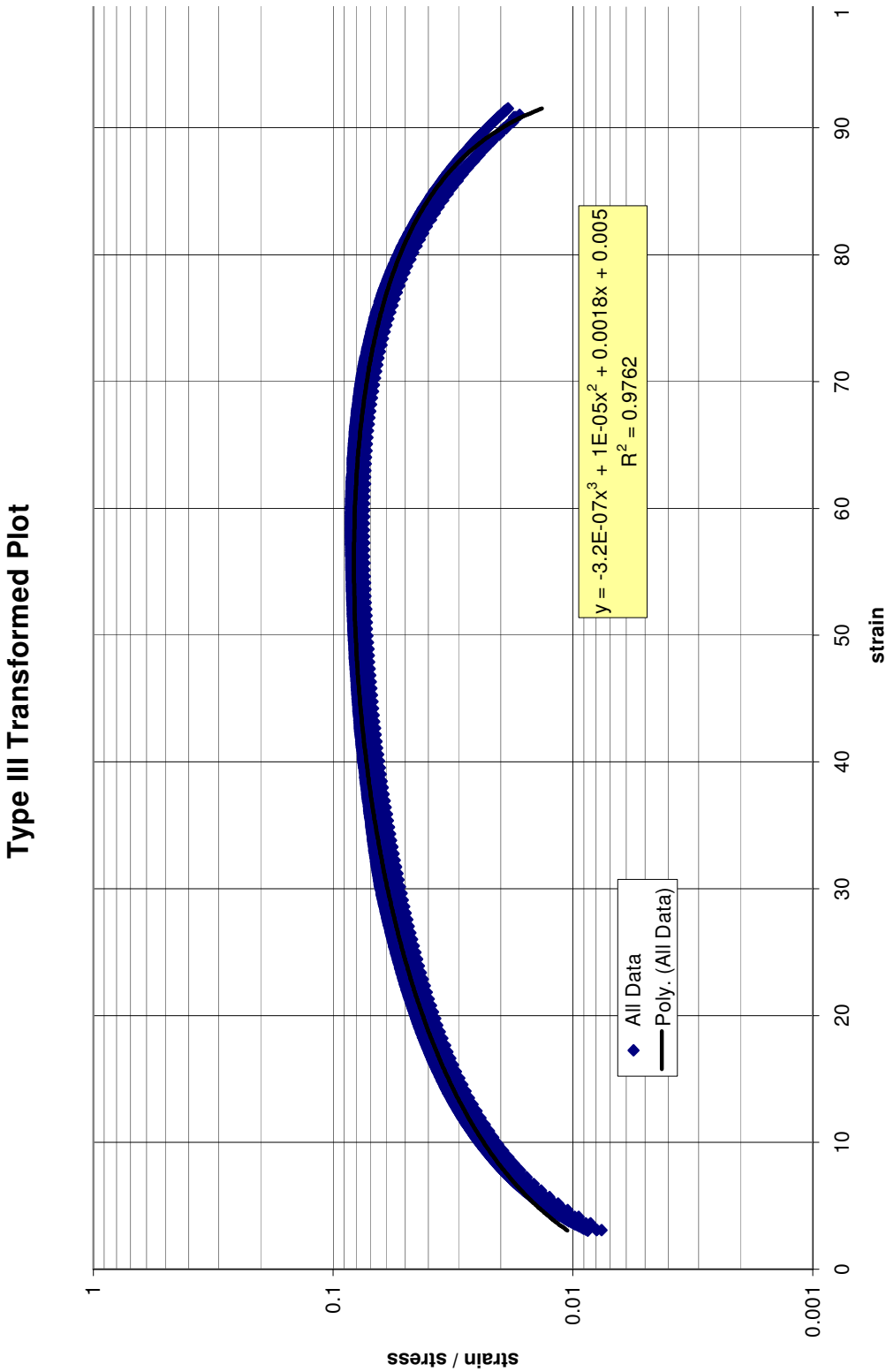

Figure 151. EPS 39 transformed hyperbolic plot

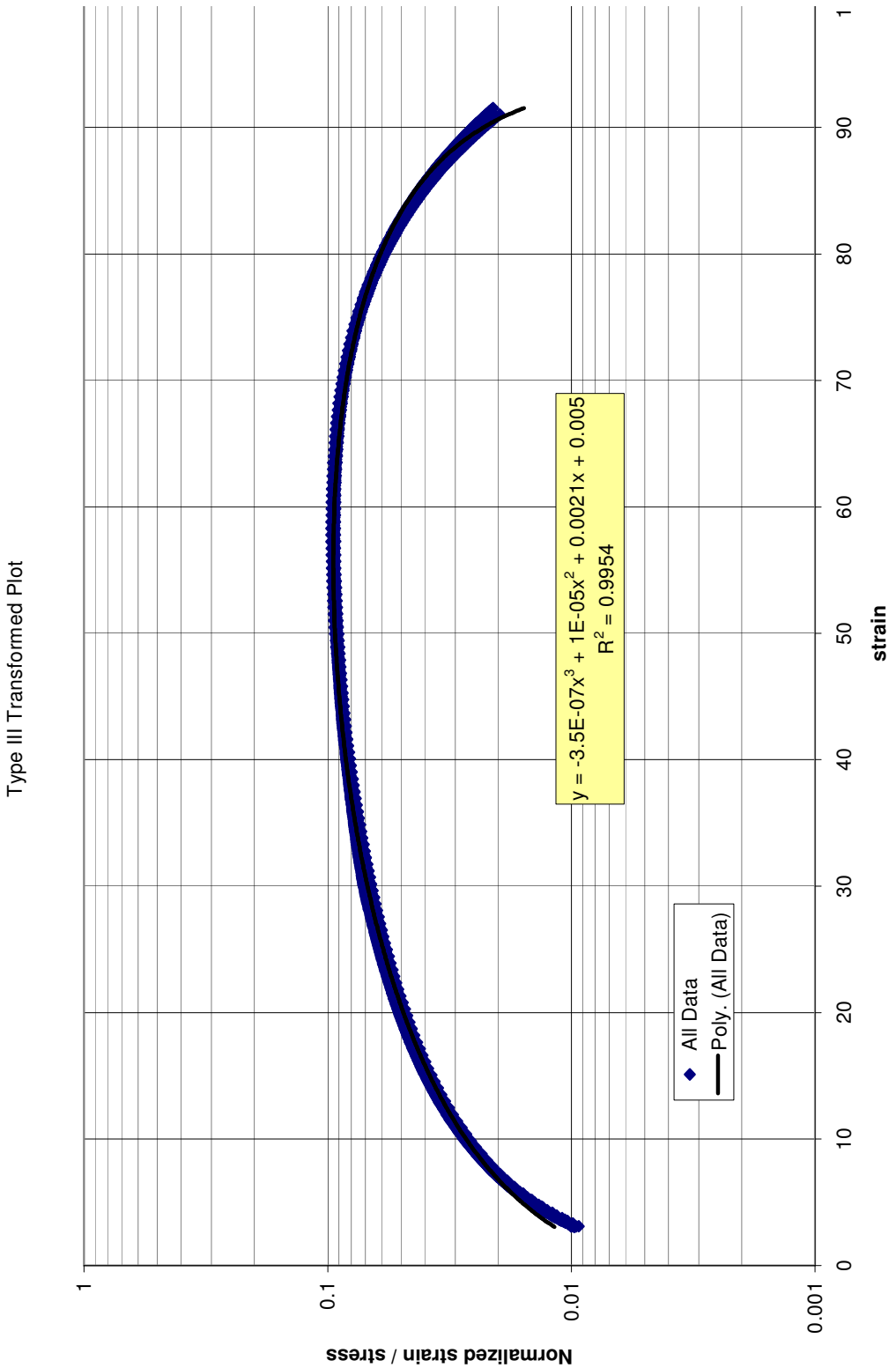

Figure 152. EPS 39 normalized transformed hyperbolic plot

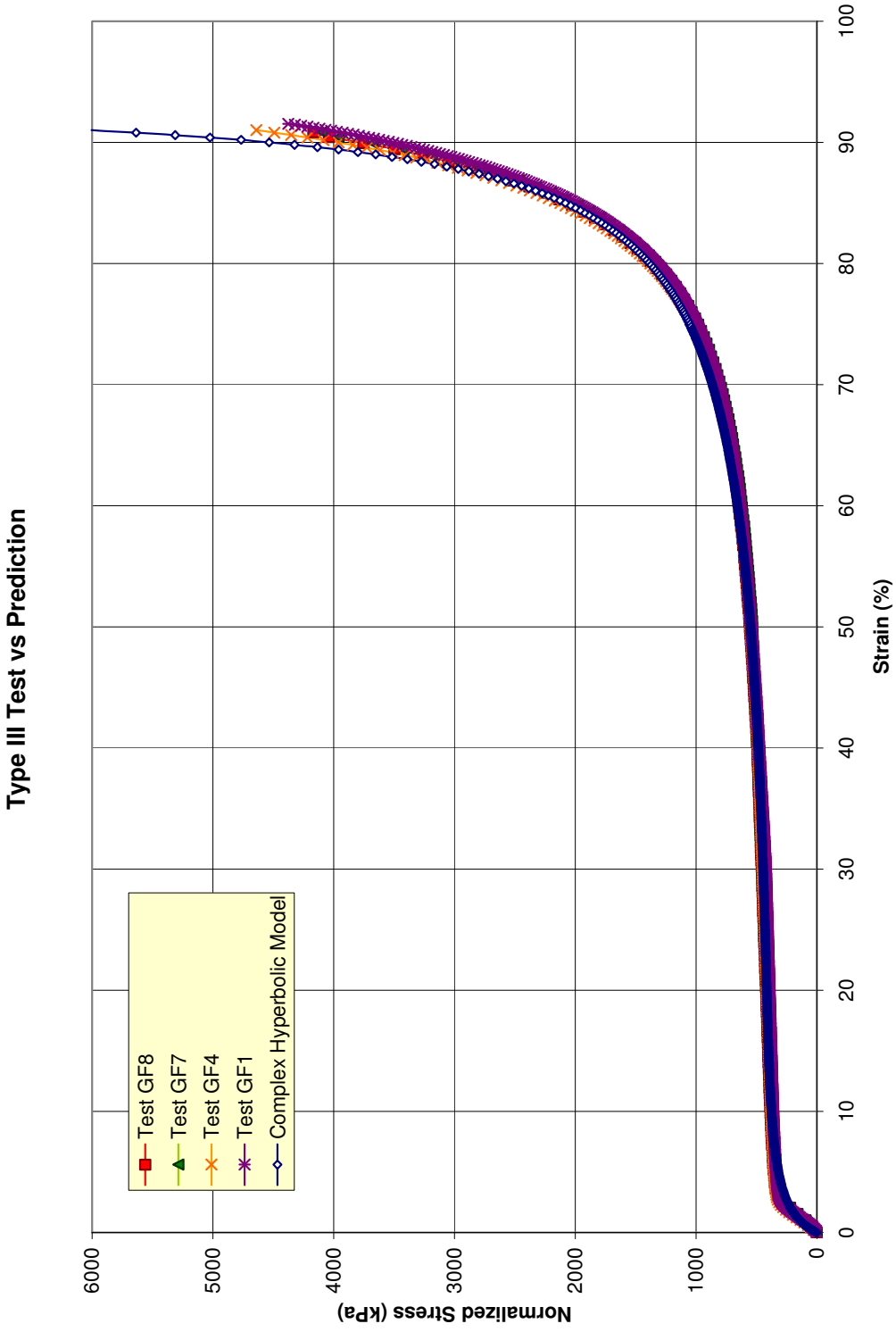

Figure 153. EPS 39 normalized compression comparison plot

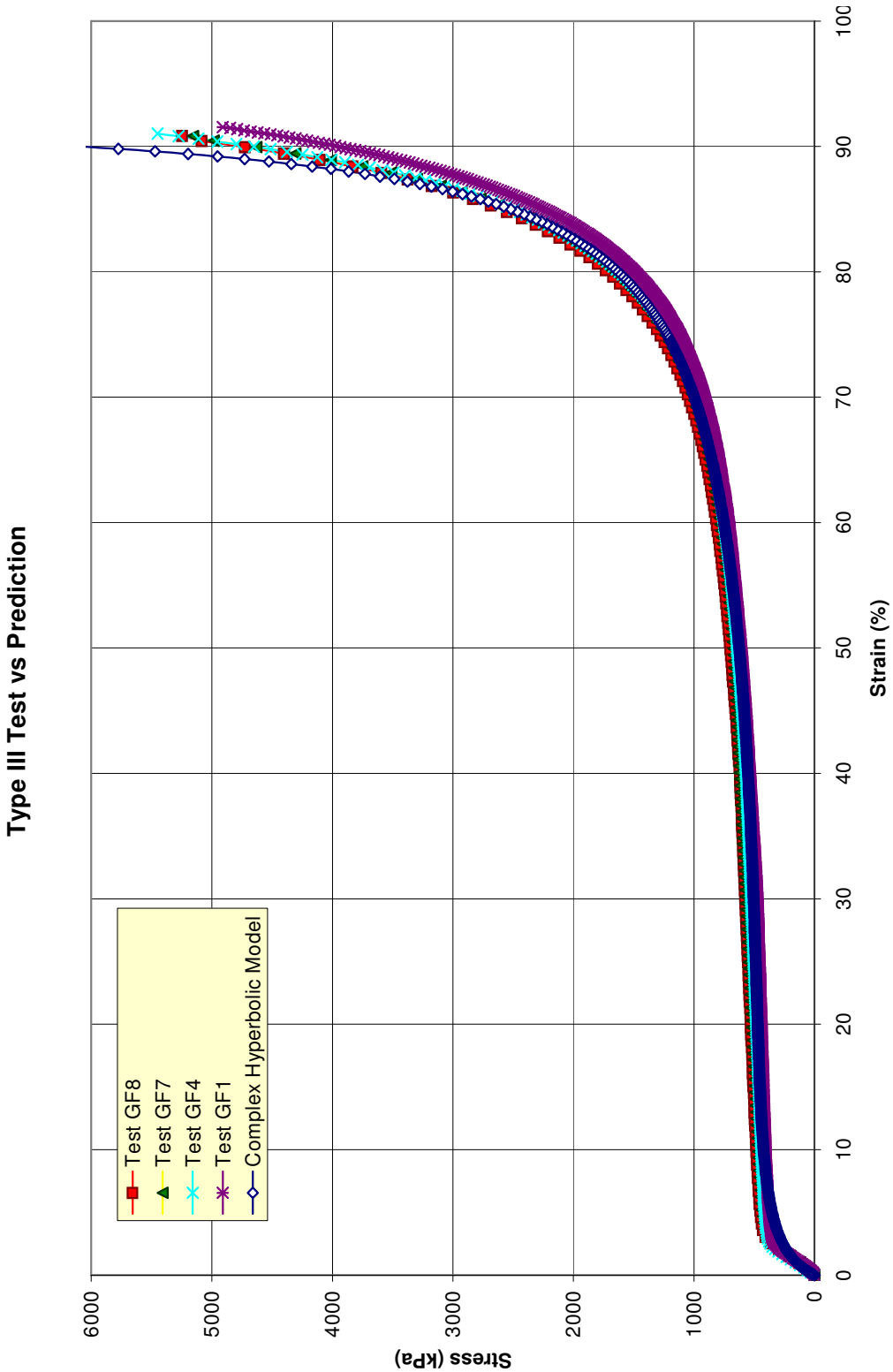

Figure 154. EPS 39 compression comparison plot

APPENDIX C

DIRECT SHEAR TESTS BETWEEN EPS GEOFOAM AND GEOMATERIALS

In an effort to better understand the mechanisms involved in the uplift field tests, a series of direct shear tests were conducted. The purpose of the tests is to find the stiffness and strength of interfaces between EPS Geofoam and the geo materials used in the uplift tests including the native trench wall materials. These tests were conducted in a standard direct shear apparatus with the Geofoam comprising one half of the test specimen. The interface between the two materials in each test was carefully aligned with the small gap between the top and bottom rings of the direct shear device. The following figures show the results of the tests. Included in the figures are the force-displacement curves as well as the Mohr-Coulomb failure envelopes found by a series of tests at different normal loads.

The native soils and clayey fill were remolded to nearly the same density and water content as the conditions of the field tests as no undisturbed samples were left after triaxial testing. The bedding sand used for the uplift tests was placed in a very loose condition by pouring the sand from a 150 mm height into the direct shear ring. Figures 155 to 159 show these laboratory test results.

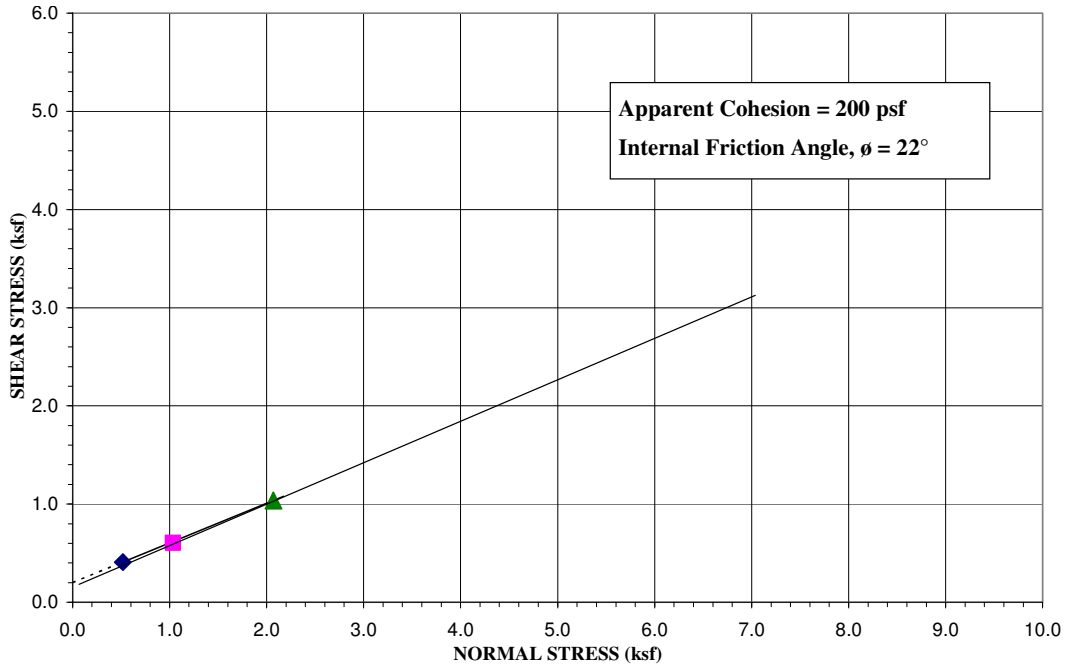

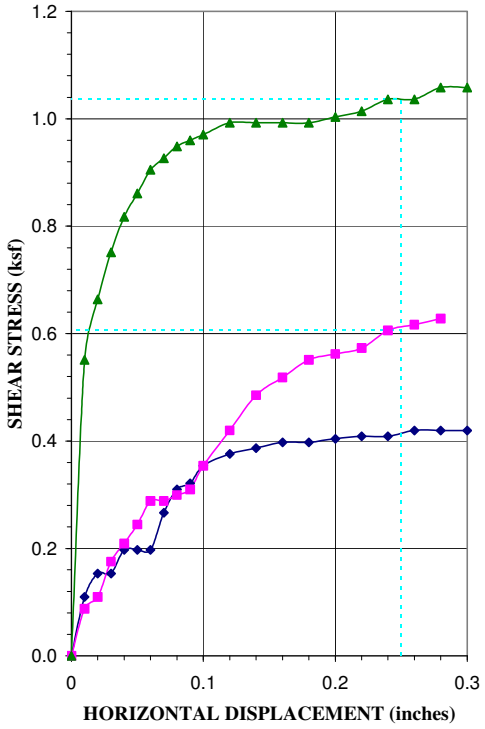

Source: B-2 @ 40'	**Depth:** 40'
Type of Test:	Consolidated Drained

Test No. (Symbol)	**1 (◆)**	**2 (■)**	**3 (▲)**
Sample Type	REMOLDED		
Height, in.	1	1	1
Diameter, in.	2.42	2.42	2.42
Dry Density Before, pcf		#DIV/0!	#DIV/0!
Dry Density After, pcf		1591.1	104.6
Moisture % Before		#DIV/0!	#DIV/0!
Moisture % After		19.0	19.0
Consolidation Load, kg	0.8	1.5	3.0
Normal Load, ksf	0.52	1.04	2.07
Shear Stress, ksf	0.41	0.61	1.04
Strain Rate	0.8 mm/min		

Sample Properties	
Liquid Limit, %	---
Plasticity Index, %	---
Cohesion, psf	200
Friction Angle, ϕ	22
Percent Gravel	---
Percent Sand	---
Percent Passing No. 200 sieve	---
Classification	EPS 15 and Native Clay

Figure 155. Direct shear results between EPS 15 and native clay

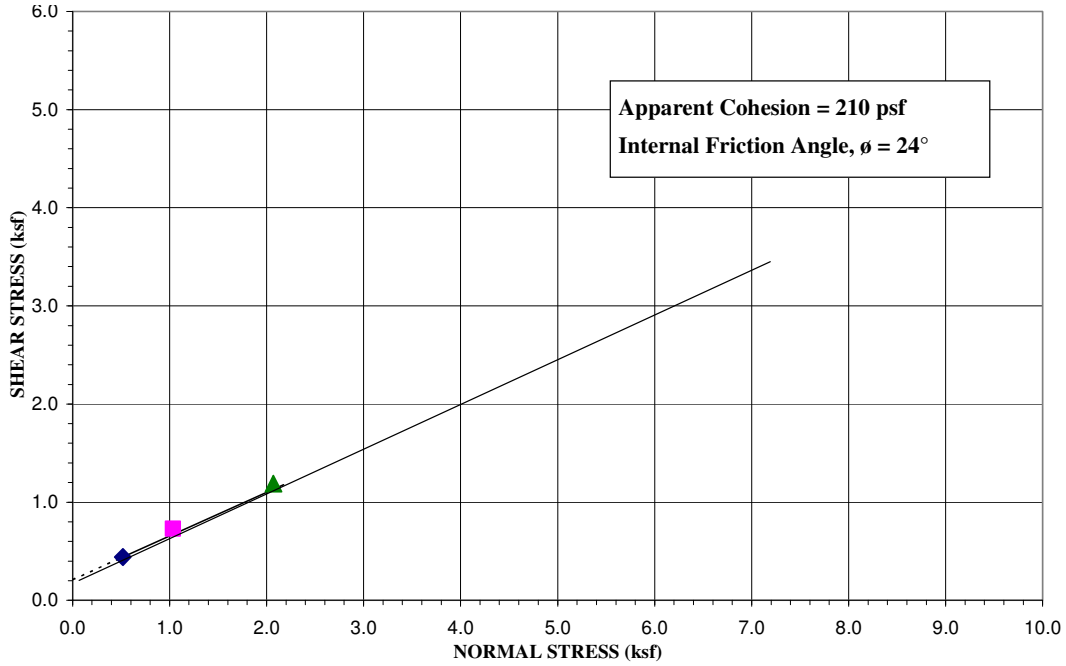

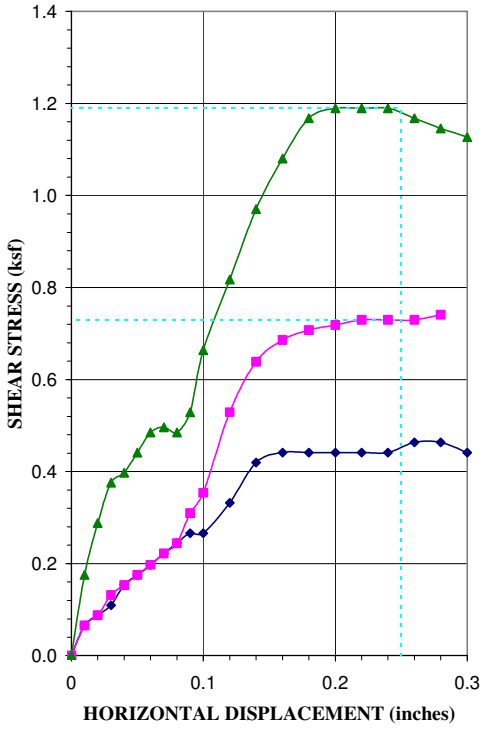

Source: B-2 @ 40'	**Depth:** 40'
Type of Test:	Consolidated Drained

Test No. (Symbol)	**1 (◆)**	**2 (■)**	**3 (▲)**
Sample Type	REMOLDED		
Height, in.	1	1	1
Diameter, in.	2.42	2.42	2.42
Dry Density Before, pcf		#DIV/0!	#DIV/0!
Dry Density After, pcf		1591.1	104.6
Moisture % Before		#DIV/0!	#DIV/0!
Moisture % After		19.0	19.0
Consolidation Load, kg	0.8	1.5	3.0
Normal Load, ksf	0.52	1.04	2.07
Shear Stress, ksf	0.44	0.73	1.19
Strain Rate	0.8 mm/min		

Sample Properties	
Liquid Limit, %	---
Plasticity Index, %	---
Cohesion, psf	210
Friction Angle, ϕ	24
Percent Gravel	---
Percent Sand	---
Percent Passing No. 200 sieve	---
Classification	EPS 12 and Native Clay

Figure 156. Direct shear results for EPS 22 and native clay

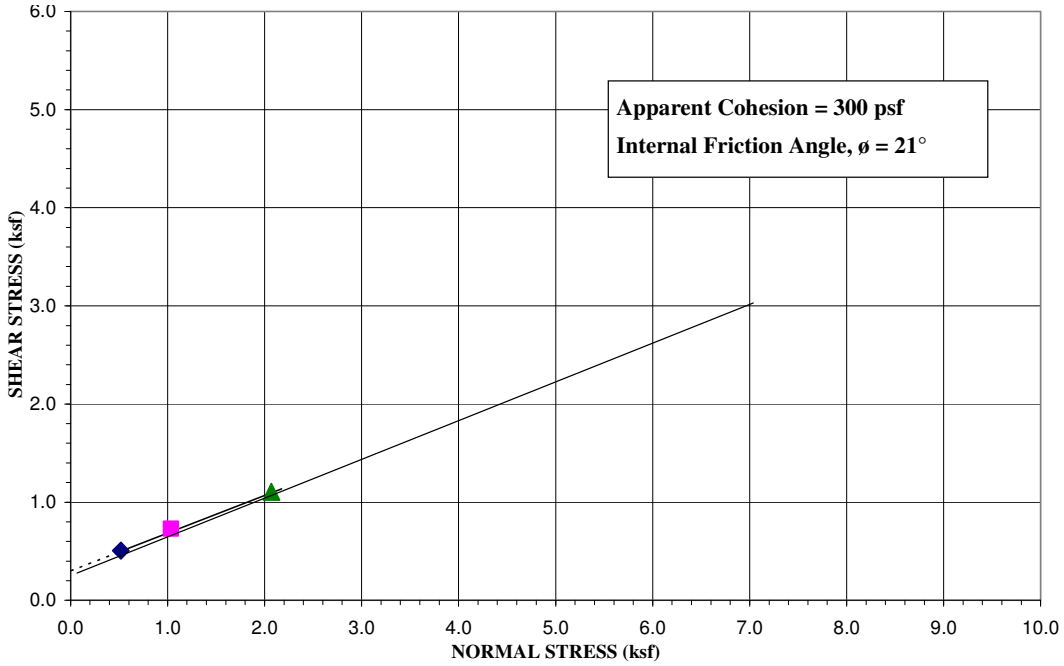

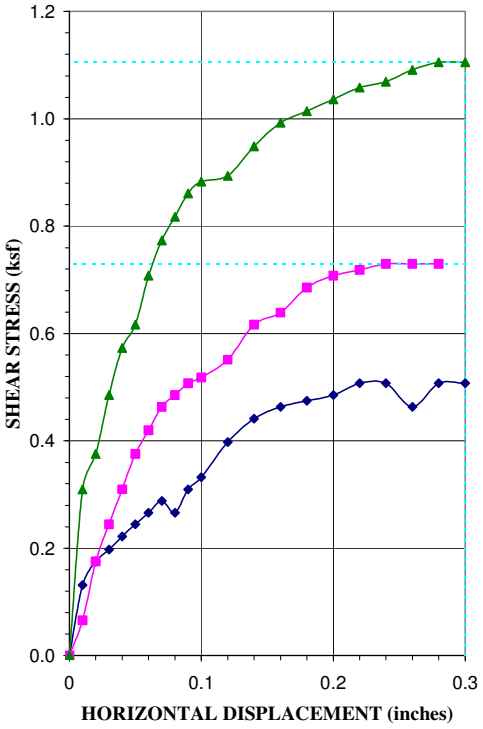

Source: B-2 @ 40'	**Depth:** 40'
Type of Test:	Consolidated Drained

Test No. (Symbol)	**1 (◆)**	**2 (■)**	**3 (▲)**
Sample Type	REMOLDED		
Height, in.	1	1	1
Diameter, in.	2.42	2.42	2.42
Dry Density Before, pcf		#DIV/0!	#DIV/0!
Dry Density After, pcf		1591.1	104.6
Moisture % Before		#DIV/0!	#DIV/0!
Moisture % After		19.0	19.0
Consolidation Load, kg	0.8	1.5	3.0
Normal Load, ksf	0.52	1.04	2.07
Shear Stress, ksf	0.51	0.73	1.11
Strain Rate	0.8 mm/min		

Sample Properties	
Liquid Limit, %	---
Plasticity Index, %	---
Cohesion, psf	300
Friction Angle, ϕ	21
Percent Gravel	---
Percent Sand	---
Percent Passing No. 200 sieve	---
Classification	EPS 15 and Clayey Fill

Figure 157. Direct shear results for EPS 15 and clayey fill

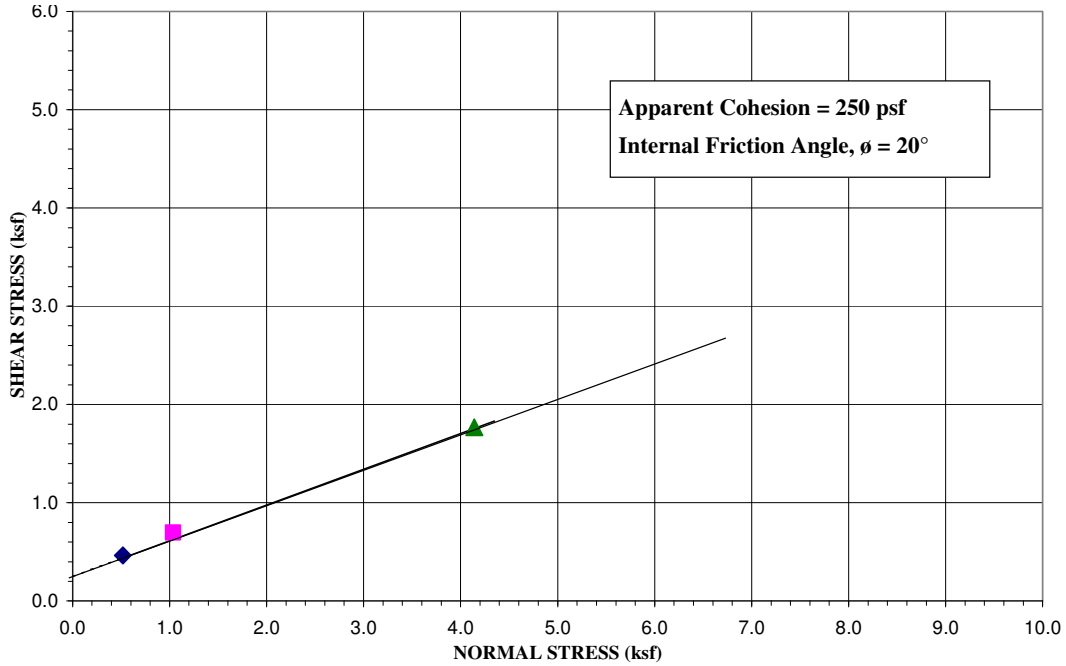

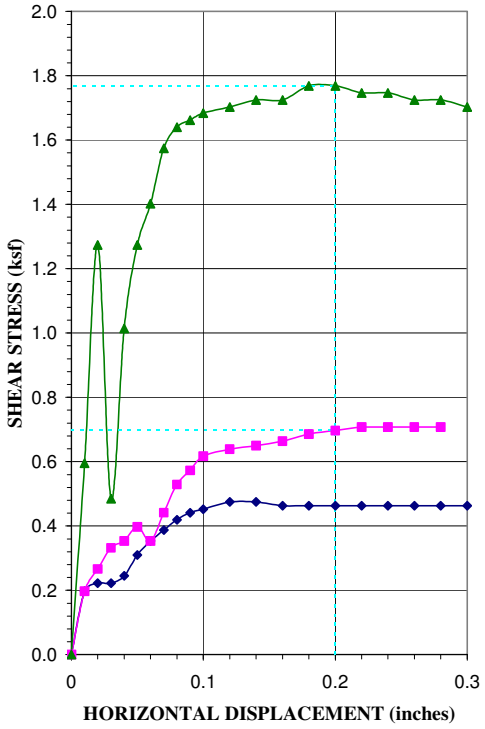

Source: B-2 @ 40'	Depth: 40'
Type of Test:	Consolidated Drained

Test No. (Symbol)	1 (◆)	2 (■)	3 (▲)
Sample Type	REMOLDED		
Height, in.	1	1	1
Diameter, in.	2.42	2.42	2.42
Dry Density Before, pcf		#DIV/0!	#DIV/0!
Dry Density After, pcf		1591.1	104.6
Moisture % Before		#DIV/0!	#DIV/0!
Moisture % After		19.0	19.0
Consolidation Load, kg	0.8	1.5	6.0
Normal Load, ksf	0.52	1.04	4.14
Shear Stress, ksf	0.46	0.70	1.77
Strain Rate	0.8 mm/min		

Sample Properties	
Liquid Limit, %	---
Plasticity Index, %	---
Cohesion, psf	250
Friction Angle, ϕ	20
Percent Gravel	---
Percent Sand	---
Percent Passing No. 200 sieve	---
Classification	EPS 22 and Clayey Fill

Figure 158. Direct shear results for EPS 22 and clayey fill

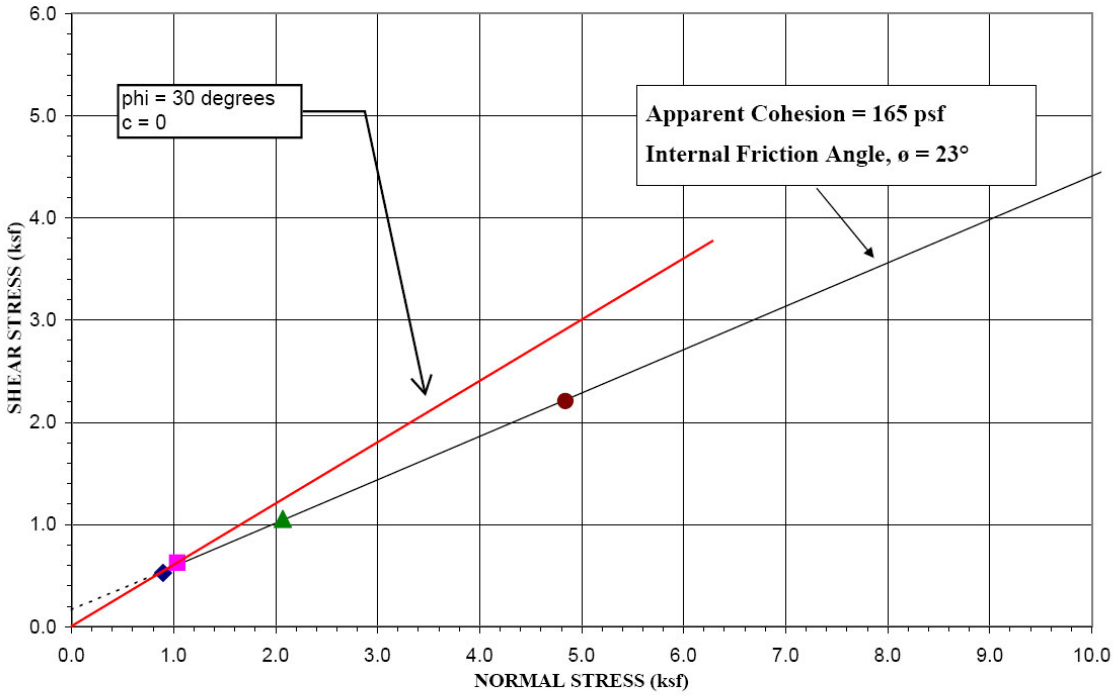

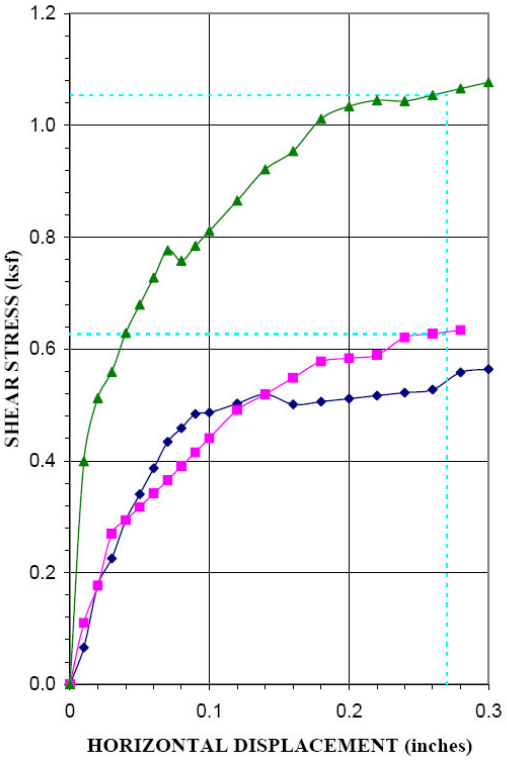

Source: B-2 @ 40'	**Depth:** 40'
Type of Test:	Consolidated Drained

Test No. (Symbol)	**1 (◆)**	**2 (■)**	**3 (▲)**
Sample Type	REMOLDED		
Height, in.	1	1	1
Diameter, in.	2.42	2.42	2.42
Dry Density Before, pcf		#DIV/0!	#DIV/0!
Dry Density After, pcf		1591.1	104.6
Moisture % Before		#DIV/0!	#DIV/0!
Moisture % After		19.0	19.0
Consolidation Load, kg	1.3	1.5	3.0
Normal Load, ksf	0.90	1.04	2.07
Shear Stress, ksf	0.53	0.63	1.05
Strain Rate	0.8 mm/min		

Sample Properties	
Liquid Limit, %	---
Plasticity Index, %	---
Cohesion, psf	165
Friction Angle, ϕ	23
Percent Gravel	---
Percent Sand	---
Percent Passing No. 200 sieve	---
Classification	Sand (SC)

Figure 159. Direct shear results for EPS 15 and bedding sand

APPENDIX D

TRIAXIAL SOIL TEST DATA PLOTS FOR FIELD UPLIFT TESTS

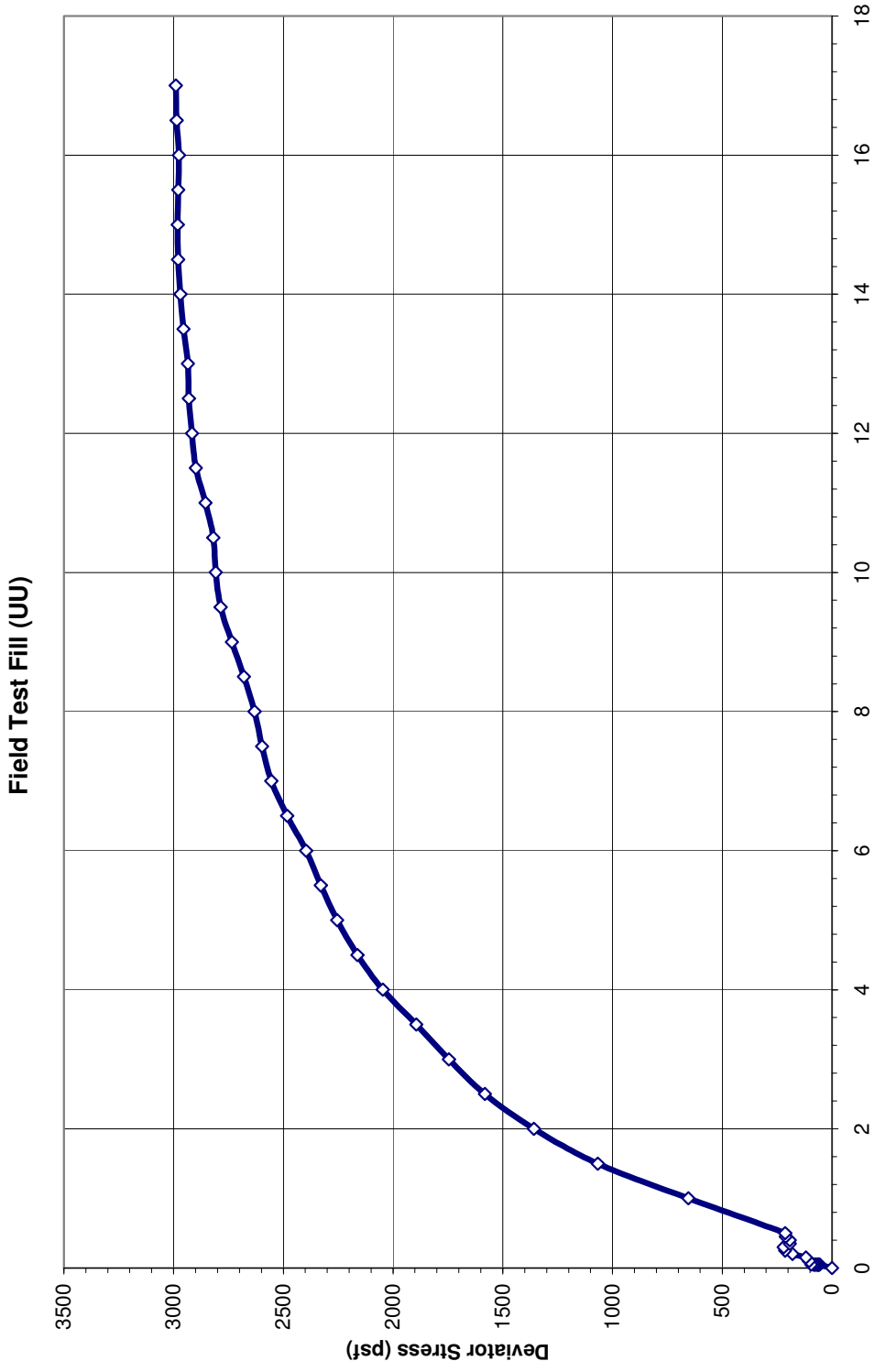

Figure 160. Clayey fill UU triaxial test data

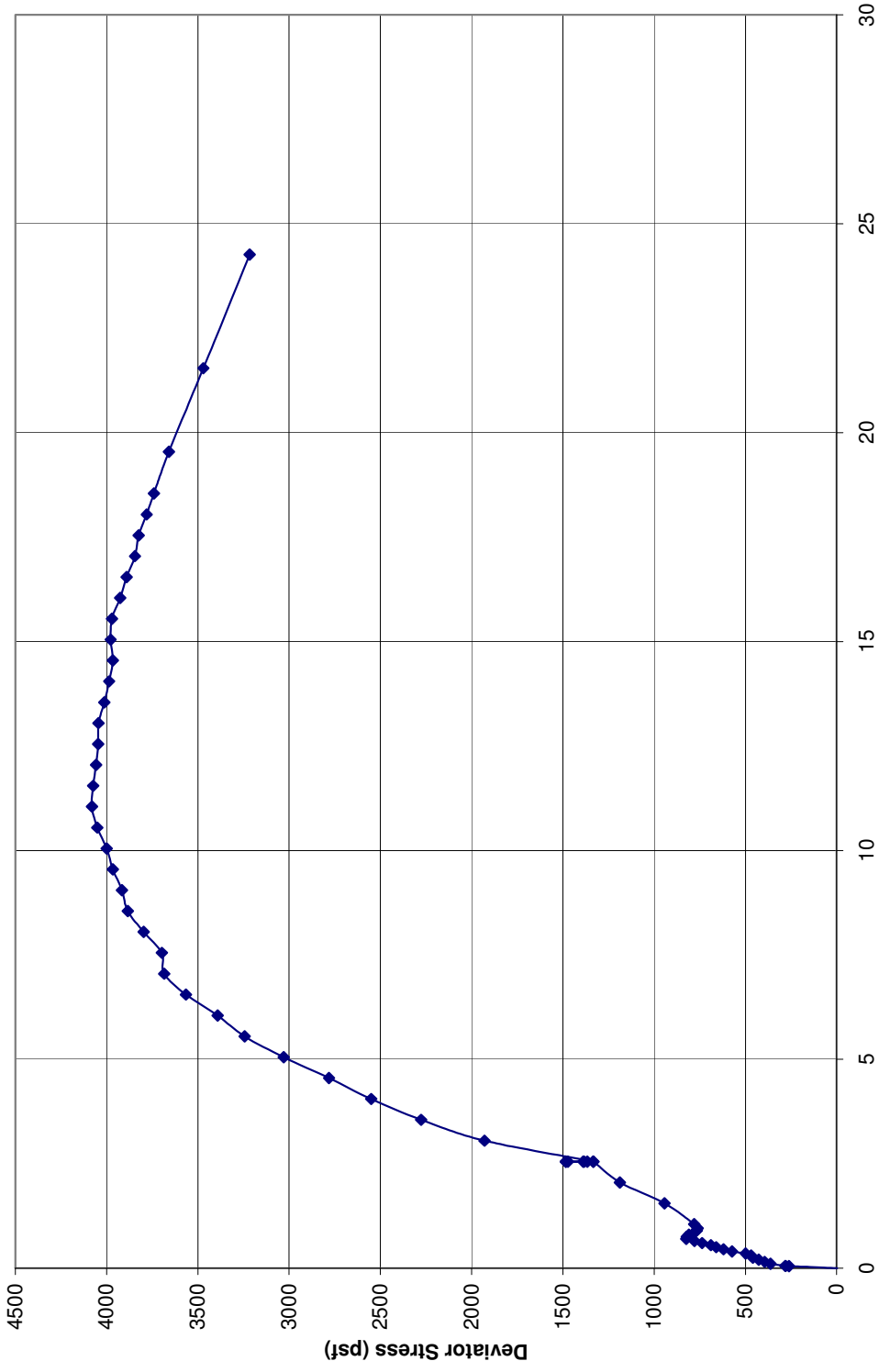

Figure 161. Clayey fill CD saturated triaxial test data

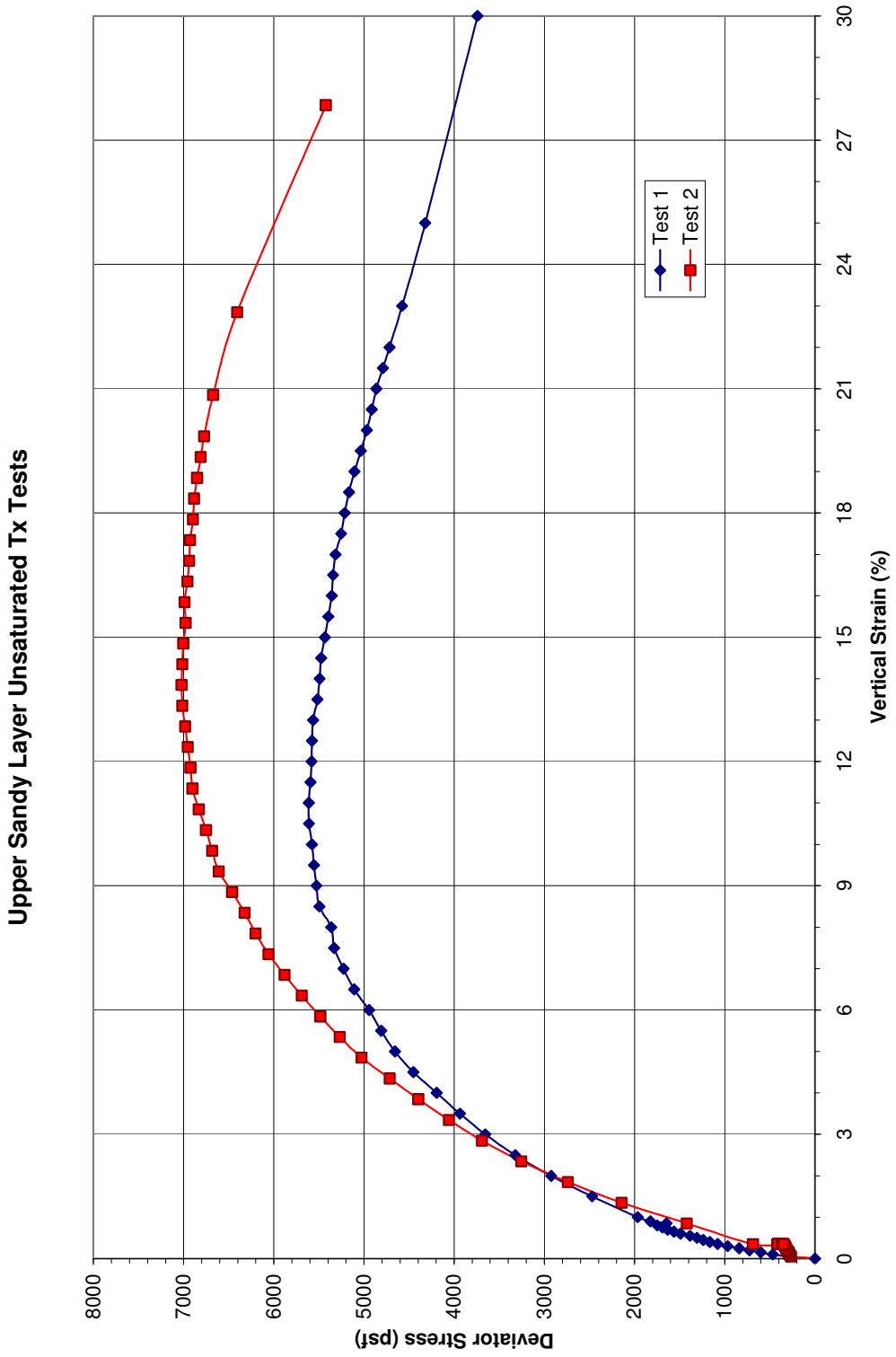

Figure 162. Triaxial test data for upper sand CD unsaturated

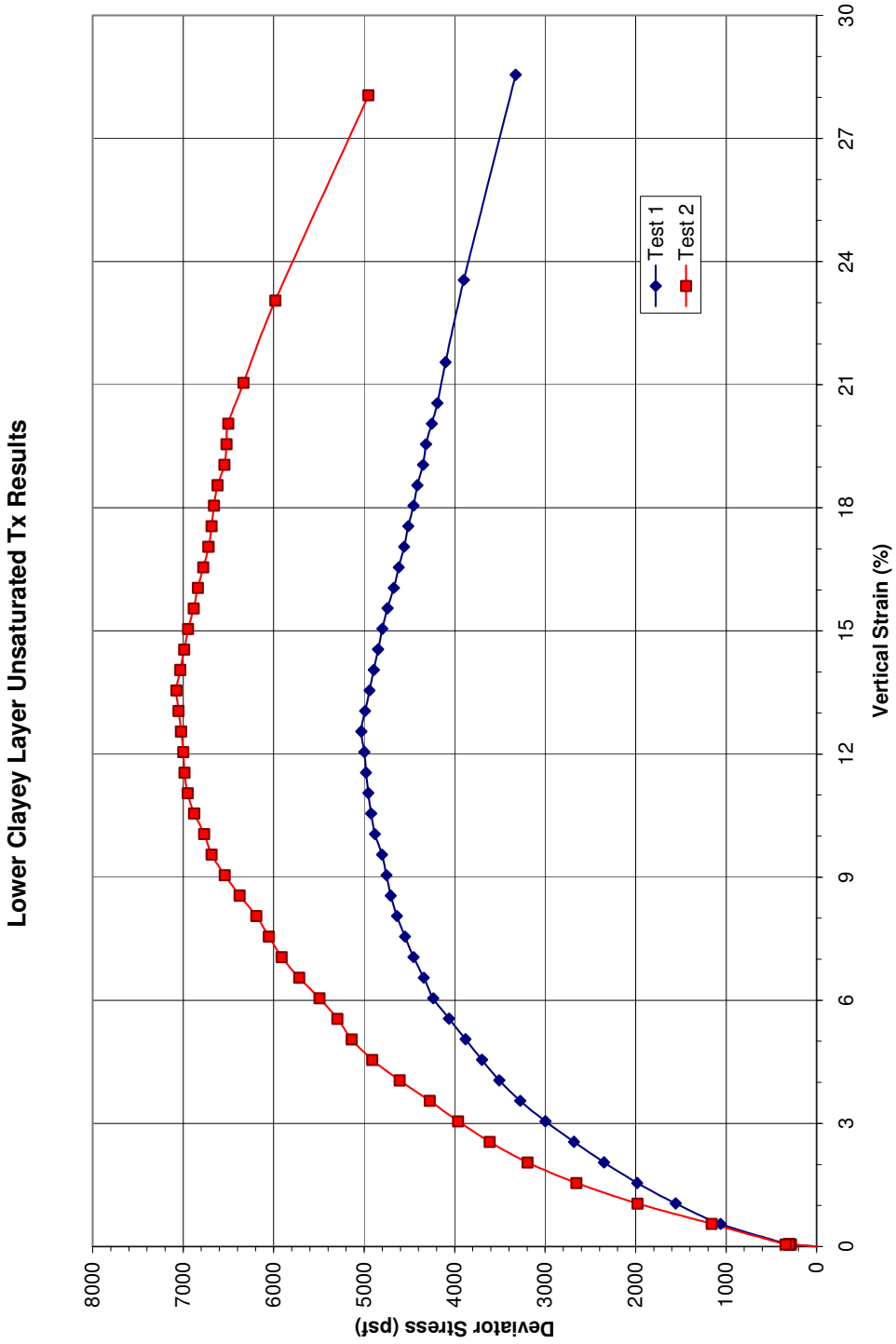

Figure 163. Triaxial test data for lower clay CD unsaturated

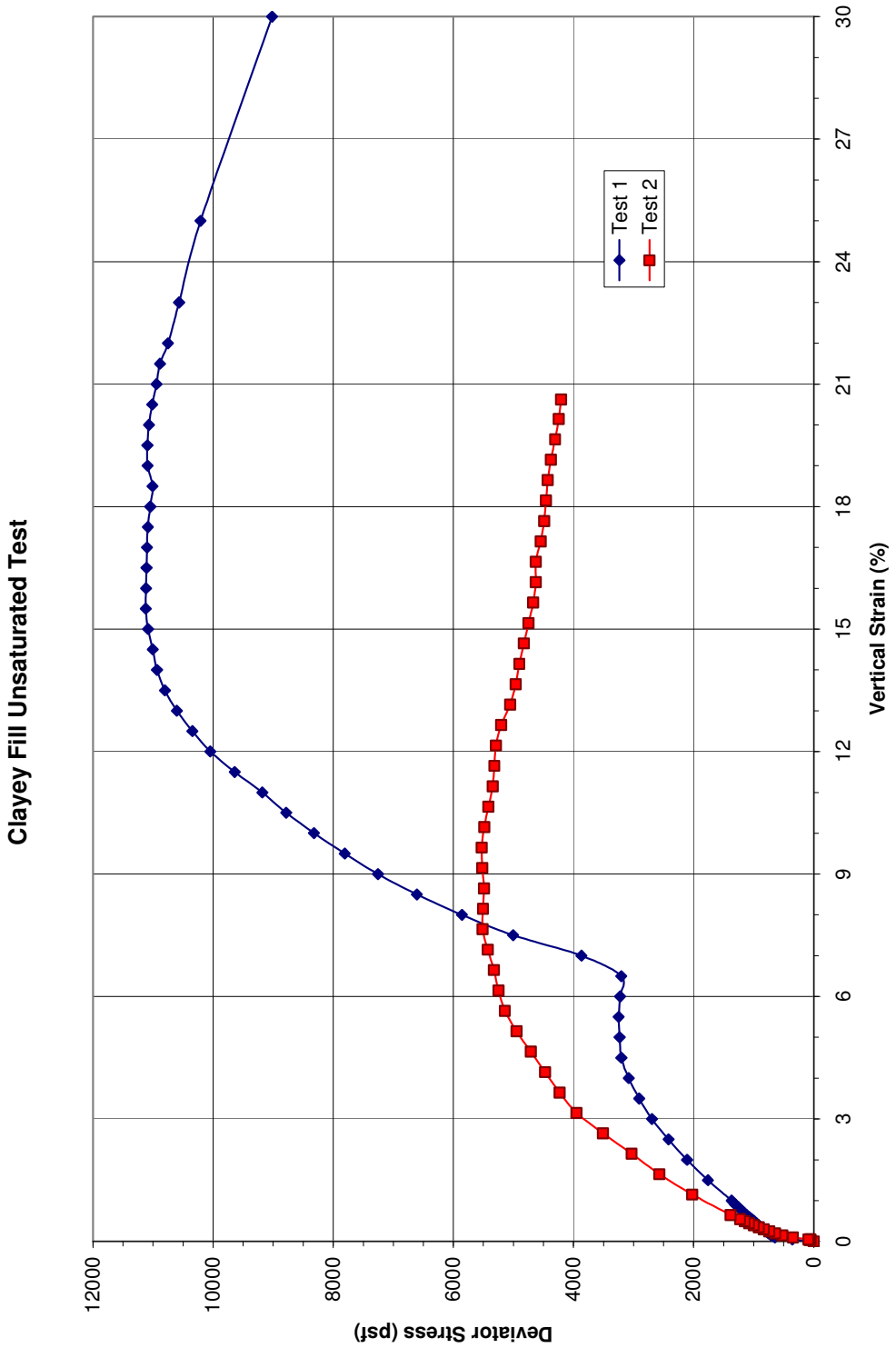

Figure 164. Triaxial test data for clayey fill CD unsaturated

APPENDIX E

CYCLIC TESTING OF EPS GEOFOAM

A series of cyclic triaxial tests were conducted on EPS Geofoam cylinders as part of the testing program of this research project. Doctor Aurel Trandafir of the University of Utah's Geology Department conducted this part of the research program. The cyclic triaxial test cycles the specimen rapidly at relatively small strains, simulating earthquake and other rapid dynamic cyclic loading of the EPS. These tests were conducted at the University of Utah's Geologic Engineering Laboratory.

Test Equipment

A cyclic triaxial apparatus manufactured by Geocomp Corporation (Massachusetts Ave., Boxborough, MA) was used in this investigation to study the cyclic stress-strain behavior of EPS Geofoam. This is fully-automated equipment which can be employed to carry out both cyclic and static triaxial tests on cylindrical specimens utilizing cyclic and triaxial software, respectively. Once the specimen to be tested was placed in the triaxial device and the test conditions are selected, the cyclic triaxial system runs all of the phases automatically. Test data were stored in a file for subsequent reduction and plotting by way of a report capability built into the software. Different parts of the cyclic triaxial

apparatus are shown in Figure 165. Figure 166 shows a photo of the cyclic triaxial equipment utilized in the present experimental program.

Materials and Testing Procedure

Stress-controlled cyclic uniaxial tests were conducted on 3 types of EPS specimens characterized by nominal densities of 15 kg/m^3 (EPS15), 22 kg/m^3 (EPS22) and 39 kg/m^3 (EPS39). The tests involved EPS cylinders with a diameter of 50 mm and a height to diameter ratio of 2:1 (Figure 167). An initial static deviator stress ($(\sigma_a - \sigma_r)_{static}$) with a magnitude greater than the amplitude of the applied cyclic deviator stress ($\Delta(\sigma_a - \sigma_r)_{cyclic}$) was imposed on the specimen prior to starting cyclic loading. The term σ_a is the vertical, axial, compressive stress on the specimen, and σ_r is the lateral confining stress.

The cyclic phase started after the specimen attained equilibrium under the applied static deviator stress. All cyclic tests were performed under zero confining pressure. The amplitude of the applied cyclic deviator stress ranged within 5 kPa to 39 kPa, and the loading frequency was 0.5 Hz. The number of loading cycles in the triaxial tests. Table 39 summarizes the parameters of each cyclic test, along with the type and the actual measured density of the corresponding EPS specimen.

Figures 168 to 170 show the position of the initial deviator stress points for cyclic uniaxial tests on the stress-strain curve derived from uniaxial monotonic loading with a strain rate of 5%/min for each type of EPS. For EPS15, points A1 and B1 correspond to static deviator stresses representing 45% and 76% of the deviator stress at yield, $(\sigma_a - \sigma_r)_{yield}$ (Figure 169). Points A2, B2 and C2 characterizing the initial stress conditions for

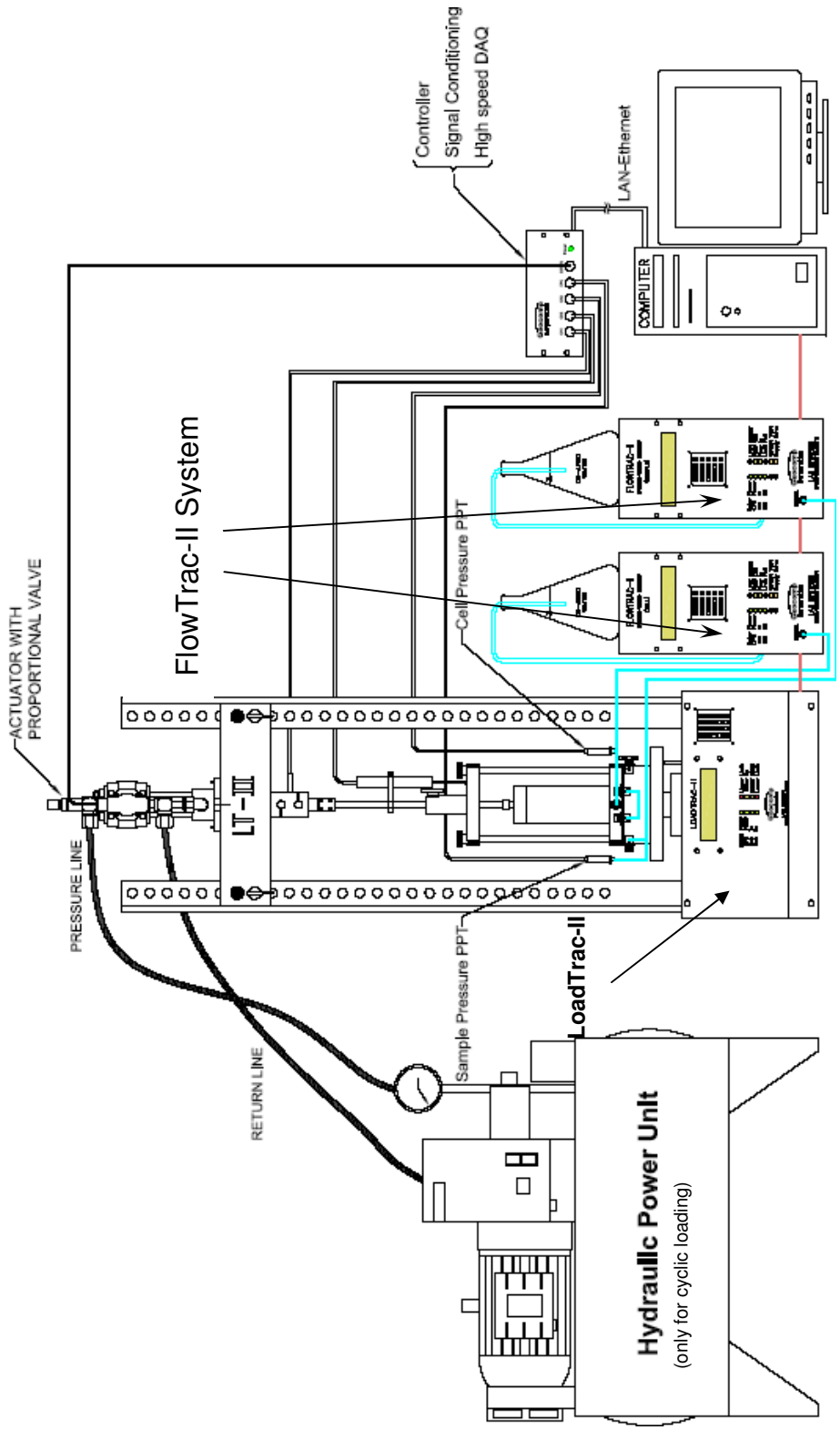

Figure 165. Set-up of the cyclic triaxial equipment available in the Soil Mechanics Laboratory, Department of Geology and Geophysics, University of Utah (after Geocomp Corporation, 2006)

Figure 166. Photo of the cyclic triaxial equipment available in the Soil Mechanics Laboratory, Department of Geology and Geophysics, University of Utah

Table 39. Cyclic test parameters, and type and measured density of tested EPS specimens

Test no.	EPS type	EPS density (kg/m^3)	$(\sigma_a - \sigma_r)_{static}$ (kPa)	$\Delta(\sigma_a - \sigma_r)_{cyclic}$ (kPa)	Frequency, f (Hz)	Number of cycles, N
1-1	EPS15	14.9	15 (Point A1 in Fig. 4)	13	0.5	20
1-2*)	EPS15	14.9	25 (Point B1 in Fig. 4)	10	0.5	20
2-1	EPS22	24.9	21 (Point A2 in Fig. 5)	20	0.5	20
2-2	EPS22	24.9	42 (Point B2 in Fig. 5)	39	0.5	20
2-3	EPS22	24.9	76 (Point C2 in Fig. 5)	38	0.5	20
3-1	EPS39	52.0	21 (Point A3 in Fig. 6)	20	0.5	20
3-2	EPS39	52.0	41 (Point B3 in Fig. 6)	39	0.5	20
3-3	EPS39	52.0	81 (Point C3 in Fig. 6)	39	0.5	20
4-1	EPS22	31.8	40 (Point B2 in Fig. 5)	5	0.5	5
4-2	EPS22	31.8	40 (Point B2 in Fig. 5)	10	0.5	5
4-3	EPS22	31.8	40 (Point B2 in Fig. 5)	15	0.5	5
4-4	EPS22	31.8	40 (Point B2 in Fig. 5)	20	0.5	5
4-5	EPS22	31.8	40 (Point B2 in Fig. 5)	25	0.5	5
4-6	EPS22	31.8	40 (Point B2 in Fig. 5)	35	0.5	10
4-7	EPS22	31.8	40 (Point B2 in Fig. 5)	39	0.5	10

**) The specimen did not achieve equilibrium under the applied static deviator stress, and was still yielding at the beginning of the cyclic loading phase. The cyclic phase started just before the triaxial equipment reached the axial strain limit for monotonic loading.*

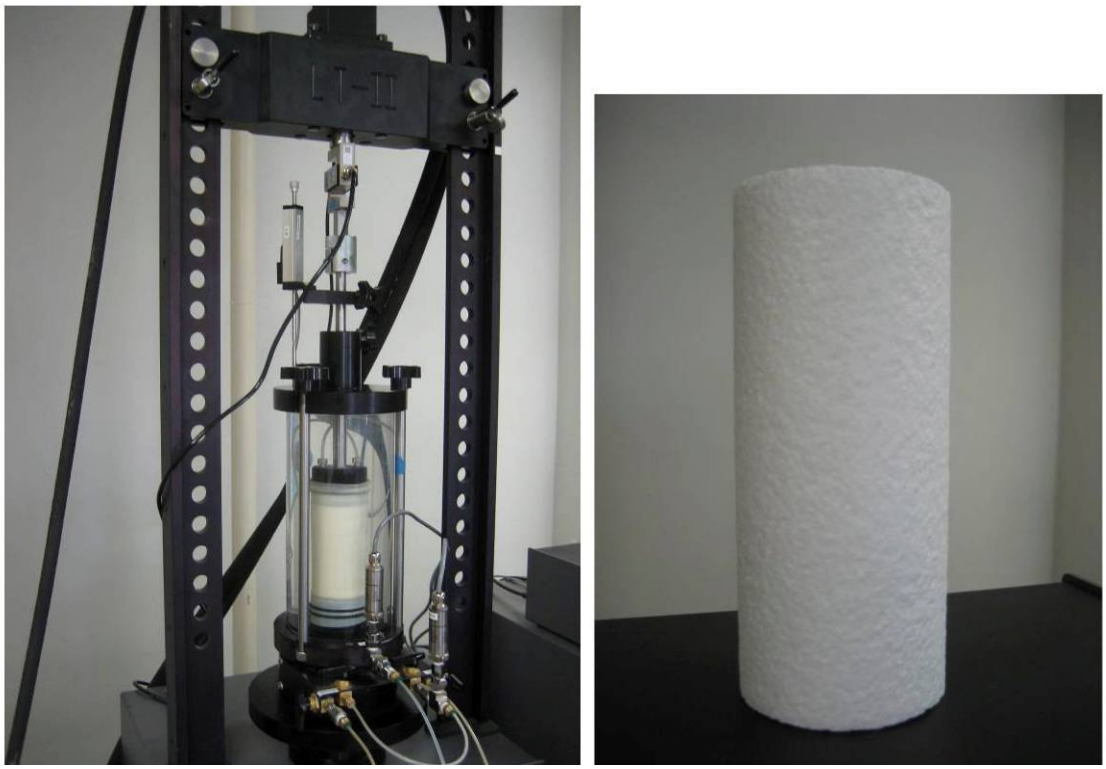

Figure 167. EPS cylindrical specimen subjected to cyclic uniaxial testing

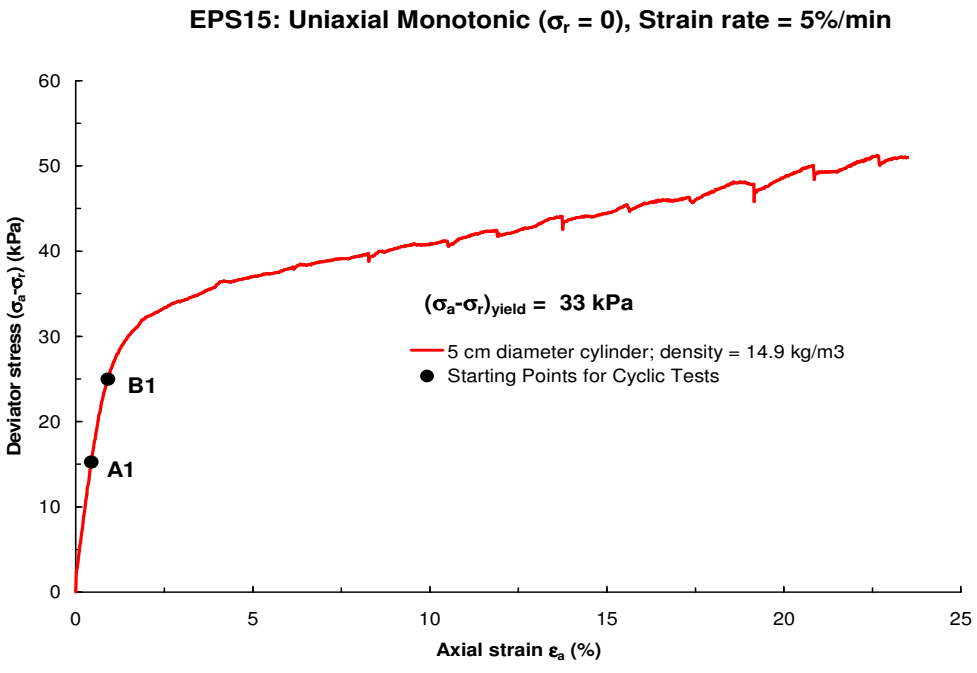

Figure 168. Uniaxial monotonic test result on EPS15

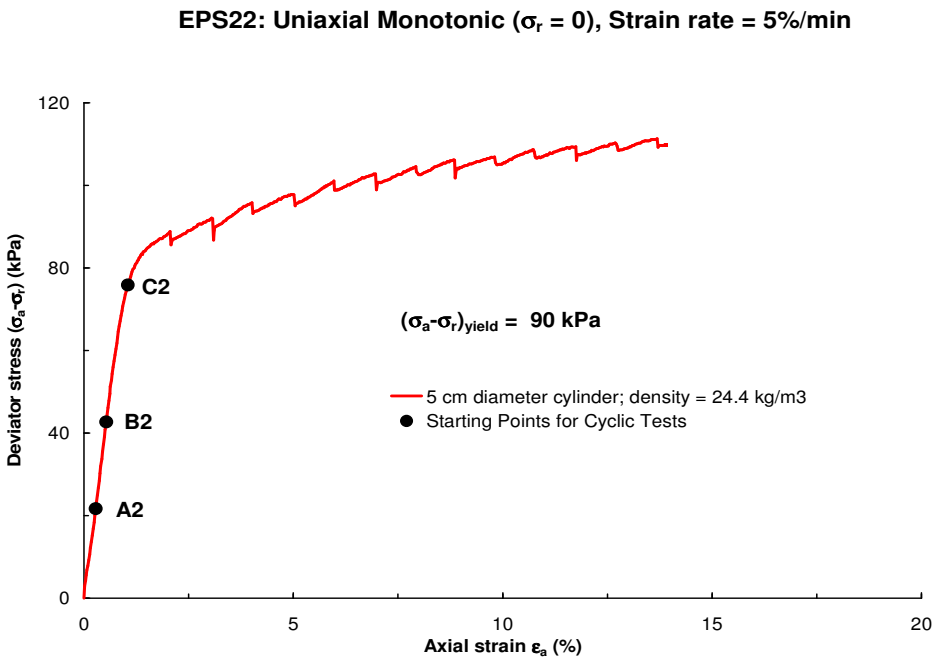

Figure 169. Uniaxial monotonic test result on EPS22

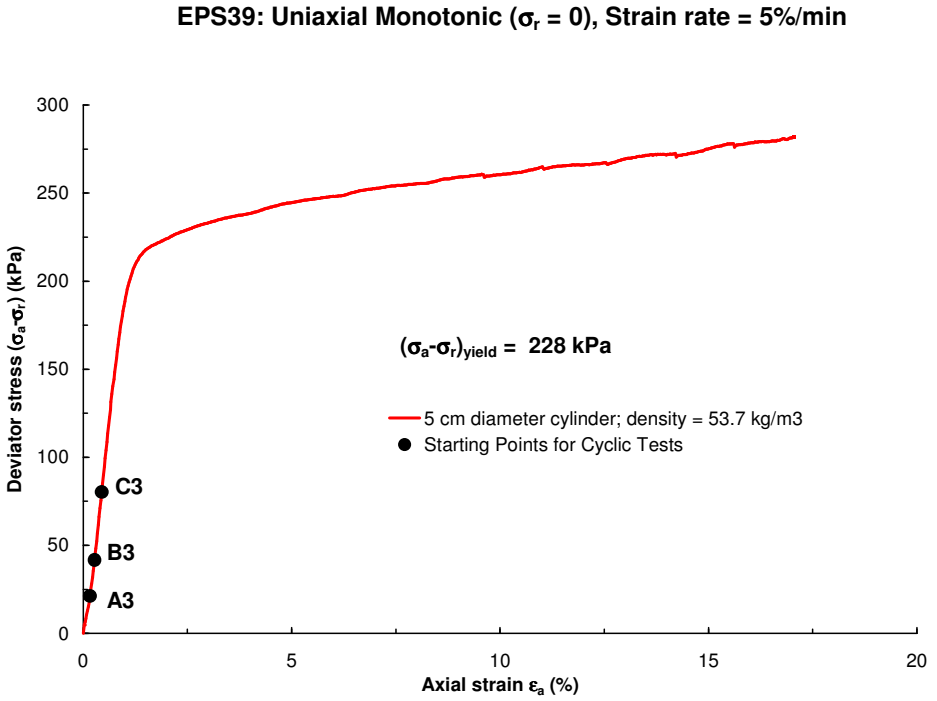

Figure 170. Uniaxial monotonic test result on EPS39

the cyclic uniaxial tests on EPS22, correspond to static deviator stresses representing 23%, 47% and 85% of the deviator stress at yield.

Cyclic Stress-Strain Behavior of EPS Geofoam

The response of EPS to cyclic loading is illustrated in Figures 171 to 185. EPS15 demonstrated in both tests (i.e., tests 1-1, 1-2) a nonlinear elasto-plastic response. The higher the initial deviator stress, the higher the amount of permanent residual deformation. For an initial deviator stress corresponding to 23% of $(\sigma_a - \sigma_r)_{yield}$, the cyclic behavior of EPS22 also appears to be nonlinear elastic. However, this behavior changes to nonlinear elasto-plastic for initial deviator stress levels of 47% and 85% of the yield stress. As seen before, the amount of permanent residual deformation increases with increasing initial deviator stress for the same amplitude of applied cyclic loading. Because of its higher density and stiffness, EPS39 shows a nonlinear elastic behavior for all considered initial (static) deviator stress levels.

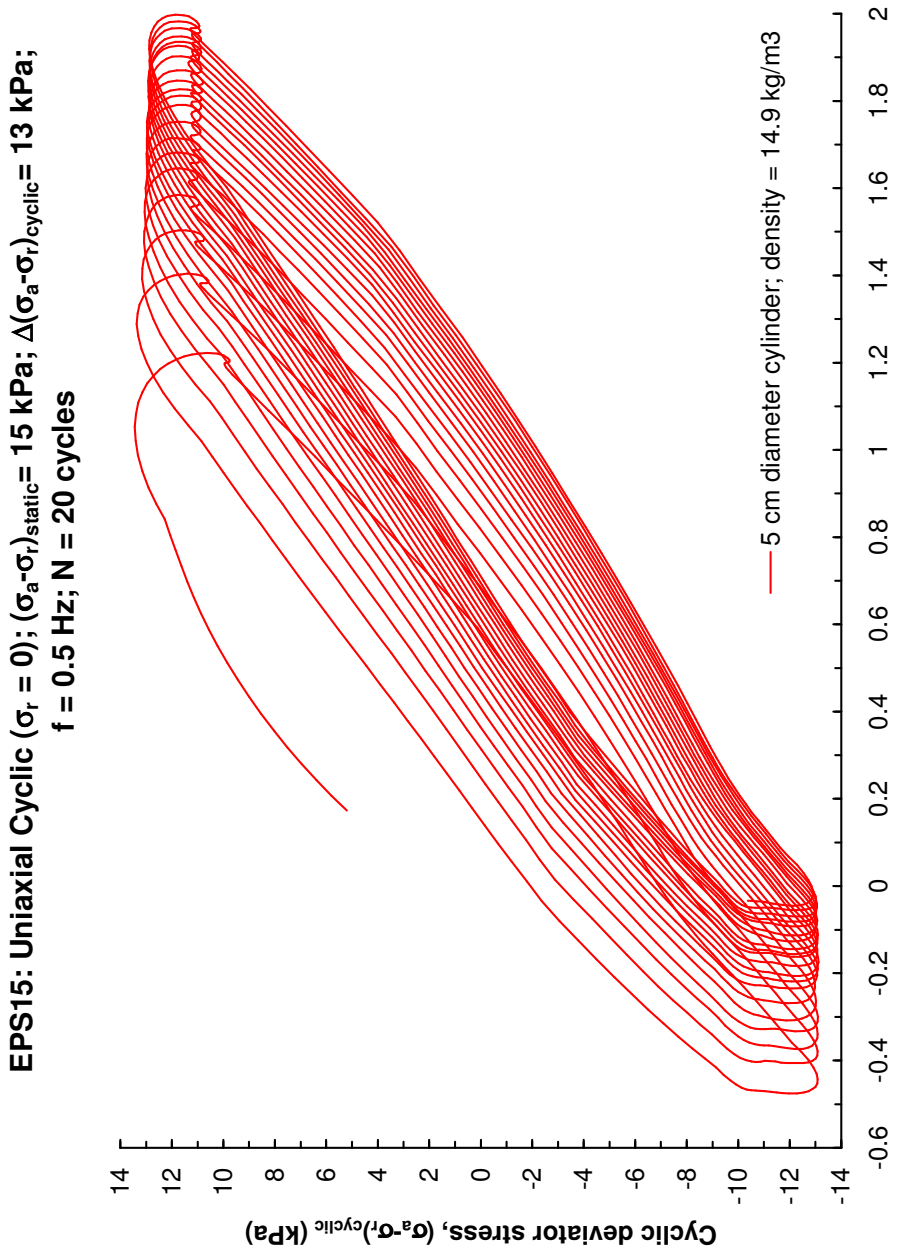

Figure 171. Uniaxial cyclic test 1-1 on EPS15

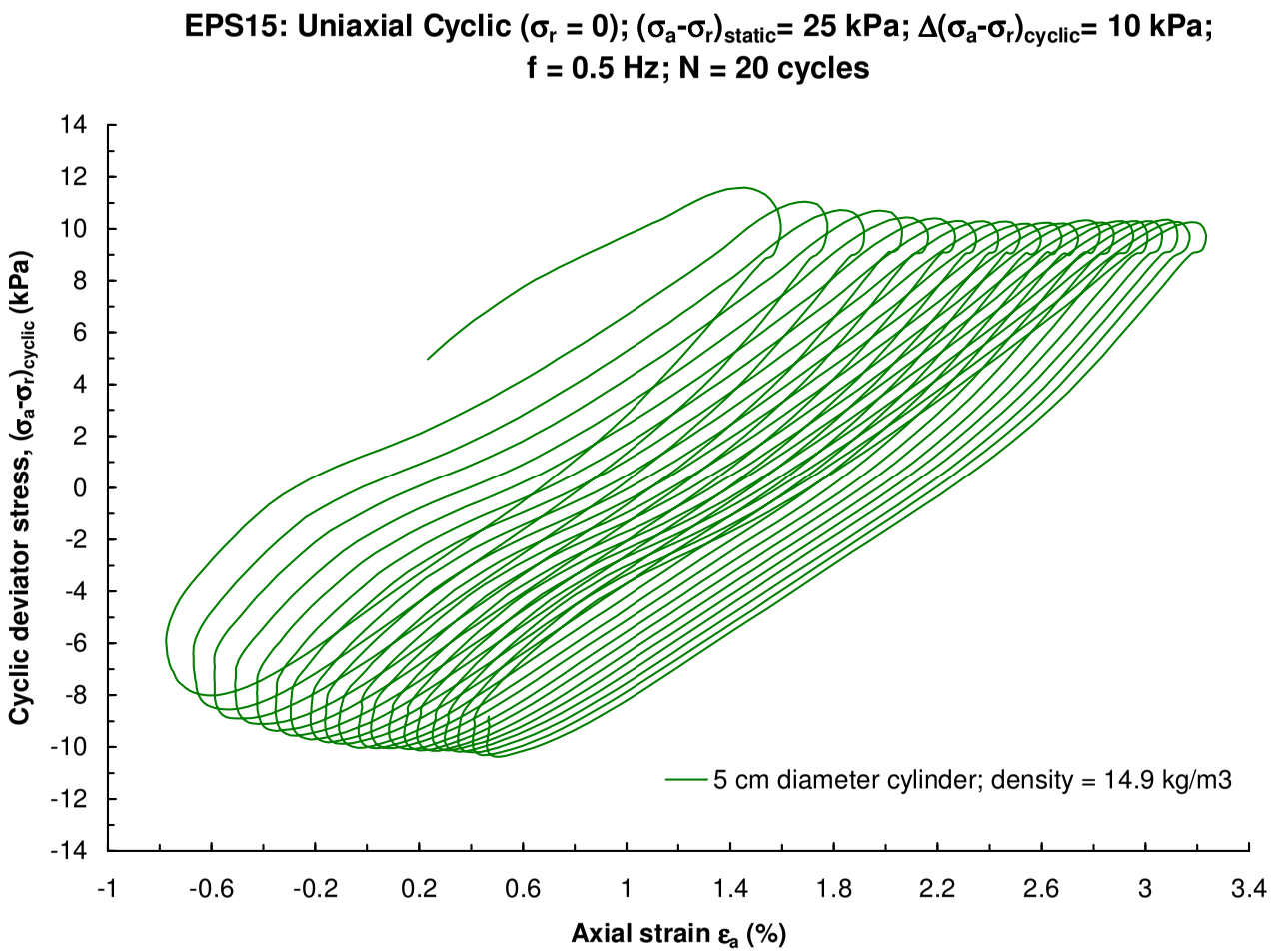

Figure 172. Uniaxial cyclic test 1-2 on EPS15

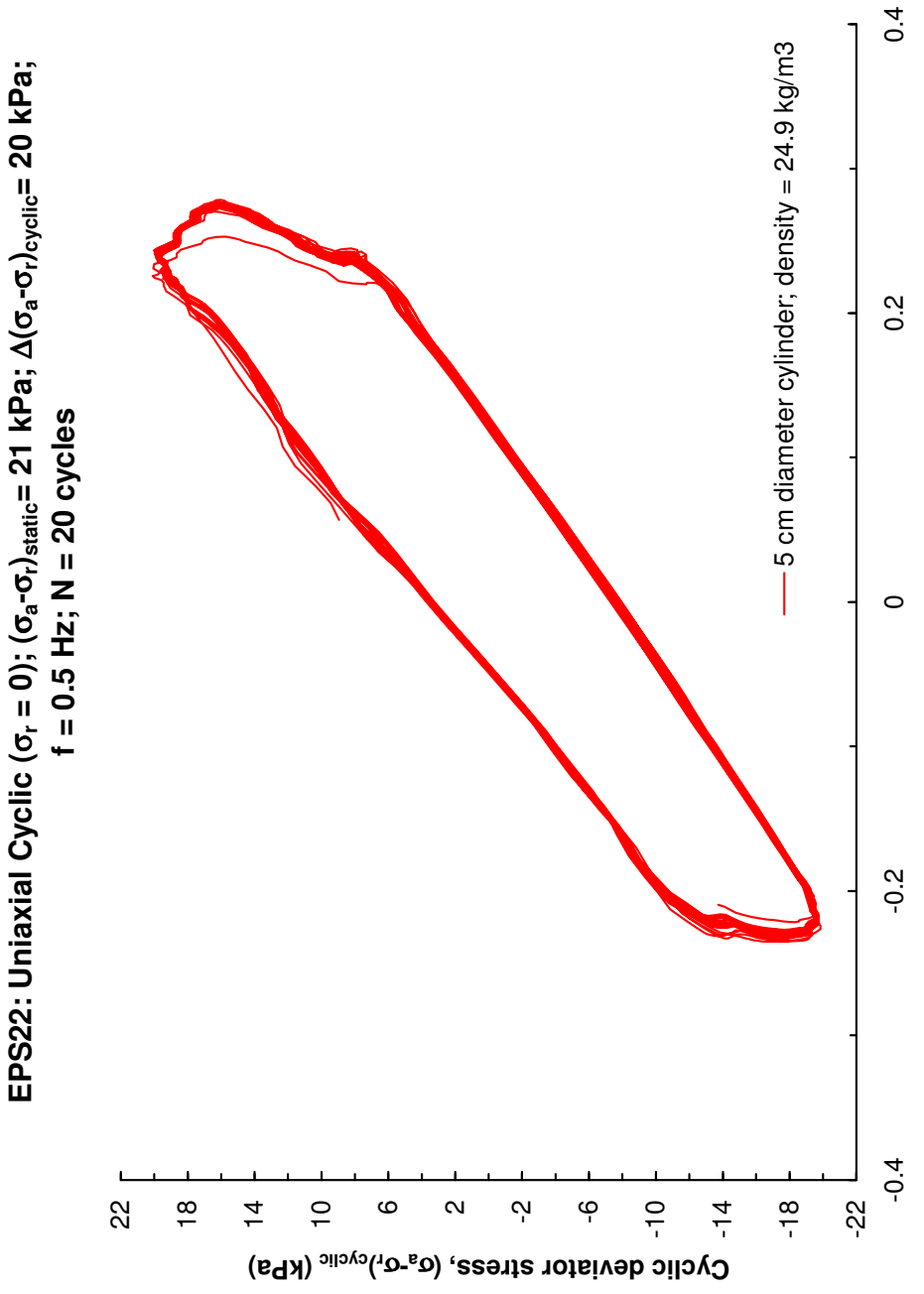

Figure 173. Uniaxial cyclic test 2-1 on EPS22

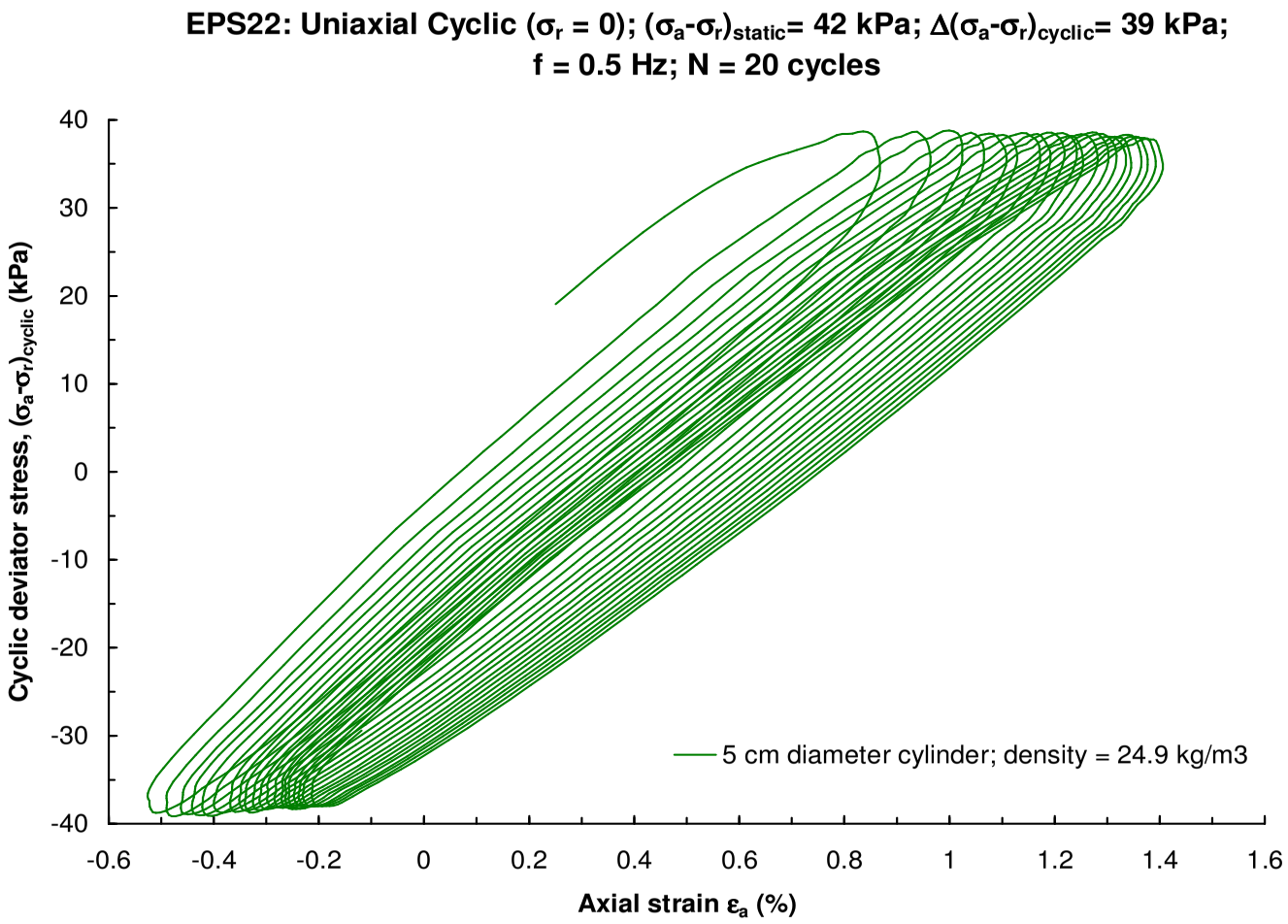

Figure 174. Uniaxial cyclic test 2-2 on EPS22

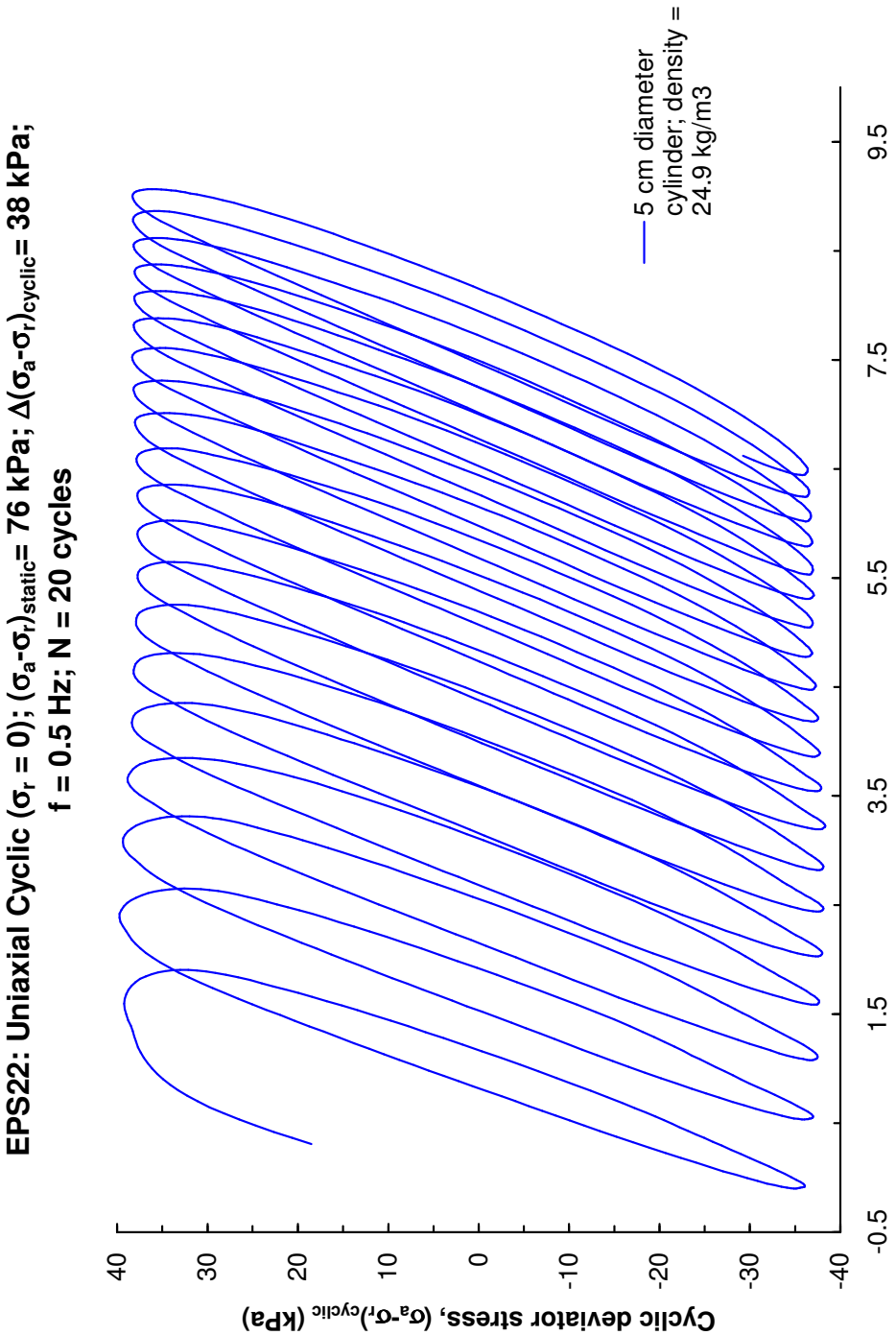

Figure 175. Uniaxial cyclic test 2-3 on EPS22

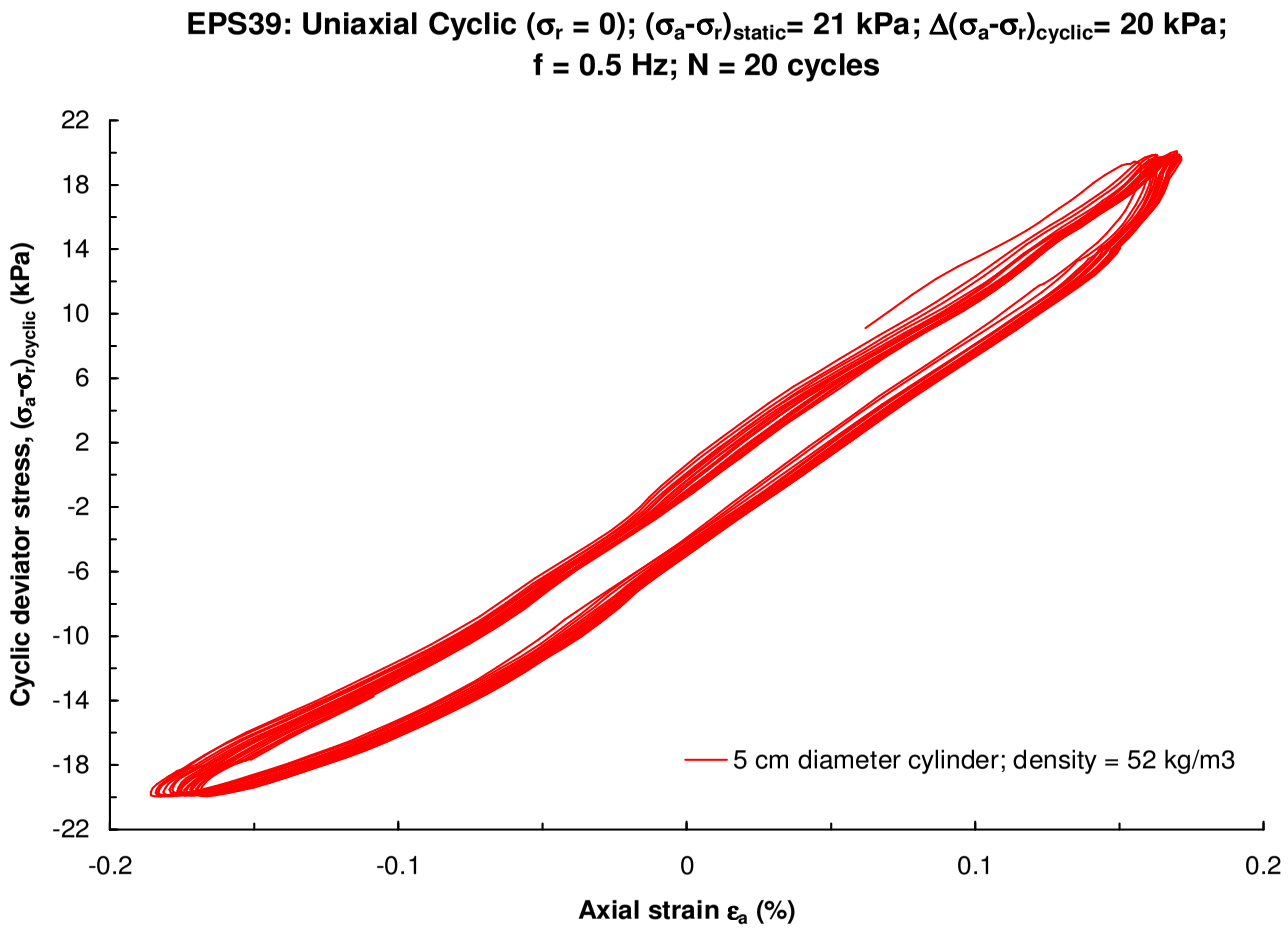

Figure 176. Uniaxial cyclic test 3-1 on EPS39

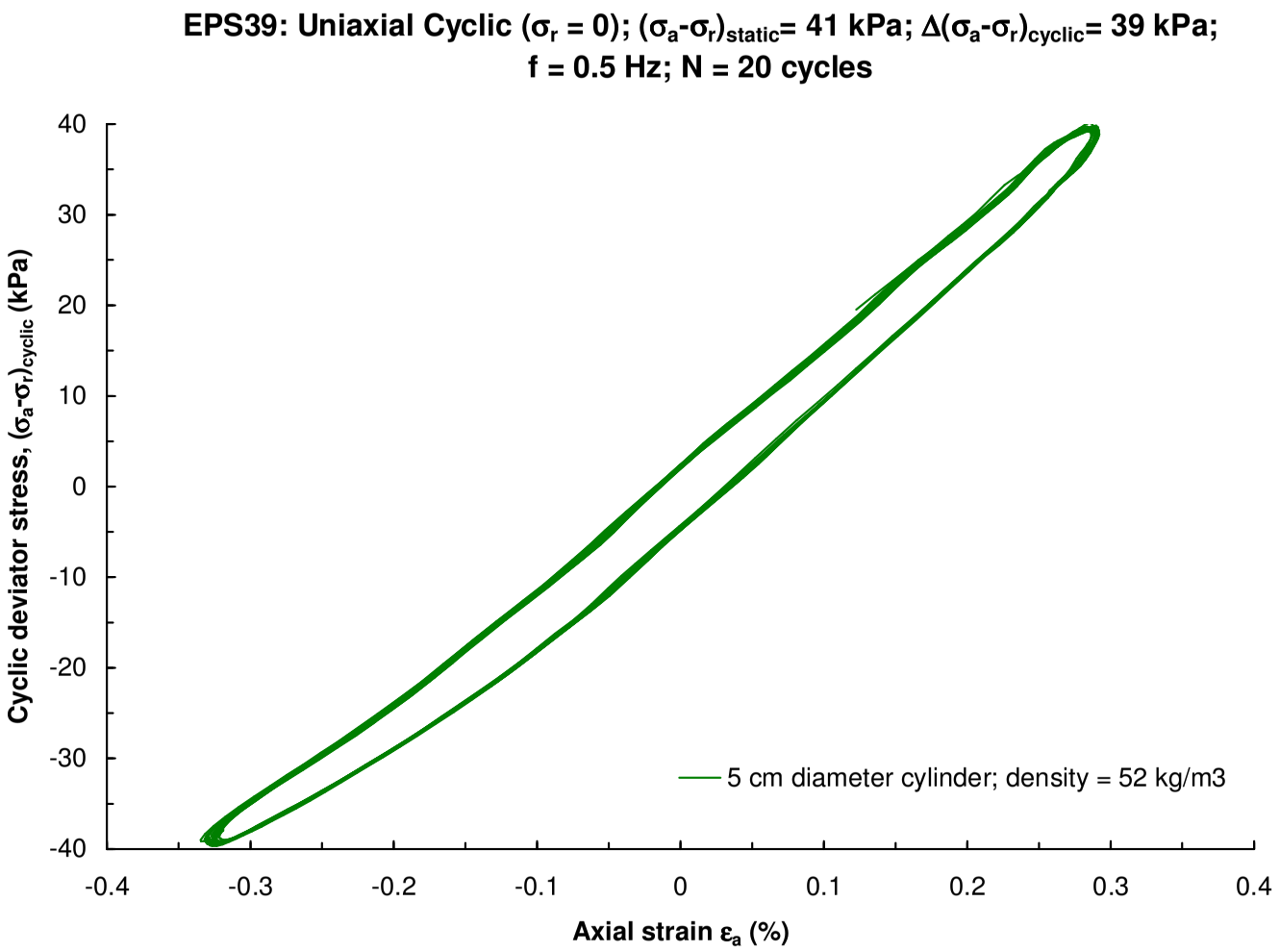

Figure 177. Uniaxial cyclic test 3-2 on EPS39

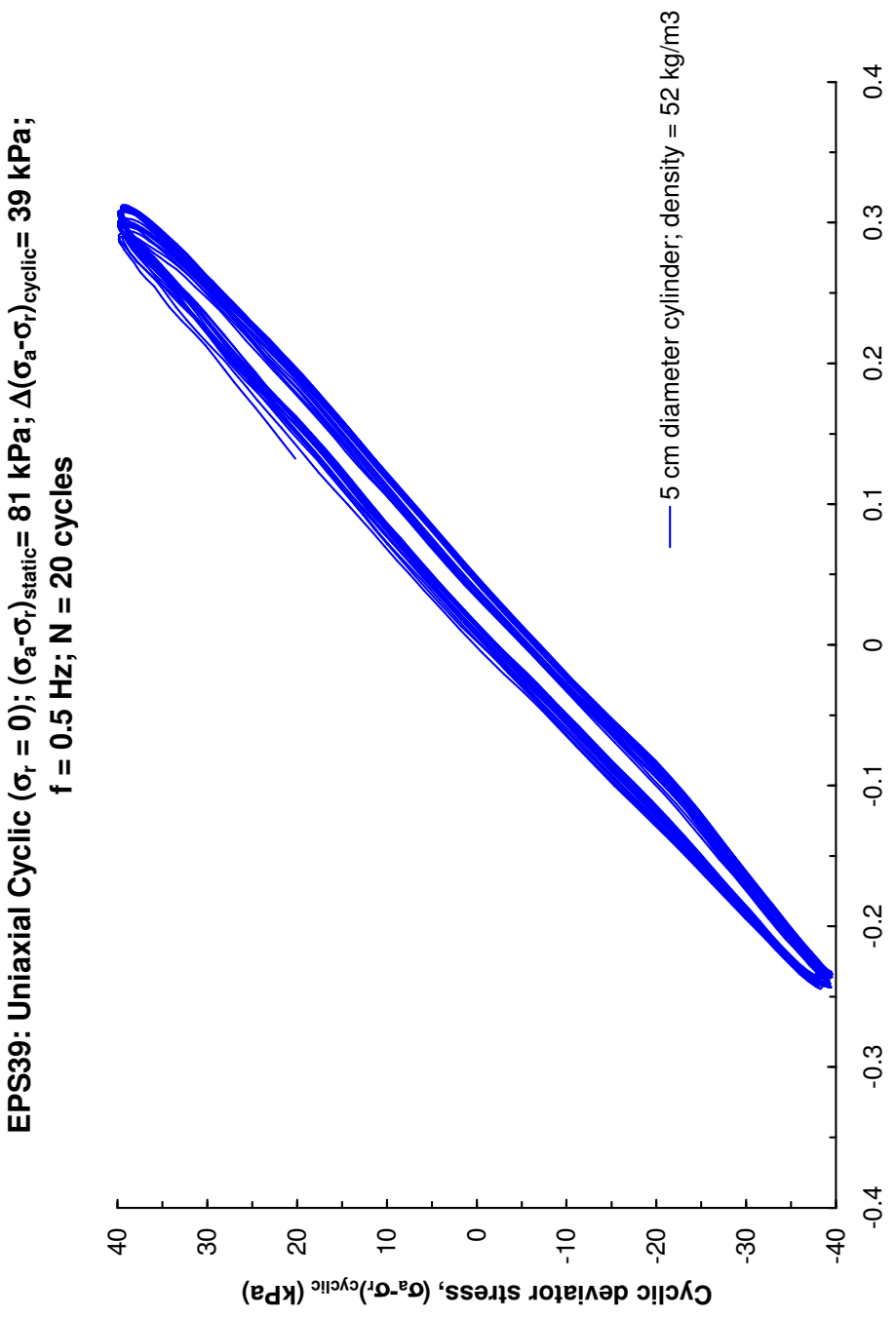

Figure 178. Uniaxial cyclic test 3-3 on EPS39

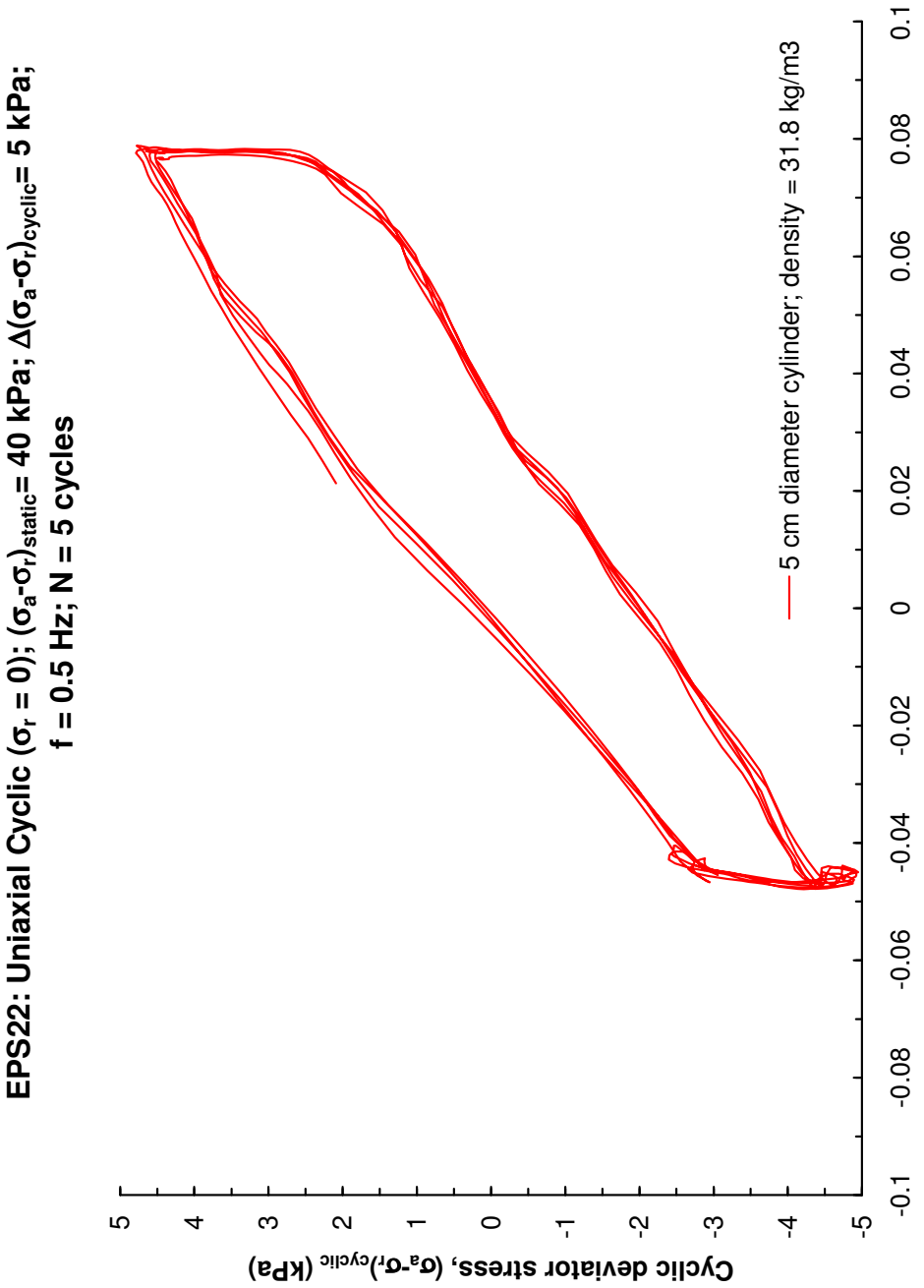

Figure 179. Uniaxial cyclic test 4-1 on EPS22

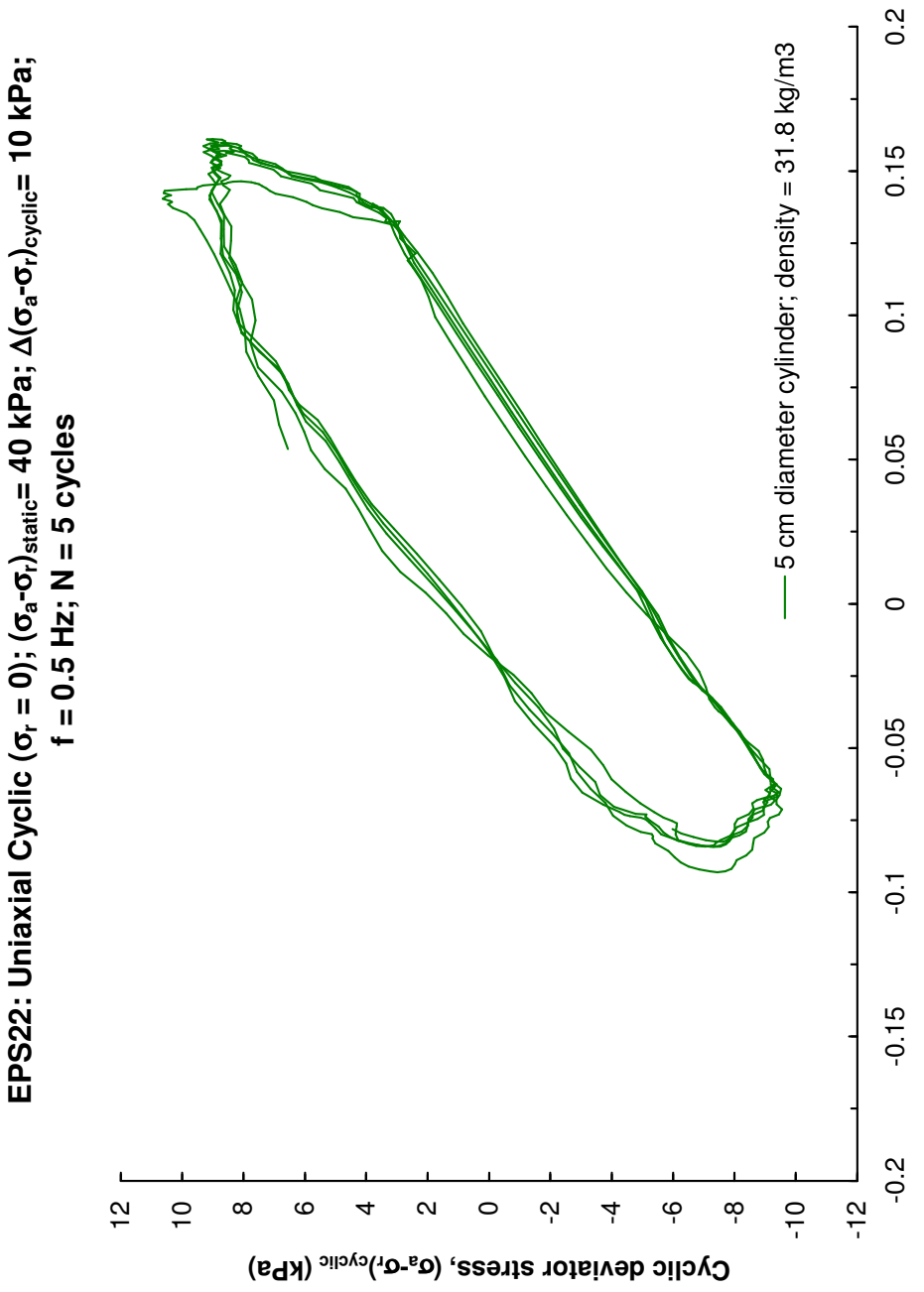

Figure 180. Uniaxial cyclic test 4-2 on EPS22

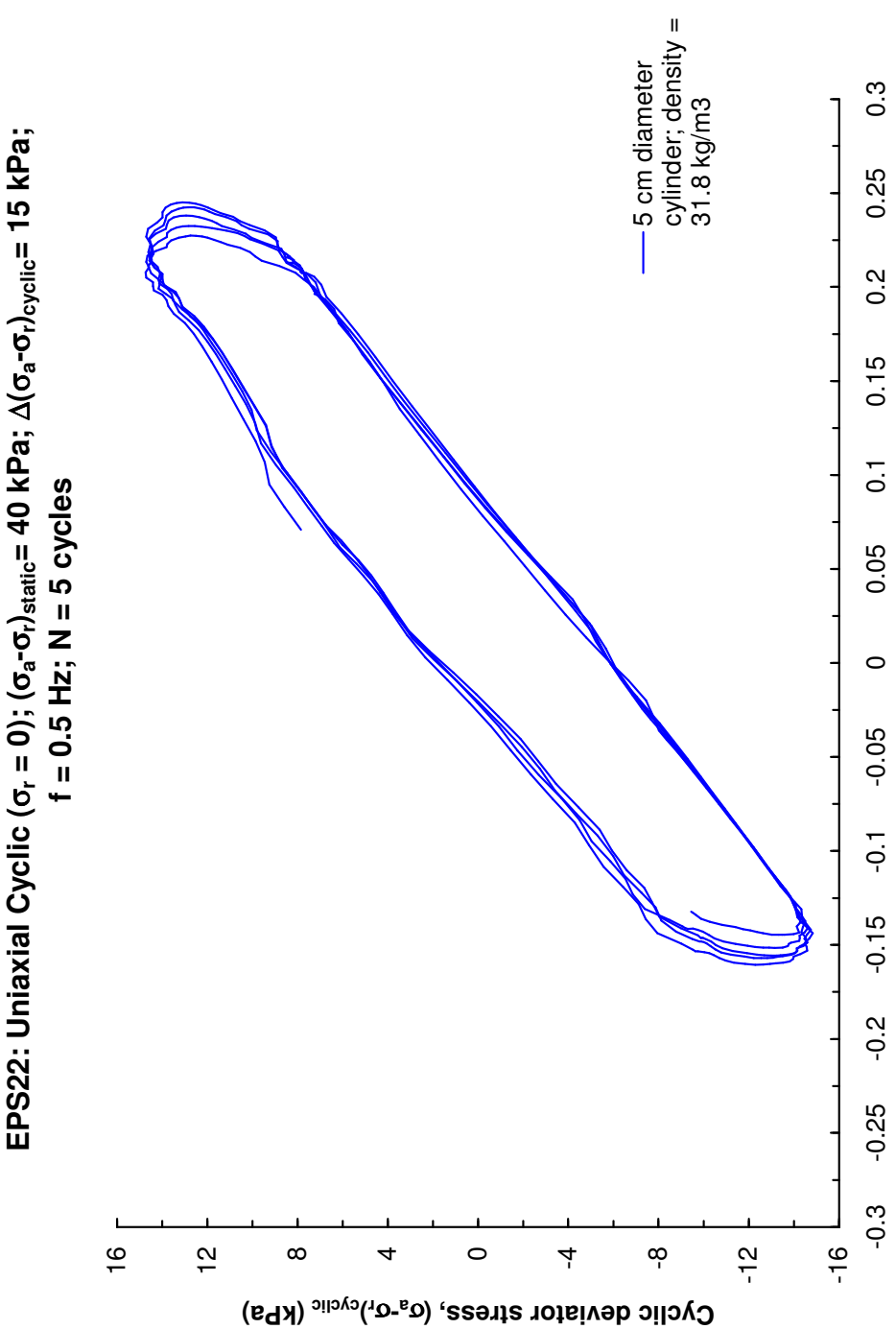

Figure 181. Uniaxial cyclic test 4-3 on EPS22

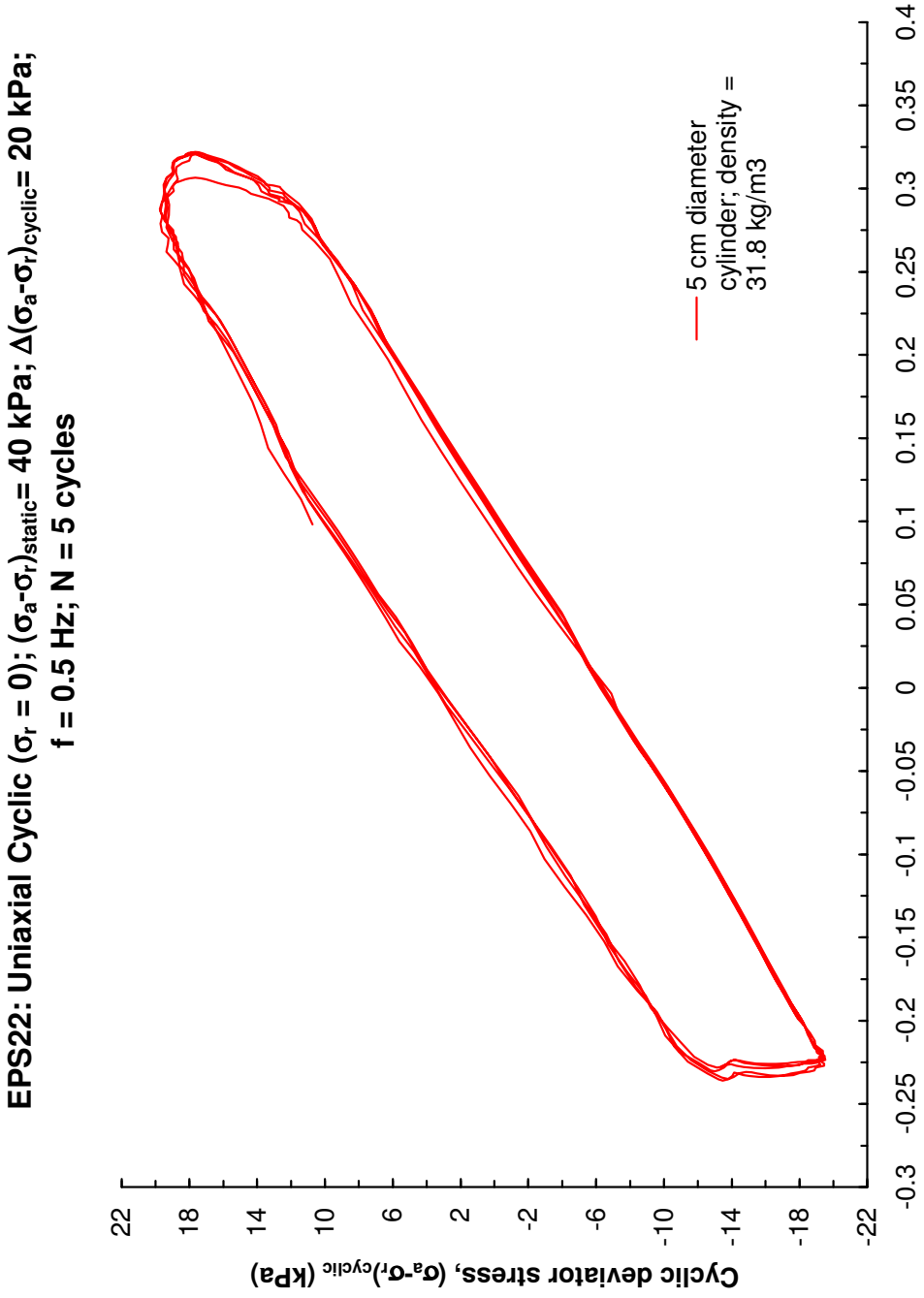

Figure 182. Uniaxial cyclic test 4-4 on EPS22

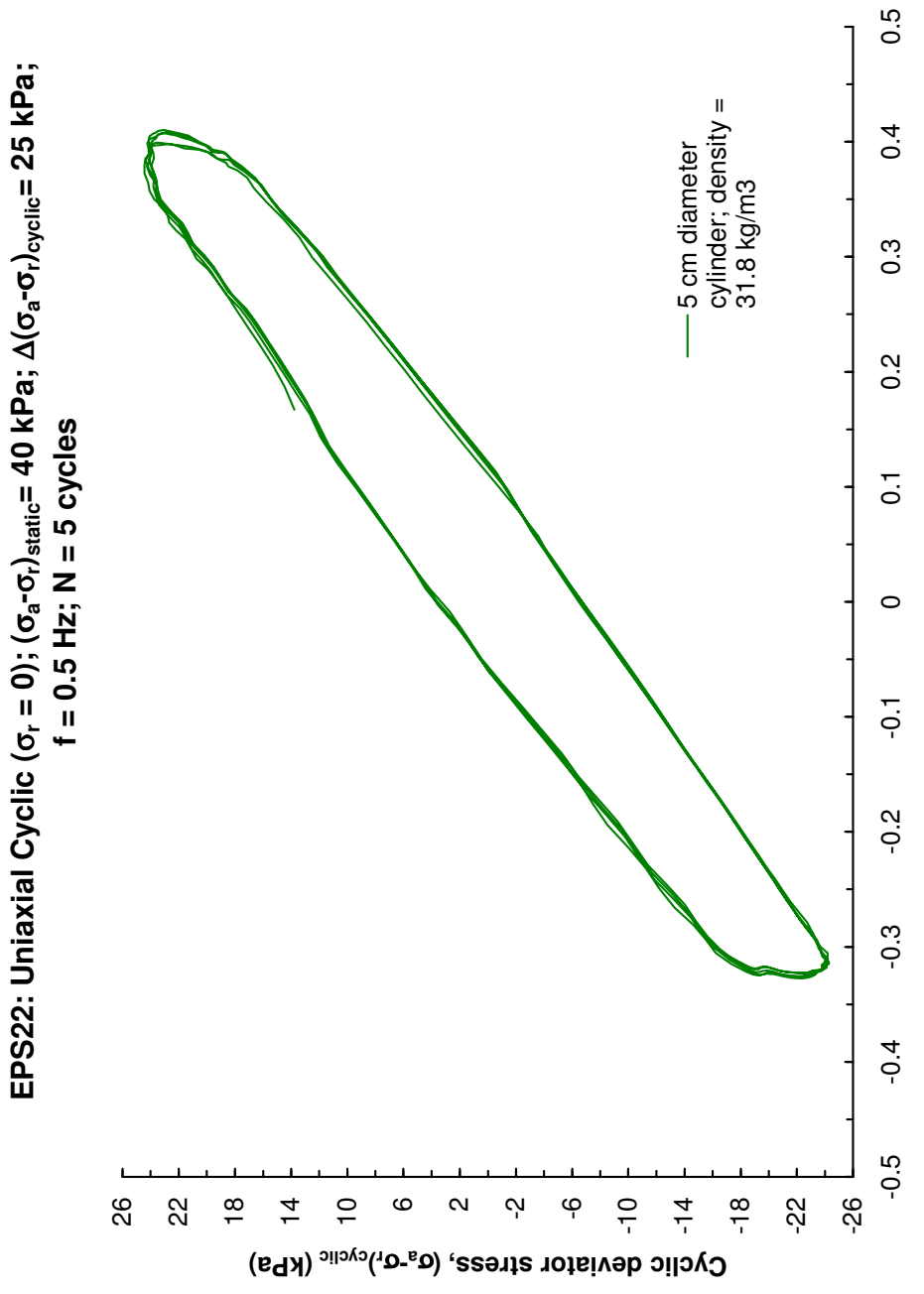

Figure 183. Uniaxial cyclic test 4-5 on EPS22

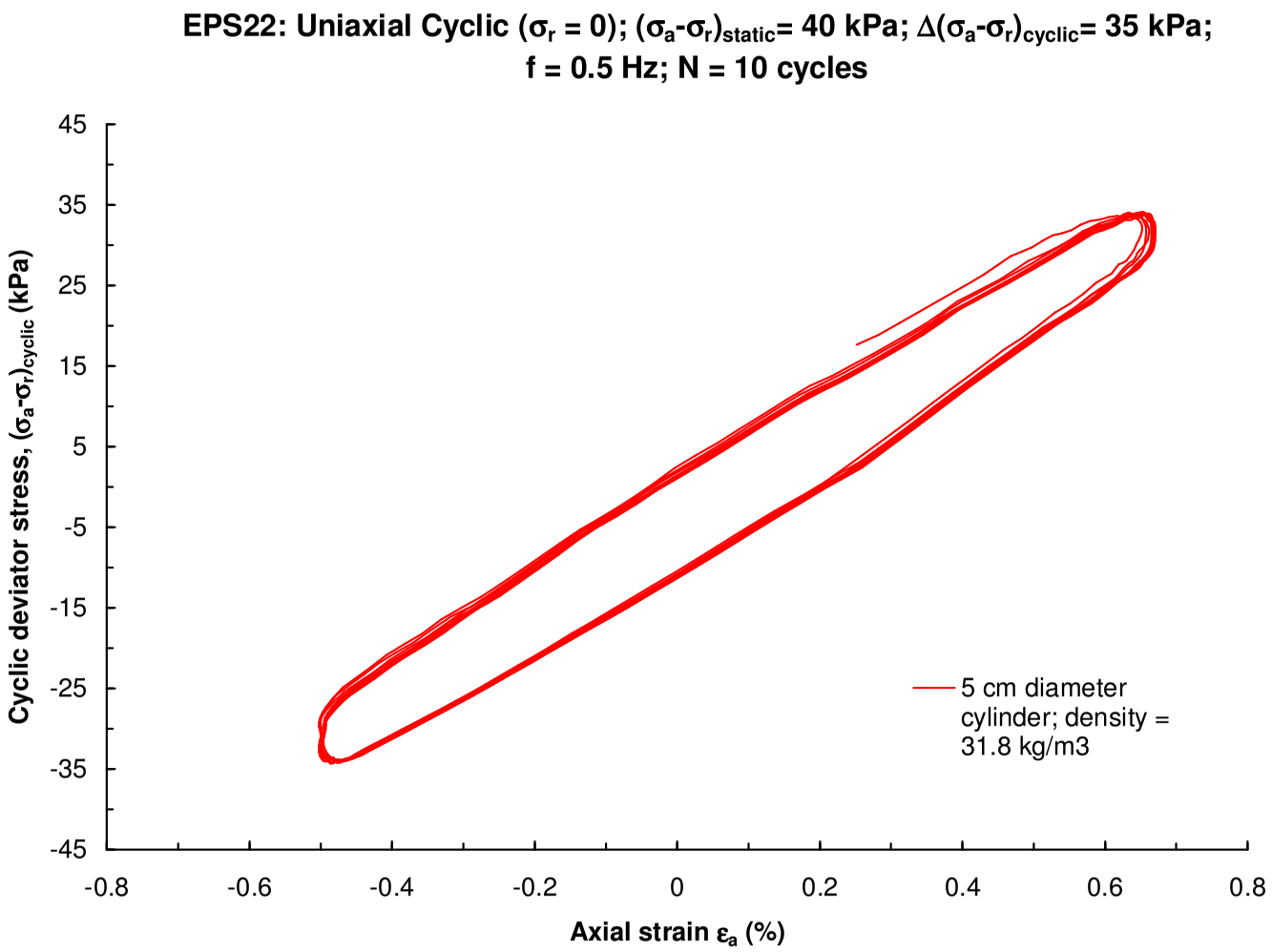

Figure 184. Uniaxial cyclic test 4-6 on EPS22

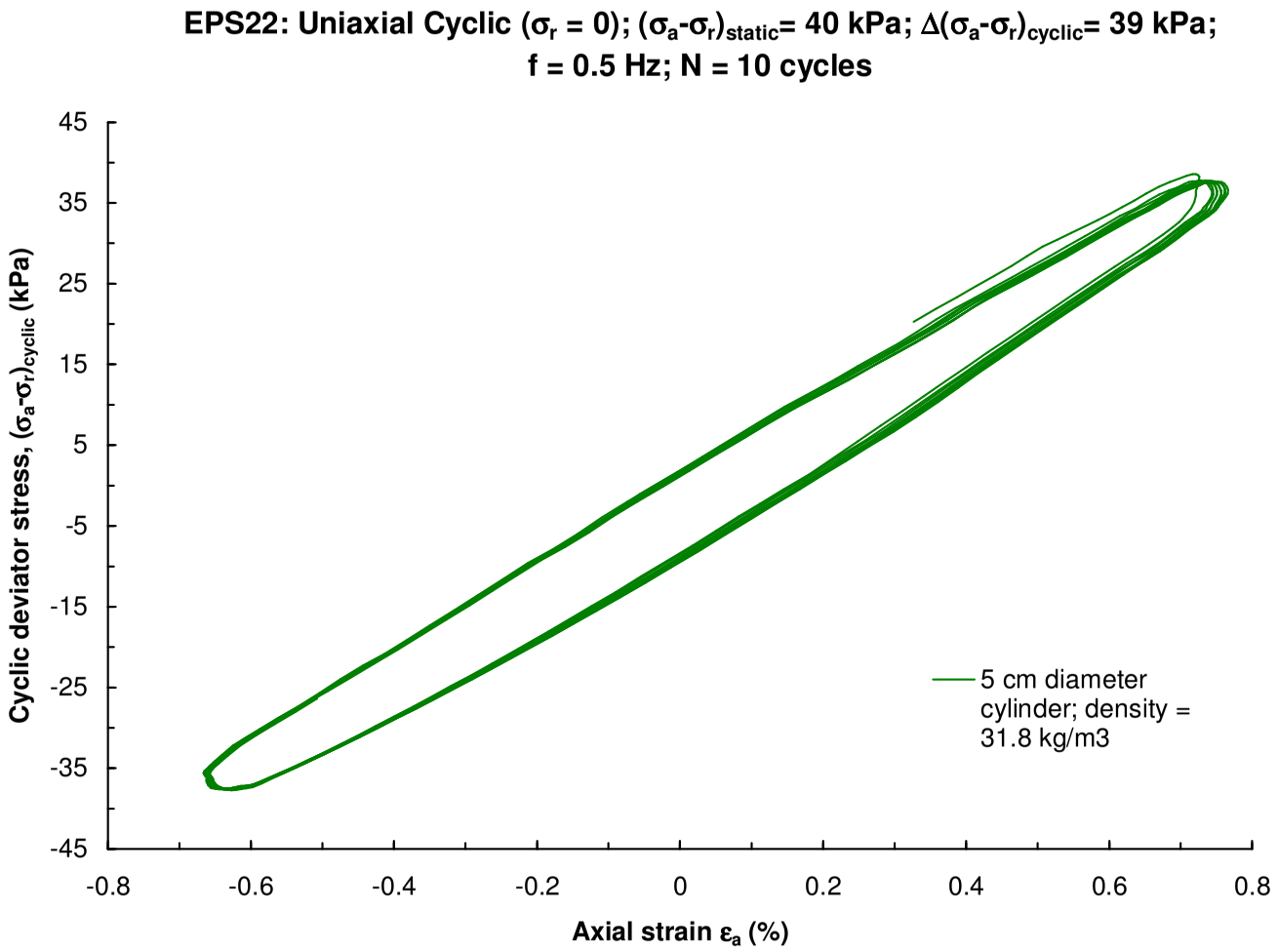

Figure 185. Uniaxial cyclic test 4-7 on EPS22

Dynamic Properties of EPS Geofoam

The results from tests 4-1 to 4-7 in Table 40 were used to derive the dynamic elastic modulus (*E*) and damping ratio (*D*) for EPS22. These cyclic uniaxial tests cover a range of cyclic axial strain amplitudes from 0.079% to 0.745%. The calculated *E* and *D* values are given in Table 40.

The dynamic shear modulus (*G*) and cyclic shear strain amplitude (γ_c) can be calculated based on the dynamic elastic modulus (*E*) and cyclic axial strain amplitude (ε_{ac}) values from cyclic triaxial tests using the following equations from the elasticity theory:

$$G = \frac{E}{2(1+\upsilon)} \tag{3113}$$

$$\gamma_c = (1+\upsilon)\varepsilon_{ac} \tag{3214}$$

where ν represents the Poisson's ratio.

Figure 186 shows the dynamic shear modulus ratio (G/G_0) versus the cyclic shear strain amplitude (γ_c) from cyclic uniaxial tests in comparison to the relationship proposed by Athanasopoulos et al. (1999) which is based on Equation 33.

Table 40. Dynamic properties of EPS 22 from cyclic uniaxial tests

Cyclic Strain Amplitude *%*	Dynamic Elastic Modulus *kPa*	Dynamic Elastic Modulus Ratio ----------	Damping Ratio *%*
0.07877	5990	0.9599	11.82
0.16116	5588	0.8956	16.33
0.23782	5324	0.8532	14.32
0.32157	5548	0.8891	13.74
0.40699	5629	0.9021	1097
0.65771	4801	0.7694	9.63
0.74516	4910	0.7868	6.90

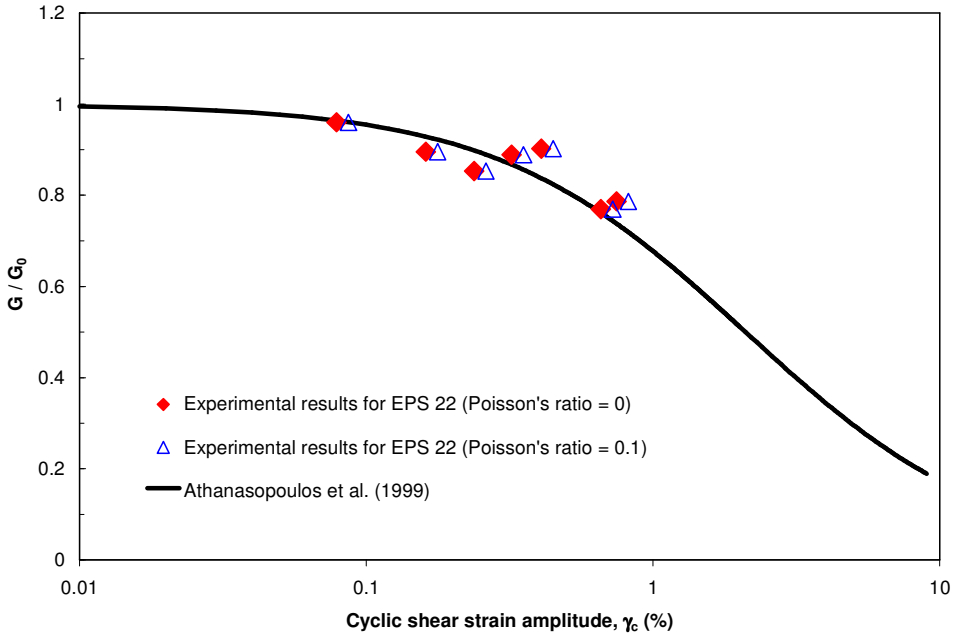

Figure 186. Dynamic shear modulus ratio versus shear strain amplitude for EPS22

$$\frac{G}{G_0} = \frac{1}{1 + \frac{\gamma_c}{\gamma_{c0}}} \tag{3315}$$

In Equation 33, G_0 is the initial elastic modulus, and γ_{c0} is a constant with a value equal to 2.1%. To be able to compare the experimental results with the relationship provided by Equation 33 and since there is no available information on the G_0 value for the tested EPS22, a G/G_0 value at a cyclic shear strain amplitude of 0.079% equal to that provided by Equation 33 was assumed (i.e., $G/G_0 = 0.96$). The experimental results plotted for various values of the Poisson's ratio (i.e., $\nu = 0$ and $\nu = 0.1$) are quite narrowly scattered and follow the trend of the Athanasopoulos et al. (1999) relationship, therefore being in agreement with Eq. 33.

On the other hand, the experimental damping ratio values (Figure 187) obtained from cyclic uniaxial tests on EPS22 indicate a completely different trend when compared to the relationship proposed by Athanasopoulos et al. (1999) which is given by the Equation 34:

$$D = 10 - \frac{10 - D_0}{1 + \frac{\gamma_c}{\gamma_{c0}}} \tag{34}$$

where $D_0 = 0.55\%$ and $\gamma_{c0} = 2.1\%$. Apparently, the experimental results indicate a logarithmic decrease in the damping ratio with increasing amplitude of cyclic axial strain for EPS22 (Figure 187). For a Poisson's ratio $\nu = 0$, the following equation can be used to

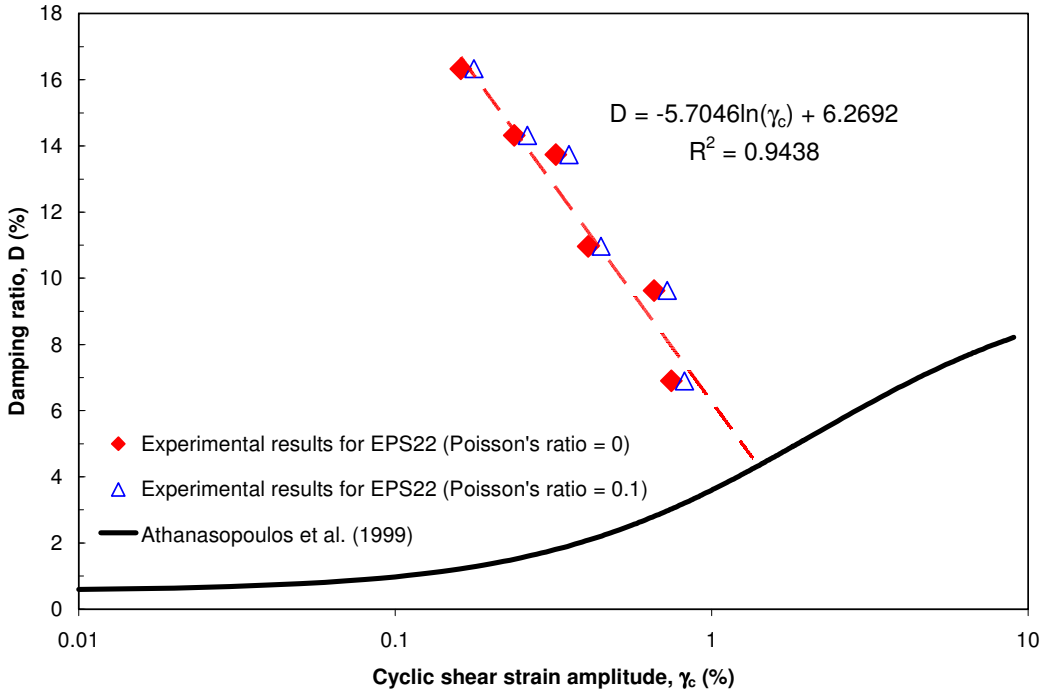

Figure 187. Damping ratio versus shear strain amplitude for EPS22

evaluate the damping ratio of EPS22 at cyclic shear strain levels between 0.1% and 0.75% (Figure 188):

$$D\ (\%) = 6.2692 - 5.7046\ \ln(\gamma_c) \qquad (35)$$

with γ_c expressed in% (%).

Conclusions and Recommendations for Cyclic EPS Testing

The cyclic uniaxial test results for EPS Geofoam indicate a nonlinear elastic material behavior for cyclic axial strain amplitudes up to approximately 0.8%. In this context, the dynamic properties required for implementation of the equivalent linear elastic model have been evaluated for EPS22. This testing considered a range of cyclic axial strains from 0.079 to 0.745%. The dynamic shear modulus and damping ratio values from this testing were also compared with available published relationships. This showed that the shear modulus ratio-cyclic shear strain curve obtained from this program agreed well with the published relationships.

However, the experimentally obtained damping values decrease with increasing cyclic shear strain amplitude, which is opposite to that shown in previously published relations. For cyclic axial strain amplitudes greater than 0.8%, this study shows that EPS22 exhibits a nonlinear elasto-plastic behavior that is associated with the occurrence of permanent plastic deformation; thus, equivalent linear elastic models may not be appropriate for evaluations where the calculated dynamic strains are greater than 0.8%. A more elaborate constitutive model that accounts for yielding of the EPS and the accumulation of permanent plastic strains is recommended for higher strain cyclic cases. It is also important to mention here that the EPS shear modulus degradation and damping curves shown herein were unconfined. Therefore, it is recommended that a more detailed experimental program involving cyclic triaxial tests on EPS samples subjected to various confining stresses and strain levels be conducted in the future to study the effects of these factors on the cyclic stress-strain behavior and associated dynamic properties.

APPENDIX F

LATERAL BOX TEST EQUIPMENT

Loading Device

The actuator used in this test program utilized a MTS electronic control and data acquisition system. The actuator has a maximum capacity of 445 kN with a maximum stroke of 381 mm. The maximum displacement rate for the ram is 3.048 m per minute. The ram is powered by a MTS pneumatic pump (Figure 188) with computer controlled manifold and servo. Feedback for the system is through the displacement transducer and the tests were done as displacement controlled tests. (The system is capable of cyclic testing though this capability was not utilized in this test program.) The actuator was controlled by an MTS control box with a signal provided to it by a National Scientific DC signal generator and Lab View™ to control the rate of the piston extension.

Instrumentation

Several types of measurements were taken during the test program. The total load applied to the pipe by the actuator was measured by a Houston Scientific load cell (Figure 189). The displacement of the actuator was measured with a displacement. Vibrating wire and resistant base total earth pressure cells were placed in the backfill to measure the horizontal and vertical stresses that developed.

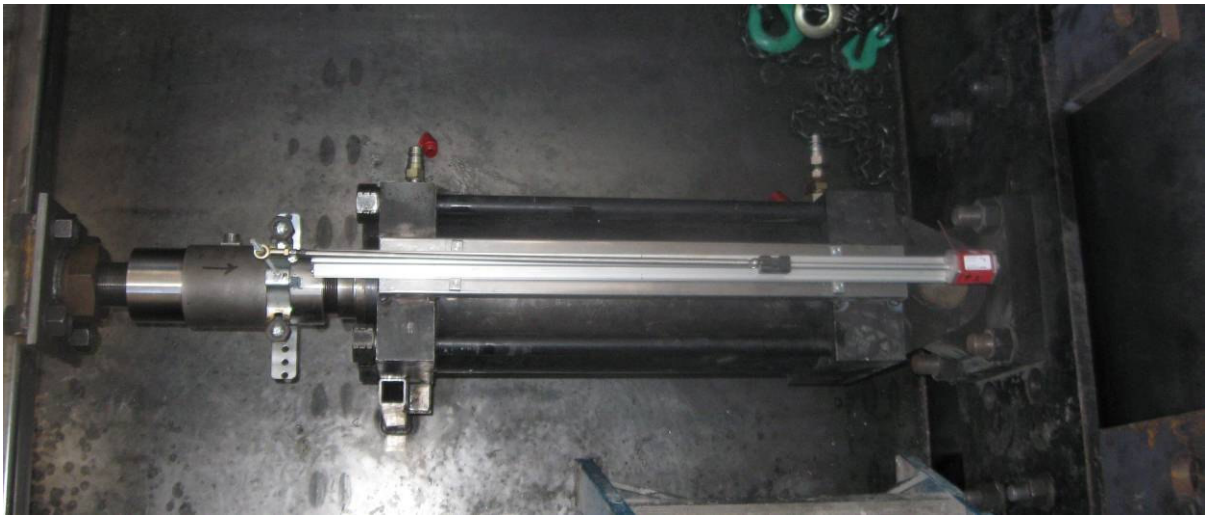

Figure 188. MTS actuator ram used as loading device mounted to the back wall of the trench box. Displacement transducer is resting atop the actuator

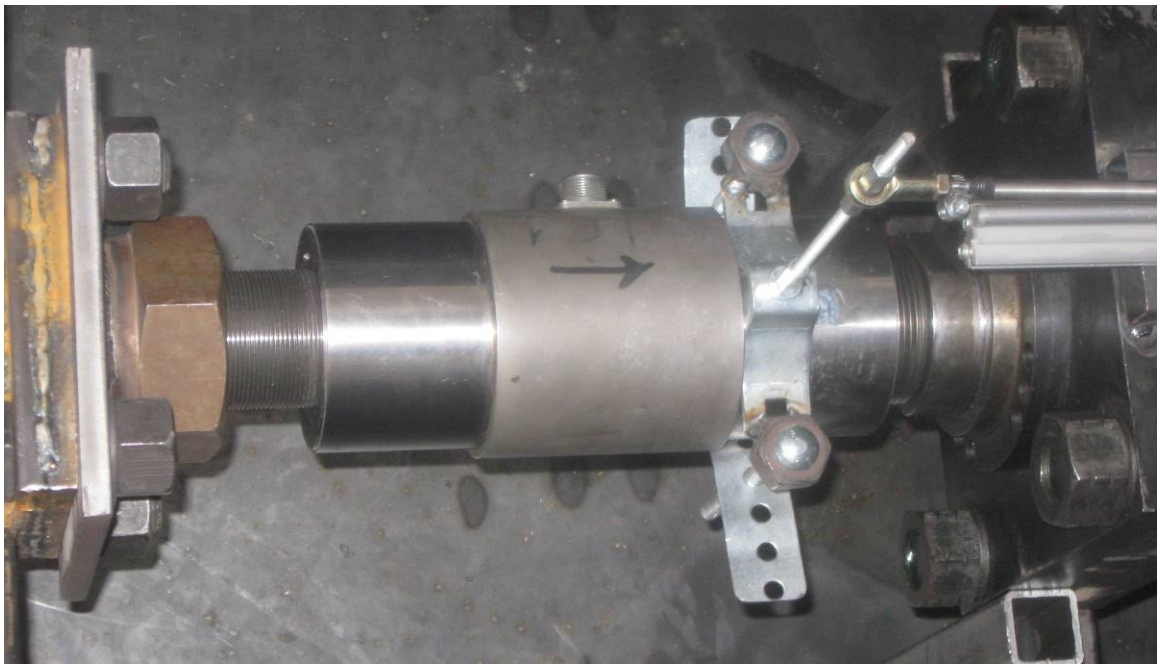

Figure 189. Houston Scientific force-based load cell mounted between the actuator at the horizontal struts

The load cell used was a Houston Scientific Force Link™. (This type of force load cell is also referred to as a rod type load cell as it is placed in line with the load application). The electronics of the load cell are 4 resistors that are arranged in a Thevanin Bridge configuration. The load cell was accurate to +/- 0.1% of its range with a working range of measurements of +/- 445 kN in both tension and compression. The load cell threaded onto the actuator and sits between the load cell and the push rods that extend through the partition wall into the sand chamber. Figure 190 shows how the load cell attached to the struts that extend through the partition wall.

The displacement transducer used in the tests was a Temposonics™ magnetic slider displacement transducer (Figure 191). This sensor measures absolute displacement to an accuracy of 0.025 mm. The transducer was mounted atop the ram and had an extension arm that connected to the load cell at the end of the ram. Thus configured, it tracked the displacement of that load cell in a line parallel with the extension of the actuator (Figures 191 and 192). Both the load cell and the displacement transducer were calibrated prior to their use in the subsequent test program.

The horizontal and vertical stresses developed in the sand backfill were measured with Geokon™ series 4100 total earth pressure cells. The cells used were flat “pancake” cells and were less than a 12.7 mm thick and 230 mm in diameter. Two types of Geokon series 4100 cells were used. Some of the cells were resistance type and others were vibrating wire (VW) cells. For the resistance type cells, data acquisition was rapid and occurs in milleseconds. For the VW cells, data can only be gathered every 10 to 30 seconds. All earth pressure cells were rated to 1 MPa. Figure 192 shows three of the earth pressure cells used in this testing program.

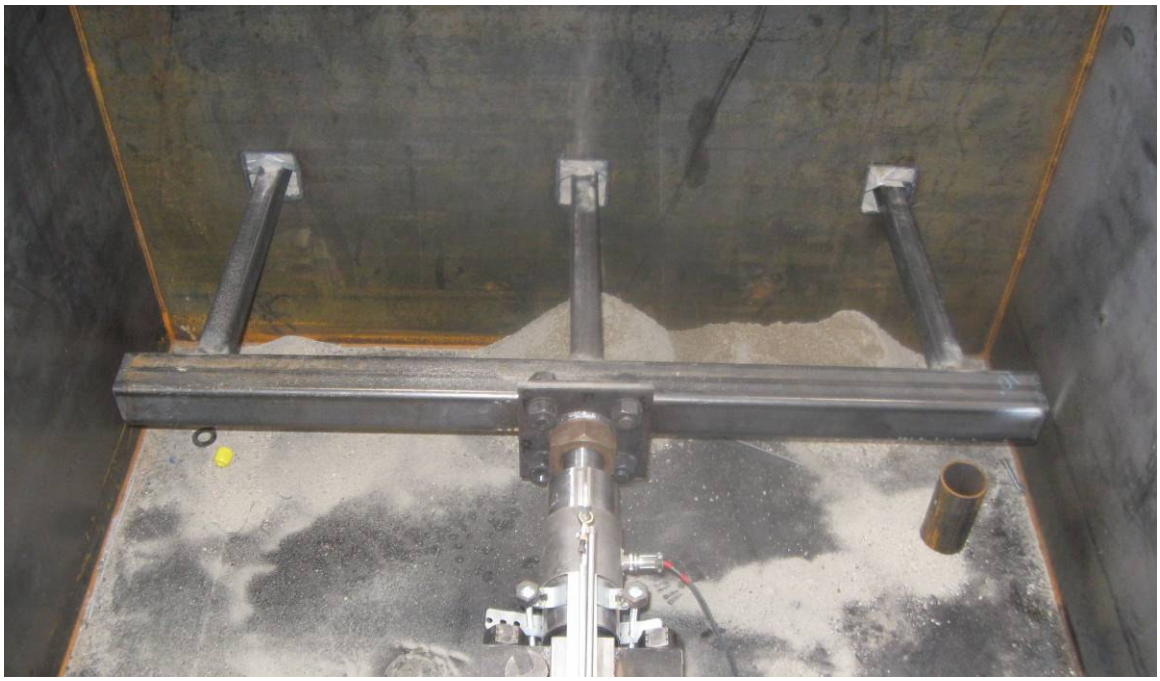

Figure 190. Load cell connecting to push rods

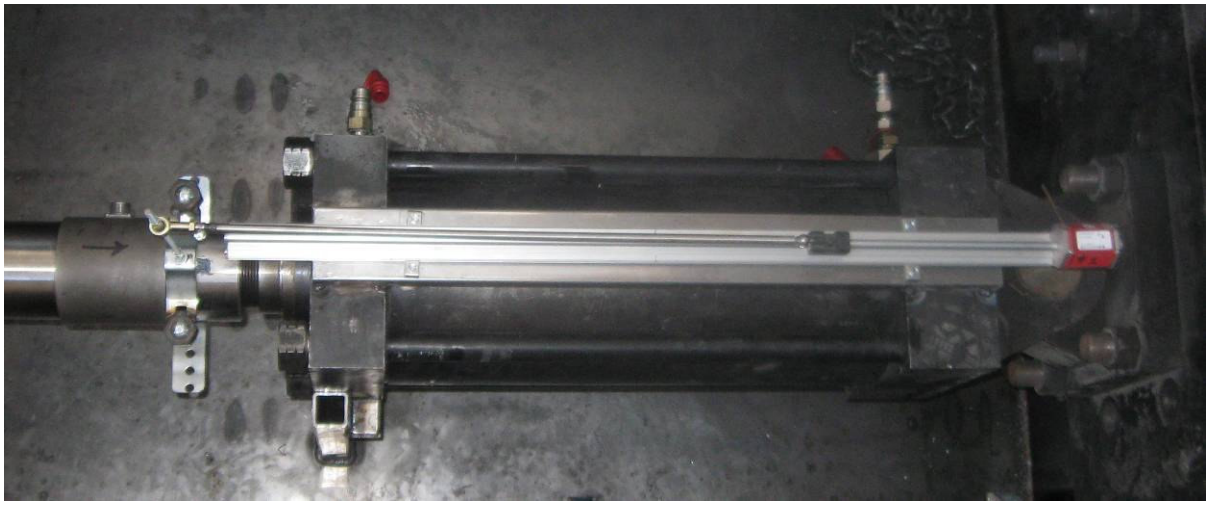

Figure 191. Temposonics displacement transducer

Figure 192. Geokon total earth pressure cells

Data Acquisition

The data from the load cell and total pressure cells were acquired, stored and processed by a Campbell Scientific CR1000 data-logger and its LoggerNet software. The CR1000 is shown in Figure 193. The CR1000 is capable of measuring or sampling different types of electrical signals at frequencies of 100 Hz, or less. These measurements include differential voltages, conditioned signals and single-ended voltages (as originating from a thermistor). The CR1000 stores the signals from each instrument, at the programmed sampling increment, in its internal memory until called for by an external PC running the LoggerNet software. The software displays the data in real time on graphs and tables, allowing the user to monitor all measurements as the test progresses. The CR1000 also processes the raw voltage readings from the instruments

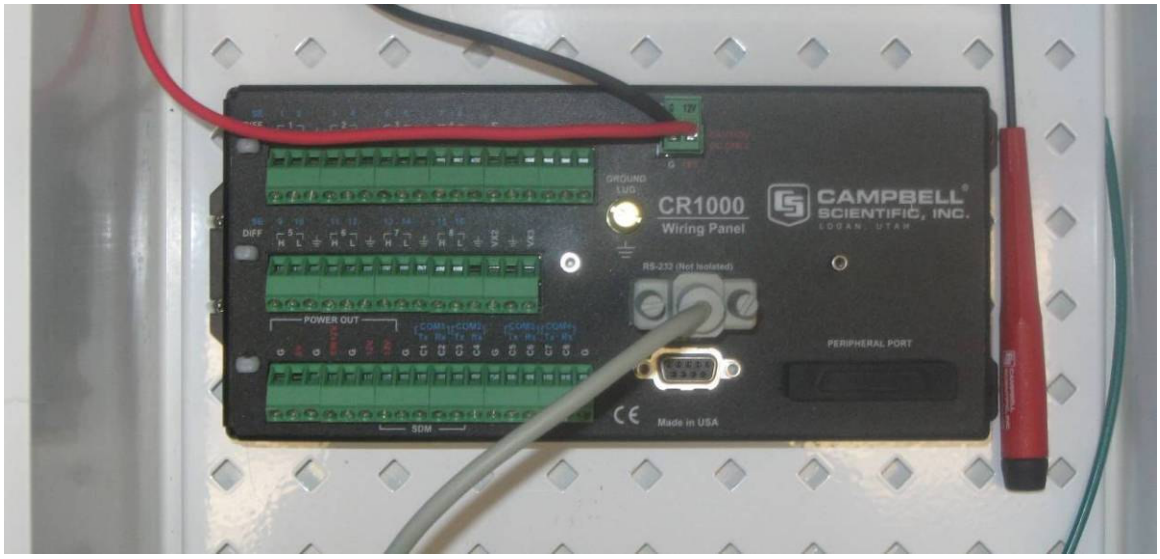

Figure 193. Campbell Scientific CR1000 data collector

into engineering units if desired. When the user provides calibration factors for each instrument, the data can be exported directly for interpretation.

Calibrations for each instrument were conducted by the University of Utah in addition to the factory supplied calibrations. In addition, each instrument was recalibrated after each experiment to verify that the data processed were accurate. The load cell and earth pressure cells were full-bridge circuits that returned a differential voltage, while the Temposonics displacement transducer was a conditioned signal that returned a differential voltage. The wire leads from each instrument were connected to the CR1000 directly as shown in Figure 194. Each wire lead was assigned a particular port on the CR1000 by the LoggerNet software, which was dedicated for the test program to that particular wire from a given instrument.

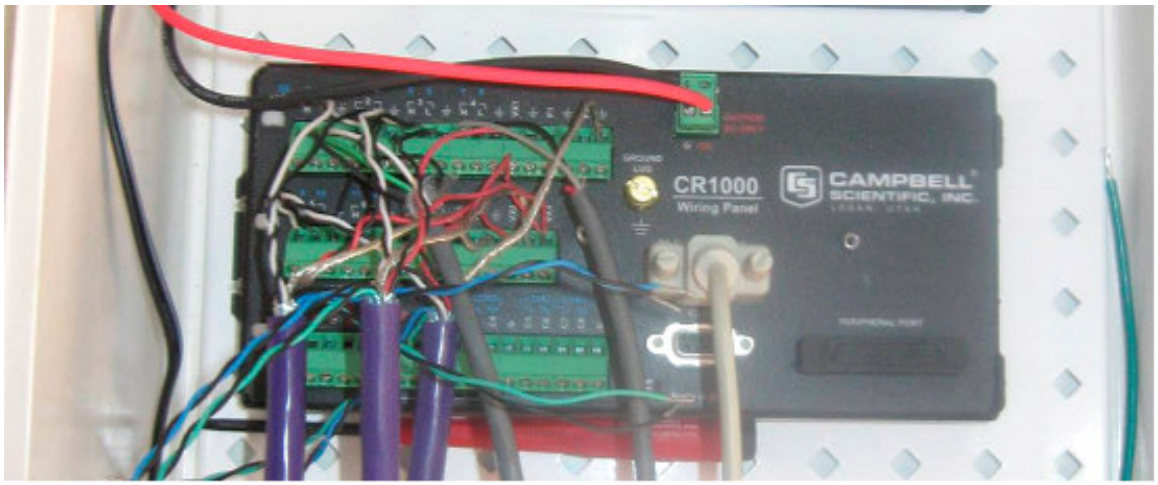

Figure 194. CR1000 wired to instrumentation

APPENDIX G

UPLIFT TEST EQUIPMENT

Instrumentation

For the uplift tests, several types of measurements/recordings were taken. The total vertical uplift load applied to the pipe by the crane was measured by a force-tension load cell. The displacement of the pipe as it moved upward through the cover was measured with linear displacement transducers. In addition, the vertical earth pressure within the backfill system was measured with pancake earth pressure cells.

The load cell used to measure the total uplift force was a Strainsert inline Tension Force Link. This type of force-tension load cell is also referred to as a shackle type load cell because it is placed in line with the load application of the crane cable and shackles. A picture of this load cell is shown in Figure 195. The Strainsert load cell is accurate to +/- 0.1% of its range with a working range of 712 kN in tension. The Strainsert cell connects to two clevises by a hole in its ends (Figure 196). Figure 197 shows the cell and shackles in line with the crane cable used for uplift. The electronics of the load cell are 4 resistors that are arranged in a Thevanin Bridge configuration. The displacement transducers used in the tests were Celesco Brand stringpot potentiometer displacement transducers. The stringpot potentiometers measure voltage potential change as a string is

Figure 195. Strainsert tension load cell and shackles

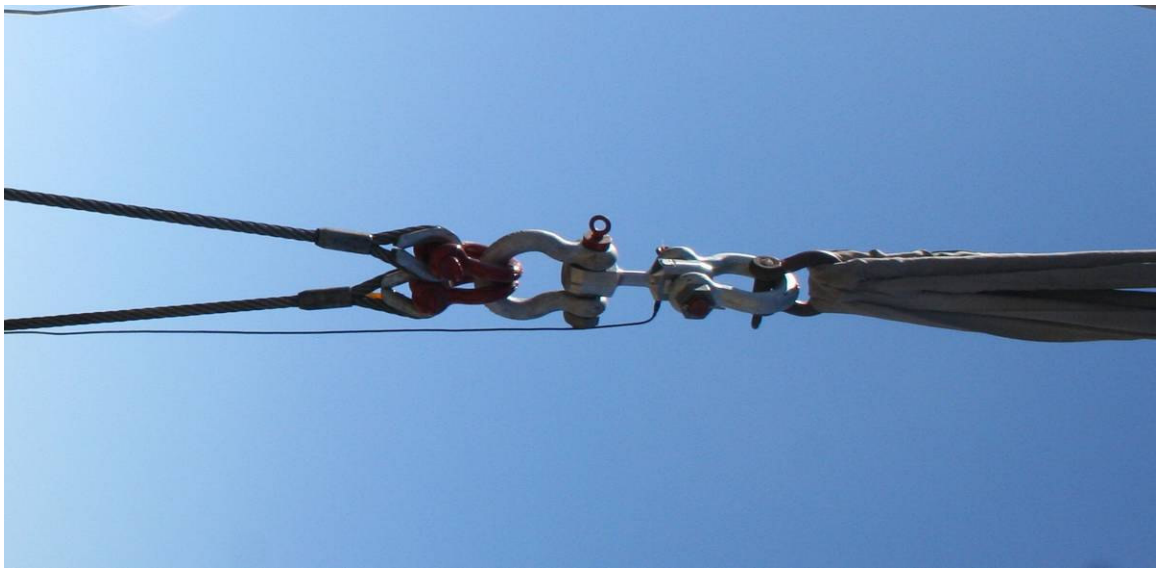

Figure 196. Strainsert tension load cell and crane cables

pulled out of the housing. The electronics are a 3 wire half bridge. These sensor measures have an accuracy of 0.25 mm.

The vertical earth pressure cells placed in the backfill of the trenches were measured with Geokon earth pressure cells. These cells were flat “pancake” cells that are less than a half an inch thick and 9 inches (229 mm) in diameter. Two types of Geokon series 4100 earth pressure cells were used: resistance-based and vibrating wire. The primary difference between these types is the manner of data acquisition. For the resistance-based cells, data acquisition is automatic and data sampling occurs on a subsecond basis. For the vibrating wire cells, data can only be gathered every 10 to 30 seconds. Both types of earth pressure cells were all rated to 1MPa.

Data Acquisition

The data from the instruments used in the tests were acquired, stored, and processed by a Campbell Scientific CR1000 data-logger and its LoggerNet software. The CR1000 is shown in Figure 198. The CR1000 is capable of measuring different types of electric signals at sampling rates of 100 hertz, or higher. These measurements include differential voltages, conditioned signals and single ended voltages (e.g., thermistors). The datalogger collects data according to a measurement schedule provided by the user on a PC communicating with the CR1000. The CR1000 stores the signals from each instrument for each sampling increment in its internal memory until called for by an external PC running the LoggerNet software.

The software displays the data in real time on graphs and tables on a PC or laptop, allowing the user to monitor all measurements as the test progresses. The CR1000 also

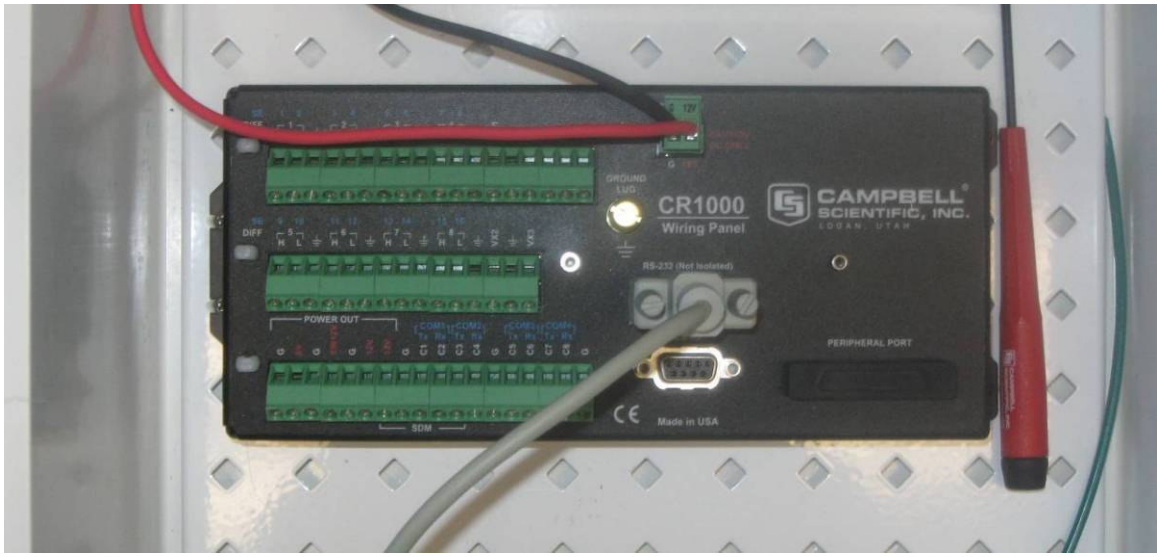

Figure 197. Campbell Scientific CR1000 Datalogger

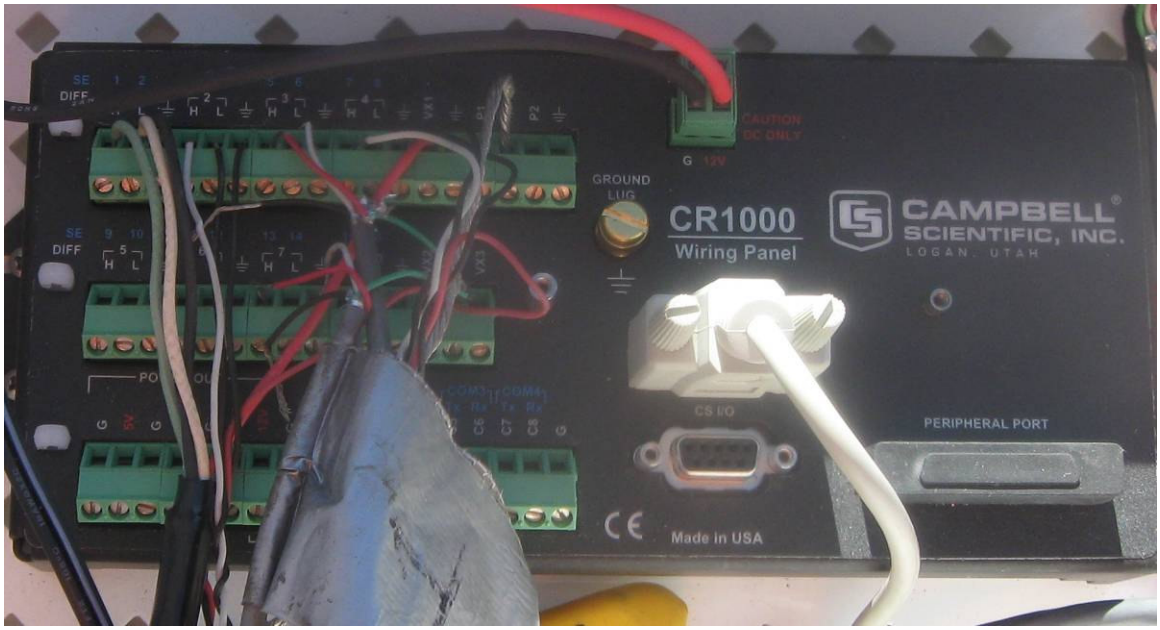

Figure 198. CR1000 with instrumentation attached

processes the raw voltage readings from the instruments into engineering units if desired. With calibration data for each instrument supplied by the user, the data can then be exported for engineering purposes. The calibrations for each instrument were conducted by the University of Utah in addition to the factory supplied calibrations. In addition, each instrument was recalibrated after the field testing to verify that the data were processed accurately.

The tension load cell and earth pressure cells were full-bridge circuits that returned a differential voltage; the stringpot displacement transducers were 3 wire half bridge configurations that also returned a differential voltage. The leads from each instrument were connected to the CR1000 directly. Each wire lead was assigned a particular port on the CR1000 by the LoggerNet software, which was dedicated for the test program to that particular wire from a given instrument. After testing, the data from the CR1000 datalogger were sent to the computer which was running the LoggerNet software. Two backup test files containing all the data were automatically made by LoggerNet. One of these backup files was immediately transferred to an independent data storage device as a secondary data backup.

APPENDIX H

FLAC STRAIN SOFTENING MATERIAL MODEL

The FLAC strain softening model is based on the Mohr-Coulomb model with non-associated shear and associated tension flow rules. The difference, however, lies in the possibility that the cohesion, friction, dilation and tensile strength may harden or soften after the onset of plastic yield (prior to yield, the properties of the material are constant and elastic). In the Mohr-Coulomb model, cohesion, friction, dilation and tensile strength are assumed to remain constant. In the strain softening constitutive model, the user can define the cohesion, friction and dilation as piecewise-linear functions of a hardening parameter measuring the plastic shear strain. A piecewise-linear softening law for the tensile strength can also be prescribed in terms of another hardening parameter measuring the plastic tensile strain. The FLAC FISH code measures the total plastic shear and tensile strains by incrementing the hardening parameters at each timestep and causes the model properties to change according to the user-defined parameters. The yield and potential functions, plastic flow rules and stress corrections are identical to those of the Mohr-Coulomb model. See Itasca (2005) for complete details on numerical implementation of the strain softening material model.

In the FLAC code, the friction, dilation, cohesion and tensile strengths are input in tables as functions of plastic strain. If the user desires, the properties may remain constant, just like in the Mohr-Coulomb material model, by defining the same properties

at a large range of plastic strains. In Chapter 10, tables show the properties used in FLAC models. The derivation of those properties from triaxial test results is contained in this appendix.

The theoretical basis of the strain softening model is shown in Figure 199. Figure 199 is a triaxial test stress:strain curve overlain by two lines. The solid line is a representation of the Mohr-Coulomb material model, while the dashed is a representation of the strain softening material model.

In Figure 199, the friction angle of the material has been decreased at 6.25% plastic strain. In the strain softening and Mohr-Coulomb material models in Figure 199, the onset of yield was at 7.25% total strain. The material was softened at 13.5% total strain, or 6.25% plastic strain (plastic strain is defined as the total strain minus the strain at which yield occurred).

In the FLAC strain-softening material model, reduction of friction or dilation produces a gradual reduction in strength, while a reduction of cohesion or tension produces a sudden decrease in strength.

The derivation of the properties for use in the strain softening model is not straight-forward (Itasca, 2005). The derivation has three steps. The first step is to conduct triaxial or other testing to define stress:strain curves at different stress levels. Mohr circles are then drawn for the failure state (onset of plastic flow), and at levels of plastic strain from the suite of stress:strain curves that show similar behavior at same amount of plastic strain. Once a set of Mohr circles is drawn, Mohr-Coulomb failure envelopes are drawn to determine the properties at the differing plastic strain levels. It is best to change the cohesive strengths as little as possible in the drawing of the Mohr-Coulomb failure

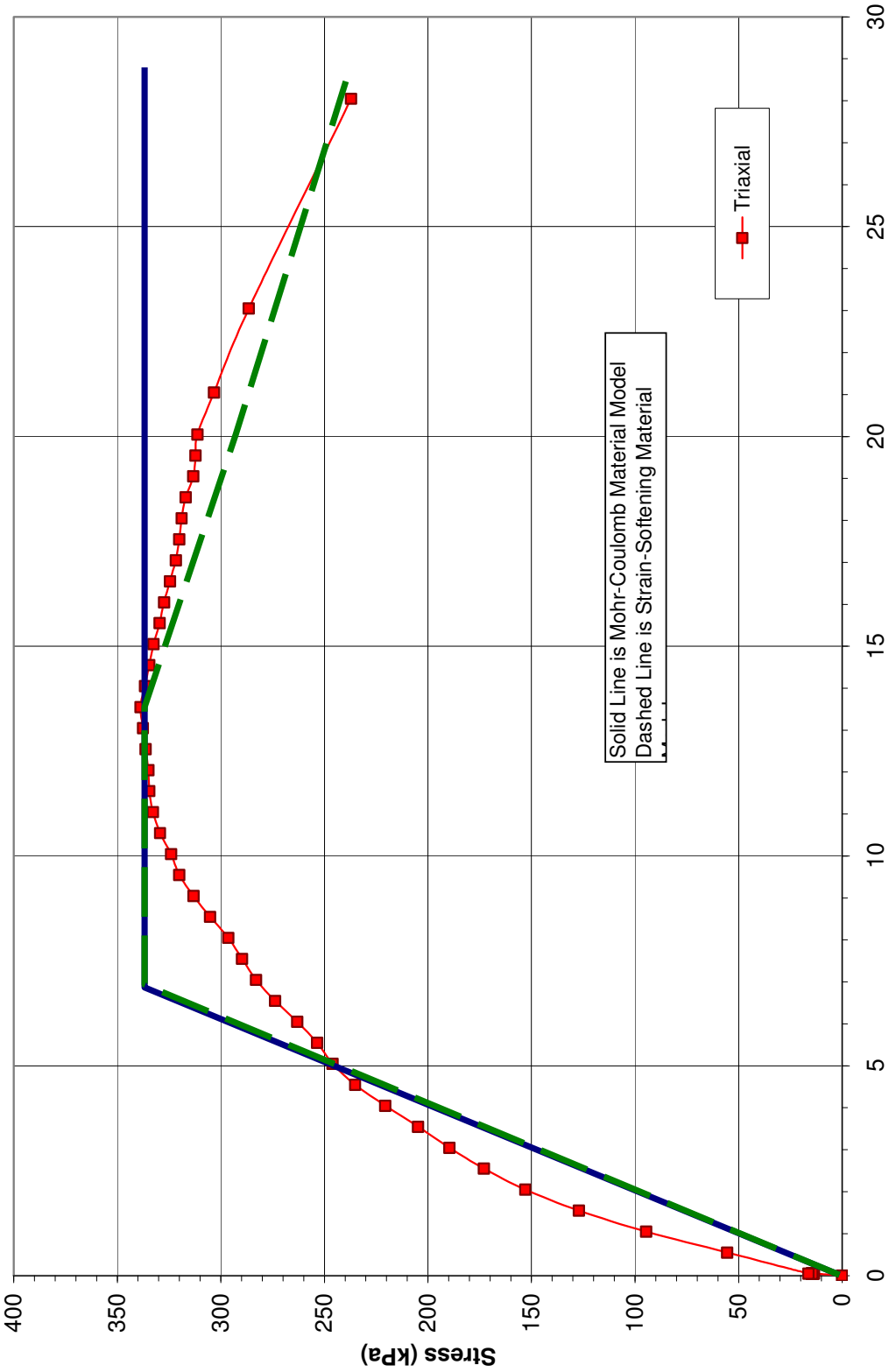

Figure 199. Conceptual strain softening model

envelopes as a change in cohesive or tensile strength is sudden in the FLAC implementation of the model. In the triaxial testing done in this project, no tension or tensile strength was directly measured. For numerical stability, tensile strengths one order of magnitude less than the cohesive strengths at a given plastic strain were chosen.

Figure 200 shows two triaxial test stress:strain curves (in terms of principle stress ratio) used in the derivation of strain-softening material properties for the native sand at the uplift test site. Plastic strains of 0%, 9% and 15% (12, 21 and 27% total strain) are chosen for Mohr circles. The Mohr circles for the three strain levels are shown in Figure 201. The confining stresses for the two tests, and all three strain levels, were held constant during testing. The effective confining stress for Test 1 was 77.8 kPa, while Test 2 had an effective confining stress of 143.6 kPa.

In Figure 201, the larger the circle, the smaller the plastic strain level. The solid circles and lines represent the strength at failure. The dashed lines are for 9% and 15% plastic strain, respectively. The friction angle at failure is 28 degrees, while the apparent cohesion is 35.9 kPa. At 9% plastic strain, the friction angle is 26 degrees, while the apparent cohesion is 36 kPa. At 15% plastic strain, the friction angle is 21 degrees, while the apparent cohesion is 35 kPa. Table 25 shows that these values were used in FLAC and FLAC3D modeling for the Native Sand.

Using the strain softening material model parameters in Table 25, simple FLAC models of the triaxial specimens were created and run in axial compression. The stress and strain across the block were tracked using FISH codes. This procedure was used to validate the model parameters against the actual testing.

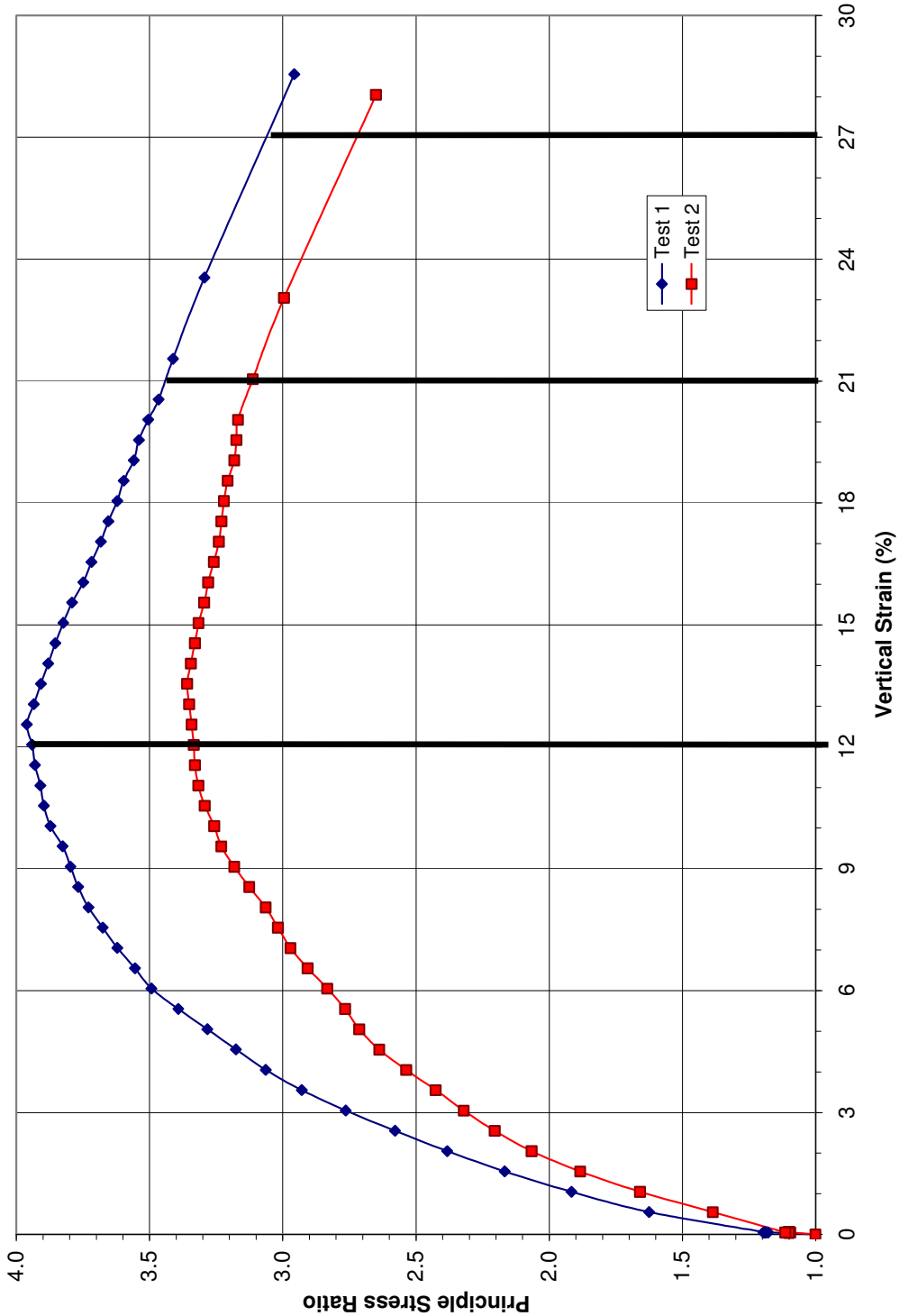

Figure 200. Stress:strain curve for strain softening model derivation

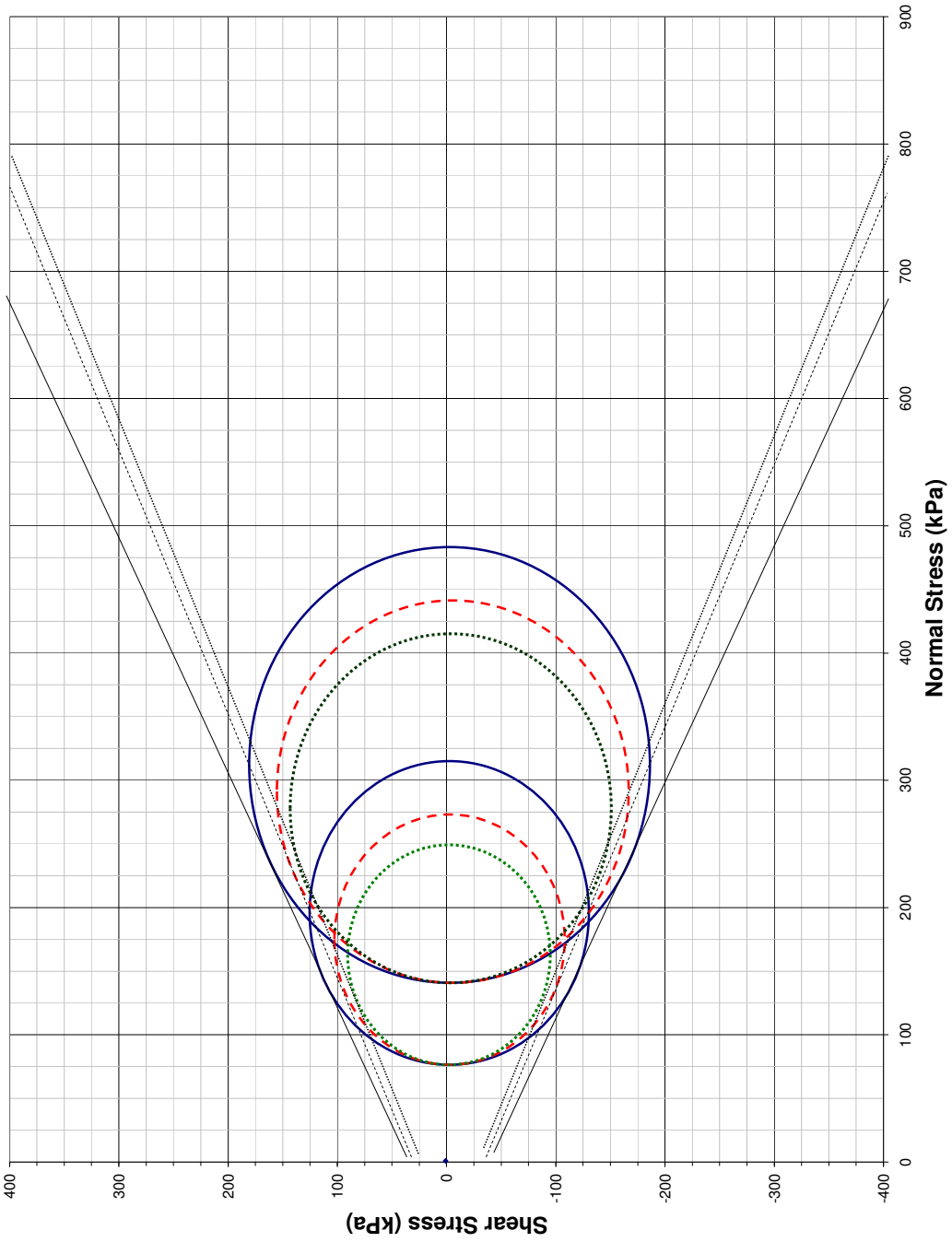

Figure 201. Mohr circles for strain softening derivation

Three FLAC models were produced, one for the native sand found at the uplift test site, one for the native clay, and one for the random clayey fill used in the uplift test. In the FLAC models, to assist in the fit of the curves, a nonlinear modulus function was used for the prefailure state. The nonlinear modulus function was from Duncan et al. (1980) and used the initial tangent modulus found from the laboratory testing. Figures 202 to 204 show the laboratory testing compared to FLAC models using the strain softening model. In Figure 202, the Mohr-Coulomb material model is also shown for comparison purposes. Note in Figure 204 that the Mohr-Coulomb material model run had constant stress at plastic strain compared to the strain softening model and the laboratory test data.

The modeling exercise shown in Figures 202 to 204 demonstrates for triaxial test models that the strain softening model in FLAC can reasonably match laboratory test data with numerical simulation with relative ease. This demonstration indicates that the strain softening model is acceptable for modeling of full scale uplift tests provided that detailed laboratory testing is available.

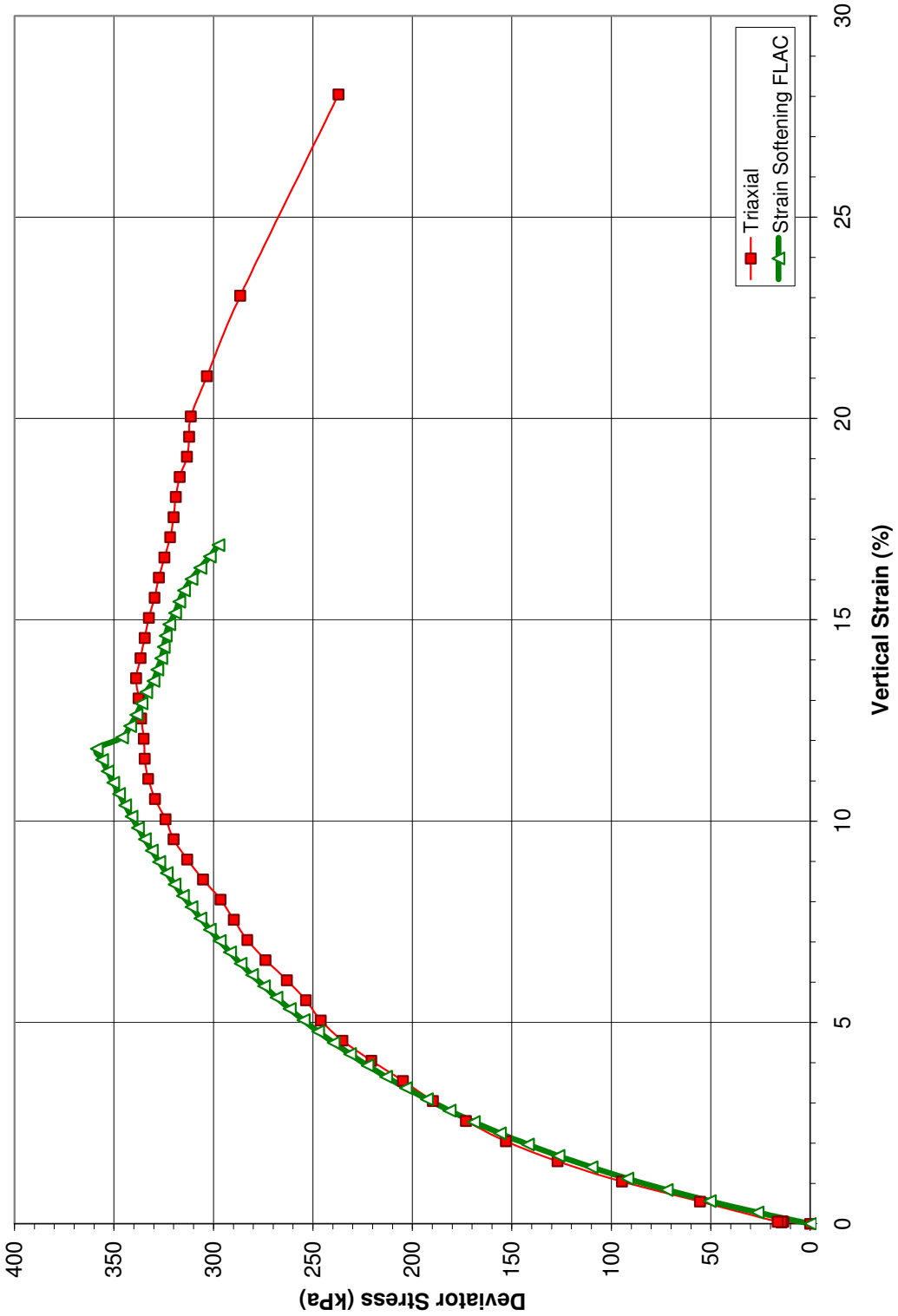

Figure 202. Native sand FLAC with strain softening model

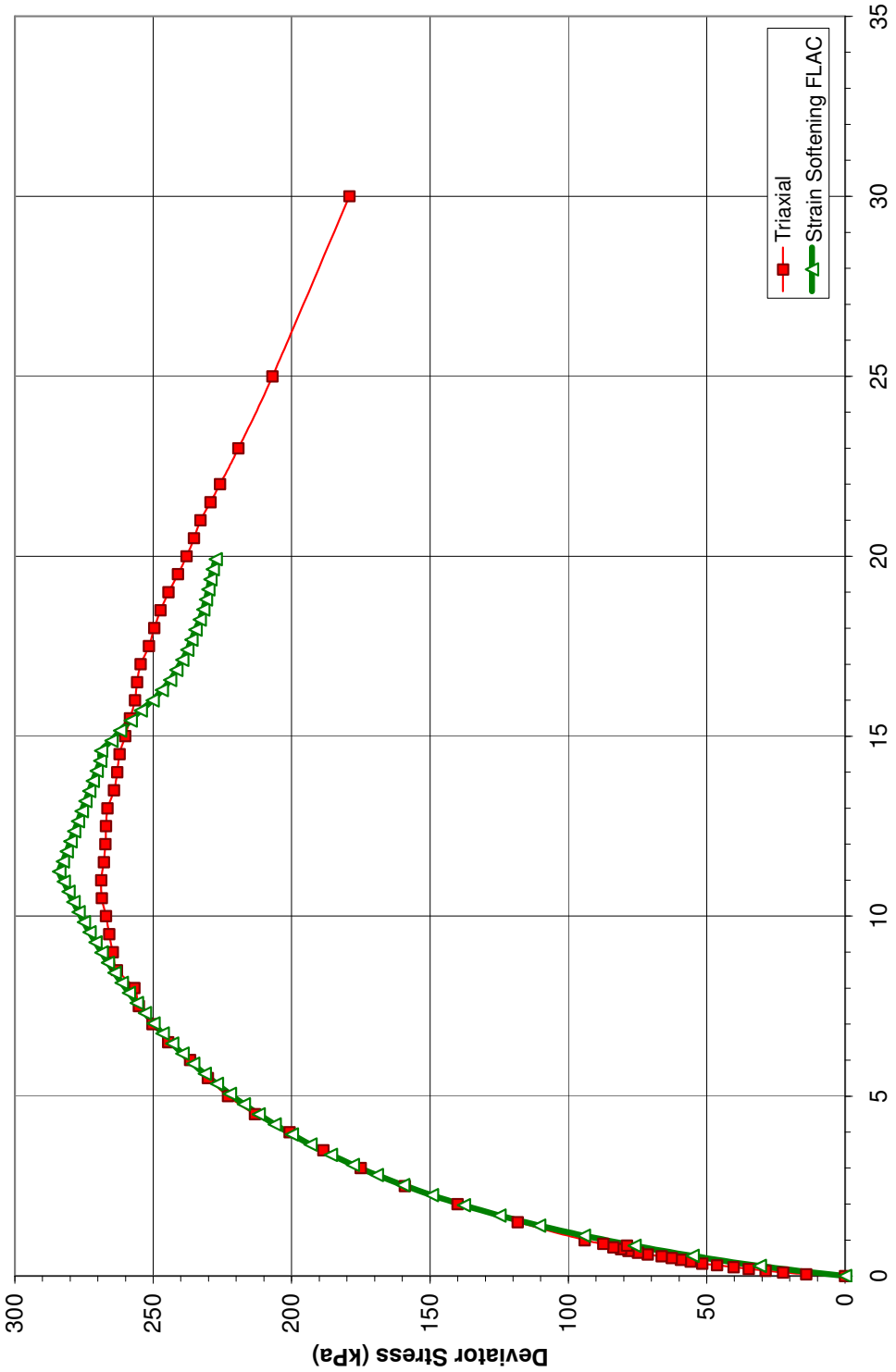

Figure 203. Native clay FLAC with strain softening model

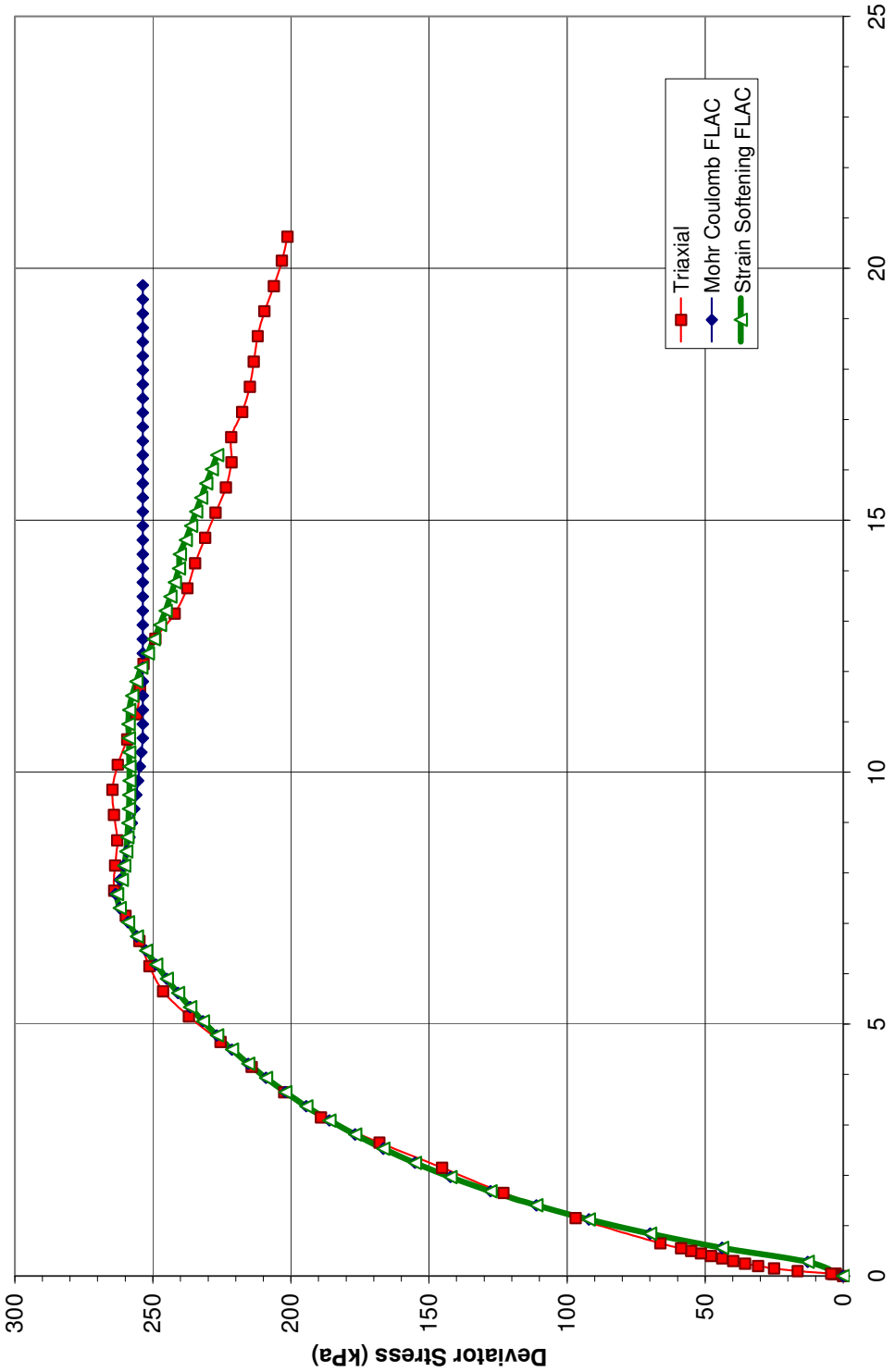

Figure 204. Clayey fill FLAC with strain softening model

APPENDIX I

FLAC BENCHMARKING RESULTS

All test data from Trautmann and O'Rourke (1984).

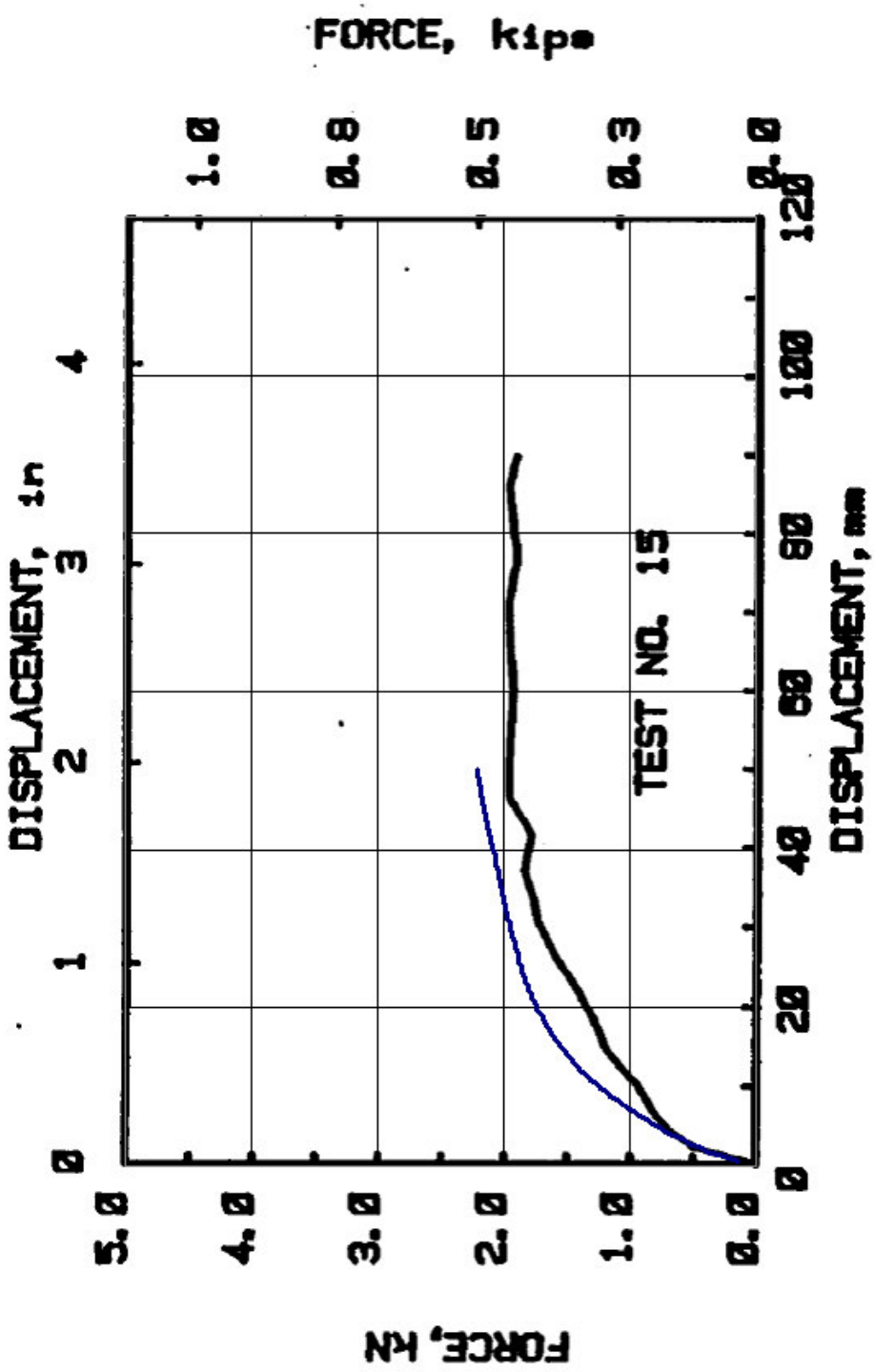

Figure 205. FLAC model 1 compared to test data

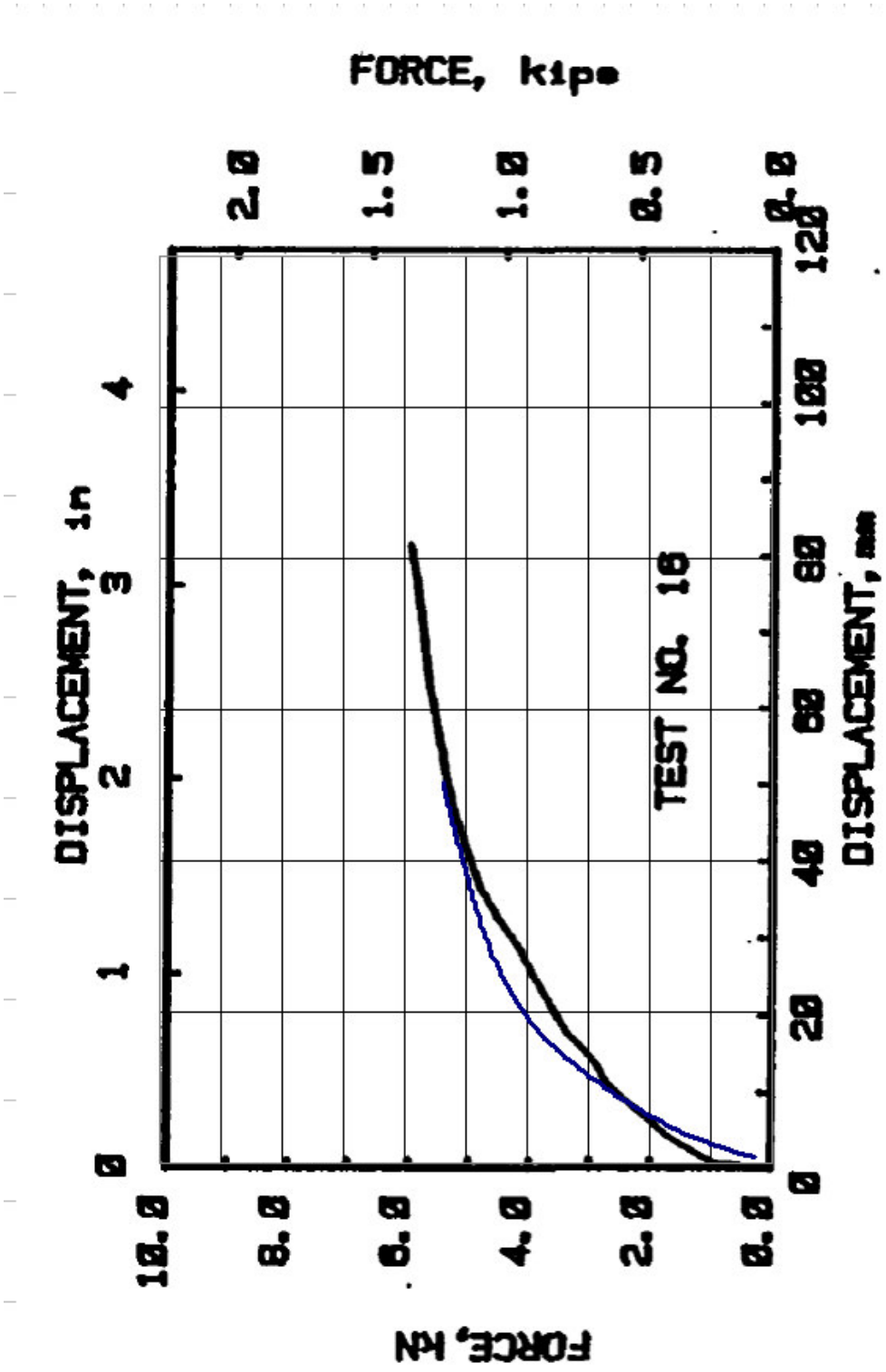

Figure 206. FLAC model 2 compared to test data

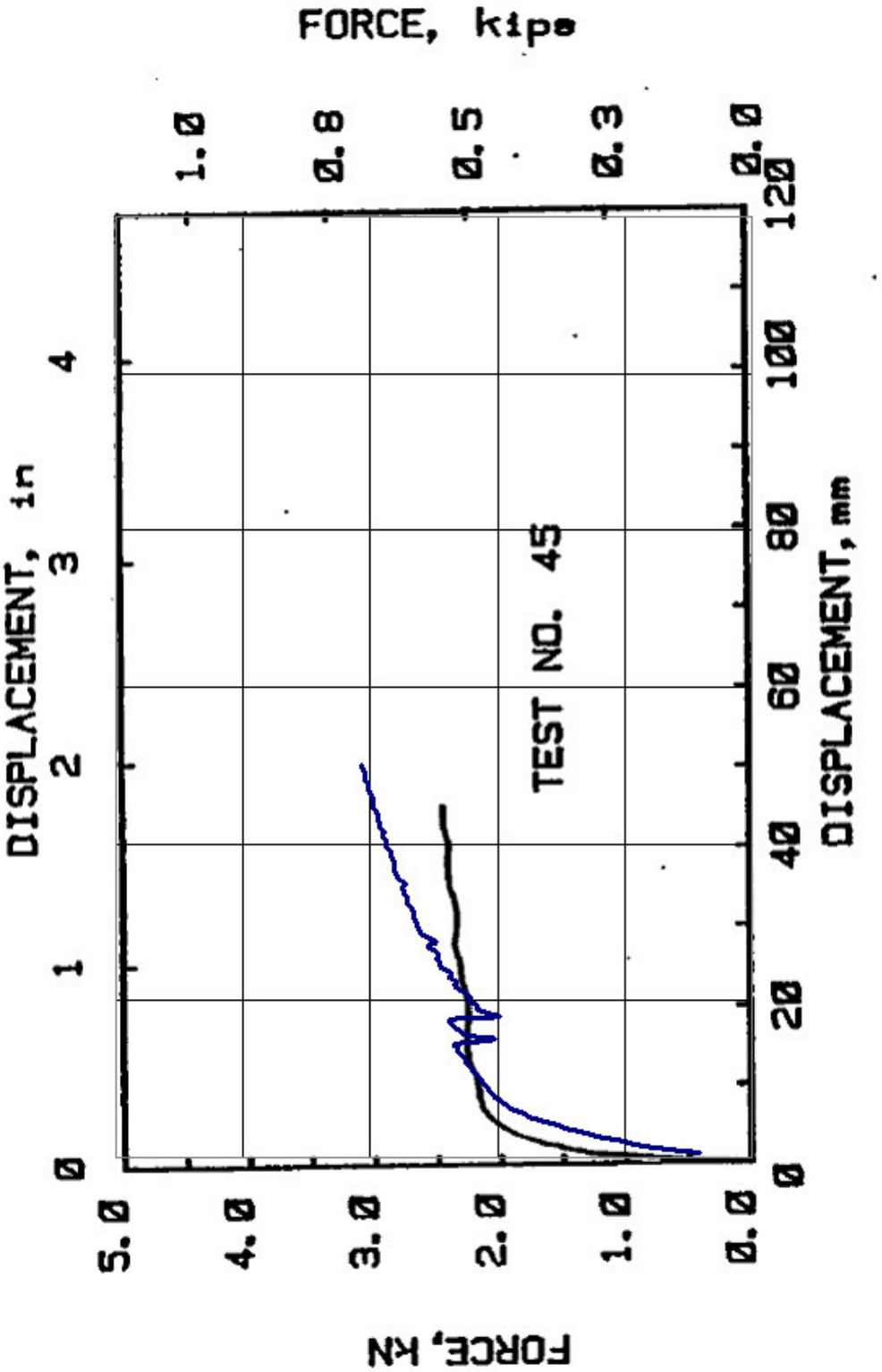

Figure 207. FLAC model 3 compared to test data

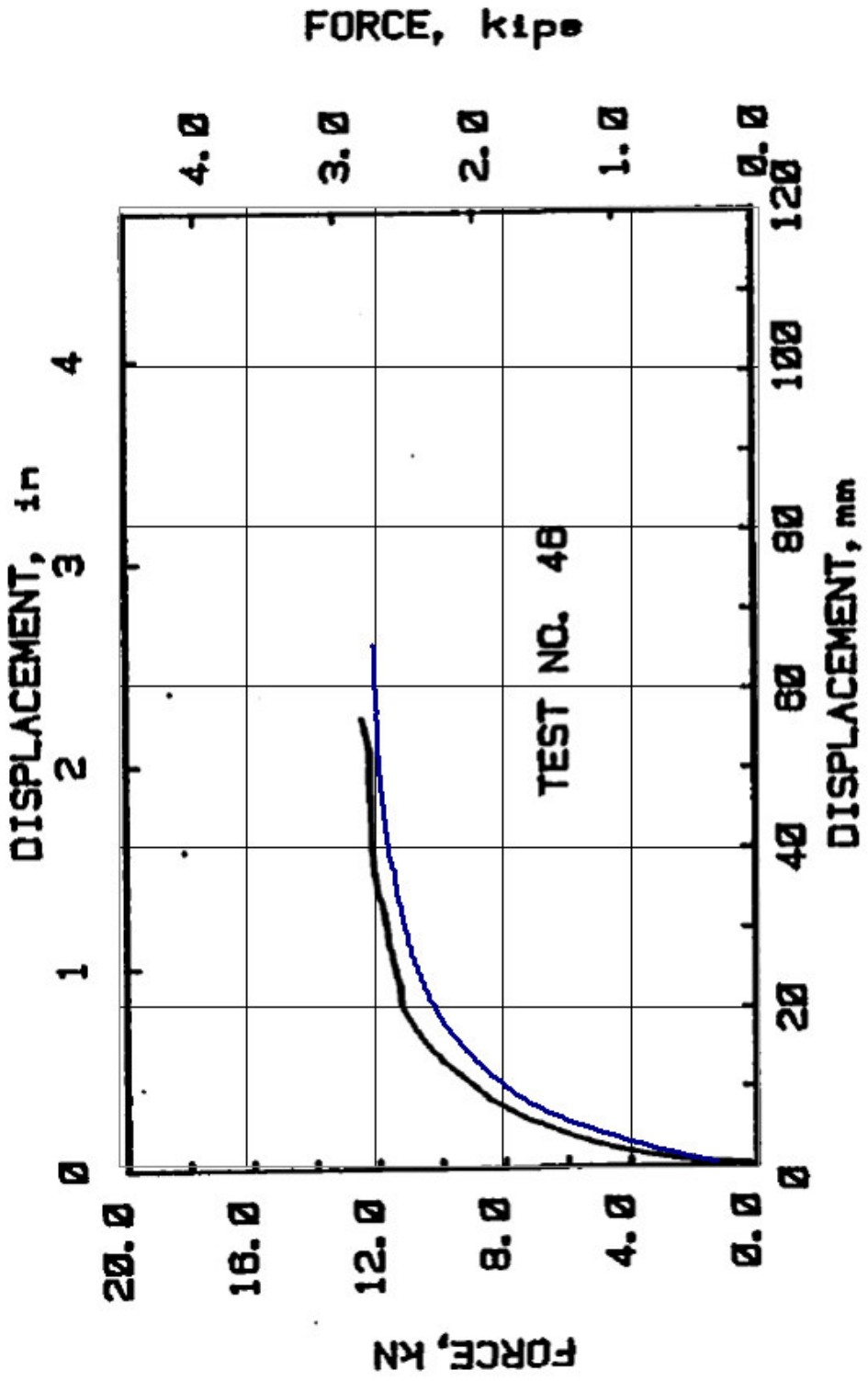

Figure 208. FLAC model 4 compared to test data

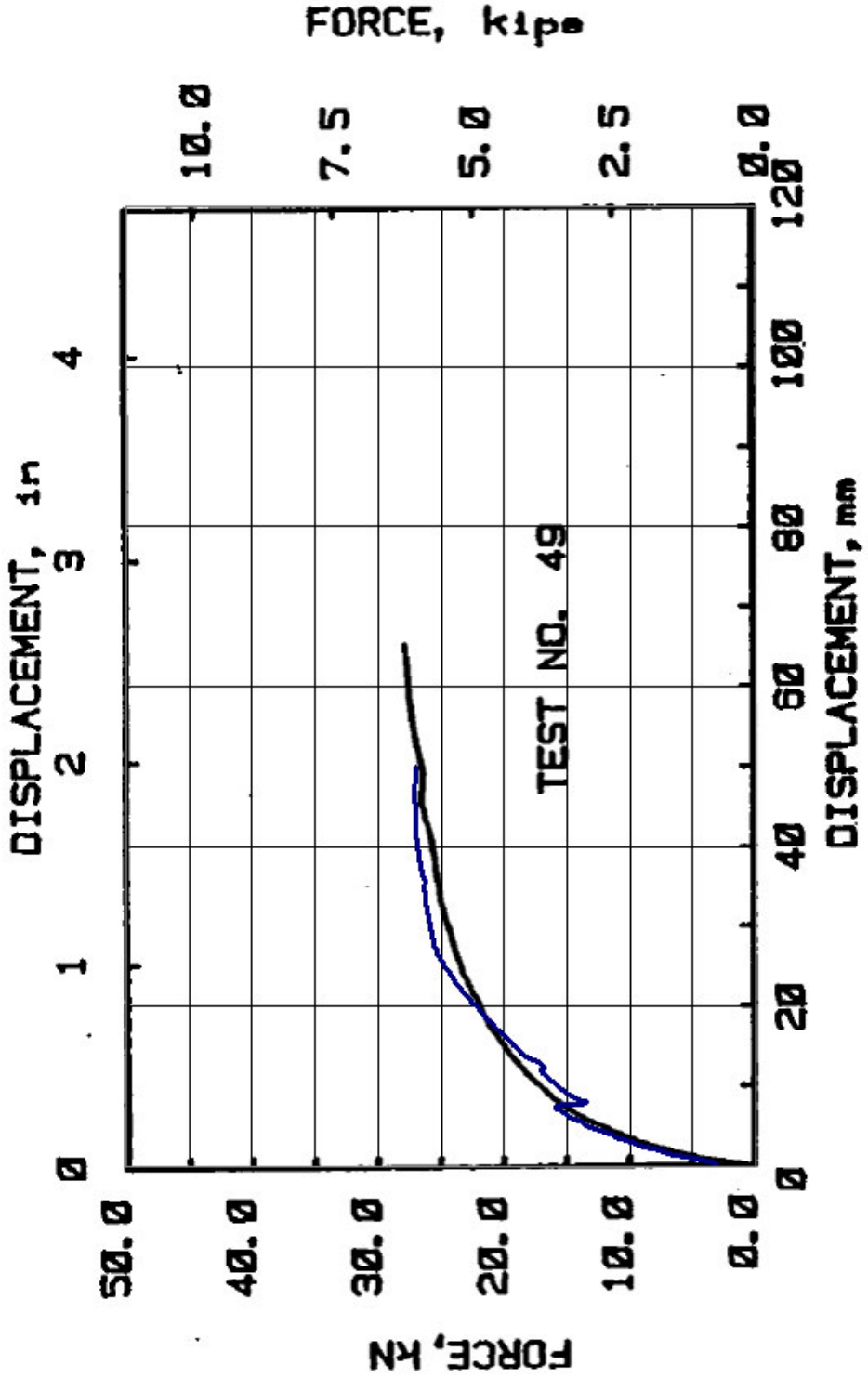

Figure 209. FLAC model 5 compared to test data

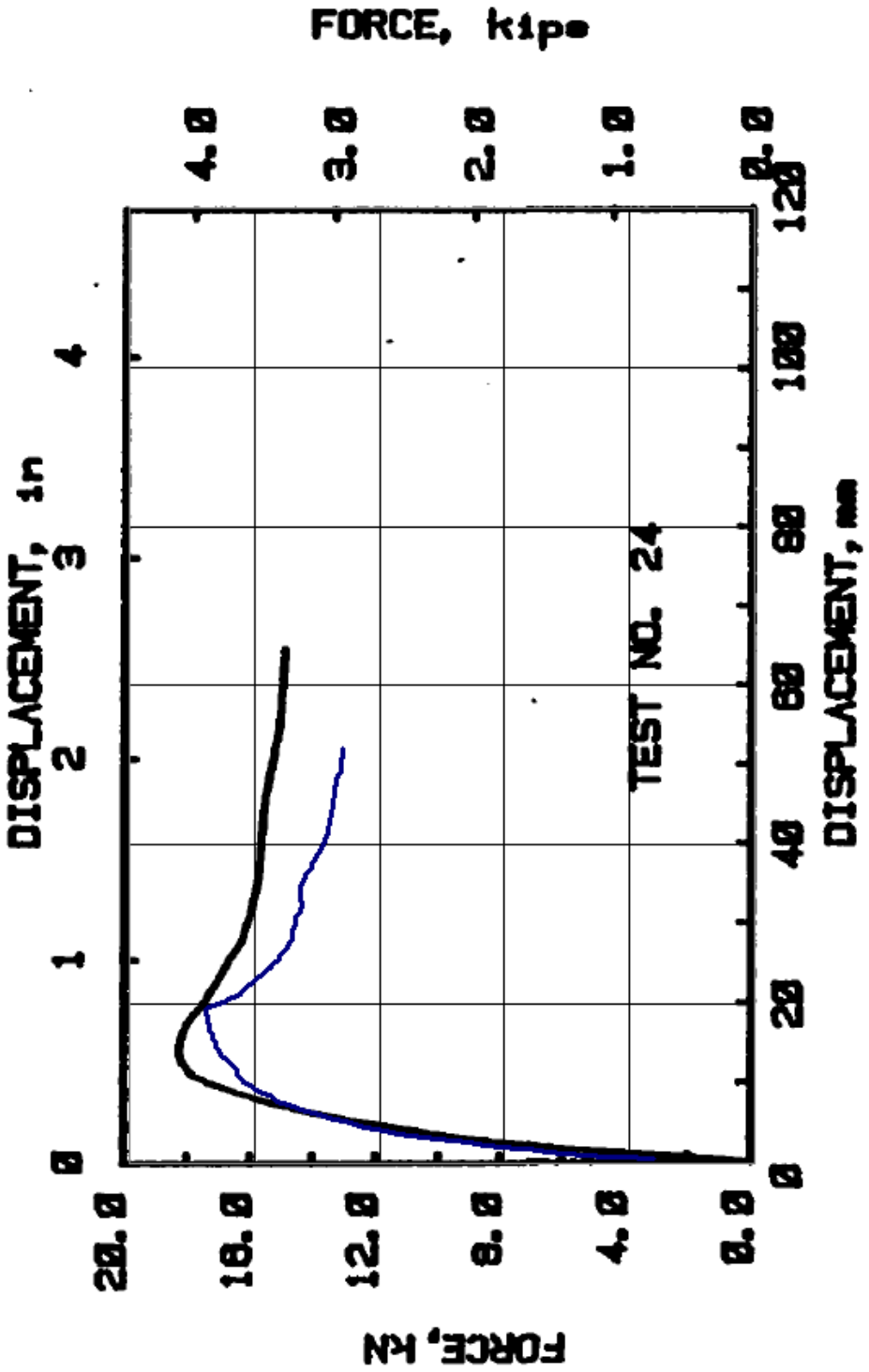

Figure 210. FLAC model 6 compared to test data

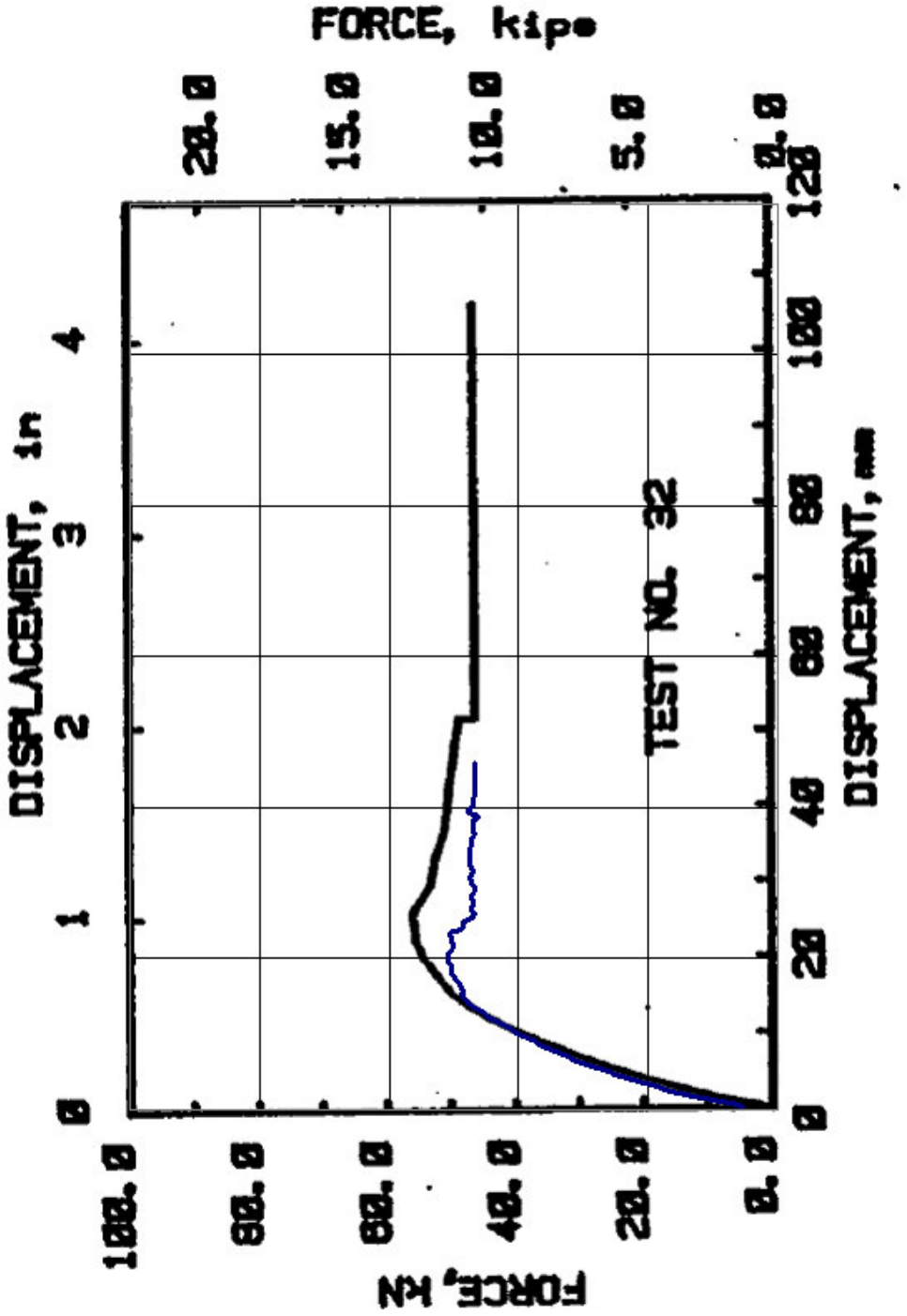

Figure 211. FLAC model 7 compared to test data

REFERENCES

American Lifeline Alliance, American Society of Civil Engineers (2005). *Guidelines for the Design of Buried Steel Pipelines*. ASCE Press, Reston, VA.

American Society of Civil Engineers (1984). *Guidelines for the Seismic Design of Oil and Gas Pipeline Systems*. Technical Council on Lifeline Engineering, Committee on Gas and Liquid Fuel Lifelines, ASCE Press, Reston, VA.

American Society for Testing and Materials (1994). *Test Method for Consolidated-Undrained Triaxial Compression Test on Cohesive Soils designation* D4767. ASTM Press, Reston, VA.

Ariman, T., and Lee, B.J. (1991). "On beam mode of buckling of buried pipelines," *Proceedings of the Second US-Japan Workshop on Liquefaction, Large Ground Deformations, and their Effects on Lifelines, Buffalo, New York, Technical Report NCEER-89-0032*, Multidisciplinary Council on Earthquake Engineering Research, Buffalo, New York, 401-412.

Athanasopoulos, G.A., Pelekis, P.C. and Xenaki, V.C. (1999). "Dynamic properties of EPS Geofoam: an experimental investigation." *Geosynthetics International*, 6(3), 171-194.

Bartlett, S.F., and Farnsworth, C. (2004). "Monitoring and modeling of innovative foundation treatment and embankment construction used on the I-15 reconstruction project, project management plan and instrument installation report." *Report No. UT-04.19,* Utah Department of Transportation Research Division, Salt Lake City, Utah.

Bartlett, S.F., Negussey, D., Kimble, M., and Sheeley, M. (2000). "Use of Geofoam as super-light-weight fill for I-15 reconstruction." *Transportation Research Board 79th Annual Meeting*, Federal Highway Administration, Washington, D.C, 40-47.

Bartlett, S.F., Farnsworth, C., Negussey, D., and Stuedlein, A.W. (2001). "Instrumentation and long-term monitoring of Geofoam embankments, I-15 reconstruction project, Salt Lake City, Utah." *Proceedings of the 3rd International EPS Geofoam Conference*, Salt Lake City, Utah.

Bathurst, R.J., Keshavarz, A., Zarnani, S., and Take, W.A. (2007). "A simple displacement model for response analysis of EPS Geofoam seismic buffers." *Soil Dynamics and Earthquake Engineering*, 27, 344–353.

Bathurst, R.J., Zarnani, S., and Gaskin, A. (2007). "Shaking table testing of Geofoam seismic buffers." *Soil Dynamics and Earthquake Engineering*, 27, 324–332.

Bishop, A.W., and Henkel, D.J (1957). *The Measurement of Soil Properties in the Triaxial Tests.* Edward Arnold Ltd., London, England.

Bishop, A.W., and Henkel, D.J (1962). *The Measurement of Soil Properties in the Triaxial Tests.* Edward Arnold Ltd., London, England.

Black, D.K., and Lee, K.L. (1973). "Saturating laboratory samples by back pressure." *Journal of Geotech. Engrg. Div.*, ASCE, 99(1), 75-93.

Cheuk, C.Y. White, D.J., and Bolton, M.D. (2005). "Deformation mechanisms during uplift of buried pipes in sand." *1st International Conference on Soil Mechanics and Geotechnical Engineering,* September 2005, Osaka, Japan, 1685-1688.

Chun, B.S., Lim, H., Sagong, M., and Kim, K. (2004). "Development of a hyperbolic constitutive model for expanded polystyrene (EPS) Geofoam under triaxial compression tests." *Geotextiles and Geomembranes,* 22 (2004), 223-237.

Choo Y.W., Abdoun, T.K., O'Rourke, M.J., and Ha, D. (2007). "Remediation for buried pipeline systems under permanent ground deformations." *Soil Dynamics and Earthquake Engineering,* 27 (2007), 1043-1055.

Clough, G.W., and Duncan, J.M. (1971). "Finite element analysis of retaining wall behavior." *Journal of Soil Mechanics and Foundations Division,* 97(12), 1657-1673.

Desmod, T.P., Power, M.S., Taylor, C.L., and Lau, R.W. (1995). "Behavior of large-diameter pipeline at fault crossings." *Technical Council on Lifeline Earthquake Engineering Nomograph 6*, ASCE TCLEE, Reston, VA, 296 –303.

Duncan, J.M., and Chang, C.Y. (1970). "Nonlinear analysis of stress and strain in soils." *Journal of Geotech. Engrg. Div.*, 96(5), 1629-1953.

Duncan, J.M., Bryne, P., Wong K.S., and Chang, C.Y. (1980). "Strength, stress-strain, and bulk modulus parameters for finite element analysis of soils." *Report UCB/GT/80-02*, University of California, Berkeley.

Duncan, J.M., and Mokwa, R.L. (2001). "Passive earth pressures: theories and tests." *Journal of Geotechnical and Geoenvironmental Engineering, ASCE*, (127)3, 248-257.

Duskov, M. (1997). " EPS as a light-weight sub-base material in pavement structures," thesis, presented to Delft University of Technology of The Netherlands, in partial fulfillment of the requirements for the degree of Doctor of Philosophy.

El-Aziz, A., and Zahw, M. A., (1999). “Influence of temperature on the mechanical properties of hot mix asphalt concrete mixes.” *Annual Conference of the Canadian Society for Civil Engineering*, Regina, Saskatchewan, 91-100.

El-Naby, R.M. A., El-Aleem, A.M. A., and Saber, S. H., (2002). “Evaluation of the shear strength of asphalt concrete mixes: experimental investigation.” *Annual Conference of the Canadian Society for Civil Engineering*, Montreal, Quebec, 1-9.

Farnsworth C. F., Bartlett S.F., Negussey, D., and Stuedlein, A. (2008). “Construction and post-construction settlement performance of innovative embankment systems, I-15 reconstruction project, Salt Lake City, Utah.” *Journal of Geotechnical and Environmental Engineering*, 134(2), 289-301.

Federal Emergency Management Agency (1991). *Siesmic Vulnerability and Impact on Disruption of Lifelines in the Conterminous United States*. Applied Technology Council, ATC-25, FEMA 224, Washington, D.C.

Geocomp Corporation, (2006). *Triaxial User’s Manual*. Geocomp Corporation, Boxborough, Mass.

Gomez, J.E., Filz, G.M., and Ebeling, R.M. (2003). “Extended hyperbolic model for sand-to-concrete interfaces.” *Journal of Geotechnical and Geoenvironmental Engineering*, 129(11), 993-1000.

Goetz, W. H., and Chen, C. C. (1950). “Properties of hot-mix asphalt.” *Proceedings of the Association of Paving Technologists*, 19(55), 40-47.

Hazarika, H. (2006). “Stress-Strain modeling of EPS Geofoam for large strain applications.” *Geotextiles and Geomembranes*, 24(2006), 79-90.

Hills, J. F., and Heukelom, W., (1969). “Modulus and Poisson Ratio of asphalt mixes.” *Journal of the Institute of Petroleum*, 55(541), 27-35.

Holtz, R.D., and Kovacs W.D. (1981). *An Introduction to Geotechnical Engineering.* Prentice Hall, Upper Saddle, New Jersey.

Horvath, J. S. (1991). "Using geosynthetics to reduce earth loads on rigid retaining structures." *Geosynthetics '91*, Industrial Fabrics Association International, St. Paul, MN, 409-424.

Horvath, J.S. (1995). *Geofoam Geosynthetic*. Horvath Engineering, New York, USA.

Horvath, J.S., (2005). “Expanding the use of EPS Geofoam in Practice.” *Boston Society of Civil Engineers Section/American Society of Civil Engineers Geo-Institute 2005 Geotechnical Engineering Seminar,* ASCE, Waltham, MA, 7-80.

Itasca Consulting Group, Inc. (2005). *FLAC: Fast Lagrangian Analysis of Continua: User's Guide*. ITASCA, Minneapolis, Minnesota.

Itasca Consulting Group, Inc. (2005). *FLAC3D: Fast Lagrangian Analysis of Continua in 3 Dimensions: User's Guide*. ITASCA, Minneapolis, Minnesota.

Jaky, J., (1944). "The coefficeint of earth pressure at rest." *J. Society of Hungarian Architects and Engineers*, October, Budapest, Hungary, 335-358.

Karamitros, D.K., Bouckovalas, G.D., and Kouretzis, G.P. (2007). "Stress analysis of buried steel pipelines at strike-slip fault crossings." *Soil Dynamics and Earthquake Engineering*, (27), 200-211.

Kennedy, R.P., Darrow, A.C., Short SA. (1979). "Seismic design of oil pipe systems." *Journal of Technical Councils of ASCE*, 105(TCI), 119–134.

Kennedy, R.P., and Kincaid, R.H. (1983). "Fault crossing design for buried gas oil pipelines." *ASME PVP*, 77(1)**,** 1–9.

Kondner, R. L. (1963). "Hyperbolic stress-strain response: Cohesive soils." *J. Soil Mech. and Found. Div.*, 98(1), 115–143.

Li, B., Wu, S.P., Cheng, Q.P., and Lui, Q. T., (2008). "Investigation of mechanical properties of conductive asphalt mixtures using indirect tensile test." *2nd International Conference on Heterogeneous Material Mechanics*, Chinese Institute of Engineering, Huangshan, China, 1250-1253.

Matsubara, K., and Hoshiya, M. (2000). "Soil spring constants of buried pipelines for seismic design." *Journal of Engineering Mechanics*, 126(1), 46-64.

Multidisciplinary Council on Earthquake Engineering Research (MCEER), (1999). *Response of Buried Pipelines Subject to Earthquake Effects, Monography No. 3*, MCEER Buffalo, NY.

Meyersohn, W.D. (1991). "Analytical and design considerations for the seismic response of buried pipelines." thesis, presented to Cornell University, NY, in partial fulfillment of the requirements for the degree of Doctor of Philosophy.

Negussey, D. (2006). "Design parameters for EPS Geofoam." *Soils and Foundations*, 47, 161-170.

Negussey, D., and Huang, X. (2006). "Modulus of subgrade reaction for EPS Geofoam." *Proceedings of ASCE GeoShanghai*, Shanghai, China,165-172.

Negussey, D., Stuedlin, A. W., Bartlett, S. F., and Farnsworth, C.F. (2001). "Performance of Geofoam embankment at 100 South, I-15 reconstruction project, Salt Lake City, Utah." *EPS Geofoam 2001, 3rd International Conference*, Salt Lake City, Utah, 229-301.

Negussey, D. and Studlein, A. (2003). "Geofoam fill performance monitoring." *Utah Department of Transportation Research Division Report No. UT-03.17*. Utah Department of Transportation, Salt Lake City, UT.

Negussey, D. and Sun, M.C. (1996). "Reducing lateral pressure by Geofoam (EPS) Substitution." *Proceedings of the 2nd International Conference on EPS*, Tokyo, Japan, 201-211.

Newmark, N.M., and Hall, W.J. (1975). "Pipeline design to resist large fault displacement." *Proceedings of U.S. National Conference on Earthquake Engineering*, Ann Arbor, MI, 416–425.

Patros, A.M. and Kazawinsky, P.M. (1987). "Geoboard reduces lateral earth pressures." *Geosynthetic '87,* Geosynthetics International, New Orleans, LA, 325-337.

Pellinen, P. K., and Xiao, S. (2005). "Relationship between triaxial shear strength and indirect tensile strength of hot mix asphalt." *Asphalt Paving Technology*, 74, 347-379.

Santaga, M., Germaine, J.T., and Ladd, C.C. (2007). "Small-strain nonlinearity of normally consolidated clay." *Journal of Geotechnical and Geoenvironmental Engineering.* 133(1), 72-82.

Santaga, M., and Germaine, J.T. (2002). "Sampling disturbance effects in normally consolidated clays." *Journal of Geotechnical and Geoenvironmental Engineering.* 128(12), 997-1006.

Skempton, A.W. (1954). "The pore pressure coefficients A and B." *Geotechnique*, 4(3), 143-147.

Skempton, A.W., and Bjerrum, L. (1957). "A contribution to the settlement analysis of clays." *Geotechnique*, 7(4), 168-178.

Sheeley, M., and Negussey, D. (2000). "An investigation of Geofoam interface strength behavior." *Proceedings of the Soft Ground Technology Conference*, ASCE Geotechnical Special Publication 112, Delph, Netherlands, 292-303.

Takada, S., Hassani, N., and Fukuda, K. (2001). "A new proposal for simplified design of buried steel pipes crossing active faults." *Earthquake Engng Struct. Dyn*., 30, 1243–1257.

Trautmann, C.H., and O'Rourke, T.D. (1984). "Lateral force-displacement response of buried pipes." *Journal of Geotechnical Engineering,* 111(9), 1077-1092.

Trautmann, C.H., and O'Rourke, T.D. (1984). "Uplift of buried pipes." *Journal of Geotechnical Engineering,* 111(9), 1061-1076.

Vougioukas, E.A., Theodossis, C., and Carydis, P.G. (1979). "Seismic analysis of buried pipelines subjected to vertical fault movement." *Journal of Technical Councils of ASCE* 1979, 105(TCI), 432–441.

Xenaki, V.C. and Athanasopoulos, G.A., (2001). "Experimental investigation of the interaction mechanism at the EPS Geofoam-sand interface by direct shear testing." *Geosynthetics International*, 8(6), 471-499.

Wang, L.L.R., and Wang, L.J. (1995). "Parametric study of buried pipelines due to large fault movement." *Technical Council on Lifeline Earthquake Engineering Nomograph 6*, ASCE TCLEE, Reston, VA,152–159.

Wang, H., Lui, X., and Hao, P. (2008). "Evaluation of the shear resistance of hot mix asphalt by the direct shear test." *Journal of Testing and Evaluation*, 36(6), 485-492.

Winkler, E. (1867). *Die lehre von elastizität und festigkeit*, H. Dominicus, Prague.

Yoshizaka, K., and Sakanoue, T. (2003). "Experimental study on soil-pipeline interaction using EPS backfill." *Pipelines 2003*, ASCE, Baltimore, MD, 1126-1134.

Zou, Y., Small, J.C., and Leo, C.J. (2000). "Behavior of EPS Geofoam as flexible pavement subgrade material in model tests." *Geosynthetics International*, 7(1), 1-22.